UCLouvain
Institute for Information
and Communication Technologies,
Electronics and Applied Mathematics

Exploring relevant properties of superparamagnetic nanoferrites towards inductive sensing

Margo HAUWAERT

Thesis submitted in partial fulfillment
of the requirements for the degree of
Docteur en sciences de l'ingénieur et technologie

Dissertation committee:

Prof. Jean-Pierre RASKIN	*supervisor*	UCLouvain, Belgium
Prof. Laurent FRANCIS	*chairperson*	UCLouvain, Belgium
Prof. Denis FLANDRE	*secretary*	UCLouvain, Belgium
Prof. Sophie HERMANS		UCLouvain, Belgium
Prof. Luc DUPRÉ		UGent, Belgium
Dr. Simo SPASSOV		KMI/IRM, Belgium
Prof. Montserrat RIVAS		Universidad de Oviedo, Spain

The 10th of June 2026

This template is powered by LaTeX and was created by Pierre-Yves Gousenbourger (2020).
© Margo HAUWAERT, UCLouvain (2026), all rights reserved.

Hun toegewijde handen,
Leurs coeurs en couleurs,
To my grandparents

Declarations

Originality

I hereby declare that this thesis is the result of my own original work. It has not been submitted, in whole or in part, for any other degree or diploma at this or any other institution. All sources and contributions have been properly acknowledged.

Funding

This research was made possible by a FRIA grant from the Fonds de la Recherche Scientifique (F.R.S.-FNRS). Additional funding for mobility was granted by Erasmus+ and Wallonie-Bruxelles International.

Use of AI-assisted tools

Portions of this manuscript were written with the assistance of large language models : Claude Opus 4.6 (Anthropic) and Gemini 2.5 (Google). These tools were used for writing assistance only. The scientific content, analysis, and conclusions remain entirely the responsibility of the author.

Acknowledgments

This thesis would have been impossible without my promotor Jean-Pierre Raskin who I wish to thank for his trust, for opening doors, for his encouragement and insights. My sincerest gratitude towards my thesis jury: Denis Flandre, Sophie Hermans, Simo Spassov, Luc Dupré, Montserrat Rivas as well as to Sébastien Toussaint who was in the accompanying committee of this work. Their feedback and advice have strongly contributed to my learning curve. Genuine recognition to the president of the jury, Laurent Francis, for taking his role to heart.

Nanoparticle synthesis by thermal decomposition was entirely done in the IMCN-MOST lab led by Sophie Hermans. I was fortunate enough to be accompanied by Sophie and Louise Lejeune: their patience and involvement have been a backbone from the very first day of my work. Special thanks to Jean-François Statsyns for his good spirits and to Alessia Tonelli and Fabien Drault for careful and numerous TEM imaging.

I was warmly welcomed in the applied physics lab of the Universidad de Oviedo, led by Montserrat Rivas and Jose-Carlos Martinez-Garcia. Especially for you, some montserrat fonts are hidden in this manuscript. Hats off to Vanessa Pilati, Maria Salvador, Leyre Fraille, Jose-Luis Marques-Fernandez and Mona Fadel: "Si necesitas algo, me dices" is one of the first sentences I learned because I heard it so often, applied to both their unvaluable knowhow and uncountable coffees (can I finally confess I never drank any before arriving?).

Many magnetic measurements were performed in collaboration with IRM-KMI in Dourbes: I cannot thank Simo Spassov enough for his work, open mind, dedication and talent.

Heartfelt gratefulness for Ron Goldfarb who generously shared time and knowledge. For Yves Gossuin who welcomed me at UMons and guided me through his equipment. Luc Piraux and Tristan Da Camara who performed valuable AGFM measurements.

Without logistical, technical and administrative support, PhD students are nothing more than limbless lambs. I am grateful for the reliable and strong support of

Souley Djadjandi, Benoit Hubert, Christel Derzelle, Anne Gillet, Pascal Simon, Simon De Jaeger, Pierre Eloy, Isabelle Dargent, Emilie Brichart, Nicolas André and Nathalie Ponet.

A big thanks to my colleagues Sébastien Toussaint, Grégoire Le Brun, Sami Yunus, Martin Lefebvre, Nicolas Roisin, Fares Tounsi, Charles Wiame, Pieter Cardinael, Brieuc Pinon and Noémie Bidoul for their guidance, critical questions and genious insights. To Thibault Pirson, Arash Masrouri, Louis Golard, Clara Whyte, Antoine Laterre, Aurélia Hernandez, Eléonore Masarweh, Clémentine Geevers and Oriane de Leuze for stimulating discussions. And last but not least to all the co-inhabitants that have come and gone in our "free electrons" office: Ramy, Rose, Brock, Alex, Ju, Rom, Greg, Rik and Rafael. Ramy and Nordin deserve a special mention for helping out with "les aléas" literally day and night.

Ignace Adant for always putting students forward and going crescendo when colouring outside the lines. Stephanie Merle for questioning the bigger picture, beyond "la pate droite du transistor". The AILouvain team for painting the vast horizon of engineering. The folks of "Ingés en Transition": it was a pleasure cocreating an emulsion of challenging thoughts and beautiful people.

"Chapeau bas" for Nordin Trifiro, François Clinquart, Eléonore Terryn, Amélia Moore, Alexandre Loffet and Richard Ekoue with whom collaborating was both pleasant and enriching. Séverin Berthet has been the most dedicated volunteering scrum-master and deserves a medal (that sparkles).

It is a privilege to have friends that give you wings and prevent you from flying too close to the sun: Ornella, Miguel, Camille, Emeline, Célia. OLG De Keimelschieters for navigating through the landscape of "My mate does a pee aadj dee". Sjoe, Dorien and Abuela with skills ranging from dinosaurs, over sewing, to singing. Daan and Emily whose citizenship is inspiring. Lise and Hanne, my favourite walking club.

My roommates for supplying daily sunshine despite belgian weather. Lidia, Laurent, Martin, Anne and Pancho for their open doors. The home at Montald: Vincent and Sophie the leading sparrows. Elise, Célestine and Léonor the blossoms.

My parents for paving the way and shaping my values. My grandparents for the rich roots they have watered carefully. My dear brother, both a pillar and my yang ever since he stole my only-child ying. Nathan, Jos, Sue and Aida for the beautiful songs added to the forest.

Seb, the rock on which I cannot only build, but also grow.

Abstract

Lateral flow assays (LFA) provide rapid point-of-care diagnostics, but their standard colourimetric readout with gold nanoparticle labels is only semi-quantitative. Replacing these labels with superparamagnetic nanoferrites (SPNF) and reading the strip with magnetic sensors enables quantification that is insensitive to the optical and electrochemical variability of biological matrices. Leveraging these advantages requires understanding how SPNF composition, size, coating, substrate and measurement conditions jointly determine the effective magnetic properties. This thesis investigates Fe_3O_4, $MnFe_2O_4$ and $CoFe_2O_4$ nanoparticles from synthesis to inductive detection. Their magnetic properties are characterised from DC to the GHz range, and from 2 K to 300 K. Studied configurations are compacted powder, cellulose membranes and aqueous suspensions. A combined Debye fitting procedure applied simultaneously to mobile and immobilised suspensions separates the Néel and Brownian relaxation contributions, resolving the effective anisotropy–diameter degeneracy that limits single-configuration analysis. Inductive detection is demonstrated with affordable and portable sensors.

Four main findings emerge. First, SPNF dispersed in membranes exhibit initial susceptibilities three to four times higher than in powder, attributed to reduced interactions; characterisation in a configuration representative of the final application is therefore necessary to avoid underestimating the available signal. Second, manganese ferrite consistently yields higher susceptibility than iron oxide across all methods and configurations, a consequence of its lower magnetocrystalline anisotropy. Third, drying nanoparticle-loaded membranes under a 500 mT static field improves the inductive signal by 8 to 16 %, by pre-aligning the easy axes of the nanoparticles with the sensing field before immobilisation upon evaporation; the effect requires no modification to the SPNF or the sensor electronics. Fourth, while the inductive sensor's lowest sensed mass (7 μg for $MnFe_2O_4$) remains at least two orders of magnitude above the levels relevant for low-abundance biomarker detection on lateral flow assays, the sensor still provides genuine insight into the mobility and alignment of the nanoparticles, and classifies the materials by

their effective magnetic properties consistently with the advanced laboratory measurements.

Contents

Abstract v
Contents vii
List of acronyms xv
List of symbols xvii
List of Figures xxi
1 Introduction 1
1.1 Goal of the thesis and research questions 5
1.2 Navigation tools throughout this thesis 5
2 Nanomagnetism : relevant concepts for this work 9
2.1 Magnetism: the coexistence of unit systems 10
2.1.1 This Work (mainly) uses SI Units 12
2.2 Magnetism: The Bulk Material Story 13
2.2.1 Ferromagnetic Hysteresis: the Textbook Example 13
2.2.2 Dia-, Para- and Ferromagnetism 16
2.2.3 The Energy Landscape of Magnetic Materials 23
2.3 Magnetism: the Nano Material Story 27
2.3.1 Superparamagnetism in Ferromagnetic Materials 27
2.3.2 Key Concepts to superparamagnetism 30
2.3.3 Brownian and Effective Relaxation 34
2.3.4 Describing DC Superparamagnetic Behaviour 36
2.3.5 Describing (linear) AC Superparamagnetic Behaviour 40
2.3.6 Interactions between Magnetic Nanoparticles 45
2.3.7 Peculiarities of SPNF 47
2.4 Magnetic nanoparticles in biomedical applications 50
2.4.1 Biosensing Label 50
2.4.2 Magnetic (cell) Separation 51
2.4.3 MRI Contrast Agents 51
2.4.4 MPI 52
2.4.5 Targeted Drug Delivery 52
2.4.6 Magnetic Hyperthermia Therapy 53

Chapter Summary 54

I Magnetic Nanoparticles : Synthesis and Properties

3 Synthesis, Coating, Structural Characterisation 59
3.1 Measuring and Comparing MNP Sizes 60
3.1.1 Indirect Measurement techniques 61
3.1.2 Nanoparticle size distribution quantification 62
3.1.3 Multiplicative spread: The Lognormal Distribution 64
3.1.4 How is a "monodisperse" synthesis defined? 70
3.1.5 Methods: determining size distribution 72
3.2 MNP Synthesis by Thermal Decomposition 75
3.2.1 Thermal Decomposition of Iron Precursors : Literature Overview . 75
3.2.2 TD synthesis : Materials and Methods 79
3.2.3 TD Synthesis : Results and Discussion 81
Section Summary 87
3.3 MNP Synthesis by Coprecipitation 89
3.3.1 Coprecipitation of Iron Salt : Literature Overview 89
3.3.2 Coprecipitation : Experimental Findings 92
Section Summary 95
3.4 Silica coating of MNP 96
3.4.1 Theory and Literature: Silica Coating 96
3.4.2 Results: Silica coating around TD SPIONs 100
Section Summary 109
Chapter Summary 111

4 Magnetic Characterisation and Metrology 113
4.1 Motivation: configuration-dependent susceptibility 114
4.1.1 The central role of MNP 114
4.1.2 Measurement conditions differ fundamentally from end-use 116
4.2 Chapter Scope and Methods 117
4.2.1 Convention: Mass Density and Specific Magnetisation of MNP . . 120
4.2.2 Convention: Units 122
4.3 Nearly-DC Magnetisation Curves, at 300K 123
4.3.1 Materials and Methods 123
4.3.2 Magnetisation of Powder Samples (300 K) 127
4.3.3 Magnetisation of MNP spread in Cellulose (300K) 134
4.3.4 Perspective: Low-temperature magnetisation as a complementary diagnostic. 139
Section Summary 140
4.4 Nearly-DC FC-ZFC Curves 142
4.4.1 Theory and Literature benchmarks: FC-ZFC Curves 142
4.4.2 Methods: IFCC-ZFCW Measurement Protocol in this work 147
4.4.3 Results: A clear Tb for Mn–CP2 in cellulose membranes 150
4.4.4 Results: SPIONs in cellulose membranes 153

Section Summary 156
4.5 AC Susceptibility Measurement 159
4.5.1 Theory: Interpreting the $\chi'(T)$ and $\chi''(T)$ Data 159
4.5.2 Theory: Fitting Models for Dynamic Susceptibility 161
4.5.3 Methods: ACS measurements 163
4.5.4 Results: AC $\chi(T)$ 165
4.5.5 Sensitivity of Vogel-Fulcher Parameters to pre-exponential factor boundaries 172
4.5.6 Susceptibility for membrane Mn–CP2 and Fe–CP1 (up to 1 kHz) . 174
Section Summary 175
4.6 MHz-GHz Complex Susceptibility at Room Temperature 177
4.6.1 Theory: MHz-GHz toroid susceptometry 177
4.6.2 Materials and Methods 179
4.6.3 Results: Complex Susceptibility of MNP powders 182
4.6.4 Discussion on relevance of E4991 measurements 188
Section Summary 191
4.7 Conclusions and Perspectives on MNP Characterisation 193
4.7.1 Summary of the workflow 193
4.7.2 Conclusion regarding nanoparticle properties 197
4.7.3 Conclusion regarding membrane versus powder configuration 199
4.7.4 Conclusion regarding applied models and frameworks 200
4.7.5 Key contributions of this chapter 202
Chapter Summary 204

II Detection of Magnetic Nanoparticles : Towards Inductive Sensing on LFA's

5 Sensing MNP : State of the Art 209
5.1 Magnetic Sensing 210
5.1.1 General Overview of Magnetic sensor principles 210
5.2 Inductive sensing: Core Concepts 212
5.2.1 Inductors 212
5.2.2 Phenomena Causing Inductor's Impedance Variations 213
5.2.3 Readout Architectures 214
5.3 Sensing of MNP in Literature 217
5.4 Literature Focus: Sensing MNP in LFA 223
5.4.1 The optical signal: pros and cons 223
5.4.2 Quantifying MNP on LFA 224
5.5 Commercial Platforms for MNP detection 227
Chapter Summary 231

6 Inductive Detection of Magnetic Nanoparticles 233
6.1 "Start with Why" 234
6.2 Materials and Methods: Inductive sensing of MNP 236
6.2.1 Colpitts Oscillator Design on PCB 236

6.2.2 Coils . . . 239
6.2.3 Measurement Protocol: MNP in NC . . . 241
6.3 Results: linearity within working range . . . 243
6.3.1 Sensitivity: Frequency change induced by known MNP mass . . . 243
6.3.2 Results: Constant signal ratio with varying Oscillation Frequency . 248
Section Summary . . . 251
6.4 EA orientation within Nitrocellulose . . . 253
6.4.1 Pre-Orientating EA: Materials and Methods . . . 253
6.4.2 Results: Pre-orienting EA improves inductive sensing . . . 255
6.4.3 Discussion on EA Pre-Orientation . . . 256
Section Summary . . . 259
6.5 Inductive Sensing: characterising particle mobility . . . 261
6.5.1 Literature: Mobility affects susceptibility . . . 261
6.5.2 Observing MNP mobility with LCR4284 . . . 262
6.5.3 Observing Particle Mobility with the Colpitts Oscillator . . . 270
Section Summary . . . 274
6.6 Conclusion and Perspectives . . . 276
6.6.1 Summary of the workflow . . . 278
6.6.2 Conclusions regarding the nanoparticle samples . . . 278
6.6.3 Conclusions regarding the measurement set-up . . . 279
6.6.4 Conclusions regarding the applied models . . . 280
6.6.5 Key contributions of this chapter . . . 281
Chapter Summary . . . 284

7 Conclusions and Perspectives: MNP in Biosensors . . . 287
7.1 Scientific Questions on SPNF Properties . . . 288
7.2 Engineering Questions on Inductive LFA Design . . . 297
7.3 Contributions and key findings . . . 303
7.4 Perspectives . . . 305
7.4.1 High effort, medium impact . . . 306

Appendices . . . 309
A.1 Electromagnetism : Maxwell Equations . . . 310
A.1.1 Steady Current generates a Magnetic Field (1820's) . . . 310
A.1.2 Changing Magnetic Field generates a Current (1830's) . . . 311
A.1.3 Maxwell : One Ring to Rule all Fields (1870's) . . . 312
A.1.4 Lorentz : Forces on Electrical Charges . . . 315
A.1.5 Recurring Spatial Configurations . . . 315
A.2 Interpreting the Bohr Magneton with Classical Physics . . . 317
A.3 Verwey Transition in Iron Oxide Nanoparticles . . . 318
A.3.1 Verwey Transition in Larger Nanoparticles ($>$ 20 nm) . . . 319
A.4 Literature Review for TD synthesis and Silica coating . . . 321
A.4.1 Literature Review for TD synthesis . . . 321
A.4.2 Alternatives to LaMer Nucleation . . . 331
A.4.3 Competing Mechanisms of Surfactant Influence on Particle Size . . 331

A.4.4 Coating Hydrophilic (and vitrophilic) Magnetic Nanoparticles with Silica 332
A.5 Magnetisation Curves at Room Temperature 338
A.5.1 Validation of SQUID measurements with AGFM measurements . . 338
A.5.2 Validation of superparamagnetism in manganese ferrite Superparamagnetic Nanoferrite (SPNF) and Superparamagnetic Iron Oxide Nanoparticle (SPION) 338
A.5.3 Correcting Magnetisation Curves for Measurement 340
A.6 Reported Mydosh parameters for SPIONs 344
A.7 RF analysis of magnetic samples 346
A.7.1 Notifying an Error in the Internal Correction of the E4991 Permeability Mode 346
A.8 Sensors - Key Concepts 349
A.9 Commercial MNP Sensors applications, patents and evolution 350
A.10 Coil Geometries 355
A.10.1 Solenoid Coils 355
A.10.2 Planar Coils 356
Bibliography **359**

Related journal papers

[JP1] G. Le Brun, M. Hauwaert, R. Moumneh, S. Yunus, and J.-P. Raskin, "Studying ion transport dynamics in electrochemical measurements of lateral flow assays," *Journal of Electroanalytical Chemistry*, vol. 966, p. 118399, 2024. DOI: 10.1016/j.jelechem.2024.118399.

[JP2] F. Tounsi, M. Hadj Said, M. Hauwaert, S. Kaziz, D. Flandre, et al., "Variation Range of Different Inductor Topologies with Shields for RF and Inductive Sensing Applications," *Sensors*, vol. 22, no. 9, p. 15, 2022. DOI: 10.3390/s22093514.

[JP3] G. Le Brun, M. Hauwaert, A. Leprince, K. Glinel, J.-P. Raskin, et al., "Electrical Characterization of Cellulose-Based Membranes towards Pathogen Detection in Water," *Biosensors*, vol. 11, no. 2, p. 57, 2021. DOI: 10.3390/bios11020057.

Related conference papers

[CP1] M. Hauwaert, N. Trifiro, V. Pilati, L. Lejeune, S. Spassov, M. Lefebvre, R. Moumneh, S. Hermans, M. Rivas, and J.-P. Raskin, "Improving Inductive Sensing of Superparamagnetic Nanoparticles Through Orientation of Easy Axes," in *2025 IEEE Sensors*, 2025. DOI: 10.1109/SENSORS59705.2025.11330555.

[CP2] G. Le Brun, M. Hauwaert, A. Leprince, K. Glinel, J.-P. Raskin, et al., "Electrochemical Characterization of Nitrocellulose Membranes towards Bacterial Detection in Water," in *Proceedings*, vol. 60, no. 1, p. 61, 2020. DOI: 10.3390/IECB2020-07080.

Conference Speeches

[CS1] M. Hauwaert, V. Pilati, L. Lejeune, N. Trifiro, M. Lefevre, M. Rivas, S. Hermans, and J.-P. Raskin, "Superparamagnetic Nanoparticles: bridging traditional Characterization and Real-World Biosensing Applications," in *IEEE Magnetics*, West Palm Beach, FL, USA, Nov. 2025.

[CS2] M. Hauwaert, N. Trifiro, V. Pilati, L. Lejeune, S. Spassov, M. Lefebvre, R. Moumneh, M. Rivas, S. Hermans, and J.-P. Raskin, "Improving Inductive Sensing of Superparamagnetic Nanoparticles through Orientation of Easy Axes," in *IEEE Sensors*, Vancouver, Canada, Oct. 2025.

[CS3] M. Hauwaert, V. Pilati, L. Lejeune, N. Trifiro, M. Lefevre, M. Rivas, S. Hermans, and J.-P. Raskin, "Inductive detection of magnetic nanoparticles : from sensor design to physical questions," in *IEEE Nano*, Gijon, Spain, Jul. 2024.

[CS4] M. Hauwaert, L. Lejeune, T. da Câmara Santa Clara Gomes, A. Engel, J.-P. Raskin, et al., "Tuning Nanoparticle Coating and Size for inductive biodetection," in *Frontiers in Magnetic Nanoparticles*, Greenville, SC, USA, Jun. 2023.

Conference Posters

[CPo1] M. Hauwaert, L. Lejeune, T. da Câmara Santa Clara Gomes, A. Engel, J.-P. Raskin, et al., "Nanoparticle Coating and Size : Key for optimal magnetic Biosensors," in *ENFI*, ULB - Brussels, Belgium, Jul. 2023.

[CPo2] M. Hauwaert, G. Le Brun, J. Vandeputte, J. Mahy, J.-P. Raskin, et al., "Nanoparticles for impedimetric biodetection on paper-based substrates," in *Micro and Nano Engineering Conference – MNE 2021*, Torino, Italy, Sep. 2021.

[CPo3] G. Le Brun, M. Hauwaert, I. Adant, and J.-P. Raskin, "Conception responsable de capteurs de qualité de l'eau," in *Conference on interdisciplinary and transdisciplinary research for sustainable development*, Louvain-la-Neuve, Belgium, Nov. 2021.

[CPo4] G. Le Brun, M. Hauwaert, A. Leprince, K. Glinel, J.-P. Raskin, et al., "Electrochemical paper-based biosensors for bacteria detection in water," in *The 1st International Electronic Conference on Biosensors (IECB)*, On-line conference, Nov. 2020.

List of acronyms

A2S	Approach to Saturation
ACS	AC Susceptometry
AGFM	Alternating Gradient Force Magnetometer
AuNP	Gold Nanoparticles
CA	Citric Acid
CGS	Centimeter-Gram-Second System
CP	Coprecipitation
CV	Coefficient of Variation
DI	deionised water
DLS	Dynamic Light Scattering
EA	Easy Axis
EDX	Energy Dispersive X-ray Spectroscopy
EMF	Electromotive Force
emu	Electromagnetic Units
FC	Field Cooled
FC-ZFC	Field Cooled - Zero Field Cooled
GMR	Giant Magnetoresistance
ICP	Inductively Coupled Plasma
IFCC	In Field Cooled cooling
IRF	Instrumental Remanent Field
LFA	Lateral Flow Assay
LoD	Limit of detection
MNP	Magnetic Nanoparticles
MPI	Magnetic Particle Imaging
MRI	Magnetic Resonance Imaging
NC	Nitrocellulose
PCB	Printed Circuit Board
PDF	Probability Density Function

PDI	Polydispersity Index
SEM	Scanning Electron Microscopy
SG	Spin Glass Behavior
SI	International System of Units
SPION	Superparamagnetic Iron Oxide Nanoparticle
SPM	Superparamagnetism
SPNF	Superparamagnetic Nanoferrite
SQUID	Superconducting Quantum Interference Device
SRF	Self-Resonant Frequency
SSE	Sum of Squared Errors
SSG	Super Spin Glass Behavior
SW	Stoner-Wohlfarth
TD	Thermal Decomposition
TEM	Transmission Electron Microscopy
TEOS	Tetraethyl Orthosilicate
VNA	Vector Network Analyser
VSM	Vibrating Sample Magnetometer
VT	Verwey Transition
XPS	X-Ray Photoelectron Spectroscopy
XRD	X-Ray Diffraction
ZFC	Zero Field Cooled
ZFCW	Zero Field Cooled warming

List of symbols

B	Magnetic flux density	[T]
χ	Magnetic susceptibility (volume)	[–]
χ_0	Static susceptibility (zero-frequency limit of the Debye model)	[–]
χ''	Imaginary (out-of-phase) component of AC susceptibility	[–]
χ_i	Initial susceptibility (slope of $M(H)$ at $H \to 0$)	[–]
χ'	Real (in-phase) component of AC susceptibility	[–]
D_{mag}	Magnetic diameter	[nm]
$\tilde{D}_{\mathrm{mag}}$	Median magnetic diameter from lognormal fitting (Chantrell, Debye)	[nm]
$\tilde{D}_{\mathrm{TEM}}$	Median diameter derived from TEM images	[nm]
E_a	Anisotropy energy barrier	[J]
η	Carrier fluid dynamic viscosity	[Pa s]
$\Delta f / f$	Relative frequency shift	[–]
γ	Lognormal shape factor	[–]
H	Magnetic field strength	[A/m]
h	Hydrodynamic-to-magnetic volume ratio (V_H / V_{mag})	[–]
H_c	Coercive field	[A/m]
k_B	Boltzmann constant	[J/K]
K_{eff}	Effective anisotropy constant	[J/m^3]
K_{m}	Magnetocrystalline anisotropy constant (intrinsic to crystal structure; contributes to K_{V})	[J/m^3]
K_{S}	Surface anisotropy constant	[J/m^2]
K_{V}	Volume anisotropy constant (includes K_{m}, strain, shape contributions)	[J/m^3]
L	Coil inductance	[H]
$\Delta L / L$	Relative inductance change	[–]
$\mathcal{L}(\xi)$	Langevin function: $\coth(\xi) - 1/\xi$	[–]
M	Volume magnetisation	[A/m]
m_{NP}	Magnetic moment of a nanoparticle	[A m^2]

M_r	Remanent magnetisation (volume)	[A/m]
M_s	Saturation magnetisation (volume)	[A/m]
μ_0	Vacuum permeability	[H/m]
μ_r	Relative permeability	[–]
ω	Angular frequency	[rad/s]
$p(D, \gamma)$	Lognormal size distribution function	[1/m]
Φ	Mydosh parameter: relative shift of peak temperature per decade of frequency	[–]
σ_M	Specific magnetisation (per unit mass)	[A m^2/kg]
$\sigma_{M,r}$	Specific remanent magnetisation (per unit mass)	[A m^2/kg]
$\sigma_{M,s}$	Specific saturation magnetisation (per unit mass)	[A m^2/kg]
T_0	Vogel-Fulcher temperature (inter-particle interaction strength parameter)	[K]
T_B	Blocking temperature	[K]
T_f''	Temperature at which χ'' peaks at frequency f	[K]
T_f'	Temperature at which χ' peaks at frequency f	[K]
T_{irr}	Irreversibility temperature	[K]
τ_0	Attempt time (Néel–Arrhenius prefactor)	[s]
τ_B	Brownian relaxation time	[s]
τ_{eff}	Effective relaxation time	[s]
τ_{meas}	Measurement time	[s]
τ_N	Néel relaxation time	[s]
V_{NP}	Nanoparticle volume	[m^3]
v_f	Volume filling factor of nanoparticles within a sample	[–]
V_H	Hydrodynamic volume	[m^3]
V_{mag}	Magnetic volume of a single-domain nanoparticle, derived from Langevin/Chantrell fitting	[m^3]
ξ	Langevin parameter ($\mu_0 m_{\text{NP}} H / k_B T$)	[–]
ζ	Anisotropy energy barrier in units of thermal energy ($E_a / k_B T$)	[–]

List of Figures

1.1 MNP-enhanced LFA workflow for pneumococcal pneumonia diagnosis 2
1.2 Chapter overview and key outputs per chapter 6

2.1 Ferromagnetic hysteresis loop with M_r, H_c and M_s 13
2.2 Qualitative $M(H)$ curves for dia-, para-, ferro- and superparamagnetic materials 18
2.3 Critical diameters D_p and D_c for nanoparticle magnetic behaviour . . 29
2.4 Energy landscape of a monodomain nanoparticle: anisotropy barrier and Néel switching 31
2.5 Effective relaxation time and frequency versus core diameter for magnetite nanoparticles in water 37
2.6 Langevin magnetisation curves for SPNFs of varying core diameter . . 39
2.7 Debye AC susceptibility spectrum for a monodisperse system. 42
2.8 Dead (magnetically disordered) surface layer in magnetic nanoparticles 48
2.9 Lattice change at the Verwey transition in Fe_3O_4 and coexistence with T_B 49

3.1 TEM vs XRD mean diameters: example of variation 61
3.2 Influence of shape factor γ on normal and lognormal distributions . . 67
3.3 TEM analysis interface: equivalent diameter and roundness metric . . 74
3.4 LaMer nucleation model for iron oxide nanoparticle synthesis 76
3.5 TEM images of TD synthesis results 82
3.6 Thermal Decomposition Protocol : Correlation with size 86
3.7 TEM images and size histograms for coprecipitation samples 93
3.8 Effect of Igepal volume on silica shell formation: illustration 100
3.9 Pham protocol on FCN4 and Fe–TDH1: core-free silica outcome . . . 102
3.10 Pham protocol on Fe–TDH2 and Fe–TDH3 with 400 μl Igepal 103
3.11 Hou et al. Silica coating protocol, varying initial MNP mass 105
3.12 Hou et al. Si coating protocol: EDX results 106
3.13 Hou et al. Si coating - starting from MNP suspension 107

4.1 Characterisation techniques in temperature–frequency space 117
4.2 Room-temperature magnetisation of SPION powders 128
4.3 Room-temperature magnetisation of Mn-SPNF powders 131
4.4 Magnetisation of Fe–CP1 and Mn–CP2: powder vs. membrane 135
4.5 Magnetisation of Fe–TDH4 with and without silica coating 138
4.6 Model FC-ZFC curves for monodisperse and polydisperse SPNF . . . 142
4.7 FC-ZFC of ∼11 nm SPION powders: variability across studies 148
4.8 FC-ZFC measurements on Mn–CP2 in powder and cellulose membrane 149
4.9 FC-ZFC measurements on Fe–CP1 in powder and cellulose membrane 151
4.10 FC-ZFC measurements on Fe–TDH4 with and without silica coating . 152
4.11 AC susceptibility of Mn–CP2 in membrane and powder 168
4.12 AC susceptibility of Fe–CP1 in cellulose membrane 169
4.13 AC susceptibility of Fe–TDH4 with and without silica coating 171
4.14 Frequency-dependent χ' of Mn–CP2 and Fe–CP1 membranes (1 Hz–1 kHz) 174
4.15 E4991 test fixture dimensions and toroidal capsule design 180
4.16 Complex susceptibility of CP powders and Fe–Comm at 1 MHz–1 GHz 183
4.17 Debye model fit to complex susceptibility of Fe–CP1 and Mn–CP3 powders 185
4.18 Complex susceptibility of Fe–TDH4 with and without silica coating (1–50 MHz) 187
4.19 Effect of prior magnetisation on complex susceptibility of CP and TD powders 190
4.20 Workflow summary of magnetic characterisation in Chapter 4 193

5.1 Equivalent circuit of an inductor 212
5.2 Equivalent circuit of a planar differential transformer 215
5.3 Working principle of the frequency mixing technique 216

6.1 Colpitts Oscillator: standard representation 238
6.2 Coil geometries: planar coil (LDC) and wound coil L1 on 3D-printed support 239
6.3 Example of timeseries for measurement of nanoparticles in nitrocellulose242
6.4 Relative frequency change vs. nanoparticle mass, Colpitts oscillator (L1), 600 kHz and 5.9 MHz 244
6.5 Inductance change vs. nanoparticle mass, planar LDC coil (2 MHz) . 247
6.6 Inductive signal of Mn–CP3 samples over frequency, coils L1 and L2 . 250
6.7 Normalised differential signal $D_{\mathrm{norm}}(f)$ for Coprecipitation (CP) samples in nitrocellulose, 3–19 MHz 251
6.8 Experimental workflow for Easy Axis (EA) pre-orientation and dual-coil inductive measurement 254

6.9 Scanning Electron Microscopy (SEM) images of magnetite nanoparticles in glass fibre membrane: field-free vs. field-dried 256
6.10 Inductive signal per mass for three ferrite types with and without EA pre-orientation 257
6.11 AC Susceptometry (ACS) spectra of FeraSpin XL nanoparticles in water, glycerol and freeze-dried 262
6.12 Real relative permeability of SPNF and Nanomag-D samples in deionised water (DI) water and agar-agar (LCR4284) 264
6.13 Debye fitting on LCR-derived real susceptibility: DI water and agar-agar conditions 269
6.14 Measurement timeseries for SPNF in eppendorf (DI / agar-agar protocol)272
6.15 Colpitts oscillator frequency shift per mass for Mn–CP3, Fe–CP1 and Nanomag-D in agar-agar and DI water (coils LE1 and LE2) 273

7.1 Susceptibility response regimes as a function of nanoparticle diameter: (A) frequency dependence and (B) excitation field amplitude (representative values for magnetite) 296
A.3.1 Example of observed Verwey Transition in nanoparticles 318
A.5.1 Comparison of magnetisation of magnetite powders (commercial 50 nm MNC and thermally decomposed 10 nm TD) extracted by both SQUID and AGFM magnetometers. Note : 70 kOe magnetic field corresponds to 7 T flux density. 339
A.5.2 Magnetisation of Manganese, Iron, Cobalt and Nickel Ferrites. Mass Magnetisation relative to total powder mass, in emu/g corresponds to Am^2/kg 340
A.7.1 The light blue curve illustrates an error in the fixture compensation from E4991. 347

1

Introduction

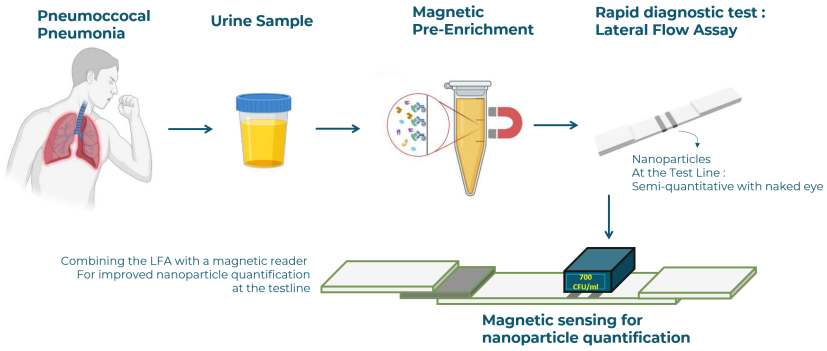


Fig. 1.1 Based on [1] : schematic workflow of an MNP-enhanced Lateral Flow Assay for Pneumococcal Pneumonia diagnosis. The process begins with the collection of a urine sample from a symptomatic patient. Magnetic nanoparticles are utilised for pre-enrichment to concentrate the target analyte before it is applied to the LFA strip. While the test line provides a semi-quantitative visual signal, the integration of a portable inductive magnetic reader allows for precise nanoparticle quantification and objective determination of the targeted biomolecule.

The demand for portable sensing devices is increasing across point-of-care healthcare, environmental monitoring, and food quality control. These devices enable the detection of pathogens in aqueous analytes at or near the sampling site, adhering to the World Health Organization's ASSURED guidelines: Affordable, Sensitive, Specific, User-friendly, Rapid and robust, Equipment-free, and Deliverable to end-users [2]. Paper-based substrates are relevant for these applications as they leverage the natural capillarity of paper to perform microfluidics without complex pumping systems. The most prevalent example is the Lateral Flow Assay (LFA), such as pregnancy tests and COVID-19 self-tests. Traditional LFAs typically rely on the visual inspection of colored labels like colloidal gold (yielding characteristic red test-lines) or latex nanoparticles. Expansion of this technology to other use cases faces technical bottlenecks :

- Semi-quantitative : Because results depend on naked-eye interpretation, sensitivity is subjectively bounded by human perception. This complicates differentiation in concentrations, effectively reducing the assay to a qualitative positive/negative threshold reading [3, 4].
- Surface-Only Detection: Optical readout only probes labels at the membrane surface, leaving the vast majority of them distributed across the thickness of the nitrocellulose strip undetected [3]. Test lines below a certain label density remain invisible, regardless of analyte presence [5].

Consequently, there is a growing interest in replacing visual readout with

instrument-based detection to enable true quantification [1, 3, 5]. Research is shifting toward technologies combining paper substrates such as Nitrocellulose (NC) with electrical and magnetic detection [6, 7]. This work focuses on LFAs leveraging Magnetic Nanoparticles (MNP) as labels in immuno-assays combined with magnetic sensors. This is a promising research track for various reasons :

- MNP are an established material class in biomedicine [8, 9]. Their applications range from in vivo targeted drug delivery to in vitro bioseparation and relaxation-based biosensing [9–11].
- Magnetic readout probes the entire volume of a test line rather than just the surface [7]. It maintains performance in turbid or opaque biological samples where optical methods would probably fail [7].
- Background noise remains low across diverse analytes (urine, blood, or groundwater). While changes in conductivity can affect sensing in electrochemistry or impedance, they do not directly alter the magnetic signal[1].
- Through magnetic pre-enrichment, MNPs allow for the active extraction and concentration of target analytes from complex matrices prior to application on the strip. This overcomes the volume limitations of standard paper microfluidics and lowers the Limit of detection (LoD) by increasing local analyte density.

The relevance of this synergy is illustrated by Salvador et al. [1], who report the detection of *Streptococcus pneumoniae*, a leading cause of global mortality, particularly among paediatric and geriatric populations. By coupling magnetic pre-enrichment with an inductive LFA reader as illustrated in Fig. 1.1, sensitive detection is achieved directly from urine samples at the point of care, enabling near real-time monitoring of the patient at each voiding event. A promising sub-class of MNP are SPNF. When particle size is reduced below a critical diameter (10–20 nm), the energy barrier for magnetic moment reversal becomes comparable to room-temperature thermal energy. These particles magnetize strongly under an external field but retain no residual magnetism (remanence) once the field is removed. This "on/off" magnetic behaviour is particularly relevant for use in biomedical applications, as it prevents the magnetic dipole-dipole interactions that would otherwise lead to particle agglomeration, affecting specificity and dynamics of the sensing system [12]. Furthermore, clustering complicates homogeneous mixing with the targeted biomolecules and repeatable immunological binding. This work utilizes inductive sensors, chosen for their cost-effectiveness and "appropriability,"

[1] Although changes in conductivity may affect agglomeration of nanoparticles and thus indirectly change the magnetic signal.

allowing for a simplified electronic architecture that provides objective digital quantification while remaining consistent with the low-cost ethos of the LFA.

Interdisciplinarity is the cornerstone of the developments of biosensors : obviously biology and electronics come together, but chemistry and fluidics are equally important. No electrical repeatability without biological stability. No linear sensitivity without controlled colloidality. A same variation in measurements can be considered "repeatable" in a biology lab but completely unreliable in an electronics lab. Optimising this integrated system requires to speak the language of the other disciplines involved : a local optimum from a sensor point of view might deteriorate the global optimum of the system. This intrinsic complexity is one of the main reasons explaining the “Valley of Death” between the high load of research and publications in the field of biosensors and the low fall-out towards society [13, 14]. The trajectory of MNP-based diagnostics illustrates this vividly: despite decades of promising laboratory results across theranostics [15], magnetic biosensing [10], and point-of-care platforms [11, 15], only a handful of commercial magnetic readers have survived to clinical deployment (cf. Section 5.5).

This work has been no exception to the need for interdisciplinarity, even without addressing the biological aspects: starting to design a magnetic sensor to integrate with LFA leverages the seemingly simple question “What additional magnetic field do you expect to measure?” or “What permeability change do you expect?”. Exploring literature reveals a wide spectrum of properties and characterisation results, all corresponding to superparamagnetism for different applications : MRI contrast optimisation [8, 10], hyperthermia dosimetry [9], magnetic particle imaging [16], and point-of-care biosensing [11]. Traditionally, MNP are characterised in well-dispersed ferrofluid or dense compacted powder. But what is the relevance of these measurements in predicting the behaviour of magnetic nanoparticles in biosensing applications? The effective magnetic environment in LFA applications bears little resemblance to these configurations : SPNF are confined within the pores of a nitrocellulose membrane : during and after evaporation of the suspending liquid, inter-particle distances are dictated by capillary flow and clustering dynamics. To the best of our knowledge, no study yet analysed the macroscopic magnetic properties of magnetic nanoparticles in a substrate resembling the LFA-application.

Before arriving to actual inductive sensing in Part II of this work, Part I focuses on the synthesis and characterisation of nanoparticles and explores their properties over frequency and temperature. A detour? Maybe. But to cite the introduction of a well-known reference handbook for magnetic materials [17] : *”One lesson from a study of the history of magnetism is that fundamental understanding of the science may not be a prerequisite for technological progress. Yet fundamental understanding helps. The*

progression from the poorly differentiated set of hard and soft magnetic steels that existed at the start of the twentieth century to the wealth of different materials available today, with all sorts of useful properties described in this book, owes more to metallurgy and systematic crystal chemistry than it does to quantum physics." In the final chapter of this work, we try to answer the following question : given the multiple parameters that can affect the actual properties of nanoparticles, what characterisations should a sensor designer dispose of to start his job? A common dutch expression says "Meten is weten."[2] The mantra of this work would be "Weet wat je meet."[3]

1.1 Goal of the thesis and research questions

The research questions addressed in this work are separated between understanding the configuration-dependent magnetic properties of SPNF ("Scientific Questions, SQ") and the design process of inductive sensors for SPNF ("Engineering Questions, EQ").

SQ1 *What intrinsic parameters set the magnetic response of SPNF?*

SQ2 *How do configurations modify these intrinsic properties?*

SQ3 *How are appropriate SPNF with required properties for Lateral Flow Assays made?*

SQ4 *What models are appropriate to describe macro-properties of MNP at room temperature, from DC to 1 GHz?*

SQ5 *Which MNP properties govern the signal of an inductive LFA reader?*

EQ1 *What magnetic characterisation steps are necessary for inductive SPNF sensor design on specific substrates?*

EQ2 *What sensor properties are achieved with the proof-of-concept sensor, how do these compare to the literature, and what recommendations can be drawn for improved figures of merit?*

EQ3 *Are inductive LFA good candidates to fulfil the ASSURED standards?*

1.2 Navigation tools throughout this thesis

How to sail this work

This work aims to address the thematic of nanoparticle within (bio)sensors under different angles of attack. It is meant to be read by people from different disciplines. For anyone with a background in applied physics, the Curie-Weiss Law is considered redundant background information while for an electrical engineer, the

[2] "To measure is to know."
[3] "Know what you measure."

concept of Curie Temperature is not a given. Fig. 1.2 represents the main outputs per chapter.

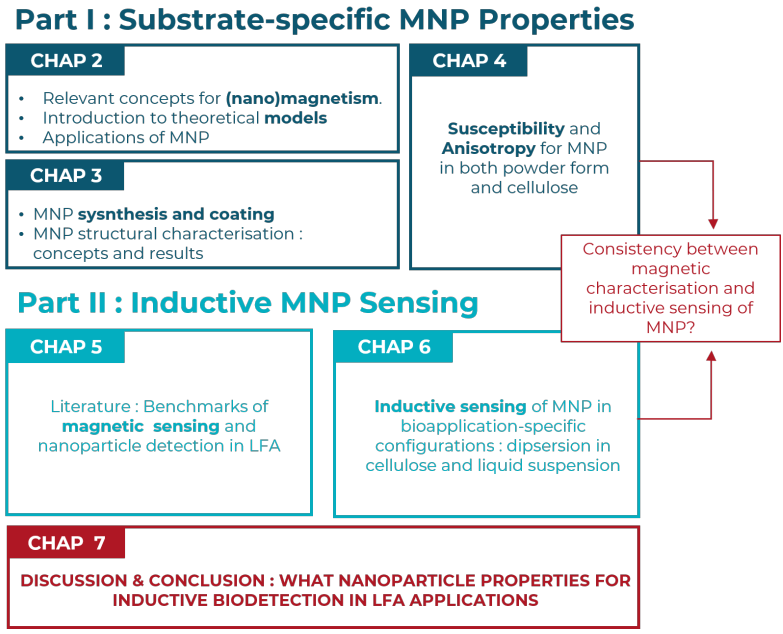


Fig. 1.2 Chapter overview in this work. Light blue boxes in chapters of part 1 refer to main take-aways for part 2. MNP stands for Magnetic Nanoparticles.

Conventions

Here are some conventions applied in this work :

- Vectors and vector fields are written in bolt letters $\mathbf{V}$. The authors trust it will be deducible for the reader whether it refers to a vector or a vector field.
- The field of magnetism is a "rebel" in the adoption of SI units. While these standards are more and more adopted, CGS units are still common in both literature and characterisation tools. A comprehensive overview of conversion is offered in Table 2.1 of Chapter 2. While all main summary tables will contain SI units, throughout the core of this work CGS units will emerge. Corresponding SI units will often be indicated. Intuitive reference values : the field within an IRM scanner is expressed in T, your fridge magnets have about 5 mT field strength and the Earth's magnetic field strenght is expressed in tens of μT.

- By default, the size of nanoparticles is given with their diameter unless mentioned differently.

The nomenclature applied in this work requires some specifications :

- "Agglomerates" refer to individual nanoparticles that attach together (by magnetic attraction, insufficient of colloidal stability,...). They interact only by dipolar interactions. "Aggregates" refer to nanoparticles that grew together and share a plane : both dipolar interactions and exchange interactions have to be considered.
- "Corona" refers to any surface species surrounding the nanoparticle (ligands, surfactants, grafted molecules, or shells). "Coating" specifically refers to a distinct shell with measurable thickness (e.g. silica, gold).

Three categories of nanoparticles are discussed :

- **MNP** is a general label for all nanoparticles with magnetic properties, no matter the magnetic behaviour nor the elemental composition of the nanoparticle.
- **SPION** refers to iron oxide (γ-Fe_2O_3 and Fe_3O_4) nanoparticles with superparamagnetic behaviour. This subgroup exists in literature due to e.g. its low toxicity, for in vivo applications.
- **SPNF** refers to ferrites (i.e. any iron oxide with spinel structure) with nanoscale dimensions and superparamagnetic behaviour. In this work, this term is used to refer to both pure iron oxide nanoparticles SPION and mixed ferrites (e.g. manganese ferrite superparamagnetic nanoparticles)

2

Nanomagnetism : relevant concepts for this work

Every magnetic nanoparticle carrying remanent magnetisation behaves as a magnetic dipole. The resulting dipole-dipole interactions promote agglomeration in suspension, which is undesirable for biomedical applications. Superparamagnetic nanoparticles combine high saturation magnetisation with zero remanence, avoiding permanent agglomeration [18]. Describing this behaviour quantitatively requires a theoretical framework that this chapter introduces.

The chapter starts with unit conventions and fundamental magnetic quantities, with a reminder of the underlying electromagnetism in Appendix A.1. It then reviews ferromagnetic hysteresis and the classification of magnetic materials from a bulk-material perspective. The focus narrows to nanoscale magnetism: the transition to single-domain behaviour, Néel and Brownian relaxation [19], the Langevin model for DC magnetisation, the Debye model for AC susceptibility, and the role of dipolar interactions. A final section positions the work within the landscape of biomedical applications of magnetic nanoparticles. The parameters introduced here, in particular M_s, K_{eff}, τ_N, τ_B, T_B, D_{mag} and χ_0, are applied in Chapters 3 through 6 to interpret experimental data.

2.1 Magnetism: the coexistence of unit systems

The Centimeter-Gram-Second System (CGS) (centimeter, gram, second) system of electromagnetic units (EMU) was formulated by William Thomson, James Clerk Maxwell, and others through the British Association for the Advancement of Science. It was established during a period of historical development of electrical and magnetic units. In EMU, the unit for magnetic moment is often incorrectly referred to simply as "emu," when the actual unit is erg per gauss or erg[1] per oersted. Furthermore, magnetisation (magnetic moment per unit volume) is commonly expressed either as M in "emu per cubic centimeter" or as $4\pi M$ in units of gauss, leading to confusion because these expressions are dimensionally equivalent but differ numerically by 4π.

Despite international efforts to transition to modern systems, EMU remains in common use for expressing magnetic data among generations of physicists, making magnetics a notable exception to the general acceptance of the SI across most scientific disciplines [20, 21]. Table 2.1 introduces the correspondence between CSG and SI units.

[1]The 'erg' unit's name is derived from the Ancient Greek $\epsilon\rho\gamma o\nu$ which means 'work'. It is a unit of energy equivalent to $10^{-}7$[J].

SI Symbol	SI Quantity	Conversion from EMU to SI Units[a]
Φ	Magnetic flux	$1\ \mathrm{Mx} = 1\ \mathrm{G}\cdot\mathrm{cm}^2 \to 10^{-8}\ \mathrm{Wb} = 10^{-8}\ \mathrm{V}\cdot\mathrm{s}$
B	Magnetic flux density, magnetic induction	$1\ \mathrm{G} \to 10^{-4}\ \mathrm{T} = 10^{-4}\ \mathrm{Wb/m}^2$
μ[b]	Permeability	$1\ (\mathrm{EMU}) \to \{\mu_0\}\ \mathrm{H/m} = \{\mu_0\}\ \mathrm{N/A}^2 = \{\mu_0\}\ \mathrm{Wb}/(\mathrm{A}\cdot\mathrm{m})$
H	Magnetic field strength, magnetizing force	$1\ \mathrm{Oe} \to 10^3/(4\pi)\ \mathrm{A/m}$
m	Magnetic moment	$1\ \mathrm{erg/G} = 1\ \mathrm{emu} \to 10^{-3}\ \mathrm{A}\cdot\mathrm{m}^2 = 10^{-3}\ \mathrm{J/T}$
j	Magnetic dipole moment	$1\ \mathrm{erg/G} = 1\ \mathrm{emu} \to 10^{-3}\{\mu_0\}\ \mathrm{Wb}\cdot\mathrm{m}$
M	Magnetization, volume magnetization	$1\ \mathrm{erg}/(\mathrm{G}\cdot\mathrm{cm}^3) = 1\ \mathrm{emu/cm}^3 \to 10^3\ \mathrm{A/m}$
J, I	Magnetic polarization, intensity of magnetization	$1\ \mathrm{G} \to 10^{-4}\ \mathrm{T} = 10^{-4}\ \mathrm{Wb/m}^2$
σ	Specific magnetization, mass magnetization	$1\ \mathrm{erg}/(\mathrm{G}\cdot\mathrm{g}) = 1\ \mathrm{emu/g} \to 1\ \mathrm{A}\cdot\mathrm{m}^2/\mathrm{kg}$
χ	Susceptibility, volume susceptibility	$1\ (\mathrm{EMU}) \to 4\pi\ (\mathrm{SI})$
χ_ρ, χ_m	Specific susceptibility, mass susceptibility	$1\ \mathrm{cm}^3/\mathrm{g} \to 4\pi \times 10^{-3}\ \mathrm{m}^3/\mathrm{kg}$
w, W[c]	Energy product, volume energy density	$1\ \mathrm{erg/cm}^3 \to 10^{-1}\ \mathrm{J/m}^3$
N, D	Demagnetizing factor	$1\ (\mathrm{EMU}) \to (4\pi)^{-1}\ (\mathrm{SI})$

[a] EMU are the same as Gaussian units for magnetostatics: Mx = maxwell, G = gauss, Oe = oersted. SI: Wb = weber, T = tesla, H = henry, N = newton, J = joule.
[b] In the SI, relative permeability $\mu_r = \mu/\mu_0 = 1 + \chi$. In EMU, permeability $\mu = 1 + 4\pi\chi$. Relative permeability μ_r in the SI corresponds to permeability μ in EMU.
[c] In the SI, $w\ [\mathrm{J/m}^3] = B\ [\mathrm{T}]\cdot H\ [\mathrm{A/m}] = \mu_0\ [\mathrm{Wb}/(\mathrm{A}\cdot\mathrm{m})]\cdot M\ [\mathrm{A/m}]\cdot H\ [\mathrm{A/m}]$. In EMU, $w\ [\mathrm{erg/cm}^3] = (4\pi)^{-1}B\ [\mathrm{G}]\cdot H\ [\mathrm{Oe}] = M\ [\mathrm{erg}/(\mathrm{G}\cdot\mathrm{cm}^3)]\cdot H\ [\mathrm{Oe}]$.

Table 2.1 Conversion of units for magnetic quantities. In the right column, $\{\mu_0\}$ refers to the numerical value of μ_0, the recommended value of which may change slightly over time. Factors of 4π originate from the conversion of unrationalized EMU to rationalized SI units. In the absence of units, a dimensionless quantity is labeled with its associated system of units (EMU or SI). The arrows ($\to$) indicate correspondence, not equality. From [21]

2.1.1 This Work (mainly) uses SI Units

In this work we will apply SI units (unless stated otherwise) and more precisely the Sommerfeld Convention: $\mathbf{B} = \mu_0(\mathbf{H} + \mathbf{M})$ [T] or $\left[\frac{\mathrm{H{\cdot}A}}{\mathrm{m}^2}\right]$.

$$B\,[\mathrm{T}] : \textbf{Magnetic Flux Density} \tag{2.1}$$

$$H\left[\frac{\mathrm{A}}{\mathrm{m}}\right] : \textbf{Magnetic Field} \tag{2.2}$$

$$M\left[\frac{\mathrm{A}}{\mathrm{m}}\right] : \textbf{Static Volume magnetisation} \tag{2.3}$$

$$\mu_0 \approx 4\pi \times 10^{-7}\left[\frac{\mathrm{H}}{\mathrm{m}}\right] : \textbf{Vacuum Permeability} \tag{2.4}$$

Magnetisation **M** is defined as the extent to which a material becomes magnetised when placed within a magnetic field, and is a measure of the net magnetic dipole moment per unit volume. It is sometimes called the 'induced magnetisation'. Note that historically μ_0 was considered exactly equal (by definition) to $4\pi \times 10^{-7}\left[\frac{\mathrm{H}}{\mathrm{m}}\right]$ while under the revised SI convention, it is an experimentally determined constant that corresponds to this value for 9 digits [20]. For the scope of this work, this will not be further elaborated.

The magnetic volume susceptibility $\chi\,[-]$ is a dimensionless quantity that indicates the degree of magnetisation of a material in response to an external magnetic field:

$$\chi = \frac{\partial \mathbf{M}}{\partial \mathbf{H}} \tag{2.5}$$

In many cases, the $\mathbf{M}(\mathbf{H})$ relationship depends on the external field strength. However, at 'low' external field (referred to as "the linear range" in this work), linearity can be considered:

$$\begin{aligned} \mathbf{B} &= \mu_0(\mathbf{M} + \mathbf{H}) \\ \mathbf{B} &\approx \mu_0(\chi + 1)\mathbf{H} \\ &= \mu_0\mu_r\mathbf{H} \\ &= \mu\mathbf{H} \end{aligned} \tag{2.6}$$

The relative permeability μ_r is the ratio of permeability of a specific medium μ to the permeability of free space μ_0. Note that our results are presented in the SI system of units, and hence the magnetic susceptibility is dimensionless [22].

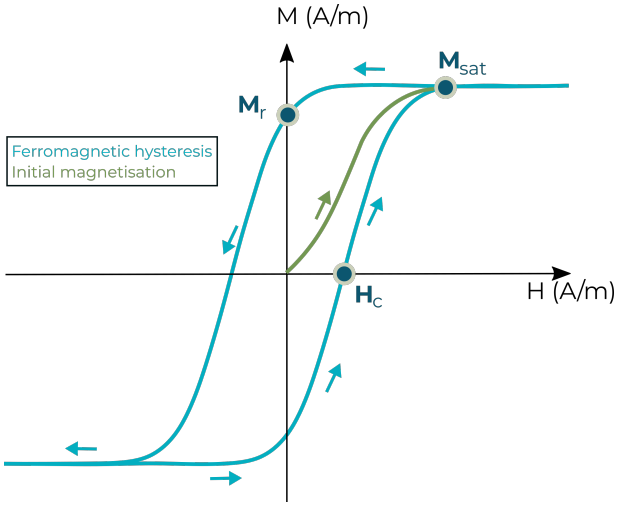


Fig. 2.1 Remanent magnetisation M_r, coercivity H_c, saturation magnetisation M_s.

2.2 Magnetism: The Bulk Material Story

2.2.1 Ferromagnetic Hysteresis: the Textbook Example

The most direct manifestation of magnetism in solid materials is the remanent magnetisation of ferromagnetic materials such as magnetite (Fe_3O_4), which can be so strong the material becomes a permanent magnet. This is usually associated with hysteresis[2], a phenomenon studied by James Ewing, and named by him in 1881[3]. Hysteresis is a physical phenomenon where the current state depends on its history. The existence of coercivity and remanence is fundamentally linked to a multivalley energy landscape in magnetic configuration space. Given the tangible nature of ferromagnetic hysteresis, and given their relevance for this work since superparamagnetism occurs in ferromagnetic materials, we dedicate this subsection in detailing the qualitative hystersis curve in Fig. 2.1.

The steps of the hysteresis curve trace the material's process of modifying and eventually eliminating its microstructure of ferromagnetic domains [23]. This is

[2] 'Hysteresis', coming from the Ancient Greek *'ὑστερος' 'husteros'*, 'additional, posterior'. Note that *husteros* also denotes 'more external', leading to *'ὑστέρα 'hustera'*, meaning 'uterus'. 'Hysteria' is related to 'uterus'...

[3] J. Ewing studied and named hysteresis while he was working in Japan as professor in civil engineering and mechanics. He had been recruited *'to help the modernisation'*. Later in his career he would work at Cambridge University. His wife was a descendent of president George Washington's brother.

represented in Fig. 2.1, with external magnetic field as the abscissa and typical ferromagnetic magnetisation as the ordinate.

- The $(0,0)$ point corresponds to the "initial state" of the material that has not been submitted to any H field. In the demagnitized state of the sample, magnetic moments of all individual domains are oriented in various directions such that they cancel each other out, resulting in zero net magnetisation for the macroscopic sample. In practice, this "demagnetised" state can be reached by either heating or submitting the sample to an oscillating field with decreasing amplitude.

- The response of the material as the magnetic field (H) is imposed and increased from zero is traced by the initial magnetisation curve [17]. This happens through two primary mechanisms that alter the domain structure:

  Domain Wall Motion: Domains that are favourably aligned with the applied field grow at the expense of unfavourably aligned domains. This growth occurs by the movement of domain walls, mainly as Barkhausen jumps[4].

  Domain Rotation: As the field increases further, the magnetisation within individual domains may rotate to align more closely with the applied field direction. This process typically occurs in higher fields and, importantly, involves work done against anisotropy forces.

- Saturation magnetisation $M_s \left[\frac{\mathrm{A}}{\mathrm{m}}\right]$ is maximum magnetisation value towards which a material can converge when subjected to very high external field. At this point, all the magnetic moments within the material are aligned parallel to the direction of the external field [24].

- The key to hysteresis lies in the irreversible nature of this domain wall motion. When the external field is decreased, the magnetisation does not simply retrace its path, due to the existence of a multivalley energy landscape within the magnetic material. Furthermore, domain walls are subject to hindrances to their motion caused by various crystal imperfections and internal stresses.

- Due to these hindrances, even after the applied field is reduced to zero from saturation, a portion of the magnetisation remains. This is the remanent magnetisation $M_r \left[\frac{\mathrm{A}}{\mathrm{m}}\right]$, the visible proof of magnetic hysteresis, because the

[4] A Barkhausen jump represents a discontinuous change in magnetisation. These jumps, when summed up, constitute the hysteresis loop of a macroscopic sample. Heinrich Barkhausen detected these jumps in 1919 by measuring flux jumps in a long pick-up coil filled with nickel wires using an amplifier connected to a loudspeaker. Each discontinuous jump in magnetisation induced a small EMF (electromotive force) in the coil, which was heard as a click [23].

magnetisation "lags behind" the applied field [25]. The material is "stuck" in a metastable state where domains are preferentially oriented, rather than returning to the original demagnetised state.

- To reduce this remanent magnetisation to zero, a reverse magnetic field is required. The magnitude of this reverse field is called the coercivity. The coercive field $H_c \left[\frac{\mathrm{A}}{\mathrm{m}}\right]$ is the point at which reverse domains nucleate or pinned domain walls are freed, allowing the magnetisation to reverse direction. It is also referred to as "switching field".

2.2.1.1 Saturation Magnetisation and Spontaneous Magnetisation

Between the low-field and the high-field region near saturation there exists a large section of the magnetisation curve, comprising most of the change of magnetisation between zero and saturation. The main processes occurring here are large Barkhausen jumps, and the shape of this portion varies widely from one kind of specimen to another. It is not possible to express M as a simple function of H in this intermediate range. In the high-field region, however, domain rotation is the predominant effect, and changes in magnetisation with field are relatively small. The relation between M and H in this range is called the "law of approach" to saturation and is usually written as [22, 26]:

$$M = M_s \left(1 - \frac{a}{H} - \frac{b}{H^2}\right) + \chi H \tag{2.7}$$

The term χH represents the field-induced increase in the spontaneous magnetisation of the domains, or forced magnetisation; this term is usually small at temperatures well below the Curie point and may often be neglected. Constant a is mainly dependent on microstress, and b is generally considered dependent on crystal anisotropy [26]. While the physics behind these constant will not be considered further, the mathematical "approach to saturation" will be helpful for magnetisation data correction as explained in Section 4.3 in Chapter 4.

It is important to note that for ferromagnetic materials, the amplitude of local magnetisation within a magnetic material does not change when a material (de)magnetises: (de)magnetisation is nothing more than the (de)alignment of local magnetisation vectors. The more the local vectors are aligned, the larger the bulk magnetisation vector. The magnetisation within a domain is called the spontaneous magnetisation M_s, defined by the local magnetic order within the lattice [27, 28]. In the ideal case, macroscopic saturation magnetisation equals M_s[5]. In

[5]Strictly speaking, M_s denotes the spontaneous magnetisation within a domain. The macroscopic saturation magnetisation equals M_s only in the ideal case; real samples may not reach this value due to strain, surface effects and lattice imperfections. For single-domain nanoparticles, the focus of this work, the distinction is immaterial and M_s is used throughout.

practice, due to strain, surface effects and lattice imperfections, real samples may not reach M_s [24, 29].

2.2.1.2 The area of the hysteresis curve corresponds to hysteresis losses

Coercivity and remanence are fundamentally determined by the stability of metastable magnetic configurations and the energy barriers that hinder the reversal of magnetisation. These barriers arise from the effective magnetic anisotropy (K_{eff}), which is influenced by numerous factors: sample shape, surface roughness, microscopic defects, thermal history,... which will be further explained in Subsection 2.2.3.

From the first law of thermodynamics, consider

$$\mathrm{d}U = \partial Q + \partial W \tag{2.8}$$

for a constant density system of unit volume, with U the internal energy, Q the heat added to the system, and W the magnetic work done on the system. Consider an adiabatic process ($\partial Q = 0$) and the magnetic work given in general by $\partial W = \mathbf{H} \cdot \mathrm{d}\mathbf{B}$ [30]. Note that this is a macroscopic energy-storage concept, different from the work on a single charge, therefore not contradicting the maxwell equations. As a result, $\partial U = \mathbf{H} \cdot \mathrm{d}\mathbf{B}$. Under the hypothesis that $\mathbf{B}$ and $\mathbf{H}$ are colinear[6], the relation simplifies to $\mathrm{d}U = H\mathrm{d}B$. Substituting in Eqn. 2.8, one obtains

$$\Delta U = -\mu_0 \oint M \mathrm{d}H \tag{2.9}$$

As a result, the surface of the hysteresis loop of a sample in an external applied field $\mathbf{H}$ corresponds to the hysteresis loss [28, 31]. This energy is mainly dissipated as heat, and should not be confounded with eddy current losses. Hyperthermia applications with magnetic nanoparticles exploit these heat losses: when nanoparticles are excited at high frequency, their hysteresis loop enlarges.

2.2.2 Electron Choreographies determine Dia-, Para- and Ferromagnetism

More generally speaking than the textbook example above, magnetism is closely related to the "perpetuous motion of electrons" - even though any quantum physicist would frown, since wave-particle duality describes electrons as standing waves so they do not actually "move". The nucleus also has a small magnetic moment,

[6] This hypothesis of colinearity is not automatically satisfied since $\mathbf{B} = \mu_0(\mathbf{M} + \mathbf{H})$. The resulting magnetisation within a sample is not necessarily aligned with $\mathbf{H}$ since it is also influenced by anisotropy, exchange energy,... However, incrementally, one can assume that $\mathrm{d}\mathbf{B}$ is colinear with $\mathrm{d}\mathbf{H}$. When omitting the colinearity hypothesis, the expressions are less simplified but the conclusion is the same: the area in the hysteresis curve corresponds to hysteresis losses [30].

but it is insignificant compared to that of the electrons, and it does not affect the gross magnetic properties. In this work, we will stick to the simplification of electrons being moving charges. They have two sources of angular motion: spin and orbital motion around the nucleus. The "building block" of magnetic moment is the Bohr Magneton: $\mathbf{m_B} = 9.274 \times 10^{-24} [\mathrm{A} \cdot \mathrm{m}^2]$, just like the electron charge $e = 1.602 \times 10^{-19} [\mathrm{C}]$ is a natural unit of electric charge.

- **Orbital Motion** of electrons around the nucleus: the elementary magnetic moment m can be represented by a tiny current loop with surface A and current I, of which the shape is unimportant provided the current flows in a plane $m = I \times A$ The order of magnitude of the Bohr magneton can be demonstrated with orbital motion in classical physics as done in Appendix A.2.

- **Intrinsic spin** is quantized in such a way that it can have just two possible orientations in a magnetic field, 'up' and 'down'. [17] The moment induced by spin equals one Bohr Magneton. The spin of the electron, and its associated magnetic moment, has to be accepted as a fact, consistent with wave mechanics.

The magnetic moment due to spin and that due to motion in the first Bohr orbit are exactly equal to the Bohr Magneton [32]. The total magnetic moment of an atom or molecule is the vector sum of all orbital and spin contributions: it is always a *quantization* of $\mathbf{m_B}$. This cannot be demonstrated with classical physics and requires *the addition of some Quantum Physics salt and pepper* as Walter Dewin famously said.[7]

In what follows, we introduce diamagnetism, paramagnetism and ferromagnetism. These are magnetic states of matter that are mainly linked to how electrons are distributed around the nucleus and how magnetic effects cancel each other out internally. The description of magnetism in solids is fundamentally different depending on whether the electrons are localised on ion cores, or delocalised in energy bands [33]. Magnetisation curves can significantly vary from the "ferromagnetic textbook example" given in Fig. 2.1: they give us some interesting ideas of the properties of the materials as illustrated in Fig. 2.2. These are characterised by susceptibility, corresponding to the slope of the magnetisation curve: $\chi = \mathrm{d}M/\mathrm{d}H$. Note that susceptibility as it is discussed here referes to "nearly DC" properties in the "linear range" (i.e. before approaching saturation).

[7] https://www.youtube.com/watch?v=u36QpPvEh2c

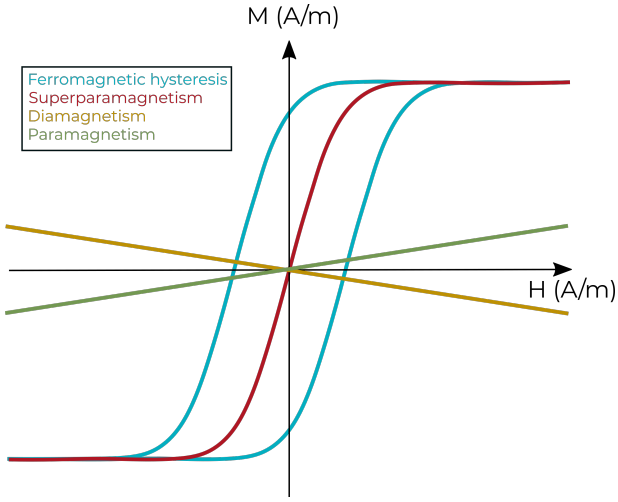


Fig. 2.2 Qualitative hysteresis curves for diamagnetic, ferromagnetic and paramagnetic materials, and for superparamagnetic behaviour. Note: paramagnetic materials saturate too but at external fields that are several orders of magnitude above the occurrence of ferromagnetic saturation.

2.2.2.1 Diamagnetism

Orbital moment is related to diamagnetism [33]. The induced moment within the material slightly opposes the external field. [8] This is a fundamental property of all materials, although sometimes overruled by other forms of magnetism, such as para- or ferromagnetism. Diamagnetism is the dominant susceptibility when there are no partially filled shells (unpaired spins) present that could generate a larger paramagnetic contribution [33]. Indeed, electrons which constitute a closed shell in an atom usually have their spin and orbital moments oriented so that the atom as a whole has no net moment. This is the case for mono-atomic gases (He, Ne) and most polyatomic gases and ionic solids (e.g. NaCl) since their molecule formation usually leads to filled electron shells. However not all gases are diamagnetic, nor are all ionic or covalent solids. Generalisations in this regard should be avoided[34]. One valid generalisation was found by Pierre Curie (°1859, France[9])

[8] This is again due to quantum-mechanical 'salt and pepper'. It is sometimes suggested as a 'intuition' that magnetic field would alter the motion of nanoparticles which in turn has an induced magnetic field opposing the initial change, as suggested by Lenz's Law. One should note it is *not* a correct vulgarisation since diamagnetism occurs without time-varying magnetic flux.

[9] Pierre Curie is a descendent of Jean Bernoulli. During his youth education is not yet compulsary in France, but qualitative home education is assured by his parents and tutors. Besides his works on magnetism, P. Curie is famous for the discovery of piezo-electricity with his brother, and his works on radio-activity with his wife M. Curie. The couple won the

who reported in 1895 that diamagnetic susceptibility is independent on temperature. [33]

2.2.2.2 Curie Paramagnetism described by Langevin and Weiss

Curie also observed that unlike diamagnetic materials, some paramagnetic materials do have a volume susceptibility χ_v $[-]$ which is inversely proportional to the absolute temperature and proportional on a constant C [K] (later called "the Curie Constant"). This observation is true for paramagnetic materials in which dipoles do not significantly interact with each other.

$$\chi_v = \frac{C}{T} \tag{2.10}$$

In 1905 Langevin (°1872, France[10]) theoretically explained Curie's observations. Qualitatively, a paramagnetic material is made up of atoms or molecules, each with a net magnetic moment, due to unbalanced spin and orbital contributions from electrons. Without an external magnetic field, these magnetic moments are randomly oriented by thermal agitation and cancel out, resulting in zero net magnetisation. When a magnetic field is applied, the atomic moments tend to align with this field. In the absence of any opposing influence, they would all orient in the field direction, and the material would develop a strong net magnetic moment. However, thermal agitation counteracts this tendency by keeping the moments disordered. As a result, only partial ordering is achieved, leading to a weak but positive magnetic susceptibility. As temperature increases, thermal fluctuations grow stronger, further disrupting this ordering and reducing the susceptibility, hence the inverse proportionality.

2.2.2.3 Curie Paramagnetism described by Langevin

Note: Langevin's model is also used to describe superparamagnetic behaviour, hence this section dedicated to its origin observation in paramagnetic materials.

Consider an external field $\mathbf{H}$, ϕ the angle between an atomic moment and the external field and a unit volume of material containing n atoms, each having an atomic moment $\mathbf{m}$. Each magnetic moment has a certain potentiel energy E_p

$$E_p = -\mathbf{m} \cdot \mathbf{H} \cos\phi \tag{2.11}$$

Physics Nobel Prize in 1903. Their two daughters would also win a prestigious Nobel Prize: Irène Curie would win the Chemistry Nobel Prize in 1935 for her works on radio-activity while Eve Curie wins the Peace Nobel Prize in 1965 as director of UNICEF.

[10] Paul Langevin was a friend of P.Curie and it is while returning from a diner with Langevin that Curie would die in traffic in 1906. Known for major contributions in the domains of magnetism and relativity, he's also famous for strong political opinions. In 1898 he's a signatory of the petition to exonerate Alfred Dreyfus. After the First World War he advocates for the social responsibility of scientists. From 1944 to 1946 he's president of the French Human Rights Liga.

In a state of thermal equilibrium at temperature T [K], the probability of an atom having an energy E_p is proportional to the Boltzmann factor $e^{\frac{-E_p}{k_B T}}$ with k_B the Boltzmann constant $k_B = 1.380649 \cdot 10^{-23} \left[\frac{\text{J}}{\text{K}}\right]$. The total magnetic moment in the direction of the field acquired by the unit volume, thus the magnetisation $\mathbf{M}$, is

$$\mathbf{M} = \int_0^n \mathbf{m} \cos\phi dn \tag{2.12}$$

with dn with number of moments between ϕ and $\phi + d\phi$. The maximum possible moment the material can have, corresponding to a perfect alignment of all n moments $\mathbf{m}$, is $\mathbf{M_s} = n\mathbf{m}$.

The Langevin function expresses that

$$\frac{M}{M_s} = \coth\xi - \frac{1}{\xi} \tag{2.13}$$

with $\xi = \frac{\mu_0 \mathbf{m} H}{k_B T}$.

For $\xi << 1$ this can be expressed as a Taylor series:

$$L(\xi) = \frac{\mathbf{M}}{\mathbf{M_s}} = \frac{1}{3}\xi - \frac{1}{45}\xi^3 + \frac{2}{945}\xi^5 - \frac{1}{4725}\xi^7 + ... \tag{2.14}$$

The number of atoms per unit volume $n = \frac{N\rho}{A}$ with N the number of Avogadro, ρ the density and A the atomic weight. It then follows that

$$\mathbf{M} = \frac{n\mathbf{m}\xi}{3} = \frac{n\mathbf{m}^2 H}{3k_B T} \tag{2.15}$$

$$\chi_v = \frac{M}{H} = \frac{n\mathbf{m}^2}{3k_B T} \tag{2.16}$$

$$= \frac{N\mathbf{m}^2}{3Ak_B T} \tag{2.17}$$

$$\tag{2.18}$$

This allows us to determine the Curie constant C for $\xi << 1$:

$$C = \frac{N\mathbf{m}^2}{3Ak_B} \tag{2.19}$$

$$\theta = \rho C \lambda \tag{2.20}$$

Two major conclusions can be drawn from Langevin's theory:

- When $\xi = \frac{\mu_0 \mathbf{m} \mathbf{H}}{k_B T}$ is large, $L(\xi)$ tends to 1. Physically, saturation occurs when the external field $\mathbf{H}$ is large enough or the temperature T is low enough.

- When $\xi << 1$ is, $L(\xi) \approx \xi/3$ and magnetisation M varies proportionally with $\mathbf{H}$ and $\frac{1}{T}$, thus confirming Curie's observation for this particular case.

2.2.2.4 Weiss' contribution

The aforementioned Langevin theory and Curie Law are based on the assumption that individual carriers of magnetic moment do not interact with each other. Their orientation is determined solely by thermal agitation and applied field. Many paramagnetic and ferromagnetic materials do not obey this condition. Curie's Law was therefore generalised by Pierre Weiss (°1865) as the Curie-Weiss Law:

$$\chi_m = \frac{C}{(T-\theta)} \tag{2.21}$$

with χ_m the mass susceptibility $\left[\frac{\mathrm{m}^3}{\mathrm{kg}}\right]$, C the Curie Constant $\left[\frac{\mathrm{Km}^3}{\mathrm{kg}}\right]$ and θ [K].

Weiss suggested in 1907 that these interactions could be expressed in terms of a fictitious internal field, the "molecular field" H_m, directly proportional to the magnetisation M through a constant λ: $H_m = \lambda M$. As a result, $\theta = \rho C \lambda$ is a measure of the strength of the interactions. It is important to note that this field is in no sense a real field; it is rather a force, which tends to align or misalign the atomic or molecular moments. The strength of this force depends on the amount of ordering already attained, because H_m is proportional to the magnetisation. [34]

For temperatures above the Curie temperature T_C, susceptibility often follows the Curie-Weiss Law:

$$\chi = \frac{C}{T - T_C} \tag{2.22}$$

where C is the Curie constant.

The magnetic response to an applied field of materials which do not order magnetically may be either paramagnetic or diamagnetic. In isotropic paramagnets, the induced magnetisation M is in the same direction as H, whereas in diamagnets it is in the opposite direction. [29]

2.2.2.5 Pauli Paramagnetism

Pauli paramagnetism is a magnetic phenomenon associated with delocalised electrons in metallic solids. It is derived from the free-electron model. Like Curie paramagnetism (originating from localised, noninteracting electrons), Pauli paramagnetism generates a small, positive magnetic susceptibility and materials lose their induced magnetisation immediately when the external field is removed. At room temperature, it is approximately two orders of magnitude smaller than the Curie susceptibility [33]. Unlike Curie paramagnetism, Pauli susceptibility is temperature independent to the first order [17]. This behaviour occurs in some 3d and 4d metals and alloys such as palladium (Pd). The temperature-independent nature of the induced magnetisation in palladium, as well as its high purity and stabil-

ity, make it a reliable calibration standard for magnetometers: this will be used for calibration of the MPMS measurements in Subsection A.5.3.2.

2.2.2.6 Ferromagnetism

Ferromagnetism is strongly related to the concept of molecular field $\mathbf{H_m}$ introdued by Weiss in 1906: this very strong internal field causes ferromagnetic materials to be self-saturated or "spontaneously magnetised". The origin of this molecular force would later be explained by Werner Heisenberg (°1901, German Empire[11]) as electrostatic in nature and originating from quantum mechanics. It is now known as exchange forces. These forces make the material saturated at all points, which is called **spontaneous magnetisation**, i.e. the inherent automatic alignment of atomic magnetic moments that occurs in ferro-and ferrimagnetic materials below the Curie temperature. They make it energetically favourable for adjacent atomic moments to align parallel to each other.

This poses a paradox: how can a ferromagnetic material have zero net magnetisation if it is spontaneously magnetised in all points? The answer lies in another hypothesis of Weiss, later confirmed experimentally: the domain hypothesis. Ferromagnetic material is composed of small regions called domains, each spontaneously magnetised to saturation in a specific direction. In the demagnetised state, the magnetic moments of these regions are oriented in different directions, resulting in zero net magnetisation for the entire specimen. Within each domain, the material is fully magnetised to its saturation value without requiring an external magnetic field. Once the material has been magnetised, it will have a net magnetic moment even with zero external field: the remanent magnetisation M_r. Their formation helps to minimise the total free energy of the system, particularly the magnetostatic energy. This is the fundamental cause for hysteresis observed in ferromagnetic materials.

Some materials, such as iron metal, can exist as either hard or soft magnets. Whether cubic iron is a hard or soft magnet depends on its crystal grain size. When crystal grains in iron are sub-micron size, and comparable to the size of the magnetic domains, the magnetic domains are pinned by crystal grain boundaries: a stronger coercive magnetic field needs to be applied to cause them to re-align. When iron is annealed, the crystal grains grow and the magnetic domains become more free to align with applied magnetic fields. This decreases the coercive field and the material becomes a soft magnet. The spontaneous magnetisation due to alignment of the atomic magnetic moments depends on temperature, and it falls

[11] Heisenberg is one of the founders of nowadays quantum mechanics. During the 1920's he was a student of Niels Bohr in Copenhagen. Interestingly, Heisenberg would work on the german atomic bomb during the Second World War while Bohr had fled the german occupation in Denmark and collaborated on the Manhattan Project in the USA.

precipitously to zero at the Curie temperature T_C. Above the Curie Temperature, a phase transition occurs and the materials becomes paramagnetic.

We distinguish two main types of ferromagnetism. Hard magnetic materials have broad, square $M(H)$ loops, while for soft magnetic materials these are narrow. The coercivity value determines stability of the remanent state and gives rise to the classification of magnets into hard magnetic materials (permanent magnets), semi-hard materials (storage media), and soft magnetic materials. The coercivity of magnetic samples has a strong dependence on their grain size. As the grain size decreases, the coercivity increases to maximum and then decreases. The change in coercivity is attributed to its change from the multidomain nature to single-domain superparamagnetic state; a further decrease in grain size results in an unstable state where spin fluctuations dominate [35].

2.2.3 The Energy Landscape of Magnetic Materials

The creation of domains occurs as a minimisation of the total free energy of the material.

2.2.3.1 Exchange Energy

The exchange constant $A\left[\frac{\mathrm{J}}{\mathrm{m}}\right]$ can be related to the Weiss constant θ of the molecular field theory introduced by Eq. 2.21. The molecular field $\mathbf{H_m}$ introduced by Weiss is proportional to the existing magnetisation $\mathbf{M}$ that aligns atomic moments. This molecular field is a phenomenological way of approximating the effect of the quantum-mechanical exchange interaction.

In bulk ferromagnetism, exchange energy is the dominant, active force that forces atomic spins to align. The competition between exchange energy and magnetostatic energy is the cause of domain formation.

In single-domain nanoparticles, the exchange energy is so strong within that tiny volume that it rigidly locks all the internal spins together, forcing the entire particle to act as one single "macro-spin," because it is a fixed, constant force.

2.2.3.2 Self-Energy or Magnetostatic Energy

In a single, uniformly magnetised ferromagnetic body, free magnetic poles form on the surfaces, creating a large external demagnetising field[12]. This field stores considerable magnetostatic energy. This is the major type of energy reduced by domain creation (opposing exchange energy which is increased by wall creation). The magnetostatic interactions are rather weak compared to the short-range exchange forces responsible for ferromagnetism, but they are important in ferromagnets

[12]This explains the classical U-shape for magnets: in that case, the demagnetising field does not run through the magnet. Historically, when hard alloys were not mastered industrially, this was the easiest way to maintain remanent magnetisation.

nonetheless because the domain structure and magnetisation process depends on them. It is the long-range nature of the dipole–dipole interaction, varying as r^{-3}, that allows these weak interactions to determine the magnetic microstructure [28].

Consider the demagnetising field $\mathbf{H_d}$ created by a magnet. The energy E_d of the demagnetising field is

$$E_d = -\frac{\mu_0}{2}\int_V \mathbf{M}\cdot\mathbf{H_d}dV \tag{2.23}$$

where V is the volume of the magnet and $\mathbf{M}$ the material's own magnetisation. Demagnetisation field occurs in para-, dia- and ferromagnetic materials but is mostly critical in the latter.

In single-domain nanoparticles, the concept is the same, but exactly like the exchange energy this is now a constant since the particle cannot form domains to reduce this energy. This energy now acts as a type of anisotropy, known as shape anisotropy.

2.2.3.3 Anisotropy Energy

Magnetic anisotropy refers to the phenomenon where the magnetic properties of a material depend on the direction in which they are measured. This means that it is easier to magnetise the material along certain crystallographic or geometric directions, known as "easy axes," and harder along others. The tendency for magnetisation to lie along an easy axis is quantitatively represented by the anisotropy energy density ($\mathcal{E}_a$), with the leading term often expressed as

$$\mathcal{E}_a = K\sin^2\phi\left[\frac{J}{m^3}\right] \tag{2.24}$$

where ϕ is the angle between the magnetisation and the easy axis, and K is the anisotropy constant. The total anisotropy constant is determined by different physical mechanisms:

- Magnetocrystalline Anisotropy is an intrinsic property of the material that dictates the preferred crystallographic directions for magnetisation[13]. Crys-

[13]Magnetocristalline anisotropy is mainly due to spin-orbit coupling. This coupling involves the interaction between the electron's spin and its orbital motion. The electron's orbit is strongly "fixed" to the crystal lattice (via orbit-lattice coupling). When an external field attempts to reorient the electron's spin, its orbit also tends to reorient, but this is resisted by the strong coupling to the lattice. The energy required to overcome this resistance to rotate the spin system away from an easy direction is the crystal anisotropy energy. It can also arise from the electrostatic interaction of electron orbitals with the crystal field and interatomic dipole-dipole interactions

tal anisotropy generally decreases with increasing temperature and vanishes at the Curie point [23].

- Stress anisotropy is an induced anisotropy that results from the interaction between mechanical stresses (applied or residual) and the magnetostriction of the material. For example, materials with positive magnetostriction under tension are easily magnetised in the direction of tension, while materials with negative magnetostriction under tension are harder to magnetise along the tension direction.
- Anisotropy induced by Thermal/Mechanical Treatments. These anisotropies are created by treatments like magnetic annealing, stress annealing, or plastic deformation. Unlike crystal anisotropy, they are not intrinsic properties.
- Shape anisotropy arises from the shape of the magnetic body. A nonspherical body is easier to magnetise along its long axis than along a short axis. It originates from the demagnetising field. Minimising this self-energy drives the preference for magnetisation along the long axis.
- Surface anisotropy occurs in thin films and nanoparticles. It primarily comes from the single-ion mechanism at the surface, where atoms experience a different crystal field due to their anisotropic surroundings (broken symmetry) compared to the bulk. It extends to the first few monolayers and can be significant enough to impose perpendicular magnetisation in very thin films. This will be further discussed in Section 2.3.

Additionally, exchange anisotropy arises in systems with intimate contact between ferromagnetic and antiferromagnetic materials but is out of scope for this work. Strong easy-axis anisotropy is a prerequisite for hard magnets, while near-zero anisotropy is required for soft magnets.

In the case of magnetic nanoparticles, it is more relevant to discuss anisotropy energy E_a than anisotropy energy density $\mathcal{E}_a$:

$$E_a = KV\sin^2\phi \tag{2.25}$$

2.2.3.4 Zeeman Energy

Zeeman[14] energy provides the main aligning force for magnetic moments placed in an external field.

[14]The dutch scientist Pieter Zeeman (°1865) submitted a detailed drawing and description of the aurora borealis above The Netherlands in 1883 and was published at the age of only 18. He studied in Delft and Leiden under supervision of Hendrik Lorentz. Zeeman and Lorentz closely collaborated on the effects of magnetic field on a light source. Both won the Physics Nobel Prize in 1902.

For a uniform external field, it is obtained by integrating the rotational work (Eq. 15) done by the **H**-field's torque over the angle (θ) between the magnetic moment and the magnetic field.

$$E_z = -\mu_0(\mathbf{m} \cdot \mathbf{H}) = -\mu_0 mH\cos(\theta) \tag{2.26}$$

Importantly, the minus sign states that the change in potential energy of the magnetic material is the negative of the work done by the field. Note that it is assumed that turning the moment has no effect either on its amplitude or on the **H** field.

If **H** is uniform, there is no net force on the magnetic moment, only a torque: the potential energy does not depend on its position. However, potential energy becomes position-dependent in non-uniform fields. This results in a force $\mathbf{F_z}$ which is the negative gradient of the potential energy:

$$\mathbf{F_z} = -\nabla E_z \tag{2.27}$$

$$= \mu_0 \nabla(\mathbf{m} \cdot \mathbf{H}) \tag{2.28}$$

The energy E_Z is minimised for a ferromagnet or paramagnet by $\mathbf{f_z}$ tending to pull the material into a region where the field is greatest, but a diamagnet is pushed out to a region where the field is smallest [28].

In paramagnetic materials, Zeeman energy competes with thermal energy to align atomic magnetic moments. An applied field acts to turn these moments towards its direction. The ratio of Zeeman energy to thermal energy dictates the degree of alignment, which in turn determines the material's magnetisation (described by the Langevin or Brillouin functions). In ferromagnetic materials, the applied field exerts a "pressure" on the walls, changing the Zeeman energy and causing the walls to move, which is a key part of the magnetisation process in low fields.

2.2.3.5 Thermal Energy

Thermal energy E_T [J] refers to the energy associated with the random motion and agitation of atoms, molecules, or spins within a material at a given temperature. It is defined as

$$E_T = k_B T \tag{2.29}$$

with k_B the Boltzmann constant $\approx$ 1.381 $\left[\frac{\mathrm{J}}{\mathrm{K}}\right]$.

In ferromagnetic materials, thermal energy directly opposes the alignment of atomic magnetic moments caused by exchange forces. It also plays a key role in the irreversible nature of domain wall motion by providing the necessary energy for domain walls or single-domain regions to surmount energy barriers (such as pinning sites or nucleation barriers), leading to sudden, discontinuous changes in magnetisation known as Barkhausen jumps. Above the Curie Temperature, thermal energy is high enough to lead to the collapse of spontaneous magnetisation, causing the transition to paramagnetic state where atomic moments experience random thermal fluctuations resulting in zero net magnetisation.

Energies	**Diamagnetism**	**Paramagnetism**		**Ferromagnetism**	
		Curie	Pauli	Soft	Hard
Exchange	/	/	/	Dominant	Dominant
Self-Energy	/	/	/	Important	Important
Anisotropy	/	/	/	Important	Dominant
Zeeman	Important	Dominant	Dominant	Important	Important
Thermal	/	Dominant	/	Important	Important

Table 2.2 Relative importance of different energy terms in bulk magnetic materials.

2.3 Magnetism: the Nano Material Story

While pure metal nanoparticles possess superior intrinsic magnetic properties that are highly desirable for applications like microwave absorption, their inherent instability due to oxidation necessitates the use of more stable metal oxide nanoparticles [24, 36].

2.3.1 Superparamagnetism: Ferromagnetic materials, paramagnetic behaviour

Superparamagnetism occurs in certain monodomain ferromagnetic nanoparticles (which have fixed magnetostatic and exchange energy), when the thermal energy exceeds the anisotropy barrier. Their behaviour becomes fundamentally different than the bulk counterpart. These phenomena were first documented by Louis Néel in 1949 and William Brown in 1963 [19]. The name 'superparamagnetism' was given by Bean and Livingston in 1959 [37]. In general single-domain particles are expected to be less than 1000 atoms in diameter. Most importantly, hysteresis

vanishes. Furthermore, they show specific behaviours such as surface spin canting, superspin glass behaviour and large surface anisotropies [38].

If the particle is smaller than the thickness of a domain wall, it cannot consist of two domains separated by a domain wall. Another way to approach the problem is to note that the total magnetostatic energy of a single domain particle of diameter D will vary as the particle volume, which is proportional to D^3, while the domain wall area and energy will vary as the cross-sectional area of the particle, which is proportional to D^2. If these are the only energies to consider, there must be a critical diameter D_c below which the single-domain state is favoured [39].

Fig. 2.3 illustrates the magnetic behaviour of the nanoparticles as a function of two critical diameters D_p and D_c.

- $D = D_p$: When nanoparticle size decreases, the 'competition' between different energies in the ferromagnetic material - responsible for domain creation- comes out of balance. An increasing proportion of the magnetic concent is located amidst a domain wall. When $D = D_p$, it reaches a comparable size to the walls average thickness, it is energetically more favourable to arrange as a single domain particle [24], thus D_p is the diameter above which poly-domain nanoparticles exist.

- $D_c < D < D_p$: The biggest monodomain magnetic nanoparticles exhibit higher coercive energies than their bulk counterparts. This is mainly due to the fact that energies required to reverse the spin orientation are usually larger than those needed to induce domain-wall movements. Higher applied magnetic fields are thus required to overcome the system anisotropy energy and perform such a rotation that moves the domain away from its easy magnetisation axis [24].

- $D = D_c$: If the nanoparticle diameter decreases even further, coercivity decreases rapidly to zero. The amount of exchange-coupled spins resisting spontaneous magnetic reorientation is decreased and the overall anisotropy energy drops. A critical volume is thus reached, below which thermal agitation overcomes the coercivity of the particle and switches its magnetic configuration intermittently [24].

When $D < D_c$, their magnetic anisotropy energy (proportional to the volume, cf Eq. 2.25) becomes so small that the thermal energy at room temperature is sufficient to overcome the energy barrier separating two opposite orientations of the magnetisation vector. As a result, these two orientations become equally probable and the net magnetisation, averaged over the observation time window, becomes zero in the absence of an external field. This null remanence resembles the

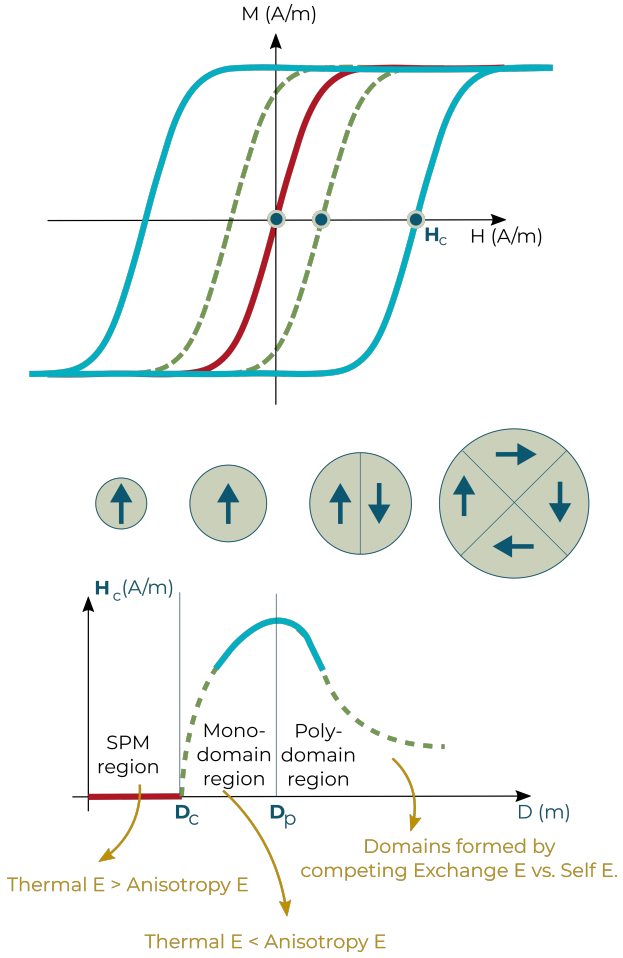


Fig. 2.3 SPM: superparamagnetism. Dc critical diameter for monodomain transition, Dp critical diameter for SPM behaviour. Adapted from [24].

paramagnetic state, but the nanomaterial retains the high saturation magnetisation characteristic of ferromagnets. If an external magnetic field is applied under these conditions, the magnetisation of single-domain nanoparticles follows, almost instantly, the field variations so that no hysteresis cycle can be observed. Likewise, the H_c values are null or close-to-zero. In fact, the system, from a magnetic point of view, displays paramagnetic behaviour.

Table 2.3 collects literature values of D_p and D_c for three ferrite compositions relevant to this work. The values depend on particle shape, crystallinity and, for D_c, on the measurement timescale; the ranges listed correspond to DC magnetometry conditions ($\tau_{\text{meas}} \approx 100$ s) at room temperature.

Material	$\mathbf{D_p}$ (nm)	$\mathbf{D_c}$ (nm)
Fe_3O_4	76–128 [40, 41]	25–30 [42, 43]
γ-Fe_2O_3	∼60 [44, 45]	10–15 [45]
$MnFe_2O_4$	*	∼15 [45]

* Not well established; the very low bulk K_m (Table 4.3) makes the single-domain/multi-domain boundary difficult to determine experimentally.

Table 2.3 Literature values of the critical diameters D_p (single-domain limit) and D_c (superparamagnetic limit at 300 K) for selected ferrites.

For magnetite, the superparamagnetic window ($D_c < D < D_p$) spans roughly 25 to 80 nm, leaving a broad single-domain but magnetically blocked regime that is further discussed in Chapter 7.

2.3.2 Key Concepts to superparamagnetism: Neel Relaxation, Easy Axis, Anisotropy and Blocking Temperature

In a single-domain particle, the magnetisation direction is naturally constrained to lie along one or more easy axes, due to magnetic anisotropy. This anisotropy creates an anisotropy energy barrier $E_a = KV$ that prevents the magnetisation vector from freely rotating [44]. The magnitude of this energy barrier is proportional to the anisotropy constant $K\left[\frac{\text{J}}{\text{m}^3}\right]$ and the volume V of the particle, as illustrated in Fig. 2.4. Néel relaxation is the mechanism describing the spontaneous reversal (flipping) of the magnetic moment due to thermal agitation ($k_B T$). This thermal energy competes with the anisotropy energy barrier: the higher the thermal energy, the higher the chance that the magnetic moment can overcome the barrier. The characteristic time for this reversal process, the Néel relaxation time (τ_N) is described by the Neel-Arrhenius law:

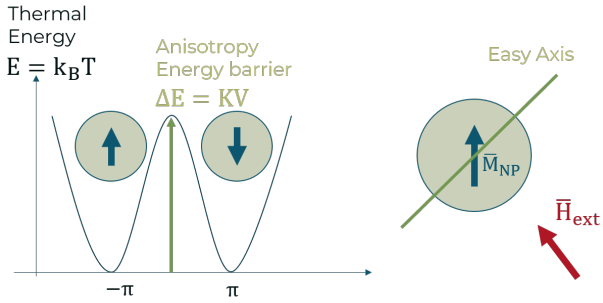


Fig. 2.4 Illustration of the energy landscape of a monodomain nanoparticle, dominated by anisotropy energy and thermal energy. When the thermal energy is higher than the anistotropy energy, it triggers spontaneous switching of the nanoparticle's magnetisation between two opposite orientations along the easy axis.

$$\tau_N = \tau_0 e^{\left(\frac{KV}{k_B T}\right)} \tag{2.30}$$

with k_B the Boltzmann constant and T the system temperature. Usually, the microscopic jump, or attempt time τ_0 is included in the following range $\approx \left[10^{-11}, 10^{-9}\right]$ [s] [29, 38, 46].

In practical conditions, the time interval in which the relaxation process is registered, known as the **measurement time (τ_{meas})**, determines the actual magnetic behaviour observed. The magnetic behaviour depends critically on how this relaxation time, τ_N, compares to τ_{meas}. This comparison defines two distinct regimes:

1. **Blocked State:** If the observation time is much shorter than the relaxation time ($\tau_{\text{meas}} \ll \tau_N$), the particle's magnetic moment will not have sufficient time to flip during the measurement. From the perspective of the experiment, its magnetism appears static or **"blocked"** [47].
2. **Superparamagnetic (SPM) State:** If the observation time is much longer than the relaxation time ($\tau_{\text{meas}} \gg \tau_N$), the magnetic moment will flip many times during the measurement. The particle is classed as superparamagnetic, as thermal fluctuations are large enough to cause the time-averaged magnetisation to be zero in the absence of an external field [47]

The **blocking temperature (T_B)** is the temperature that marks the transition between these two behaviours. It is formally defined as the temperature at which the average time for the magnetic moment to escape its energy well is equal to the

characteristic measurement time. This is the limit where the system has sufficient thermal energy to overcome the energy barrier, and it is expressed as:

$$\tau_{\text{meas}} = \tau_N = \tau_0 \exp\left(\frac{KV}{k_B T_B}\right) \tag{2.31}$$

$$T_B = \frac{KV}{k_B \ln\left(\frac{\tau_{\text{meas}}}{\tau_0}\right)} \tag{2.32}$$

This equation reveals a critical insight: the blocking temperature is not an intrinsic, fundamental property of the material. Its value explicitly **depends on the observation time (τ_{meas})** of the experimental technique. A faster measurement (smaller τ_{meas}) will yield a higher blocking temperature, while a slower one will yield a lower one. For instance, the same nanoparticles can be in the superparamagnetic state in static magnetisation experiments ($\tau_{\text{meas}} \approx 1$ s) and in the blocked state in Mössbauer spectroscopy measurements ($\tau_{\text{meas}} \approx 10^{-8}$ s) [24]. Therefore, the blocking temperature is **not a true thermodynamic constant**.

The concept of a single, sharp blocking temperature T_B is an idealization. The experimentally observed transition from a blocked to a superparamagnetic state occurs over a finite temperature width for two primary reasons. First, the Néel relaxation process itself is stochastic; τ_N represents a statistical average of a random, thermally-driven process, meaning the switch is inherently probabilistic [48]. Second, any real-world sample consists of an ensemble of particles with a statistical distribution of volumes (V) and anisotropy energies (K). Since T_B is directly proportional to the energy barrier KV, this spread in particle properties results in a corresponding distribution of blocking temperatures, which manifests as a broad transition.

In practice, this distribution implies that at any given temperature below the maximum blocking temperature of the ensemble, a fraction of particles is blocked while the remainder is superparamagnetic. The temperature above which *all* particles in the ensemble are superparamagnetic, i.e. the upper bound of the blocking temperature distribution, is called the irreversibility temperature T_{irr}. It corresponds to the blocking temperature of the largest (or most strongly interacting) particles. The gap $\Delta T = T_{\text{irr}} - T_B$ therefore provides a qualitative measure of the width of the energy barrier distribution: a narrow gap indicates a uniform ensemble, while a large gap points to a broad size or interaction distribution [48, 49]. Its experimental determination via FC-ZFC measurements is discussed in Section 4.4.1.3.

The most important simplification underlying Neel's solution is based on the

formal separation between non-switching and switching processes. The Shliomis-Stephanov-Raikher model takes into account the effects of the thermal energy and provides a solution for the linear susceptibility of isolated, uniaxial particles, which is valid over the entire range of temperatures [50]. Further study of this is out of scope for this work.

2.3.2.1 Deriving The Anisotropy Constant

Traditionally the following equation is used to determine the effective anisotropy constant K_{eff} from the blocking temperature:

$$K_{\text{eff}} = \frac{\ln(\tau_{\text{meas}}/\tau_0)\, k_B T_B}{V} \approx \frac{25\, k_B T_B}{V} \tag{2.33}$$

with V the volume corresponding to the magnetic diameter D_{mag}, and the numerical factor $25 \approx \ln(100\,\text{s}/10^{-9}\,\text{s})$ valid for DC magnetometry ($\tau_{\text{meas}} \approx 100\,\text{s}$, $\tau_0 \approx 10^{-9}\,\text{s}$) [39, 51]. The commonly cited factor of "25" arises directly from this logarithmic term by assuming standard DC magnetometry conditions for measurement time $t_m \approx 100$ s (a typical Vibrating Sample Magnetometer (VSM) or Superconducting Quantum Interference Device (SQUID) measurement time) and $\tau_0 \approx 10^{-9}$ s. This substitution yields $\ln(100/10^{-9}) = \ln(10^{11}) \approx 25.3$, which is rounded to 25. Consequently, the approximation $K \approx 25kT_B/V$ is only valid for T_B values derived from these specific DC measurements. This "25" factor is invalid and should not be used for T_B values obtained from techniques with different characteristic times, such as AC susceptibility (where $t_m = 1/f$ and the factor is closer to 10–15) or Mossbauer spectroscopy (where $t_m \approx 10^{-8}$ s and the factor is ~ 2.3).

In [38] it was shown that MNP with diameters between 2.5 and 5.0 nm show a very large magnetic anisotropy, which decreases sharply when $D > 8$ nm with increasing size until reaching asymptotically the value of the bulk magnetite. The rapid increase of K_{eff} at small diameters is frequently observed in MNP and is attributed to the much larger magnetic anisotropy of the surface ions resulting from the broken symmetry. For nanoparticles smaller than 8nm, the following phenomenological expression determines the effective anisotropy constant K_{eff} by considering both volume anisotropy energy density K_{V} (which includes magnetocrystalline anisotropy K_{m} as well as strain and magnetoelastic contributions) and surface density of anisotropy energy K_{S} [38, 44, 52]

$$K_{\text{eff}} = K_{\text{V}} + (6\Phi/D)K_{\text{S}} \tag{2.34}$$

with $6\Phi/D$ the surface to volume ratio, and $\Phi > 1$ expressing the deviation of a perfect sphere.[38]

2.3.2.2 Stoner-Wohlfarth Nanoparticles

Defining the total energy of superparamagnetic particles as a balance between their internal anisotropy energy (which wants to align the moment with the easy axis) and the Zeeman energy (from an external magnetic field, which tries to align the moment with the field), is the most simple way of analysing them and corresponds to the Stoner-Wohlfarth (SW) model (1948) [23].

It is important to keep in mind the three main assumptions which are made:

- **Single-Domain**: The particle is so small that it contains only one magnetic domain. All the atomic spins inside it act as a single "giant" magnetic moment.
- **Coherent Rotation**: When the magnetisation reverses, all the spins rotate together, in unison. A coherent process is one where the direction of magnetisation remains everywhere the same during reversal whereas an incoherent reversal process involves an intermediate state which is not uniformly magnetised.
- **Anisotropy**: The particle has a "preferred" magnetic direction, called an easy axis. It takes energy to point the magnetisation away from this axis.

The SW model considers 3 types of energies: Zeeman energy, anisotropy energy and demagnetisation energy (most often put under the denominator of shape anisotropy for superparamagnetic nanoparticles). Zeeman energy dictates the equilibrium direction of magnetisation relative to the field and contributes to coercivity and hysteresis (e.g. when in blocked state). Literature often refers to "SW nanoparticles" [53]: it is important to keep these fundamental underlying assumptions in mind.

2.3.3 Brownian and Effective Relaxation for SPNF Suspensions

For SPNF suspended in a liquid, two primary mechanisms allow the magnetic moment to relax, or return to equilibrium: the Néel relaxation introduced in the previous section, and Brownian relaxation.

When a time-varying external magnetic field is applied to a suspension of such nanoparticles, the field exerts a magnetic torque on each particle's magnetic moment, attempting to align it with the field direction. However, this rotation is opposed by a viscous drag torque exerted by the surrounding fluid medium, which resists the particle's motion. Brownian relaxation[15] is the mechanical process de-

[15] Brownian relaxation is not a separate concept from rotational Brownian motion but is the direct manifestation of its dynamics within a magnetic measurement.

scribing the interplay between the aligning magnetic torque and the retarding viscous drag from the nanoparticle carrier fluid [54]. The characteristic time for this physical rotation is the Brownian relaxation time, τ_B, derived from the rotational case of the Stokes-Einstein relation [46]:

$$\tau_B = \frac{3\eta V_H}{k_B T} \tag{2.35}$$

with η the dynamic viscosity of the fluid and V_H the **hydrodynamic volume** of the particle. V_H is a critical parameter, as it includes the magnetic core, any surface coatings (like polymers [55] or surfactants), a layer of solvent that moves with the particle [54, 56] but also aglomeration. Note that Brownian relaxation is fundamentally a mechanical process, independent from the magnetic nature of the nanoparticles (as opposed to Neel relaxation). The magnetic field provides a coherent, aligning torque, while the thermal energy continues to provide a randomizing influence, tending to disrupt this alignment. The viscous drag of the fluid determines how quickly the particle can respond to either of these torques [57].

Effective Relaxation and Size Dependence

Both Néel and Brownian relaxation are present simultaneously in a liquid suspension. Their main characteristics are summarised in table 2.4. The particle's magnetic moment will relax via the fastest available mechanism, following the "path of least resistance".[16] The combined effect of these two parallel pathways is described by the **effective relaxation time (τ_{eff})**:

$$\frac{1}{\tau_{\text{eff}}} = \frac{1}{\tau_N} + \frac{1}{\tau_B} \tag{2.36}$$

The dominant mechanism is determined by particle size, due to the different dependencies of τ_N and τ_B.

- τ_N depends **exponentially** on the magnetic core volume.
- τ_B depends **linearly** on the hydrodynamic volume.

This leads to a critical size threshold. For smaller nanoparticles (e.g., iron oxides with core diameters below 10-15 nm), τ_N is extremely short, making Néel relaxation the dominant process. As the core size increases, τ_N increases exponentially and becomes very long. τ_B also increases, but much more slowly. Consequently, for larger nanoparticles (e.g., core diameters above 15-20 nm), τ_B becomes shorter than τ_N, and Brownian relaxation becomes the dominant relaxation pathway. Fig. 2.5 offers a theoretical overview of relaxation time constants and frequencies for

[16] It is no coincidence that the equation determining effective relaxation time, is similar to the resulting resistance of two parallel resistances.

Feature	Brownian Relaxation (τ_B)	Néel Relaxation (τ_N)
What rotates?	The **entire particle** physically rotates in the fluid.	The **magnetic moment** flips *inside* the fixed particle.
Alignment Force	External field's torque.	External field's torque.
Opposing Force	**Viscous drag** from the fluid (driven by thermal motion).	**Anisotropy energy barrier (E_A)** within the crystal.
Role of Thermal E.	Causes **external collisions** (Brownian motion).	Provides **internal energy** to jump the barrier.
Effect of Field (H)	Provides an aligning torque that *competes with* thermal motion, suppressing random disorientation.	Field tilts the energy landscape, lowering the effective barrier (E_A) and accelerating the internal flip.
Depends on...	Fluid viscosity (η), Particle size (V_H).	Anisotropy (K), Magnetic volume (V_{mag}), Temperature (T).

Table 2.4 Comparison of Brownian and Néel Relaxation Mechanisms.

While both Neel and Brown relaxation are present in MNP suspended in liquid, the particle will relax (i.e. "return to equilibrium") according to the fastest mechanism (i.e. "the "path of least resistance").

Note that in [55] τ_N decreases by many orders of magnitude in the presence of a field (affecting the energy wells of nanoparticles). In contrast, τ_B is comparatively insensitive to the field strength. This has a critical consequence: a nanoparticle system that is strongly Brownian-dominant at zero field ($\tau_B \ll \tau_N$) can easily transition to being Néel-dominant when a strong operational field is applied, as τ_N plummets to become the shorter relaxation time. This insight is vital for material design: optimising a nanoparticle based on zero-field assumptions could lead to a device that fails to perform as expected under its intended operating conditions. However in this work, τ_B τ_N are measured within the linear response regime, thus when $\mu_0 m_{\text{NP}} H << k_B T$.

2.3.4 Describing DC Superparamagnetic Behaviour

2.3.4.1 DC susceptibility and Langevin Function

Note: the Langevin function shouldn't be confused with the Langevin Equation.

Magnetisation is thus a mesoscopic volumic average of dipole moments, the elementary magnetic quantity. The representation of the magnetisation of a solid by the quantity M(r) which varies smoothly on a mesoscopic scale is the continuous

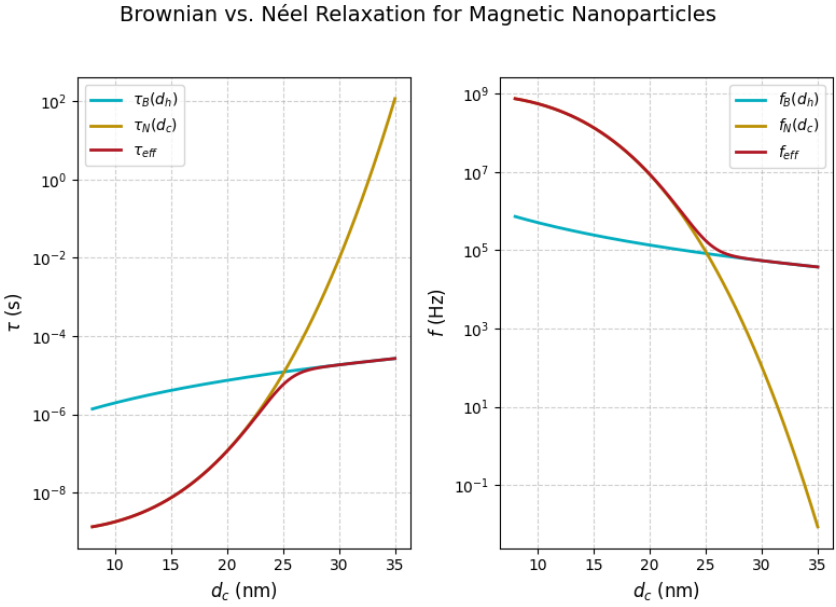


Fig. 2.5 Effective time constant and frequency equivalent over particle core diameter dc for a fixed shell of 4 nm thickness. The following constants have been considered: temperature $T = 300\ K$, attempt time $\tau_0 = 1e-9$, anisotropy constant relevant for magnetite 10nm particles $K = 4700\ J/m^3$, water viscosity $\eta = 0.89e-3\ Pa \cdot s$.

medium approximation. It is fundamental in magnetostatics. [28]. The concept of magnetisation of a ferromagnet is often extended to cover the macroscopic average over a sample.

$$M = \frac{\sum_i M_i V_i}{\sum_i V_i} \tag{2.37}$$

where M_i is the magnetisation of domain i and V_i its corresponding volume.

A single monodomain nanoparticle is at its saturation magnetisation since it consists of a ferromagnetic material. As a consequence, the average magnetic moment $\overline{m}$ $[10^{-3} A \cdot m^2]$ of a monodomain particle can be expressed as the saturation magnetisation M_s $[\frac{A}{m}]$ times the particle volume V_{NP}. Because only the core contributes to the magnetisation, one should consider the magnetic core volume V_{mag} determined by the magnetic diameter D_{mag} (explained in 2.3.7.1).

$$\overline{m_{\mathrm{NP}}} = M_s V_{\mathrm{mag}} \tag{2.38}$$

The $M(H)$ magnetisation curve of a set of non-interacting superparamagnetic nanoparticles in a ferrofluid can be described via the Langevin function $\mathcal{L}(\xi)$, which was introduced previously to model Curie paramagnetism in Section 2.2.2.3. This model predicts a characteristic S-shaped, nonlinear magnetisation curve that is completely reversible and shows no hysteresis [58, 59]. Note that this implies coherent rotation, as established by the Stoner-Wolhfarth model.

$$\mathcal{L}(\xi) = \frac{M(\xi)}{M_s} = \coth(\xi) - \frac{1}{\xi} \tag{2.39}$$

with ξ the ratio of magnetic energy $\mu_0 m_{\mathrm{NP}} H$ and thermal energy $k_B T$:

$$\xi = \frac{\mu_0 m_{\mathrm{NP}} H}{k_B T}$$

with m_{NP} $\left[\mathrm{A} \cdot \mathrm{m}^2\right]$ the magnetic moment of the nanoparticle and H $[\mathrm{A/m}]$ the intensity of the external magnetic field. As established in Subsection 2.2.2.2 this can be approximated by $\mathcal{L}(\xi) = \frac{\xi}{3}$. Considering no magnetic interaction between nanoparticles and substituting $m_{\mathrm{NP}} = M_s V_{\mathrm{mag}}$ (Eq. 2.38), the intrinsic susceptibility χ_i of a single superparamagnetic nanoparticle is [60]:

$$\chi_i = \frac{\mu_0 m_{\mathrm{NP}}^2}{3 k_B T} = \frac{\mu_0 M_s^2 V_{\mathrm{mag}}^2}{3 k_B T} \tag{2.40}$$

The initial susceptibility thus scales as V_{mag}^2: doubling the magnetic volume quadruples χ_i. In the low-field limit ($\xi \ll 1$), χ_i is inversely proportional to temperature by Taylor series approximation, following the Curie Law $\chi = C/T$ as developed in Section 2.2.2.2. This linearity means that the initial magnetisation curve of non-interacting SPNF does not exhibit an inflection point [61].

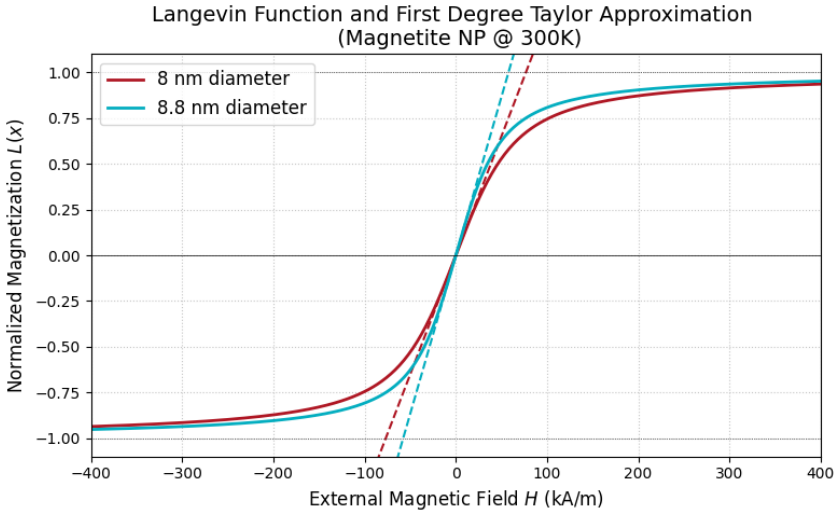


Fig. 2.6 Langevin function and first degree approximation as defined in Eq. 2.39 for nanoparticles of different diameter sizes with $M_s = 4.810^5 A/m$

Langevin function is dominantly a function of the particle's magnetic volume V_{mag}. Small magnetic cores possess a shallow magnetisation curve with large fields required to saturate the particles as illustrated in Fig. 2.6. With increasing core diameter the magnetisation curve becomes steeper and saturation is reached at moderate external fields [46]. Intuitively, it should be seen as follows: when the diameter is smaller, the magnetic energy $\mu_0 m_{NP} H$ within nanoparticle is smaller, it is thus more "tossed around" by thermal energy and needs a stronger external field to be aligned.

2.3.4.2 Chantrell's Equations

Using the low field and high field portions of the room temperature magnetisation curves, Chantrell's Equations [62] obtain the median magnetic diameter $\tilde{D}_{mag}$ of nanoparticles - given two hypothesis:

1. The MNP are non-interacting.
2. The size distribution is lognormal[17].

[17] While methods like Transmission Electron Microscopy (TEM) can directly measure size distribution, most other techniques, including static magnetisation measurements, rely on solving an inverse problem to obtain a core size distribution that would best match the measured signal. Assuming a predefined distribution function, such as the lognormal distribu-

For non-interacting nanoparticles with a polydisperse, moderately wide distribution, the dependence of the magnetisation on the field is:

$$M(H) = v_f M_s \int \mathcal{L}\left\{\frac{\mu_0 m_{\mathrm{NP}}(D) H}{k_B T}\right\} p(D,\gamma)\mathrm{d}D \tag{2.41}$$

with v_f the volume filling factor of the nanoparticles within the sample, $m_{\mathrm{NP}}(D)$ the magnetic moment of a particle with diameter D and $p(D,\gamma)$ the lognormal size distribution function [64]. This was first proposed by Chantrell in 1978 [62].

2.3.4.3 Temperature effect on DC Magnetisation Curves

The transition from the superparamagnetic to the blocked state can be observed in the temperature evolution of the hysteresis loop. Above the blocking temperature T_B, an ideal SPNFs system is characterized by a hysteresis-free, S-shaped curve with zero coercivity and remanence. As the temperature is lowered below T_B, thermal energy becomes insufficient to induce rapid magnetisation reversals against the anisotropy energy barrier. The magnetic moments become "blocked," and the system exhibits ferromagnetic-like behaviour, marked by the emergence of an open hysteresis loop with non-zero coercivity and remanence [44]. Bloch's Law completes Langevin: The thermal decrease of the magnetisation between 5 and 300 K can be fitted to a spin-wave-type dependence (Bloch law). This is out of scope for this work but the reader is redirected to [38, 65, 66] for further reference.

2.3.5 Describing (linear) AC Superparamagnetic Behaviour

Throughout this section we assume linear behaviour of the nanoparticles. This implies that no harmonics are considered during AC analysis. At AC excitation with strong external field, e.g. for Magnetic Particle Imaging (MPI), there harmonics become a cornerstone in the analysis.

The complex susceptibility is expressed as:

$$\chi(\omega) = \chi'(\omega) - i\chi''(\omega)$$

with $\chi'(\omega)$ the real (in-phase) component of the susceptibility, which represents the ability of the material to store magnetic energy ; and $\chi''(\omega)$ the imaginary (out-of-phase) component, which represents the dissipation of energy due to the relaxation processes.

tion, reduces the solution space to the variables of that function, simplifying the inverse problem. The log-normal distribution, specifically proposed by Chantrell et al., is a commonly assumed curve shape in this context [63].

2.3.5.1 The Ideal (Simple-Core) Debye Model

While Neel and Brown relaxation were introduced previously as linked to a single time constants, it should be noted that these are stochastic processes. The Neel and Brown time constants represent the average time it takes for relaxation to occur, i.e. the characteristic time-scale of the process. As soon as $\chi'' > 0$, relaxation is occurring and energy is being converted to heat (or "magnetically lost").

Consider the effective relaxation time τ_{eff} of a system (which could be either due to Neel, Brown or both as introduced in Eq. 2.36) and a measurement frequency ω:

- **Following** ($\omega \ll 1/\tau_{\text{eff}}$): the particles can reorient (relax) before the field changes much. The lag is small, so χ'' is small.
- **Lagging** ($\omega = 1/\tau_{\text{eff}}$): the field's frequency is perfectly matched to the particle's response time. The particles lag significantly and move (resonate) with a large amplitude, leading to the maximum possible friction and heat, the peak of χ''.
- **Freezing** ($\omega \gg 1/\tau_{\text{eff}}$): the particles do not have time to move at all before the field reverses. They are "frozen" in place. The amplitude of their motion is tiny, so the total energy loss χ'' is again small.

This is described by the Debye model for a system of non-interacting and identical dipoles. Because all dipoles are assumed to be uniform, their collective response is defined by a **single characteristic relaxation time**, τ_{eff}.

$$\chi(\omega) = \frac{\chi_0}{1 + j\omega\tau_{\text{eff}}} \tag{2.42}$$

$$\chi' = \frac{\chi_0}{1 + (\omega\tau_{\text{eff}})^2} \tag{2.43}$$

$$\chi'' = \frac{\omega\tau_{\text{eff}}}{1 + (\omega\tau_{\text{eff}})^2}\chi_0 \tag{2.44}$$

Here, χ_0 is the **static susceptibility**, or the total response in a static ($\omega = 0$) field. For non-interacting superparamagnetic particles, χ_0 is identical to the ensemble susceptibility derived from the Langevin low-field approximation (Eq. 2.40): both equal $n\mu_0 m_{\text{NP}}^2/(3k_BT)$, i.e. both scale as V_{mag}^2 per particle. We retain distinct symbols because χ_i is conventionally used in the DC magnetometry context, while χ_0 is the standard notation in Debye relaxation models. Fig. 2.7 illustrates a characteristic AC susceptibility plot for $\tau_{\text{eff}} = 10^{-5}$ and $\chi_0 = 1$.

This "simplified" Debye model is used e.g. in [31] to model the heat dissipation caused by the imaginary part of susceptibility of ferrofluids, and in [67] to study

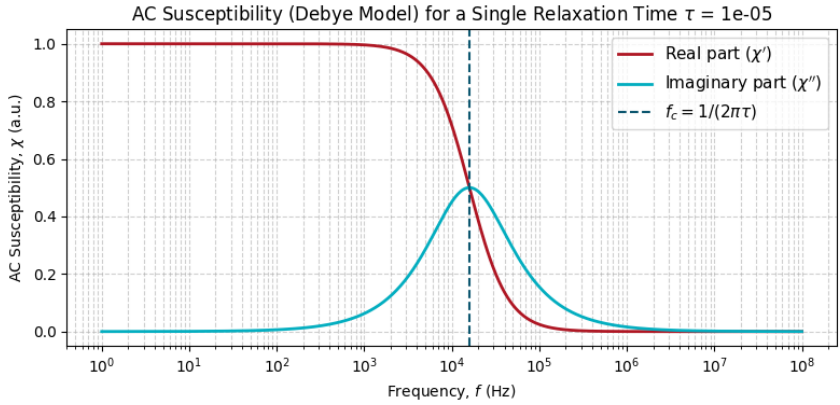


Fig. 2.7 Example of AC susceptibility according to Debye with a single relaxation time tau = 1e-5.

the correlation between AC susceptibility and external field strength, for 200nm nanomagnetic aggregates containing 10nm nanomagnetic cores.

2.3.5.2 The "real-world" Model assuming lognormal size distribution

Real systems contain a distribution of particle sizes and thus a spectrum of relaxation times. To model this, we must sum the contributions of all different particle sizes. The integral formula is the mathematical tool for this summation:

$$\chi(\omega) = C \int_0^\infty \frac{(D_{\text{mag}}/2)^6}{(1 + j\omega\tau_{\text{eff}}(D_{\text{mag}}, \delta))} p(D_{\text{mag}}, \gamma) \mathrm{d}D_{\text{mag}} + \chi_{\text{hf}} \tag{2.45}$$

Here, C is a coefficient that includes temperature, particle number density and intrinsic particle magnetisation. $p(D_{\text{mag}}, \gamma)$ is the **particle size distribution** (the fraction of particles with magnetic diameter D_{mag}). When fitting, the lognormal distribution is parametrised by its median $\tilde{D}_{\text{mag}}$ and shape factor γ. The term $\tau_{\text{eff}}(D_{\text{mag}}, \delta)$ is the **size-dependent relaxation time**, with δ the thickness of the hydrodynamic surface layer. The χ_{hf} term accounts for other high-frequency effects. Developing for the real and imaginary part gives:

$$\chi'(\omega) = C \int \frac{(D_{\text{mag}}/2)^6 \, p(D_{\text{mag}}, \gamma)}{1 + (\omega\tau_{\text{eff}}(D_{\text{mag}}, \delta))^2} \mathrm{d}D_{\text{mag}} + \chi_{\text{hf}} \tag{2.46}$$

$$\chi''(\omega) = -C \int \frac{\omega\tau_{\text{eff}}(D_{\text{mag}}, \delta) \, (D_{\text{mag}}/2)^6 \, p(D_{\text{mag}}, \gamma)}{1 + (\omega\tau_{\text{eff}}(D_{\text{mag}}, \delta))^2} \mathrm{d}D_{\text{mag}} \tag{2.47}$$

This model is used in e.g. [68] where monodisperse nanoparticles were charac-

terized over seven decades. Note that the static susceptibility χ_0 from the simple model is equivalent to the total result of the integral when $\omega = 0$:

$$\chi_0 = C \int_0^\infty (D_{\mathrm{mag}}/2)^6 \, p(D_{\mathrm{mag}}, \gamma) \mathrm{d}D_{\mathrm{mag}} \tag{2.48}$$

Note that δ does not appear in this expression: at DC, every particle has sufficient time to reach equilibrium, so the static susceptibility depends only on the magnetic moment (i.e. the magnetic volume), not on the hydrodynamic shell thickness that governs relaxation dynamics.

Model	What is correlated? What is expressed?	Conditions of Validity
Stoner-Wohlfarth	Correlates the magnetic energy of a particle with its orientation relative to its internal anisotropy axis and an external field. Expresses the critical field (H_{sw}) needed to flip the magnetization.	- Strictly at $T = 0$ K (no thermal energy). - Single-domain particle. - Coherent rotation (all spins flip together). - Uniaxial anisotropy. - No inter-particle interactions.
Langevin-Chantrell	Correlates the bulk magnetization of a nanoparticle assembly with the applied field (H) and temperature (T). Langevin Function expresses the characteristic S-shaped, non-hysteretic curve of superparamagnetism. Chantrell integrates over log-normal size-distribution.	- System is in the superparamagnetic state (i.e., above the blocking temperature, $T > T_B$). - Particles are non-interacting and show coherent roation. - The system is in thermal equilibrium. - Isotropic distribution of anisotropy axes. - $k_B T >> KV$, i.e. "unblocked" particles.
Néel-Arrhenius	Correlates the magnetic relaxation time (τ) with the energy barrier ($K_u V$) and temperature (T). Expresses the time it takes for a particle's moment to spontaneously flip due to thermal energy. This law defines the blocking temperature T_B. The Vogel-Fulcher law adds a T_0 term to account for inter-particle interactions.	- **Néel-Arrhenius:** Valid for non-interacting (or very weakly interacting) superparamagnetic particles. Assumes $K_u V \gg k_B T$. - **Vogel-Fulcher:** An empirical model used to describe systems with significant interactions (e.g., concentrated ferrofluids, spin glasses). T_0 is the "Vogel-Fulcher temperature," related to interaction strength.
Debye AC Susceptibility	Correlates the in-phase (χ') and out-of-phase (χ'') components of the magnetic response to the frequency (ω) of a small AC field. Expresses the energy dissipation (via χ'') and the characteristic relaxation time (τ) of the system.	- Linear response regime (AC field amplitude is very small). - System contains a single relaxation process (or can be modeled as such). - Valid for both Néel (internal) and Brownian (physical rotation) relaxation.

Table 2.5 Summary of Models for Magnetic Nanoparticle Behavior used later in this work.

2.3.6 Interactions between Magnetic Nanoparticles

For systems having strong inter-particle interactions, the parameters deduced from magnetic measurements such as the blocking temperature and saturation magnetisation can be strongly modified.

2.3.6.1 Exchange Interactions

Exchange interactions are short-range quantum mechanical interactions that tend to align neighboring magnetic moments. This interaction is responsible for ferromagnetism and the "molecular field" in Weiss' model. In the context of nanoparticles, this interaction can occur between atoms within the same nanoparticle. It can also occur between two nanoparticles in direct contact if their is atomic contact between surfaces [39, 69], i.e. if they form "aggregates". Cabreira-Gomes et al. [70] observed significant inter-particle exchange coupling for very small (5 nm) aggregated particles (i.e. grown together), confirming that this effect is tied to intimate surface contact rather than mere proximity. In this work, only agglomerated nanoparticles with core diameters above 5 nm are considered; inter-particle exchange coupling is therefore not expected to play a significant role and is not discussed further[18].

2.3.6.2 Dipolar Interactions

Dipolar interactions are magnetostatic forces that are dominant in systems of well-dispersed but concentrated nanoparticles [73]. They act as locally effective fields within the sample [74]. The strength of the dipolar interaction energy between two spherical particles E_{dd} can be estimated from the nanoparticle magnetic moment $\mathbf{m}_{\mathrm{NP}}$ and the centre-to-centre distance d [44]:

$$E_{dd} = (\mu_0/4\pi)(\mathbf{m}_{\mathrm{NP}}{}^2/d^3) \tag{2.49}$$

Because E_{dd} scales with m_{NP}^2 and therefore with V^2, dipolar interactions become rapidly more significant for larger particles at shorter separations. In the work of Demortiere et al. [38], dipolar interactions in powders are negligible for 5 nm particles but non-negligible for 9 nm particles: for the smaller ones, the moment per nanoparticle is small enough that the dipolar interaction energy remains negligible compared to the anisotropy barrier.

Interactions as an additional (uniaxial) contribution to K_{eff}: Dipolar interactions between neighbouring magnetic moments modify the energy landscape of

[18] For the sake of completeness: If nanoparticles have a core-shell structure, exchange interactions *can* occur at the interface between both materials. They promote strong parallel (ferromagnetic) or antiparallel (antiferromagnetic) alignment of spins across the interface [71, 72].

each particle, and no consensus exists as to how to account for this modification within existing models [69, 75–77].

The most widely used framework for incorporating interactions into the energy barrier is the Dormann–Bessais–Fiorani (DBF) model [75, 78, 79]. Within it, each particle experiences an effective interaction field from its neighbours, which raises its energy barrier. The corresponding interaction energy for particle i due to its nearest neighbours is approximated in a uniaxial form.

Qualitatively, the DBF model predicts that dipolar interactions *always raise* the energy barrier, and hence always increase the blocking temperature.

A subtle but important consequence affects τ_0: these interactions simultaneously steepen the Arrhenius slope (higher apparent barrier) and shift the intercept (lower apparent τ_0).

Regime dependence of interaction effects: Mørup et al. [69] raised a fundamental objection to the DBF model. The key distinction, which follows from the model's structure, is that anisotropy defines a preferred *axis*, whereas the interaction field defines a preferred *direction*: interactions not simply raise or lower the energy barrier height; they make the double-well potential *asymmetric*, creating two unequal minima with two different barrier heights for forward and reverse switching [69]). This qualitative change in the energy landscape cannot be captured by simply increasing K_{eff}. Two regimes are considered:

- **Weak dipolar interactions** can lower the effective energy barriers between the two magnetisation minima, resulting in *faster* superparamagnetic relaxation than predicted by the single-particle Néel–Arrhenius model. This has been observed in Mössbauer studies of maghemite (γ-Fe_2O_3) nanoparticles, where interacting samples showed enhanced relaxation compared to non-interacting ones [69].

- **Strong dipolar interactions** suppress superparamagnetic relaxation and can lead to collective magnetic ordering below a critical temperature $T_0 \approx E_{dd}/k_B$. The system then exhibits spin-glass-like dynamics (discussed in Section 2.3.6.3) or, when particles form chains, ferromagnetic alignment of the moments [69]. In DC magnetisation, this manifests as an increase of the apparent blocking temperature [38]. In practice, the strong-interaction regime approach developed by Morup et al. reconciles with the interaction-anisotropy approach of the DBF model.

Chosen convention in this work: Garcia-Acevedo et al. [80] propose a methodology for characterising changes in energy landscape by dipolar interactions based on controlled thickness shells (thus known E_{dd}). Morup et al. [69] instead suggest studying different concentrations. Both approaches are more precise than DBF, but more time-consuming and complex, and they do not yield a single scalar param-

eter that can be tracked across measurement techniques and sample configurations.

Since this work aims at comparing nanoparticle behaviour across fundamentally different measurement techniques (magnetisation, Field Cooled - Zero Field Cooled (FC-ZFC), ACS, impedance analysis) and sample configurations (powder, membrane, suspension), a consistent parameter is required. The interaction anisotropy approach from the DBF model is therefore adopted: K_{eff} serves as such a parameter, absorbing the set-up specific, average dipolar interaction contribution into a single effective constant. This allows direct comparison of the effective energy barrier from one technique or configuration to another. The validity of this approach, and the limitations it entails, will be discussed in due time.

2.3.6.3 Spin-Glass behaviour

The glass-like behaviour observed in ensembles of SPNF is referred to as superspin glass behaviour. This collective magnetic state arises when inter-particle dipolar interactions are sufficiently strong to overcome the individual anisotropy energy barriers, coupling the particle moments into a frustrated, disordered configuration [38, 44]. AC susceptibility measurements are particularly suited to distinguish superspin glass dynamics from simple superparamagnetic blocking, as the frequency dependence of the peak temperature differs qualitatively between both cases [69]. This distinction is revisited in the context of the Mydosh parameter in Chapter 4.

2.3.7 Peculiarities of SPNF

2.3.7.1 Magnetic Diameter and Spin Canting

Different methods can be used to determine the sizes characterizing nanoparticles. However, "size" is an ambiguous concept. First, it can define different parts of the nanoparticle: the crystalline part of the core, the whole iron core (crystalline and amorphous), the core, the shell, and the hydrated layer, or even a size with no geometrical meaning on the particle but just a physical meaning. Second, in almost all cases, nanoparticles are polydisperse. [58]

The concept of magnetic diameter is introduced in [81] based on the works of Chantrell et al. [62]

Unlike bulk materials, nanoparticle material properties are very sensitive to surface properties, due to their significant surface/volume ratio. Surface effects can lead to a decrease of the magnetisation of small particles, for instance oxide nanoparticles, with respect to the bulk value. This reduction has been associated with different mechanisms, such as the existence of a magnetically dead layer on the particle=s surface, the existence of canted spins, or the existence of a spin-glass-like behaviour of the surface spins. [82]

The **Dead Layer** is a surface phenomena which results from surface atoms having a different coordination and symmetry since they have fewer neighbours than

those at the heart of the particle. This disturbs the alignment of the spins and leads to a reduction in magnetisation of the MNP. Unni et al. propose to add molecular oxygen as one of the reactive species in the thermal decomposition to obtain similar physcial and magnetic diameter. distributions.[81]

The values of saturation magnetisation lower than those of bulk magnetite and maghemite were found to be related to this composition evolution and to the presence of oxidation defects, surface spin canting and volume spin canting as a function of NPs diameter. Small NPs presented mainly a surface spin canting. NPs with large sizes display Ms which depends on their oxidised shell thickness, defects and surface spin canting. NPs with intermediate sizes display a surface and in particular a volume spin canting due to a disordered structure induced by a perturbed oxidation state in these NPs[83].

In [38] demonstrated that a typical thickness for the shell is 1 nm in the case of iron oxide particles smaller than 15 nm. This is further discussed in Section 4.3.2.1. Independently, Kahmann and Ludwig confirmed this effect by comparing the effective magnetic moment obtained from AC susceptibility with the geometric particle volume from TEM: the resulting saturation magnetisation values fall well below bulk references for both single-core and multi-core iron oxide systems [84].

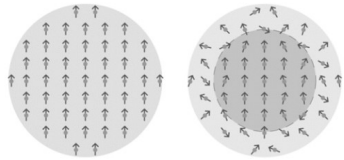


Fig. 2.8 Illustration of the dead layer in Magnetic Nanoparticles, from [24].

2.3.7.2 Verwey Transition in Nanoparticles

Zooming out to bulk magnetite:

In 1939, E.J.W. Verwey reported a remarkable and abrupt phenomenon in magnetite: upon cooling, its electrical conductance dropped discontinuously by two orders of magnitude below a critical temperature, subsequently named the verwey temperature [85]. This drop signifies a transition from a relatively conductive state at higher temperatures to an insulating state at lower temperatures. This change in electrical properties is correlated with changes in lattice symmetry and magnetic properties.

In bulk magnetite, the Verwey Transition (VT) is a well-established phenomenon with a Verwey temperature of approximately 120-125 K for stoichio-

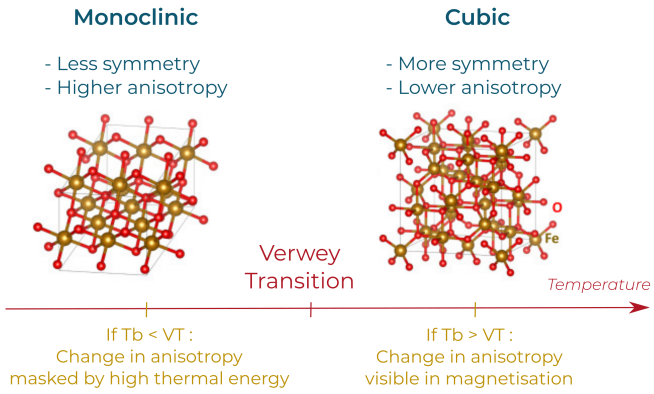


Fig. 2.9 Adapted from [94]: Illustration of lattice change in Fe_3O_4 caused by the Verwey Transition and coexistence with blocking temperature for superparamagnetic mangetite nanoparticles.

metric crystals [86–88]. When temperature drops below that point, the crystal structure transforms from cubic to a lower-symmetry phase as shown in Fig. 2.9[19] [85, 89, 90]. This lower-symmetry lattice implies an increase in K_m [91, 92], thus the magnetite becomes significantly magnetically harder, resulting in a large increase in coercivity and remanent magnetisation when T < VT [87, 93]. The VT is highly sensitive to the stoichiometry of magnetite: oxidation can suppress VT to lower temperatures and broaden the transition [89, 90].

Zooming back in to magnetite nanoparticles:

The Verwey transition can also occur in nanomaterials, though its manifestation is often size- and shape-dependent, and can be influenced by surface effects and interparticle interactions. Surface spin disorder, surface oxide layers, and oxygen vacancies contribute to non-stoichiometry in nanoparticles, which can suppress the Verwey transition [95]. On the other hand, shape control or surface functionalization (e.g. amine ligands) can improve surface coordination and preserve stoichiometry, enabling the transition in smaller particles [92].

The Superparamagnetism (SPM) behaviour of nanomaterials and anisotropy are intrinsically linked. When K_m increases at temperatures below VT, the effects

[19] In simple terms... In magnetite lattice, both Fe^{2+} and Fe^{3+} are present. Well above the Verwey Temperature, the lattice is in a cubic phase with rapidly hopping additional electrons (from Fe^{2+}) that create an averaged symmetric arrangement. When the electrons "slow down" due to temperature decrease, they group into a fixed order of Fe^{2+} and Fe^{3+} ions, creating a new 'landscape' of electrostatic forces and breaking the aforementioned symmetry. The old cubic structure is no longer the lowest energy state, causing a shift in atom positions.

on the superparamagnetic behaviour depend on the blocking temperature.

- *When TV > Tb:* the magnetic signature of the Verwey transition can be smeared or suppressed. This happens because thermal energy is still high enough to cause strong magnetic fluctuations and overcome the anisotropy barrier even at VT, preventing the clear manifestation of the magnetic easy axis switching associated with the Verwey transition [91].
- *When TV < Tb:* the Verwey transition can be sharply defined [92]. In such cases, the magnetic moments are already "blocked" against thermal fluctuations before VT is reached, allowing the anisotropy changes at TV to be clearly observed. This can happen e.g. when shape anisotropy is high or in assemblies of nanoparticles, such as magnetosome chains [91].

2.4 Magnetic nanoparticles in biomedical applications

Biosensing is not the only field in which an interest for SPION exists. The small size, zero H_c, and large M_s make SPNF useful for both in vivo and in vitro biomedical applications [18]. These can broadly be divided into *in vivo* applications, where the nanoparticles are introduced into the body (targeted drug delivery, MRI contrast enhancement, magnetic hyperthermia therapy), and *in vitro* applications, where they are used outside the body for diagnostic purposes (biosensing, bioseparation, magnetic relaxation-based detection) [9]. In all cases, two common requirements apply. First, the nanoparticles must exhibit superparamagnetic behaviour, ensuring zero remanence and preventing unwanted agglomeration once the external field is removed. Second, biocompatibility must be ensured. While bulk magnetite is generally considered non-toxic, at the nanoscale the cytotoxicity profile becomes strongly dependent on particle size, shape, surface coating, and dose [96]. Smaller particles present a higher surface-to-volume ratio that increases chemical and biological reactivity. Coating chemistry also plays a decisive role, as iron oxide nanoparticles coated with oleic acid or silica have been shown to exhibit lower cytotoxicity than PEG-coated counterparts at comparable diameters [96].

2.4.1 Biosensing Label

In biosensors, they can be efficient labels for biomolecules due to their tunable size and surface chemistry, and are used e.g. in quantitative immuno-sensors such as lateral flow assays (LFAs) whose best examples are pregnancy selftests. In Lateral Flow Assays, magnetic signals do not degrade significantly with time, and sense not only particles on the surface but in the whole volume of the test line [97]. With respect to other types of markers (radioactive, enzymes, fluorophores, luminescent, etc.), magnetic ones have many potential advantages: lower cost, higher stability (when oxidation is mastered) and low intrinsic toxicity of magnetite when

appropriately coated [96]. In the context of next-generation LFAs, magnetic readout offers two distinct quantification approaches: inductive sensing, where a coil interrogates the change in magnetic permeability at the test line, and magnetic particle quantification (MPQ), where a non-linear magnetic field alternating between two frequencies excites the nanoparticles and the resulting harmonics are recorded [7]. Both methods measure the signal generated in the entire test line volume rather than only at the surface, yielding wide dynamic ranges and superior performance in opaque or complex biological matrices where optical readout is hindered [7]. A broader perspective on how nanomaterials, including magnetic nanoparticles, are being integrated into LFAs to address challenges of sensitivity, multiplexing, and quantification at the point of care is provided by Sena-Torralba et al. [7] and Wang et al. [11].

2.4.2 Magnetic (cell) Separation

To improve the performances of biosensors, magnetism of SPIONS can be used for pre-concentration or separation of the target analyte from the biological fluid, increasing detection sensitivity and specificity [97]. This separation does have other applications. A key advantage for point-of-care applications is that magnetic fields penetrate non-magnetic materials (plastics, glass), enabling integration into closed, sterile microfluidic systems. For example, magnetic cell separation is a widely used *in vitro* technique for isolating target cell populations from heterogeneous biological samples [98]. The principle relies on magnetophoresis: cells are labelled with antibody-conjugated magnetic beads and a magnetic field gradient exerts a force on the labelled cells, selectively retaining them while unlabelled cells are washed away. The same principle applies beyond cells: surface-functionalised MNPs can selectively capture antibodies, DNA, proteins, or pathogens from complex biological fluids using an external permanent magnet [9, 98].

2.4.3 MRI Contrast Agents

MRI is one of the most established biomedical imaging techniques, generating images of tissues based on nuclear magnetic resonance. MNPs serve as contrast agents by creating local magnetic field gradients that disrupt the coherent precession of neighbouring water protons. Cross-linked iron oxide nanoparticles, consisting of a 3–5 nm monocrystalline iron oxide core coated with dextran, have been the standard magnetic contrast agent for research purposes [10]. Clinical and experimental MRI scanners operate with static fields of 1–11 T generated by superconducting magnets [9, 10]. Several iron oxide nanoparticle formulations have received regulatory approval for clinical use, including ferumoxytol (Feraheme®), a carboxymethyl-dextran-coated SPION with a $\sim$7 nm iron oxide core and 17–31 nm overall diameter, originally approved by the FDA for the treatment of iron deficiency anaemia but increasingly repurposed as an MRI contrast agent and cell

tracking probe [8]. Beyond standard anatomical imaging, MNPs have been explored for more specialised MRI applications. Champagne et al. [99, 100] reported that SPION agglomeration in solution could be modulated by the magnetic fields generated by neuronal tissue, suggesting a possible route to detecting brain activity via MRI. Pant et al. [101] have studied SPION for early-stage *in vivo* detection of osteoporosis.

2.4.4 MPI

MPI is a tracer-based imaging technique that visualises SPION concentration with no background signal from surrounding tissue [102]. It exploits the non-linear magnetisation of SPIONs, driving them into saturation rather than operating in the linear regime used by inductive biosensors. A static selection field with a strong gradient produces a field-free point (FFP) where SPIONs remain unsaturated, and a superimposed oscillating drive field rasters this FFP across the field of view [103]. Only SPIONs located at the instantaneous FFP respond to the drive field; their non-linear magnetisation generates higher harmonics of the drive frequency, which are picked up by a receive coil and correlated with the FFP trajectory to reconstruct a three-dimensional image. MPI performance depends strongly on nanoparticle properties: a narrow size distribution is essential [16, 68]. A small hysteresis loop raises the susceptibility in the transient region and improves the signal, provided that field and frequency remain low enough to avoid heating [46, 104]. Dual-frequency schemes, such as the 25 kHz/10 kHz approach of Viereck et al. [105], can further discriminate particle mobility for binding detection.

2.4.5 Targeted Drug Delivery

In targeted drug delivery, MNPs are functionalised with biocompatible coatings (PEG, SiO_2, PLA) and loaded with therapeutic agents, either within the particle structure or conjugated on the surface. An external magnetic field gradient is then used to guide the drug-loaded nanoparticles towards the target site, typically a tumour [9]. This approach focuses the drug at the lesion, reduces systemic side effects, and requires lower dosages compared to conventional chemotherapy. Drug release can be triggered by local conditions such as pH changes, enzymatic activity, or temperature elevation [9]. A core diameter in the range of 10–40 nm is generally employed, balancing magnetic responsiveness against the ability to cross capillary walls and maintain prolonged blood circulation [9]. High saturation magnetisation is essential to ensure effective magnetic guidance against the drag of blood flow. Further discussion of challenges and opportunities in magnetic drug delivery can be found in [106, 107].

2.4.6 Magnetic Hyperthermia Therapy

In magnetic hyperthermia therapy (MHT), MNPs act as thermal seeds: under a high-frequency alternating magnetic field (AMF), energy dissipation through Néel and Brownian relaxation losses heats the surrounding tissue. When the temperature of cancerous cells and tissues is raised to 42–45 °C, the cells undergo apoptosis; above 48 °C, necrosis (thermo-ablation) occurs, while healthy tissue is comparatively less affected [9]. MHT has gained significant clinical attention, with trials demonstrating its efficacy when combined with low-dose radiotherapy in the treatment of glioblastoma, pancreatic and prostate tumours [108].

The efficiency of heat dissipation is quantified by the specific absorption rate (SAR, in $\mathrm{W\,g^{-1}}$), which depends on the anisotropy, saturation magnetisation, particle size and shape, as well as the AMF parameters [9]. Reported operating conditions span AMF frequencies from 63 kHz to 1 MHz and field amplitudes from 4.5 to 65 kA/m, depending on the formulation and target tissue [9]. Néel and Brownian relaxation of the magnetic domains are the dominant contributors to local heating; to achieve high heating rates, neither mechanism should entirely dominate, as the interplay between the two determines the optimal operating point [31]. Smaller, superparamagnetic MNPs with high M_s and proper surface modification have been identified as the best candidates for MHT, with core diameters in the range of 8 to 34 nm reported across different studies [9]. Particle shape also plays a role: cubic nanoparticles and one-dimensional nanorods can outperform spheres owing to enhanced shape anisotropy [9]. Tackett et al. [109] show how Néel relaxation can be measured in frozen conditions (heat absorption), while Mehdaoui et al. [110] study optimal size properties for hyperthermia.

Chapter Summary

This chapter aimed to introduce the concepts, both variables and models, that will be applied throughout the rest of this thesis to describe the magnetic behaviour of superparamagnetic nanoferrites. The framework is built up from unit conventions and bulk magnetism, narrows to the nanoscale regime where superparamagnetism is defined, and closes with the broader context of biomedical applications in which SPNFs are used.

Unit conventions: Magnetism is a notable exception to the general adoption of the International System of Units (SI) system, with the CGS-Electromagnetic Units (emu) system still widely used in the literature. Unless specified otherwise, this work adopts SI units with the Sommerfeld convention, $\mathbf{B} = \mu_0(\mathbf{H} + \mathbf{M})$. Magnetisation M is expressed in A/m and the volume susceptibility χ is dimensionless.

Bulk magnetism: Ferromagnetic hysteresis is traced to irreversible domain wall motion within a multivalley energy landscape, and the area of the $M(H)$ loop quantifies hysteresis losses. Materials are classified as diamagnetic, paramagnetic or ferromagnetic depending on the competition between the principal energy contributions: exchange, magnetostatic (self) energy, anisotropy, Zeeman and thermal energy. Superparamagnetism is not a distinct class of matter but a behaviour occurring in ferromagnetic materials when the anisotropy energy approaches the thermal energy.

From bulk to nanoscale: Below a critical diameter D_c, nanoparticles become single-domain: the exchange energy rigidly locks the internal spins together and the particle behaves as a single macro-spin. The anisotropy barrier KV becomes comparable to the thermal energy k_BT, and thermal agitation can reverse the magnetisation along both directions of the easy axis. The resulting superparamagnetic state combines a high saturation magnetisation with zero remanence and coercivity above the blocking temperature T_B.

Relaxation mechanisms: Two relaxation mechanisms coexist. Néel relaxation (τ_N) describes the internal reversal of the magnetic moment over the anisotropy barrier and depends exponentially on the magnetic core volume. Brownian relaxation (τ_B) describes the physical rotation of the particle in the carrier fluid and depends linearly on the hydrodynamic volume. The effective relaxation time is governed by the faster of the two, which links the choice of characterisation technique to the particle property it actually probes.

DC and AC susceptibility models: The Langevin function describes the field-dependent magnetisation of non-interacting superparamagnetic parti-

cles, and the initial susceptibility scales as V_{mag}^2. For polydisperse samples, the Langevin function is integrated over a lognormal size distribution using Chantrell's equations. In the AC regime, the Debye model relates the complex susceptibility to the effective relaxation time, and is extended to a lognormal size distribution to describe real samples.

Interactions: Exchange interactions between nanoparticles are neglected in this work when agglomerates rather than aggregates are considered. Dipolar interactions modify the energy landscape of each particle. This work adopts the Dormann-Bessais-Fiorani (DBF) convention, in which dipolar interaction contribution is absorbed into an effective anisotropy constant K_{eff}. This allows energy barriers to be compared across measurement techniques and sample configurations without an explicit model of the dipolar field.

Biomedical context. SPNFs are used in a range of *in vivo* applications (MRI contrast agents, magnetic hyperthermia, targeted drug delivery) and *in vitro* applications (biosensing labels, magnetic separation, magnetic particle imaging). In all cases, two requirements generally apply: superparamagnetic behaviour to avoid permanent agglomeration once the external field is removed, and biocompatibility which at the nanoscale depends strongly on size, surface chemistry and dose.

Towards Parts I and II. The quantities introduced in this chapter, in particular M_s, K_{eff}, τ_N, τ_B, T_B, D_{mag} and χ_0, are applied throughout Parts I and II to interpret experimental results. Part I (Chapters 3 and 4) uses this framework to characterise nanoparticles in membrane and powder form with "traditional" equipment for magnetic characterisation, while Part II (Chapters 5 and 6) applies it to the design and interpretation of inductive detection experiments on LFA membranes and within aqueous media.

PART I
Nanoparticles : Synthesis and Properties

3

Superparamagnetic Nanoparticles : Synthesis, Coating and Structural Characterisation

The synthesis route of magnetic nanoparticles determines their size, size distribution, shape, crystallinity and surface chemistry, all of which influence their magnetic properties [51, 111] and, ultimately, their suitability for inductive biosensing on lateral flow assays. This chapter first establishes the methodology for measuring and comparing nanoparticle size distributions, with particular attention to the biases introduced by different measurement weightings and distribution models. Two synthesis routes are then presented. Thermal Decomposition (TD) is studied in detail: protocol parameters, their influence on the resulting size distribution and the repeatability across batches are discussed. CP samples, synthesised by collaborators from Universidad de Oviedo, are characterised in terms of size, morphology and elemental composition to verify that their properties are consistent with expectations from literature. The scope is the appropriation and characterisation of existing protocols rather than their optimisation. Finally, a reverse microemulsion silica coating is developed for the hydrophobic TD products as a step towards biocompatibility and biomolecule conjugation. The resulting nanoparticle library (Tables 3.4 and 3.5), spanning different compositions, sizes and surface chemistries, provides the material basis for the magnetic characterisation and inductive sensing experiments of Chapters 4 and 6.

3.1 Literature overview: Measuring and Comparing Size distributions of MNP batches

Properties of magnetic nanoparticles depend on their size. Characterising diameters within a batch of nanoparticles is essential to anticipate their behaviour within biosensing applications. Generally speaking, the narrower the size distribution of a batch, the more predictable and "sharp" their behaviour will be. Three main sources of bias exist in the evaluation and comparison of nanoparticle size distribution, which can significantly affect the corresponding estimated magnetic properties. For example, the Neel relaxation time $\tau_N \propto e^{\frac{KV}{k_b T}}$ (Eq. 2.30). Since $V \propto d^3$, bias in the estimation of average size can significantly increase the gap between the estimated and actual τ_N.

1. **Indirect measurement of different quantities**: the spatial resolution of optical microscopy is constrained by the wavelength of visible light (400–700 nm), rendering it unsuitable for observing features at the 10 nm scale. Consequently, nanoparticle characterisation requires X-Ray Diffraction (XRD) ($\lambda \approx$ 0.1–10 nm) or electron microscopy. These techniques are inherently indirect, as they measure physical interactions rather than providing direct visualisation, which can introduce systematic biases. E.g. the **crystallite size (D)**

measured by XRD is not necessarily the same as the particle size TEM. A single particle may be composed of multiple, smaller crystallites (a polycrystalline material). Moreover, the proximity of the magnetite and maghemite diffraction peaks makes phase distinction difficult by XRD alone [112].

2. **Polydispersity creates bias:** size dispersity can result in a several fold difference in the measured size when using different analytical techniques. Such variability in the measured size hampers the comparison of studies performed by different research groups, in particular when only one analytical technique is used to measure particle size [113]. The more the material is polydisperse, the more volume-weighted and intensity-weighted measurements will deviate from the number-weighted measurements. E.g. for polydisperse samples, volume-weighted XRD will obtain a higher average diameter than number-weighted Transmission Electron Microscopy (TEM) analysis.
3. **Approximative fitting models:** it is impossible to produce sets of particles which all have the exact same size, and their radii inevitably present some size distribution, which is typically log-normal (sometimes, normal) [18]. However, the fitting is never perfect. The less a distribution fits a lognormal distribution, the more incorrect the "theoretical correlation" between shape factor and standard deviation will be. Furthermore, mathematical/statistical concepts are sometimes (incorrectly) used and (incorrectly) compared to previously published values.

3.1.1 Indirect Measurement techniques

Table 1 Average diameter from TEM and XRD measurements: polydispersity–lattice parameter of iron oxide nanocrystals

$\langle D \rangle$ TEM/nm	σ (%)	$\langle D \rangle$ XRD/nm	a lattice/Å
14	20	12.8	8.389
11	15	10.3	8.372
9.0	11	8.3	8.365
5.0	07	5.1	8.361
3.5	08	3.7	8.360
2.5	09	3.1	8.360

Fig. 3.1 From [38]: difference between diameters obtained by TEM and DRX measurements; and corresponding variations.

In Fig. 3.1 from [38], discrepancies can arise between mean diameters $\langle D \rangle$ derived from TEM and XRD. The three larger samples correspond to a common case in literature, related to the fact that the physical diameter measured by TEM must, by definition, be greater than or equal to the crystallite size determined

by XRD. In the three smaller samples however, the diameter obtained by XRD is nevertheless larger than the TEM diameter. This can probably be explained by the statistical treatment of the data: XRD provides a volume-weighted average [114], whereas TEM typically yields a number-weighted average. Therefore, the presence of larger outliers within a polydisperse sample may result in a higher mean diameter for XRD [115]. The next section deepens the concepts of number and volume weighted distributions.

Generally speaking, measurement of nanoparticle sizes is indirect and based on different fundamental concepts: Dynamic Light Scattering (DLS) measures how light scattering through the solution is influenced by Brownian motion of the particles (dependent on their hydrodynamic diameter) [116], TEM measures how electrons are transmitted through the measured sample [117], and XRD depends on X-ray diffraction in crystal planes [58]. In theory, monodomain, monocrystal, spherical and non-agglomerated nanoparticles would result in similar TEM, DLS and XRD measurements. In practice, nanoparticles batches are rarely perfect, resulting in different sizes that cannot be easily compared.

3.1.2 Nanoparticle size distribution quantification

Method	Classification	Weighting	Signal Origin
XRD	Structural	Volume (d^3)	Diffracting crystalline material.
SEM/TEM	Structural	Number (d^0)	Direct imaging counts individual particles equally.
DLS	Structural	Intensity (${d_H}^6$)	Light scattering intensity is proportional to the sixth power of the hydrodynamic diameter d_H

Table 3.1 Classification and Weighting of Nanoparticle Characterisation Methods, based on [117].

3.1.2.1 Intensity, volume and number weighing

In this work, the size distribution of synthesis will be mainly characterised by TEM images, resulting in number-weighted contribution of all diameters to the representative diameter. Since monodispersity is a figure of merit for our synthesis protocol, we aim at comparing our measurements with size dispersities obtained in literature. Therefore, we also elaborate volume and intensity weighting in this section.

Nanoparticle sizes are often described as a "central value" with a standard deviation or other metric to describe distribution width. The raw data of DLS is proportional to the scattering intensity $\propto d_H^6$, resulting in an "intensity weighed" mean

diameter, with a practical limit for resolving bimodal distributions of a 2:1 to 3:1 size ratio [118], while XRD is $\propto d^3$ i.e. "mass weighted or volume weighted". As a result, different measurement techniques do not only measure different physical quantities, the extent to which larger nanoparticles dominate the signal will also differ, affecting the deduced mean diameter. This makes comparison more difficult.

A clear illustration is provided by Woodward et al. [119], who measured the same coprecipitation magnetite ferrofluid with three independent techniques. Number-weighted TEM yielded a mean diameter of 9.8 nm, while volume-weighted Langevin fitting and SANS gave 12.7 and 17.3 nm respectively. The discrepancy grows with distribution width: for a narrow thermal-decomposition sample, all three techniques converged to ∼3.7 nm. This confirms that weighting differences become practically negligible for monodisperse samples but can exceed 75 % for polydisperse ones. For any measurement type, conversions are often done to obtain either a number-weighed or volume-weighed size distribution [113]:

$$\text{Mean Number Diameter: } \mu(D_{1,0}) = \left(\frac{\sum n_i D_i}{\sum n_i}\right) \tag{3.1}$$

$$\text{Mean Volume Diameter: } \mu(D_{3,0}) = \left(\frac{\sum n_i D_i^3}{\sum n_i}\right)^{1/3} \tag{3.2}$$

where n_i is the number of particles in a given size class and D_i is the diameter of the particles in that size class. Mean-Volume Diameter answers the question "If the considered mass of nanoparticles was spread over identical spheres, what would the diameter of this sphere be?". The De Brouckère Mean (or Volume Moment Mean), $D[4,3] = \sum n_i D_i^4 / \sum n_i D_i^3$, answers the question “What is the average particle size when each particle’s contribution to the average is weighted by its volume (or mass)?” [120].

3.1.2.2 Additive and Multiplicative Measure of Spread

Fundamentally, two "syntaxes" exist to describe a distribution: additive and multiplicative spread of measure [121].

Additive spread: Additive spread characterises symmetric distributions, such as the Normal distribution, where variation is conceptualized as a fixed quantity added to or subtracted from a central point. The central tendency is measured by the arithmetic mean (μ), calculated as the sum of the observations divided by the count. The dispersion is quantified by the standard deviation (σ), which represents the typical deviation from the mean. For a sample of data $X_1, X_2, \ldots, X_n$, these are

defined as:

$$\text{Arithmetic Mean: } \mu(X) = \frac{1}{n}\sum_{i=1}^{n} X_i \tag{3.3}$$

$$\text{Standard Deviation: } \sigma(X) = \sqrt{\frac{1}{n-1}\sum_{i=1}^{n}(X_i - \mu(X))^2} \tag{3.4}$$

This framework is encapsulated in the interpretation of confidence intervals, where a range is described additively, such as $\mu(X) \pm \sigma(X)$ for approximately 68% of the data.

Multiplicative Spread: Conversely, multiplicative spread is characteristic of skewed, non-negative distributions, such as the lognormal, where variation is proportional to the magnitude of the data. The central point is best represented by the geometric mean (GM), which is the n-th root of the product of the observations. The dispersion is described by the unitless geometrical standard deviation (GSD), which is derived from the standard deviation of the natural logarithm of the data ($\sigma_{\ln}$). The formulas are:

$$\text{Geometric Mean: GM} = \left(\prod_{i=1}^{n} X_i\right)^{1/n} \tag{3.5}$$

$$\text{Geometrical Std. Dev.: GSD} = \exp\left(\sigma_{\ln}\right) \tag{3.6}$$

where $\sigma_{\ln}$ is the standard deviation of $\ln(X_1), \ldots, \ln(X_n)$. The GSD acts as a multiplicative factor, with the 68% confidence interval being defined by the range $\left[\frac{\text{GM}}{\text{GSD}}, \text{GM} \cdot \text{GSD}\right]$.

Multiplicative statistics are relevant in nanoparticle analysis because nanoparticle formation, via processes like aggregation or Oswald ripening (cf 3.2.1), **is inherently multiplicative**, leading to right-skewed, lognormal-like distributions (cf 3.1.3). However, additive concepts remain essential: standard deviation is an intuitive value for most scientists. While it is calculable for any definition, it is mostly interpretable and useful for symmetric and more precisely gaussian distributions. The less the distribution is symmetrical (e.g. lognormal distribution with pronounced right-skewness), the more the concept of standard deviation is misleading.

3.1.3 Multiplicative spread: The Lognormal Distribution

The main sources for this section are: [63, 121–124].

A continuous random variable X is said to be lognormally distributed if its natural logarithm $Y = \ln(X)$ is normally distributed: $Y \propto \mathcal{N}(\xi, \gamma^2)$ with ξ and γ

the mean and variance of Y (thus, the logarithm of the data and not the data itself!). The Probability Density Function (PDF) is

$$f(x;\xi,\gamma) = \frac{1}{x\gamma\sqrt{2\pi}} \exp\left(-\frac{(\ln(x)-\xi)^2}{2\gamma^2}\right) \quad \text{for } x > 0 \tag{3.7}$$

Key characteristics of this distribution are:

- Since a lognormal variable can never be zero or negative, the function is **only defined for** $x > 0$ (corresponding to the physical reality of size which cannot be negative)
- The lognormal distribution is always **skewed to the right**. Visually: it has a long tail extending towards very large positive values.

Two main parameters are:

- ξ the "location on the log-scale": when it increases, distribution shifts to the right and becomes more spread out
- γ the "shape factor": when it tends to zero, the distribution becomes more symmetric and resembles a normal distribution. When it increases, the distribution becomes more heavily skewed to the right. Note that when a data-series represents radii and those are doubled to be diameters, γ remains unchanged.

The mean $\mu(X)$, median $M(X)$ and variance $\sigma^2(X)$ (additive spread parameters) of a lognormal distribution are determined as follows:

$$\mu\,(X) = e^{\left(\xi+\frac{\gamma^2}{2}\right)} \tag{3.8}$$

$$M(X) = e^{\xi} \tag{3.9}$$

$$\sigma^2\,(X) = e^{(2\xi+\gamma^2)}(e^{\gamma^2}-1) \tag{3.10}$$

$$\sigma\,(X) = \mu\,(X)\,\sqrt{e^{\gamma^2-1}-1} \tag{3.11}$$

$$CV = \sqrt{e^{\gamma^2}-1} \tag{3.12}$$

$$\tag{3.13}$$

Three things are worth noting:

- The mean is always greater than the median, which is a typical indicator for right-skewness.
- The standard deviation $\sigma\,(X)$ of values that are lognormally distributed, is dependent on both the mean $\mu\,(X)$ and the lognormal shape factor $\gamma\,(Y)$

- For a lognormal distribution, the coefficient of variation (relative standard deviation) $CV = \frac{\sigma(X)}{\mu(X)}$ depends only on the shape factor

Due to the multiplicative nature of the lognormal spread, the link with multiplicative spread parameters is more straightforward:

$$GM = e^{\xi} \tag{3.14}$$

$$GSD = e^{\gamma} \tag{3.15}$$

Fig. 3.2 illustrates the effect of the shape factor γ on the difference between a lognormal distribution and a normal distribution with matching mean and standard deviation. For small values ($\gamma = 0.05$), both distributions are virtually indistinguishable, justifying the common practice of fitting nanoparticle size data to either model. As γ increases ($\gamma = 0.2$), the right-skewness of the lognormal becomes apparent and the mean shifts away from the median. For $\gamma = 0.5$, the discrepancy is pronounced: a normal fit would significantly misrepresent the tail of the distribution and underestimate the proportion of larger particles. This highlights why the choice of distribution model matters when reporting size dispersity, and why converting between lognormal and normal parameters (Eqs. 3.8 to 3.12) should only be trusted for small γ.

3.1.3.1 Fitting the distribution model

The Kolmogorov-Smirnov[1] (K-S) test is a non-parametric goodness-of-fit test. It expresses how probable it is that a collection of samples comes from a given probability distribution. It quantifies a distance between the empirical distribution function of the sample and the cumulative distribution function of the reference distribution. Performing such a test can avoid mistakes such as deriving a standard deviation σ from a shape factor γ which is obtained from an invalid lognormal fitting.

Importantly: the less a measured distribution fits the lognormal distribution, the less the conversion from lognormal to normal (eqn. 3.8 to 3.12) is valid.

3.1.3.2 Standard Deviation and Polydispersity Index

The Polydispersity Index (PDI) is a ubiquitous yet frequently misinterpreted parameter in the field of nanoparticle characterisation. While it is widely used as a figure of merit for the width of a particle size distribution, its physical origin is rooted in the dynamics of particle diffusion as measured by Dynamic Light Scattering (DLS).

[1] Andrey Kolmogorov (°1903) and Nikolai Smirnov (°1900) were Soviet Russian Mathematicians. While Kolmogorov is known as father of modern probability by laying the modern axiomatic foundation in a 1933 publication, he also contributed to the field of ecology and generalised the Lotka-Volterra model of predator-prey systems.

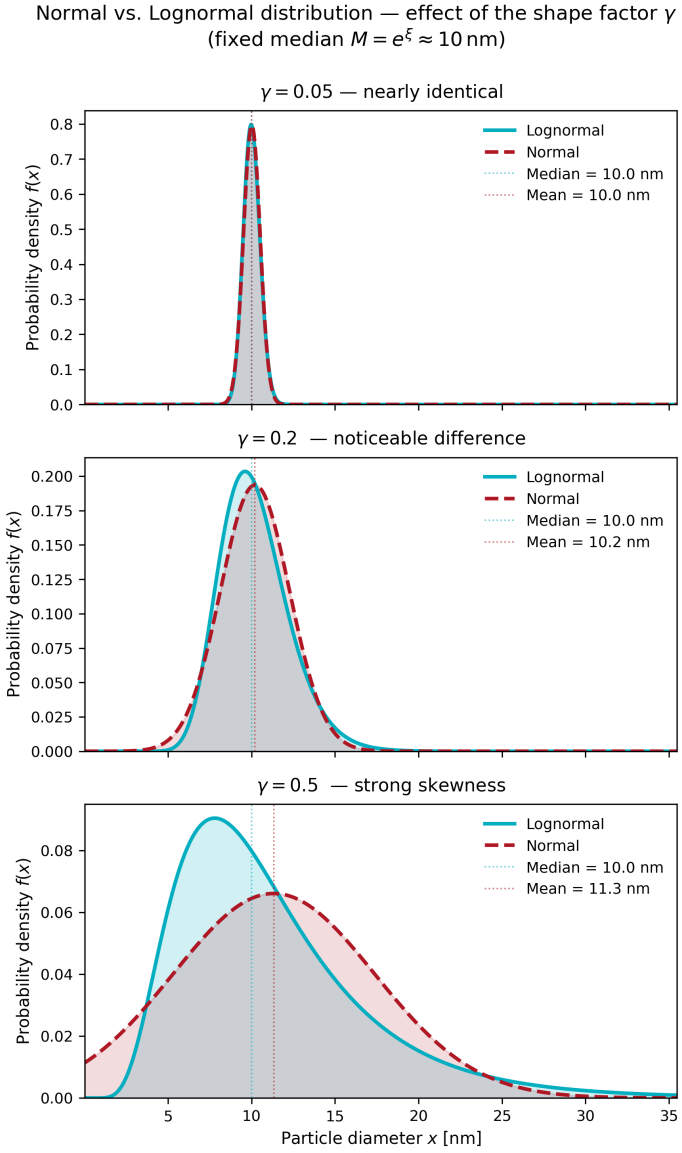


Fig. 3.2 Comparison of normal and lognormal distributions with matching mean and standard deviation, for three values of the shape factor γ. The fixed median is $M = e^{\xi} \approx 10\,\text{nm}$.

Actual (to the best of our knowledge) definition of PDI: While it is rarely recommended to compare PDI obtained with DLS and TEM [125], it is interesting to explain the mathematical link between these two concepts, leading to misinterpretation and confusion. The diffusion coefficient D_{eff} is inversely proportional to the hydrodynamic radius R_h via the Stokes-Einstein equation [116]. This makes the connection between the PDI of diffusion coefficients and the distribution of particle hydrodynamic sizes. **Thus a first important hypothesis when linking DLS metrics to TEM metrics is the fact that the nanoparticles are 'nearly perfect' spheres, implying their radii R are 'similar' to their hydrodynamic radii R_h.**

The effective mean diffusion coefficient D_{eff} is dependent on the intensity-weighed density function q (i.e. the distribution of diffusion coefficients):

$$D_{eff} = \int_0^\infty Dq(D)dD \tag{3.16}$$

Variance of the diffusion coefficient is given by:

$$Var(D) = \int_0^\infty (D - D_{eff})^2 q(D)dD \tag{3.17}$$

Polydispersity Index (PDI) describes the relative width of the distribution if normalised by D_{eff}^2. According to ISO 22412, it is given by [116]:

$$PDI = \frac{Var(D)}{D_{eff}^2} \tag{3.18}$$

It is a dimensionless quantity, typically ranging from 0.0 for a perfectly uniform (monodisperse) sample to 1.0, that describes the heterogeneity of the diffusional behaviour of the particles as observed by the DLS instrument. Note that some publications define the PDI differently [2].

Analysing size distribution we consider the constant $C = \frac{k_B T}{6\pi\eta}$. Furthermore, let's remember $Var(Cx) = C^2 Var(x)$. As a result,

[2] Publication [113] states "The polydispersity index is commonly reported to describe the width of the particle size distribution of a sample. This is obtained from the ratio of the weight average molecular weight to the number average molecular weight with values increasing from 1 as the polydispersity increases." This interpretation is also used in [126] where a PDI of 1.03 is associated with 'highly monodispersed' samples while a PDI of 1.09-1.3 is labelled as "polydisperse".

$$PDI = \frac{C^2 Var(\frac{1}{R_h})}{C^2 \langle \frac{1}{R_h} \rangle} = \frac{Var(\frac{1}{R_h})}{\langle \frac{1}{R_h} \rangle} \approx \frac{Var(\frac{1}{R})}{\langle \frac{1}{R} \rangle} \tag{3.19}$$

For **narrow distributions (second hypothesis)** the harmonic mean and the inverse of the arithmetic mean are close. One can state that $\langle \frac{1}{R} \rangle = \frac{1}{\langle R \rangle}$. Furthermore, applying Taylor expansions for the moments of functions of random variables:

$$Var\left(\frac{1}{R}\right) \approx \frac{Var(R)}{\langle R \rangle^4} \tag{3.20}$$

This approximation is also valid if and only if the size distribution is narrow, rendering higher-order terms negligible. Combining 3.19 and 3.20 yields:

$$PDI \approx \frac{Var(\frac{1}{R})}{\langle \frac{1}{R} \rangle} \approx \frac{Var(R)}{\langle R \rangle^2} = \left(\frac{\sigma}{\mu}\right)^2 \tag{3.21}$$

Consider a lognormal distribution. Based on Eqs. 3.8 and 3.10

$$PDI \approx \frac{\sigma^2}{\mu^2} = e^{\gamma^2} - 1 \tag{3.22}$$

The Taylor expansion is

$$e^{\gamma^2} \approx 1 + \gamma^2 + (higher\ order\ terms) \tag{3.23}$$

$$PDI \approx e^{\gamma^2} - 1 \approx \gamma^2 \tag{3.24}$$

It is important to keep in mind that the conversion between "shape factor" associated with PDI (and DLS measurements) and "standard distribution" associated with measuring nanoparticle sizes on TEM images, cannot always be done. **This is only valid when the distribution is only slightly skewed.** For $\gamma = 0.5$, $\gamma^2 = 0.25$, while $e^{\gamma^2} - 1 = 0.284$ which can already induce a significant difference. If one wishes to compare data, one should validate that the TEM size distribution fits a lognormal distribution, and then compare the lognormal figures of merit.

Another source of confusion lays in the parallel use of "polydispersity" and "polydispersity index". In [127] "polydispersity" corresponds to the shape factor of the lognormal distribution called γ in this work. This is actually the square root of what we call PDI.

3.1.4 How is a "monodisperse" synthesis defined?

In Table 3.2 different figures of merit for distribution width are listed, as well as their corresponding qualifications throughout literature.

Polydispersity Index (γ^2): The PDI of a monodisperse distribution is defined by $\gamma^2 < 0.05$ according to ISO 22412. Pazik et al. [130] use the term "uniform" for a synthesis which is not strictly monodisperse, i.e. with $\gamma^2 = 0.096$. While the ISO norm states that polydispersity occurs with $\gamma^2 > 0.7$, this term is already applied by Wulandari [131] for $\gamma^2 = 0.1$. When $\gamma \in [0.05,\ 0.7]$ qualifications such as "broad size distribution" can be used [130].

Polydispersity (γ): When distributions measured on TEM data are fitted to a lognormal distribution, "polydispersity γ" or "lognormal standard deviation" are commonly indicated. Both Roca [128] and Cavelius [129] indicate that $\gamma = 0.15$ correspond to "narrow size distribution". This is consistent with $\gamma^2 < 0.05$ but comparison should be done carefully: as explained in Subsection 3.1.2, small particles are more easily "overshadowed" in DLS measurements than in TEM measurements. Ribiero et al. compare synthesis batches and obtain $\gamma \in [0.2,\ 0.3]$ which they label as "repeatable distribution width". However, the higher boundary cannot be qualified as monodisperse while the lower could.

Coefficient of Variation (CV): Data from TEM images can also be fitted on normal distributions. The coefficient of variation (CV), i.e. relative standard deviation, is commonly used to quantify the distribution width, although no standardised name exists: in [132–134] is it called "PDI" (which is erronous according to the best of our knowledge) while [129] names it "dispersity". Assuming a small distribution, i.e. monodispersity, Eq. 3.12 states that $\gamma^2 < 0.05$ corresponds to $CV < 22\%$. This is consistent with the labels used by Balakrishnan, Sarifi, Unni, and Cavelius. Xu uses this indirectly by claiming monodispersity based on standard deviation (conversion is left to the reader). For polydispersity, no conversion can be made correctly between longormal and normal distributions since Eqs. 3.8 to 3.12 are only valid when γ is "small enough" (i.e. when linearisation by Taylor expression is valid).

Quality of the fitting: is not indicated in the aforementioned articles: the larger de spread, the more this matters. Throughout literature, it is quite arbitrary whether TEM data is fitted on lognormal parameters (γ) or normal parameters (CV). However, this has an impact on the interpretation of the "most occuring diameter" as shown in figure It would be good practice for authors to add the value of the K-S test, as explained in Subsection 3.1.3.1. Furthermore, no standard norm exists regarding the number of data points. The fewer the data points, the less failing to reject a lognormal fit actually confirms that the distribution truly is lognormal. Table 3.3 offers an overview of counts used in literature: it varies between 100 and 2000 data points.

Value	Interpretation (measurement method)	Reference
Polydispersity ($\gamma = \sqrt{PDI}$), i.e. "Logarithmic Standard Deviation"		
$\approx 15\%$	"Narrow size distribution" (TEM)	Roca et al. [128]
15%	"Narrow distribution" (TEM)	Cavelius et al. [129]
20% - 30%	Distribution width is not qualified but fit on lognormal spread to compare synthesis batches (TEM)	Ribeiro et al. [127]
Polydispersity Index (γ^2)		
< 0.05	"Monodisperse"	ISO 22412:2017 [117]
0.096	"Highly uniform" (DLS)	Pazik et al. [130]
0.247	"Broad size distribution" (DLS)	Pazik et al. [130]
0.1–0.4	"Moderately polydisperse" (DLS)	Wulandari et al. [131]
> 0.4–0.5	"Highly polydisperse (DLS)"	Wulandari et al. [131]
> 0.7	"Polydisperse"	ISO 22412:2017 [117]
Coefficient of Variation (CV, σ/μ)		
5%	"Highly Monodisperse" (TEM)	Balakrishnan et al. [132]
$<$ 7–8%	"Truly monodisperse" (TEM)	Sharifi et al. [133, 134]
10–19%	The variation between synthesis distributions is qualified as "similar" (TEM)	Unni et al. [81]
15%	"Narrow size distribution" (TEM)	Cavelius et al. [129]
32–65%	"Quite broad" magnetic diameter distribution (TEM)	Unni et al. [81]
40%	"Significantly polydisperse" (TEM)	Cavelius et al. [129]
Standard Deviation (σ)		
7 ± 0.5, 8 ± 0.4, 9 ± 0.6, 10 ± 0.8 nm	"Very narrow". Note that this corresponds to CV between 6.5 and 8 %. (TEM)	Xu et al. [135]

Note: Sharifi et al. [133] and Balakrishnan et al. [132] use the term "PDI" but apply the CV formula (σ/μ). In Cavelius et al. [129] the term "dispersity" is used, but the applied formula corresponds to CV.

Table 3.2 Nanoparticle size throughout literature (converted to metrics as defined in this chapter) and their interpretations

Count	Reference
Not specified[a]	Balakrishnan et al. [132], Sharifi et al. [133]
Not specified[b]	Park et al. [136]
100	Roca et al. [128], Guardia et al. [137]
300	Pichon & Baaziz [83]
500	Lin et al. [138]
600	Manuelli et al. [108]
600–1000	Belaid et al. [139]
900	Patsula et al. [126]
> 2000	Sharifi et al. [133, 140]

[a] TEM histograms with a.u. scales; mean and standard deviation communicated but not exact count
[b] Supplementary materials have "relative count" as y-axis but overshoot 100, we interpret this might be absolute count with erronous axes labeling.

Table 3.3 Number of nanoparticles counted for size distribution determination in TEM analysis

3.1.5 Materials and Methods: How size distribution is obtained in this work

In this work, TEM proved to be the most reliable technique for size characterisation: DLS measurements were performed but did not provide satisfying repeatability (despite attempts in standardising sonication time,...).

Diameters are often determined using tools such as ImageJ, allowing to "draw diameters and count their length according to a set scale".

- When nanoparticles are not perfect shapes, some 'interpretation' exists on the exact diameter. For example, in [133, 141], despite the fact that they are reported to be "faceted" or "polygonal", no clear metric exists as to how an average diameter is obtained. This is, however, far from negligible: for regular hexagons, the circumscribed radius R is over 15% larger than the inscribed radius r. For regular triangles $R = 2r$. For any triangle, $R \geq 2r$.

- Methods consisting of "drawing diameters" only approximately pass through the center, which can lead to accumulated bias.

We therefore developed a tool[3] of which the interface is shown in Fig. 3.3 that determines their shape using Bezier curves (splines) after identifiying four (or more depending on shape irregularity) points on the contour. This offers several advantages:

- Identifying the "average diameter" based on the surface of the shape, assuming a circle.
- The inscribed and outscribed circle is considered: comparing these diameters allows to identify batches with more irregular/polygonal shaped nanoparticles.

For logistical reasons, it was not possible to have the same amount of nanoparticle count on TEM images. However, care was taken not to count doubles (i.e. when the same ones occur on several images). The validity of a lognormal distribution is assessed with the Kolmogorov-Smirnov test mentioned in Subsection 3.1.3.1, applying a p-value ≤ 0.05 to reject the null hypothesis.

[3]Implementation of the tool was done with the kind help of Sebastien Janssens who knows the TKinter Python Packages by heart ;)

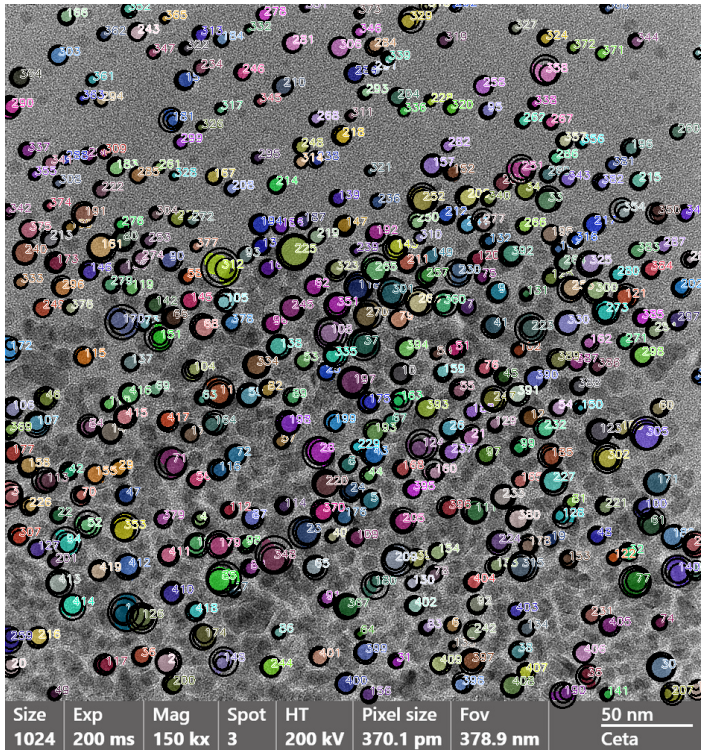


Fig. 3.3 Example of an analysed TEM image. Measuring nanoparticle diameter based on their surface. Determining the inscribed and circumscribed circle to validate the "roundness" of the nanoparticles.

3.2 MNP Synthesis by Thermal Decomposition

The main protocol used for thermal decomposition comes from [135] and includes oleylamine as surfactant. The principal questions we wish to address are :

> Given the small amount of nanoparticle yield per run, it is relevant to explore increasing reagent quantities. Are results significantly affected by doubling the reagents?
>
> Is the obtained size distribution monodisperse? Is lognormal fitting relevant and correct?
>
> How repeatable is the obtained median diameter and size distribution?
>
> What parameters of the synthesis protocol have most effect on median diameter and size distribution?

3.2.1 Thermal Decomposition of Iron Precursors : Literature Overview

3.2.1.1 Main Principles of Thermal Decomposition

TD is a non-aqueous, kinetically controlled process. It is one of the best synthesis procedures to obtain SPION with a narrow size dispersion, excellent size control, good cristallinity, and a higher saturation magnetisation [142]. However, the TD canonical route is rather limited to produce SPION with larger sizes (+/-12 nm), and generally they're not biocompatible. Another challenge of synthesis by thermal decomposition is the small amount of product, although progress is made to improve the yield and increase the reactant mass [12].

The synthesis principle relies on organometallic compounds (i.e. metal acetylacetonates, cupferronates) which are decomposed in high-boiling organic solvents containing stabilising surfactants (i.e. fatty acids, oleic acid, hexadecylamines). These molecules dynamically coordinate to the surface of the growing nanocrystals, mediating their growth and preventing agglomeration. The resulting nanoparticles are capped with a hydrophobic ligand shell, making them readily dispersable in non-polar organic solvents like hexane or toluene, but requiring subsequent surface modification steps to render them water-soluble for biological applications [142]. They can be made hydrophilic by e.g. ligand exchange [143]. The principle of the thermal decomposition process through nucleation can be interpreted by the LaMer model (1950) as summarised in Fig. 3.4. It has four main steps [144, 145] :

1. **Formation of Monomers:** An organometallic precursor is dissolved in a boiling organic solvent under the addition of surfactants. The dissolved

organometallic precursor liberates monomers which will later constitute the nanoparticles. The concentration of this monomers increases progressively in the solution. This process typically occurs between 180°C and 240°C depending on the precursor [130, 136]. Advanced in-situ characterisation techniques, such as small-angle X-ray scattering, have revealed that these monomers are not simple iron atoms or ions but are more complex intermediate species stabilised by the surfactant molecules [146].

2. **(Burst) nucleation:** When the concentration of monomers reaches a critical concentration (i.e. 'supersaturation' [147]) nucleation is triggered : monomers assemble themselves to form nanoparticle cores. This phase is ended as soon as the monomer concentration drops back below the critical point. Nucleation typically happens between 240°C and 280°C [83, 136]. By confining nucleation to a short time window, the method ensures that all particles are created with essentially the same size at essentially the same moment.
3. **Growth:** When the monomer concentration drops below the critical point, the formation of new nuclei is inhibited and existing nuclei start growing. The remaining monomers in the solution, along with those generated by the continued slow decomposition of the precursor, diffuse through the solvent to the surface of the existing nuclei and deposit onto them, causing the particles to grow in size [146]. Since all the nuclei were formed at approximately the same time, they essentially grow for the same duration under the same conditions of monomer concentration.
4. **Ostwald Ripening :** in this process, smaller particles, which have a higher surface energy and are thus less thermodynamically stable, tend to redissolve back into the solution. The monomers released from these dissolving small particles then deposit onto the surfaces of the larger, more stable particles [143]. The driving force behind this is the minimisation of total surface energy.

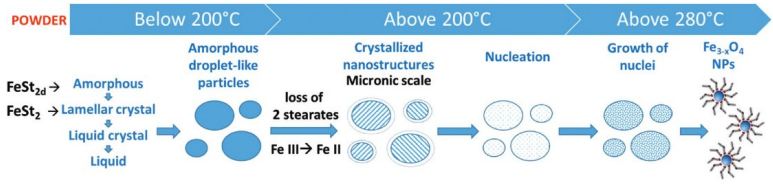


Fig. 3.4 Schematic example of LaMer nucleation for synthesis of iron oxide nanoparticles, starting with iron stearates as precursor.

The LaMer model implies that successful synthesis of monodisperse nanocrystals can be attributed to the effective separation of nucleation and growth processes,

which result from the different temperature dependence of nucleation and growth kinetics. Different improved models have been developed, considering for example continuous nucleation rather than burst nucleation, or competitive growth [144, 148, 149]. However, the basic LaMer model remains relevant for a conceptual understanding of the main phenomena occuring during TD. This model also highlights that the **surfactant has a double role**. On the one hand, it interferes in the kinetics of nucleation and growth by (a) confining the nuclei and limiting their growth ; or (b) influencing the stability of the iron precursor, affecting the decomposition temperature. On the other hand, it stabilises them and improves their colloidal stability [145]. Note that the LaMer approach to study nucleation and growth has also been duplicated to other metal oxides, such as Cu_2O in [149]. Alternatives to LaMer nucleation exist for decomposition of metal precursors, such as seed-mediated growth [150] and Finke's method [147]. These are not employed in this work; details are given in Appendix A.4.2.

3.2.1.2 Parameters Influencing Thermal Decomposition Products

In principle, the ratios of the starting reagents including organometallic compounds, surfactant, and solvent are the decisive parameters for the control of the size and morphology of magnetic nanoparticles. However, heating curve, reaction timeand aging period may also be crucial for the precise control of size and morphology [82]. While the method excels at producing small (<15 nm), highly uniform particles, extending this control to larger sizes (>20 nm) becomes progressively more challenging. To produce larger particles, one must either start with fewer nuclei or allow for a much longer growth phase. Both strategies can compromise the ideal separation of nucleation and growth. Longer reaction times at very high temperatures can introduce competing processes like uncontrolled Ostwald ripening, which, if not perfectly managed, can broaden the size distribution over time [151].

Precursor-to-Surfactant Ratio : The precursor-to-surfactant ratio is a commonly discussed parameter. Generally speaking, it is pointed that more surfactant relative to the precursor leads to smaller particles [117]. For example, in [29], the final particle size of iron oxide nanoparticles was observed to increase as the amount of oleic acid in the reaction medium was reduced. Specifically, using 1.4 g, 0.7 g, and 0 g of oleic acid yielded nanoparticles with approximate sizes of 8 nm, 12 nm, and 23 nm, respectively. However, the role of surfactant molecules is often complex : they actively participate by coordinating to the iron precursor, stabilising the intermediate monomer species, and dynamically binding to the different crystal facets of the growing nanoparticles. This modulation of surface energy and monomer accessibility controls both the nucleation barrier and the subsequent growth rate, ultimately dictating the final size [152]. Studies specifically focussing on the surfactant concentration identify an optimum [83], and map competing mechanisms. On the one hand, increased surfactant can stabilise intermediates and slow nucleation,

resulting in fewer nuclei that grow larger [83, 133, 153]. On the other hand, excess ligands can block growth sites or stabilise more nuclei, leading to smaller particles [126, 153]. Beyond the optimum, desorption of the surfactant from the nanoparticle surface can trigger uncontrolled growth and polydispersity [133]. A detailed breakdown of these competing mechanisms is given in Appendix A.4.3.

The precursor-to-surfactant ratio also significantly impacts the size distribution (polydispersity) of the nanoparticles [132, 151]. Too high or low ratios can lead to broader size distributions [139, 154]. Broadening of the size distribution can also be explained by processes like Ostwald ripening, where monomers redistribute from smaller to larger particles, which is facilitated at high oleic acid concentrations [154, 155], or a second nucleation[4] [154].

Type of Solvent : Solvents with higher boiling points enable higher reaction temperatures, influencing particle size [83, 136, 153, 156]. The nature of the solvent (and their polarity) also affects the stability and decomposition kinetics of the iron complex [83]. In [38] the nanoparticle yield is noted to be low when using solvents with low boiling points : only a part of the precursors is decomposed and then converted into nanocristals.

Reaction Temperature and Duration : The reaction temperature profile, including the reflux temperature and the ramp rate (the speed at which the temperature is increased), provides kinetic control.

Nucleation typically occurs at lower temperatures, initiated by the dissociation of weakly bound ligands from iron centers or the decomposition of the iron precursor, while particle growth occurs at higher temperatures through the dissociation of strongly bound ligands [132, 136, 153].

- For iron oleate complexes, nucleation can occur around 200–240°C, and major growth around 300°C [136].
- For iron stearate complexes, nucleation is observed in the 200–300°C range, with stable nuclei appearing around 280°C [145].

Growth rate is often increased when the reaction temperature is higher, leading to larger particles [83, 139, 143, 151, 156]. This can lead to narrower size distributions and better monodispersity, because a distinct separation between

[4]When a high oleic acid concentration is used, there can be an increase in the dissolution of as-formed iron oxide nuclei, and thereby the nucleation process becomes more difficult and only the large nuclei can survive the re-dissolution. As a result, the particle size increases with the increase of oleic acids concentration. However, the thermal decomposition of iron oleate is very rapid under high temperatures and hence a high concentration of monomer will be present due to the lack of nucleation. When the super-saturation of the monomer is attained, the second nucleation occurs. As a consequence, the particle size distribution becomes very broad.

nucleation and growth steps is achieved [126, 129, 136, 149, 153, 156]. This is why solvents with different boiling points are used. For example in [132] MNP are synthesised at 320°C (octadecene) and 370°(docosane). All parameters during the thermal decomposition are kept the same, including the heating rate. Since the heating rate is the same, the amount of nuclei (generated at a temperature less than 250°) is the same in both syntheses. However, the amount of monomers available for the particle growth would be higher at 370°than at 320°due to more decomposition of strongly bound ligands or increased reactivity of the iron oleate, resulting in larger particles at 370°.

Increasing the reaction time ('aging') mostly leads to larger nanoparticles, as more time is allowed for grain growth. Nevertheless, too long an annealing time can lead to a broader or bimodal size distribution [83, 156]. Conversely, too low a reaction temperature (close to the nucleation peak) can hinder precursor decomposition and lead to low reaction yield and high polydispersity [153].

The heating rate also plays an important role. Lower heating rates can lead to larger particles because nucleation occurs at lower temperatures where nucleation rates are smaller, resulting in fewer nuclei that grow larger [156]. An intermediate heating rate (3 K/min) may produce significantly more spherical and uniform particles compared to faster (9 K/min) rates, as it allows for a cleaner separation between the precursor decomposition and burst nucleation phases [146].

Water Traces : The presence of water can stabilise the iron complex, leading to decomposition at higher temperatures, which in turn causes the formation of a large number of nuclei and thus limits grain growth, resulting in smaller nanoparticles [83]. Most protocols contain a heating step at 120 °for 30 min which aims at removing traces of water before starting the experiment ("dehydratation"). A systematic comparison of thermal decomposition protocols and the resulting size control strategies reported in literature is given in Appendix A.4.1.

3.2.2 TD synthesis : Materials and Methods

In the main TD protocol we applied, is a variation on the synthesis developed by Hyeon et al. in 2001 [157] with dioctyl ether as solvent (boiling temperature : 287 °C). In our case iron acetylacetonate $Fe(acac)_3$ operates as precursor and oleylamine is used both as a surfactant and reducing agent [135]. It will be specifically mentioned for some synthesis that the reagents of the protocols were doubled, to increase the nanoparticle yield.

> In a typical synthesis of 10 nm Fe_3O_4 NPs, $Fe(acac)_3$ (3 mmol) was dissolved in 15 mL of dioctyl ether and 15 mL of oleylamine. The mixture was sonicated for 10 minutes in order to disperse the precursor, resulting

> in a vivid red and homogeneous suspension. It was heated to 110°and dehydrated for 1h. The resulting solution is brown. Then, a condenser was connected to the flask and the solution was heated to 300°C using a heating mantle. Once the temperature reached, the reaction mixture was refluxed for 1 hour. After the reaction, the solution was cooled down to room temperature. The Fe_3O_4 NPs were extracted upon the addition of 50 mL of ethanol, followed by centrifuging. Washing of the nanoparticles is done at least 5 times by alternating water and ethanol. Storage is done in ethanol.

Heating was done mainly in a heating mantle "Steinberg Systems SBS-LHM-1000/DH". An oil bath was explored as well but the heating plates at our disposal could not consistently sustain 298 °during more than an hour. In the naming of batches, "FCN" are only used for structural characterisation in this chapter and are all made with the heating mantle. The heating rate was not a tunable parameter and varied from 12 to 15 °C/min. The heating process was as follows :

- The heating curve starts after one hour of dehydratation, between 110 °C and 140 °C. This difference is due to drifting of the dehydratation temperature : the heating mantle is less precise at lower temperature.
- According to [136], nucleation of intermediate iron–surfactant complexes begins around 200 °C (cf Subsection 3.2.1.2). In the present system, this intermediate is an iron–oleylamine complex rather than an iron oleate, but the temperature range is expected to be comparable [146].
- Between 240 and 265 °C, an opaque white smoke forms, likely corresponding to volatile decomposition products released during precursor transformation.
- Around 280 °C, explosions start. These bring the temperature down temporarily.
- The duration of the reflux plateau was varied between 51 and 68 minutes.

Care was taken for these synthesis details which are not (consistently) reported in literature.

- It is often mentioned that the reaction takes place under "vigorous stirring", e.g. in [38]. Using a magnetic stirrer is not recommended since it agglomerates most of the magnetic mass. The thermal decomposition process is one of boiling with constant movement within the mixture. We used to manually shake the heating mantle every 15-30 min to avoid the formation of a fixed solid residu on the necked bottle.

- Sonicating the mixture of precursor, ligand/surfactant and solvent was necessary for good homogeneity of the reagent suspension before starting the heating process, as specifically suggested in [83].
- Washing by magnetic separation was done at least 8 times per batch, varying water and ethanol. Hydrophobic surfactant containing nanoparticles "climbs the walls" of the erlenmeyer when water is added and needs to be reincorporated in the solution by stirring of the erlenmeyer. The solution was sonicated for at least 10 minutes before each separation.

3.2.3 TD Synthesis : Results and Discussion

3.2.3.1 Structural and elemental properties

Table 3.4 contains ICP and TEM results for 11 synthesised samples. TEM imaging was performed by Fabien Drault and Alessia Tonelli at UCLouvain. Fe–Comm samples are commercial magnetite with $\tilde{D}_{\mathrm{TEM}}$ = 130 nm (according to the data sheet) magnetite nanoparticles and high polydispersity. They are a control sample throughout this work an relevant in this case for comparison on ICP analysis data. Fig. 3.5 gives example TEM images for FCN3, 5, 6 and 12.

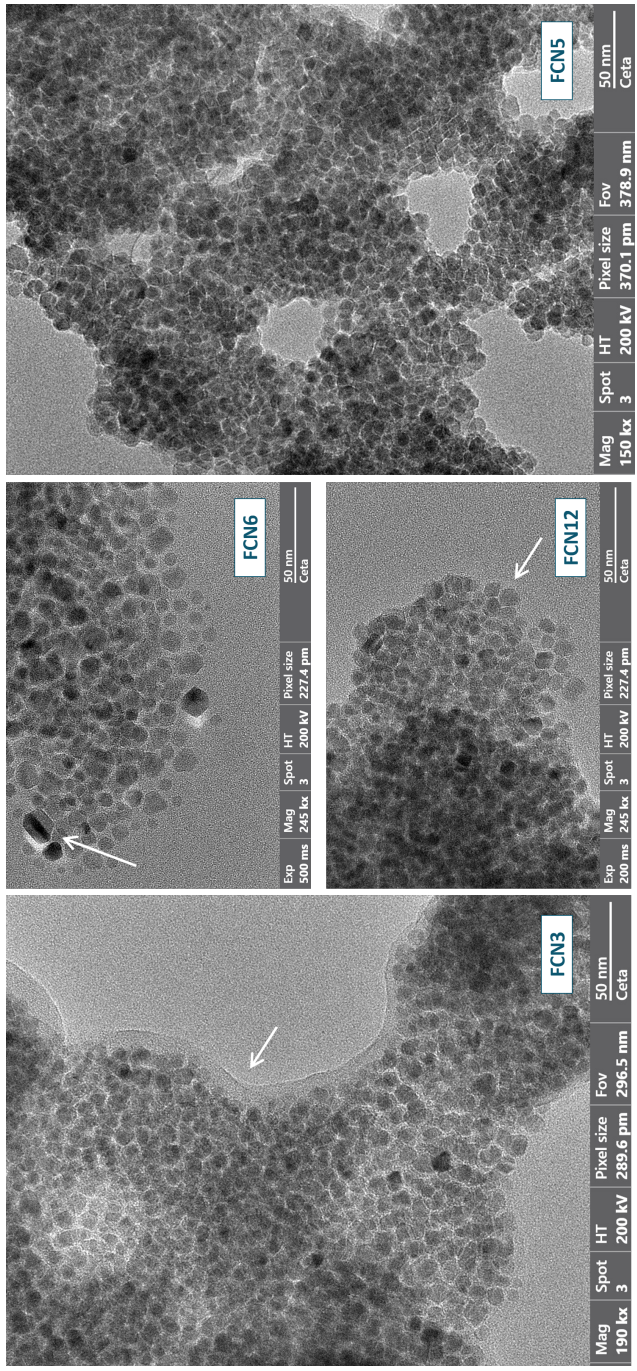


Fig. 3.5 TEM images of TD synthesis results

Elemental properties : Table 3.4 contains the mass percentage of iron in the different nanoparticle powders, obtained by ICP. Powder is obtained by drying the nanoparticle suspenstion (stored in ethanol). To minimise oxidation, the drying of the nanoparticle suspension is done at room temperature. The importance of this has been assessed. Indeed, Fe–TDH4 is a mix of FCN7, FCN8, FCN12. Given the large amount of this mixture, part of it was dried in the oven (Fe–TDH4W), and the rest was dried by natural evaporation for 3 days on the lab bench (Fe–TDH4C). The powder obtained by oven-drying was brown, indicating oxidation (a greater fraction of γ-Fe_2O_3) while the other remained black. This different mass fraction of iron cannot be attributed to differences in surfactant fraction since the initial suspension was identical. FCN3 was a "brownish" powder which had been stored for over a year and oxidated as well (despide the large layer of surfactant observed on TEM images). ICP also reflects this by a lower mass fraction.

The iron mass fraction depends both on its oxidation state and the presence of surfactant. However, Inductively Coupled Plasma (ICP) cannot quantify the mass fraction of oleylamine (organic molecular structure) since it only detects elemental ions. Approximations can be made. In stoichiometric maghemite Fe_2O_3 the mass fraction of iron is 69-70% while in magnetite it is at 72%. For dark powders, assuming 70% magnetite and 30% maghemite would lead to a theoretical iron mass fraction of 71.25%. A measured 68% Fe mass fraction would mean that the surfactant mass fraction m_s is defined by $m_s = \frac{0.7125-0.68}{0.7125} = 4.5\%$.

The presence of surfactant : We could not find a correlation between the number of washing cycles and the amount of surfactant present on the TEM images (qualitatively assessed in Table 3.4). One explanation might be the "randomness" of the TEM images, not representative for the whole batch. TGA analysis would allow to have a more global and representative evaluation of surfactant fraction per batch. Another explanation would be that the amount of surfactant "clinging" to them is influenced by the cooling down phase, consistent with the dual role of the surfactant discussed in Subsection 3.2.1: beyond its kinetic role during nucleation and growth, it dynamically coordinates to the nanoparticle surface and its binding state evolves with temperature. Indeed we observed that the surfactant becomes "thick and soapy" when the mixture approaches room temperature. The addition of ethanol was done when the mixture was below 60 °C, well below the reaction temperature threshold [155]. However, the exact temperature of the mixture at the start of the washing was not monitored. The correlation between manipulations during the cooling down and the persistence of the surfactant layer deserves further study.

Fig. 3.5 clearly shows spacing between the nanoparticles: even if they are agglomerated, they are not aggregated (i.e. they do not share a crystallographic plane). This underlines that sufficient surfactant was present around them, also during the synthesis dynamics. It confirms the validity of an important hypothesis made

Table 3.4 List of samples, iron mass fraction according to ICP and size distribution according to TEM data. Fitting on lognormal size distribution is validated and the shape factor is given. "x2?" is checked when the double of the initial reagent amount was used. "Surf?" assesses an appreciation of the amount of surfactant present on the TEM images. Names of samples in bold indicate that they have been used later in this work for magnetic characterisation. The list is ordered according to chronology of synthesis (except for Fe–Comm which is store-bought and Fe–TDH4 which is a mix.)

Sample	**x2?**	**ICP**	**TEM**				**Note**
		Mass Fe %	**Median $\tilde{D}_{\mathrm{TEM}}$ (nm)**	**Shape factor γ**	**Count**	**Surf.?**	
Fe–TDH1			7.54	0.27	714	None	
FCN3		60.43	8.31	0.19	448	Much	ICP: "brown-ish" powder
FCN4			9.26	0.24	2089	None	
FCN5	x	68.87	10.68	0.16	316	Little	
FCN6	x		8.37	0.24	1431	None	TEM: some larger polygons
FCN7			9.05	0.16	529	Little	
FCN8			9.15	0.16	635	Much	
Fe–TDH2	x	68.61	9.56	0.21	407	Much	
Fe–TDH3		67.2	11.15	0.25	596	Little	TEM: some larger polygons
FCN11	x		9.91	0.20	589	Little	
FCN12	x		8.21	0.17	878	None	
Fe–TDH4C		65.59	9.26	0.20	184	Little	Mix of FCN7, FCN8 and FCN12. Powder for ICP obtained by drying in ambient conditions.
Fe–TDH4W		61.71				"	Mix of FCN7, FCN8 and FCN12. Powder for ICP obtained by drying in oven.
Fe–Comm		68.44	135.8	St. dev. 98	256		No lognormal distribution[a]

[a] No lognormal distribution could be fitted given Coefficient of Variation (CV) = 68%; the standard deviation of the raw distribution is given instead of a shape factor.

in this work: inter-particle exchange interactions are not considered dominant (cf. Subsection 2.3.6.1).

Size Distribution : As can be observed in Table 3.4, lognormal distribution was validated for all synthesised samples. The communicated data are median diameter $\tilde{D}_{\mathrm{TEM}}$ and shape factor γ : these are chosen because the distributions are narrow, i.e. conversion between normal and lognormal distribution is valid. Indeed median $M(X)$ refers directly to position and can be converted to ξ ("position on the log scale") independently from the distribution width, while γ depends only on distribution width and can be converted to CV without ξ (cf Eqs. 3.12).

TEM image analysis was performed according to the method described in Subsection 3.1.5. Lognormal distribution was validated by the K-S test for all synthesised samples, although the particle count of Fe–TDH4C (184) and FCN5 (316) might be a little low for statistical significance. The shape factor of the fitted lognormal distributions varies from 0.16 to 0.27. This is larger than the "narrow size distribution" of 15% obtained by Roca et al. for ≈11 nm particles [128] but still below $\gamma^2 = 0.096$ labelled as "highly uniform" by Pazik et al. [130]. When considering the PDI, 7 out of 11batches are below the monodispersity threshold determined by ISO 22412 (cf. 3.1.3.2).

Note that TDH4 is a mix of FCN7, FCN8 and FCN12. However, the median diameter of this mix ($\tilde{D}_{\mathrm{TEM}}$ = 9.26 nm) is higher than the median diameter of the three individual samples (resp. 9.05, 9.15, 8.21). This is a perfect illustration of the limitation of TEM as a size characterisation tool. It is coherent that the shape factor of the mix (0.20) is larger than those of the composing solutions (0.16–0.17).

No lognormal distribution could be fitted on the Fe–Comm sample (commercial sample) : its CV is 68% and therefore it is undoubtedly polydisperse.

Shape : It can be observed in Fig. 3.5 that some polygons exist within the nanoparticles. In FCN6 (γ = 0.24) these form a subpopulation with larger diameter. In FCN12 (γ = 0.17) their diameter remains consistent. The presence of faceted particles is consistent with the high heating rates used in this work (12–15 °C/min), well above the 9 °C/min threshold identified by Lassenberger et al. [146] beyond which uneven thermal gradients promote irregular morphologies (cf. Subsection 3.2.1.2).

3.2.3.2 Correlations : synthesis protocol and resulting size properties

Elemental and size parameters are extracted from Table 3.4. Correlations are established based on the Pearson correlation coefficient (r). A correlation between two datasets is considered significant when $|r| > 0.5$. However, the dataset being small, any outcome should be interpreted cautiously.

Doubling the reactant quantities : Doubling the amount of reagents has lead to no statistically significant alteration of median diameter nor size distribution. Given the low yield per nanoparticle synthesis, this is a useful observation.

Reflux Plateau : Subplots A and B in Fig. 3.6 display the correlation between reflux duration and, respectively, median diameter and polydispersity (i.e. the shape factor γ of the corresponding lognormal distribution). As illustrated by Fig. 3.4 and discussed in Subsection 3.2.1.2, the main process during the reflux plateau is monomer-addition growth: the remaining iron–oleylamine precursor reservoir is consumed by the existing nuclei [146]. Ostwald ripening, whereby smaller particles dissolve in favour of larger ones, acts as a secondary mechanism. It therefore makes sense that median diameter increases as the reflux time is made longer. No correlation is found between reflux time and polydispersity. This could be explained by the fact that γ is more sensitive than median diameter to faceted outliers, whose occurrence depends on both the heating rate and the reflux duration, making it difficult to isolate the effect of reflux time alone.

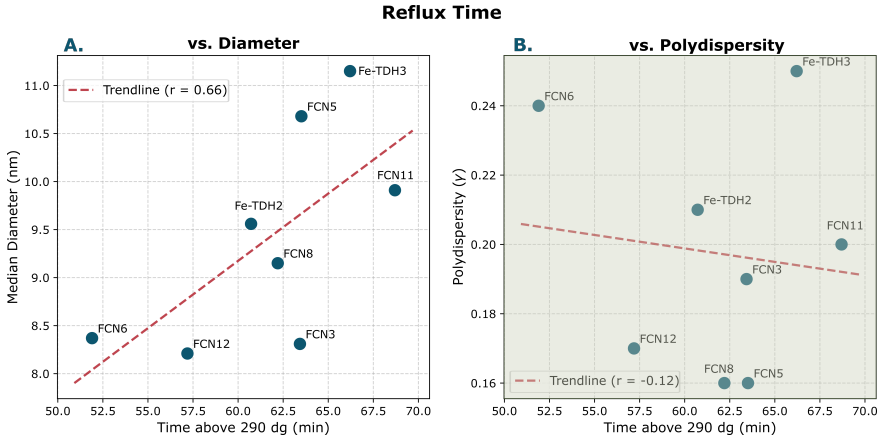


Fig. 3.6 Correlation between median diameter and shape factor (polydispersity) of the fitted lognormal distribution vs (1) duration of reflux time. The variable r refers to the Pearson correlation coefficient.

Section summary

Consolidated conclusions: The thermal decomposition protocol of [135] consistently produces lognormally distributed SPION in the 7–11 nm median diameter range with shape factors between 0.16 and 0.27. The polydispersity index remains below the ISO 22412 monodispersity threshold for the majority of batches, confirming that the protocol yields monodisperse nanoparticles. Doubling the reagent quantities did not affect the size distribution, which is relevant given the low nanoparticle yield per run. However, the median diameter is not repeatable across batches: it varies by nearly a factor of 1.5 between the smallest (Fe–TDH1, 7.54 nm) and the largest (Fe–TDH3, 11.15 nm) batch. While TD synthesis leverages the creation of monodisperse nanoparticle batches, the difficulty of repeatability is acknowledged as a bottleneck in [132, 156, 158].

TEM images (Fig. 3.5) show clear inter-particle spacing, confirming that they are agglomerated but not aggregated (i.e. they do not share a crystallographic plane). This validates the hypothesis that inter-particle exchange interactions are negligible (cf. Subsection 2.3.6.1), an assumption on which the magnetic characterisation in Chapter 4 relies.

Post-synthesis handling affects stoichiometry. The Fe–TDH4 pair, prepared from the same suspension but dried differently, shows a measurable difference in iron mass fraction (65.59% for ambient drying vs 61.71% for oven drying), attributable to oxidation of magnetite towards maghemite. Long-term storage under air leads to the same effect (FCN3), even in the presence of a surfactant layer. For non-oxidised powders, the surfactant mass fraction is estimated at approximately 4.5% from ICP data.

Some batches exhibit faceted (polygonal) morphologies on TEM images. Their presence is consistent with the high heating rates applied in this work (12–15 °C/min), well above the 9 °C/min threshold identified by [146] beyond which uneven thermal gradients promote irregular shapes. In FCN6, the faceted particles form a subpopulation with larger diameter, contributing to polydispersity.

Observed trends requiring further investigation:

A positive correlation was identified between reflux duration and median diameter (Fig. 3.6). While the low number of data points requires caution and does not allow to consider this as a robust conclusion, it is consistent with continued monomer-addition growth from the iron–oleylamine precursor reservoir during the reflux plateau [146]. This observation should be reinforced with additional datapoints and can not be considered independently from the heating rate and cooling rate.

No correlation was found between the number of washing cycles and the amount of residual surfactant observed on TEM images (Table 3.4). The cooling-down phase is proposed as a more likely factor influencing surfactant persistence: the surfactant becomes viscous as the mixture approaches room temperature, and the exact temperature at which washing begins was not controlled.

Perspectives:

Based on the observations above, four directions are identified for further work:

1. Controlling the heating rate in the 3–9 °C/min range [146] to assess whether median diameter repeatability and particle sphericity improve when nucleation

and growth are better separated. The faceted morphologies observed in several batches at 12–15 °C/min support this direction.

2. Monitoring the cooling rate systematically. The cool-down phase was not recorded with sufficient precision in this work to allow for quantitative analysis. Literature reports that cooling conditions affect both Ostwald ripening and ligand–surface interactions [129, 143, 156], and their influence on the final size distribution deserves dedicated study.
3. Performing the synthesis under inert atmosphere to reduce oxidation and to enable a cleaner interpretation of the influence of other process parameters, in particular the cooling rate.
4. Replacing the qualitative TEM-based surfactant assessment by thermogravimetric analysis (TGA) to quantify the surfactant mass fraction and correlate it with washing and cooling parameters.

Towards integration into lateral flow assays, it should be noted that the resulting nanoparticles carry a hydrophobic oleylamine corona. Phase transfer or ligand exchange would be required before use in aqueous environments.

3.3 MNP Synthesis by Coprecipitation

The CP samples used in this work were synthesised by collaborators. This section does not aim to discuss the synthesis protocol in detail but rather to identify the size, morphology and elemental properties of the available samples, as they will be used throughout the remainder of this work. The principal questions we wish to address are:

> What are the size distributions and morphologies of the CP samples?
>
> How does the polydispersity of CP batches compare with that of TD batches?
>
> What is the elemental composition of the manganese ferrite samples, and does it match the expected stoichiometry?
>
> What colloidal stability can be expected from these hydrophilic, citric-acid-coated nanoparticles?

3.3.1 Coprecipitation of Iron Salt : Literature Overview

3.3.1.1 Main Principles of Coprecipitation

Coprecipitation is a water-based, thermodynamically driven process involving the precipitation of a solid from a liquid phase when the concentration of solute species exceeds the solubility limit, creating a state of supersaturation [141]. These protocols have several advantages compared to thermal decomposition, such as simplicity, rapidity, gram-scale production and high yield [158]. The method was first demonstrated by Massart in 1981 [159]. Almost all commercially available iron-oxide based MRI contrast agents are fabricated by this route [12].

For the synthesis of magnetite (Fe_3O_4), the method involves the stoichiometric mixing of ferrous (Fe^{2+}) and ferric (Fe^{3+}) iron salts, typically chlorides ($FeCl_2$, $FeCl_3$) or sulfates ($FeSO_4$, $Fe_2(SO_4)_3$), in an aqueous solution. To achieve the correct stoichiometry for the magnetite spinel structure, a molar ratio of Fe^{3+}:Fe^{2+} of 2:1 is theoretically required and commonly employed [160]. Common bases include sodium hydroxide (NaOH) or weaker ones like ammonium hydroxide. The addition of the base rapidly increases the solution's pH, providing the hydroxide ions (OH^-) necessary to react with the dissolved iron ions. This leads to the simultaneous precipitation (hence "coprecipitation") of iron hydroxides, which subsequently transform into the iron oxide phase.

The reaction can be simplified as:

$$Fe^{2+} + 2\,Fe^{3+} + 8\,OH \longrightarrow Fe_3O_4(s) + 4\,H_2O$$

The sequence of physical and chemical transformation can be summarised as follows :

1. **Nucleation:** The process begins with the addition of the base. As the local concentration of OH^- ions increases, the solution becomes supersaturated with respect to the solubility products of iron hydroxides. This high degree of supersaturation drives a rapid and often uncontrolled burst of nucleation, where tiny, solid-phase nuclei of ferrous hydroxide ($Fe(OH)_2$) and ferric hydroxide ($Fe(OH)_3$) are formed throughout the solution [161]. The rate and density of this nucleation event are extremely sensitive to local fluctuations in pH, temperature, and reactant concentration. In a typical batch reactor, where a concentrated base is added to the iron salt solution, these parameters are notoriously difficult to control uniformly, leading to nucleation occurring at different times and rates in different regions of the reactor. This spatial and temporal inhomogeneity during the nucleation stage is a primary source of the final product's polydispersity.
2. **Growth and Transformation:** Following nucleation, the initially formed hydroxide precursors undergo a complex process of growth, dehydration, and structural rearrangement to form the thermodynamically more stable inverse spinel structure of magnetite [161]. This transformation is typically facilitated by a subsequent heating or "aging" step, where the reaction mixture is held at an elevated temperature (e.g., 60–90°C) for a period to promote crystallization and drive the reaction to completion [162].

3.3.1.2 Parameters influencing Coprecipitation Products

In general, the most important parameters to control are

- **pH** of the reaction medium is a dominant factor. A sufficiently high pH, typically in the range of 8 to 14, is necessary to ensure the complete precipitation of the iron ions. Beyond this, the rate of pH change is crucial. The rapid addition of a strong base like NaOH can cause a sharp, localised spike in pH, leading to massive, uncontrolled nucleation and a very broad size distribution [131].

- **Temperature** exerts a strong influence on both nucleation and growth kinetics. To achieve better control, a two-stage temperature profile is often employed. The initial precipitation (base addition) is conducted at a low temperature, often below 10°C and ideally below 4°C, to slow down the kinetics and better manage the nucleation process. Following precipitation, the temperature is raised to an aging temperature, typically between 60°C and 90°C, to provide the thermal energy needed to drive the dehydration and crystallization of the hydroxide precursors into the final magnetite phase [131, 162].

- **Stirring Rate** : while insufficient stirring leads to poor mixing and high polydispersity, some studies have found that excessively high stirring rates can paradoxically lead to larger hydrodynamic sizes due to increased particle agglomeration. Consequently, there is often an optimal stirring speed that must be determined empirically. For instance, one study optimising the synthesis of citrate-stabilised SPION identified an optimal stirring speed of 9000 rpm to achieve the most desirable particle size and stability [163].

- **Stabilisers and Coating:** Due to their high surface-area-to-volume ratio and inherent magnetic attraction, bare SPNFs are thermodynamically unstable in aqueous suspension and will readily agglomerate to minimise their surface energy. To prevent this and ensure long-term colloidal stability, the synthesis is almost always performed in the presence of, or followed by coating with, a stabilising agent. These agents can be small molecules like dextran or citrate. The stabiliser is not a passive component; it can actively influence the particle growth kinetics by binding to the surface [164]. Tourinho et al. determined a semi-empiric formula on how much citric acid is needed depending on the diameter, to guarantee saturation at the nanoparticle surfaces[165]. It is also possible to cover the nanoparticles with different polymers such as polyethylene glycol (PEG) [166], polyacrilic acid (PAA) [167] or polyethylenimine (PEI) [168], increasing the repulsion between nanoparticles and achieving a stable solution by steric stabilisation.

The nature of the coprecipitation method, the rapid, thermodynamically driven precipitation from bulk aqueous solutions, is the direct cause of its primary limitation: poor control over size distribution. The process is characterized by the simultaneous and overlapping occurrence of nucleation and growth, a classic recipe for producing polydisperse particle populations. The difficulty in maintaining uniform conditions (pH, temperature, concentration) throughout a batch reactor means that nuclei form at different times and in different locations, and subsequently grow for different durations, inevitably leading to a wide range of final particle sizes [12, 46]. It was shown that precise control of pH improves the polydispersity of the obtained batch [165, 169, 170]. By optimising stirring speed, stabiliser concentration, and temperature, a PDI of 0.215 was achieved in [131]. However, these optimisations can only mitigate, not eliminate, the inherent challenge of separating the nucleation and growth steps in a single pot. Post-synthesis purification was applied in [125] : a crude sample with a PDI of 0.28 was subjected to sequential centrifugation, yielding highly monodisperse fractions with PDI values of approximately 0.10 (measured with DLS). Compared to typical PDI values for thermal decomposition products, summarised in Table 3.2, these can be considered "moderately polydisperse".

3.3.2 Coprecipitation : Experimental Findings

This section does not aim to discuss the properties of the samples since elaboration was done by a partner. It mainly aims at identifying their size and elemental properties since they will be used later throughout this work. For practical applications it is worth emphasising that colloidal stability of these samples was very high and that coprecipitation yields, by nature, hydrophillic nanoparticles.

3.3.2.1 Structural Characterisation

The CP samples at our disposal were made by our colleagues at the Universidad de Oviedo[5]. The applied protocol is described in [170, 171]. They have a citric acid corona. Both powder form (obtained by evaporation at room temperature) and ferrofluid (highly concentrated suspension) were available. TEM imaging, particle counting and histogram construction were performed by the collaborators who synthesised the samples. The mean diameter and shape factor γ of the lognormal fit are communicated directly; the median diameter listed in Table 3.5 is deduced from these values assuming a lognormal distribution rather than counted independently. In Fig. 3.7 a representative TEM image and corresponding histogram (obtained by manual diameter selection of at least 1500 particles per sample) are illustrated. Mn–CP1 has large polygons among its population and Co–CP1 has a double population (two lognormal distributions are required to accurately fit the size distribution). Note that for Mn–CP2 the light blue circles indicate nanoparticles which were not included in the analyses, because of the uncertainty about their individual or agglomerated nature. If these are single nanoparticles, the histogram might be biased.
The main characteristics of the manganese ferrite and mangetite samples made by coprecipitation are summarised in Table 3.5 with γ the shape factors of the fitted lognormal curve. Compared with TD batches in Table 3.4, obtained distribution width is significantly larger. According to the ISO 22412 norm, only Mn–CP2 would be classified as "monodisperse".

3.3.2.2 Elemental Characterisation

TGA analysis suggests that the citric acid (CA) takes up 7 - 16 % of the sample mass. This is higher than the estimated surfactant masses based on ICP results for the iron oxide nanoparticles obtained by thermal decomposition in Subsection 3.2.3.1. It is probable that this higher relative corona mass contributes to the overall better colloidal stability of these CP nanoparticles compared to the TD in this work.

The stoichiometric Mn/Fe mass ratio is expected to be 30/61 for $MnFe_2O_4$, corresponding to a Fe/Mn mass ratio of 2.03. While the larger Mn–CP1 (Fe/Mn = 1.94) is acceptably close to this value, Fe is more dominant in Mn–CP2 (Fe/Mn =

[5] A huge thanks to Vanessa Pilati for sharing her samples with stunning colloidal stability.

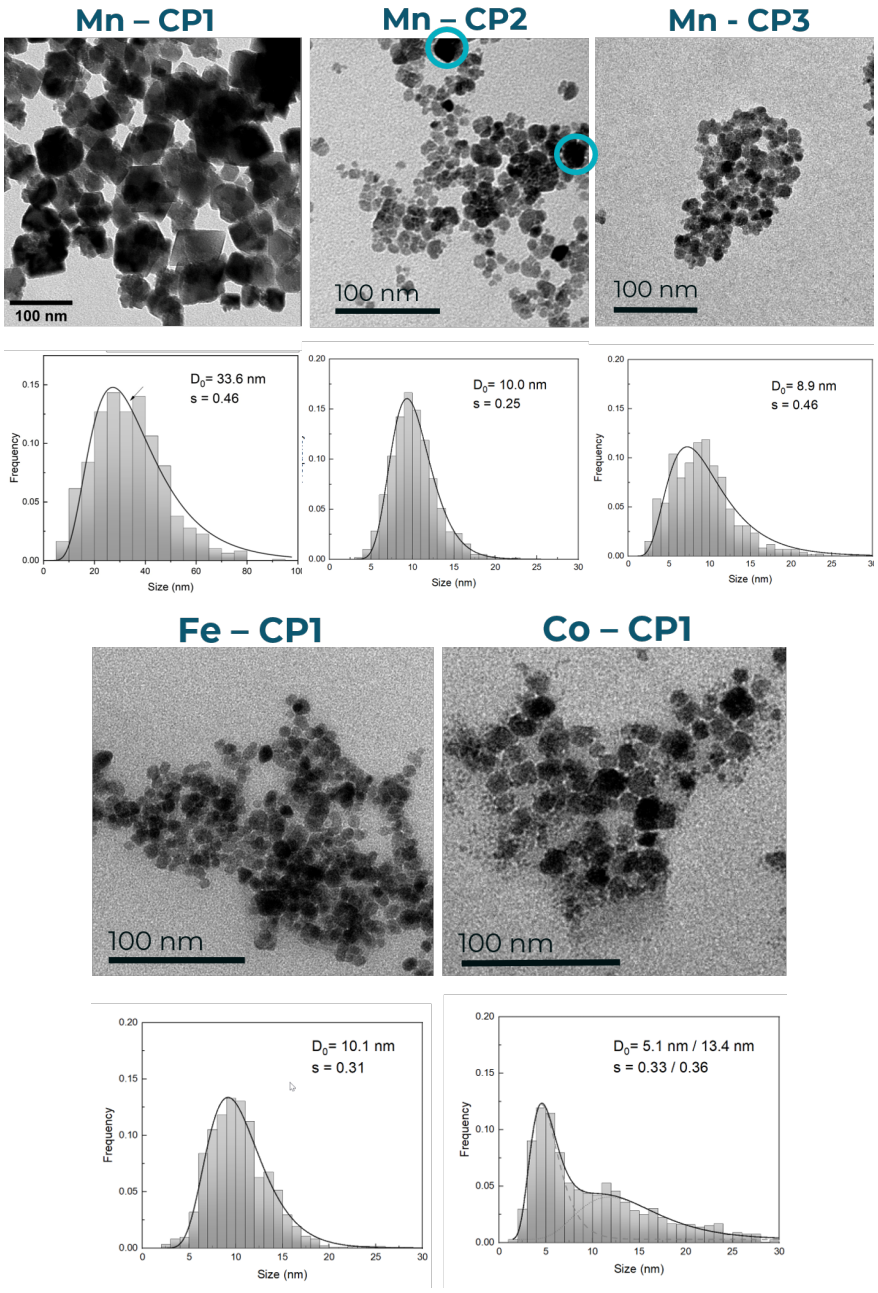


Fig. 3.7 Example TEM image and corresponding histograms for size characterisation of Mn–CP2 and Mn–CP3. The histograms contain 2000 individual nanoparticles counted over more than 15 images per sample. "s" indicated on the histograms represents the lognormal distribution shape factor. In Co–CP1, two "populations" are considered.

2.82) and Mn–CP3 (Fe/Mn = 2.66), as observed in Table 3.5. This is attributed to preferential Mn dissolution at the particle surface. Ma et al. [172] demonstrated that Mn^{2+} is selectively released from $MnFe_2O_4$ nanoparticles while Fe remains stable in solution. The release follows the reaction $MnO + 2\,H^+ \longrightarrow Mn^{2+} + H_2O$ and is strongly size-dependent: at pH 4.8, the fraction of Mn released after 12 h reaches 61.9% for 3 nm particles, 26.0% for 10 nm, and only 6.4% for 18 nm [172]. In the present case, the citric acid coating locally reduces the pH at the nanoparticle surface, promoting this dissolution mechanism. The effect is more pronounced in the smaller Mn–CP2 and Mn–CP3 due to their larger surface-to-volume ratio. Pilati et al. [170] showed that acid treatment produces a core/shell structure: the core retains the mixed-ferrite stoichiometry while the surface becomes enriched in Fe, forming a thin ($\sim$0.5 nm) maghemite-like (γ-Fe_2O_3) shell. This observation is consistent with the ICP data of the present work: the Mn-depleted composition measured for Mn–CP2 and Mn–CP3 likely reflects a volume-averaged signal from a near-stoichiometric core surrounded by an Fe-rich surface layer, rather than a homogeneous departure from stoichiometry throughout the particle. Surface-sensitive characterisation (e.g. XPS or STEM-EDX) would be required to confirm this interpretation for the present samples.

Table 3.5 List of samples made by coprecipitation and results of (1) ICP quantification of Fe& Mn (2) TEM analysis for mean and median diameter (nm) and (3) Citric Acid (CA) mass fraction deduced from TGA analysis. Italic median is deduced from TEM counted mean, assuming lognormal distribution.

Sample	ICP		TEM			TGA
	Element	Mass %	Mean D	Median D_{TEM}	γ	CA Mass %
Fe–CP1	Fe	67.49	10.1	*9.6*	0.31	9 - 11 %
Mn–CP1	Fe	47.41	33.6	*30.2*	0.46	
	Mn	24.55				
Mn–CP2	Fe	48.04	10.0	*9.7*	0.25	7 - 10 %
	Mn	17.14				
Mn–CP3	Fe	48.58	8.9	*8.0*	0.46	
	Mn	18.22				
Co–CP1[a]			5.1/13.4	–	0.33/0.36	13 - 16 %

[a] A double lognormal population was fitted on this sample; values are given for each population.

Section summary

Consolidated conclusions: Coprecipitation is a simple, rapid and scalable water-based route that produces hydrophilic SPNFs with high colloidal stability. The CP samples used in this work, synthesised following the protocol of [170, 171], cover median diameters from approximately 8 to 30 nm for manganese ferrites and roughly 10 nm for magnetite. Shape factors range from 0.25 to 0.46, confirming that the size distributions are significantly broader than those obtained by thermal decomposition (Table 3.4). Only Mn–CP2 ($\gamma = 0.25$) satisfies the ISO 22412 monodispersity criterion. The citric acid corona accounts for 7–16 % of sample mass (TGA), which is higher than the surfactant fractions measured for TD nanoparticles and likely contributes to the superior colloidal stability of these samples.

Observed trends requiring further investigation:

ICP analysis reveals a systematic Mn depletion in the smaller manganese ferrite samples (Fe/Mn mass ratio of 2.82 for Mn–CP2 and 2.66 for Mn–CP3 versus the stoichiometric value of 2.03), consistent with the size-dependent preferential dissolution of Mn^{2+} reported by [172]. Following the interpretation of [170], this likely reflects a core/shell structure with a near-stoichiometric mixed-ferrite core surrounded by a thin Fe-rich maghemite-like shell, rather than homogeneous Mn depletion. Confirming this interpretation for the present samples would require surface-sensitive characterisation, such as XPS depth profiling to resolve the radial Fe/Mn gradient, STEM-EDX mapping to visualise the elemental distribution at the single-particle level, or Mössbauer spectroscopy to distinguish the cation site occupancy between core and shell.

Perspectives:

Based on the observations above, two directions are identified for further work:

1. Quantifying the effect of the core/shell compositional gradient on the magnetic properties of the Mn-ferrite CP samples, in particular whether the Fe-rich surface layer modifies the effective anisotropy or saturation magnetisation relative to a homogeneous mixed ferrite of the same size.
2. Exploiting the inherent hydrophilicity and colloidal stability of CP nanoparticles for direct integration into aqueous-based lateral flow assay protocols, without the phase-transfer step required for TD products.

3.4 Silica coating of MNP

To enable dispersion of SPION in aqueous media and at physiologic salt concentrations, iron oxide cores are functionalized or coated, preventing agglomeration through interactions between themselves or with biological molecules and precipitate out of solution. Coating and functionalisation can also provide valuable binding sites for biomolecules and improve biocompatibility [46]. Typical coatings include polymers (i.e. poly-ethylene-glycol, PEG), glucans (i.e. dextran, starch), silanes or ionic residual groups (i.e. carboxyl groups in citric acid). It can also be a metal coating (i.e. gold) or multicomponent encapsulation (i.e. micelles). In any case, steric hindering or repulsive forces keep them from interacting magnetically.

Colloidal stability of magnetic nanoparticles is a competition of forces. Attractive forces are Van der Waals forces[6] and magnetic dipole-dipole attraction. Repulsing forces can be electrostatic and osmotic. Therefore agglomeration associated with magnetite nanoparticles can be avoided in different ways: by creating an electrostatic double layer [174–176] as done e.g. with citric acid, by using an amphiphilic surfactant stabiliser creating steric hindrance [158, 173] such as oleyamine, or by shifting the isoelectric point[7]. For general colloids, stability is determined by a balance of attractive and repulsive interactions, classically described by DLVO theory (named after Derjaguin, Landau, Verwey, and Overbeek) [178, 179]. For stability of ferrofluidics specifically, Campos et al. [180] use an "Extended DLVO" model in which magnetic forces are added. While worth mentioning, these models are out of scope for this work.

3.4.1 Theory and Literature: Silica Coating

Silica shells around magnetic nanoparticles offer major advantages:

1. Since neutral pH (e.g., pH 7.4, physiological pH) is significantly higher than silica's IEP of 2.0, the silanol groups are largely deprotonated ($Si-OH \longrightarrow SiO^- + H^+$) leading to a strong negative surface charge [177]. This contributes to colloidal stability by enhancing Coulomb repulsion [173].
2. Chemical inertness: It protects the magnetic core from being dissolved in acidic environments (due to its lower IEP) and reduces its tendency to oxidation [181].

[6] Van der Waals forces are short-range and tend to pull particles together, causing them to agglomerate and eventually settle out of the suspension. The smaller the nanopaticles, the higher the surface-area-to-volume ratio, the more this short-range attraction dominates [173].

[7] The isoelectric point is the specific pH at which the surface of a particle suspended in a liquid has a net electrical charge of zero. Below this point, the electrostatic double layer collapses, making the (attracting) Van Der Waals forces to dominate. For bare magnetite, the IEP is around pH 6.8-8.0 while it is around 2.0 for silica [58, 177].

3. Easy Functionalization: The silanol groups on the surface are a perfect chemical "handle" for attaching other molecules (like drugs, antibodies, or targeting agents) using well-established silane chemistry [58, 182].
4. Biocompatibility: Silica provides scaffold for enzyme immobilization and serves as template for radical polymerization with other molecules. It has a large surface area, does not require utilisation of organic solvent, thus resulting in reduced toxicity [12].

Vitrophobic[8] nanoparticles, like gold nanoparticles or hydrophobic SPION inherently resist direct coating with silica, often due to a lack of surface hydroxyl groups that would act as anchor points for silica precursor. An additional challenge is chemical instability in the presence of ammonia, which is a common catalyst in silica synthesis, as it can lead to oxidation and dissolution [183]. Coupling agents like APTES can be used to modify the nanoparticle surface, effectively converting them from vitrophobic to vitrophilic [173, 182]. Vitrophilic nanoparticles on the other hand have surface hydroxyl groups that readily interact with silica precursors, using methods like the Stober process [184].

3.4.1.1 Stöber Method for Silica formation

A sol-gel process represents a highly versatile and widely adopted "wet-chemical" technique for the fabrication of solid materials, especially metal oxides, from small molecular precursors. The process is defined by the controlled conversion of molecular monomers or precursors in a solution into a colloidal solution, known as a "sol," which subsequently evolves into a continuous, integrated network, or "gel". The sol-gel approach is a versatile paradigm of synthesis under kinetic control[9]. The final architecture of the material is not necessarily the most thermodynamically stable state. Instead, it is dictated by the relative rates of the underlying chemical reactions, which are exquisitely sensitive to experimental parameters such as pH, temperature, solvent, and precursor concentration. This sensitivity is the foundation of the "fine control" over chemical composition and microstructure that characterizes the method. This contrasts sharply with traditional high-temperature ceramic processing, which operates closer to thermodynamic equilibrium [185]. The chemical foundation of the sol-gel process rests upon two fundamental reaction types: hydrolysis of a precursor and condensation [164].

- Hydrolysis of a metal alkoxide precursor: replacement of an alkoxy group ($-OR$) by a hydroxyl group ($-OH$). It can be base-catalyzed or acid-catalyzed: respectively, the OH^- or H^+ overload lower the energy barrier

[8] Indeed: hydrophobic and hydrophilic apply to water, vitrophobic and vitrophilic apply to silica...

[9] Sol-gel based protocols do exist for nanoparticle synthesis, but since the obtained product is not in the most thermodynamically stable state, this implies that the nanoparticles are often less crystalline, thus less magnetic [58, 97]. This can be improved by post-processing but partly undermines the simplicity of the method.

to overcome in order to bind OH^- groups to the metal precursor nucleus: $M-OR + H_2O \longrightarrow M-OH + R-OH$

- Condensation: Following hydrolysis, the resulting molecules containing hydroxyl groups undergo polycondensation to form a network of metal-oxygen-metal (M−O−M) bonds, which constitutes the solid backbone of the gel. These condensation reactions are responsible for the growth of the solid network. Even after the initial gel point is reached, these reactions continue in a process known as aging, which leads to further cross-linking, strengthening of the gel network, and changes in the material's structural properties [186].

The Stober Process is a sol-gel process to make a silica SiO_2 network with Tetraethyl Orthosilicate (TEOS), $Si(OC_2H_5)_4$, as precursor. The process begins with the base-catalyzed hydrolysis of the four ethoxy groups of the TEOS molecule, which are replaced by hydroxyl (silanol) groups, and culminates in the condensation of these silanol groups to form stable siloxane (≡Si−O−Si≡) bridges. The overall reaction for the complete hydrolysis of TEOS can be written as:

$$Si(OC_2H_5)_4 + 4\,H_2O \xrightarrow{NH_3} Si(OH)_4 + 4\,C_2H_5OH \tag{3.25}$$

The Stöber process was first published in 1968 by Werner Stöber, Arthur Fink, and Ernst Bohn as a synthesis protocol for monodisperse, spherical silica nanoparticles [184], with diameters typically ranging from 50 to 2000 nm. Traditionally, the 'nucleation phase' refers to the stage where hydrolysis dominates the reaction rate, generating silanol monomers, while 'growth phase' refers to the stage where condensation dominates the reaction rate [187]. Nanoclusters and nanoparticles are formed in conditions where the condensation rate which is higher than the nucleation rate: immediately consuming created silanol monomers/oligomers results in highly banched, compacted clusters that grow into spherical particles rather than extended polymer networks. The concentration of ammonia is a primary determinant of the final particle size and number density. An increase in ammonia concentration significantly accelerates the rates of both hydrolysis and condensation [188]. Crucially, studies have shown that as the ammonia concentration increases, the diameter of the obtained particles tends to increase [188, 189].

3.4.1.2 Coating nanoparticles with silica

The Stöber method can be directly applied to hydrophilic nanoparticles (e.g. made with CP) or to hydrophobic nanoparticles (e.g. from TD synthesis) which are made hydrophilic by silanisation. Appendix A.4.4 summarizes 13 variants of this protocol that resulted in articles with "convincing" TEM images, a useful pre-selection of methods for e.g. enrobing CP nanoparticles with silica. For coating nanoparticles in polar media, the reversed-microemulsion method offers a complementary

approach, particularly for nanoparticles that are initially dispersed in non-polar organic solvents such as the nanoparticles made by TD in this work. It consists of two main stages:

1. Creation of a reversed ("water-in-oil" [190]) microemulsion, which is dispersion of nanosized water droplets stabilised by a layer of surfactant molecules (e.g. Igepal CO-520) within a continuous oil phase (e.g., cyclohexane or heptane). As surfactants are amphiphillic [191], the hydrophilic headgroups of the surfactant face inwards towards the water core, while the hydrophobic tails extend into the continuous oil phase. These droplets are often called reverse micelles or "nanoreactors" [192].
2. The TEOS is soluble in the oil phase. It diffuses through the oil until it reaches the interface of these aqueous nanoreactors. Once at the interface, it can enter the water core where the ammonia catalyst promotes its hydrolysis using the water that is already present, creating reactive silanol monomers.
3. A ligand exchange occurs between the original hydrophobic ligand (e.g., oleic acid) and the surfactant (e.g., Igepal CO-520) in the microemulsion, and subsequently between the surfactant and hydrolyzed TEOS, transferring the nanoparticle to the water phase [175, 191].
4. The hydrolyzed TEOS then condenses and grows on the nanoparticle surface to form a silica shell. They then confined within that tiny droplet, which favours monodispersity and inhibits agglomeration [192].

The main control parameters are identified:

- Water-to-surfactant molar ratio: Affects the size of the water pool, monomer occupancy, and intermicellar exchange rate, thus influencing particle size [192]. Pham et al. demonstrate how this controls the size and number of the aqueous domains within the microemulsion system [193], as represented in Fig. 3.8. Low surfactant volumes can lead to agglomerated core-free silica nanoparticles. Conversely, excessively high volumes can cause micelle fusion, also resulting in agglomerated nanoparticles and core-free silica

- TEOS concentration, especially when added in fractionated drops, influences shell thickness [190, 192].

- Ammonium hydroxide (catalyst) concentration affects the hydrolysis rate of TEOS. While increasing ammonia can slightly increase shell thickness, an excessive amount can promote core-free silica formation. This is because an enlarged aqueous domain (due to higher ammonia content [191]) can accelerate TEOS hydrolysis, causing the monomer supply rate to exceed its consumption rate as demonstrated by Ding et al. [175].

- The number of nanoparticles should match the number of acqueous domains to avoid the formation of core-free silica particles. Ding et al. demonstrated that the size and number of aqueous domains are determined by the ratio of ammonia to surfactant [175]. If the mass of nanoparticles is kept constant while their size increases, the number of NPs will decrease and may not match the fixed number of aqueous domains, leading to core-free silica particles. This was confirmed by Pham et al. [193] that identified an optimal MNP mass for their coating protocol: below the optimum range, core-less particles are formed. Above that optimum range, there is not enough TEOS to coat all nanoparticles.

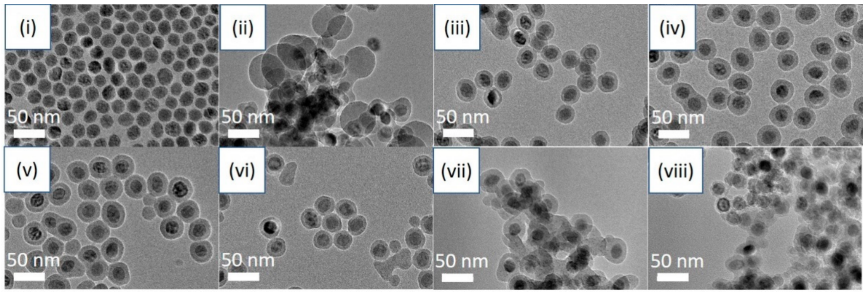


Fig. 3.8 From [193]: Igepal content varying between (i) 0 μl, (ii) 100 μl, (iii) 200 μl, (iv) 300 μl, (v) 400 μl, (vi) 500 μl, (vii) 2500 μl, and (viii) 5000 μl in the presence of 5 mg of MNPs, 100 μl of TEOS, and 100 μl of NH4OH.

Reversed micro-emulsion can be more generally used for core-shell nanoparticles: it is reported for polymer coating [182], gold-coated nanoparticles [58] or silver-coated nanoparticles [183]. In this work two syntheses are tested: Pham et al. [193] coat 5 mg of SPION with a single TEOS addition step and 16h of incubation. Hou et al. propose the coating of 40 mg SPION with 14 additions of TEOS, incubating 16 hours each. Note that this method often requires a large amount of solvent and surfactants to synthesise a relatively small amount of nanoparticles, limiting industrial scalability [158] as opposed to some direct Stober coating processes (such as Gao et al. [194] use up to 400 mg, cf Appendix A.4.4).

3.4.2 Results: Silica coating around TD SPIONs

The SPION synthesised by thermal decomposition in this work carry an oleic-acid corona and are initially dispersed in non-polar solvents, making them vitrophobic in the sense recalled earlier in this section. Rather than rendering them vitrophilic by APTES silanisation as a preliminary step to a Stöber-type coating, the two protocols tested below rely on reverse microemulsion, in which the surfactant itself

mediates the transfer of the particles into the aqueous nanoreactors where silica forms. This motivates the choice of protocol family for the TD particles of this work. TEM and EDX imaging of the coated samples was performed by Alessia Tonelli at UCLouvain.

3.4.2.1 Reverse micro-emulsion Pham et al

Table 3.6 Applied coatings (and variations) based on the reversed micro-emulstion protocol of Pham et al. [193]. The initial chloroform volume is not specified. Properties of initial MNP are listed in Table 3.4. For all experiences the initial state of the nanoparticles was powder form.

	Igepal CO-520 (µl)	Cyclohexane (ml)	MNP (mg)	Chloroform (ml)	NH_4OH (ml)	TEOS (ml)	Incubation Time (h)
Pham et al	variation	11	5	?	0.1	0.1	16
Fe – Comm powder	300	11	5	0.5	0.1	0.1	16
Fe–TDH1 & FCN4 powder	300	11	5	0.5	0.1	0.1	16
Fe–TDH2 & Fe–TDH3 powder	400	11	5	0.5	0.1	0.1	16

The protocol prescribed by Pham et al. [193] is as follows:

> MNPs were coated with silica by the reverse microemulsion method. Various volumes of Igepal CO-520 (0.1 to 5 mL) were added into 11 mL cyclohexane and sonicated for 10 min. Subsequently, 5 mg of MNPs in chloroform was added to the solution and mixed for several minutes to disperse the MNPs into the Igepal CO-520 solution. Next, NH4OH (100 uL) and TEOS (100 uL) were added drop-wise, and the mixture was incubated for 16 room temperature. Next, the mixture was precipitated by adding 20 mL EtOH and centrifuged at 8500 rpm for 30 min. The precipitate was washed five times with EtOH. Finally, the MNPs-SiO2 were re-dispersed into EtOH to obtain a 1 mg/mL MNP-SiO2 solution.

For better control on the MNP mass, the initial sample was in powder form and suspended in 0.5ml chloroform with 15 min sonication. The starting point has been to apply the mass ratios from the Pham et al. protocol. Based on Fig. 3.8 the volume chosen for Igepal was 300 μl which corresponds to nicely enrobed particles in subfigure (iv). As shown in table 3.6 this has been applied on Fe-Comm and a mix of Fe–TDH1 and FCN4 (properties summarized in Table 3.4). For the very large Fe-Comm ($\tilde{D}_{\mathrm{TEM}}$ = 130 nm) this has resulted in the formation of pure silica spheres (50 nm diameter) completely separated from the MNP. For the mix of Fe–TDH1 and FCN4, nanoparticles and the created SiO_2 were observed together, but no clear coating was observed: silica mainly formed spheres as shown in Fig. 3.9. This is unsurprising: as explained in 3.4.1.2, respecting mass ratios from an example protocol does is not necessarily recommended if the used particles

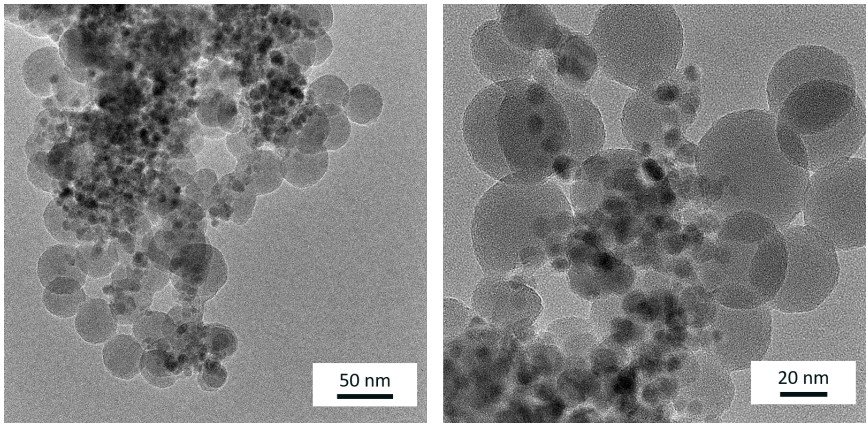


Fig. 3.9 Silica coating with Pham et al. protocol on FCN4 and Fe–TDH1 with 300 μl Igepal for 5 mg SPION.

have different sizes. Matching the number of aqueous domains ("nanoreactors") with the number of nanoparticles is a more dominant parameter. Pham et al. used 20 nm SPION while Fe-TDH1 has $\tilde{D}_{\mathrm{TEM}}$ = 7.54 nm and FCN4 has $\tilde{D}_{\mathrm{TEM}}$ = 9.26.

Tuning reactant ratio for better enrobement of the formed SiO_2 around the SPION has been done based on Fig. 3.8: subfigure (ii) was matched to the situation obtained for Fe–TDH1 and FCN4 (Fig. 3.9), suggesting a shortage of Igepal. Therefore the applied volume was increased from 300 μl to 400 μl and tested on both Fe-TDH2 ($\tilde{D}_{\mathrm{TEM}}$ = 9.56 nm) and Fe-TDH3 ($\tilde{D}_{\mathrm{TEM}}$ = 11.15 nm). Note that the latter contains some polygons (γ = 0.25 as summarized in Table 3.4). Fig. 3.10 shows the results. On the upper row (subfigures A and B) it is observed that SiO_2 is well attached around Fe-TDH2 SPION even though the layer is thin and non-homogeneous. Importantly, no loose silica masses were found. Subfigures C and D show the results for Fe-TDH3: silica is attached to nanoparticles but some pure silica masses do exist. This can probably be exlained by the larger median diameter of Fe-TDH3 compared to Fe-TDH2 (influencing, again, the number of SPION) for a given mass. This indicates that 400 μl Igepal approaches the equilibrium for SiO_2 enrobement of 9.56 nm TD nanoparticles while the amount should probably be decreased for 11.56 nm TD.

The Pham et al. protocol has the advantage of incubating only 16 h, all the TEOS is added at once. However, th amount of nanoparticles handled per batch (5 mg) is however very small. Furthermore, the quality of the enrobement is very dependent nanoparticle size and requires precise tuning of the Igepal volume among the inital reagents. For the TD protocol that was applied in this work, variabil-

ity of medium size per synthesis batch is significant, forming a bottleneck in the straightforward application of the Pham protocol. The elaboration of a systematic "calibration" curve, linking $\tilde{D}_{\mathrm{TEM}}$ with appropriate Igepal volume, would require some effort but could make subsequent applications easier. In such a calibration, the water-to-surfactant ratio would be worth tracking alongside the absolute Igepal volume, since Bagwe et al. [192] identify it as a primary control parameter for the size and number of the aqueous domains, and therefore for the number of nanoreactors available to host the nanoparticles.

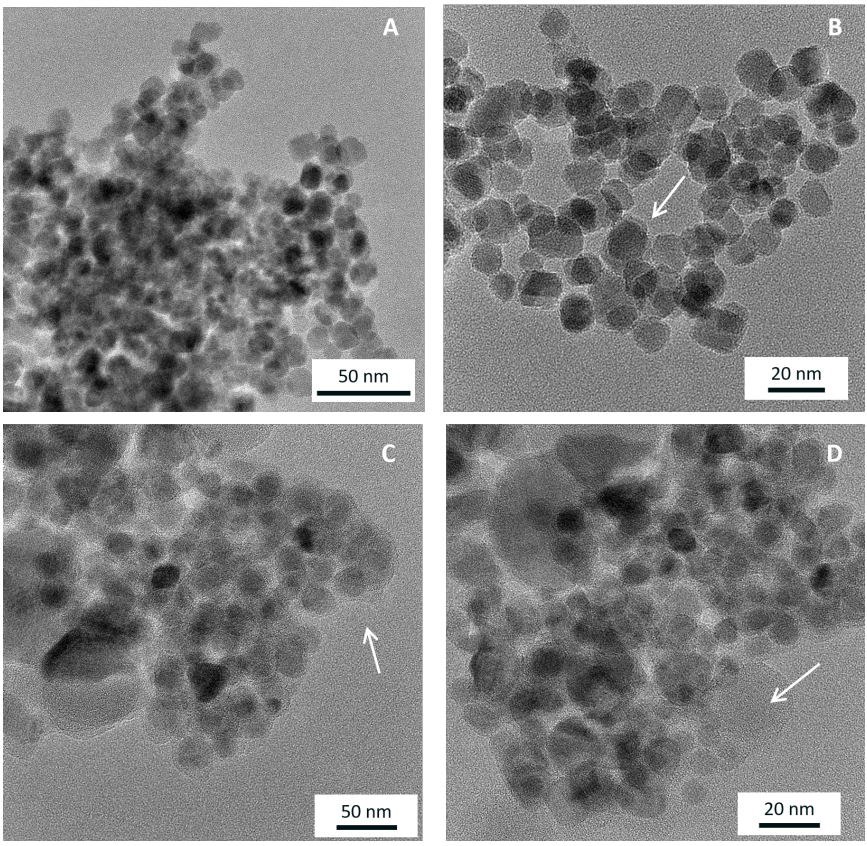


Fig. 3.10 Silica coating with Pham et al. protocol on Fe–TDH2 (A, B) and Fe–TDH3 (C,D) with 400 μl Igepal for 5 mg SPION.

3.4.2.2 Reverse micro-emulsion by Hou et al.

Another reverse micro-emulsion protocol for silica coating is proposed by Hou et al. [195]. In essence, it is similar to Pham et al. but differs on (1) initial nanopar-

ticle mass (8-fold, an advantage) and (2) incubation time (14-fold, a -substantial-disadvantage).

> 6.8 g of Igepal CO-520 was dispersed in 20 mL of cyclohexane and sonicated for 10 min. Then, 200 mL of cyclohexane containing 40 mg of Fe3O4 was added to the above solution with continuous stirring. Subsequently, 0.5 mL of ammonium hydroxide was added to the above mixture solution. Finally, 0.5 mL of TEOS was added in the above mixture solution via the equivalently fractionated drop method (adding 35 uL per 16 h). The resulted Fe 3O4@SiO2 core-shell MNPs were centrifuged and washed, and then redispersed in ethanol.

	Igepal CO-520 (g)	Cyclohex. for Igepal (ml)	MNP (mg)	Cyclohex. for MNP (ml)	NH_4OH (ml)	TEOS (ml)	TEOS drop volume (µl)	incubation steps (h)
Hou et al	6.8 g	20	40	200	0.5	0.5	35	14×16 h
Fe–Comm powder	6.8 g	20	40	200	0.5	0.22	$3 \times 50 + 70$	24, 0.75, 24
Fe–TDH 2 & 3 powder	6.8 g	20	40	200	0.5	0.24	40	4, 12, 4, 4, 20
Fe–TDH3 powder	6.8 g	20	**18**	200	0.5	0.24	40	4, 12, 4, 4, 20
Fe–TDH 2 & 3 suspension	6.8 g	20	40	200	0.5	0.32	40	4, 12, 4, 4, 20, 4, 20
Fe–TDH 4 powder	6.8 g	20	**63**	200	0.5	0.28	40	4, 12, 4, 4, 20, 4

Table 3.7 Reagents used for the silica coating experiences based on the protocol of Hou et al. Cyclohex. refers to cyclohexane.

None of the experiences done respected the total added TEOS volume proposed by Hou et al. The shell in their article is signficantly thick and the incubation time (14 times 16h) poses a signficiant constraints. The main goal of these tests was to observe wether deposition around the TD nanoparticles was more uniform than for the Pham et al. protocol due to drop-wise application of TEOS: to reduce incubation time for practical reasons, it was preferred to half the total added TEOS than to double the dropsize.

An interesting benchmark are the Fe–Comm MNP: it was observed in Pham et al. that single addition of TEOS resulted in loose silica spheres completely disattached from the MNP. Dropwise addition of TEOS done here resulted in attachement of SiO_2 on the particles. The MNP were very clustered given their low colloidal stability (due to their size and the large incubation time) and the silica was not spread evenly around the clusters. Nevertheless, this observation is consistent with the mechanism invoked by Ding et al. [175]: slow step-wise TEOS

addition is expected to keep the monomer supply rate below the condensation rate, favouring silanol condensation onto the existing nanoparticle surface rather than the formation of independent core-free clusters.

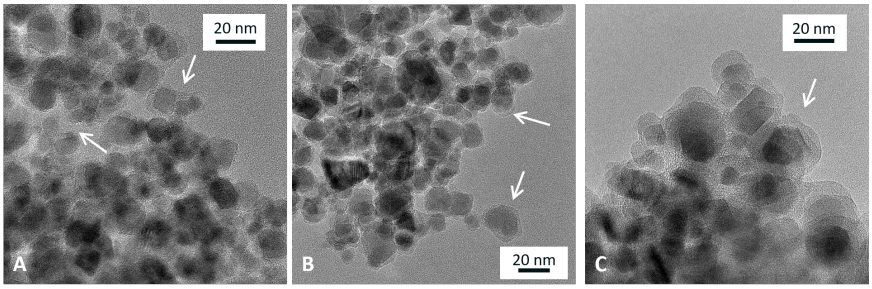


Fig. 3.11 Hou et al. Silica coating protocol on (A) Fe–TDH2, (B) Fe–TDH3 and (C) halved Fe–TDH3 mass. All initial SPION were in powder form.

TEM and EDX on Fe-TDH2@Si and Fe-TDH3@Si: Fig. 3.11 shows TEM results of coating applied to FeTDH 2 & 3 in initial powder form (sonicated for 20min after suspension in cyclohexane). Subfigures (A) and (B) show the results of applying Hou et al. protocol to Fe–TDH2 and Fe–TDH3, with some variations the applied drops were 40 µl instead of 35 and the incubation time varied between 4 and 20 h instead of 16 consistently. Despite that, silica coating consistently enrobes both samples. Even though homogeneity of the coating can be improved (by respecting the 16 h incubation more strictly?) the Hou et al. protocol seems to be more robust to their size variation than Pham et al: no loose silica masses were observed. Fig. 3.12 shows EDX results on the Fe–TDH3 sample: the presence of silica is confirmed and for some particles a higher concentration at the shell, combined with a lower concentration in the center, is visible, which is encouraging. In Fig. 3.11 (C) the initial nanoparticle mass was halved: this results in thicker shell thickness but no loose SiO_2. It confirms that this protocol is less sensitive than Pham et al. to matching the amount of nanoreactors with the amount of nanoparticles: TEOS in lower concentrations has lower tendency to form core-free silica in empty micelles. Furthermore, halving the nanoparticle mass at constant TEOS volume effectively doubles the TEOS-per-particle ratio, so that a thicker shell is the outcome expected from the scaling reported by Chang et al. [190] and Bagwe et al. [192].
Starting with nanoparticles in liquid suspension form resulted in less clustered images (thus corresponding samples) than starting with them in powder form. Fig. 3.13 shows the results of coatings on Fe–TDH 2 & 3 where liquid was the starting point. The fact that the SPION have not been dried results in clearly less agglomerated states on the TEM grid, therefore probably in suspension too, which

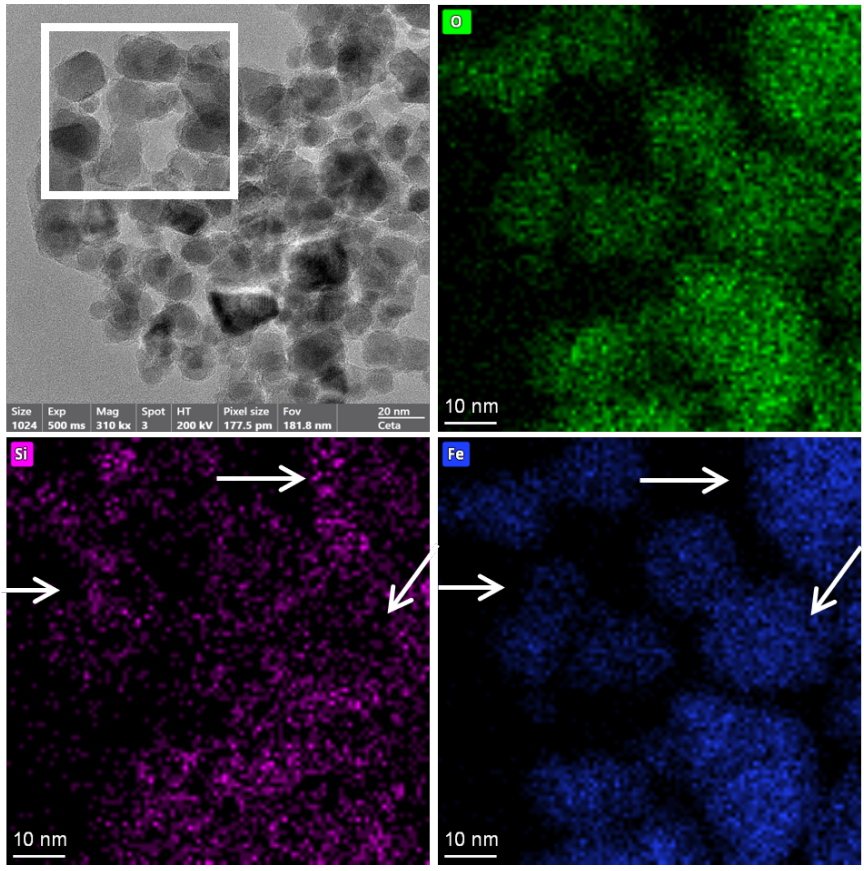


Fig. 3.12 Hou et al. Si coating protocol on Fe–TDH3: EDX results.

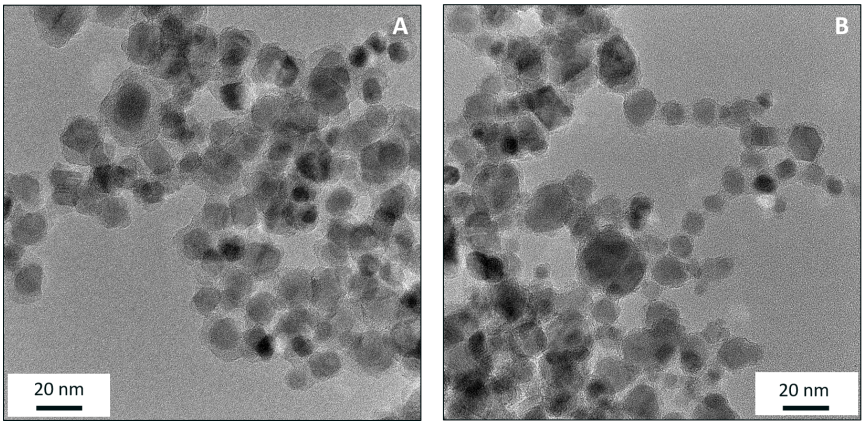


Fig. 3.13 Hou et al. Si coating - starting from MNP suspension

is a necessary condition towards individual enrobement of SPION. A tentative mechanism for this difference can be formulated in terms of the ligand exchange described earlier in this section. Starting from suspension preserves the original oleic-acid corona largely intact, whereas drying to powder may partially disturb it through capillary and contact forces during solvent removal. A degraded starting corona might compromise the first step of the oleic-acid to Igepal exchange, favouring partial agglomeration before they are transferred into the aqueous nanoreactors. This explanation remains a working hypothesis, since the state of the corona prior to coating has not been directly characterised in this work.

ICP on Fe-TDH4@Si: ICP analysis was performed on the Fe–TDH4@Si powder (starting core properties in Table 3.4; post-coating size was not re-characterised). The results are reported in Table 3.8. Assuming pure maghemite (γ-Fe_2O_3, 69.94 % Fe) and pure silica (SiO_2, 46.75 % Si), the 60.36 % Fe and 1.41 % Si mass fractions correspond to 86.30 % Fe_2O_3 and 3.02 % SiO_2, leaving $\approx$ 10.7 % residual mass attributed to the organic corona (oleylamine from the TD synthesis, Igepal residue from the microemulsion). The pure-maghemite assumption is an upper bound on the iron oxide mass fraction: in practice the core is a magnetite/maghemite mix (Fe mass fraction between 69.94 and 72.36 %), so the Fe_2O_3-equivalent fraction may be slightly overestimated, whereas the SiO_2 estimate is unaffected. The $\sim$ 3 % SiO_2 fraction obtained here is lower, per nanoparticle, than what would be expected for the halved-mass Fe–TDH3 batch of Fig. 3.11(C), consistent with the lower TEOS-per-MNP ratio used for Fe–TDH4 compared to Fe–TDH3 (Table 3.7).

Despite its long incubation time, the protocol of Hou et al. has proven to be a robust protocol for silica coating, less impacted than Pham et al. by nanoparticle size

Sample	Fe (%)	Si (%)	Fe_2O_3 (%)	SiO_2 (%)	Residual (%)
Fe–TDH4@Si	60.36	1.41	86.30	3.02	10.68

Table 3.8 ICP analysis of the coated Fe–TDH4@Si powder. Fe_2O_3 and SiO_2 mass fractions are derived assuming pure maghemite and pure silica. The residual mass is attributed to the organic corona (oleylamine + Igepal residue). Starting core properties ($\tilde{D}_{\mathrm{TEM}}$, γ) for Fe–TDH4 are reported in Table 3.4; post-coating size was not re-characterised.

(thus amount, for a given mass), suggesting less need for tuning when systematically applied to TD batches which may have some variability in median diameter. Partial drop addition of TEOS encourages condensation of silica on the SPION and avoids corefree silica. A correlation is observed between shell thickness and total TEOS mass. Further studies should aim for more homogeneous coating (by e.g. less variable incubation time, which was the case here for practical constraints). Little aggregation is observed when they are not in powder form, favouring individual enrobement. While reversed micro-emulsion handles small nanoparticles masses which is a major bottleneck for industrial use [1], it can be a reliable method for research purposes where controlled shell thickness allows to study the impact of dipolar interactions by controlling interparticle distance.

Section summary

Silica coating of TD SPION was investigated using two reverse microemulsion protocols, Pham et al. [193] and Hou et al. [195]. Coating quality was assessed by TEM imaging and by Energy Dispersive X-ray Spectroscopy (EDX). The goal is to achieve a homogeneous and individual silica shell around each particle while avoiding core-free silica spheres, given the batch-to-batch variability of $\tilde{D}_{\mathrm{TEM}}$ inherent to the TD protocol of this work. Fe–Comm was included as an informative benchmark only.

Consolidated conclusions:

- Reverse microemulsion is a suitable route for the hydrophobic TD SPION of this work: the Igepal CO 520 mediates the ligand exchange from the oleic acid corona and transfers them into the aqueous nanoreactors where silica forms, avoiding the preliminary silanisation step that a direct Stöber protocol would require.
- The Pham et al. protocol, with a single TEOS addition, is strongly sensitive to the initial particle diameter which influences the ratio between the amount of nanoparticles and the amount of nanoreactors (for a given MNP mass): core-free SiO_2 nucleation occurs in empty micelles. Applying the published mass ratios to TD batches whose median diameter differs from Pham's reference produced predominantly core-free silica spheres (Fig. 3.9, Table 3.6). Tuning the Igepal volume to match a smaller median diameter yielded genuine shell attachment on Fe–TDH2 without core-free silica, but the same conditions applied to the slightly larger Fe–TDH3 still left loose silica masses (Fig. 3.10). A single fixed Igepal volume is therefore insufficient across the size range obtained by the TD protocol of this work.
- The Hou et al. protocol, which delivers TEOS by fractionated drops over long cumulated incubations, is robust to nanoparticle size variations. Silica enrobement was obtained on Fe–TDH2, Fe–TDH3 and Fe–TDH4, with no core-free silica observed (Fig. 3.11, Table 3.7). This is consistent with the Ding et al. [175] picture in which a slow monomer supply keeps the concentration below the level at which core-free clusters form, favouring condensation onto existing nanoparticle surfaces. The same dropwise strategy also produced silica attached to Fe–Comm, where the single-addition Pham protocol had failed.
- Within the Hou protocol, shell thickness is correlated with the total TEOS mass per particle: halving the initial nanoparticle mass at constant TEOS volume increased the shell thickness without producing core-free silica (Fig. 3.11C), as expected from doubling the TEOS-per-particle ratio following the trends reported by Chang et al. [190] and Bagwe et al. [192].
- Starting the Hou protocol from a liquid SPION suspension rather than from redispersed powder produced visibly less agglomerated coated samples (Fig. 3.13). Preserving the native dispersion before coating is therefore a practical leverage towards individualised silica shells, which is directly relevant for later studies where interparticle distance is a controlled variable.

Observed trends requiring further investigation:

- The homogeneity of the silica shells obtained with the Hou protocol remains visibly irregular (Fig. 3.11). Whether this reflects the shortened and non-constant incubation times adopted here (4–20 h between drops, instead of the 16 h constant step prescribed by Hou et al.) or the intrinsic size dispersion of the TD batches cannot be disentangled from the present data.

- The superior dispersion obtained from liquid starting suspensions is attributed to a better-preserved oleyamine corona before the ligand exchange step, since drying to powder may degrade the corona.

Perspectives:

- Establishing a systematic calibration curve linking $\tilde{D}_{\mathrm{TEM}}$ to the optimal Igepal volume for the Pham protocol, with the water-to-surfactant ratio identified by Bagwe et al. [192] as the primary control parameter, would make the Pham protocol practical for the TD batches of this work despite their batch-to-batch variability in median diameter. Since this protocol is 14 times shorter than the Hou protocol, exploring the relevance of such a calibration curve may be relevant if practical applications require to perform the coating often. Indeed, the variability of median nanoparticle size is not proper to the TD batches used in this work, it has been confirmed multiple times on both research-grade as commercial nanoparticles [5].

- The EDX analysis of the coated Fe–TDH3 sample shows, for some particles, a silicon-rich shell and an iron-rich centre, but no systematic quantification of shell thickness across the population has been performed. This would be relevant for confirming homogeneity and the correlation between initial TEOS concentration, nanoparticle diameter and shell thickness.

- The Hou protocol should be repeated with the originally prescribed 16 h constant incubation between TEOS drops, on a TD batch of well-characterised $\tilde{D}_{\mathrm{TEM}}$, to test whether coating homogeneity can be improved while preserving the protocol's robustness to particle size.

- The coated Fe–TDH samples prepared here feed into the magnetic characterisation of Chapter 4, where the (thin) silica shell is associated with an improved initial susceptibility and lower effective anisotropy. Reproducing the coating on several batches with varying shell thickness, and comparing samples that underwent the ligand exchange without silica deposition, would allow to disentangle the contribution of (1) ligand exchange improving surface state of the SPION, (2) the silica shell improving surface state of the SPION and (3) the affected dipolar interactions due to physically controlled distance between particles.

Chapter Summary

This chapter addresses the synthesis, structural characterisation and silica coating of SPNFs intended for inductive biosensing on lateral flow assays. Two synthesis routes are compared, TD and CP, and a reverse microemulsion silica coating is developed for the hydrophobic TD products.

Size characterisation. Comparing nanoparticle sizes across measurement techniques requires attention to their respective weighting: TEM provides number-weighted distributions, XRD is volume-weighted and DLS is intensity-weighted. For monodisperse samples these converge, but for polydisperse batches discrepancies can exceed 75 %. The lognormal distribution is the appropriate model for nanoparticle size data, and its validity is assessed throughout this work with the Kolmogorov–Smirnov test. Conversion between lognormal parameters (shape factor γ) and normal parameters (coefficient of variation) is only reliable for narrow distributions. A Bezier-curve-based tool was developed for TEM analysis, which determines an equivalent circular diameter from the contour of each particle and quantifies shape irregularity via the inscribed-to-circumscribed circle ratio.

Thermal decomposition. The TD protocol, based on [135], produces lognormally distributed SPION with median diameters in the 7–11 nm range and shape factors between 0.16 and 0.27. The majority of batches satisfy the ISO 22412 monodispersity criterion ($\gamma^2 < 0.05$). Doubling the reagent quantities does not alter the size distribution, which is relevant given the low yield per run. A positive correlation between reflux duration and median diameter is observed, consistent with continued monomer-addition growth during the reflux plateau. However, the median diameter is not repeatable across batches, varying by nearly a factor of 1.5. TEM images confirm clear inter-particle spacing, indicating that they are agglomerated but not aggregated, which validates the assumption that inter-particle exchange interactions are negligible. They carry a hydrophobic oleylamine corona and require phase transfer before use in aqueous media.

Coprecipitation. The CP samples, synthesised by collaborators following the protocol of [170, 171], cover iron oxide, manganese ferrite and cobalt ferrite compositions with median diameters from approximately 8 to 34 nm. Size distributions are significantly broader than those of TD batches, with shape factors ranging from 0.25 to 0.46. The citric acid corona (7–16 % of sample mass) renders them hydrophilic and results in higher colloidal stability compared to the TD nanoparticles of this work. ICP analysis reveals a systematic Mn depletion in the smaller manganese ferrite samples, consistent with size-dependent preferential dissolution of Mn^{2+} and the formation of a core/shell structure with an Fe-rich surface layer [170, 172].

Silica coating. Two reverse microemulsion protocols were compared for coating the hydrophobic TD SPION with silica. The protocol of Pham et al. [193], which adds TEOS in a single step, is sensitive to the particle-to-nanoreactor ratio and produced core-free silica when applied to batches whose median diameter differed from the reference value. The protocol of Hou et al. [195], which delivers TEOS by fractionated drops each followed by 16 h of incubation, yielded consistent silica enrobement without core-free by-products across the range of median diameters encountered in this work, and the shell thickness scales with the total TEOS-per-particle ratio. Depending on the target shell thickness, 5 to 15 additions may be required, bringing the total incubation time to several days or even weeks, which is the main practical constraint of this protocol. Starting the coating from a liquid SPION suspension rather than from redispersed powder appears to reduce agglomeration, favouring individual particle coating. While the silica-coated nanoparticles remain dispersed in organic solvent at this stage, the silica shell is a step towards biocompatibility and provides silanol surface groups suitable for biomolecule conjugation. The controlled shell thickness is also directly relevant for later studies in which the silica spacer is used to investigate the effect of dipolar interactions on magnetic properties (Chapter 4).

Towards integration in lateral flow assays. All median diameters obtained by TD (7–11 nm) fall well below the critical superparamagnetic diameter D_c reported for magnetite and maghemite (Subsection 2.3.1, Table 2.3), confirming that these particles are in the superparamagnetic regime. The CP samples span a wider range: the smaller batches are superparamagnetic while the largest (Mn–CP1, 34 nm) likely exceeds D_c for manganese ferrite and may exhibit partial magnetic blocking. The two synthesis routes present complementary advantages and limitations for integration in LFA biosensors. TD nanoparticles have monodisperse size distributions, which are expected to yield a more uniform magnetic response, but they are hydrophobic and produced in small quantities per batch. Silica coating provides a route towards biocompatibility and functionalisation, yet the coating step introduces additional complexity and limits throughput. CP nanoparticles are hydrophilic, colloidally stable and produced at higher yield, making them closer to the requirements of the aqueous environment of a lateral flow strip. Their broader size distributions, however, are expected to produce a less uniform magnetic response (Chapter 4). The fluidic behaviour of these nanoparticles within a lateral flow membrane, including the effects of agglomeration and surface chemistry on capillary transport, is discussed in Chapter 7. The nanoparticle libraries assembled here, summarised in Tables 3.4 and 3.5, span different compositions, size ranges and surface chemistries and provide the material basis for the magnetic characterisation and inductive sensing experiments presented in Chapters 4 and 6.

4

Superparamagnetic nanoparticles : Magnetic Characterisation and Metrology

Magnetic susceptibility of SPNFs is not a fixed material property: it depends on particle volume, surface state, inter-particle interactions, and the configuration in which the sample is measured. Section 4.1 develops this motivation and identifies the LFA geometry (nanoparticles immobilised within a nitrocellulose membrane after capillary flow and drying) as particularly under-characterised in the literature.

To address this, the chapter applies four complementary characterisation techniques (magnetisation curves at 300 K, FC-ZFC, ACS, and MHz–GHz impedance analysis) to identical SPNF batches in four configurations (powder, nitrocellulose membrane, water suspension, agar-agar suspension), varying composition (Fe, Mn, Co ferrites), synthesis route (TD vs CP), size and coating. The scope, overview figure and unit conventions are introduced in Section 4.2. Suspension configurations are deferred to Chapter 6, which uses inductive coils better suited to volumetric samples.

The original contribution of this chapter is the systematic paired powder/membrane characterisation of the same batches across the four techniques. Results are interpreted within the framework of Chapter 2, consolidated with TEM data from Chapter 3, and summarised in Tables 4.14 and 4.15.

4.1 Motivation: configuration-dependent susceptibility

When aiming for quantitative biosensor integration of SPNF, one needs to correlate a measurable transduction signal with a quantity of nanoparticles. This requires characterisation of SPNF, modelling and calibration. In what follows, we discuss how (i) particle volume plays a dominant role in every relevant magnetic property, (ii) the effective magnetic volume is itself highly variable, (iii) measurement conditions may fundamentally differ between characterisation and end-use, and (iv) the specific configuration of a lateral flow assay remains poorly characterised magnetically.

4.1.1 The central role of MNP

The volume of SPNF enters almost every magnetic quantity introduced in Chapter 2, but through different functional forms. Table 4.1 collects these dependencies on both hydrodynamic V_H as magnetic V_{mag} volumes.

The contrast between these functional forms is the central point: a 10 % increase in diameter D translates to a $\sim$33 % increase in volume. While T_B shifts proportionally, the Néel relaxation time τ_N shows exponential dependence. Initial and static susceptibilities (χ_i and χ_0) are proportional to V_{mag}^2 (a 33 % volume increase aug-

Quantity	Dependence on V_{mag} or V_H	Equation
Néel relaxation time τ_N	exponential ($e^{K_{\mathrm{eff}} V_{\mathrm{mag}} / k_B T}$)	Eq. 2.30
Brownian relaxation time τ_B	linear (V_H)	Eq. 2.35
Blocking temperature T_B	linear ($K_{\mathrm{eff}} V_{\mathrm{mag}}$)	Eq. 2.32
Initial susceptibility χ_i	quadratic ($\propto V_{mag}^2$)	Langevin Eq. 2.40
Static susceptibility χ_0[†]	quadratic ($\propto V_{mag}^2$)	Debye Eq. 2.47

[†]For non-interacting particles above T_B, χ_0 (derived by Debye) and χ_i (derived by Langevin/Chantrell) are identical; the distinct symbols reflect DC vs. AC convention (cf. Section 2.3.5).

Table 4.1 Dependence of key magnetic quantities on particle volume. All equations are derived in Chapter 2.

ments χ_i with 80 %) [1]. Two samples with the same median diameter but different size distributions (quantified by the lognormal shape factor γ, cf. Section 3.1.3.2) can yield very different magnetic signatures, as was demonstrated by Woodward et al. [119].

4.1.1.1 The magnetic diameter $\tilde{D}_{\mathrm{mag}}$ depends on synthesis, storage and set-up

Assuming the physical SPNF diameter D_{TEM} is well characterised (Chapter 3), the *magnetically active* volume V_{mag} relevant to the equations above is subject to multiple sources of variability.

- **Dead layer and spin canting.** The magnetic diameter D_{mag} is systematically smaller than D_{TEM} due to magnetically disordered surface spins (Section 2.3.7.1), reducing the effective moment $m_{\mathrm{NP}} = M_s V_{mag}$. This is mainly determined for the batch at the moment of synthesis but can be affected by any surface state modification.

- **Oxidation state and stoichiometry.** Partial oxidation and non-stoichiometric cation distributions lower $\sigma_{M,s}$ below bulk values. The SPNF state of oxidation is variable over time and is influenced by surfactant and conservation conditions.

- **Inter-particle interactions.** Dipolar interactions modify the effective energy barrier and break the uniaxial symmetry assumed by the Stoner–Wohlfarth and Néel–Arrhenius models, altering τ_N in ways that are difficult to predict analytically [47, 50]. Depending on the interaction strength, consequences range from subtle modifications of the effective energy barriers to collective spin-glass ordering [69].

[1]Note that the Debye expression for χ' and χ'' depends on effective relaxation time τ_{eff}, therefore depending on both V_{mag} and V_H (if MNP are free to rotate).

4.1.1.2 The hydrodynamic volume is variable

Even when the magnetic core is well characterised, the hydrodynamic volume V_H that governs Brownian relaxation (Section 2.3.3) can vary by orders of magnitude depending on the physico-chemical environment. Because $\tau_B \propto V_H$ and V_H enters the Debye model through the effective relaxation time, any change in V_H directly shifts the frequency-dependent susceptibility spectrum.

- **Coating and surfactant shell.** The hydrodynamic volume includes the magnetic core, any organic or inorganic coating, and a solvation layer that moves with the particle [54, 56]. Coating thickness is itself subject to batch-to-batch variability (cf. Chapter 3).
- **Agglomeration and clustering.** Even in nominally stable colloids, a fraction of particles may form dimers, trimers or larger clusters, whose hydrodynamic volume scales with the agglomerate, not the individual core. Affecting pH or ionic strength of the nanoparticle medium affects the agglomeration state [178, 180]. This is particularly relevant for biomedical applications: physiological saline and functionalisation buffers can have higher ionic strengths than suspension media during characterisation [2].
- **Carrier fluid viscosity.** Since $\tau_B = 3\eta V_H / k_B T$, the dynamic viscosity η of the carrier medium acts as a multiplicative factor on the Brownian relaxation time. Replacing water by a biological matrix shifts τ_B proportionally, without any change in particle size.

V_H is not a fixed particle property but a system-level quantity that depends on coating, solvent composition, pH, ionic strength and agglomeration state. Transferring a Brownian relaxation time measured under one set of conditions to a different environment therefore requires explicit knowledge of, or control over, each of these parameters.

4.1.2 Measurement conditions differ fundamentally from end-use

The main models describing superparamagnetism impose ideal conditions (cf. Table 2.5). In any real physical configuration, these hypotheses are not all fulfilled. When conditions vary between characterisation and sensing, the sources of bias vary as well:

4.1.2.1 The LFA configuration is poorly characterised for MNP

In a LFA, nanoparticles are captured on a NC membrane at the test line. Once dried, particles are immobilized so no Brownian contribution exists. The drying

[2] Tombácz et al. [167] showed that the salt tolerance of magnetite nanoparticles depends critically on the adsorbed organic acid, with citrate-coated particles remaining stable up to ∼500 mM NaCl while uncoated particles agglomerate at much lower concentrations.

and capillary flow steps likely affect agglomeration.

Comprehensive characterisation of the core size, magnetic behaviour and agglomeration state are identified by Salvador et al. as essential for optimising the sensitivity and performance of magnetic LFA [97]. Characterising nanoparticles in conditions as close as possible to this final system thus motivates the inclusion of membrane-based samples and the direct comparison with powder (in this Chapter) and suspension configurations (in Chapter 6).

4.2 Chapter Scope: techniques, parameters, and configurations

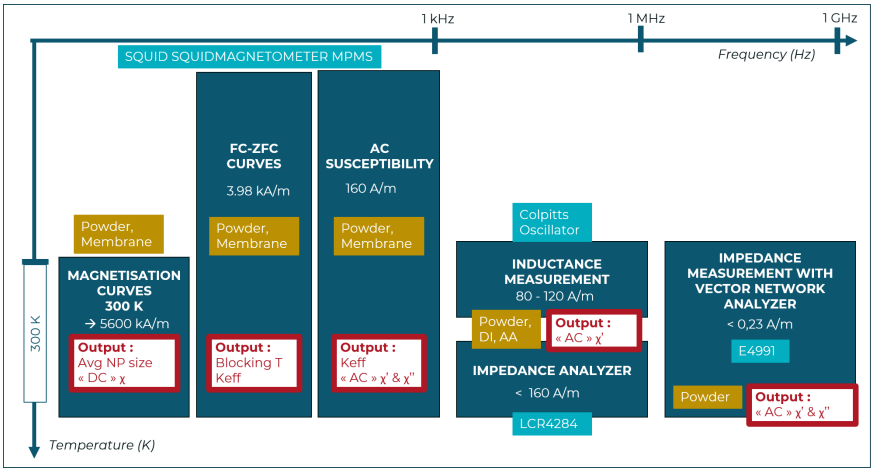


Fig. 4.1 Measurements and relevant output as a function of temperature and frequency. Note: frequency and temperature are not at scale.

Fig. 4.1 offers an overview of the main characterisation methods used in this work and applied. All these are well below the linearity limit, justifying a fundamental assumption in what follows: the susceptibility χ is configuration-dependent, and not H-dependent. Table 4.2 summarizes the main parameters we wish to (indirectly) deduce per measurement-type.

Data collected between 1 kHz and 1 MHz is measured with different inductors, connected to either a portable Colpitts Oscillator or an impedance analyzer. Due to the flexibility offered by the inductor shape, these are the only measurements that allowed to measure nanoparticles suspended in water (i.e. free to rotate) and compare them with nanoparticles at the same concentration suspended in

	Magnetisation at 300 K	**FC – ZFC Curves**	**AC Susceptibility Data**	**Coil Impedance Measurements**	**VNA measurements**
Average Magnetic Diameter D_{mag}	Langevin Eqn. for Stoner - Wohlfarth MNP				
Nanoparticle Size Distribution with (γ)	Chantrell Eqn (lognormal)			Hydrodynamic size (distribution), from Brown relaxation	
Effective Anisotropy Constant K_{eff}		Based on blocking T.	Néel-Arhennius & Vogel-Fulcher		
Blocking Temperature T_b		Derived from max difference btwn FC and ZFC magnetisation curves (depending on τ_{meas})	At temperature where χ'' is max (depending on frequency)		
Initial Susceptibility χ_i	Magnetisation slope in linear range				
Neel Relaxation time constant τ_N		Based on blocking T. & msmt freq.	Decrease in χ', increase in χ''		Decrease in χ', increase in χ''
Brownian Relaxation time constant τ_B			Debye Model	Decrease in χ'	Debye model
Nature of Interactions	Rate at which saturation is reached	Diff. irreversibility & blocking T.	Mydosh Parameter	« sharpness of slopes »	« sharpness of slopes »

Table 4.2 Overview of significant data extract from characterisation methods. Turquoise font refer to properties which are **"directly observable" from data**. Green font refer to models **implying hypotheses** (cf. Table 2.5 for the hypotheses). Gray font refers to **qualitative information**. Note : brownian relaxation is only applicable when the SPNF are free to rotate.

agar-agar (i.e. blocked rotation). Given that these inductors correspond rather to a "sensor" set-up, they are discussed in Chapter 6. This Chapter is dedicated to conventional metrology equipment for magnetic materials: below 1 kHz with the SQUID magnetometer (cf. Sections 4.3 - 4.5) and above 1 MHz with a Vector Network Analyser (VNA) (Section 4.6). All SQUID magnetometer measurements were performed in collaboration with the IRM-KMI, specifically by Dr. Simo Spassov.

The work of Garcia et al. [196] identifies good practices and characterisation errors to avoid. Unless mentioned differently, samples were handled with plastic or paper tweezers to avoid contact with metals and measurements were corrected

for diamagnetic effects of the holder (i.e. kapton tape or cellulose).

In this work, we introduce four characterisation techniques, four varying nanoparticle parameters and four different substrates.

Introduced Characterisation Techniques in this Chapter:

1. **Magnetisation curves up to 7 T**: full hysteresis and initial magnetisation at 300 K (room temperature).
2. **FC-ZFC Curves ranging from 4 K to 300 K**: in In Field Cooled cooling (IFCC) and Zero Field Cooled warming (ZFCW). Probing field is 50 Oe unless mentioned differently.
3. **ACS between 10 Hz and 1 kHz**. Probing field is 2 Oe unless mentioned differently.
4. **Impedance analysis between 1 MHz and 1 GHz**, probing field is varying but below 20 Oe unless mentioned differently.

Nanoparticle Parameters:

1. Varying **nanoparticle elemental composition**: samples of manganese ferrite oxide, cobalt ferrite oxide and magnetite are compared.
2. Varying **synthesis method**: magnetite nanoparticles, originating from both TD and CP, resulting in different crystallinity, coating and oxidation, are compared. The synthesis protocols have been introduced in Chapter 3. Tables 3.4 and 3.5 contain the available TEM and ICP data for the batches used in this chapters. The naming of the samples is consistent throughout the work.
3. Varying **size**: several sizes of MNP are studied: 50 nm polydisperse magnetite nanoparticles (commercially bought, Fe–Comm), 8-10 nm SPION made by TD and 8-33 nm SPNF made by CP.
4. Varying **coating**: SPION synthesized by TD, with and without silica coating, are characterised.

Nanoparticle Configurations:

1. Powder form: dry, conventional form. Easily adaptable to characterisation set-ups (can be encapsulated in various manners). Nanoparticles are packed, highly interacting and immobilized.
2. Agar-Agar suspension: dispersed nanoparticles, immobilized nanoparticles. Interactions depend on suspension concentration.
3. Water suspension: allow to mimic identical concentrations as agar-agar suspensions. Comparison between both configurations allows to isolate the effect of mobility of the nanoparticle agglomerations.

4. Dispersion in cellulose: less conventional configuration but closest to mimic the LFA system.

Magnetisation measurements and Field Cooled (FC)-Zero Field Cooled (ZFC) curves are obtained for both powder samples and these respective samples pipetted and dried on cellulose membranes. Given their time-consuming nature, ACS measurements are mainly made for nanoparticles in membranes (which is closest to a LFA-like set-up), with a few powder measurements for comparison. VNA measurements are made on nanoparticles in powder form only, as attempts on cellulose membranes stacked within the toroidal sample holder did not exceed the noise floor (cf. Section 4.6). The complementary case of nanoparticles in agar-agar and water suspensions, and how rotational mobility affects the change in inductance, is studied in Chapter 6.

4.2.1 Convention: Mass Density and Specific Magnetisation of MNP

Formula	$\sigma_{M,s}$ (Am^2/kg)	$\mathbf{K_m}$ (kJ/m^3)
Fe_3O_4	92	11
γ-Fe_2O_3	80	4.6
$MnFe_2O_4$	80	3
$CoFe_2O_4$	80	200
$NiFe_2O_4$	50	6.2

Table 4.3 Room temperature magnetic properties of bulk ferrites. Saturation magnetisation's equivalent units are emu/g.

Table 4.3 lists saturation magnetisation and magnetocrystalline anisotropy for bulk ferrites. These compounds are strictly ferrimagnetic, but are referred to as ferromagnetic throughout this work, as the sublattice structure does not enter the macroscopic measurements and models used here. Because these compounds have well-defined crystal structures and densities, literature values are conventionally reported as specific (mass) magnetisation $\sigma_{M,s}$ (Am^2/kg, equivalent to emu/g). Converting to volumetric magnetisation M_s (A/m) is then straightforward once the bulk density is known. For magnetite nanoparticles we consider

$$\mathrm{M_s(A/m)} = 91(\mathrm{A\cdot m^2/kg}) \times 5180(\mathrm{kg/m^3})$$

For manganese ferrite we consider

$$\mathrm{M_s(A/m)} = 80(\mathrm{A\cdot m^2/kg}) \times 5000(\mathrm{kg/m^3})$$

These conversions assume ideal stoichiometry, pure Fe_3O_4 or $MnFe_2O_4$, which is rarely the case for real nanoparticles. Farshidfar et al demonstrated e.g. that

their magnesium ferrite nanoparticles (around 10nm diameter) have a theoretical density of 4.51 $\left[\frac{g}{cm3}\right]$ but an observed one of 3.77 $\left[\frac{g}{cm3}\right]$ [197]. Even for highly crystalline single-crystal magnetite, $\sigma_{M,s}$ is size-dependent: values ranging from 84.7 emu/g (287 nm) down to 54.7 emu/g (9.6 nm) have been reported, compared with ∼92 emu/g for the bulk [41]. Similarly, the nanoparticles employed in magnetic biosensing studies exhibit saturation magnetisations well below the bulk values of Table 4.3: Marquina et al. report 40 emu/g for commercial magnetite nanoparticles [5] and Moyano et al. 50 emu/g for Fe_3O_4@C nanoflowers with 10–20 nm crystallites [4], i.e. roughly 40–55 % of bulk magnetite. As will be confirmed in Section 4.3, the SPION and Mn-SPNF characterised in this work follow the same trend.

It is important to keep in mind that SPION are prone to oxidation, which leads to phase transformations that fundamentally alter their magnetic properties. The typical pathway proceeds from ferrimagnetic magnetite to ferrimagnetic maghemite [198]. This chemical change affects saturation magnetisation M_s: oxidation typically causes a marked reduction in M_s [199] which is consistent with the M_s values for bulk counterparts in Table 4.3. However, exceptions exist: some studies report an increase in M_s after controlled post-synthesis oxidation, attributed to improved crystallinity and the reduction of the magnetically disordered "dead layer" at the nanoparticle surface [198].

As shown in Chapter 3, the iron mass fraction in thermally decomposed magnetite powders varies between 60 and 69 % depending on oxidation conditions and surfactant mass (Table 3.4), while the Mn/Fe ratio in coprecipitated manganese ferrite deviates from the stoichiometric value due to Mn depletion at the nanoparticle surface (Table 3.5). The actual $\sigma_{M,s}$ of a given powder or nanoparticle suspension is therefore an effective rather than intrinsic quantity.

In practice, two normalisation conventions coexist in this chapter. The default is magnetisation per gram of powder (emu/g), which allows direct comparison with most published data. When the oxidation state or composition may have changed between sample preparations, for instance when the same batch is measured both as a dried powder and after pipetting a dilution on a membrane, , or when different stoichiometrically imperfect batches are compared, normalising per gram of iron (emu/g Fe) is sometimes preferred, because the iron content was determined independently by ICP without any assumption on the oxidation state or metal ratio (Tables 3.4 and 3.5). This convention has its own limitations: it prevents direct comparison with bulk reference values, and for mixed ferrites it attributes the full magnetisation to only one of the magnetic cations. However, ICP data in Tables 3.4 and 3.5 allow the reader to convert between conventions where needed. Normalisation per iron mass was also done in [200].

Another option would be to normalise per total magnetic metal mass, as done for instance by Iacovita et al. for the specific absorption rate[3] in [201]. While this accounts for all magnetic cations present, it implicitly treats their contributions to the net moment as equivalent, which is not strictly correct since Fe and Mn ions carry different magnetic moments and their effective contribution depends on site occupancy in the spinel lattice. This convention does not allow straightforward comparison either: it was not applied in this work.

The normalisation basis is stated explicitly for each dataset in the sections that follow.

4.2.2 Convention: Units

1. In literature it is common practice to normalise the magnetisation data as M/M_{max}. While this is relevant for Langevin fitting, comparing saturation rate,... it should be common practice for authors to specify the order of magnitude of measured magnetisation.
2. Fundamentally, **magnetisation M is the volume density of magnetic moment**, as required e.g. in the Sommerfeld convention $B = \mu_0(H + M)$ where H is the magnetic field strength $\left[\frac{\mathrm{A}}{\mathrm{m}}\right]$ and M is the volume magnetisation in $\left[\frac{\mathrm{A}}{\mathrm{m}}\right]$ equivalent to magnetic moment $\left[\mathrm{A}\cdot\mathrm{m}^2\right]$ divided by volume [29, 34]. This is further detailed in Chapter 2, Subsection 2.1.1. As a consequence, susceptibility $\chi = \frac{M}{H}$ (dimensionless in SI units) is a volume susceptibility and relative permeability $\mu_r = \chi + 1$ is also volume-based [46, 202]. It is incorrect to apply this to mass-based units!
3. When expressing magnetic moment per mass of material, this is called **specific magnetisation** σ_M. This can be relevant in specific cases, e.g. when handling nanoparticle samples that are weighted but which exact volume is unknown.
4. Since the ICP analysis (cf Chapter 3) does not allow to differentiate oxygen mass from surfactant mass, and since the magnetite/maghemite ratio in synthesised nanoparticles is not exactly known, we prefer referring to mass of iron instead of mass of powder for exact comparison.
5. Similarly, for manganese ferrite, ICP might reveal a Mn/Fe ratio which does not completely correspond to $MnFe_2O_4$. This is because the manganese ferrite nanoparticles, surrounded by a citric acid corona, might have "lost" some Mn at their surface. This is because manganese within ferrite is chemically

[3] The specific absorption rate (SAR) quantifies the power dissipated per unit mass of magnetic material under an alternating magnetic field, and is the central figure of merit in magnetic hyperthermia.

less stable in acid environments. For further reference, the reader is referred to [165, 170, 172, 203, 204]. As a result, it is sometimes preferred to normalise for mass of iron, an objective base for comparison based on ICP results.

4.3 Nearly-DC Magnetisation Curves, at 300K

4.3.1 Materials and Methods

4.3.1.1 Magnetometers: SQUID and AGFM

The main measurement tool for magnetisation curves is the SQUID magnetometer integrated in the MPMS3 from Quantum Design. SQUIDs are among the most sensitive magnetic sensors available [205] for static or low-frequency magnetic flux. They integrate one or two Josephson Junctions[4] allowing to detect magnetic flux with the precision of a magnetic flux quantum. Further details of this working principle are out of scope for this manuscript. It should however be noted that SQUIDs, while precise, must be cooled below the critical temperature of the superconducting loop (either liquid hydrogen or liquid nitrogen can be used), causing bulky infrastructure and significant maintenance constraints.

The Alternating Gradient Force Magnetometer (AGFM) is fundamentally a force magnetometer. Its operation is based on detecting magnetisation by measuring the force exerted on a magnetised sample when the sample is placed a constant DC field to which an alternating gradient magnetic field is superposed. This varying field produces an alternating force on a sample that possesses a net magnetic moment (depending on the DC field). This alternating force is quantified by a piezo-resistance interfaced with a lock-in amplifier [207]. The alternating gradient field is typically applied at a frequency that matches the mechanical resonance frequency of the probe (cantilever), usually in the range of 100–1000 Hz [208]. Another common magnetometer principle is the VSM in which the sample is mechanically oscillated, causing AC flux depending on the sample's magnetic moment caused by the DC field [209]. While AGFM and VSM magnetometers are less precise than SQUIDs, they are generally less expensive. It is worth citing Sankhi et al. who designed a low cost vibrating sample magnetometer based on audio components [210].

It should be noted that for the hysteresis curves, **no error bars are plotted** nor are the datapoints marked: the measured samples have a magnetisation which is

[4]Josephson Junctions consists of two superconductors separated by a thin non-superconducting barrier (a weak link). They exploit the Josephson effect, a macroscopic quantum phenomenon where Cooper pairs can tunnel across the barrier, creating a supercurrent without any voltage. Applying an external magnetic flux induces a spatial variation in the quantum phase across the junction. For further reference, the reader is redirected to [206].

high enough to allow for repeatable, smooth measurement curves.

4.3.1.2 Sample selection and preparation

Selecting studied SPNF samples

In Appendix A.5.2 it is demonstrated that manganese ferrite SPNF and iron oxide SPION have (nearly) SPM behaviour in powder form, while cobalt nanoferrites are blocked at room temperature due to high K_m (cf Table 4.3): fitting Chantrell equations or exploring the initial susceptibility χ_i for different configurations (dried membrane dispersion vs. powder form) is not relevant given their hysteresis. Therefore, Mn-SPNF and SPION (both CP and TD) are the main object of study in this Chapter. Note that Co–CP1 samples will be used in Chapter 6: their blocked state at room temperature make them an interesting benchmark for observing Brownian relaxation when the nanoparticles are suspended in water.

Sample preparation

Powder samples for the SQUID magnetometer consist of 0.5-2 mg of powder (specified in due time) within a small polymer tube while for AGFM, 0.05-0.1 mg of powder was encapsulated in a small peace of kapton tape. Appendix A.5.1 validates that both measurement methods yield coherent conclusions for powders, confirming consistency of results for both set-ups. **For the rest of this chapter, we use SQUID data generated on both powder capsules and cellulose membrane samples.**

Membrane samples were prepared by pipetting nanoparticle suspensions of known concentration onto cellulose squares (2.8×2.8 mm, 3 mm thick). This cellulose is used as a proxy for NC, the relevant membrane for LFA configurations. The membranes were never overflown. Inbetween droplet applications, supernatant was left to evaporate at ambient air for at least 25 minutes. This was repeated until the required mass of nanoparticles was deposited within the membrane. Two membrane attachment methods were used for the SQUID sample holder: membranes cut with scissors and fixed with glue (referred to as "SG"), and membranes laser-cut and attached with tape ("LT").

All membrane measurements in this chapter (magnetisation, FC-ZFC and AC susceptibility) used the standard Quantum Design quartz paddle sample holder. This holder consists of a flat paddle (∼4 mm wide) redrawn from a fused-silica rod, attached to a glass-filled polycarbonate adapter. Fused silica is electrically insulating, which eliminates eddy-current background during AC measurements, and its diamagnetic susceptibility ($\chi \approx -1.1 \times 10^{-5}$ SI) is small, temperature-independent, and therefore straightforward to subtract.

4.3.1.3 Measurement protocol

All magnetisation curves presented in this chapter were acquired using the MPMS3 from Quantum Design [211], operated in DC scan mode. In this mode, the sample is physically translated through a set of gradiometer superconducting pickup coils over a scan length of approximately 35–40 mm; the position-dependent voltage induced in the SQUID sensor is recorded and fitted to extract the magnetic dipole moment. Key instrument specifications relevant to these measurements are given by Quantum Design [211].

The applied field is calculated from the magnet current via a calibrated field-to-current ratio. Superconducting magnets can trap residual magnetic flux in their windings, creating a remanent field (typically ≈5 Oe after using the oscillate approach mode from 7 T) that causes the actual field at the sample to differ from the nominal set point. This Instrumental Remanent Field (IRF) is the primary motivation for the field-axis correction described in Section A.5.3.2 and Appendix A.5.3.

The measurement temperature was stabilised at 300 K with a 5-minute settling time. Before each measurement, the sample was centred in the gradiometer pickup coils using the instrument's DC locate scan. Two field sequences were employed depending on the measurement objective:

1. **Initial magnetisation curve** (0 to +7 T): the field was first ramped to 0.5 T, then brought to 0 T using the oscillate approach mode (progressively smaller oscillations to minimise trapped flux), followed by a 2-minute settling time. The field was then swept from 0 to $+7$ T at 350 Oe/s using linear field steps. These measurements do not require IRF correction, since the measurement starts at 0 T and does not cross zero field again, so the artefacts caused by trapped flux (apparent loop opening, branch shifting) do not arise.
2. **Full hysteresis loop** (± 7 T, four quadrants): starting from +7 T, the field was swept through a full four-quadrant loop (+7 T $\rightarrow -7$ T $\rightarrow$ +7 T). Each half-cycle was divided into segments: linear steps at high field (7 T to 1.5 T and 1.45 T to 0.4 T) and logarithmic steps near the origin (0.39 T $\rightarrow 0 \rightarrow -0.39$ T), concentrating data points in the region where magnetisation changes most rapidly. The field ramp rate was 350 Oe/s during measurement sweeps and 700 Oe/s for transit between sequences. This sequence is sensitive to IRF near zero field and therefore requires the correction described in Appendix A.5.3, using a Palladium standard measured with the identical field sequence.

4.3.1.4 Correction of Magnetisation Curves

Two types of corrections are applied: High Field slope Correction and IRF & Approach to Saturation (A2S). These are elaborated in Appendix A.5.3. In summary:

- High Field Slope Correction: corrects only the magnetisation axis by subtracting a linear slope (attributed to diamagnetic and paramagnetic contributions). It is a straightforward first-order correction, but it assumes complete saturation of the SPNF moments above 5 T, which may not hold due to dead layer effects.
- **IRF + A2S Correction:** corrects both axes: first corrects the field axis for instrumental remanent field (frozen flux trapped in the SQUID superconducting magnet), which otherwise produces artefacts such as apparently open hysteresis loops. A paramagnetic standard (Palladium) measured with the identical sequence is used to model the field error and shift the nominal field to the true field. The second step then models the high-field convergence accounting for the fact that the ferromagnetic component may not be fully saturated, and extracts M_s more precisely than the simple linear subtraction. These corrections were performed by Dr. Simo Spassov.

4.3.1.5 Chantrell Equation Fitting to Model Nanoparticle Size Distribution

Fitting the Langevin function to a magnetisation curve as to obtain magnetic diameter, can be done both for a single diameter as for a lognormal diameter distribution, as expressed by the Chantrell Equation (Eq. 2.41 in Chapter 2). Note that Chantrell model assumes perfectly spherical and non-interacting nanoparticles (Table 2.5). The validity of this will be discussed throughout this chapter, e.g. for powder samples.

IRF and A2S corrected data allow to determine the most suitable lognormal PDI of nanoparticle diameter distribution to fit the magnetisation data. In order to avoid over-representation of (nearly identical) saturated datapoints, the data is cut off at $4 \cdot 10^6$ [A/m] DC field amplitude (both positive and negative) corresponding to 5 [T]. The main fitting steps are:

1. Normalise the magnetisation data by scaling the entire loop to the range [-1, 1], using the loop's measured minimum and maximum moments.
2. Create a single, averaged curve by averaging the forward and backward branches of this normalised loop. For IRF corrected data of superparamagnetic samples, these should be nearly overlapping.
3. Performs a simple curve fit with the basic Langevin function to get a "single-size" initial guess for the diameter.
4. Use this guess to seed a minimisation routine, which fits the full Chantrell (log-normal distribution) model to the averaged data by finding the $\tilde{D}_{\mathrm{mag}}$ and γ.
5. Keep track of Sum of Squared Errors (SSE) to compare fitting accuracy for different samples

The SSE quantifies the goodness of fit by summing the squared differences between each measured data point and its corresponding model prediction:

$$\mathrm{SSE} = \sum_{i=1}^{N} \left(M_i^{\mathrm{meas}} - M_i^{\mathrm{model}} \right)^2 \tag{4.1}$$

where N is the number of measured field points, M_i^{meas} is the measured magnetisation at the i-th field value after IRF and A2S correction and normalisation between 0 and 1, and M_i^{model} is the corresponding value predicted by the Chantrell model (Eq. 2.41). A lower SSE indicates a better agreement between the Chantrell model and the experimental magnetisation curve. Comparing SSE values across samples therefore highlights cases where the ideal Langevin model is insufficient, e.g. due to spin canting or inter-particle interactions.

4.3.2 Magnetisation of Powder Samples (300 K)

4.3.2.1 SPION Powders at Room temperature: Magnetisation Curves

Fig. 4.2 contains the magnetisation data of SPION powders: 10 nm synthesised by CP (Fe–CP1) and nanoparticles made TD of different median sizes (Fe–TD). Commercial magnetite (130 nm) MNP are measured for comparison. In Table 4.5 the magnetic diameters obtained by fitting the Chantrell equation to superparamagnetic samples is compared to TEM observations. The reader's attention is drawn to the following observations:

Fe–Comm ($\tilde{D}_{\mathrm{TEM}}$ = 135.8 nm) do not show superparamagnetic behaviour: In the upper graph of Fig. 4.2 a coercivity of 5 mT is observed. This coercivity is consistent with Fig. 2.3: at 130 nm median diameter, iron oxide MNP are not considered superparamagnetic as summarised in Table 2.3. Due to its high PDI (cf Table 3.4) this batch is composed of monodomain SPION, monodomain nanoparticles with high coercivity, and polydomain nanoparticles.

- They reach saturation at the lowest external field (cf upper graph), since the magnetisation is dominated by non-SPM monodomain particles (higher initial moment) and polydomain particles (wall motion instead of coherent rotation).
- Despite reaching saturation at lowest external field, their initial susceptibility calculated from the initial magnetisation curve between 0 and 1 mT (not shown on the graph) is lower than the CP and TD powder samples, as summarised in Table 4.14. This can be explained by their coercivity of 5 mT.
- Fe-Comm show the highest $\sigma_{M,s}$ per iron mass (lower graph). Assuming Fe_3O_4 stoichiometry, they saturate at $\sigma_{M,s}$ = 93 emu/g which corresponds

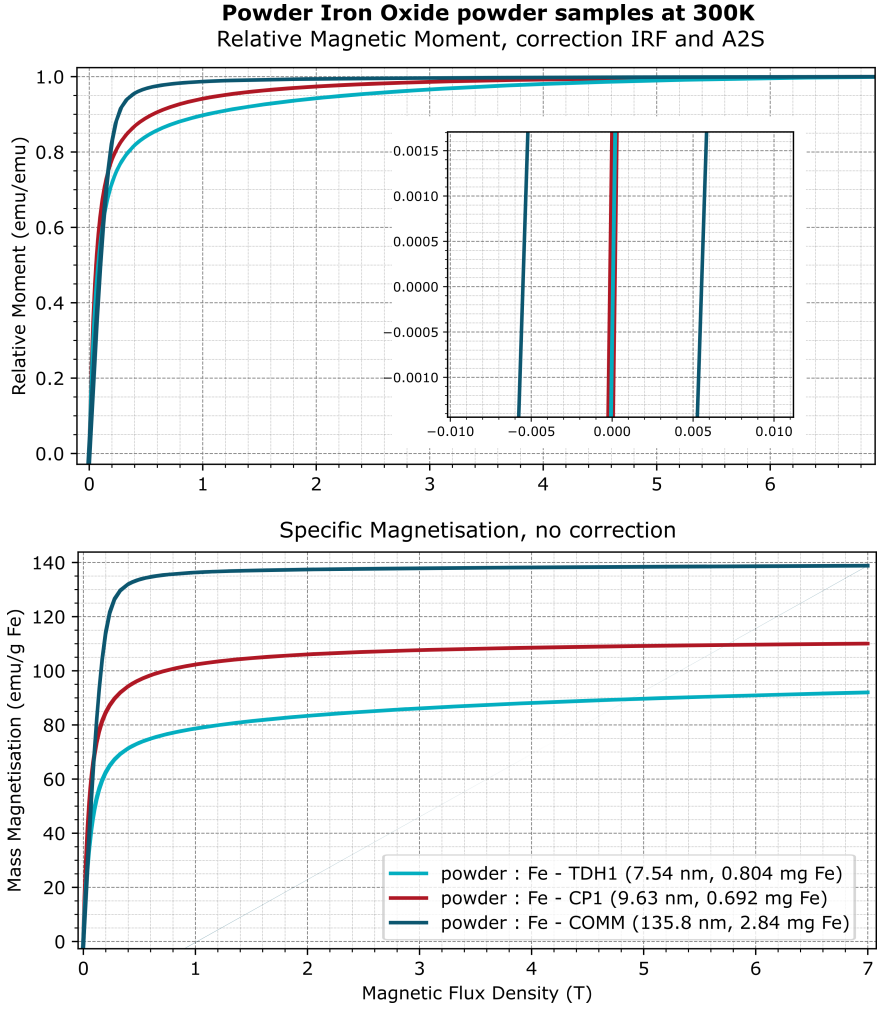


Fig. 4.2 Powders of iron oxide nanoparticles. Iron masses in the samples are specified in the legend. Dimensions are median diameters. Upper graph shows relative magnetisation with IRF and A2S correction. Lower graph shows specific magnetisation per iron mass, not corrected.

to the bulk counterpart in Table 4.3. This indicates that surface effects are little significant for the sample, even though the large size distribution (CV = 68%): the surface effects present for the sample fraction with the smallest diameters, are barely visible.

10.1 nm SPIONs made by CP show quasi-ideal superparamagnetic behaviour: The 10.1 nm nanoparticles made by CP (red) have a lower saturation magnetisation per iron mass than Fe–Comm: assuming Fe_3O_4 stoichiometry, we would expect them to saturate at 80% of their bulk counterpart. Saturation is nearly reached around 3 T. In the lower graph of Fig. 4.2 it can be observed that no (apparent) paramagnetism exists in uncorrected magnetisation curve.

TD SPIONS show a superposition of superparamagnetic and paramagnetic behaviour: Compared to the CP sample, SPION made by TD saturate at lower $\sigma_{M,s}$ and that their saturation occurs at higher field: when IRF and A2S correction are applied (upper graph), saturation is reached around 4.5 T. They saturate at $\approx$ 62 % of the bulk counterpart, consistent with Baaziz et al. [83] who analysed TD SPION.

Interestingly, when no correction is applied (lower graph), a paramagnetic component is clearly present. While the varying median diameters and size distribution of TD and CP samples cause differences in surface effects, this alone cannot explain these significant differences: no correlation is found between $\sigma_{M,s}$ and $\tilde{D}_{\mathrm{TEM}}$. The nanoparticles made by TD seem to have a significant paramagnetic component (lower graph, non-corrected). This might be due to the presence of dead layer or cation disorder. Indeed, Baaziz et al. [83] reveal a clear size-dependent evolution of composition and magnetic structure for SPION (made by TD):

- SPION smaller than $\sim$8 nm are almost entirely oxidised and display a composition close to maghemite. The smallest nanoparticles ($\sim$5 nm) exhibit mainly *surface* spin canting, with a canted shell thickness of approximately 0.4 nm (one atomic layer).
- 8–12 nm particles show intermediate composition with a perturbed oxidation state that does not present a well-defined core–shell boundary. They display both surface *and volume* spin canting, with a thicker canted layer of $\sim$0.7 nm (two atomic layers). The proportion of iron deviates from the expected values for either pure magnetite or maghemite, indicating cation disorder that destabilises the ferrimagnetic superexchange coupling within the volume.
- Nanoparticles larger than $\sim$12 nm consist of a stoichiometric magnetite core surrounded by a thin maghemite shell. They possess a well-defined magnetite core, show negligible volume canting and mainly residual surface spin canting whose relative contribution decreases with increasing size.

These findings offer a consistent explanation for the differences observed between CP and TD SPION. Fe-TDH1 and Fe-TDH4 both show this paramagnetic slope and fall precisely within the intermediate size regime identified by Baaziz et al., where volume spin canting is most pronounced. Disordered spins located deep within the particle volume, unlike surface-canted spins, require very large applied fields to align, which accounts for the persistent paramagnetic-like slope observed in all TD samples up to 7 T. Furthermore, the lower specific saturation magnetisation of TD samples compared to the CP counterpart (Fe–CP1: 10.1 nm), despite comparable sizes, is consistent with a larger fraction of canted volume spins reducing the net magnetic moment. The CP nanoparticles, synthesised in aqueous conditions without organic surfactant coating, may be less susceptible to the internal structural defects and cation disorder that Baaziz et al. attribute to the thermal decomposition route at these sizes.

Unni et al. [81] demonstrated that standard TD synthesis produces nanoparticles whose magnetic diameter distribution is significantly smaller and broader than the physical diameter distribution, indicating a thick magnetically dead layer. They attribute this to the fact that TD of iron oleates proceeds in an oxygen-poor organic solvent at high temperature (∼300°C). This strongly reducing environment favours Fe^{2+} over Fe^{3+}, promoting non-stoichiometry and crystal defects (cation vacancies on octahedral sites). By introducing controlled molecular oxygen during synthesis, they obtained particles with nearly identical physical and magnetic diameters, directly proving that the dead layer in TD particles is a synthesis-induced artefact rather than a purely geometric surface effect. In comparison, CP occurs in an aqueous alkaline environment where the Fe^{2+}/Fe^{3+} ratio is set by precursor stoichiometry, resulting in a thinner dead layer estimated at 0.5–0.9 nm [38].

4.3.2.2 Mn-SPNF Powders at Room temperature: Magnetisation Curves

Fig. 4.3 contains the magnetisation data of different manganese ferrite powders, all three of them synthesised by CP. Table 4.4 summarises the Fe/Mn fractions in each sample (values copied from Subsection 3.3.2.2) and the deduced specific saturation magnetisation either per sample mass or per iron mass.

Mn-CP1 (mean diameter 33 nm) do not show superparamagnetic behaviour: From the upper graph of Fig. 4.3, the 33 nm Mn–CP1 nanoparticles have the significant coercivity (3 mT). While the limit diameter between monodomain and pluridomain manganese ferrite nanoparticles is not easily determined due to low magnetocrystalline anisotropy K_m, the mean diameter is far above the SPM limit (D_c = 15 nm according to Table 2.3), explaining the observed coercivity. Furthermore, TEM images on Fig. 3.7 show that part of the nanoparticles is tetrahedric, probably contributing to shape anisotropy. As with Fe–Comm, these larger nanoparticles saturate at lower external field than their superparamagentic counterparts.

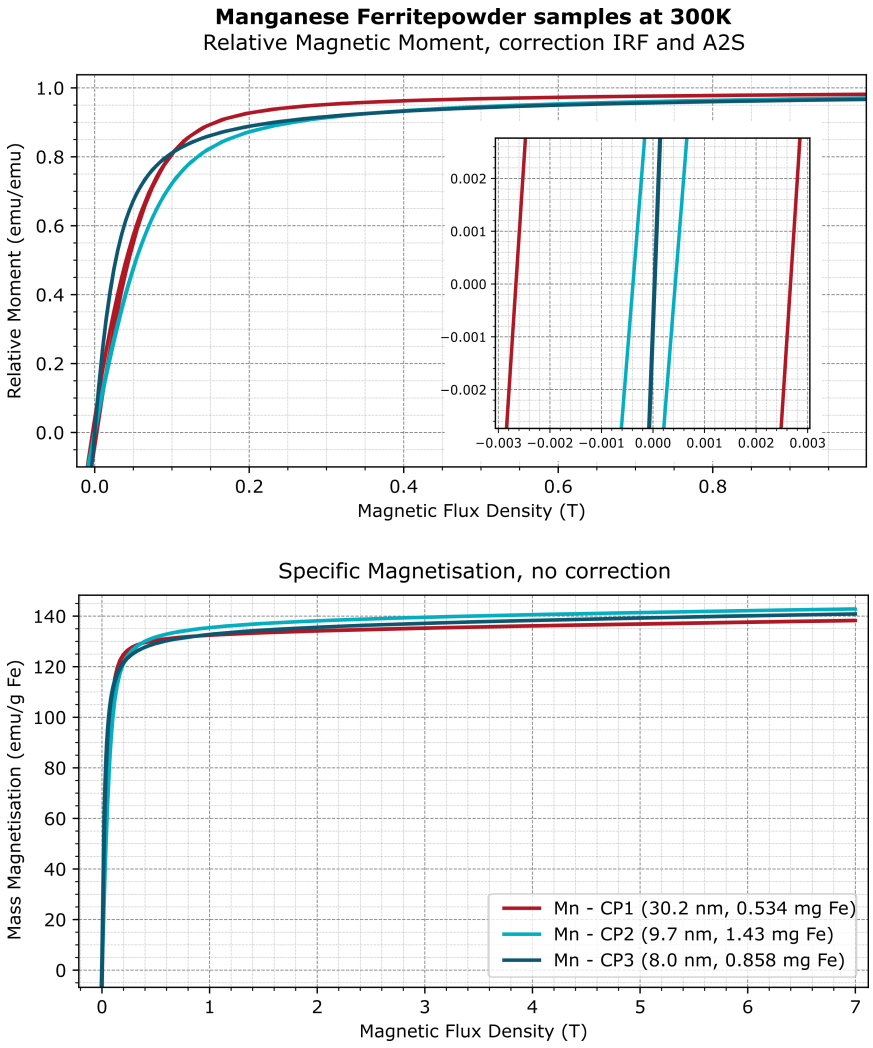


Fig. 4.3 Relative magnetisation and specific magnetisation per iron mass for powders of manganese ferrite nanoparticles. Masses of iron in the sample are specified in the legend. Note (1) that the diameters are mean and not median diameters derived from TEM images (cf. Fig. 3.7) and (2) that the x-axis of the upper graph goes from 0 to 1 T.

Mn–CP2 and Mn–CP3 (mean diameter resp. 10 and 8.9 nm) do show superparamagnetic behaviour: On the upper graph of Fig. 4.3, one observes that 10 nm Mn–CP2 and 8.9 nm Mn–CP3 have converging relative magnetisation curves beyond 200 mT. Below that point, a steeper magnetisation is observed for Mn–CP3: since they have a large size distribution (γ = 0.46), a fraction of their content is larger than Mn–CP2 (γ = 0.25), inducing dominating larger moments per nanoparticle thus contributing to a "quicker magnetisation" at lower external field (cf. Fig. 2.6).

Similar σ_M graphs for the three Mn–CP samples: In general, despite changes in Fe/Mn ratio and sizes for the three samples, their specific magnetisation curves (lower graph of Fig. 4.3) show less variation than for the SPION in Fig. 4.2. Two effects may contribute to this relative stability.

- The lower graph of Fig. 4.3 shows that Mn–CP1 has a slightly smaller $\sigma_{M,s}$, both per sample mass and per iron mass (Table 4.4). Given their larger diameter, we would expect less influence of surface effects and thus a higher $\sigma_{M,s}$ (as for magnetite nanoparticles in Subsection 4.3.2.1). This can be interpretated in light of the compositional differences reported in Subsection 3.3.2.2: Mn–CP1 (Fe/Mn = 1.94) is close to the stoichiometric $MnFe_2O_4$ composition, whereas Mn–CP2 and Mn–CP3 are Mn-depleted (Fe/Mn = 2.82 and 2.66 respectively). As demonstrated by Ma et al. [172], Mn depletion produces an Fe-enriched surface that structurally resembles maghemite. Since the bulk saturation magnetisation of γ-Fe_2O_3 is similar to that of $MnFe_2O_4$ (cf. Table 4.3), the Fe-enriched shell of the smaller particles may partially compensate for the dead-layer reduction that would otherwise lower their M_s.

- Manganese ferrite is less sensitive to the magnetite-to-maghemite oxidation pathway that dominates SPION variability, because the divalent Mn^{2+} ions are already in their most stable oxidation state under ambient conditions, unlike Fe^{2+} in magnetite which readily oxidises to Fe^{3+} [170].

	Mn–CP1	**Mn–CP2**	**Mn–CP3**
Magnetisation $\sigma_{M,s}$ @7T (emu/g powder)	63.5	67	66.2
Magnetisation $\sigma_{M,s}$ @7T (emu/g iron)	138	143	140
Fe mass fracion %	47.41%	48%	48.5%
Mn mass fraction %	24.5%	17%	18.2%
Fe/Mn mass ratio	1.94	2.82	2.66

Table 4.4 Specific Magnetisation σ_M and metal mass fractions. The stoichiometric Fe/Mn mass ratio for $MnFe_2O_4$ is 2.03.

4.3.2.3 Superparamagnetic Mn–CP3 have higher χ_i than Fe–CP1 (powder form)

In Table 4.14 the initial susceptibilities χ_i for powder forms, are derived from the slope between 0 and 1 mT of initial magnetisation curves (not shown on the graphs). For Mn–CP3, χ_i = 14.8 while for Fe–CP1, χ_i = 6.36. This can be directly attributed to the lower K_m of manganese ferrite (cf Table 4.3) and underlines the attraction for manganese ferrite nanoparticles as biosensing labels in e.g. LFA [171].

4.3.2.4 Fitting Powder Magnetisation Curves to the Chantrell Equation

In Table 4.5 the median magnetic diameters obtained by fitting the Chantrell equation (as described in Subsection 4.3.1.5) are compared to TEM observations. Langevin Function assumes no interactions, but these are undoubtedly significant in powder samples [97]. Dipolar interactions can be considered as increasing the effective anisotropy constant K_{eff} as explained in Subsection 2.3.6.2. When K_{eff} is significant, aligning all moments requires a larger external field. A signature of significant anisotropy is that higher external field is required to achieve saturation. As shown in Fig. 2.6, this tends to decrease the equivalent fitted Langevin diameter. Unsurprisingly, the fitted median magnetic diameter $\tilde{D}_{mag}$ in powder form is smaller. Except for Mn–CP2, the fitted shape factor of the lognormal distribution γ is similar.

	TEM data			Chantrell Fitting		
Powders	Mean D (nm)	$\tilde{D}_{TEM}$ (nm)	γ	Median $\tilde{D}_{mag}$ (nm)	γ	SSE
Fe–CP1	10.1	*9.6*	0.31	7.95	0.29	0.037
Fe–TDH1	7.89	7.54	0.27	7.3	0.39	0.20
Mn–CP2	10.1	*9.7*	0.25	8.95	0.01	0.043
Mn–CP3	8.9	*8.0*	0.45	11.0	0.32	0.058

Table 4.5 Mean and Median ($\tilde{D}_{TEM}$) particle diameters & distributions for Mn-SPNF and SPION obtained by TEM images. Comparison with median $\tilde{D}_{mag}$ obtained by fitting a lognormal distribution into the Chantrell Equation. γ is the shape factor of the (fitted) lognormal distribution as introduced in Subsection 3.1.3.2. Upright numbers are extracted directly from the TEM data. Italic data are deduced assuming perfect lognormal distribution.

The fitted magnetic diameter of CP nanoparticles is larger then for TD particles, consistent with the TEM data. The exact proportionality is not maintained, probably due to different enrobement type (oleyamine vs CA) and mass fractions, altering interactions. Interestingly, the SSE for Chantrell equation fitting is 6 to 10

times higher for TD nanoparticles than for CP nanoparticles. The presence of a dead layer is not considered in the ideal Chantrell model, which might explain the decreased fitting quality when dead layer is more significant.

The estimated magnetic diameter for Mn–CP2 is smaller than for Mn–CP3, while TEM diameters indicate the opposite. However, given the large γ_{TEM} of Mn–CP3, the validity of a lognormal fitting can be questioned and the associated representative diameter can be questioned. It is reassuring that the fitted γ is smaller for Mn–CP2 than for Mn–CP3. The very low fitted γ and SSE for Mn–CP2 is probably explained by the fact that their global behavior is nearly perfectly superparamagnetic (no significant dead layer,...) and can be fitted by a single equivalent diameter.

4.3.3 Magnetisation of MNP spread in Cellulose (300K)

This study compares the effect of nanoparticle disposition, i.e. the difference in magnetisation curves when the MNP are dispersed in cellulose (close to LFA set-up) are in powder form. Cellulose membrane samples were prepared as described in Subsection 4.3.1.1. Specific magnetisation σ_M is expressed in emu per gram of Fe. This is the most objective metric since ICP was carried out separately on powder samples and dilutions that were pipetted on membranes: it enables us not to make any hypothesis on the oxidation state for magnetite and on the Mn/Fe ratio in manganese ferrite.

4.3.3.1 CP SPIONs and Mn-SPNFs: powder vs membrane

Fig. 4.4, shows specific magnetisation for Fe–CP1 and Mn–CP2 samples in both powder form and suspended in membranes.

Subfigures (A) and (C) show the initial magnetisation curve between 0 and 1 mT, allowing to deduce initial susceptibility χ_i from the slope (summarized in Table 4.14).

- For SPIONs, we observe that the initial mass susceptibility is four times higher for samples spread in the membrane, compared to compacted powder.
- No initial magnetisation curve was available for Mn–CP2 powders, but based on the full magnetisation curve on subplot (D) this factor is estimated between 3.5 and 4.5.

For both iron as manganese ferrite, it is observed in B. subplots that initial susceptibility decreases slightly when nanoparticle mass within the membrane increases. While there are not enough datapoints to make a quantified correlation, all measurements confirm this trend. A possible explanation resides in the fact that clusters might be bigger, thus dipolar interactions and shape anisotropy

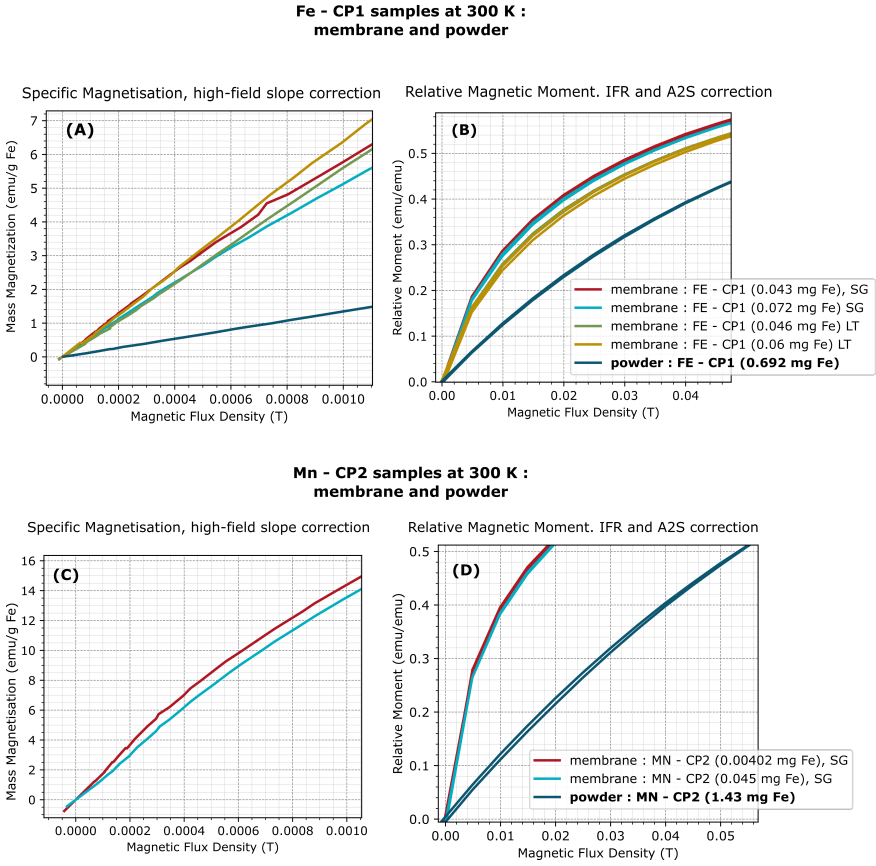


Fig. 4.4 SG: the membrane was cut with siscors and glued on the measurement support. LT: the membrane was lasercut and taped on the measurement support. (A) and (C) display initial mangetisation curves, which were not measured for Mn-CP2 powder.

stronger, when concentration is higher. This needs further analysis, e.g. with SEM imaging of clusters. It is encouraging that this mass-dependent ordering in initial susceptibility is independent from the variations in saturation magnetisation, which is independent from dipolar interactions.

From subfigures (B) and (D) we can conclude that powders not only have lower initial susceptibility, they also reach saturation less quickly, confirming that for the exact same samples, significantly higher interactions increase the anisotropy. Strong magnetic anisotropy, imposes an energy barrier that resists the alignment of the macro-spin with the external field. This results in a slower approach to saturation compared to the Langevin prediction [212]. Note that the Fe–CP1 membranes, a small distinction exists between the "SG" and "LT" membranes: the former are cut with scissors and glued on the measurement pad while the latter are lasercut and taped on the measurement pad. This explains the sligth grouping in subplot (B) between the two types of membranes.

Table 4.6 summarises the fitted $\tilde{D}_{\mathrm{mag}}$ and allows for comparison with fitting results for powder (values copied from Table 4.5). The fitted magnetic diameter is consistently larger for membrane measurements than for powder measurements, confirming that increasing dipolar interactions cause a lower equivalent magnetic diameter according to the Langevin equation. Note that the fitted size distribution tends to be larger for the fitting on membranes: this might be due to varied cluster sizes. It is probable that the capillary flow induces more varied clustering than the static evaporation that leads to powder. LT membranes (cut with laser, attached with tape on sample holder) induce a slightly larger SSE, the samples tend to saturate less quickly as shown in Fig. 4.4 (B): either the laser cutting combustion residues on the membrane induce a bias that is not completely corrected for with A2S and IRF correction, or the pore structure in the cellulose boundaries was affected.

4.3.3.2 Silica Coated TD SPIONs

Fig. 4.5 shows magnetisation curves for SPION made by TD, both uncoated (enrobed with oleyamine) and coated according to the procedure detailed in Subsection 3.4.2.

- Subplot (A) shows how specific saturation magnetisation per iron mass for Fe–TDH4 in both cellulose membranes and in iron form, both with and without silica coating. For powder, an increase in $\sigma_{M,s}$ is observed due to the coating. For the membrane this is not the case: however, given the low yields of the silica synthesis and the poor colloidal stability of TD nanoparticles, an error in exact nanoparticle mass may have occurred.

- Interestingly, despite the lower $\sigma_{M,s}$ for coated Fe–TDH4 in membranes, its

	TEM data			Chantrell Fitting		
	Mean D	$\tilde{D}_{\text{TEM}}$	γ	$\tilde{D}_{\text{mag}}$	γ	SSE
Fe–CP1 p.	10.1	*9.6*	0.31	7.95	0.29	0.037
6.0 ug m. LT				9.02	0.43	0.1078
46.4 ug m. LT				9.06	0.42	0.1192
43.44 ug m. SG				9.47	0.45	0.0974
Fe–TDH4 p.		9.20	0.20			
12.7 ug Fe m. SG				8.06	0.48	0.268
Fe–TDH4@Si p.		""	""	7.32	0.29	0.039
8.4 ug Fe m. SG				8.39	0.38	0.041
Mn–CP2 p.	10.0	*9.7*	0.25	8.95	0.01	0.043
5.89 ug m. LT				12.95	0.68	0.1050
4.02 ug m. SG				12.42	0.48	0.0312
45.0 ug m. SG				12.37	0.48	0.0255

Table 4.6 Fitted median diameters $\tilde{D}_{\text{mag}}$ (nm) for powder measurment (p.) and membrane measurements (m.) of the same sample, compared to TEM data. LT membranes are cut with a laser and attached with tape on sample holder while SG membranes are cut with scissors and attached with glue. γ is the shape factor of the (fitted) lognormal distribution as introduced in Subsection 3.1.3.2.

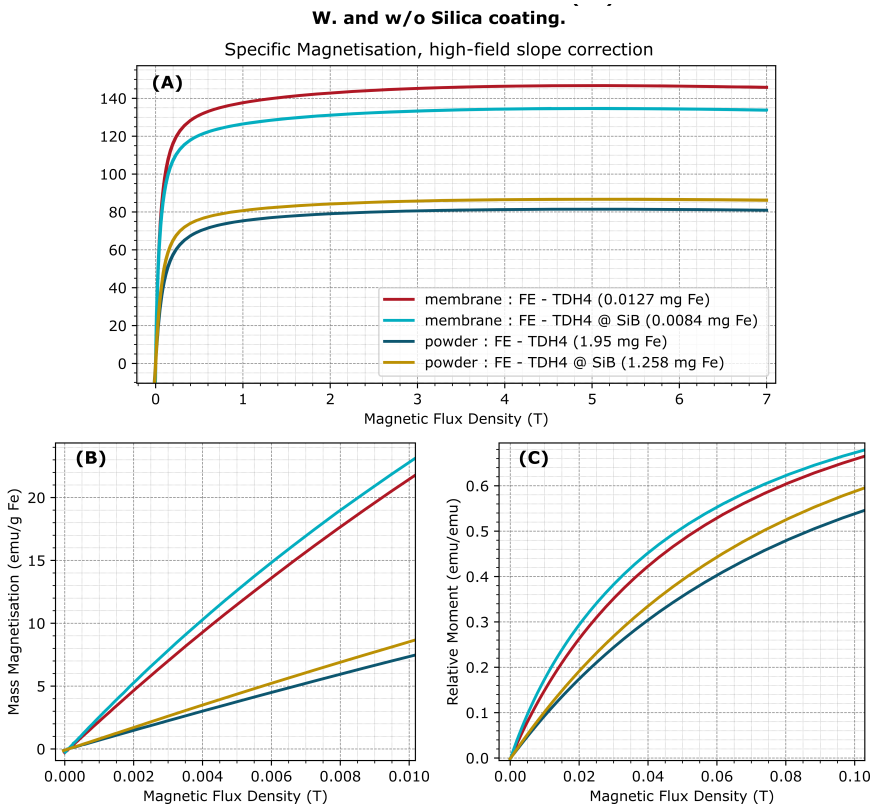


Fig. 4.5 All membranes are cut with siscors and glued on the measurement support. (B and C) are obtained from the measurement of the initial magnetisation curve (i.e. after demagnetisation, no full hysteresis cycle.)

initial susceptibility, displayed on subplot (B) is still higher. This confirms that the measured χ_i increase is not related to weighing or pipeting artefacts. For the powder samples, silica coating also improves the initial susceptibility per iron mass. Looking at relative magnetisation in subplot (C), it is confirmed that samples with coating saturate at lower field, indicating reduced anisotropy.

In Table 4.6 it is observed that the fitted magnetic diameter $\tilde{D}_{\mathrm{mag}}$ is 0.30 nm higher due to coating, but most importantly that the SSE of the Chantrell fitting is lower, indicating more ideal SPM behavior. This is corroborated by the sharper χ''(T) peaks and improved Vogel–Fulcher fit quality ($R^2 = 0.99$) observed for Fe–TDH4@Si in ACS measurements (Fig. 4.13). These observations are pointing to-

wards an improved surface state of the nanoparticles due to the silica coating. To confirm this observations, several coated batches should be made. It cannot be distinguished wether the silica coating improves the surface state, or the ligand exchange which happens during the inverse micro-emulsion coating protocol [195].

4.3.4 Perspective: Low-temperature magnetisation as a complementary diagnostic.

The observations above regarding probable dead layer contributions in Fe–CP1 and changes in dipolar interactions between membrane and powder, are drawn from room-temperature curves fitted with the Chantrell model and supported by literature analogy. Low-temperature magnetisation measurements (at 5 K) would provide more direct complementary insights:

- At 5 K thermal fluctuations are frozen out and the hysteresis loop reaches a well-defined saturation, so M_s can be read off directly rather than extracted through Chantrell fitting. The deficit of M_s(5 K) relative to the expected bulk value provides a more direct estimate of the fraction of magnetically disordered spins than room-temperature measurements. Converting this deficit into a dead layer thickness still requires knowledge of the nanoparticle composition (the expected bulk M_s depends on the magnetite/maghemite ratio) and a geometric model, but the measurement itself avoids the Langevin fitting step [83].

- Third, at 5 K all nanoparticles are magnetically blocked and exhibit hysteresis, which makes it possible to apply the interaction diagnostic proposed by Thamm and Hesse [213]. For an ensemble of non-interacting single-domain particles with uniaxial anisotropy, the initial magnetisation curve equals the average of the upper and lower hysteresis branches. The initial magnetisation curve should fit this mean for non-interacting particles; a deviation indicates demagnetising dipolar interactions. This analysis requires only one demagnetisation cycle and would provide a model-free, field-resolved measure of interaction strength. It could be applied to both powder and membrane samples, directly testing whether the reduced dipolar interactions inferred from the Chantrell fitting (Section 4.3.1.5) are confirmed by an independent method. Importantly, this analysis is not applicable at 300 K because the superparamagnetic samples studied here show no coercivity and no distinct initial curve at room temperature.

Section summary

Room-temperature magnetisation curves were measured for SPION and Mn-SPNF in both powder form and dispersed in cellulose membranes, the latter serving as a proxy for a LFA configuration. The effect of silica coating on TD SPION was also investigated.

Consolidated conclusions:

- Commercial magnetite (Fe–Comm, 135.8 nm) and Mn–CP1 (33 nm) are not superparamagnetic at room temperature, consistent with their diameters exceeding the critical SPM size for their respective compositions.
- SPION synthesised by CP (Fe–CP1, 10.1 nm) exhibit quasi-ideal superparamagnetic behaviour, confirmed by low SSE when fitted with the Chantrell equation.
- SPION synthesised by TD exhibit a persistent paramagnetic-like slope and lower specific saturation magnetisation than CP counterparts of comparable size. The Chantrell SSE is 6 to 10 times higher for TD than for CP nanoparticles. The most probable explanation, consistent with the findings of Baaziz et al. [83] and Unni et al. [81], is that the reducing conditions inherent to thermal decomposition promote volume spin canting and a thicker magnetically dead layer through cation disorder and non-stoichiometry for TD SPION below 12 nm. The lower initial volume susceptibility of TD nanoparticles compared to CP SPION is attributed to both smaller medium diameter and increased presence of dead layer.
- Mn–CP3 powder has a higher initial susceptibility χ_i than Fe–CP1 powder, directly attributable to the lower magnetocrystalline anisotropy K_m of manganese ferrite.
- Dispersing nanoparticles in cellulose membranes yields a substantially higher initial susceptibility compared to compacted powder, for both iron oxide and manganese ferrite samples. Membrane samples also reach saturation at lower applied field. Both observations are consistent with reduced dipolar interactions in the dispersed configuration.
- The fitted magnetic diameter from the Chantrell equation is systematically larger for membrane samples than for powder, confirming that stronger dipolar interactions in powder form increase the effective anisotropy and reduce the equivalent Langevin diameter.

Observed trends requiring further investigation:

- The Chantrell-fitted shape factor γ is systematically larger for membrane samples than for powder (Table 4.6). While the larger fitted median magnetic diameter $\tilde{D}_\mathrm{mag}$ in membranes indicates globally weaker dipolar interactions, the broadened γ suggests that the interactions that do occur are more varied in nature. This is consistent with a distribution of cluster sizes forming during capillary

flow and drying within the cellulose matrix: nanoparticles in large clusters experience stronger dipolar coupling than isolated particles or small agglomerates, producing a wider apparent size distribution when fitted with a single lognormal model.

- The three Mn–CP samples show similar specific saturation magnetisation despite significant differences in Fe/Mn ratio and size. A plausible interpretation is that the Mn-depleted, Fe-enriched surface shell of the smaller particles partially compensates for the dead-layer-induced reduction in magnetisation. Targeted structural characterisation, for instance through X-ray absorption spectroscopy or Mössbauer spectroscopy, could confirm the proposed compensation mechanism by resolving the cation distribution within the nanoparticle volume.
- Silica-coated TD SPION show improved initial susceptibility and faster approach to saturation compared to their uncoated counterparts, both in powder and membrane form. This points towards an improved magnetic surface state. However, only one coated batch was measured; it remains unclear whether the improvement originates from the silica shell itself or from the ligand exchange that occurs during the inverse micro-emulsion coating protocol. Repeating the coating procedure on multiple batches would allow to assess reproducibility, and comparing samples that underwent ligand exchange without silica deposition would help isolate the two effects.

Perspectives:

- The substantially higher initial susceptibility measured for membrane-dispersed nanoparticles, compared to compacted powder, is directly relevant for LFA design: nanoparticles captured on a test line are in a dispersed configuration closer to the membrane samples than to powder. This favourable susceptibility, combined with the advantage of manganese ferrite over iron oxide in terms of χ_i, supports the choice of Mn-SPNF as labels for inductive LFA detection.
- Mossbauer spectroscopy could confirm a more substantial dead layer in TD than CP SPION. Alternative TD synthesis routes that reduce the size of the death layer, such as adding molecular oxygen as proposed by Unni et al. [81], are interesting points of comparison to confirm the physical origin of the non-staturation of TD particles while maintaining their size.
- Low-temperature magnetisation measurements (5 K) on the samples studied in this chapter would complement room-temperature data: observing $\sigma_{M,s}$ below blocking temperature can give complementary insights on strength of dipolar interactions and how they vary between powder and membrane sample [213].
- The higher initial susceptibility of silica coated nanoparticles, if confirmed on multiple batches, suggest a route to further improve the magnetic response of TD SPION by mitigating the dead-layer penalty inherent to this synthesis method.
- These static magnetisation results provide the baseline for interpreting frequency-dependent measurements in the following sections (FC-ZFC, ACS) and for the inductive sensing experiments in Chapter 6.

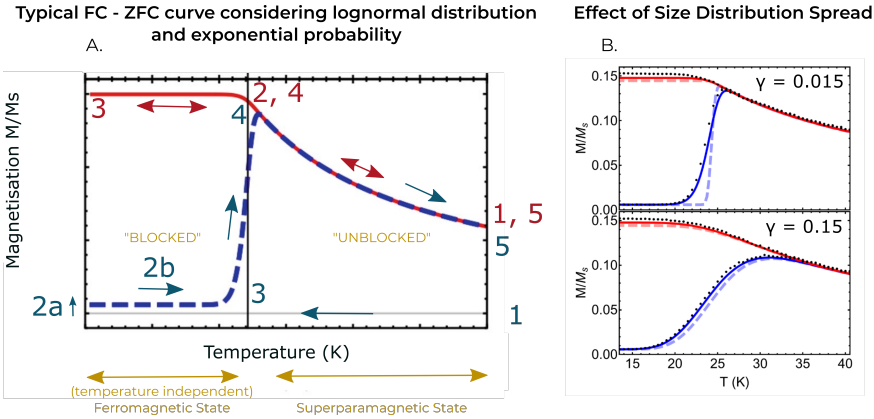


Fig. 4.6 Adapted from [48]. (left) Typical FC-ZFC curve considering one SPNF size but stochastic T_B distribution. (right) Graphs considering lognormal size distribution with varying shape factor γ: a larger distribution "flattens" the curve.

4.4 Nearly-DC FC-ZFC Curves

4.4.1 Theory and Literature benchmarks: FC-ZFC Curves

4.4.1.1 FC-ZFC measurements: what and how

The FC-ZFC measurement is an experiment allowing to determine the blocking temperature T_B. Consider Fig. 4.6 that represents an ideal measurement for non-interacting, monodisperse superparamagnetic samples. An overview of the main steps in FC-ZFC measurements is given below.

ZFC Curves (blue numbers in Fig. 4.6 A):

1. Consider a superparamagnetic sample in zero field at room temperature. It has no net magnetisation since all the macrospins are randomly oriented. Temperature is reduced without any external field (zero field cooling). Net magnetisation remains zero.
2. When the temperature is at its lowest point, an external field is applied. (2a) Since we are -supposedly- well below the blocking temperature, we are in a ferromagnetic state. The external field causes a coherent rotation of the magnetic moments resulting in a non-zero but very small magnetisation. The temperature then starts increasing again. (2b) As long as we stay below the blocking temperature, we are in purely ferromagnetic state so magnetisation is not temperature dependent: it remains constant. **Note: the name "zero field cooling" can be misleading since the warming up and measurement occur in a non-zero field!**
3. When the blocking temperature is approached, thermal energy becomes comparable to field energy and much more important than anisotropy energy. An abrupt increase in

magnetisation occurs: the macrospins being "unblocked", they align with the external field. Note: saturation is not reached since the applied field is very small (cf infra)

4. As temperature is further increased, the random fluctuations from thermal energy begin to dominate and the macrospins become randomly oriented once again, producing the 1/T exponential decrease of the magnetisation, asymptotically reaching to zero following the Curie-Weiss Law (cf Subsection 2.2.2.2).

FC Curves (red numbers in Fig. 4.6 A):

1. Consider a superparamagnetic sample in a small external field at room temperature that is cooled from 'high' temperature (well above T_B). Above T_B, the magnetisation is dependent on temperature and applied field. During this cooldown, temperature and external field are the same in every point as during the ZFC warming up: the magnetisation curves overlap.
2. As the particles cool past their blocking temperatures, their magnetic moments lock into alignment with the external field. Since this is a ferromagnetic state, the magnetisation remains constant when temperature is further decreased.
3. The lowest temperature is reached. While keeping the same magnetic field on, the sample is slowly heated, and its magnetisation is measured.
4. When temperature exceeds T_B, magnetisation becomes temperature-dependent again given that thermal energy exceeds anisotropy energy again and becomes comparable to field-energy.
5. As temperature increases further, thermal energy increases the flipping rates and decreases the net measured magnetisation. The path followed is the same since conditions have not changed.

Note that on Fig. 4.6 (A) the transition from blocked to unblocked state is not sharp, despite the single size which is considered by the model in [48]. Given the stochastic nature of the thermally induced switching of nanoparticle magnetic moment, the transition between "blocked" and SPM never occurs instantaneously at a single T_B. Note that VSM has a shorter measurement time than SQUID, which shifts the apparent blocking temperature to higher values and sharpens the ZFC peak.

Fig. 4.6 (B) and (C) show that for an assortment of particle sizes, the transition from blocked to SPM state is smoothed out. Indeed, $T_B \propto V_{\text{mag}}$: as temperature increases, more and more particles 'unblock' and are able to align with the small external field applied for measurement.

The probing field lowers the effective anisotropy energy barrier. In the absence of a field, the energy landscape is a symmetric double-well with barrier height $E_a = K_{\text{eff}} V_{\text{mag}}$ (cf. Fig. 2.4 and Eq. 2.25). When an external field H is applied along the easy axis, the Zeeman energy $-\mu_0 m_{\text{NP}} H \cos\phi$ tilts this landscape: the

well aligned with the field deepens while the opposing well becomes shallower. The effective barrier for moment reversal is thereby reduced, and consequently the thermal energy required to induce superparamagnetic fluctuations is lower. This is observed experimentally as a decrease in T_B with increasing probing field, illustrating once more that blocking temperature is not a thermodynamic constant nor a phase transition.

4.4.1.2 Deriving Blocking Temperature

The blocking temperature T_B is the key characteristic temperature for superparamagnetic systems, defined as the temperature at which the mean time for a magnetic nanoparticle moment to escape an energy well is equal to the characteristic measurement time τ_{meas}: the nanoparticles go from "blocked" to "unblocked" state [48, 95]. This happens when the measurement time constant equals the Néel relaxation time constant, as introduced in Subsection 2.3.2. **We insist again on the fact that unlike Curie Temperature, the blocking temperature is not a thermodynamic constant: it depends on the measurement conditions.**

In much experimental work, T_B is conventionally estimated as the location of the peak maximum in the ZFC magnetisation curve Tmax [69, 214, 215]. While this method is widely used, it is often inaccurate. The actual mode blocking temperature is generally lower (to the left) of the ZFC peak. This discrepancy arises because the ZFC magnetisation is disproportionately large for unblocked particles at high temperatures, skewing the weighted sum of particle contributions towards higher temperatures [48, 49, 95].

The most robust method for determining the blocking temperature involves mathematical analysis of the relationship between the FC and ZFC curves with the second derivative method. This consists in evaluating where the second derivative of the difference between the FC and ZFC magnetisation is zero:

$$\frac{d^2(M_{FC} - M_{ZFC})}{dT} = 0$$

This method aligns with kinetic Monte Carlo simulations and indicates that T_B occurs near the inflection point in the ZFC curve, to the left of the peak position.

From the blocking temperature, the effective anisotropy constant K_{eff} of the measured sample is then given by:

$$K_{\text{eff}} = \frac{\ln(\tau_{\text{meas}}/\tau_0)\, k_B T_{\text{B}}}{V_{\text{mag}}} \approx \frac{25\, k_B T_{\text{B}}}{V_{\text{mag}}} \tag{4.2}$$

This is further detailed in Subsection 2.3.2. The numerical factor 25 $\approx$

$\ln(100\,\mathrm{s}/10^{-9}\,\mathrm{s})$ assumes $\tau_0 = 10^{-9}\,\mathrm{s}$[5] and $\tau_{\mathrm{meas}} = 100\,\mathrm{s}$. It is strictly valid in interaction anisotropy approach (Subsection 2.3.6.2): any interaction contribution goes entirely into K_{eff} with no possibility of adjusting τ_0.

Table 4.7 collects literature benchmarks for T_B obtained from FC-ZFC measurements on SPNF of various sizes and sample forms and with varying probing fields.

4.4.1.3 Irreversibility Temperature T_{irr}

In FC-ZFC curves, T_{irr} (introduced in Subsection 2.3.2) is observed as the temperature where both curves merge: above it, the magnetic response is independent of the sample's thermal history; below it, the two different starting conditions (zero-field vs. in-field cooling) lead to two different magnetisation paths, the definitive experimental proof that magnetic moments are being blocked [22, 69]. In concentrated samples, the gap $\Delta T = T_{\mathrm{irr}} - T_B$ is attributed to distributed cluster sizes inducing a range of interaction-anisotropy contributions rather than a broad intrinsic size distribution, as demonstrated by Salvador et al. [97] and Frandsen et al [95].

4.4.1.4 Benchmark values in literature

Table 4.7 summarizes benchmark values from literature. The applied field during the measurement varies from 10 Oe [217] to 500 Oe [49, 218] across studies, and is not always reported; since higher fields lower the effective energy barrier, direct comparison requires caution.

Crystallographic quality highly influences T_B:

- Nedelkoski et al. [216] observe that antiphase boundaries (crystallographic defects formed during nanoparticle growth) and grain boundaries act as pinning sites that inflate the effective anisotropy. They report $T_B \approx 115$ K for single-crystal and $\sim$200 K for defective Fe_3O_4 of comparable size

- Unni et al. Unni, Uhl, Savliwala, Savitzky, Dhavalikar, Garraud, *et al.* [81] demonstrate that polycrystalline 21 nm particles ($T_B = 267$ K) exceed the blocking temperature of smaller but single-crystalline 18 nm particles ($T_B = 98$ K).

CP seems to yield higher T_B at comparable sizes:

- At 5 nm: CP gives 45 K (Goya, at 500 Oe), while TD gives 22–25 K (at 75–100 Oe). Since higher applied fields lower T_B, the CP value measured at 500 Oe would be even higher if remeasured at 75 Oe. The gap is therefore larger than it appears.

[5] With "acceptable" validity down to $\tau_0 = 10^{-11}$ as detailed in Subsection 2.3.2

Reference	Synthesis	Size [nm]	Form	H [Oe]	T_B [K]	Notes
Unni [81]	TD	18	polymer matrix (0.02 wt% Fe)	10	98	Single-crystal, no dead layer
Unni [81]	TD	21	polymer matrix (0.02 wt% Fe)	10	267	Polycrystalline, large dead layer
Demortière [38]	TD	3.5	powder	75	18	—
Demortière [38]	TD	5	powder	75	22	—
Demortière [38]	TD	9	powder	75	36	—
Demortière [38]	TD	11	powder	75	61	—
Baaziz [83]	TD	5.4	powder	75	25	
Baaziz [83]	TD	8.1	powder	75	75	—
Baaziz [83]	TD	11.3	powder	75	160	—
Baaziz [83]	TD	15.9	powder	75	202	—
Nedelkoski [216]	TD	12.3	powder	100	∼115	Single-crystal, crystallographic defects (synthesis [150])
Nedelkoski [216]	TD	14.2	powder	100	∼200	crystalline defects, broad ZFC (synthesis from [157])
Orozco [143]	TD	5	powder	—	—	T_B below measurement range
Frandsen [95]	TD	5	powder	100	24	
Martins [141]	CP	9.3	powder	100	155	—
Goya [49]	CP	5	powder	500	45	—
Goya [49]	CP	10	powder	500	107	—
Orozco [143]	TD	8	powder	—	24	—
Salvador [97]	TD	8	powder	—	87	—
Salvador [97]	TD	12	powder	—	101	—
Salvador [97]	TD	23	powder	—	225	—

Table 4.7 Literature benchmarks for blocking temperature of ferrite nanoparticles obtained from FC-ZFC measurement with probing field H [Oe]

- At 9–10 nm: CP gives 107 K (Goya, 500 Oe) and 155 K (Martins, 100 Oe), while TD gives 36 K (Demortière, 9 nm) to 87 K (Salvador, 8 nm). Again, the CP values exceed TD values despite the high probing field in Goya et al.

While a more advanced study would be required to draw rock-solid conclusions, a hypothesis would be to attribute this to (1) higher polidispersity obtained with CP synthesis [38, 51, 128] and (2) improved crystalline quality achieved for optimised TD protocols [216].

Differences in interactions, agglomeration or crystalline properties? ∼11 nm Fe_3O_4 particles in powder form yield various T_B values: ranging from 61 K in Demortière et al. [38] and 160 K in Baaziz et al. [83]... for identical probing fields (75 Oe) and similar synthesis protocols (TD). Fig. 4.7 illustrates corresponding FC-ZFC graphs graphs. Regarding the exact reasons for this T_B, one can only guess.

- Neither paper reports the powder packing density or sample mass, so one cannot verify whether the difference is purely due to packing.
- Demortière explicitely explains a final step: "The crystal solutions were dispersed in 5 mL of hexane and finally a last centrifugation was performed to eliminate unstable nanoparticles or agglomerates in solution." This may have produced a less agglomerated powder.
- Baaziz report volume spin-canting and an oxidation gradient: these defects increase K_{eff} beyond the bulk value, contributing to a higher T_B independently of interactions. We can however not exclude that this did not occur in the sample of Demortière.

It should be observed that the 11 nm graph from Demortière et al. strongly resembles the 8 nm graph of Baaziz et al. For the latter, the evolution in sizes is attributed to $K_{\text{eff}}V_{\text{mag}}$ scaling. The paper reports that the 8 nm SPION are composed of 5% magnetite while the 11 nm SPION are composed of 15%. However, this is not explicitely linked to T_B evolution. The CV (15%) in Demortière et al. is twice as broad, but a broader distribution primarily flattens the T_B distribution rather than shifting it.

4.4.2 Methods: IFCC-ZFCW Measurement Protocol in this work

Distinction should be made between field-cooled cooling (FCC) and field-cooled warming (FCW) procedures. In FCC, the magnetic field is applied first and the magnetic moment is measured while cooling the sample in a constant field. In FCW, the sample is first cooled in the field, then the magnetic moment is measured while slowly warming in the same field [219]. The FC measurement is ideally a reversible process; irreversibility between FCC and FCW can occur due to

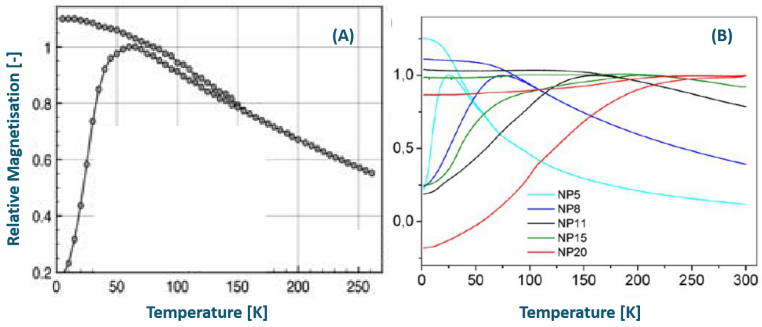


Fig. 4.7 FC-ZFC measurements on 11 nm SPION in powder form. **(A)** Demortière et al. [38] and **(B)** Baaziz et al. [83] where 11 nm SPION are displayed in black.

phenomena such as the Paramagnetic Meissner Effect or vortex pinning [219], which are out of scope for this work. In this work, we applied ZFCW and IFCC.

Measurements were performed on a Quantum Design MPMS® 3 SQUID Magnetometer, by Dr. Simo Spassov in collaboration with IRM-KMI. A probing field of 50 Oe was used. The protocol is as follows:

1. Zero field is established at 300 K by ramping to 0.5 T, then applying the oscillate approach mode down to 0 T with a 2-minute settling time. The sample is then cooled in two steps: first to 20 K at 5 K/min, then to 1.8 K at 2 K/min, followed by a 20-minute thermal stabilisation
2. A probing field of 50 Oe is applied using no-overshoot mode at 10 Oe/s, followed by a 1-minute settling time
3. The magnetic moment is measured in VSM mode (2-second averaging, 4 mm scan length) during a continuous temperature sweep from 1.8 K to 300 K at 5 K/min in the 50 Oe probing field (ZFCW)
4. While maintaining the 50 Oe field, the sample is cooled back to 1.8 K at 5 K/min and the magnetic moment is measured (IFCC)

4.4.2.1 Sample Preparation

The samples used for the FC-ZFC measurements, both in powder form (gelatin capsules) and as dried dispersions in cellulose membranes (quartz paddle, see 4.3.1.2), were the same as for the magnetisation curves, cf Subsection 4.3.1.2.

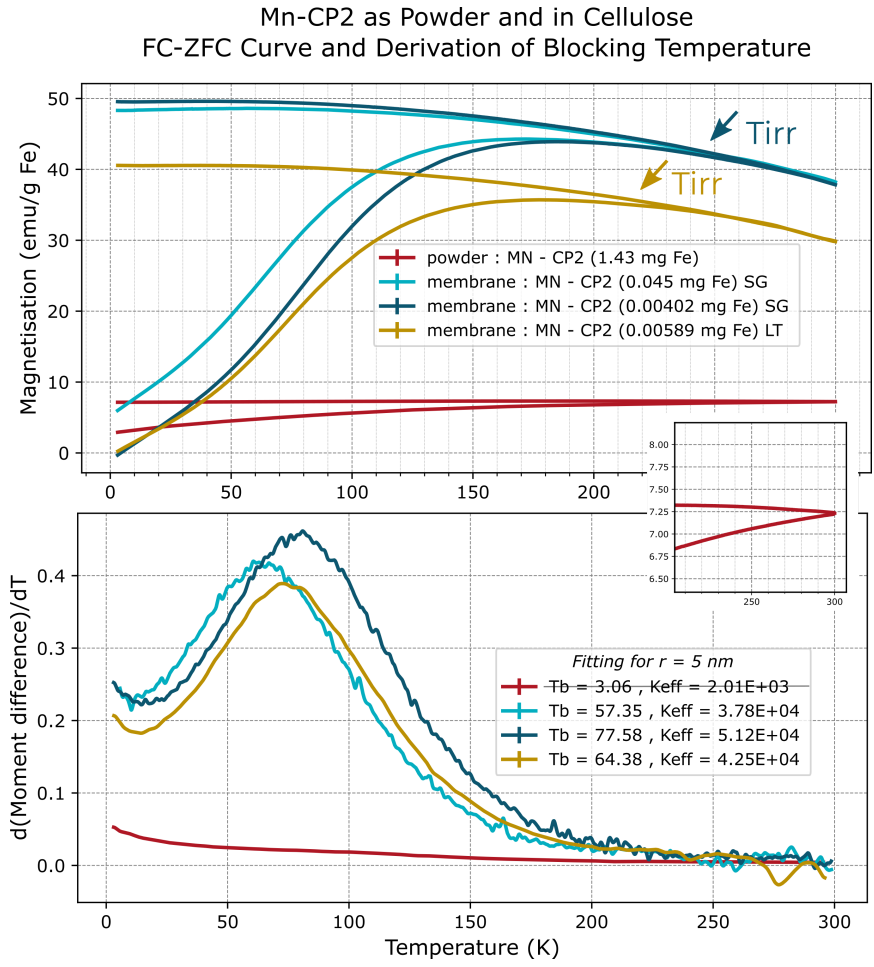


Fig. 4.8 FC-ZFC measurements on Mn–CP2 samples. LT stands for laser cut and taped on the sample holder, while SG stands for scissor cut and glued on the sample holder. A radius of 4.5 nm is considered to derive K_{eff}.

4.4.3 Results: A clear Tb for Mn–CP2 in cellulose membranes

Fig. 4.8 shows the FC-ZFC curves for Mn–CP2 particles in both powder form and membrane. For powder, the curves join by metrological reason: once the temperature has reached 300 K, the sample is cooled again and IFCC measurement starts. Given the same magnetisation state is the end of one measurement and the start of another, it makes sense that both curves join. It is very likely however that powder (compacted in the measurement holder) is in blocked state, probably due to high interactions. This is coherent with the fact that dipolar interactions (supposedly highly dominant in powder) increase the observed blocking temperature as explained in Subsection 2.3.6. As a result, the derived blocking temperature and anisotropy constant have no physical meaning. The corresponding magnetisation curves in Fig. 4.3 (made with the same sample and sample holder) show nevertheless very small to no hysteresis for the Mn–CP2 sample. This might be explained by the fact that only a minority of the particles is still fully blocked at room temperature.

The three membranes have a blocking temperature between 57 and 77 K. These blocking temperature and anisotropy constant can be correlated using Eqn. 2.32.

- considering the median diameter obtained by TEM analysis $\tilde{D}_{\mathrm{TEM}}$, the corresponding effective anisotropy K_{eff} constants are 37.6 – 50.8 kJ/m^3
- considering the magnetic size obtained by Chantrell fitting (cf Table 4.6), the corresponding anisotropy constants are between 19.8 – 26.8 kJ/m^3

Thus when Mn–CP2 SPNF are spread in membranes, their effective anisotropy K_{eff} (including the surface effects, shape effects, interactions within clusters,...) is 7–17 times higher than magnetocrystalline anisotropy K_{m} (cf Table 4.3), depending on the considered value for diameter and T_B.

The FC- and ZFC-curves for powder fully merge between 230 K and 250 K, placing T_{irr} well above T_B. The large gap $\Delta T = T_{\mathrm{irr}} - T_B$ indicates a wide distribution of energy barriers [48, 49]. This is traditionally attributed to large size distribution (cf Subsection 4.4.1.3). However, both TEM imaging and Chantrell fitting on powder indicate narrow size distribution of the nanoparticles (cf Table 4.5): it is therefore more probable that the nanoparticles form clusters of distributed sizes within the membrane, inducing an integrated distribution of added anisotropy due to interparticle interactions [95]. This is aligned with the larger Chantrell-fitted γ for Mn–CP2 in membranes (cf Table 4.6) , which was also attributed to agglomerate size distribution.

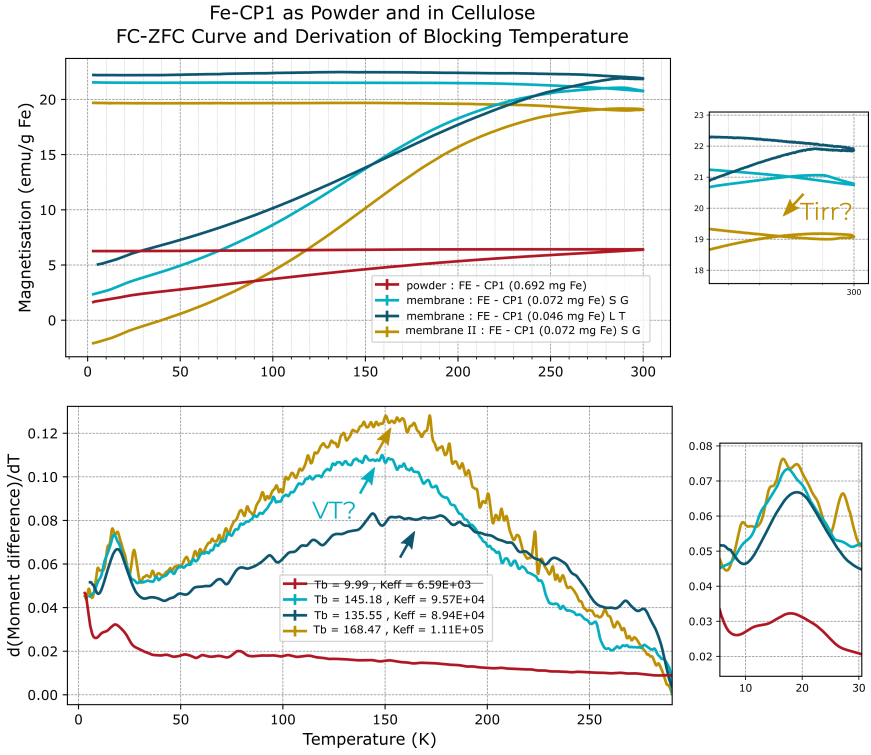


Fig. 4.9 FC-ZFC measurements (upper graph) and derived $d(M_{FC} - M_{ZFC})/dT$ (lower graph) for Fe–CP1 samples in cellulose and powder. LT stands for laser cut and taped on the sample holder, while SG stands for scissor cut and glued on the sample holder. A radius of 4.5 nm is considered to derive K_{eff}: for the powder sample this is invalidated due to measurement noise at low temperature (amplified with the derivative operation). The iron masses per sample are specified in the legend of the upper graph.

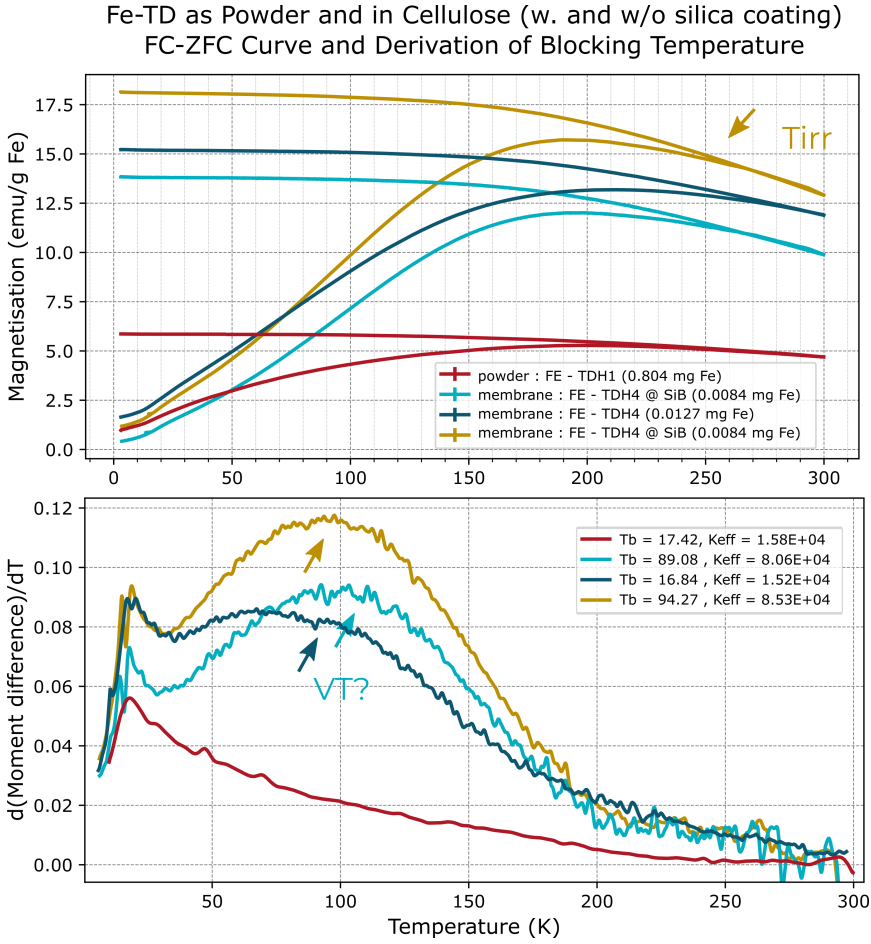


Fig. 4.10 FC-ZFC measurements (upper graph) and derived $d(M_{FC} - M_{ZFC})/dT$ (lower graph) for Fe–TD samples in cellulose and powder. All membranes are cut with scissors and glued. A radius of 4.5 nm is considered to derive K_{eff}. The iron masses per sample are specified in the legend of the upper graph.

4.4.4 Results: SPIONs in cellulose membranes

Figs. 4.9 and 4.10 represent the FC-ZFC curves for SPION made by CP and TD respectively, in both powder and membrane form. For the TD synthesis, both silica coating and pristine particles are considered.

As for manganese ferrite made by CP, the FC and ZFC powder curves of Fe–CP1 join exactly at 300 K which is a measurement artefact. As for Mn–CP1, this is attributed to a minority of unblocked particles at room temperature. On the other hand, Fe–TDH1 powder are in superparamagnetic state at room temperature with T_{irr} around 220 K. This is consistent with the slightly lower coercivity at room temperature observed in the magnetisation curves, Fig. 4.2. Note that the powder samples in the literature benchmark Table 4.7 appear unblocked at room temperature because the probing field H is > 75 Oe (up to 500 Oe) while the probing field in this case is at 50 Oe. Notably, above T_{irr} the ZFC magnetisation of Fe–TDH1 powder decays more slowly than that of the corresponding membrane samples (Fig. 4.10). This is consistent with dipolar interactions reducing the effective field seen by individual particles, thereby flattening the $1/T$ Curie decay expected for non-interacting SPNFs [69]. This comparison cannot be extended to Mn–CP2 and Fe–CP1 powders, since their FC-ZFC curves do not fully merge within the 300 K measurement window. Extending the temperature range would enable the same analysis, but would require careful control of oxidation at elevated temperatures.

4.4.4.1 Deriving T_B on membranes: the large peak...

Deriving the blocking temperature T_B as explained in Subsection 4.4.1.2 yields a large distribution for both TD and CP samples dispersed in membranes, centered around 80 - 100 K for TD and 150-160 K for CP. This is consistent with the (cautious) observation in Table 4.7 that the CP samples have higher T_B.

For both CP and TD SPION in membranes, as for Mn–CP2 in membranes, the $\Delta T = T_{\text{irr}} - T_B$ is above 100 K. Again, this confirms the hypothesis of a distribution of cluster sizes formed within the cellulose membrane during drying.

Since a smaller bump in $d(M_{FC} - M_{ZFC})/dT$ is also observed around 18-20 K (cf infra), the question is raised wether the first wouldn't correspond to T_B and the second to VT. Indeed in [89] the Verwey Temperature is determined by analysing the first derivative of the magnetisation (dM/dT) from the ZFC curve and fitting a gaussian function to its peak: the center being attributed to VT. Three arguments allow to discard this:

- Frandsen et al. [95] demonstrate that this transition would also be seen as a "kink" in the FC curve (at 120 K for 20 nm SPION, in this specific paper), cf. Fig. A.3.1 in Appendix A.3.
- Above T_B, the thermal energy is supposedly large enough to "overshadow" the change

in crystalline anisotropy induced by the Verwey transition, cf. Fig. 2.9. If the peak at 18 K would indeed correspond to T_B, VT at 100 - 150 K would be doubtful.

- As demonstrated literature benchmark in Appendix A.3, Verwey transition - if observed in superparamagnetic nanoparticles- tends to occur at the bulk phenomenon temperature (120 - 125 K) or 10 - 20 K below, but no report is made of VT above the bulk counterpart: while for TD it would be lower, for CP it would not.

4.4.4.2 Deriving T_B on membranes: ... and the small peak

Both powders and membrane show a peak at 15-20 K. It is worth stressing that this is not an artefact, for two reasons:

- This "low temperature peak" is consistently present throughout both iron oxide samples (TD and CP) but never observed for manganese ferrite SPNF
- The double peak in M(T), with a smaller one at lower temperature and a dominant one at higher temperature, is also observed in ACS measurements for SPION (and not for Mn-SPNF).

From the examples in literature given in Subsection 4.4.1.2, this would be surprisingly small for 10 nm particles subject to interactions. Indeed, the empirical relationship $T_B \propto D^2$ established by Frandsen et al. predicts $T_B \approx 54$ K for 10 nm magnetite nanoparticles [95], further confirming that the 15-20 K peak cannot correspond to the blocking of the entire particle core. It is confirmed by the observations in literature (Table 4.7) that no mention is made of such low T_B for nanoparticles with 10 nm diameter.

A possible explanation would be that in the cellulose membrane, the nanoparticles deposited on the outer part of the membrane would form clusters of strongly oxidized nanoparticles, reducing drastically the $\tilde{D}_{\mathrm{mag}}$: down to 4-5 nm according to Table 4.7. This oxidated fraction would be less subject to dipolar interactions as studied in [38]. This would also be consistent with the presence of the peak in powder form: during drying, a fraction (smaller than for the membrane) is also exposed to air and might show SPM behavior when the majority is blocked. When the probing field is higher (as in most cases of Table 4.7), most particles unblock and this peak is not dominant anymore.

4.4.4.3 The effect of coating

On Fig. 4.10 measurements of Fe–TDH4 and Fe–TDH4@Si suspended in cellulose membranes are compared. The specific magnetisation in emu/g Fe does not show clear tendency, probably due to limited weighing accuracy because of lower colloidal stability (as for the magnetisation curves on Fig. 4.5). However, in relative terms, the peak at 15-20 K is consistently less dominant for the coated samples. This would be consistent with the fact that oxidation is reduced due to the coating offering protection of the SPION surface.

4.4.4.4 Deducing K_{eff}

Two phenomena, potentially related to two different anisotropy behaviours, coexist. The deduced anisotropy constants are summarised in Table 4.8. Note that if hypothesis of associating the 18 K - peak with a fraction of the sample that has reduced D_{mag} due to oxidation, it makes little sense to deduce K_{eff} with $\tilde{D}_{\text{mag}}$ extracted from Chantrell fitting.

Sample	**Radius**	K_{eff} **at** T_B	
		$\mathbf{T_B \approx 18\ K}$	**High** T_B
Fe–CP1 m.	$\tilde{D}_{\text{TEM}}$: 9.6 nm	13.4	111.7 (T_B = 150 K)
	$\tilde{D}_{\text{mag}}$: 9.06 nm	–	133.0 (T_B = 150 K)
Fe–TDH4 m.	$\tilde{D}_{\text{TEM}}$: 9.2 nm	15.2	84.65 (T_B = 100 K)
	$\tilde{D}_{\text{mag}}$: 8.06 nm	–	125.9 (T_B = 100 K)
Fe–TDH4@Si m.	$\tilde{D}_{\text{TEM}}$: 9.2 nm	15.2	77.88 (T_B = 92 K)
	$\tilde{D}_{\text{mag}}$: 8.39 nm	–	102.7 (T_B = 92 K)

Table 4.8 Derived anisotropy constants [kJ/m3] for Fe–CP1 and Fe–TDH4 in membranes (m.). Diameters are obtained by TEM images (physical) or Chantrell fitting (magnetic), with blocking temperature depending on the interpretation of the ZFC-curves.

Consistent with higher T_B for similar sizes, the effective anisotropy of Fe–CP1 is higher than that for Fe–TDH4. This is aligned with the literature overview in 4.4.1.2.

Comparing K_{eff} deduced from $\tilde{D}_{\text{TEM}}$ to the bulk magnetocrystalline anisotropy of the corresponding iron oxide phase (Table 4.3), Fe–CP1 in membranes exhibits an effective anisotropy 10 to 24 times larger than K_{m} (considering magnetite and maghemite respectively), while Fe–TDH4 yields a ratio of 8 to 18. As for Mn–CP2 (7–17 times above K_{m}), the effective anisotropy of SPION in membranes is thus approximately one order of magnitude above the bulk magnetocrystalline value for both compositions.

Considering the ratio between compositions, the effective anisotropy of the SPION in membrane dispersion is 2.1 (for TD) to 2.7 (for CP) times larger than K_{eff} obtained for Mn–CP2 in membranes. Similar ratios are found for the bulk counterparts: magnetite's K_{m} is 3.6 times larger than for manganese ferrite, while maghemite's K_{m} is 1.5 times larger. The approximate preservation of the

cross-composition ratio suggests that the interaction contribution to K_{eff} is not a composition-independent additive constant, but rather scales with the intrinsic anisotropy of the material. If the interaction contribution were purely additive (i.e. $K_{\text{eff}} = K_{\text{m}} + K_{\text{int}}$ with K_{int} identical for both compositions in the same membrane configuration), the ratio $K_{\text{eff}}(\text{Fe})/K_{\text{eff}}(\text{Mn})$ would be compressed towards unity as K_{int} grows. Instead, the observed ratio (2.1–2.7) falls within the bulk range (1.5–3.6). This observation is consistent with the scaling framework proposed by Serantes et al. [220], in which the influence of dipolar interactions on T_B is governed by a dimensionless parameter: the dipolar contributions are reported to have a K_{m}-scaled effect rather than an absolute. Sanchez et al. [221] provide experimental support for this interpretation: in Co-doped maghemite compacts at fixed packing fraction, the peak temperature of the interacting system scales linearly with the blocking temperature of isolated particles (slope ≈ 1), confirming that the anisotropy contribution dominates over the interaction offset.

Section summary

FC-ZFC measurements were performed on SPION and Mn-SPNF in both powder form and dispersed in cellulose membranes. A probing field of 50 Oe was used. The blocking temperature T_B was derived using the second derivative method, and the effective anisotropy K_{eff} was deduced from the Néel–Arrhenius relation.

Consolidated conclusions:

- For Mn–CP2 dispersed in cellulose membranes, a clear blocking temperature is observed between 57 and 77 K (Fig. 4.8). The corresponding effective anisotropy K_{eff} is 7–17 times higher than the bulk magnetocrystalline anisotropy K_{m} of manganese ferrite (Table 4.3), depending on whether $\tilde{D}_{\text{TEM}}$ or $\tilde{D}_{\text{mag}}$ from Chantrell fitting is used. For SPION in membranes, K_{eff} is 8–24 times larger than K_{m} (considering magnetite and maghemite respectively). The cross-composition ratio $K_{\text{eff}}(\text{Fe})/K_{\text{eff}}(\text{Mn}) \approx 2.1$–$2.7$ falls within the bulk range $K_{\text{m}}(\text{Fe})/K_{\text{m}}(\text{Mn}) \approx 1.5$–$3.6$ (Table 4.3). This approximate preservation of the bulk ratio is consistent with the scaling framework [220], in which the dipolar interaction effect is material-scaled rather than a composition-independent additive constant.
- For SPION in membranes, the dominant blocking temperature is centred around 80–100 K for TD and 150–160 K for CP samples. The higher T_B of CP samples at comparable sizes is consistent with the literature benchmark (Table 4.7).
- For all compositions, the large gap $\Delta T = T_{\text{irr}} - T_B$ (exceeding 100 K for membrane samples) cannot be attributed to a broad intrinsic size distribution, since both TEM and Chantrell fitting on powder indicate narrow distributions (Table 4.5). Instead, it is attributed to a distribution of cluster sizes formed during membrane drying, consistent with the elevated Chantrell-fitted γ observed for membrane samples in Section 4.3 (Table 4.6).

- Powder samples of both Fe–CP1 and Mn–CP2 appear blocked at 300 K, , as expected by observed coercivity in their magnetisation curves. The blocked state of powders is attributed to strong dipolar interactions in the compacted configuration, consistent with the reduced initial susceptibility observed for powder versus membrane samples in Section 4.3. Fe–TDH1 powder is superparamagnetic at room temperature ($T_{\text{irr}} \approx 220$ K) confirming the very low measured coercivity, which is attributed to smaller diameter and better monodispersity.

Observed trends requiring further investigation:

- A secondary peak at 15–20 K is consistently present in the $d(M_{FC} - M_{ZFC})/dT$ curves of all iron oxide samples (both TD and CP, in powder and membrane) but is never observed for manganese ferrite (Fig. 4.9, Fig. 4.10). This double-peak structure is corroborated by ACS measurements (Section 4.5). Given that the empirical relationship $T_B \propto D^2$ [95] predicts $T_B \approx 54$ K for 10 nm magnetite, the 15–20 K peak cannot correspond to the blocking of the full particle core. A plausible hypothesis is that a fraction of SPION, exposed to air during membrane drying, undergoes strong oxidation that reduces the effective magnetic diameter to 4–5 nm, yielding a correspondingly lower T_B.

- Silica-coated TD SPION (Fe–TDH4@Si) show a less dominant 15–20 K peak relative to their uncoated counterparts (Fe–TDH4) in cellulose membranes (Fig. 4.10). This is consistent with the silica shell protecting the SPION surface against oxidation, and aligns with the improved initial susceptibility observed for coated samples in Section 4.3. However, this observation is based on two membrane samples from a single batch; confirmation on additional batches is required.

- The literature benchmark (Table 4.7) reveals that nominally identical nanoparticles (e.g. $\sim$11 nm Fe_3O_4 by TD, measured at 75 Oe in powder) can yield T_B values differing by a factor of 2.5 across studies [38, 83]. Crystallographic quality, powder packing density, and degree of oxidation are identified as the most likely sources of variability, but their relative contributions remain unquantified.

Perspectives:

- Repeating the FC-ZFC measurement at a higher probing field (e.g. 100–200 Oe) would serve two purposes: (1) verifying that both the dominant and the 15–20 K peak shift with field, thereby confirming that both correspond to superparamagnetic blocking rather than to a structural phase transition, and (2) enabling direct comparison with the majority of literature benchmarks in Table 4.7.

- The cluster-size distribution hypothesis, proposed here to explain both the large $\Delta T = T_{\text{irr}} - T_B$ and the elevated γ from Chantrell fitting (Section 4.3), could be validated by systematic SEM imaging of membrane cross-sections, as already suggested in the perspectives of Section 4.3.

- The FC-ZFC characterisation of nanoparticles dispersed in cellulose membranes, rather than as compacted powder, is not common practice. Yet the membrane configuration is directly relevant for LFA applications, where captured nanoparticles are dispersed on a nitrocellulose test line. The observation that membrane

dispersion yields a well-defined T_B (as opposed to the blocked state observed in powder) reinforces the conclusion from Section 4.3 that the dispersed configuration is more favourable for magnetic sensing.

4.5 AC Susceptibility Measurement

4.5.1 Theory: Interpreting the $\chi'(T)$ and $\chi''(T)$ Data

The ideal Debye model introduced in Section 2.3.5 (Eq. 2.44) assumes a constant static susceptibility χ_0 and no high-frequency contribution ($\chi_{\text{hf}} = 0$). More generally, χ_0 depends on temperature and χ_{hf} is non-zero:

$$\chi'(\omega, T) = \chi_{\text{hf}} + \frac{\chi_0(T) - \chi_{\text{hf}}}{1 + \omega^2\tau(T)^2} \tag{4.3}$$

$$\chi''(\omega, T) = \frac{[\chi_0(T) - \chi_{\text{hf}}]\,\omega\tau(T)}{1 + \omega^2\tau(T)^2} \tag{4.4}$$

Crucially, $\chi_0(T)$ is not constant: for superparamagnetic particles, $\chi_0 \propto \mu^2/(3k_BT)$ (eq. 2.40) and $\chi_0 \propto V^2/T$ (Curie-like behaviour). This temperature dependence has important consequences for interpreting the peaks in $\chi'(T)$ and $\chi''(T)$.

4.5.1.1 The $\chi''(T)$ Peak: Blocking Condition

We denote by T_f' and T_f'' the temperatures at which $\chi'(T)$ and $\chi''(T)$ peak, respectively, at measurement frequency f. Setting $\mathrm{d}\chi''/\mathrm{d}T = 0$, the dominant contribution comes from the $\omega\tau/(1+\omega^2\tau^2)$ factor, provided that $\chi_0(T) - \chi_{\text{hf}}$ varies slowly compared to the exponential variation of $\tau(T)$. This yields the standard blocking condition [44, 222]:

$$\omega\tau(T_f'') = 1 \quad \Longleftrightarrow \quad \tau(T_f'') = \frac{1}{2\pi f} \tag{4.5}$$

At this temperature, the phase lag between the oscillating field and the magnetisation response is maximal, producing maximum energy dissipation. Below T_f'', moments are blocked ($\tau \gg 1/\omega$) and cannot follow the field; above T_f'', moments flip freely ($\tau \ll 1/\omega$) with minimal lag.

Livesey et al. [48] showed that the stochastic nature of thermal switching produces an **irreducible broadening** of the blocking transition even for perfectly monodisperse particles. For a polydisperse ensemble, each particle size contributes its own χ'' resonance at a different temperature (since τ depends on KV). The observed peak is the superposition of all contributions, weighted by the equilibrium susceptibility of each sub-population. In this sense, the $\chi''(T)$ peak temperature reflects the **mean blocking temperature** of the ensemble [223].

4.5.1.2 The $\chi'(T)$ Peak: Competition Between Unblocking and Thermal Decay

Recall that for χ'', the condition $\omega\tau = 1$ emerges because $\chi_0(T)$ varies slowly compared to the exponential $\tau(T)$. For χ', however, $\chi_0(T)$ appears as a factor of the relaxation term (Eq. 4.3), so its $1/T$ decay enters the derivative $\mathrm{d}\chi'/\mathrm{d}T$ on equal

footing with $\tau(T)$. The peak therefore arises from the competition between two opposing effects:

1. **Unblocking**: as T increases, τ decreases exponentially, causing $1/(1+\omega^2\tau^2)$ to increase, moments become responsive to the field.
2. **Curie decay**: simultaneously, $\chi_0(T) \propto 1/T$ decreases, thermal fluctuations reduce the equilibrium response.

Derivation of the χ' peak condition: In the idealized case where $\chi_0(T) = C/T$ (Curie law) and $\chi_{\text{hf}} \approx 0$, the real susceptibility reduces to $\chi'(T) = C/[T(1+\omega^2\tau^2)]$. Setting $\mathrm{d}\chi'/\mathrm{d}T = 0$:

$$\frac{\mathrm{d}}{\mathrm{d}T}\left[\frac{1}{T}\right] \cdot \frac{1}{1+\omega^2\tau^2} + \frac{1}{T} \cdot \frac{\mathrm{d}}{\mathrm{d}T}\left[\frac{1}{1+\omega^2\tau^2}\right] = 0 \tag{4.6}$$

The first term gives $-1/T^2$. For the second, from the Néel-Arrhenius law $\tau = \tau_0 \exp(E_a/k_BT)$:

$$\frac{\mathrm{d}\tau}{\mathrm{d}T} = -\frac{E_a}{k_BT^2}\,\tau \qquad \Longrightarrow \qquad \frac{\mathrm{d}}{\mathrm{d}T}\left[\frac{1}{1+\omega^2\tau^2}\right] = \frac{2\omega^2\tau^2\,E_a/(k_BT^2)}{(1+\omega^2\tau^2)^2} \tag{4.7}$$

Substituting and defining $u = \omega\tau$ and $\zeta = E_a/(k_BT)$:

$$-\frac{1}{1+u^2} + \frac{2\zeta\,u^2}{(1+u^2)^2} = 0 \qquad \Longrightarrow \qquad -(1+u^2) + 2\zeta\,u^2 = 0 \tag{4.8}$$

which yields:

$$\omega\tau(T_f') = \frac{1}{\sqrt{2\zeta-1}} \qquad \text{with} \quad \zeta = \frac{E_a}{k_BT_f'} \tag{4.9}$$

Unlike the χ'' condition $\omega\tau = 1$, this is not a universal constant. The condition $\zeta > 1/2$ (required for the peak to exist) is always satisfied for systems with non-negligible energy barriers.

Since $\omega\tau(T_f') < 1 = \omega\tau(T_f'')$ and $\tau(T)$ is monotonically decreasing, it follows that:

$$T_f' > T_f'' \tag{4.10}$$

The χ' peak always occurs at a higher temperature than the χ'' peak, even for a perfectly monodisperse system. Note that in the frequency domain, $\chi'(\omega)$ is monotonically decreasing and has no peak at all [222, 224], the χ' peak exists only in the temperature domain, precisely because of the $\chi_0(T)$ variation.

Bias toward the largest particles for χ': The V^2 dependence of χ_0 means that larger particles contribute disproportionately to χ'. As shown in the polydisperse Debye integral (Eq. 2.38 and Eq. 2.45), the integrand is weighted by $m_{\text{NP}}^2 \propto V^2 \propto$

$(D_{\mathrm{mag}}/2)^6$. In the temperature domain, the $1/T$ factor in $\chi_0(T)$ further shifts the χ' peak toward higher temperatures, i.e. toward the blocking temperatures of the largest particles. Ludwig et al. [225] state that this makes ACS-derived size distributions effectively volume-weighted. The recurring claim that the χ' peak reflects the "largest particles" [69, 223] is therefore more accurately described as a m_{NP}^2-weighted average. The χ' peak temperature T_f' lies between the mean T_B (probed by χ'') and the T_B of the very largest particles.

4.5.2 Theory: Fitting Models for Dynamic Susceptibility

4.5.2.1 Néel-Arrhenius Linearization

At the χ'' peak temperature, $\tau = 1/(2\pi f)$ (Eq. 4.5). Substituting into the Néel-Arrhenius law (Eq. 2.30) and taking the logarithm yields:

$$\ln\left(\frac{1}{2\pi f}\right) = \ln(\tau_0) + \frac{E_a}{k_B T_B} \tag{4.11}$$

For a non-interacting system, a plot of $\ln(1/f)$ versus $1/T_B$ is a straight line. The slope gives the energy barrier $E_a = KV$, and the intercept gives the attempt time τ_0.

4.5.2.2 The Vogel-Fulcher Law

For systems with significant dipolar interactions, the Néel-Arrhenius model is insufficient: fitting yields unphysical parameters. The interactions introduce an additional effective energy barrier that shifts T_B to higher temperatures, causing $\ln(1/f)$ versus $1/T_B$ to deviate from a straight line. This behaviour is captured by the empirical Vogel-Fulcher law:

$$\tau = \tau_0 \exp\left(\frac{E_a}{k_B(T_B - T_0)}\right) \tag{4.12}$$

The parameter T_0, the Vogel-Fulcher temperature, measures the inter-particle interaction strength. If $T_0 = 0$, the equation reduces to the Néel-Arrhenius law. Originally an empirical relation for the viscosity of supercooled liquids, the law was first applied to magnetic systems by Shtrikman and Wohlfarth [226], who interpreted T_0 as arising from interactions between superparamagnetic clusters in spin glasses.

Note that in this work, interactions are already absorbed into K_{eff} contributing to E_a, as defined by the DBF model (Subsection 2.3.6). Adding T_0 creates a three-parameter fit: T_B, E_a and T_0 are correlated. Therefore, exact benchmarks for T_0 in nanoparticle systems do not exist; reported values span from ∼40 K to ∼270 K [22, 80, 223, 227] depending on the material, sample form and... fitting parameters (not often reported in literature). Note that T_0 does not only account for dipolar

interactions: de Araújo et al. [22] showed that exchange coupling between touching $MgFe_2O_4$ nanoparticles can also inflate T_0. The Vogel-Fulcher law is therefore best used only as a *relative* measure of interaction strength between samples, not as an absolute determination of anisotropy.

4.5.2.3 The Mydosh Parameter

The frequency dependence of T_B provides a model-independent classifier: the Mydosh parameter Φ [228].

$$\Phi = \frac{\Delta T_B / T_B}{\Delta(\log_{10} f)} \tag{4.13}$$

It quantifies the relative shift of the peak temperature per decade of frequency. Unlike the Vogel-Fulcher or Arrhenius analyses, Φ requires no fitting and no assumption about K_{eff}, τ_0, ... Through its frequency-dependence, Φ reflects a fundamental change in what governs the peak temperature, progressing from a purely kinetic artifact of the measurement timescale (large Φ) to a thermodynamic property of the material (small Φ). Table 4.9 summarises the four commonly distinguished regimes, together with the Φ boundaries reported by different groups. There is no universally accepted set of boundary values: the original classification from [228] was developed for atomic spin glasses, and different nanoparticle studies adopt different thresholds depending on the source cited (Dormann et al. [79], Masunaga et al. [229], Ramos-Guivar et al. [230]). In Appendix A.6 a more detailed overview is given on reported Mydosh parameters in literature, for SPION. Despite the ambiguous threshold values, the underlying physical trend is unambiguous: as interactions strengthen, the peak temperature evolves from a kinetic blocking condition, where T_B is the temperature at which $\tau(T)$ crosses $1/f$ along an exponential curve, toward a cooperative freezing transition whose temperature is an intrinsic property of the interacting ensemble and therefore nearly frequency-independent.

4.5.2.4 Choosing Between χ' and χ'' for Fitting

Because the χ'' peak condition ($\omega\tau = 1$) provides a direct extraction of τ at each frequency, the Arrhenius or Vogel-Fulcher linearization is exact within the Debye framework when applied to χ'' peak temperatures. Applying the same linearization to χ' peak temperatures implicitly absorbs the factor $1/\sqrt{2\zeta - 1}$ (Eq. 4.9) into the fitted τ_0, yielding a systematically larger apparent τ_0. For polydisperse systems, the distinction goes further as explained in 4.5.1: χ'' probes the mean T_B, while χ' probes the dynamics of a larger, m_{NP}^2-weighted sub-population, yielding different effective energy barriers. The choice of component also depends on the physical regimes explained in Table 4.9:

- **SPM regime:** χ'' is preferred because the peak condition $\omega\tau = 1$ provides the most direct extraction of $\tau(T)$, as done by e.g. Goya et al. [49] and García-Acevedo et al. [80].

		Φ boundaries by source				
Regime and Relaxation law	**Physical origin of Φ**	[228]	[79]	[229]	[230]	[231]
Non-interacting SPM: $\tau = \tau_0 e^{KV/k_BT}$	T_B is purely kinetic: defined by $\tau(T_B) = 1/f$; shifting f by one decade moves T_B substantially	>0.1	>0.13	>0.1	0.3–0.5	>0.05
Interacting SPM: $\tau = \tau_0 e^{E_a/k_B(T-T_0)}$	Interactions modify individual barriers (Vogel-Fulcher T_0) but each particle still relaxes mostly independently	—	0.05–0.13	0.05–0.1	0.18–0.3	—
Super Spin Glass Behavior (SSG)	Collective freezing via dipolar frustration; nearly f-independent	—	0.005–0.05	<0.05	0.05–0.18	0.01–0.05
Canonical Spin Glass Behavior (SG)	True phase-transition; residual f-dependence from finite-ω probing only	<0.01	<0.005	—	—	∼0.005

Table 4.9 Classification of dynamic magnetic regimes via the Mydosh parameter Φ, with boundary values reported by different groups. The rightmost columns give the Φ ranges adopted in five representative classification schemes from the literature. The "Physical origin" column explains why Φ takes its characteristic value in each regime.

- **SSG regime:** The cooperative freezing transition manifests most characteristically as a cusp in $\chi'(T)$ [228]. Aslibeiki et al. [232] and Tiwari et al. [233] both used χ' peak temperatures for Vogel-Fulcher fitting of SSG systems. Hiroi et al. [234] explicitly distinguished the two regimes: χ'' for SPM samples and χ' for SSG samples.

In this work, Vogel-Fulcher fitting and Mydosh parameter extraction will be systematically done on χ''(T); and on χ'(T) when these show maxima.

4.5.3 Methods: ACS measurements

4.5.3.1 AC Susceptometers

Alternating Current (AC) Susceptometry is a non-destructive technique for investigating the dynamic magnetic properties of materials. The fundamental principle involves applying a weak, sinusoidally oscillating magnetic field, $H(t) = H_0 \cos(\omega t)$, to a sample and measuring the resulting induced magnetisation, $M(t)$. In an ideal material with no relaxation effects, the magnetisation would respond instantaneously and in-phase with the applied field. However, in a real system like a nanoparticle suspension, the relaxation processes introduce a time delay or phase lag, which induces a real and imaginary part of susceptibility as explained in Section 2.3.5.

The most common solution is to use a gradiometric or balanced coil configuration. This involves two identical pickup coils wound in opposition and connected in series. The uniform field from the excitation coil induces equal and opposite voltages in the two coils, which cancel each other out. The nanoparticle sample is then placed inside only one of the coils. The magnetisation of the sample creates an additional, localised magnetic flux that is not balanced, producing a net voltage signal that is proportional to the sample's magnetisation [235]. The voltage induced in this balanced pickup system, according to Faraday's law of induction, is proportional to the rate of change of the sample's magnetic moment. This voltage signal is then analysed, often with a lock-in amplifier, to separate its in-phase (χ') and out-of-phase (χ'') components [236]. To enhance specificity and sensitivity, particularly for biosensing, a mixing-frequency method can be employed, as demonstrated by Tu et al. in [237].

4.5.3.2 Methods

Instrument: AC susceptibility measurements were performed on the same Quantum Design MPMS® 3 SQUID magnetometer described in Subsection 4.3.1.1, equipped with the AC susceptibility option. They were performed in collaboration with IRM/KMI by Dr. Simo Spassov. In AC mode the instrument uses a dc SQUID sensor coupled to a second-order superconducting gradiometer via a flux transformer. Because the SQUID output is proportional to the magnetic flux threading the pickup coils rather than to its time derivative, sensitivity is essentially independent of the excitation frequency over the calibrated range (0.1 Hz to 1 kHz) [211]. The AC excitation field is generated by a copper solenoid immersed in the liquid-helium bath; an iterative drive-nulling procedure suppresses direct coupling between the drive coil and the gradiometer by a factor of approximately 10^7. Each data point is acquired in a two-point measurement: the sample is measured successively in the bottom and centre (counter-wound) pickup coils, and the difference eliminates residual direct-coupling artefacts.

Samples: Although the same quartz paddle holder was used (see 4.3.1.2), the specific membrane and powder samples prepared for AC susceptibility measurements differed from those used for DC magnetisation and FC-ZFC (Subsection 4.3.1.2). Membrane samples were prepared and mounted on the quartz paddle as described in Subsection 4.3.1.2. The used nanoparticles were Mn–CP2, Fe–CP1, Fe–TDH4 and Fe–TDH4@Si. Powder samples were compacted into a Quantum Design standard sample holder straw (P/N 8000-001), a translucent plastic tube with a weakly diamagnetic background. This differs from the gelatin capsules used for DC magnetisation and FC-ZFC powder measurements. Applied masses are specified alongside the individual measurement results.

Measurement parameters: For all samples, the AC driving field amplitude was set to 2 Oe (peak). Temperature sweeps were performed upon warming from 3 K

to 300 K with approximately 62 temperature points per sweep (the exact number varied between samples). Measurements were carried out at 5 to 15 frequencies spanning 5 Hz - 900 Hz. The instrument recorded both the in-phase and out-of-phase AC susceptibility components, χ' and χ'', along with their standard errors, the AC moment amplitude, and the phase angle, all as a function of temperature. Sample masses are reported with the individual measurement results.

4.5.3.3 Methods: Extracting K_{eff}, T_B, T_0, Φ

Treatment of the obtained data was done as follows:

- To locate the temperature of maximum susceptibility (T_f) at each frequency, raw data were first resampled onto a uniform temperature grid (200 points) by linear interpolation, then smoothed using a Savitzky–Golay filter (polynomial order 2; window lengths of 15, 20 and 30 points were tested as a robustness check). Peaks were identified on the smoothed curves using a minimum-distance constraint. For iron oxide samples they were classified into a low-temperature group ($T_f < 50$ K) and a high-temperature group ($T_f \geq 100$ K).

- The frequency dependence of T_f was quantified by the Mydosh parameter, obtained by Eq. 4.13.

- The Néel-Arrhenius and Vogel-Fulcher models were fitted to the $(1/T_f,\ -\ln 2\pi f)$ data by nonlinear least-squares regression. Bounds on τ_0 (10^{-11}–10^{-9} s) and K_{eff} (1×10^4–50×10^4 J/m^3) were shared between the two models to ensure a fair comparison; T_0 was additionally constrained to remain below 90 % of the lowest observed T_f. Goodness of fit was assessed by R^2 and convergence onto a bound was flagged.

4.5.4 Results: AC $\chi(T)$

Figs. 4.11, 4.12, 4.13 represent AC susceptibility data curves: on the ordinates are χ' and χ'', on the abscis temperature. Different curves within a same graph correspond to different excitation (sensing) frequencies. In theory, extrapolating the tendency towards 0 Hz should result in an identical blocking temperature as the FC-ZFC curves (τ_{meas} = 100 s), but in this case the probing field for ACS (2 Oe) is lower than for FC-ZFC (50 Oe) so no one-on-one conclusion can be drawn. Note that the real component is one order of magnitude larger than the imaginary component. On the right of these susceptibility figures, Arrhenius and Vogel-Fulcher fitting are represented.

The most notable structural difference across samples is the presence or absence of a second peak in $\chi''(T)$. Furthermore, a higher symmetry exists in the

these peaks. This is consistent with χ'' being directly sensitive to energy dissipation at the blocking condition $\tau(T_B) = 1/\omega$, whereas χ' peaks are broader and more easily masked by the monotonic Curie-like background. Table 4.10 summarizes the fitting parameters obtained for each sample. In the following subsections the corresponding graphs per sample family are discussed.

4.5.4.1 ACS Results: Mn–CP2 in membrane and powder

Both for the real and imaginary part, the peak temperature is lower for the powder than for the membrane sample. This is unconsistent with the FC-ZFC measurements where membranes are unblocked at room temperature while powders are not, cf. Fig. 4.8. The signature of Mn–CP2 on membrane was double-checked and confirmed with a duplicate sample. We cannot exclude that the difference in sample mass (14 mg Fe for powder, 45 μg Fe for the dispersion in cellulose membrane) affects the measurement dynamics.

- χ': The powder sample shows $T'_f > T''_f$, consistent with the expectation that the real-part peak (1) reflects the blocking of the largest particles in the distribution and (2) competes with Curie-decay (Eq. 4.10 in 4.5.1). It is therefore unsurprising that neither Neel-Arrhenius nor Vogel-Fulcher fitting yield reliable results with R being very low (Section 4.5.2.4).

- χ'': Powder and membrane exhibit a single peak in the imaginary susceptibility ($\bar{T}_f \approx 178$ K for powder, ≈ 241 K for membrane). While the symmetry of both peaks is satisfying (according to the fact that it is not subject to Curie decay, cf 4.5.1), it is interesting to observe the shape of these peaks: the T_B distribution seems wider for the samples on membranes, consistent with the hypothesis that various cluster sizes are formed in the membrane. Vogel-Fulcher yields a reliable linearisation, confirming SPM behavior with interactions. Interestingly, the fitted T_0 for powder is lower than for the membrane (T_0 = 42 vs T_0 = 152, cf Table 4.10) underlining the point made by Dorman et al. [79] that this parameter serves for comparison within similar configurations and conditions.

Mn–CP2 Mydosh Parameter: A significant difference appears between the real and imaginary phases for Mn–CP2 powder: $\Phi = 0.009$ (χ') vs $\Phi = 0.091$ (χ''). The very low Φ from the real part may reflect the fact that the real-phase peak is governed by the largest particles in the distribution, whose blocking temperatures are less sensitive to frequency. The imaginary-phase value of $\Phi = 0.091$ is more representative of the ensemble-averaged dynamic behaviour and is typically linked to interacting SPM behavior (Table 4.9), consistent with the fact that Vogel-Fulcher fitting yields reliable result. In the membranes, the χ'' Mydosh parameter ($\Phi = 0.045$) is lower than for the powder and at the boundary between SSG and interacting SPM. We cannot differentiate whether this would mainly be attributed to wider T_B distribution (making peak identification less presice) or to actual SSG

Sample	Phase	Peak type	$\bar{T}_f$ (K)	N	Φ	VF R^2	VF T_0 (K)	K_{eff} (kJ/m^3)	τ_0 (s)	On bound
Mn–CP2 powder (14 mg)	χ'(T)	single	271	6	0.009	*0.19*	—	—	—	—
	χ''(T)	single	178	6	0.091	0.99	42	68	10^{-11}	Yes
Mn–CP2 membrane (45 *ug* Fe)	χ'(T)	not unblocked	298	—	—	—	—	—	—	—
	χ''(T)	1	241	7	0.045	0.96	152	43	3.4×10^{-11}	No
Fe–CP1 membrane (72 *ug* Fe)	χ'(T)	not unblocked	—	—	—	—	—	—	—	—
	χ''(T)	Double: lowest T_f''	43	7	0.21	0.78	≈ 0	17	10^{-9}	Yes
Fe–TDH4@Si membrane (8.4 *ug* Fe)	χ'(T)	1	240	6	0.040	0.99	180	23	10^{-9}	Yes
	χ''(T)	Double: highest T_f''	189	6	0.046	0.91	110	39	10^{-11}	Yes
Fe–TDH4 membrane (12 *ug* Fe)	χ'(T)	1	238	6	0.046	0.75	113	62	10^{-11}	Yes
	χ''(T)	Double: highest T_f''	173	6	0.045	*0.30*	—	—	—	—

Table 4.10 Overview of fitter Vogel-Fulcher (VF) and Mydosch parameter. If R^2 for VF is below 0.7, other fitting parameter are considered unreliable and omitted. All fits assume $\tilde{D}_{\text{mag}} = 10$ nm. VF fits use $\tau_0 \in [10^{-11}, 10^{-9}]$ s as fitting bounds. For each sample, the table reports the peak structure: if double peak occurs, the fitted peak (lowest or highest T_f'') is specified. For Fe-CP1 samples, the high temperature peak exceeds room temperature. For Fe-TDH samples, no fitting was done on the low-temp T_f'' because the temperature-step was too high during measurement.

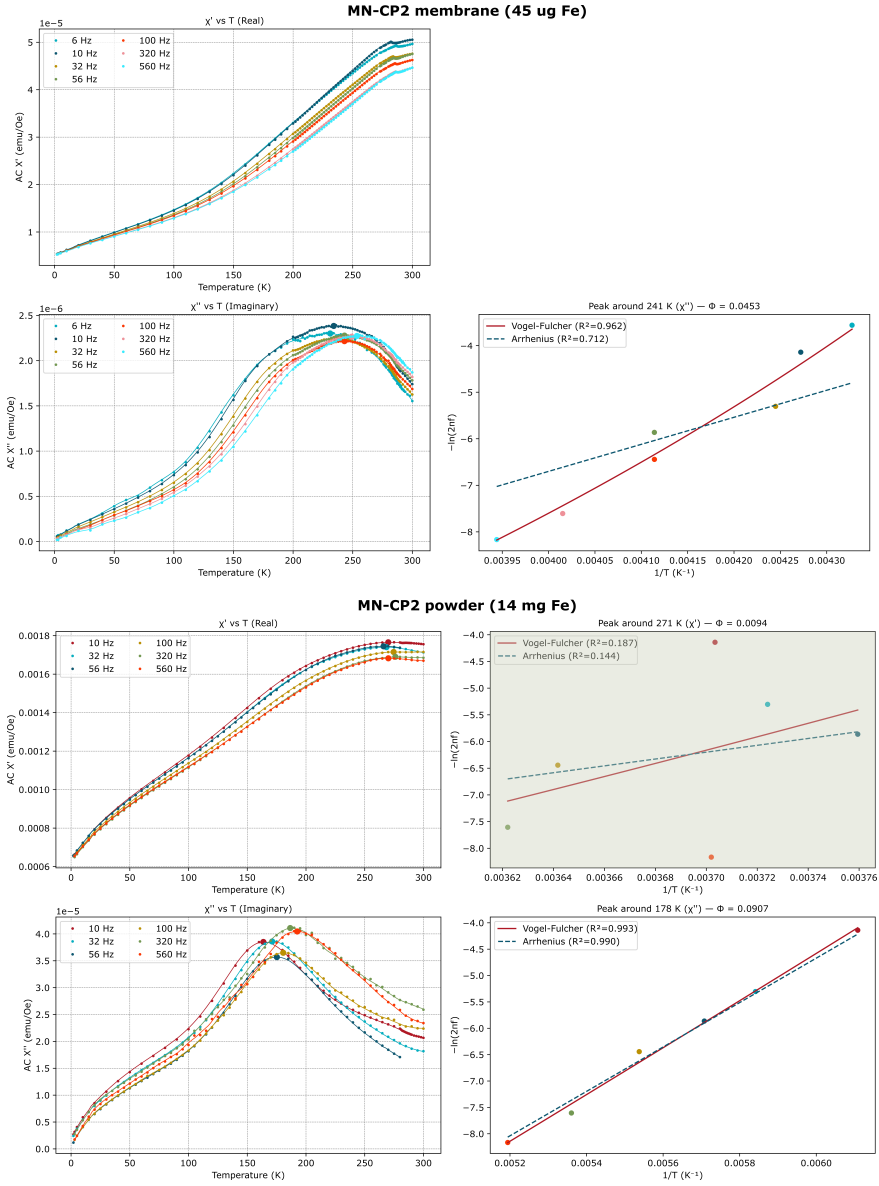


Fig. 4.11 AC Susceptibility of Mn–CP2 in cellulose dispersion and powder form. The Arrhenius, Vogel-Fulcher fitting and Mydosh parameter Φ are given for every identified susceptibility peak.

behavior in the clusters: a higher datapoint resolution around T_f'' would clarify this.

4.5.4.2 ACS Results: Fe–CP1 in membrane

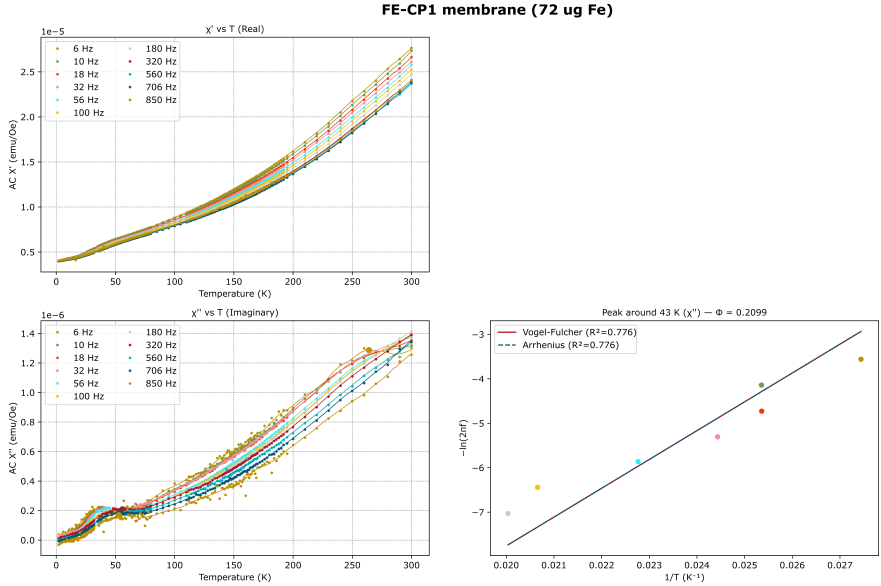


Fig. 4.12 AC Susceptibility of Fe–CP1 in cellulose dispersion

Fig. 4.12 displays ACS spectra for Fe–CP1 (72 μg Fe) in a cellulose membrane.

- χ': No peaks are detected in the real phase, indicating that nanoparticles within the largest clusters are not unblocked at room temperature when excitation field frequency is at 6 Hz or higher.
- χ'': Fe–CP1 membrane shows two groups of peaks in $\chi''(T)$: a low-temperature peak at $T_f'' \approx 43$ K and a high-temperature group for which ony the measurement at 6 and 10 Hz are unblocked at room temperature. This is consistent with the two blocking events observed in FC-ZFC curves on Fe–CP1 in membrane (Fig. 4.9). For the low-temperature peak, the temperature-step was reduced during the measurement sweep to obtain better resolution for the peak location. A key observation is the fact that both Néel-Arrhenius and Vogel-Fulcher models yield good fitting results, consequently $T_0 = 0$. This suggests that the lower temperature peak corresponds to non-interacting SPM behavior.

Fe–CP1 on membrane, Mydosh parameter: For the low-temperature χ'' peak, $\Phi = 0.21$ is attributed to non-interacting SPM behavior (Table 4.9), consistent with

the low (≈ 0) T_0 from Vogel-Fulcher fitting.

To the best of our knowledge, no consistent interpretation is offered in literature to this low-temperature peak observed in ACS and FC-ZFC measurements on iron oxide nanoparticles

- Modestino et al. [223] observe the low-temperature peak with ACS and apply the Mydosh parameter model. They agree on the fact that this peak shows nearly-ideal SPM behavior and attribute it to a subpopulation of non-interacting smaller particles. No evidence is given on the actual existence of such a subpopulation. The double-peak observation is attributed to clustering but without solid argumentation.

- Roca et al. [51] associate the low-temperature peak to "incoherent electron tunneling" in disordered magnetite (would not occur in maghemite). Frequency dependence is not further developed.

- Topping et al. [222] show an ACS graph with double peak but do not explain it at all.

This work confirms that the occurance of the double peak is element-speific: it occurs in iron-oxide SPION but not in manganese ferrite, confirmed by both ACS and FC-ZFC measurements. It is not merely the existance of a dead layer (also present in Mn–CP2 and Mn–CP3) that causes it. Furthermore, it was shown that this peak becomes less dominant after coating of TD nanoparticles (Fig. 4.10), hinting towards correlation between either this peak and surface state of SPION, or this peak and oxidatation level of SPION. ACS data offers additional insight to the FC-ZFC data: the nearly ideal Neel-Arrhenius fit ($T_B \approx 0$ in VF model) and the Mydosh parameter independently point towards non-interacting SPM-like nature of this peak. It corroborates the hypothesis in 4.4.4.2 that due to oxidation/clustering, part of the nanoparticles have a reduced magnetic core. Indeed, the corresponding T_B is generally attributed to 3-5 nm SPION (cf Table 4.7). The existance of a shell with less magnetic moment can explain the non-interacting nature of the behavior.

4.5.4.3 ACS Results: Fe–TDH4 in membrane, coated and uncoated

Fig. 4.13 shows ACS spectra for Fe–TDH4 with and without silica coating.

- χ': the Fe–TDH4 samples appear unblocked at room temperature up to 560 Hz, unlike Fe–CP1. This is consitent with the demonstration in 4.4 (based on measurements and confirmed by literature) that CP nanoparticles have higher K_{eff}. As for ACS measurements on Mn–CP2, $T'_f > T''_f$ consistent with Eq. 4.10. However the difference between both is smaller, which could be correlated to the lower γ of thermal decomposition samples. The Fe–TDH4@Si sample shows less plateau'ing, consistent with the sharper peaks in Fig. 4.10.

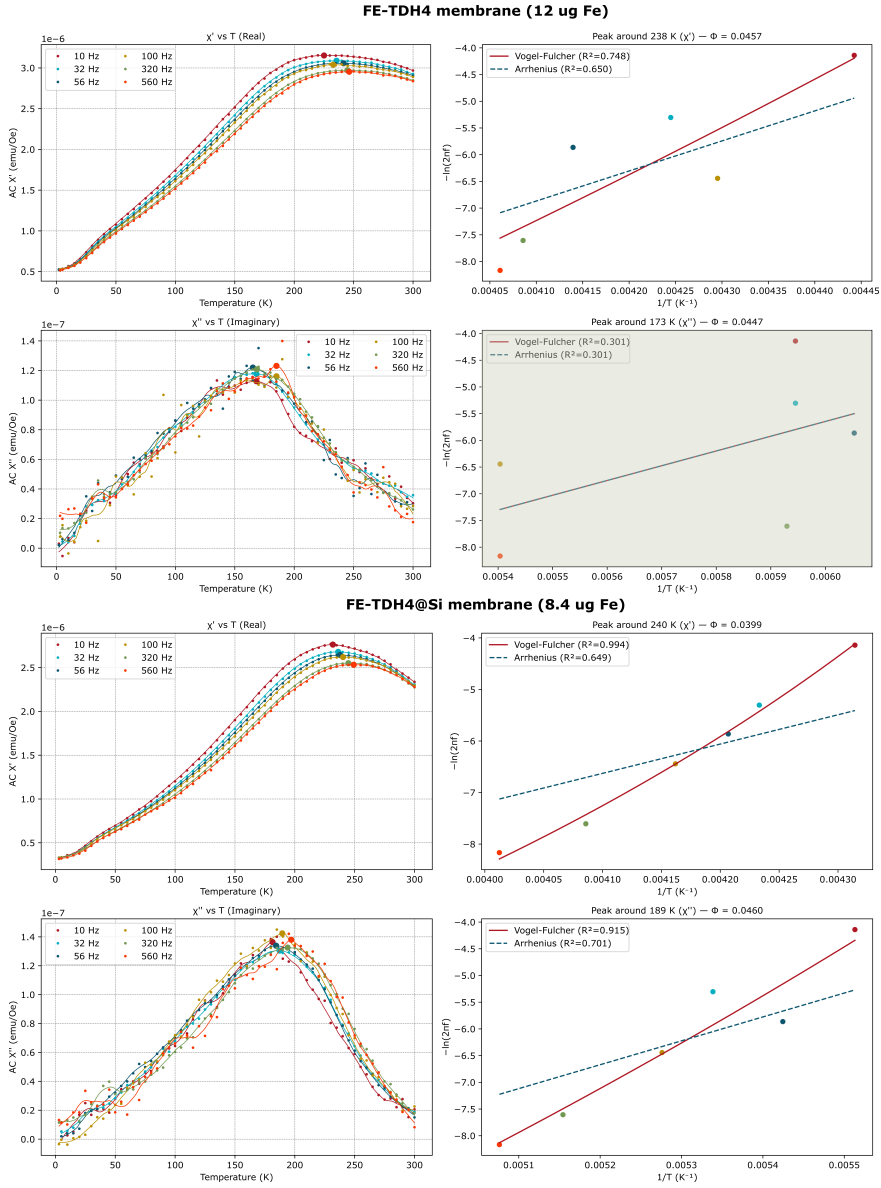


Fig. 4.13 AC Susceptibility of Fe–TDH4 in cellulose dispersion, with and without silica coating

An explanation could be that silica coating (or preceding ligand exchange) improves the colloidal stability and fosters more homogeneous clustering in the cellulose membrane. Vogel-Fulcher fitting is valid in both cases and particularly beautiful ($R^2 = 0.99$) for Fe-TDH4@Si, consistent with the lower Chantrell SSE observed for the same sample in magnetisation curves (Table 4.6). T_0 above 100 K in both cases (cf Table 4.10) indicates interactions are signficantly present. The reader is remembered to the fact that the silica coating on Fe-TDH4@Si is very thin (< 1% Si mass) so it is not expected to reduce distance between nanoparticles (therefore, dipolar interactions) significanlty.

- In T_B the existence of a double peak is confirmed. However, unlike measurements on Fe–CP1, measurements were made without improved resolution below 50 K. Therefore, no consistent low-temperature-peak identification can be done. The high-temperature peaks are occuring at higher temperature than for FC-ZFC (Fig. 4.10), consistent with the reduced τ_{meas}. Vogel-Fulcher fitting works well for Fe-TDH4@Si, but for Fe-TDH4 the measurement seems too noisy: higher resolution is required. As for Mn–CP2, fitted T_0 is lower for χ'' than χ'.

Fe–TDH4 on membrane - Mydosh Parameter: $\Phi \in [0.040 - 0.045]$ for both phases and both samples on membrane, indicating interacting SPM behavior (Table 4.9). Consistent with obtained T_0, this suggests that silica coating does not significantly alter the dynamic interaction regime.

4.5.5 Sensitivity of Vogel-Fulcher Parameters to pre-exponential factor boundaries

When the nanoparticles show non-ideal SPM behavior, the τ_0 tends to scale down. In the ideal Néel-Arhenius model, τ_0 and K_{eff} are "communicating vessels". The DBF model, which groups non-ideal effects (such as interactions) under a change (mostly increase) in K_{eff}, is just a reversed illustration of the same observation.

However, the attempt time τ_0 is not a free numerical parameter: it emerges from Brown's Fokker–Planck treatment of single-domain magnetic relaxation [75, 238] and depends explicitly on temperature, on the energy barrier $E_B = K_{\text{eff}}V$, and on a dimensionless damping parameter. Its physically admissible value therefore varies with composition, anisotropy and particle size rather than being a universal constant, so the fitting window must be chosen per system. For iron oxide nanoparticles (Fe_3O_4, γ-Fe_2O_3) above roughly 8 nm, the atomistic Landau–Lifshitz–Gilbert simulations of Moreno et al. [239] return $\tau_0 = 0.98 \pm 0.13$ ns at 300 K and confirm the commonly cited $\sim$ 1 ns benchmark, which justifies the window $[10^{-11}, 10^{-9}]$ [s] adopted in this work and is consistent with the values reported in [29, 38, 46]. Analytical estimates by Coffey and Kalmykov [238]

span 10^{-10}–10^{-11} s and partially justify an extension down to $\sim 10^{-12}$,s for high-anisotropy systems. A looser lower bound $\tau_0 \sim 10^{-13}$–10^{-9} is retained in the literature for smaller or more anisotropic SPION [49, 69, 95].

The fitting on ACS data $\tau_0 \in [10^{-11}, 10^{-9}]$ s as fitting bounds, validated for SPION at the size we consider. To the best of our knowledge, no concensus exists on the bounds for $MnFe_2O_4$ SPNF: in [232] the same are used as for Fe_3O_4, we have followed the same convention. To illustrate how this boundary choice affects the extracted parameters, the same fits were repeated with a wider range $\tau_0 \in [10^{-13}, 10^{-9}]$ s. Table 4.11 compares the results for all samples with valid Vogel-Fulcher fits.

		$\tau_0^{\min} = 10^{-13}$ s				$\tau_0^{\min} = 10^{-11}$ s			
Sample	**Phase**	τ_0 **(s)**	K_{eff} **(kJ/m^3)**	T_0 **(K)**	R^2	τ_0 **(s)**	K_{eff} **(kJ/m^3)**	T_0 **(K)**	R^2
Mn–CP2 powder	χ'	10^{-13}	87	131	0.19	10^{-11}	57	158	0.19
	χ''	10^{-13}	105	10	0.99	10^{-11}	68	42	0.99
Mn–CP2 membrane	χ''	3.4×10^{-11}	43	152	0.96	3.4×10^{-11}	43	152	0.96
Fe–CP1 membrane	χ''_{low}	10^{-9}	17	≈ 0	0.78	10^{-9}	17	≈ 0	0.78
Fe–TDH4	χ'	10^{-13}	95	85	0.75	10^{-11}	62	113	0.75
Fe–TDH4@Si	χ'	10^{-9}	23	180	0.99	10^{-9}	23	180	0.99
	χ''	10^{-13}	61	92	0.92	10^{-11}	39	110	0.91

Table 4.11 Sensitivity of Vogel-Fulcher parameters to the lower bound of τ_0. All fits assume $\tilde{D}_{\text{mag}} = 10$ nm.

Table 4.11 compares differences in VF parameters on the samples for which Vogel-Fulcher fitting had $R^2 > 0.75$. when the τ_0 bounds are lowered to 10^{-13}. Unsurprisingly, for samples that do not hit the lower bound of 10^{-11}, nothing changes. However, when τ_0 is pinned at the lower bound, decreasing the minimum pre-exponential factor from 10^{-11} s to 10^{-13} s increases K_{eff} by roughly 50% and simultaneously decreases T_0 by typically 10–30 K. This trade-off is a direct consequence of the VF equation $\tau = \tau_0 \exp\left[E_a/k_B(T_f - T_0)\right]$: a smaller τ_0 must be compensated by a larger activation energy E_a (hence higher K_{eff}) or a lower T_0 to reproduce the observed τ at the measured peak temperatures. Importantly, R^2 remains virtually unchanged between the two settings (differences < 0.01), confirming that the fit quality cannot discriminate between the two bounds. The data permit a continuous family of (τ_0, K_{eff}, T_0) solutions of comparable likelihood. These individual parameter values should therefore be interpreted with caution even though the VF fit quality is excellent, as underlined in [79]. For instance, the Mn–CP2 powder χ'' fit yields $T_0 = 10$ K with the 10^{-13} s bound but $T_0 = 42$ K

with the 10^{-11} s bound, a factor of four difference. For the Fe–TDH4@Si, the K_{eff} extracted from χ'' goes from 39 to 61 kJ/m^3.

The only sample whose VF parameters are truly bound-independent is Mn–CP2 membrane (χ''): these parameters can be considered the most reliable VF estimates in this dataset.

4.5.6 Susceptibility for membrane Mn–CP2 and Fe–CP1 (up to 1 kHz)

Fig. 4.14 displays the complex susceptibility of Fe–CP1 and Mn–CP2 in membrane between 1Hz and 1kHz. No relaxation is observed: this is unsurprising since Néel relaxation is expected to occur near GHz frequencies (cf Fig. 2.5). Unsurprisingly, the measurement confirms that Brownian relaxation, that *might* occur in clusters below 1 kHz, is not observed: the clusters are confirmed to be immobile. A slight slope is observed in Mn–CP2, which is interesting because measurements in the next section, on E4991 impedance analyzer, will show that the susceptibility slope of Mn–CP3 is stronger than the one of Fe–CP1. This should be confirmed with higher differentiation of measured masses and dupicat samples. The observed susceptibility of Mn–CP2 is also higher than Fe–CP1, consistent with previous measurements. However, given the difference in sample mass and the error propagation of mass estimation in dillutions, the exact ratio should be confirmed.

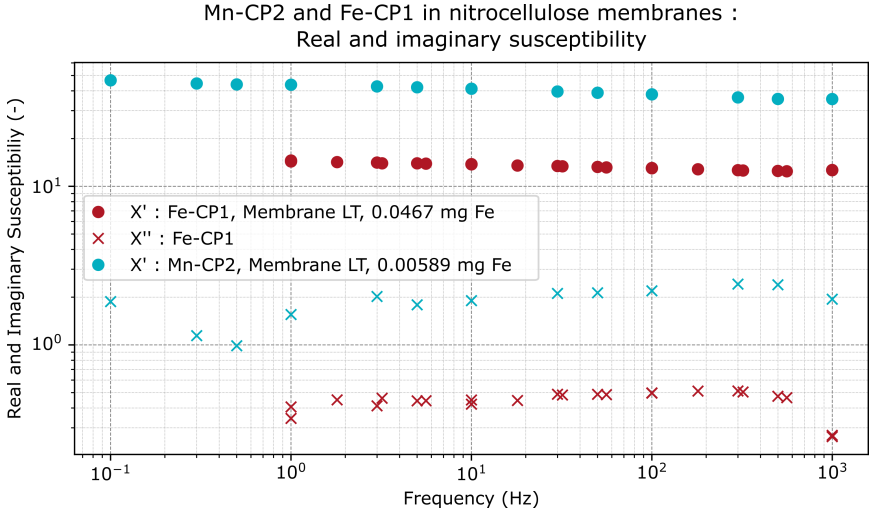


Fig. 4.14 Mn–CP2 and Fe–CP1 in membrane. Normalised for iron mass.

Section summary

ACS measurements were performed on SPION and Mn-SPNF in both powder form and dispersed in cellulose membranes, using the Quantum Design MPMS® 3 SQUID magnetometer with an AC drive amplitude of 2 Oe. Temperature sweeps from 3 to 300 K were recorded at 5 to 15 frequencies spanning 5 to 900 Hz. Peak temperatures of χ'(T) and χ''(T) (T'_f and T''_f) were extracted and used for Néel–Arrhenius and Vogel–Fulcher linearisation (with $\tau_0 \in [10^{-11}, 10^{-9}]$ s) and for Mydosh parameter extraction.

Consolidated conclusions:

- The imaginary susceptibility χ''(T) is the appropriate quantity for kinetic analysis: its peak condition $\omega\tau = 1$ provides a direct determination of τ at the peak temperature, whereas the χ'(T) peak arises from the competition between unblocking and Curie decay and is biased toward the largest particles via a m_{NP}^2 weighting (Subsection 4.5.1). Consistent with Eq. 4.10, T'_f is systematically larger than T''_f whenever both peaks are observed.

- The double-peak structure in χ''(T) observed for all iron oxide samples (Fe–CP1, Fe–TDH4, Fe–TDH4@Si in membrane) and absent for Mn–CP2 confirms, independently of the FC-ZFC measurements of Section 4.4, that this feature is element-specific to iron oxide.

- Mydosh parameters on Mn–CP2, Fe–TDH4 and Fe–TDH4@Si in membranes all follow interacting SPM behaviour, consistently through Vogel–Fulcher and Mydosh fitting. This confirms that the SPM nature is preserved in the membranes despite the supposed clustering, consistent with the absence of coercivity observed in the membrane magnetisation curves of Section 4.3 (Fig. 4.4). For Fe–CP1 this could not be confirmed since no unblocking was observed at room temperature, consistent with the higher K_{eff} derived for Fe–CP1 membranes from FC-ZFC (Table 4.8 in Section 4.4).

- The Vogel–Fulcher parameters τ_0, K_{eff} and T_0 are strongly correlated: when the lower bound on τ_0 is relaxed from 10^{-11} to 10^{-13} s, the fitted K_{eff} increases by roughly 50% and T_0 decreases by 10–30 K, while R^2 remains essentially unchanged (Table 4.11). The only sample whose VF parameters are truly bound-independent in this dataset is Mn–CP2 in membrane form. VF-derived parameters should therefore be used primarily as a *relative* measure of interaction strength across samples measured under identical conditions, as originally recommended by Dormann et al. [79].

- The low-frequency χ'(f) data on Mn–CP2 and Fe–CP1 membranes (Fig. 4.14) show no relaxation between 1 Hz and 1 kHz, consistent with Néel relaxation being expected near the GHz range (Fig. 2.5) and confirming that Brownian relaxation is suppressed for nanoparticles immobilised in cellulose membranes.

Observed trends requiring further investigation:

- The T_f' distribution width of Mn–CP1 is larger for membrane samples than for powder. This might be a strong indicator for variable cluster sizes in nitrocellulose. More comparisons between powder and membrane are needed (only one performed here).
- For Fe–CP1 membrane, the low-temperature χ'' peak yields a Vogel–Fulcher $T_0 \approx 0$ and a Mydosh parameter $\Phi = 0.21$, both signatures of non-interacting SPM behaviour (Table 4.9). This corroborates the hypothesis formulated in Subsection 4.4.4.2 that the low-temperature peak originates from a subpopulation of SPION with a reduced magnetic core ($\approx$ 3–5 nm), consistent with partial oxidation or clustering during membrane drying.
- For Fe–TDH4 and Fe–TDH4@Si membranes, the Mydosh parameter are similar, suggesting that the silica coating process did not alter the dynamic interaction regime. Since ICP reports 1.41 % Si mass on the coated powder (Table 3.8), corresponding to $\approx$ 3 % SiO_2 under the pure-maghemite/pure-silica assumption, this is consistent with the fact that no significant difference in spacing between nanoparticles exists when they are in membrane.
- For Fe–TDH4 (uncoated), the χ'' Vogel–Fulcher fit yields $R^2 = 0.30$, indicating that the data are too noisy for reliable parameter extraction on the high-temperature peak. The temperature step in TD measurements was also too coarse below 50 K to resolve the low-temperature peak, unlike the refined sweep used for Fe–CP1.

Perspectives:

- Extending the comparison between powder and membranes to other samples than Mn–CP2 would confirm the size-distribution hypothesis of clusters within membrane.
- The element-specific nature of the low-temperature χ'' peak in iron oxide, together with its non-interacting character confirmed for Fe–CP1, reinforces the interpretation of a partially oxidised outer shell on SPION. Increasing the temperature-point resolution around the χ'' low-temperature peaks of Fe-TDH4 membrane samples should confirm the ideal non-interacting SPM nature of this peak. Structural characterisation combining X-ray absorption spectroscopy or Mössbauer spectroscopy with controlled oxidation exposure would provide direct evidence of the proposed oxidation-induced magnetic shell.

4.6 MHz-GHz Complex Susceptibility at Room Temperature

4.6.1 Theory: MHz-GHz toroid susceptometry

The ACS measurements of Section 4.5.1 confirmed that the complex susceptibility remains flat up to 1 kHz, indicating that Néel relaxation occurs at considerably higher frequencies. Characterising the susceptibility in the MHz to GHz range is therefore necessary both to observe the onset of Néel relaxation and to obtain data at the operating frequencies of inductive biosensors (cf. Chapter 5). Besides the various impedance-based approaches available for this frequency range (an overview is provided in Appendix A.7.1.1), the toroidal geometry within a shorted coaxial transmission line, explained below, seems most suited to powder and liquid samples: it requires no specific sample shaping, and the azimuthal symmetry of the field eliminates the need for demagnetising-factor corrections [240].

Traditional measurement of magnetic permeability on toroidal samples often requires winding primary and secondary coils [202]. This process is not only tedious but also introduces significant experimental error at high frequencies (typically above 100 kHz) due to the distributed capacitance of the windings. The method described here, based on earlier work by Haas, Rasmussen, and Powell, involves the integration of a toroidal sample into a coaxial transmission line [241]. The Transverse Electro-Magnetic mode within a coaxial line naturally provides the required azimuthal magnetic field for probing the sample. The technique relies on measuring the impedance change of a shorted section of the line when a toroidal sample is inserted, creating a current loop. A notable advantage of the toroidal geometry is that the azimuthal field produced by the coaxial line has no demagnetising field for the composite [240]. This simplification does not hold for cylinders or disks, where demagnetising corrections would be required.

4.6.1.1 Conditions of validity

While the use of a coaxial set-up for determination of permittivity and permeability of a set-up is considered robust, several factors limit its upper frequency:

- **Higher-Order Modes:** The coaxial line can support non-TEM modes (e.g., TE_{11}) above a certain cutoff frequency (e.g., $\approx$ 9.5 GHz for a 14-mm GR-900 line used in [242]), which invalidates the theoretical assumptions.
- **Wavelength Effects:** The distance from the sample to the shorting plane must be a small fraction (e.g., $<$ 1%) of the free-space wavelength [240]. Otherwise, the transmission line section between sample and short acts as a distributed impedance element, invalidating the model underlying the ΔL and ΔR derivation below.

- **Sample Electrical Length:** The electrical length of the toroid itself, $\xi = h\sqrt{\mu_r'\epsilon_r'}$ (where ϵ_r' is the relative permittivity), must also remain small compared to the free-space wavelength to satisfy the magnetostatic approximation.

4.6.1.2 Real permeability of a toroid sample

The methodology explained below is based on the work of Dr. Goldfarb et al. [202] at NIST (National Institute of Standards and Technology, Colorado, USA). A toroidal sample with inner diameter a, outer diameter b, and height h is placed coaxially inside the sample holder, forming a single turn inductor. The inductance of the air-filled space that the toroid will occupy is given by:

$$L_a = \frac{\mu_0 h \ln(b/a)}{2\pi} \tag{4.14}$$

When the sample is inserted, this volume is filled with a material of permeability μ', and its inductance contribution becomes:

$$L_m = \frac{\mu' h \ln(b/a)}{2\pi}$$

The impedance analyser measures the total inductance of the shorted line, first without the sample (L_e) and then with the sample (L_s). The change in inductance, ΔL, is the difference between these two measurements:

$$\Delta L = L_s - L_e = L_m - L_a$$

Substituting the expressions for L_m and L_a yields:

$$\Delta L = \frac{(\mu' - \mu_0) h \ln(b/a)}{2\pi} = \frac{\mu_0(\mu_r' - 1) h \ln(b/a)}{2\pi}$$

where $\mu_r' = \mu'/\mu_0$ is the relative real permeability. Therefore:

$$\mu_r' = 1 + \frac{2\pi\Delta L}{\mu_0 h \ln(b/a)} = 1 + \frac{\Delta L}{L_a} \tag{4.15}$$

This formulation shows that the sample does not need to fill the entire coaxial line, as long as its dimensions (a, b, h) are known and the sample is "closeby enough" the short plane of the coaxial line (cf. Subsection 4.6.1.1).

4.6.1.3 Imaginary permeability of a toroid sample

In addition to the change in inductance, the analyser measures a change in the series resistance, ΔR, due to core losses in the material.

$$\Delta R = R_s - R_e = R_m$$

where R_e is the resistance of the empty fixture (assumed to be small) and R_s is the resistance with the sample. R_m represents the material's losses. The imaginary part of the permeability, μ'', is related to this measured resistance R_m and the air-space inductance L_a by:

$$\mu'' = \frac{\mu_0 R_m}{2\pi f L_a}$$

where f is the measurement frequency in Hertz. By substituting the expression for L_a (4.14), we can solve for the relative imaginary permeability, $\mu_r'' = \mu''/\mu_0$, using the measured quantities:

$$\mu_r'' = \frac{\Delta R}{\mu_0 f h \ln(b/a)}$$

4.6.2 Materials and Methods

4.6.2.1 Measurements on Keysight E4991

The measurements are made with the Keysight E4991B Impedance Analyser and the magnetic material test fixtures are the Keysight 16454A Magnetic Material Test Fixtures, a large and a small holder for toroid samples with dimensions specified in Fig. 4.15. Impedance is measured from 1 MHz to 1 GHz in a logarithmic sweep of 401 frequency points.

Attempts to measure nanoparticles spread in cellulose and nitrocellulose membranes, stacked within the capsules, were unsuccessful: the sensing signal did not exceed the noise floor. Therefore, only powders were measured. The larger capsules generally generated less noisy measurements given their higher magnetic content. However, for TD samples, only small amounts of powder were available given their low synthesis yield (Cf. Chapter 3). The large sample holder was thus used for CP powders while the small one was used for TD SPION powders.

The instrument was calibrated at the 7 mm connector plane using open, short, load, and low-loss capacitor standards. Fixture compensation (open and short) was subsequently performed at the test-fixture plane. The instrument was allowed to warm up for at least 24 h before calibration, and all measurements were carried out at room temperature.

The field in the E4991 for the maximum output current of 10 mA is only 0.23 A/m, i.e. less than 3 mOe. These test fixtures are explicitly designed for measurement of toroid magnetic materials, therefore we assume the necessary conditions in 4.6.1.1 are satisfied. Thus, considering perfect transverse electromagnetic mode, the model elaborated in 4.6.1.2 is considered valid. The experimental procedure is as follows:

1. The inductance L_e and resistance R_e of the empty, shorted sample holder are

measured and stored as a baseline over the 1 MHz to 1 GHz range. For small capsules, this frequency range was shortened to 50 MHz.

2. The toroidal sample is inserted into the holder, which is then re-shorted.
3. The inductance L_s and resistance R_s of the line with the sample are measured over the same frequency range.
4. The changes $\Delta L = L_s - L_e$ and $\Delta R = R_s - R_e$ are computed at each frequency point.
5. The relative permeability components μ_r' and μ_r'' are then calculated using the equations derived above.

The E4991 Impedance Analyser works both in permeability and impedance mode. For the former, a software error was observed: this is further elaborated in Appendix A.7.1.

4.6.2.2 Toroid Sample Holder

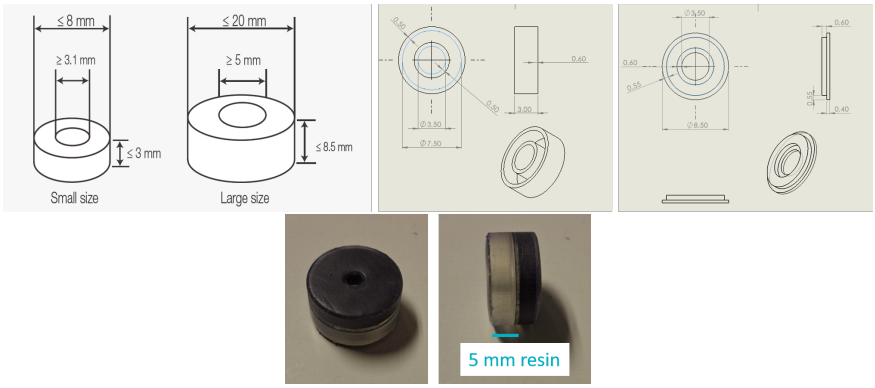


Fig. 4.15 Top: measurement of permeability properties of toroids with the E4991 impedance analyser, with maximum dimensions for the small and large test fixtures and illustration of design for a small capsule. Bottom: example of a resin cup for the large test fixture, partly filled with resin in order to comply with the available powder volumes. The side with powder is situated "facing upwards" in the holder, i.e. closest to the shortcut plane. On the picture, the powder is Fe–Comm.

Toroid "capsules" in resin (Clear Resin V4 from Formlab) that fill the whole cavity of the E4991 thoroid sample holders: the small one for TD powders and the large ones for CP powders.

- For the small ones, the thickness of the capsule walls was minimised as to maximise powder content while still assuring solidity, as illustrated in Fig. 4.15.

- The entire large capsule volume being too large for any available powder sample, a resin fill-up is added. Since the lumped-element model requires the sample to sit as close as possible to the short-circuit plane to avoid parasitic transmission-line effects (cf. 4.6.1.1), we made capsules half-filled with resin for the large test fixture as illustrated in Fig. 4.15 (bottom). The characteristics of the designed capsules and the corresponding L_a are summarised in Table 4.12.

The filling factor v_f for small capsules is around 20-25 % while for the big capsules it tends to be 30-35 %. This is due to the practical difficulty of filling the smaller cup without breaking it when pressure is applied as the lid is pressed.

Item	h (mm)	d_i (mm)	d_o (mm)	Volume (mm^3)	L_a (pH)
Small Test Fixture	3.0	6.0	8.0	65.97	173
Small Cup (SC)	1.3	4.4	7.5	37.67	139
Large Test Fixture	8.5	5.0	20.0	2503.55	2357
Large Cup (BC)	3.4	5.2	19.0	891.78	881

Table 4.12 Dimensions and Material Volume of the cavities for powder within the small and large test fixtures: height, inner diameter, outer diameter, volume and equivalent inductance for air.

4.6.2.3 Correcting for the volume filling factor

When measuring nanoparticles, the ferrite material does not take the whole sample volume: space between particles is filled by air. Consider v_{mat} the volume fraction of the matrix and v_{NP} the volume fraction of the nanoparticles. The complex volume magnetic susceptibility of the measured sample (χ_{measure}) is determined by the volume-weighted linear mixing rule [235, 240, 242], where v represents the volume fraction of the components:

$$\chi_{\text{measure}} = v_{\text{mat}} \cdot \chi_{\text{mat}} + v_{\text{f}} \cdot \chi_{\text{NP}} \tag{4.16}$$

Note that the filling factor correction is not applied to permeability (obtained by impedance measurement) but to susceptibility (volumic property). Other mixing formulas exist (Maxwell-Garnett, Bruggeman,...) which are elaborated in [243] but these require additional measurements. In [244] Lichtenecker's equation is used to account for field deformation within the sample since the authors were interested in both magnetic permeability and electric permittivity. The filling factor is obtained based on mass density of bulk equivalents and assuming perfect stoichiometry: as discussed in Subsection 4.2.1 this is an approximation, however, it has been consistently applied throughout this work. We consider that the induced error due to simplified mixing rule and incorrect mass density values, while it could be of

several tens of percents, does not affect the main messages of this section which mainly relate to relative behaviour, i.e. the variation of properties with frequency.

4.6.2.4 Debye fitting of complex susceptibility

The frequency-dependent complex susceptibility is fitted to the polydisperse Debye relaxation model (Eq. 2.45), which integrates single-particle Debye responses over a lognormal distribution of particle diameters. Since the samples are dry powders, Brownian relaxation is suppressed and only Néel relaxation is considered. The real and imaginary parts of susceptibility (Eq. 2.47) are fitted simultaneously. The free parameters are the prefactor C, the median magnetic diameter $\tilde{D}_{\mathrm{mag}}$, the lognormal shape factor γ, and the effective anisotropy constant K_{eff}. A lower bound of 10 $\mathrm{kJ/m^3}$ is imposed on K_{eff}. The static susceptibility χ_0 is not a free parameter but is computed from the fitted distribution via Eq. 2.48.

4.6.3 Results: Complex Susceptibility of MNP powders

4.6.3.1 Mn–CP2, Fe–CP1 and Fe–Comm

Fig. 4.16 plots susceptibility data for Mn–CP3, Fe–CP1 and Fe–Comm powders obtained from permeability measured in the large test fixture.

The Fe–Comm samples do not show SPM behavior and serve as a control sample. As expected, their real susceptibility does not show a decaying trend at 1 MHz, which is expected for SPM based on the Debeye model (cf. Fig. 2.7). Around 300 MHz we suspect ferromagnetic resonance (FMR): increasing real and imaginary part are a "signature" when approaching FMR. At FMR, the real part of susceptibility drops below zero: all energy is dissipated[6]. Observing this increase in χ' is reassuring: it confirms that the decrease occuring for the SPM samples is not a measurement artefact but probably related to Néel relaxation.

This decreasing trend for real susceptibility of both Mn–CP3 and Fe–CP1 is observed, which corresponds to an increase in imaginary permeability, consistent with the Debye model. Based on the magnetic diameters obtained by Chantrell fitting (Table 4.5) and the size-dependent relaxation frequency (Fig. 2.5), Néel relaxation is expected between 1 and 10 GHz for these samples. Results of Debye fitting are shown in Fig. 4.17 and summarized in Table 4.13.

- The static susceptibilities χ_0 obtained for Fe–CP1 (11.3) and Mn–CP3 (33.9) do not match the initial susceptibilities χ_i measured from the virgin magnetisation curves in Subsection 4.3.2.3 (χ_i = 6.36 for Fe–CP1 and 14.8 for Mn–CP3, cf. Table 4.14). However, the ratio $\chi_0(\text{Mn–CP3})/\chi_0(\text{Fe–CP1}) \approx 3.0$ is

[6] FMR is governed by the Landau-Lifshitz-Gilbert Equation. Ferromagnets exhibit magnetic resonance at frequencies GHz-THz yielding a change of sign to negative value of real susceptibility and a sharp peak of imaginary susceptibility. [31]

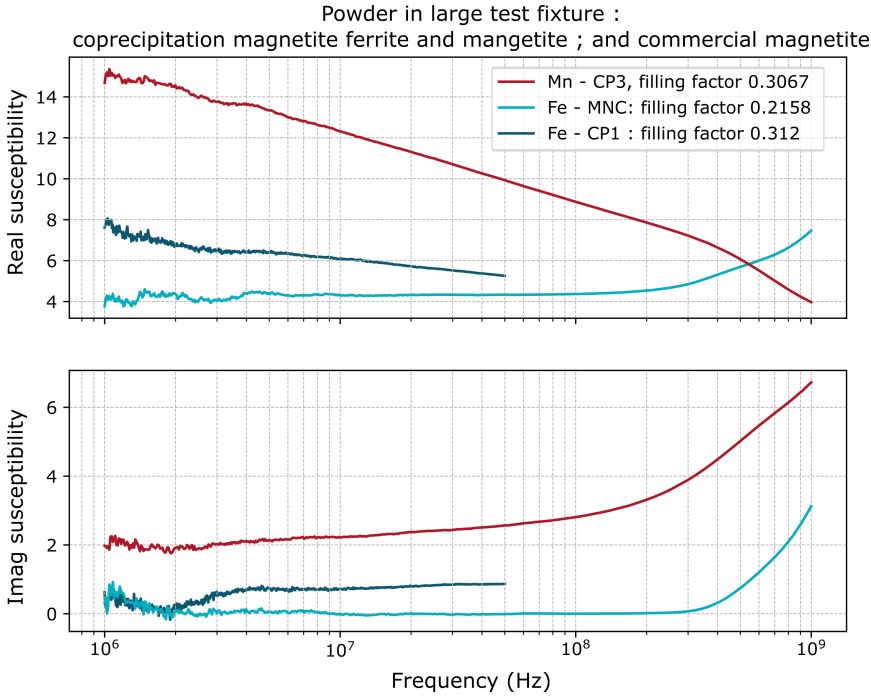


Fig. 4.16 Real and imaginary volume susceptibility of Fe–CP1, Mn–CP3 and Fe–Comm based on measurements on powder within the large test fixture.

consistent with $\chi_i(\text{Mn–CP3})/\chi_i(\text{Fe–CP1}) \approx 2.3$, confirming that Mn–CP3 susceptibility is at least twice as high as Fe–CP1 susceptibility.

- The fitted median magnetic diameters $\tilde{D}_{\text{mag}}$ are substantially smaller than those obtained by Chantrell fitting on the magnetisation curves (Table 4.5): 5.32 nm versus 7.95 nm for Fe–CP1 (a 33% reduction) and 6.30 nm versus 11.0 nm for Mn–CP3 (a 43% reduction). The fitted shape factors γ are conversely larger (0.45 and 0.44 versus 0.29 and 0.32, respectively), indicating broader fitted size distribution.

- The fitted effective anisotropies K_{eff} are both 10 kJ/m^3 which is the lower bound imposed during fitting. The anisotropy constant and fitted radius are partly "communicating vessels" since K_{eff} is multiplied V_{mag} to obtain E_a.

Different factors likely contribute to these differences in fitted values. First, the pressure on the powders in the E4991 sample is probably higher than in the gelatin capsules used for magnetisation curves and FC-ZFC measurements. Morup et al. [69] demonstrated that dipolar interactions affect magnetisation of the particles according to the interaction strenght. To validate whether this has significant impact, different toroids with varying applied pressure on the powder could be measured. The bottleneck for this is that it required much powder: it would be feasible for CP powders. Second, the Debye model extrapolates frequency-dependent data back to DC; any systematic bias in the fit, propagates into the extrapolated χ_0. Sources of bias are e.g. that v_f is obtained assuming volume density of the particles based on perfect stoichiometry of the nanoparticles. Third, the Debye model used to extract these parameters assumes monodisperse lognormal size distribution. The shape factors γ obtained on with TEM data, Langevin fitting and Debye fitting in this case all confirm that the measured powders are not. This probably implies a volume-weighted dominance of the larger particles of the sample in the obtained χ' (cf Subsection 4.5.1).

The difficulty of fitting K_{eff} from RF data alone is well documented: Goldfarb [240] reports that magnetocrystalline anisotropy ($K_{\text{eff}} \approx 0.9$ kJ/m^3 for 9.5 nm magnetite) yields Néel relaxation frequencies of ∼9 GHz, far above the measurement range, whereas effective anisotropy constants of 36–73 kJ/m^3 are needed to explain the observed MHz-range losses. This is consistent with our lower bound of 10 kJ/m^3 and suggests that surface and defect contributions dominate over bulk magnetocrystalline anisotropy for these particle sizes.

4.6.3.2 Fe–TDH4 and Fe–TDH4@Si

Fig. 4.18 shows obtained susceptibility for Fe–TDH4 and Fe–TDH4 @ Si (with a silica coating). We observe a higher real susceptibility for the silica-coated nanoparticles, consistent with the higher initial susceptibility and faster saturation

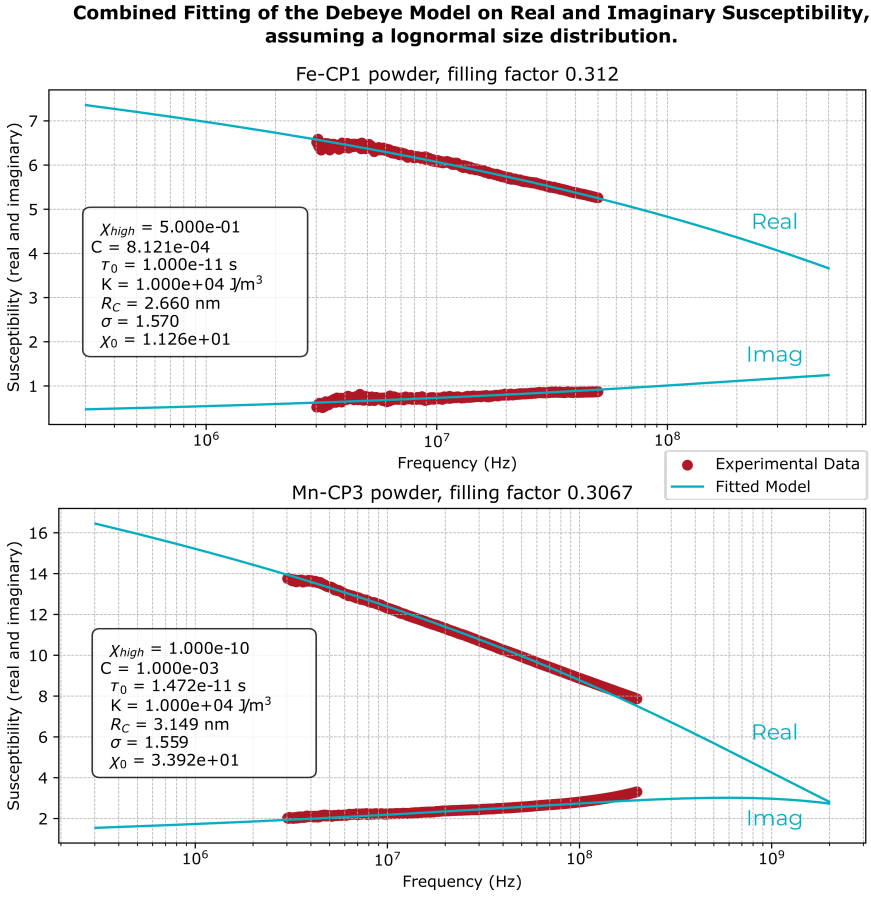


Fig. 4.17 Fitting of the Debye Equation on the real and imaginary susceptibility of Fe–CP1 and Mn–CP3 powder obtained by E4991 measurements. In this specific case σ is such that $\gamma = ln(\sigma)$. Extracted data are summarized in Table 4.13.

Material	τ_0 (s)	C (nm^{-6})	χ_{hf}	K_{eff} (kJ/m^3)	$\tilde{D}_{mag}$ (nm)	γ	χ_0
Fe–CP1 p.	1.000e-11 (b.)	8.121e-04	5.000e-01	10 (b.)	5.32	0.45	1.126e+01
Mn–CP3 p.	1.472e-11	1.000e-03	1.000e-10	10 (b.)	6.30	0.44	3.392e+01

Table 4.13 Extracted parameters from the Debye Model fitting for Fe-CP1 and Mn-CP3 powders (p.). Both fitted effective anisotropies K_{eff} hit the lower bound (b.).

observed for Fe–TDH4@Si in SQUID magnetometry on membranes (Fig. 4.5(B,C)). This suggests that the silica coating (involving ligand exchange) reduces surface spin disorder, thereby increasing the susceptibility at both quasi-static and radio frequencies. The obtained imaginary susceptibility is mostly negative which is a measurement error: it can be assumed very low. Note that this data is only measured between 1 and 50 MHz. Since this covers less than two decades, Debye fitting was not performed.

Compared with the Fe–CP1 data, the real part decreases more quickly until 2 MHz and stabilises afterwards. The rapid decrease between 1 and 2 MHz might be due to the difference in set-up, this has to be confirmed by measuring Fe–CP1 in the small capsules (the other way round is not possible since thermal decomposition yields are too small to fill the large capsules). The fact that the real part is stable beyond between 2 MHz and 50 MHz is reassuring: observations of both FC-ZFC and ACS data (Figs. 4.13 vs 4.12) indicate that blocking temperature is smaller compared to Fe–CP1, as a result, the Néel relaxation time constant would be smaller and thus occuring at higher frequency than Fe–CP1. To confirm this, new measurements up to 1 GHz are needed. For now, the only strong conclusion is that better magnetic properties due to silica coating, observed in magnetisation and FC-ZFC measurements, are consistent with E4991 measurements.

4.6.3.3 The influence of magnetisation

After the initial measurements made above, two parameters were tested: the addition of a bias current (1 mA) for the measurement, and the magnetisation of the sample. The capsules containing Fe–CP1, Mn–CP2 and Fe–TD4 were placed on a neodymium magnet and then measured again (with and without bias). Before every manipulation, the capsule was taken out and replaced in the sample holder, to validate that the observed difference was not induced by the mere fact of taking the sample out of the container (to magnetise it) and placing it back.

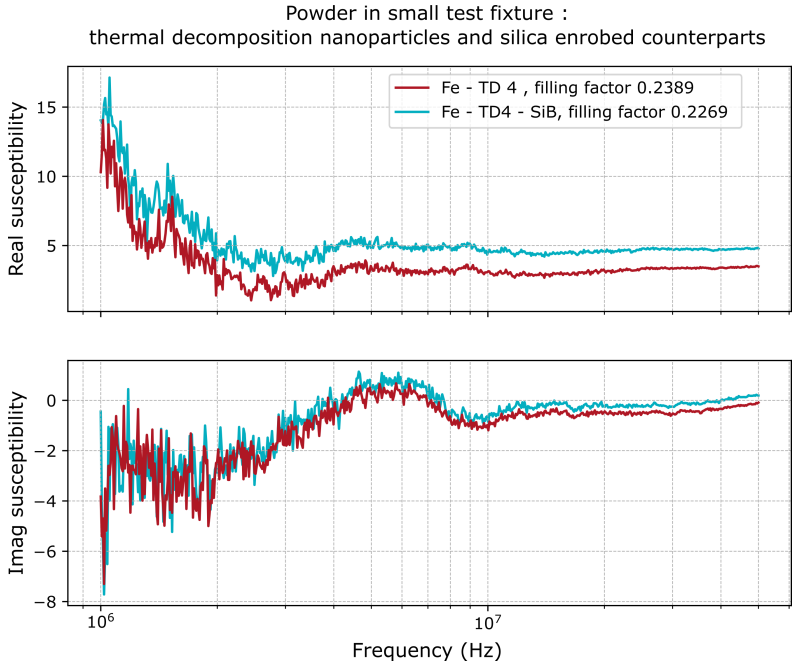


Fig. 4.18 Between every measurement, the capsule was taken out of the test fixture and put back in.

Fig. 4.19 summarises the obtained results. The presence or absence of a 1 mA bias does not affect the measurement significantly. This is unsurprising given that this changes the field by only a few mA/m, well within the linear range where $\xi \ll 1$ (cf. Section 2.2.2.2). For a 10 nm magnetite particle at 300 K, $\xi = 1$ corresponds to approximately $\mu_0 H \approx 16$ mT, so a bias of a few mA/m is negligible.

Magnetising the Fe–CP1 sample affects significantly both its real (+ 3.4% at 2 MHz) and imaginary (+ 12 %) susceptibility. For the Fe–TDH4 samples, the real part of susceptibility is clearly increased but the signal is too noisy for the imaginary part (below zero, which is not physically possible). This observation is consistent with the FC-ZFC results (Figs. 4.8, 4.9) indicating that powder samples do not display fully superparamagnetic behaviour at room temperature - probably due to dipolar interactions - thus some remanence exists and is affected by the strong magnetisation.

Two elements may contribute to the fact that Fe–CP1 is more influenced by magnetisation than Mn–CP2. First of all, the magnetocrystalline anisotropy of manganese is lower (Cf Table 4.3). The fitted effective anisotropy constants for Fe–CP1 powder (considering coexistence of two anisotropy constants) was also higher than for Mn–CP2 powder (although this is not Mn–CP3, it is close). Second, the ratio χ''/χ' is higher for Mn–CP2 than for Fe–CP1, which might explain why χ'' is more affected in the former. It is consistent with the ACS measurements between 1 Hz and 1kHz that the imaginary susceptibility of Mn–CP2 is larger (cf Fig. 4.14).

4.6.4 Discussion on relevance of E4991 measurements

Despite quantitative discrepancies in absolute values the relative ranking between samples is preserved across all three techniques. Mn ferrite consistently exhibits roughly two to three times the susceptibility of Fe-CP1, whether measured by quasi-DC magnetisation (Section 4.3), AC susceptometry up to 1 kHz (Section 4.5), or MHz-range impedance analysis. This convergence confirms the relevance of comparative conclusions even where absolute parameter extraction remains sensitive to model assumptions and filling factor corrections.

From the perspective of inductive biosensor design (Part II), the E4991 measurements confirm that the susceptibility contrast between ferrite compositions persists above 1 MHz. The manganese ferrite samples thus remain the more detectable label candidate not only at DC but also in the MHz regime relevant to sensor operation. The onset of Néel relaxation is observable below 1 GHz for CP-made powders.

In terms of LFA design, characterisation by E4991 impedance analyser offers a practical constraint: membrane-based samples did not produce a detectable signal,

limiting the technique to powders. The E4991 therefore cannot directly probe the LFA-relevant configuration. This reinforces the need for the custom inductive set-ups presented in Chapter 6, which offer the flexibility to measure nanoparticles in membranes and suspensions at intermediate frequencies.

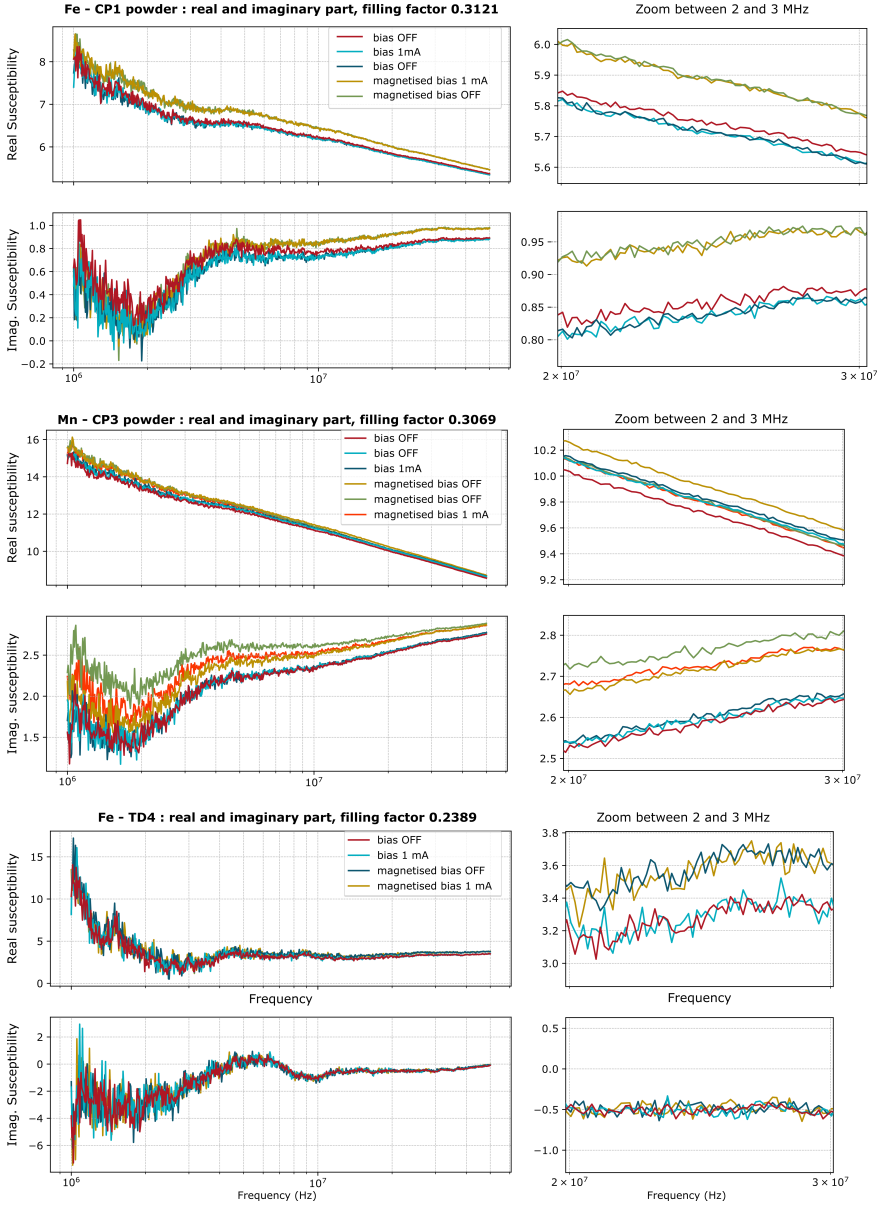


Fig. 4.19 Between every measurement, the capsule was taken out of the test fixture and put back in.

Section summary

Complex susceptibility of MNP powders was measured between 1 MHz and 1 GHz using the Keysight E4991B impedance analyser with toroidal sample holders. The frequency-dependent susceptibility of CP powders (Fe–CP1 and Mn–CP3) was fitted to the polydisperse Debye relaxation model considering Néel relaxation only. TD SPION (Fe–TDH4, Fe–TDH4@Si) were measured in smaller capsules over a reduced range (1–50 MHz). Nanoparticles dispersed in cellulose membranes were not characterised since the involved magnetic mass was too low.

Consolidated conclusions:

- Both Fe–CP1 and Mn–CP3 powders exhibit a decreasing χ' and an increasing χ'' with frequency, consistent with the onset of Néel relaxation as predicted by the Debye model. The onset of Néel relaxation is observable below 1 GHz for CP powders.
- The ratio $\chi_0(\text{Mn–CP3})/\chi_0(\text{Fe–CP1}) \approx 3.0$ obtained from Debye fitting is consistent with the ratio of initial susceptibilities from SQUID magnetometry ($\approx$ 2.3, cf. Table 4.14). Despite quantitative discrepancies in absolute values, the relative ranking between samples is preserved across all three techniques: quasi-DC magnetisation (Section 4.3), ACS up to 1 kHz (Section 4.5), and MHz-range impedance analysis. This convergence confirms the relevance of comparative conclusions even where absolute parameter extraction remains sensitive to model assumptions and filling factor corrections.
- The 1 mA bias current does not affect the measured susceptibility, consistent with the probing field (< 3 mOe) being well within the linear regime ($\xi \ll 1$).

Observed trends requiring further investigation:

- The Debye-fitted median magnetic diameters $\tilde{D}_{\text{mag}}$ are 33–43% smaller than the Chantrell-fitted values (Table 4.5), the fitted shape factors γ are larger, and the effective anisotropy K_{eff} reaches the imposed lower bound of 10 kJ/m^3 for both samples (Table 4.13). While the Debye model captures the correct qualitative trends, the absolute fitted parameters require further study. Multiple factors may contribute: stronger dipolar interactions in the toroidal capsules compared to gelatin capsules, the extrapolation of MHz data back to DC, and the volume-weighted dominance of larger particles in polydisperse samples.
- Magnetising Fe–CP1 and Mn–CP2 powder with a neodymium magnet increases its measured real susceptibilities. This is consistent with FC-ZFC results indicating that CP powders are not fully superparamagnetic at room temperature due to dipolar interactions (Section 4.4). The stronger effect on Fe–CP1 is consistent with its higher effective anisotropy compared to Mn–CP2. Fixing the nanoparticles with epoxy/agar should confirm that no physical rearrangement happened during the magnetisation.

- Fe–TDH4@Si exhibits higher real susceptibility than uncoated Fe–TDH4 between 1 and 50 MHz (Fig. 4.18), consistent with the improved initial susceptibility observed in SQUID magnetometry (Fig. 4.5) and suggesting that the silica coating reduces surface spin disorder at radio frequencies as well. However, the limited frequency range (less than two decades) and the noisy imaginary part preclude Debye fitting and limit the strength of this conclusion.

Perspectives:

- Extending small-capsule measurements to 1 GHz would allow observation of the Néel relaxation peak for TD SPION and enable Debye fitting, which was not possible on the current 1–50 MHz data.
- Preparing large capsules with varying compaction pressure would allow to quantify the influence of dipolar interactions on the extracted Debye parameters, as suggested by the discrepancy between Debye-fitted and Chantrell-fitted diameters.
- From the perspective of inductive biosensor design, the E4991 measurements confirm that the susceptibility contrast between ferrite compositions persists above 1 MHz, supporting the choice of Mn-SPNF as the more detectable label candidate not only at DC but also in the MHz regime relevant to sensor operation (Chapter 6).

4.7 Conclusions and Perspectives on Magnetic Nanoparticle Characterisation Methodology

This section synthesises the main findings from the magnetic characterisation of superparamagnetic nanoferrites. Conclusions are organised into scientific and engineering categories, with an explicit distinction between robust and tentative conclusions. A final section outlines relevant perspectives to consolidate relevant characterisation protocols for integration of nanoparticles in biosensors.

4.7.1 Summary of the workflow

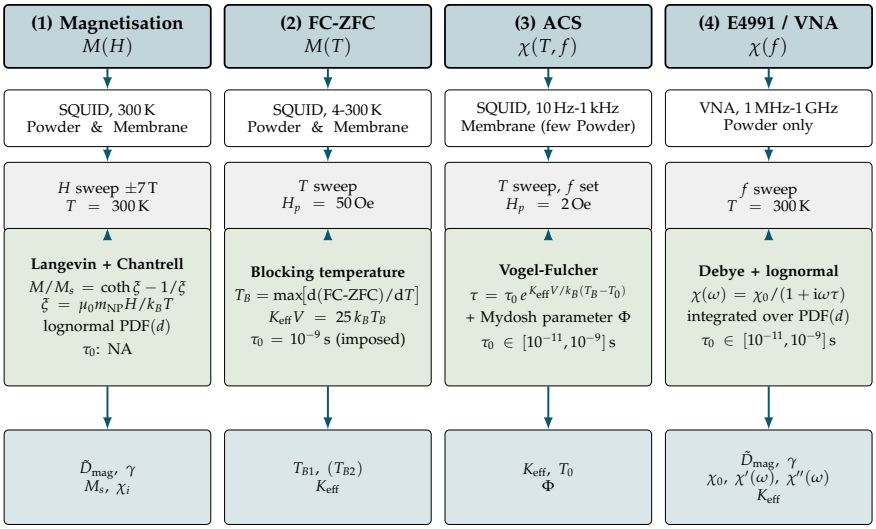


Fig. 4.20 Workflow of the four magnetic characterisation techniques presented in this chapter. Each lane reads top-down: technique header → instrument and sample configuration → measurement domain → applied model → extracted parameters. H_p refers to the probing field amplitude.

Fig. 4.20 summarises the four characterisation techniques applied in this chapter, reading top-down from measurement domain to extracted parameters. Their complementarity lies in the fact that each technique accesses the magnetic properties of SPNF through a different physical variable (field, temperature, frequency) and complementary models, resulting in partially overlapping but not identical parameter sets. The paragraphs below describe each measurement type and high-

light the role of the assumed particle diameter in extracting the effective anisotropy constant K_{eff}.

Method 1: Magnetisation curves $M(H)$ at 300 K: A full hysteresis loop is recorded under a field sweep up to $\pm 7\,\mathrm{T}$ at room temperature (Section 4.3). The Langevin–Chantrell model (Eq. 2.39 and Table 2.5) fits the equilibrium $M(H)$ curve assuming a lognormal distribution of non-interacting magnetic moments to yield the median magnetic diameter $\tilde{D}_{\mathrm{mag}}$ and shape factor γ, together with the saturation magnetisation M_s and initial susceptibility χ_i. This technique does not access K_{eff}: the equilibrium magnetisation depends on the competition between Zeeman and thermal energy, not on the energy barrier that governs dynamics.

Method 2: FC-ZFC curves $M(T)$: The blocking temperature T_B is extracted maximum of the derivative of $M_{\mathrm{FC}} - M_{\mathrm{ZFC}}$ (Section 4.4). The relation $K_{\mathrm{eff}} = 25\,k_B T_B / V_{\mathrm{mag}}$ (Eq. 2.32, with $\tau_0 = 10^{-9}\,\mathrm{s}$ and $\tau_{\mathrm{meas}} = 100\,\mathrm{s}$) then converts the measured temperature into an anisotropy constant. Critically, K_{eff} and V_{mag} appear only as the product $K_{\mathrm{eff}} V_{\mathrm{mag}}$: a single measurement of T_B constrains the product but not its factors individually. To extract K_{eff}, one must therefore impose a diameter, either from TEM or from the Chantrell fit. Because $K_{\mathrm{eff}} \propto 1/D^3$, a 20 % uncertainty on the chosen diameter propagates into a factor $\sim$1.7 on K_{eff}.

Method 3: ACS $\chi(T, f)$ between 5 Hz and 1 kHz: The frequency-dependent shift of the χ''(T) peak is fitted to the Vogel–Fulcher law $\tau = \tau_0 \exp\left[K_{\mathrm{eff}} V_{\mathrm{mag}} / k_B (T_B - T_0)\right]$ (Section 4.5). As in the FC-ZFC case, K_{eff} enters only through the direct proportionality $K_{\mathrm{eff}} V_{\mathrm{mag}}$, so the particle diameter must again be fixed externally before K_{eff} can be separated from the volume. The additional parameter T_0 accounts for inter-particle interactions but introduces a three-way correlation with K_{eff} and τ_0. The model-free Mydosh parameter Φ complements the Vogel–Fulcher fit by classifying the interaction regime without any assumption on diameter or pre-exponential factor.

Method 4: E4991 complex susceptibility $\chi(f)$ between 1 MHz and 1 GHz: The frequency-dependent complex susceptibility is fitted to the polydisperse Debye relaxation model (Eq. 2.45, Section 4.6). In contrast to the FC-ZFC and Vogel–Fulcher approaches, the Debye integral couples the diameter to the entire spectral response rather than to the energy barrier alone. The diameter D_{mag} enters the integrand through three distinct terms: (i) the Neel relaxation time $\tau_{\mathrm{eff}}(D_{\mathrm{mag}}) \propto \exp\left[K_{\mathrm{eff}} (\pi/6) D_{\mathrm{mag}}^3 / k_B T\right]$, which sets the frequency at which each sub-population relaxes; (ii) the weighting factor $(D_{\mathrm{mag}}/2)^6$, which reflects the m_{NP}^2 dependence of the equilibrium susceptibility per particle; and (iii) the lognormal probability density $p(D_{\mathrm{mag}}, \gamma)$, which determines the relative abundance of each diameter. Because these three size-dependent contributions shape different aspects of the spectral line, namely the peak frequency, the peak amplitude and the spectral breadth, the fit can, in principle, co-determine $\tilde{D}_{\mathrm{mag}}$, γ and K_{eff} simultaneously without

requiring an externally imposed diameter. In practice, however, the limited frequency window (fewer than three decades for the small capsules) and the correlation between K_{eff} and $\tilde{D}_{\text{mag}}$ restrict the reliability of the absolute fitted values, as discussed in Section 4.6.

Cross-technique perspective on K_{eff} extraction: The fundamental methodological difference is therefore that Methods 2 and 3 treat the particle volume as an external input and extract K_{eff} from the ratio E_a/V, whereas Method 4 treats both the size distribution and K_{eff} as fitting parameters constrained by the full spectral shape. The former approach is transparent and analytically simple, but any error on the assumed diameter maps directly onto K_{eff}. The latter approach avoids this imposed-diameter step, but at the cost of a larger parameter space and greater sensitivity to the frequency range covered. Table 4.15 consolidates the K_{eff} values obtained by all four routes and makes these trade-offs explicit.

Sample	Magnetometer	ACS		E4991			
	Measured initial χ_i	@ 1 Hz	@ 1 kHz	Deduced χ_0	@ 1 MHz	@ 50 MHz	@ 1 GHz
Fe–Comm p.	3.01	—	—	[a]	4.1	4.3	7.7
Fe–CP1 p.	6.36	—	—	11.3	8	5.3	—
Fe–CP1 m.	27.1	10.8	10.1	—	—	—	—
Fe–TDH4 p.	4.76	—	—	[b]	[b]	3.6	—
Fe–TDH4 m.	13.2	—	—	—	—	—	—
Mn–CP1 p.	5.35	—	—	—	—	—	—
Mn–CP2 m.	53.4	14.5	12.5	—	—	—	—
Mn–CP3 p.	14.8	—	—	33.9	15.3	9.62	4
Co–CP1 p.	21	—	—	—	—	—	—

[a] Debye model not applicable: no SPM behaviour.
[b] Signal too noisy for reliable fitting.

Table 4.14 Values for volume susceptibility either measured from the initial M(H) slope (χ_i) or obtained by Debye fitting of AC data (χ_0). Frequency-specific χ' values are also listed.

		Chantrell $M(H)$		**FC–ZFC**, high T_B		**ACS** χ'', high T_f			**E4991** Debye (powder)			
Sample	Conf.	$\tilde{D}_{\mathrm{mag}}$ (nm) fit.	γ fit.	T_B (K)	K_{eff} (kJ/m^3)	K_{eff} (kJ/m^3)	T_0 (K)	τ_0 (s)	$\tilde{D}_{\mathrm{mag}}$ (nm) fit.	γ fit.	K_{eff} (kJ/m^3)	τ_0 (s)
Fe–CP1	p.	7.95	0.29	blocked at 300 K		—			5.32	0.45	10 (b.)	1.0×10^{-11}
	m.	9.0–9.5	0.42–0.45	150	111.7	high-T peak > 300 K			—	—	—	—
Fe–TDH1	p.	7.3	0.39	SPM at 300 K ($T_{\mathrm{irr}} \approx 220$ K)		—			—	—	—	—
Fe–TDH4	p.	—	—	—		—			1–50 MHz only, no Debye fit			
	m.	8.06	0.48	100	84.7	$R^2 = 0.30$, unreliable			—	—	—	—
Fe–TDH4@Si	p.	7.32	0.29	—		—			—	—	—	—
	m.	8.39	0.38	92	77.9	39⋆	110	10^{-11}	—	—	—	—
Mn–CP2	p.	8.95	0.01	blocked at 300 K		68⋆	42	10^{-11}	—	—	—	—
	m.	12.4–13.0	0.48–0.68	66	44.2	43	152	3.4×10^{-11}	—	—	—	—
Mn–CP3	p.	11.0	0.32	—		—			6.30	0.44	10 (b.)	1.5×10^{-11}

Table 4.15 Consolidated overview of parameters fitted or extracted in Chapter 4. In the "Conf." column, "p." stands for powder and "m." for cellulose membrane. For each method, "fit." flags a fitted parameter and diameters otherwise listed are inputs to the K_{eff} extraction. For FC-ZFC and ACS, only the high-temperature ("second") peak is reported; the 15–20 K peak specific to iron oxide is discussed in Subsection 4.4.4.2. For readability of the table, FC-ZFC K_{eff} values are given based on $\tilde{D}_{\mathrm{TEM}}$ only. All ACS fits assume $\tilde{D}_{\mathrm{mag}} = 10$ nm as input; entries marked ⋆ have τ_0 pinned on a fitting bound and should be interpreted as relative only (Subsection 4.5.5). "(b.)" indicates a Debye fit pinned on the imposed lower bound $K_{\mathrm{eff}} = 10$ kJ/m^3. Non-SPM samples (Fe–Comm, Mn–CP1, Co–CP1) carry only an initial susceptibility and are reported in Table 4.14.

		FC–ZFC, low T_B		**ACS** χ'', low T_f''			
Sample	Conf.	T_B (K)	K_{eff} (kJ/m^3)	$\bar{T}_f''$ (K)	K_{eff} (kJ/m^3)	T_0 (K)	Φ
Fe–CP1	m.	≈ 18	13.4	43	17*	≈ 0	0.21
Fe–TDH4	m.	≈ 18	15.2	obs.†	—	—	—
Fe–TDH4@Si	m.	$\approx 18^\ddagger$	—	obs.†	—	—	—

Table 4.16 Cross-technique synthesis of the 15–20 K peak in iron oxide samples. All iron oxide samples in this work (powder and membrane) show the peak, but only the membrane samples listed here yielded quantitative extraction. FC-ZFC T_B is read from the bump in $\mathrm{d}(M_{FC} - M_{ZFC})/\mathrm{d}T$ at 50 Oe; ACS $\bar{T}_f''$ is the mean peak temperature of $\chi''(\mathrm{T})$ across the measured frequencies. K_{eff} is computed against $\tilde{D}_{\text{TEM}}$ rather than $\tilde{D}_{\text{mag}}$, consistent with the working hypothesis of a reduced magnetic core (Subsection 4.4.4.2). * τ_0 pinned on the upper bound 10^{-9} s (Subsection 4.5.5). † peak observed in $\chi''(\mathrm{T})$ but temperature step too coarse for reliable Vogel–Fulcher fitting (Section 4.5). ‡ attenuated relative to uncoated Fe–TDH4 (Fig. 4.10). No similar peak is observed in any Mn-SPNF sample, in either FC-ZFC or ACS.

4.7.2 Conclusion regarding nanoparticle properties

Mn-SPNF have higher susceptibility than SPION across all frequency domains: Table 4.14 quantifies the Mn versus Fe ranking across the three techniques:

- CP powders, SQUID: $\chi_i(\text{Mn–CP3})/\chi_i(\text{Fe–CP1}) = 2.3$.
- Membrane dispersions, SQUID: $\chi_i(\text{Mn–CP2})/\chi_i(\text{Fe–CP1}) = 2.0$.
- Debye-fitted χ_0 on CP powders: $33.9/11.3 = 3.0$.
- Membrane dispersions, ACS χ'(Mn–CP2)/χ'(Fe)–CP1) is 1.34 at 1 Hz and 1.24 at 1 kHz.
- E4991 at 1 MHz χ'(Mn–CP3)/χ'(Fe)–CP1) = 1.9.

Across all configurations, the conclusion supports Mn-SPNF as the preferred label candidate for inductive LFA detection. The underlying reason is the lower bulk K_{m} of manganese ferrite (Table 4.3), which translates into the lower K_{eff} extracted in membrane (Table 4.15). Mn–CP samples also show limited $\sigma_{M,s}$ variation across Fe/Mn ratios and sizes, consistent with their higher oxidation stability.

CP yields quasi-ideal SPM; TD probably carries a thicker dead layer: Fe–CP1 powder satisfies the Chantrell model with SSE = 0.037, compared with 0.20–0.33 for TD powders (Table 4.5), i.e. 6 to 10 times larger. All TD samples show a residual

paramagnetic slope up to 7 T and $\sigma_{M,s}$ at 55–65 % of bulk, against about 80 % for Fe–CP1. These observations are consistent with the framework of Baaziz et al. [83] and Unni et al. [81]: in the 8–12 nm window, the reducing conditions inherent to TD synthesis promote cation disorder, volume spin canting and a thicker magnetically dead layer.
However, a higher effective anisotropy is observed for CP SPION. From Table 4.15, Fe–CP1 in membrane reaches $T_B = 150$ K against 100 K for Fe–TDH4 and 92 K for Fe–TDH4@Si in membrane. In ACS, Fe–CP1 in membrane shows no χ'(T) peak below 300 K, while Fe–TDH4(@Si) unblock in the same range. The literature benchmark (Table 4.7) confirms the higher T_B of CP compared to TD. This is mostly attributed to the higher size distribution inherent to the CP synthesis technique.

Silica coating improves magnetic properties of Fe–TDH4 across techniques: Four independent observations point toward improved SPM behaviour after silica coating of Fe–TDH4 by reverse micro-emulsion (Section 3.4):

1. The Chantrell SSE decreases from 0.268 (Fe–TDH4) to 0.041 (Fe–TDH4@Si) in membrane (Table 4.6), and the ACS Vogel–Fulcher R^2 improves from 0.30 to 0.99, both indicating behaviour closer to the ideal SPM model.
2. The initial susceptibility χ_i per iron mass is higher for Fe–TDH4@Si, in both membrane (Fig. 4.5) and E4991 powder measurements (Fig. 4.18).
3. The effective anisotropy is lower: $T_B = 92$ K and $K_{\text{eff}} = 77.9$ kJ/m^3 for Fe–TDH4@Si against 100 K and 84.7 kJ/m^3 for uncoated Fe–TDH4 (Table 4.15).
4. The 15–20 K FC-ZFC peak attributed to oxidised surface shells is attenuated in coated samples (Fig. 4.10).

The Mydosh parameter Φ is unchanged between coated and uncoated membrane samples (Table 4.15). Since ICP reports 1.41 % Si mass on the coated Fe–TDH4@Si powder (Table 3.8), which corresponds to $\approx$ 3 % SiO_2 under the pure-maghemite/pure-silica assumption, the coating is probably too thin to affect inter-particle distances significantly. The improvement is therefore intra-particle rather than a spacing effect. The most parsimonious interpretation is that the coating procedure, or the ligand exchange that precedes it, reduces surface spin disorder and shrinks the magnetically dead layer. It cannot be determined from the present data whether the improvement originates from the silica shell itself or from the ligand exchange step; repeating the ligand exchange without silica deposition would isolate the two effects. This observation is based on a single coated batch and requires confirmation on additional batches.

The 15–20 K peak is iron-oxide-specific and non-interacting: All iron oxide samples measured in this chapter show a secondary peak near 18 K in FC-ZFC and a corresponding χ''(T) peak centered around 43 K in ACS, summarised in Table 4.16. The peak is absent from every Mn-SPNF sample, in both techniques. For

Fe–CP1 in membrane, the only sample with ACS resolution sufficient to fit the peak, Vogel–Fulcher yields $T_0 \approx 0$ and the Mydosh parameter yields $\Phi = 0.21$, both signatures of non-interacting SPM behaviour. This excludes the hypothesis of a phase change and supports the interpretation of two coexisting relaxation dynamics within SPION. The most parsimonious interpretation is a subpopulation of nanoparticles with a reduced magnetic core generated by surface oxidation: the reduced core accounts for the low apparent T_B, interparticle interactions are reduced because of lower magnetic moment and spacing between cores due to the disordered (less/non-magnetic layer). In FC-ZFC measurements, the attenuation of this 18K peak in Fe–TDH4@Si might confirm this since the silica shell limits oxidation. This attribution to oxidation deserves further study. However, this work observes undoubtedly that the peak corresponds to near-ideal SPM behavior and that is specific to iron-oxide (both CP and TD syntheses). To the best of our knowledge, literature reports this double-peak structure in ACS studies but without consistent interpretation [51, 222, 223].

4.7.3 Conclusion regarding membrane versus powder configuration

Membrane dispersion increases χ_i by a factor 3 to 4: This can directly be concluded from initial magnetisation measurements comparing identical nanoparticle batches in both membrane and powder form (Section 4.3). This is associated with decreased dipolar interactions compared to powder form, reducing K_{eff} (Subsection 2.3.6.2). The lower blocking temperature observed in FC-ZFC measurements confirms this interpretation: for example, Mn–CP2 powders appear blocked at 300 K in FC-ZFC, while the same batch dispersed in membrane yields well-defined blocking temperatures of 57–77 K. The fitted magnetic diameters from the Chantrell model are systematically larger in membranes compared to powder: $\tilde{D}_{\text{mag}}(\text{membrane})/\tilde{D}_{\text{mag}}(\text{powder})$ ranges from 1.13 to 1.19 for Fe–CP1, from 1.15 for Fe–TDH4@Si, and from 1.38 to 1.45 for Mn–CP2 (Table 4.6). Since the Chantrell model does not incorporate K_{eff}, the reduced effective energy barrier in membranes is absorbed entirely into an apparent increase of the fitted magnetic diameter.
The nanoparticle configuration on an LFA test line is closer to the membrane regime than to a compacted powder. This is a very clear example of how magnetic properties are affected by their configuration and should be studied accordingly when designing inductive sensors for LFA readouts.

Broadened fitted γ by Chantrell fitting in membrane probably reflects agglomerate distribution: The intrinsic TEM size distributions do not change between powder or membrane configuration. The systematic broadening of γ in membrane therefore probably comes from the distribution of cluster sizes, which creates a distribution of dipolar influences (and thus, K_{eff}). We put forward the hypothesis that capillary flow and drying within the NC produce a distribution of agglomerate sizes. A single hypothesis is corroborated by two additional observations:

- the broadened Chantrell γ in membrane (Table 4.15),
- the gap $\Delta T = T_{\text{irr}} - T_B$ exceeding 100 K in membrane FC-ZFC measurements (Section 4.4),
- the broader χ''(T) peak of Mn–CP2 in membrane compared with powder (Fig. 4.11),

Powder is therefore considered as the strongly-interacting limit and membrane as a weakly, heterogeneously interacting regime.

Limits in comparing membranes versus powder: Two limits of this chapter should be underlined. First, the Mn–CP2 χ''(T) peak is located at 178 K in powder and 241 K in membrane (Table 4.15), which inverts the FC-ZFC ordering on the same sample. The iron masses differ by three orders of magnitude and the sample holders are not identical, so the origin of this inversion cannot be pinned down from the current data. Second, the E4991 signal from membranes remained below the noise floor. The MHz characterisation of the LFA-relevant configuration is therefore not accessible with the conventional impedance set-up. This motivates the custom inductive geometries presented in Chapter 6.

4.7.4 Conclusion regarding applied models and frameworks

Langevin–Chantrell: equilibrium model, blind to anisotropy: The Langevin–Chantrell fit yields $\tilde{D}_{\text{mag}}$ and γ from the $M(H)$ curve but does not access K_{eff}. This is a physical property, not a fitting artefact: the equilibrium magnetisation depends on the competition between Zeeman and thermal energy, not on the energy barrier $K_{\text{eff}}V_{\text{mag}}$, which governs dynamics. Therefore, powder samples compress the fitted $\tilde{D}_{\text{mag}}$ through dipolar interactions (Table 4.15). However, the SSE of this model fitting serves as a diagnostic for how closely a sample approaches ideal SPM behaviour. For instance, Fe–CP1 powder yields SSE = 0.037 while Fe–TDH1 powder yields SSE = 0.20, a factor of five difference (Table 4.5). The higher SSE for TD samples reflects the deviation introduced by the thicker dead layer and volume spin canting identified in Subsection 4.3.2.1, which the ideal Langevin model does not account for.

$K_{\text{eff}} = 25\,k_B T_B / V_{\text{mag}}$**: valid for relative comparison:** This stems directly from the Néel-Arrhenius law. The factor 25 assumes $\tau_{\text{meas}} \approx 100$ s and $\tau_0 \approx 10^{-9}$ s. This formula is widely used for FC-ZFC but its assumption on measurement time makes it inapproprate for ACS measurements. Since $K_{\text{eff}} \propto 1/V \propto 1/D^3$, the choice between $\tilde{D}_{\text{TEM}}$ and $\tilde{D}_{\text{mag}}$ alone introduces a factor of 1.7 spread for a 20 % diameter difference. Table 4.15 reports both conventions in parallel. This is an important limitation:

- Using $\tilde{D}_{\text{TEM}}$ overestimates the magnetic volume (since it does not distinguish dead layer) which underestimates K_{eff}

- Using D_{mag} obtained by Chantrell fitting probably overestimates K_{eff} since Chantrell fitting virtually decreases the fitted magnetic diameter to compensate for anisotropy effects.

However, analysing the relative increase/decrease of anisotropy in identical configurations with different nanoparticles, or in different configurations with identical nanoparticles, can be done by relatively comparing T_B (and corresponding K_{eff}) values.

Polydisperse Debye model: reliable ranking, unreliable absolute values: The E4991 data reproduces the expected decrease of χ' and increase of χ'' with frequency due to Néel relaxation and therefore allows for Debye fitting. The cross-composition ratio $\chi_0(\mathrm{Mn–CP3})/\chi_0(\mathrm{Fe–CP1}) \approx 3.0$ is consistent with the corresponding χ_i ratio from SQUID magnetometry (≈ 2.3). However, the fitted $\tilde{D}_{\mathrm{mag}}$ is 33–43 % smaller than from Chantrell (5.32 versus 7.95 nm for Fe–CP1; 6.30 versus 11.0 nm for Mn–CP3), the fitted γ is larger, and K_{eff} systematically hits the 10 kJ/m^3 lower bound for both CP powders (Table 4.15). The absolute Debye parameters should therefore be read as relative only. Plausible contributions to the discrepancy are the stronger compaction of the toroid capsules, the limited frequency window that truncates the relaxation peak, and the volume-weighted dominance of the largest particles in χ' (cf. Subsection 4.5.1).

Vogel–Fulcher model: The three parameters τ_0, K_{eff} and T_0 are strongly correlated. The sensitivity study of Subsection 4.5.5 shows that relaxing the lower bound on τ_0 from 10^{-11} s to 10^{-13} s increases the fitted K_{eff} by about 50 % and decreases T_0 by 10 to 30 K, while R^2 remains essentially unchanged (Table 4.11). The parameter T_0 absorbs the dynamic contribution of inter-particle interactions into an effective temperature offset; its absolute value depends on the imposed τ_0 bounds and should therefore be interpreted as a relative measure of interaction strength across samples measured under identical conditions, as recommended by Dormann et al. [75]. An observation worth noting is that the Vogel–Fulcher fit quality correlates with the Chantrell SSE: the two samples with the lowest Chantrell SSE, Mn–CP2 membrane (SSE = 0.025–0.031) and Fe–TDH4@Si membrane (SSE = 0.041), also yield the best Vogel–Fulcher R^2 values ($R^2 = 0.96$ and 0.99 respectively), while Fe–TDH4 membrane (SSE = 0.268) produces $R^2 = 0.30$ (Table 4.15). Despite the Chantrell model being an equilibrium description and Vogel–Fulcher a dynamic one, both converge in identifying the same samples as closest to ideal SPM behaviour.

Mydosh parameter for distinguishing interaction regimes: The Mydosh parameter Φ requires neither a fit nor an assumption on τ_0. The exact boundaries between non-interacting SPM, interacting SPM and SSG regimes are not universally agreed upon, as illustrated by the range of threshold values reported by different groups (Table 4.9). Nevertheless, the Mydosh parameter provides a useful

complement to the Vogel–Fulcher analysis: in this work, Φ confirmed the interacting SPM regime for all membrane samples where the Vogel–Fulcher fit converged with a non-zero T_0, providing model-independent corroboration of the interaction strength inferred from the fit.

DBF framework: the K_{eff} umbrella: The Dormann–Bessais–Fiorani (DBF) approach folds inter-particle interactions, surface anisotropy and dead-layer effects into a single contribution to K_{eff} (Subsection 2.3.6). This is a deliberate simplification: the physical origins of the energy barrier are not separated, and K_{eff} is therefore not a material constant but a configuration-dependent effective parameter. The framework is retained here for a specific reason: it delivers one scalar that is comparable across techniques (SQUID magnetometry, FC-ZFC, ACS, E4991) and across configurations (powder, membrane). Although K_{eff} does not resolve the individual contributions, tracking its variation across samples and configurations allows one to translate non-ideal SPM behavior into a quantity that can inform sensor design.

Serantes scaling: K_{eff} scales with K_{m}: Serantes et al. [220] propose that the dipolar contribution scale with the intrinsic material anisotropy rather than adding a fixed offset. In membranes, the FC-ZFC-derived ratio $K_{\text{eff}}(\text{Fe–CP1})/K_{\text{eff}}(\text{Mn–CP2})$ is 2.5 (Table 4.15). For TD iron oxide in membrane, the ratio is 1.9 for Fe–TDH4 and 1.8 for Fe–TDH4@Si. The bulk reference is itself a bracket rather than a single number: $K_{\text{m}}(\text{Fe}_3\text{O}_4)/K_{\text{m}}(\text{MnFe}_2\text{O}_4) = 3.6$ and $K_{\text{m}}(\gamma\text{-Fe}_2\text{O}_3)/K_{\text{m}}(\text{MnFe}_2\text{O}_4) = 1.5$ (Table 4.3). All three membrane ratios fall within this bulk interval. The actual magnetite/maghemite fraction of the SPION cores is not known in this work, so any point within the 1.5–3.6 interval is a plausible reference. No ACS-derived ratio could be computed because the Fe–CP1 membrane χ''(T) high-temperature peak exceeds 300 K (Table 4.15).

4.7.5 Key contributions of this chapter

1. **Paired powder/membrane characterisation of identical SPNF batches across four techniques** (SQUID magnetometry, FC-ZFC, ACS and E4991 impedance analysis). To the best of our knowledge this direct comparison has not been reported before. The membrane is the configuration directly relevant to inductive LFA readout.
2. **Quantitative demonstration that χ_i is 3 to 4 times higher in cellulose dispersion than in compacted powder**, for both SPION and Mn-SPNF (Table 4.14). This factor updates the susceptibility budget used when designing inductive sensors for LFA test lines, and comes with a mechanistic interpretation in terms of agglomerate-size distribution.
3. **Indicative support for K_{m}-scaled interaction anisotropy** by comparing SPION with Mn-SPNF. The cross-composition $K_{\text{eff}}(\text{Fe})/K_{\text{eff}}(\text{Mn})$ ratios fall in the same order of magnitude as the bulk K_{m} ratio, consistent with

the scaling framework of Serantes et al. [220] rather than with an additive interaction offset. This observation should be treated as indicative rather than conclusive: the comparison involves only two compositions, the magnetite/maghemite fraction of the iron oxide cores is not known, and the Mn-depleted surface of the manganese ferrite samples (Subsection 3.3.2.2) introduces uncertainty on the effective K_{m}. Verification on additional compositions (e.g. Co ferrite, Ni ferrite) and at controlled packing fractions would be required to confirm the generality of the scaling.

4. **Cross-technique identification and interpretation of the 15–20 K peak specific to iron oxide** SPNF (Table 4.16). The peak is observed in both FC-ZFC and ACS on the same batches, is absent for Mn ferrite, and is attenuated by silica coating. For Fe–CP1 in membrane, the low-temperature χ'' peak yields $T_0 \approx 0$ and $\Phi = 0.21$, both signatures of non-interacting SPM behaviour. This supports its interpretation as a non-interacting subpopulation of reduced magnetic cores generated by surface oxidation.
5. **Filling-factor-aware volume susceptibility comparison across close to nine decades in frequency** (Table 4.14). The Mn-SPNF advantage over SPION is preserved from DC through 1 GHz, supporting Mn ferrite as the preferred label for inductive LFA detection in Part II.
6. **Observation that silica coating protocol by reversed micro-emulsion improves χ_i of TD SPION across four techniques**. This single-batch observation needs to be confirmed with several duplicates but is directly relevant for biocompatible LFA label design.

Chapter Summary

In a LFA, nanoparticles captured on a nitrocellulose test line are dispersed in a porous membrane, a configuration that differs substantially from the compacted powder or dilute suspension in which magnetic nanoparticles are conventionally characterised. This chapter investigates to what extent the magnetic properties of SPNFs depend on that configuration, by applying four complementary characterisation techniques to identical nanoparticle batches in both powder form and dispersed in cellulose membranes. The nanoparticle library assembled in Chapter 3 is used throughout: iron oxide SPIONs from TD and CP synthesis, manganese ferrite SPNFs from CP, and silica-coated TD SPIONs.

Magnetisation curves at 300 K. Room-temperature magnetisation curves were recorded by SQUID magnetometry up to 7 T. A lognormal Langevin model (Chantrell equation) was fitted to extract the median magnetic diameter $\tilde{D}_{\mathrm{mag}}$, the lognormal shape factor γ and the initial susceptibility χ_i. TD SPIONs show a residual paramagnetic-like slope up to 7 T and a specific saturation magnetisation at 55–65 % of the bulk value, with Chantrell fit residuals six to ten times larger than for CP counterparts of comparable size. This is consistent with the literature attributing a thicker magnetically dead layer and volume spin canting to the reducing conditions of TD synthesis for particles below 12 nm. Mn–CP3 powder shows a higher χ_i than Fe–CP1 powder, which we attribute to the lower magnetocrystalline anisotropy K_{m} of manganese ferrite. When the same nanoparticle batches are dispersed in cellulose membranes, the measured χ_i is three to four times higher than in powder, for both compositions. The fitted $\tilde{D}_{\mathrm{mag}}$ is systematically larger in membranes while γ is broader. We hypothesise that the broadened γ reflects a distribution of agglomerate sizes formed during capillary flow and drying within the cellulose, rather than a change in the intrinsic size distribution.

FC-ZFC curves. FC-ZFC measurements record the magnetisation as a function of temperature (1.8–300 K) under a small probing field (50 Oe), after cooling without and with that field respectively. The temperature at which the two curves diverge reveals the blocking temperature T_B, the transition between blocked and superparamagnetic states. In cellulose membranes, Mn–CP2 yields T_B of 57–77 K, while SPIONs block at 80–100 K (TD) and 150–160 K (CP). The corresponding effective anisotropy K_{eff}, obtained via the Néel–Arrhenius relation, is approximately one order of magnitude above the bulk K_{m} for all compositions. However, the cross-composition ratio $K_{\mathrm{eff}}(\mathrm{Fe})/K_{\mathrm{eff}}(\mathrm{Mn})$ of 2.1–2.7 remains within the range of the corresponding bulk ratio (1.5–3.6), which is consistent with the hypothesis that interaction-induced anisotropy scales with intrinsic material anisotropy rather than adding a fixed offset. This observation is based on two compositions and should be verified on a wider set of materials. In contrast,

Fe–CP1 and Mn–CP2 powders appear blocked at 300 K, which we attribute to stronger dipolar interactions in the compacted configuration. The gap between the irreversibility temperature T_{irr} and T_B exceeds 100 K for all membrane samples, which we attribute to the hypothesised agglomerate size distribution rather than to intrinsic size polydispersity, since TEM and Chantrell fitting on powder indicate narrow distributions. A secondary peak at 15–20 K is consistently present in all iron oxide samples but absent from every manganese ferrite sample. We hypothesise that this peak originates from a subpopulation of strongly oxidised SPIONs with a reduced effective magnetic core (4–5 nm), but this attribution requires structural confirmation. The peak is attenuated in silica-coated samples, which would be consistent with oxidation protection by the silica shell, though only one coated batch was measured.

AC susceptibility between 5 Hz and 1 kHz. ACS measurements record the in-phase (χ') and out-of-phase (χ'') components of susceptibility as a function of temperature at multiple frequencies. When the measurement frequency matches the Néel relaxation rate, the χ''(T) curve shows a peak whose frequency dependence allows to classify the interaction regime. The Mydosh parameter Φ, a model-free indicator of the relative shift of the peak temperature per frequency decade, places all membrane samples in the interacting superparamagnetic regime, indicating that the superparamagnetic nature is preserved despite clustering in the membrane. The double-peak structure observed for all iron oxide samples, and absent for manganese ferrite, independently corroborates the FC-ZFC observation. For Fe–CP1 in membrane, the low-temperature χ'' peak yields Vogel–Fulcher parameters consistent with non-interacting behaviour ($T_0 \approx 0$, $\Phi = 0.21$), supporting the hypothesis of a weakly interacting oxidised subpopulation. A sensitivity study reveals that the Vogel–Fulcher parameters (τ_0, K_{eff}, T_0) are strongly correlated: relaxing the τ_0 bound shifts the fitted K_{eff} by about 50 % with no change in fit quality. The Vogel–Fulcher law should therefore be used primarily as a relative measure of interaction strength across samples measured under identical conditions.

MHz–GHz complex susceptibility. Powder samples were measured between 1 MHz and 1 GHz using the Keysight E4991B impedance analyser with toroidal sample holders. In this geometry, the azimuthal magnetic field of a coaxial transmission line probes a toroidal powder sample without requiring demagnetising-factor corrections. Both Fe–CP1 and Mn–CP3 exhibit a decreasing χ' and increasing χ'' with frequency, consistent with the onset of Néel relaxation as predicted by the Debye model. Fitting yields a ratio $\chi_0(\text{Mn–CP3})/\chi_0(\text{Fe–CP1}) \approx 3.0$, consistent with the ratio of 2.3 obtained from quasi-static SQUID measurements, indicating that the susceptibility ranking between compositions is preserved in the MHz range. The absolute fitted parameters (median diameters 33–43 % smaller than Chantrell values, K_{eff} reaching

the imposed lower bound) should be interpreted with caution, as several factors may contribute to the discrepancy (stronger compaction in toroid capsules, limited frequency window, volume-weighted bias). Nanoparticles dispersed in membranes did not produce a signal above the noise floor in this set-up, which limits the technique to powder samples and motivates the custom inductive geometries presented in Chapter 6.

Implications for LFA integration. Three observations from this chapter are relevant for the design of inductive LFA readouts. First, the initial susceptibility measured for membrane-dispersed nanoparticles is three to four times higher than for the same batches in compacted powder. If sensor design were based on powder characterisation data alone, the susceptibility budget would be underestimated accordingly. The broadened Chantrell-fitted γ and the large $\Delta T = T_{\mathrm{irr}} - T_B$ gap in membrane FC-ZFC measurements suggest that a distribution of agglomerate sizes forms during capillary flow and drying, a process that also occurs in an LFA. To the best of our knowledge, a paired powder/membrane characterisation of identical SPNF batches across four techniques has not been reported before, and this comparison allowed to isolate the effect of the membrane substrate on the measured magnetic properties. Second, manganese ferrite SPNFs show higher susceptibility than iron oxide SPIONs across all techniques and configurations, from DC through 1 GHz. We attribute this to the lower bulk K_{m} of manganese ferrite. This ranking is observed consistently but is based on a limited number of samples per composition. Third, the observation that silica coating appears to improve the magnetic properties of TD SPIONs, with higher χ_i, lower K_{eff} and improved fit quality across techniques, suggests a possible route towards biocompatible labels with a reduced dead-layer penalty. However, this observation is based on a single coated batch and it remains unclear whether the improvement originates from the silica shell itself or from the ligand exchange step that precedes it. Confirmation on additional batches is needed before drawing a definitive conclusion.

PART II
Detection of Magnetic Nanoparticles : Towards Inductive Sensing on LFA's

5

Sensing Magnetic Nanoparticles : State of the Art

This chapter reviews the state of the art in magnetic sensing of nanoparticles, to motivate and contextualise the inductive readout developed in Chapter 6.

Section 5.1 distinguishes flux sensors from field sensors and reviews how each principle has been applied to MNP detection. Section 5.2 focuses on inductive sensing: the equivalent RLC model of a coil, the phenomena that modify its impedance in presence of MNPs, and the main readout architectures. The simplicity–sensitivity trade-off across these architectures motivates the choice retained in Chapter 6.

Section 5.3 benchmarks reported detection metrics across inductive and non-inductive approaches. Section 5.4 narrows the scope to magnetic sensing on lateral flow assays, with a comparison to the colloidal-gold optical readout that remains the commercial default. Section 5.5 reviews the ventures that have attempted to commercialise MNP detection, identifying the barriers beyond sensing physics that shape current deployment.

5.1 Magnetic Sensing

5.1.1 General Overview of Magnetic sensor principles

For magnetic sensors, a distinction should be made between magnetic flux and magnetic field sensors. This section is greatly inspired by [205]. Recall from Section 2.1 that the magnetic flux density $\mathbf{B} = \mu_0(\mathbf{H} + \mathbf{M})$ combines the applied field $\mathbf{H}$ with the material response $\mathbf{M}$. Sensors that measure *flux* integrate $\mathbf{B}$ over a finite surface area defined by the sensor geometry, while sensors that measure *field* respond locally to $\mathbf{H}$ (or its absolute value). This distinction has practical consequences for nanoparticle detection, because the dipolar field generated by a magnetic nanoparticle decays as $1/r^3$ at distances much larger than the particle radius (cf. Appendix A.1.5.2).

Flux sensors: measure magnetic flux: magnetic field is integrated over a finite surface area defined by the sensor shape. The most common example of Flux sensors are:

- Coils and Inductive Sensors: Sensitivity is proportional to frequency. Inductive sensors will be further discussed below.
- Fluxgates: A soft ferromagnetic core is driven cyclically into saturation by an AC excitation coil. An external DC or low-frequency field breaks the symmetry of the saturation cycle, generating even harmonics, principally the second, in a sensing coil wound around the same core. The amplitude of this

second harmonic is proportional to the external field [245, 246]. Fluxgates are typically used for earth and planetary magnetic field measurements and are sensitive to DC and low-frequency fields.

- SQUIDs (Superconducting Quantum Interference Devices): Based on the quantization of flux, offering ultra-high sensitivity for static or low-frequency signals, but require cryogenic cooling. For nanoparticle detection, Ladino et al. [247] used a SQUID gradiometer to detect $MnFe_2O_4$ nanoparticles, but the cryogenic requirement limits practical deployment.

Field sensors: directly measure vector components or the absolute value of H. Because they respond to a local field rather than to flux integrated over a surface, field sensors are particularly amenable to miniaturization without fundamental loss of sensitivity, an advantage exploited in CMOS-integrated Hall, GMR, and TMR devices.

- Hall Effect Sensors: Based on charge carrier deflection under the Lorentz force, producing a transverse voltage proportional to H; widely exploited in consumer and automotive applications due to simplicity and compatibility with microelectronics [248]. For MNP detection, Florescu et al. [249] demonstrated single-bead resolution using a Hall sensor with a planar drive coil and differential bridge.

- Anisotropic Magnetoresistance (AMR) Sensors: Resistance changes based on the relative orientation of the current to the magnetisation direction. Like GMR and TMR below, AMR is a magnetoresistive effect, but it arises within a single ferromagnetic layer (via spin-orbit coupling) rather than from spin-dependent transport across multilayer stacks. Quynh et al. [250] demonstrated AMR-based detection of 50 nm SPIONs in a Wheatstone bridge configuration.

- Spin Electronic Sensors (GMR, TMR): Based on magnetoresistance properties in multilayer stacks of magnetic materials; GMR and TMR have been integrated into CMOS processes for small size devices. For MNP detection, GMR sensors have been applied to lateral flow strips [5] and dried drops [251, 252], while TMR [253] and spin-valve [254] variants have also been demonstrated.

- Giant Magnetoimpedance (GMI): An external DC magnetic field changes the permeability of a soft magnetic wire, which modifies the skin depth at the AC driving frequency and thereby causes a large impedance change. Fodil et al. [255] detected nanoparticles in capillary tubes (a proxy for human blood vessels) with a GMI sensor.

- Magnetoelectric Sensors: Voltage is created by a field change due to strain induced by magnetostriction in coupled magnetic and piezoelectric materials;

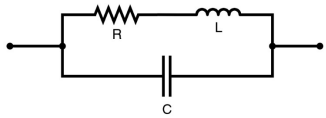


Fig. 5.1 Equivalent circuit of an inductor

they are passive (no external power supply required). Huong Giang et al. [256] applied magnetoelectric phase detection to 50 nm SPIONs in solution.

5.2 Inductive sensing: Core Concepts

In this section, a focus is made on inductive sensing of MNP since this is the underlying principle of the sensor made in this work, detailed in Chapter 6. The main reason for this choice is simplicity, consistent with the ASSURED criteria [2]. It should be acknowledged that other approaches, e.g. magnetoresistive sensors and frequency mixing techniques, can achieve lower limits of detection, as will become apparent from the benchmark later in this chapter. However, these come at the cost of nanofabricated sensor stacks, static bias fields, or dual-frequency excitation with lock-in amplification, requirements that are difficult to reconcile with a low-cost, disposable-strip format.

Beyond practical simplicity, inductive transduction offers a direct link with the metrology of Part I: inductance is directly related to effective magnetic susceptibility, the very quantity characterised across frequency and temperature in Chapter 4. The models, frequency dependencies, and substrate effects established for $\chi(\omega)$ therefore translate into expectations for the sensor response, bridging nanoparticle characterisation and sensor design.

5.2.1 Inductors

An inductor is, fundamentally, Faraday's law cast as a circuit element: a time-varying current through a coil produces a changing magnetic flux, which induces a back-EMF proportional to the rate of flux change (cf. Appendix A.1.2). The proportionality constant between total flux linkage and current defines the inductance L. In practice, every physical inductor also exhibits ohmic losses in the winding and capacitive coupling between adjacent turns, so the component is more accurately described by an equivalent RLC circuit. For detection of magnetic materials, the effective magnetic permeability μ_{eff} enters directly into the inductive impedance. The stray capacitance together with the inductance determine a Self-Resonant Frequency (SRF) exploited in several of the sensing architectures discussed below. The equivalent impedance model of an inductor is displayed in Fig. 5.1.

$$Z_R = R \tag{5.1}$$

$$Z_L = \omega L i(\mu'_{eff} - i\mu''_{eff}) \tag{5.2}$$

$$Z_C = \frac{1}{\omega C i(\epsilon'_{eff} - i\epsilon''_{eff})} \tag{5.3}$$

$$Z_Q = \left(\frac{1}{Z_L + Z_R} + \frac{1}{Z_C}\right)^{-1} \tag{5.4}$$

where Z_L stands for the inductive component of impedance Z, Z_C the capacitive one, Z_R is the resistance of the equivalent circuit, ω is the operating angular frequency, L is the coil self-inductance and C is its stray capacitance. $(\epsilon'_{eff} - i\epsilon''_{eff})$ and $(\mu'_{eff} - i\mu''_{eff})$ are the effective electric permittivity and magnetic permeability. The term effective refers to the effect of all the materials surrounding the coil [244].

In Appendix A.10 the expressions for equivalent resistance, capacitance and inductance are elaborated for planar and solenoidal coils.

5.2.2 Phenomena Causing Inductor's Impedance Variations

Eddy Current Damping: This principle allows for detecting conductive, non-magnetic samples/targets. According to Faraday's law of induction, when a conductive object, such as a metallic surgical instrument or even biological tissue with sufficient ionic conductivity, enters this magnetic field, circulating electrical currents known as eddy currents are induced within the object. These induced eddy currents generate their own secondary magnetic field. In accordance with Lenz's law, this secondary field opposes the primary magnetic field generated by the sensor coil. This has two measurable consequences on the coil's impedance: it causes a decrease in the coil's effective self-inductance and an increase in its apparent series resistance due to energy dissipation as heat within the target.

Magnetic Permeability Perturbation: This principle allows for detecting magnetic materials. In contrast to eddy current effects, the detection of magnetic nanoparticles relies on their ability to alter the magnetic permeability of the medium surrounding the sensor coil. When a material with high magnetic permeability, such as a ferromagnetic or superparamagnetic substance, is introduced into the alternating magnetic field generated by a sensor coil, it effectively acts as a magnetic core. This "core effect" concentrates the magnetic flux lines, causing a significant increase in the total magnetic flux passing through the coil. This results in a measurable increase (as opposed to decrease in case of Eddy Current Damping) in the coil's inductance since a coil's self-inductance is directly proportional to the magnetic flux [257].

5.2.3 Readout Architectures

The performance, sensitivity, and noise immunity of an inductive sensing system depend on its physical and electrical configuration. The subsections below survey the main readout strategies, ordered from the simplest single-coil measurement to the more elaborate frequency mixing technique.

5.2.3.1 Direct Impedance Measurement

The most fundamental configuration involves the direct measurement of impedance changes in a single sensor element. In a self-inductance mode, a single coil is used for both generating the excitation field and sensing the response. A variation is the mutual inductance mode, which employs a dedicated excitation coil and a separate, magnetically coupled sensing coil.

5.2.3.2 Differential and Balanced Configurations

To overcome the drift and noise limitations of single-coil sensors, differential and bridge configurations are employed. These architectures are designed for common-mode rejection, a critical requirement for translating inductive sensing into the demanding environment of biomedical diagnostics. Note that in general, differential approaches do not increase the signal, instead they lower the noise floor.

Planar differential transformer: This structure uses a primary coil to generate magnetic flux, which links with two secondary coils wound in opposite directions as illustrated in Fig. 5.2. The secondary coils are connected differentially, resulting in zero output voltage when no magnetic particles are present. When magnetic markers are placed over one coil (the "active" sensor) while the other acts as a "dummy" or reference, the presence of the markers causes a non-zero differential output voltage [258, 259]. A similar differential approach at lower frequency (10 kHz) was reported by Krishnapriya et al. [260], who achieved a LoD of 20 polystyrene microbeads using a planar bridge-and-differential-coil layout with a 4 mm^2 footprint.

Bridge configuration: A bridge circuit, such as a Wheatstone bridge, offers a similar advantage. The sensing coil forms one arm of the bridge, balanced by a reference inductor and two resistors. The bridge is excited by an AC voltage source. In the absence of a target, the bridge is balanced, and the output voltage is zero. When the inductance of the sensing coil changes, the bridge becomes unbalanced, producing an output voltage proportional to this change. This configuration provides excellent zero-point stability and high sensitivity to small inductance variations [261]. Bridge-based MNP detection has been demonstrated by Bartunik et al. [262] using a resonance bridge at 10 MHz for 50 nm SPIONs in aqueous solution, and by Makiranta et al. [263] with a planar impedance bridge at 7 MHz resolving polymer-embedded SPION clusters.

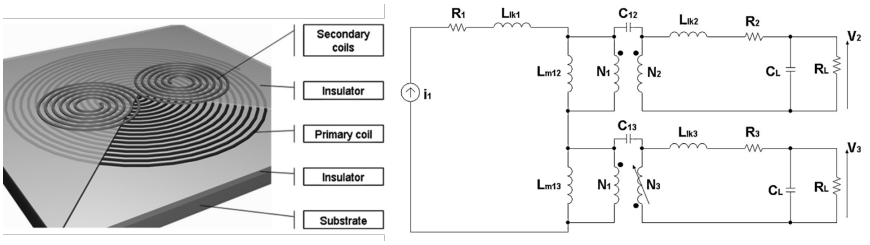


Fig. 5.2 Conceptual drawing and equivalent circuit from [259] considering non-linearities of the transformer, like the series resistance, their leakage inductance and non-ideal coupling with L_{lk} leakage inductance, L_m the magnetising inductances, R_i the series resistances, C_{1i} the parasitic capacitances between primary and secondary coils, C_L and R_L the resistance and capacitance of the signal conditioning circuit.

5.2.3.3 Resonant Frequency Shift

The coil is often paired with a capacitor to form a resonant LC circuit, where the presence of magnetic particles causes the resonant frequency to decrease. The output frequency shift is roughly linear to the inductance variation caused by the magnetic beads (cf Chapter 6). Highly stable frequency measurement techniques, such as a Phase-Locked Loop (PLL) or a cross-coupled LC oscillator, are employed to accurately measure these small frequency changes, sometimes measured in the Hertz range against a baseline of MHz [264]. Richardson et al. [265] demonstrated an early portable LC resonant frequency reader for dried SPION beads using a PLL at 529 kHz. More recently, Marques-Fernandez et al. [244] applied SRF detection directly on LFA strips with a 150 µm planar coil, scanning up to 3 GHz. Yoshida et al. [266] combined an LC resonant circuit with harmonic sensing for remote detection at centimetre-scale distances, while Moyano et al. [267] measured impedance changes of a planar inductor at 40 MHz for SPION nanoflowers on LFA strips.

At microwave frequencies, resonator-based approaches offer extreme miniaturization. Rzeszowski et al. [268] detected as few as 7 polymer-embedded MNP beads with a 45 µm planar microwave resonator at 1.4 GHz, and Dowling et al. [269] used a 20 µm microresonator at 13 GHz for SPION cluster detection. These approaches are currently limited to benchtop instruments due to their operating frequency and field requirements.

5.2.3.4 Frequency Mixing

This technique exploits the nonlinear magnetisation curve $M(H)$ of superparamagnetic nanoparticles and is conceptually similar to MPI, introduced in Section 2.4. Two AC magnetic fields are applied simultaneously: a small-amplitude excitation

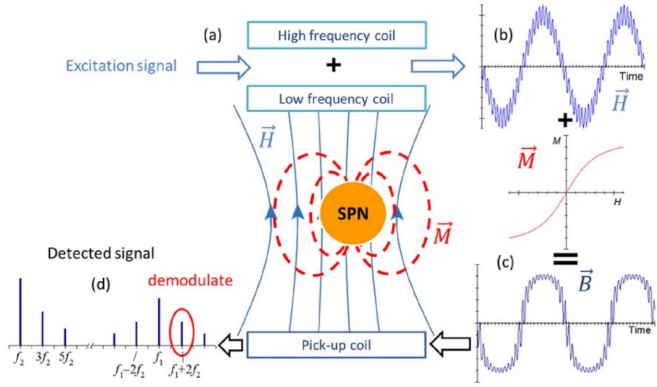


Fig. 5.3 Frequency mixing: (a) Setup of the application of the frequency mixing technique; (b) magnetic excitation field; (c) resulting magnetic flux density; (d) Fourier transform of the detected signal. The frequency component f_i selected for the detection is circled in red. $\vec{M}$ is the magnetisation direction of the MNP, $\vec{H}$ and $\vec{B}$ the excitation and the resulting magnetic field, respectively. Image from [273]

field at high frequency f_1 and a large-amplitude drive field at low frequency f_2. The drive field slowly sweeps the nanoparticles along their nonlinear $M(H)$ curve, periodically approaching saturation. As a result, the local magnetic susceptibility $\chi = \mathrm{d}M/\mathrm{d}H$ varies periodically at the drive frequency: it is high near zero field (steep part of the Langevin curve) and drops near saturation (flat part). The small excitation field probes this time-varying susceptibility: the nanoparticle response to f_1 is amplitude-modulated by the susceptibility oscillation at f_2, producing intermodulation products at combinatorial frequencies $f_i = mf_1 + nf_2$ $(m, n \in \mathbb{Z})$ [270]. Fig. 5.3 illustrates the working principle of frequency mixing. Two main advantages are:

- These mixing frequencies depend only on nonlinear magnetic material, dia- and paramagnetic backgrounds do not contribute, giving the technique intrinsic selectivity. This is demonstrated by Krause et al. [271] who detected streptavidin-coated MNP in polymer matrixes.
- The amplitude of each intermodulation component is proportional to the quantity of nanoparticles [272], and the relative amplitudes of the different components depend on the shape of $M(H)$, which is size-dependent. By analysing the harmonic spectrum, the distribution of nanoparticle sizes in a sample can therefore be inferred [270].

The excitation coils generate the two AC fields, and the resulting signal is detected with a pickup coil. It requires equipment such as lock-in amplifiers, to pre-

cisely measure the frequency response of the system. The technique has been applied across a range of configurations and substrates: Krause et al. [271] demonstrated detection on ABICAP immunofiltration columns (3D polyethylene filters) at ∼49 kHz / 61 Hz with a differential pickup coil, Orlov et al. [3] achieved subnanogram sensitivity on LFA with a portable reader, Minard et al. [274] operated at much higher frequencies (250 - 750 MHz) for cell lysate analysis, and Kuwahata et al. [275] adapted harmonic detection for sentinel lymph node phantoms. The main drawback is that this technique requires mT-range excitation fields to drive the MNP through their nonlinear regime. This implies a -generally- larger power consumption than impedance-based readers.

5.3 Sensing of Magnetic Nanoparticles in Literature

Table 5.1 Detection of magnetic nanoparticles, inductive sensing

Ref	MNP type	Size	MNP matrix	Principle	Operation	Sensor Size	LoD	Sensitivity	Range	Portability	Field (OOM)
Baglio 2005 [259]	SPION in polystyrene	4 um	Aqueous solution	Planar, Differential Transformer	10 - 15 MHz	CMOS integrated		730 mV / mg Fe		Benchtop	
Barnett 2014 [276]†	SPION in polymer (Seradyn)	760 nm	LFA	Planar, Resonant Coil Magnetometer (FLL)	~60 MHz	PCB, 5 flat spiral coils	1.5×10^6 particles (sensor); 0.8 ng/mL PSA (assay)‡	0.024 mV / 10^5 particles	0.8 - 10 ng/mL (PSA)	Portable	
Bartunik 2021 [262]	SPIONS coated with lauric acid	50 nm (hydrody-namic)	Aqueous solution	Tubular, Resonance Bridge	10 MHz	20 mm length	7 uL suspension (concentra-tion?)		7 - 80 uL (con-centration?)	Benchtop	
Dowling 2023 [269]	SPION clusters	130 um clusters	Aqueous solution	Planar, Mi-croresonator (based on FMR)	13 GHz	20 um	8 ug/ mL			Benchtop	400 mT DC polarizing field
Krause 2007 [271]	SPIONS in polymer	0.5-1 um	Immunofiltration (ABICAP column)	Tubular, Frequency mixing	HF 49.4 kHz + LF 61 Hz	4.5 mm inner coil	0.12 mg(Fe)/L		0.12 - 1300mg(Fe)/L	Portable	None (f1+2f2 mode: zero DC field)
Krishnapriya 2017 [260]	SPION beads (polystyrene)	1 um	Aqueous solution	Planar : bridge and differential coil	10 kHz	4 mm2 footprint	20 beads	0.1 uA/particle		Benchtop	uT sensing field
Kuwahata 2018 [275]	Resovist (MRI contrast agent)	60 nm (beads?)	Lymph Phantoms	Frequency mixing, harmonic detection	1-10 kHz	1 - 3 cm radius	0.28 ug Fe		0.28 ug - 2.8 mg Fe	Benchtop (intended as such)	1 mT
Minard 2013 [274]	SPIONS	12 nm	Cell lysate solution	Tubular, Frequency mixing	250 and 750 MHz	2-5 cm length	100 ng			Benchtop	10 mT excitation field (non linear range)

Continued on next page

Table 5.1 – continued

Ref	MNP type	Size	MNP matrix	Principle	Operation	Sensor Size	LoD	Sensitivity	Range	Portability	Field (OOM)
Makiranta 2006 [263]	10 nm SPIONS in polymer matrix	400 um	Dried on surface	Planar coil, impedance bridge	7 MHz	2 mm outer diam	60k particles	8.4 pV/MNP		Benchtop	
Marques - Fernandez 2023 [244]	SPIONS	12 nm	LFA	Planar, SRF detection	100 kHz - 3 GHz	150 um sensing coil width		5821 Hz / ug Fe3O4		Portable	
Moyano 2020 [267]	SPION nanoflow-ers	Core 10-20 nm, Flower 130 nm	LFA	Planar, Inductor impedance	40 MHz	cm - coil trace length		expressed in biotarget		Benchtop	
Nikitin 2007 [272]	SPION beads (Dyn-abeads)	1 um / 2.8 um	Nitrocellulose and Glass capillary	Planar, Frequency mixing	3MHz + 1kHz	50 mm cavity	3 ng		3 ng - 70 ug	Both Portable and Benchtop	
Orlov 2016 [3]	SPIONS in carboxyl	196 nm	LFA	Tubular, Frequency mixing	Freq not specified. 56 - 144 Oe		0.4 ng		ng - mg	Portable	14.4 mT excitation field (non-linear range)
Rabehi 2018 [273]	SPION flowers	20 nm per SPION	Aqueous solution	Planar, Frequency mixing	40 kHz + 80 Hz	2 cm radius	15 ug/mL			Benchtop	2 mT excitation field (non linear range)
Richardson 2001 [265]	SPION beads coated with strepta-vidin	2.8 um	Dried on plastic	Tubular, SRF measurement with PLF	up to 529 kHz	7.5 mm diameter	1.2 ug Fe	3 Hz per ug of Fe		Portable	
Rzeszowski 2010 [268]	SPION in polymer	4.5 um	Aqueous solution	Planar, Microwave resonator	1.4 Ghz	45 um diam	7 beads			Benchtop	

Continued on next page

Table 5.1 – continued

Ref	MNP type	Size	MNP matrix	Principle	Operation	Sensor Size	LoD	Sensitivity	Range	Portability	Field (OOM)
Yoshida 2011 [266]	SPIONS coated with dextran	10 - 30 nm	Dried on surface	Tubular, LC resonant circuit	Harmonic sensing, 20 and 40 kHz	3.3 cm	100 ug (3 cm distance)	7668 V/T		Benchtop (intended as such)	2.4 mT excitation field
Zheng 2016 [264]	SPIONS in bead	1.5 um	PBS solution	Planar microcoil array, LC oscillator			20 - 30 beads		1ng/ml - 1ug/ml (IgG concentration)	Portable	

† Barnett et al. report LoD as a sensor-level particle count and as an immunoassay-level analyte concentration (PSA); no conversion to nanoparticle mass is available from the source.

Table 5.2 Detection of magnetic nanoparticles, other than inductive sensing

Ref	MNP type	Size	MNP matrix	Principle	Operation	Sensor Size	LoD	Sensitivity	Range	Portability	Field (OOM)
Cardoso 2008 [254]	MNP	130 nm diam		Spin Valve	375 Hz, passband and amplifier	15 um2	3e8 particles/ml			Portable	2.5 mT DC
Florescu 2008 [249]	SPION beads	2.8 um	Drop on the sensor	Hall sensor with planar drive coil	50 kHz, differential bridge	1 - 4 um	1 single bead			Portable	0.8mT polarizing field
Huong 2017 [256]	SPION in Chitosan	50 nm (hydrody-namic?)	Aqueous solution	Magnetoelectric Effect and phase detection	100 kHz resonant freq	15 mm length	0.31 ug at 2 mm distance	15 uV/ug	0.31 - 50 ug	Benchtop	6 mT DC
Jin 2021 [253]	SPION clusters	200 nm cluster	Drop on Sensor	TMR	Resistance msmt with 4 probe method	80 um2	500 ng		0.01 - 1 mg/mL inital concentration	Benchtop	0.3 mT
Ladino 2017 [247]	MnFe2O4 with CA	17.3 nm crystal	Aqueous solution	SQUID and gradiometer coil		2 cm diameter	3.3 ug at 1 cm distance		3 - 20 ug at 1 cm	Stationary (cryogenic cooling)	145 uT AC excitation Field (10 Hz)
Li 2013 [251]	SPIONS	10 nm	Drop on sensor	GMR	DC Wheatstone bidge	800 um2	10 ng/mL (drop)			Benchtop	200 mT, polariz-ing/saturating field
Marquina 2012 [5]	SPIONS agglomer-ates, inorganic coating	156-184 nm	LFA	GMR	DC; half a.c. Wheatstone bridge	200 x 3 um2	64 ng			Benchtop	30-50 mT perpendicular field
Quynh 2019 [250]	SPIONS in chitosan	50 nm	Drop on sensor	AMR	AC Wheatstone bridge	3.2mm	0.56 memu (we deduce 50 ug)			Benchtop	
Volmer 2021 [252]	SPIONS functional-ized with PEG	10 nm	Drop on sensor	GMR	read with Keithley 2182A nanovoltmeter, 0.01Hz		1.20 ug, i.e. 0.01memu	75 emu/g		Benchtop	2.5 mT perpendicular field

In Tables 5.1 and 5.2 main benchmark values are summarised: a specific focus on inductive sensing in the former, and other magnetic sensors in the latter.

- Nanoparticle sizes are given as mentioned in the source. This can be ambiguous: when a source says "superparamagnetic, 50nm" it either means that the hydrodynamic diameter is given, or that the nanoparticle has a shell of which the mass fraction is not specified,...
- Sensitivity is only mentioned when it was specified in "measurable quantity per - nanoparticle mass"
- Operation Frequency and order of magnitude (OOM) of the 'highest involved field' are not as such figures of merit, but are mentioned for illustrative purposes. They affect power consumption, complexity of interfacing,...

Strictly speaking, sensitivity denotes the slope of the sensor's calibration curve (output change per unit of measurand), while the LoD is the minimum measurand value that produces a signal distinguishable from the noise floor, typically defined as $\text{LoD} = 3\sigma_{\text{noise}}/S$ with S the sensitivity. In practice, these definitions are inconsistently applied across the MNP detection literature: for example, Krishnapriya et al. [260] define "sensitivity" as the minimum output change that can be measured, which is in fact the noise floor. Both LoD and Sensitivity values in the tables below are reported as stated in each source; the reader should be aware that direct numerical comparison across entries is not always meaningful. Several observations emerge from Tables 5.1 and 5.2.

Heterogeneous reporting hinders direct comparison: LoD is variously reported in mass of iron (e.g. 1.2 μg Fe [265]), total nanoparticle mass (e.g. 3 ng [272]), mass concentration (e.g. 8 μg/mL [269]), particle count (e.g. 7 beads [268]), or volume of suspension without specifying concentration (e.g. 7 μL [262]). Similarly, the "Sensitivity" column mixes sensor-to-mass transfer functions (e.g. 730 mV/mg Fe [259]), sensor-to-field transfer functions (e.g. 7668 V/T [266]). Particle "size" can refer to the crystal core, the hydrodynamic diameter, or the polymer bead encapsulating the SPIONs. No standardised figure of merit exists, making a fair ranking across studies difficult.

Many demonstrations use micron-scale beads, not isolated nanoparticles: Entries such as [259] (4 µm), [272] (1–2.8 µm Dynabeads), [260] (1 µm), [265] (2.8 µm), and [249] (2.8 µm) achieve impressive detection limits with polymer microbeads. However, the magnetic moment of a particle scales with its volume ($\propto d^3$), so detecting a 4 µm bead is roughly 10^6 times easier than detecting a 40 nm SPION. For lateral flow applications, nanoparticles must be small enough to migrate through nitrocellulose pores, typically well below 500 nm. The entries most relevant to LFA,

using sub-200 nm particles on actual strips, tend to show weaker detection metrics, reflecting a fundamental tension between detectability and assay compatibility.

Frequency mixing achieves the lowest LoDs among inductive methods, but at the cost of complexity: Six of the seventeen inductive entries use frequency mixing, with the best reported LoDs (Orlov: 0.4 ng, Nikitin: 3 ng). However, the technique requires two excitation signals, milliTesla-range fields to drive MNP into the nonlinear regime, and lock-in or spectrum analysis. Simpler approaches (direct impedance, SRF shift) trade sensitivity for reduced hardware complexity and are better suited to low-cost portable readers.

Non-inductive sensors mostly require a DC polarising field: Nearly every 'non-inductive' sensor in Table 5.2 needs a static magnetic field (0.3–200 mT) to magnetise the nanoparticles before sensing their stray field. Several inductive approaches (direct impedance, SRF shift) do not require this, the AC excitation field itself probes the permeability change. This can be a practical advantage for portable, battery-operated instruments.

A sensitivity–simplicity–portability trade-off is apparent: Portable systems with sub-nanogram sensitivity exist (frequency mixing: [3, 272]), but rely on dual-frequency excitation. Simple and portable readers (SRF-based: [244, 265]; resonant coil magnetometer: [276]) sacrifice LoD but offer low component cost and handheld form factors. The highest raw sensitivities (microresonators: [268], single-bead Hall: [249]) are achieved only in benchtop setups with microscale sensor–particle distances. No single entry in the tables simultaneously optimises all three.

5.4 Literature Focus: Sensing MNP in LFA

This section narrows the scope to LFA, the target application of this thesis. The lateral flow format imposes constraints that are absent from generic MNP sensing: the nanoparticles must be small enough to migrate through nitrocellulose pores (typically below 500 nm hydrodynamic diameter), the reader must tolerate strip-to-strip variability, and the overall system should remain compatible with point-of-care deployment. The few studies that combine magnetic detection with actual LFA strips are reviewed, highlighting what drives the wide spread in reported LoDs and the recurring gap in reporting: no single study independently characterises the intrinsic susceptibility χ, the sensor-to-particle distance, and the applied field amplitude.

5.4.1 The optical signal: pros and cons

Before reviewing magnetic detection results on LFA strips, it is worth taking stock of what visual and optical readout can and cannot achieve, since they remain the

default in commercially deployed lateral flow tests. Two levels of optical readout should be distinguished.

Visual detection: Refers to naked-eye inspection of the test line: the user decides whether a coloured line is present or absent. No instrument is required, and the result is available within seconds of the assay completion, properties that align directly with the ASSURED criteria [2]. For high-concentration samples, visual readout is entirely adequate: pregnancy tests and Covid-19 self-tests have demonstrated that billions of reliable binary results can be obtained this way. The vast majority of commercial LFAs use 30–40 nm colloidal Gold Nanoparticles (AuNP), efficient colourimetric reporters due to localised surface plasmon resonance. Khlebtsov et al. [277] quantified the minimum detectable surface density on nitrocellulose via RGB colorimetric analysis: for 40 nm Au spheres, the detection limit corresponds to roughly 10 ng of gold on a typical $1\times4\,\mathrm{mm}^2$ test line. For comparison, a standard LFA strip is loaded with ∼1–4 µg of gold on its conjugate pad, of which only a fraction is captured at the test line. It should be noted that these values were obtained with monodisperse, spherical AuNP; in most commercial LFAs nanoparticles are more polydisperse, increasing detection threshold in practice [277]. An important bottleneck is subjectivity of naked-eye readout. Visual detection is operator-dependent and binary: it cannot distinguish between a weakly and a strongly positive line [278].

Optical readers: Qdd a photodetector and a controlled light source, enabling quantification of the colour intensity at the test line. They are relatively simple and inexpensive, and can extend the usable dynamic range by one to two orders of magnitude compared with the naked eye [4]. Colourimetric methods, whether by eye or by optical reader, sense only the labels located near the membrane surface. On a typical 260 µm nitrocellulose membrane, optical penetration is limited to ∼10 µm, so that roughly 96 % of the captured labels contribute nothing to the signal [3]. Magnetic readers, by contrast, probe the entire membrane volume. In literature, the visual limit of detection for SPNF is reported to be around 100 ng [5]: this is higher than AuNP due to the absence of plasmonic effect. However, when combined with magnetic sensors, integration of MNP offers opportunities for (1) improved sensitivity and analyte quantification, (2) decreasing limit of detection below the visual thresshold as achieved by Marquina et al. with a GMR sensor and (3) magnetic pre-concentration of the analyte. This underscores that replacing visual readout with a magnetic sensor is not automatically beneficial; the gain depends on the transduction principle and sensor design.

5.4.2 Quantifying MNP on LFA

Marquina 2012 - GMR: In [5], authors use a Giant Magnetoresistance (GMR) sensor ($200\times3\,\mu\mathrm{m}^2$) to detect the stray field of SPION immobilised on the test line

of an LFA. A permanent magnet applies a perpendicular field of 300–500 Oe, bringing the particles to roughly 48.5 % of their saturation magnetisation. The resulting stray field at the sensor correspond to effective fields of ≈ 0.05–1.5 Oe depending on the deposited nanoparticle mass. A linear relationship between nanoparticle mass and the detected magnetic field is confirmed. The lowest detected mass is 64 ng of SPION, below the visual detection limit.

Orlov 2016 - Inductor: In [3] authors apply the frequency mixing principle, achieving the, to the best of our knowledge, lowest reported MNP mass LoD on an LFA with an inductive readout. The labels are 200 nm carboxyl-modified SPM nanoparticles , deposited on nitrocellulose membranes. The excitation amplitudes are 144 Oe and 56 Oe for resp. the low- and high-frequency components. The calibration curve of reader signal versus mass of Fe_3O_4 follows a power law $y = 6.86\,x^{0.854}$ (from $\sim$0.01 ng to $\sim$10 mg of Fe_3O_4), with a LoD of 0.4 ng (SPION mass within beads). The power-law exponent of 0.854 is noteworthy: for an ideal frequency mixing measurement the signal should be directly proportional to the total nonlinear magnetic moment, i.e. one would expect an exponent of unity. The observed sub-linearity is not discussed by the authors but means that each additional nanogram of magnetite contributes progressively less signal. This is attributed to(i) dipolar inter-particle interactions at higher packing densities; (ii) collective demagnetisation; and (iii) a fitting artefact, whereby a single power law forced through seven decades averages over distinct physical regimes.

Marques-Fernandez 2023 - Inductor: In [244] authors demonstrate an alternative inductive approach: measuring the shift in self-resonant frequency (SRF) of a planar coil caused by nanoparticles deposited on its surface. The coil is a two-turn copper track (150 µm width, 12 mm length) on a PCB, and its impedance is scanned from 100 kHz to 3 GHz with a portable VNA. The 12 nm SPION are deposited by controlled printing onto blotting paper strips (line pattern of 25 mm $\times$ 2 mm) that are pressed against the coil surface. By modelling the coil as an equivalent RLC circuit whose SRF depends on the effective surrounding permittivity and magnetic permeability, a linear relationship between nanoparticle mass and $\ln(\mathrm{SRF})$ is predicted and confirmed experimentally for masses up to $\sim$500 µg. The measured sensitivity for magnetite is $S = 5821\,\mathrm{Hz}/\mu\mathrm{g}\,Fe_3O_4$. The demonstrated mass range ($\sim$50–500 µg) is orders of magnitude above the sub-nanogram regime reached by Orlov et al., probably reflecting the fact that SRF detection probes a bulk permeability change averaged over the coil's near-field volume, whereas frequency mixing exploits the highly specific nonlinear susceptibility of the particles.

Moyano 2020 - Inductor: In [4] authors combine magnetic and optical readout of LFA strips using multicore carbon-coated nanoparticles containing dozens of SPION. The magnetic signal is measured with a double copper line on an insulating substrate, driven at 40 MHz (500 mV excitation) via an impedance analyser,

scanned laterally across the test line by a micropositioner. The inductive impedance increase is directly proportional to the number of superparamagnetic nanoparticles at the test line. In a biotin–neutravidin affinity test, both the magnetic and the optical (reflectance) signals increase monotonically with neutravidin concentration.

Barnett 2014 - Inductor: In [276] authors demonstrate a Resonant Coil Magnetometer for quantitative readout of lateral flow strips. The reader is built around a Frequency Locked Loop circuit: planar coils on a PCB form the inductive element of a voltage-controlled oscillator at ∼60 MHz. The frequency shift caused by 760 nm multicore polymer beads captured at the test line is converted to a DC voltage via heterodyne mixing and phase detection. The assay targets total prostate specific antigen in serum using a lateral flow format. A linear dose–response is observed over the clinically relevant range 0.8–10 ng/mL, with a LoD of 0.8 ng/mL PSA. The intrinsic sensor detection limit, determined from calibration with known quantities of beads, is 1.5×10^6 particles. The estimated component cost of ∼$100 dollars and the handheld form factor make this one of the simplest magnetic LFA readers reported.

Similarities for reported MNP-LFA systems: Four of the five studies use superparamagnetic iron oxide (magnetite or maghemite) labels in the 10–200 nm core-size range, confirming that this material class remains the default for magnetic LFA. The exception is Barnett et al., who use 760 nm multicore polymer beads, still compatible with certain lateral flow formats (depending on pore size and colloidal stability). In every case the measured signal scales monotonically with the total mass of magnetic material at the test line, and calibration curves spanning at least 3–4 orders of magnitude in nanoparticle mass are routinely obtained. According to Orlov et al. [3], hydrodynamic diameters of 100–200 nm represent a practical optimum for LFA: particles below ∼50 nm carry too little magnetic moment per bead to generate a detectable signal without extreme reader complexity, while particles above ∼500 nm migrate poorly through nitrocellulose pores. The saturation magnetisations reported for the iron oxide labels (40–64 emu/g) are mutually consistent and typical of nanocrystalline magnetite with surface spin disorder [29].

Variations for reported MNP-LFA systems: LoD differs from ∼0.4 ng in [3] to ∼50–500 µg in [244], reflecting the dominance of the transduction principle. No study independently reports all three parameters that govern the signal: the intrinsic susceptibility χ of the particles (DC or AC, at the relevant frequency), the sensor-to-particle distance r (or the equivalent filling factor), and the applied field amplitude H. Marquina et al. report χ but not r; Orlov et al. circumvent the distance issue by volumetric detection but do not characterise $\chi(f)$; Marqués-Fernández et al. lump χ and ε into a single refraction-index contrast; Barnett et al. report LoD only in analyte concentration (ng/mL PSA), with no conversion to particle mass available. This makes it difficult to derive a sensor-independent figure of merit that would predict, for a given nanoparticle batch, what signal to expect on an arbitrary

reader. Harmonising the reporting by quoting a frequency-dependent mass susceptibility and the effective sensing distance, would greatly improve cross-study comparability and is a prerequisite for rational co-design of nanoparticle labels and detection hardware. Ideally, all papers should separately report sensor characteristics obtained on benchmark samples with nanoparticle applied in a controlled way rather than by immunological binding.

5.4.2.1 Bottlenecks for integration of magnetic sensors on LFA

Batch-to-batch variability: Marquina et al. [5] report that most commercial nanoparticles available at the time of their study suffer from broad size distributions, significant non-magnetic mass fractions, and poor batch-to-batch reproducibility.

Functionalization dominates assay sensitivity: The method by which antibodies are attached to the nanoparticle surface has a large impact on the immunoassay sensitivity. Marquina et al. [5] compared two functionalization strategies for hCG detection and obtained four-fold difference. This indicates that the biological recognition step, not the magnetic transduction, is often the limiting factor. Optimising the antibody orientation on the nanoparticle surface is therefore at least as important as optimising the sensor hardware. This requires very specific expertise.

Reader dynamic range $\neq$ assay dynamic range: Even when the magnetic reader can quantify nanoparticle masses over seven orders of magnitude [3], the useful analyte concentration range of the immunoassay spans only 3–4 orders. The compression arises from the sigmoidal binding kinetics of the antibody–antigen interaction: at low concentrations, captured mass scales roughly linearly with analyte concentration, but at high concentrations the test line saturates. The actual mass of nanoparticles deposited at the test line at the assay LoD is rarely reported independently, making it impossible to separate reader limitations from assay limitations. Future studies would benefit from reporting both the reader calibration (signal vs. known deposited mass) and the immunoassay calibration (signal vs. analyte concentration) as separate curves.

5.5 Commercial Platforms for MNP detection

Six ventures, founded between 1997 and 2005, have attempted to commercialise MNP detection for point-of-care diagnostics. They span inductive readout (MagnaBioSciences, LifeAssays/Magnasense), frequency mixing (Senova/FZ Jülich, Magnisense/OVVI), optomagnetic sensing (Magnotech/Philips), and GMR arrays (MagArray). Table 5.3 compiles their quantitative figures of merit; detailed descriptions of each platform's technology, patents, and corporate history are given in Appendix A.9.

From patents to products, a low conversion rate: Each of the six ventures holds or licenses granted patents, yet the path from patent to clinical product has proven to be long and uncertain. As of 2025, only the Magnotech technology, now the Siemens Atellica VTLi, has reached routine clinical deployment, for high-sensitivity cardiac troponin I [279, 280]. MagArray's REVEAL lung cancer test is commercially available and covered by Medicare in the USA, but remains classified as investigational [281, 282]. MagnaBioSciences appears inactive; LifeAssays underwent two successive acquisitions before re-emerging as Magnasense AB; Magnisense was acquired by OVVI Diagnostics and has not yet reported widespread deployment. In all cases, the delay between patent filing and any form of clinical product exceeds ten years, and most ventures never crossed the gap. The barrier is evidently not the sensing principle itself but rather regulatory approval, manufacturing scale-up, clinical validation, and reimbursement, the "valley of death" of medical device development. Furthermore, the established dominance of optical LFA, where colloidal gold strips have been manufactured at scale for decades, means that a magnetic reader must demonstrate a clear clinical advantage, not merely a lower LoD, to justify the additional hardware cost. Finally, the antibody–antigen binding step, additionally constrains the overall assay LoD (cf. Section 5.4).

Performance relative to the academic state of the art: LoD values across the six platforms span several orders of magnitude, from $\approx 9\,\mathrm{fg/mL}$ (MagArray, amplified GMR assay [281]) to $3\,\mathrm{mg/L}$ (LifeAssays, CRP on LFA [283]). This spread is dominated by the transduction principle. However, the best-performing commercial platforms are not inductive: the Atellica VTLi relies on optomagnetic detection with frustrated total internal reflection [284], while MagArray uses nanofabricated spin-valve sensor arrays on silicon [285]. The two purely inductive platforms (MagnaBioSciences, LifeAssays) show the weakest analytical sensitivity, confirming at the commercial level the sensitivity–simplicity trade-off identified in Section 5.3.

LFA coverage remains limited: Three of the six platforms (MagnaBioSciences, LifeAssays/Magnasense, Magnisense/OVVI) were designed for LFA strips, and the FMMD reader from FZ Jülich was demonstrated on the related ABICAP immunofiltration column [271]. By contrast, the two best-performing platforms (Atellica VTLi, MagArray) use proprietary cartridges or silicon chips that are incompatible with the standard nitrocellulose strip format. Among LFA-compatible platforms, the best reported LoD is $0.4\,\mathrm{ng}$ of Fe_3O_4 (Magnisense, frequency mixing [3]), obtained with dual-frequency excitation and lock-in detection, hardware that is more complex than a simple impedance or frequency-shift reader.

Portability and cost: Most platforms were designed with point-of-care use in mind, and time-to-result values fall in the 8–30 min range typical of rapid immunoassays (Table 5.3). However, true portability and low cost are difficult to

reconcile with high analytical performance. The Atellica VTLi, for instance, accepts fingerstick samples and delivers results in $\sim$8 min, but the analyser is a hospital-grade instrument, not a handheld device. MagArray requires a dedicated bench-top reader and nanofabricated consumables. The MagnaBioSciences MICT reader, designed as a handheld unit with disposable cassettes, had the profile closest to a low-cost field instrument, but the company is no longer active. Only MagArray offers multiplexing (up to 8 analytes on 64 sensors), all other platforms measure one analyte per disposable.

Table 5.3 Figures of merit for commercial MNP detection platforms. LoD values are for the best-demonstrated analyte; dynamic range is given in orders of magnitude (OOM). Entries marked with * are from academic validation studies rather than manufacturer specifications.

Platform	Sensing principle	Best LoD reported	Dynamic range	Time to result	Sample volume	Multi-plexing	Assay format	Key analytes	Concordance / comparison
MagnaBioSciences MICT [286, 287]	Inductive readout (AC, ∼100 kHz, gradiometer coils)	30 pg/mL (HIV-1 p24)* [286]; improved sensitivity over optical LFA (full-depth magnetic readout)	Not reported	15–45 min	5–50 µL	No	LFA strip	HIV-1 p24, *T. solium* antibodies, biodefence	94.5 % sens., 96 % spec. vs. parasitological diagnosis (*T. solium*)* [287]
LifeAssays / Magnasense (Magnia Reader) [283]	Magnetic permeability detection (inductance coil, temperature controlled)	3 mg/L CRP* [283]	<2 OOM	5.5 min	4 µL whole blood	No	LFA strip	CRP	CRP: $R^2 = 0.982$ vs. ref. ($n = 50$)* [283]
FMMD (FZ Jülich) / Senova substrate [271, 288]	Frequency mixing (LF 61–63 Hz + HF 40–49 kHz, detection at $f_1 + 2f_2$)	0.2 ng/mL (cholera toxin B)* [289]; 0.12 mg(Fe)/L* [271]	2–4 OOM	21–128 min	400–500 µL	No	ABICAP immunofiltration column	CRP, cholera toxin B, SARS-CoV-2 IgG	SARS-CoV-2: 97 % sens., 92 % spec. vs. DiaSorin* [290]
Magnotech / Atellica VTLi (Siemens Healthineers) [284, 291]	Optomagnetic (FTIR + magnetic actuation of 500 nm labels)	1.24 ng/L (hs-cTnI, plasma) [279, 280]	∼3 OOM (LoQ–1 250 ng/L)	∼8 min	∼30 µL fingerstick	No	Disposable cartridge	hs-cTnI, PTH	$r = 0.97$ vs. Atellica IM; $r = 0.98$ vs. Beckman hsTnI [280]; PTH: $r = 0.93$* [292]
Magnisense / MIAtek / OVVI Diagnostics [272, 293]	Nonlinear magnetisation (dual-frequency, combinatorial harmonics)	0.9 pg/mL (CYFRA 21-1)* [294]; <0.1 ng/mL (*Y. pestis*)* [272]	∼5 OOM	20–60 min	37 µL	No	LFA strip; cartridge; glass tube	*Y. pestis*, *Salmonella*, CYFRA 21-1	1–2 OOM better LoD than ELISA* [272]; 18.5× better dynamic signal range vs. optical LFA* [294]
MagArray (GMR) [281, 285]	GMR spin-valve nanosensor array (real-time, chip-based)	50 aM ≈ 9 fg/mL (CEA, amplified)* [281]; 0.9 pg/mL (unamplified)* [282]	5–6 OOM	<30 min	20–50 µL	Yes (64 sensors; 7–8 analytes)	Silicon chip	CEA, hCG, eotaxin, VEGF, lung cancer panel	$>1000\times$ more sensitive than ELISA; 3–4 OOM greater dynamic range* [281]

Chapter Summary

This chapter surveys the sensing principles used to detect MNPs, benchmarks reported performance across inductive and non-inductive transduction methods, and reviews the commercial platforms that have attempted to bring magnetic LFA readers to market. Inductive transduction is singled out because it is the principle adopted in Chapter 6.

Magnetic sensor principles: Magnetic sensors are divided between flux sensors (coils, fluxgates, SQUIDs), which integrate **B** over a finite surface, and field sensors (Hall, GMR,...), which respond locally to **H**. The distinction matters for nanoparticle detection because the dipolar field of a single particle decays as $1/r^3$, so flux sensors benefit from volumetric integration while field sensors benefit from close sensor-to-particle distance. Field sensors are more amenable to CMOS miniaturisation at the cost of nanofabrication.

Inductive sensing core concepts: An inductor is modelled as an equivalent RLC circuit in which the effective magnetic permeability of the surrounding medium enters directly into the inductive impedance. The presence of SPNFs modifies this effective permeability, which translates into a measurable change in inductance, a shift in SRF, or a modulation of the frequency of an oscillator locked on the coil. Four readout architectures are reviewed: direct impedance measurement, differential and bridge configurations, resonant frequency shift, and frequency mixing. They span the full sensitivity–simplicity range, from single-coil oscillator readers to dual-frequency excitation with lock-in detection.

Focus on LFA: The lateral flow format imposes constraints to generic MNP sensing: particles must migrate through nitrocellulose pores, the reader must tolerate strip-to-strip variability, and the system should remain compatible with point-of-care deployment. Visual readout on colloidal AuNP remains the default in commercial LFAs; its detection limit on 40 nm Au spheres corresponds to roughly 10 ng of gold per test line [277], but it is subjectively interpreted by the naked eye and limited to near-surface labels. Five representative studies of magnetic LFAs were reviewed [3–5, 244, 276]. All show monotonic signal–mass calibrations, but reported LoDs differ and no study independently reports the three parameters that govern the signal: the intrinsic susceptibility χ, the sensor-to-particle distance, and the applied field amplitude. Harmonising the reporting is identified as a prerequisite for the rational co-design of nanoparticle labels and detection hardware.

Commercial platforms: Six ventures founded between 1997 and 2005 have attempted to commercialise MNP detection, spanning inductive readout, frequency mixing, optomagnetic sensing and GMR arrays (Table 5.3, Appendix A.9). Only

the Magnotech technology (now the Siemens Atellica VTLi) has reached routine clinical deployment, and MagArray's REVEAL test is commercially available but still classified as investigational by private insurers. The best-performing commercial platforms rely on non-inductive transduction (optomagnetic, spin-valve GMR) and use proprietary cartridges incompatible with the standard nitrocellulose strip format. Among LFA-compatible platforms, the best reported LoD is 0.4 ng Fe_3O_4 with frequency mixing [3]. The recurring pattern of acquisition, pivot or cessation across the six ventures reflects barriers beyond the sensing physics: regulatory timelines, the established dominance of optical LFAs, and the fact that antibody–antigen binding is an additional limit to the overall assay LoD.

Towards Chapter 6: The benchmark establishes that simple inductive architectures (direct impedance, SRF shift, LC oscillator) offer simplicity and portability at the cost of limit of detection. They are compatible with a low-cost disposable-strip format aligned with the ASSURED criteria [2]. Chapter 6 investigates to what extent such a simple inductive readout, combined with the SPNFs characterised in Chapter 4, can be used both as a proof-of-concept LFA sensor and as a complementary characterisation tool in the kHz–MHz range.

6

Inductive Detection of Magnetic Nanoparticles

In Chapter 4, magnetic nanoparticles are characterised magnetically with conventional characterisation tools, up to 1 kHz and from 1 MHz to 1 GHz. Regardless of the set-up and measurement frequency, manganese ferrite nanoparticles are observed to have higher initial susceptibility and lower anisotropy. The importance of the nanoparticle configuration during charactisation was underscored: innovative measurements were made on nanoparticles suspended in cellulose membranes yielding interesting insights towards LFA design, such as significant increase in initial susceptibility for SPNF in membranes - compared to their powder form. This is mainly attributed to decreased dipolar interactions.

This chapter has a triple objective:

- Proof of concept demonstration of ASSURED inductive nanoparticle detection with a hand-wound copper wire and a simple Colpitts oscillator Printed Circuit Board (PCB).
- Exploring how these simple wound coils, connected to an impedance analyser or PCB reader, can serve as complementary characterisation tools for magnetic nanoparticles LFA-specific membrane dispersions between 1 kHz and 5 MHz. Correlating results with Chapter 4.
- Explore how wound coils can help characterise SPNF in another "realistic" set-ups for bio-application, i.e. in aqueous suspensions. Validate how observed Brownian relaxation completes the identified magnetic properties of the nanoparticle samples.

6.1 "Start with Why"

Part I of this work established the frequency-dependent magnetic susceptibility $\chi'(\omega)$ of superparamagnetic nanoferrites across substrates (powder, cellulose membrane, suspension) and characterisation techniques (SQUID magnetometry, FC-ZFC, ACS, E4991 impedance analysis). The present chapter addresses the integration of these samples into a sensor platform. Section 5.2 motivated the choice of inductive sensing on the grounds of hardware simplicity and compatibility with the ASSURED criteria, and acknowledged the sensitivity trade-off relative to more complex modalities. This section frames the experimental choices made in the present chapter.

Direct link between susceptibility and inductance

The inductance of a coil is proportional to the effective magnetic permeability of the medium within its field volume. The change in inductance upon introduction of a nanoparticle sample is therefore governed by $\chi'(\omega)$, the real part of the AC susceptibility at the operating frequency. This direct proportionality means that the frequency-dependent susceptibility data of Part I yield quantitative expectations for the sensor response without requiring an intermediate physical model. The present chapter tests this link experimentally: measurements with wound coils connected to an impedance analyser or Colpitts oscillator are compared with the susceptibility values obtained by SQUID magnetometry, ACS and E4991 impedance analysis in Chapter 4.

Readout architecture

The readout is based on a Colpitts oscillator whose resonant frequency shifts with the inductance of the sensing coil. This falls in the resonant-frequency-shift category discussed in Section 5.2.3.3, at the simplicity–portability end of the sensitivity–simplicity–portability trade-off identified in the benchmark (Section 5.3). The oscillator's AC excitation field probes the permeability change directly, without requiring a static polarising field.

Nanoparticles in nitrocellulose: a rarely reported configuration

The benchmark of Section 5.3 showed that many detection studies employ micron-scale polymer beads whose magnetic moment per particle is orders of magnitude above that of isolated nanoparticles. Furthermore, the few studies that address LFA substrates (Section 5.4) typically characterise nanoparticles in powder or liquid suspension, not in the porous membrane configuration of the actual assay. Part I showed that dispersing nanoferrites in nitrocellulose membranes significantly increases their initial susceptibility compared to powder form, an effect attributed to decreased dipolar interactions (Chapter 4). The present chapter extends these observations to the inductive sensing regime, providing characterisation data on 8–11 nm core nanoferrites in nitrocellulose in a frequency range (1 kHz to 5 MHz) complementary to the instruments of Chapter 4.

An additional property of inductive transduction that is relevant for LFA is its intrinsic tolerance to the biological matrix. The magnetic permeability contrast between superparamagnetic nanoparticles and any biological or environmental matrix is several orders of magnitude larger than the diamagnetic or paramagnetic background contribution. Changes in analyte conductivity affect eddy-current losses but not the permeability signal, provided the operating frequency remains below the regime where skin-depth effects in the analyte become significant.

Scope of the experimental validation

The benchmark of Section 5.3 showed that direct inductance-change and self-resonant-frequency readers report limits of detection in the microgram range [244, 265], several orders of magnitude above what frequency mixing [3] or GMR arrays [285] achieve. The setup developed in this chapter is not designed to optimise detection limits. Its purpose is twofold: to validate that the susceptibility data from Part I translate into a measurable inductive signal with a simple readout circuit, and to characterise nanoparticle-membrane systems under conditions representative of LFA operation.

6.2 Materials and Methods: Inductive sensing of MNP

The inductive measurements on nitrocellulose membranes (Section 6.3.1) and on 2 mL eppendorfs (Section 6.5) reported in this chapter were performed in collaboration with Nordin Trifiro.

6.2.1 Colpitts Oscillator Design on PCB

6.2.1.1 From inductance to frequency variation

The Colpitts Oscillator is a particular case of the architecture presented in the previous section. It was invented about a hundred years ago by E. H. Colpitts. Its core is an LC resonator, consisting of an inductor placed in parallel with a fixed capacitor. The inherent resonant frequency f of this tank circuit is defined by the inductance (L) and capacitance (C).

$$f = \frac{1}{2\pi\sqrt{LC}} \tag{6.1}$$

A simplified linear correlation exists between the relative change in frequency ($\Delta f/f$) and the relative change in inductance ($\Delta L/L$) in an LC tank circuit. Eq. 6.1 can be rewritten as:

$$d(\ln(f)) = d(-\ln(2\pi)) - d\left(\frac{1}{2}\ln(L)\right) - d\left(\frac{1}{2}\ln(C)\right)$$

$$\frac{df}{f} = -\frac{1}{2}\left(\frac{dL}{L} + \frac{dC}{C}\right)$$

For small measurable changes Δ:

$$\frac{\Delta f}{f} \approx -\frac{1}{2}\left(\frac{\Delta L}{L} + \frac{\Delta C}{C}\right) \tag{6.2}$$

Note that this linear approximation relies on the binomial (first-order Taylor) expansion $(1+x)^{-1/2} \approx 1 - x/2$ for $|x| \ll 1$. For a frequency change of 1%, the

relative error is therefore only 1.5%.

In the membrane measurements reported below, we assume $\Delta C \approx 0$ when membranes loaded with nanoparticles are inserted in L1 or L2. Indeed, the nanoparticle volume fraction within the coil is of order 10^{-4}: even assuming a bulk relative permittivity of several hundred for spinel ferrites, the Lichtenecker mixing rule [244, 295] yields a fractional capacitance change $\Delta C/C$ that is orders of magnitude below the observed $\Delta f/f$. The exact correlation between frequency change and inductance change is then derived from Eqn 6.1 as follows:

$$1 + \frac{\Delta f}{f_0} = \left(1 + \frac{\Delta L}{L_0}\right)^{-1/2} \tag{6.3}$$

Fig. 6.1 represents the typical architecture of a colpitts oscillator. The transfer function is:

$$\frac{v_{out}}{v_{in}} = \frac{g_m R_C}{1 - \omega^2 L C_2 + j\omega R_C (C_1 + C_2 - \omega^2 L C_1 C_2)}. \tag{6.4}$$

In order to have a sustained oscillation, the two conditions given by the Barkhausen criterion must be met simultaneously. Denoting the loop gain as $T(j\omega) = \frac{v_{out}}{v_{in}}$, these conditions are:

1. **Phase condition:** the total phase shift around the loop must be a multiple of 2π, i.e. $\arg\{T(j\omega_0)\} = 0$. This is equivalent to requiring that the imaginary part of the transfer function vanishes;
2. **Gain condition:** the loop gain magnitude must equal unity, i.e. $|T(j\omega_0)| \geq 1$, so that the signal is sustained (or grows until limited by nonlinearities).

The first condition determines the oscillation frequency ω_0. Setting the imaginary part of the denominator to zero:

$$\Im\left\{\frac{v_{out}}{v_{in}}\right\} = R_C(C_1 + C_2 - \omega^2 L C_1 C_2) = 0, \tag{6.5}$$

$$\omega_0 = \sqrt{\frac{C_1 + C_2}{L C_1 C_2}}. \tag{6.6}$$

This is coherent with Eq. 6.1 assuming that the total capacitance is the result of C_1 and C_2 in series: $C = \sqrt{\frac{C_1 C_2}{C_1 + C_2}}$. Unless explicitly stated otherwise, in this work C_1 and C_2 will always be identical.

6.2.1.2 Circuit Design

The component values used in the Colpitts oscillator circuit are listed in Table 6.1. The capacitors $C_1 = C_2$ are swept from 68 pF to 6.6 nF in order to vary the oscillation frequency. Frequency is then counted with a Teensy 4.1 microcontroller. The

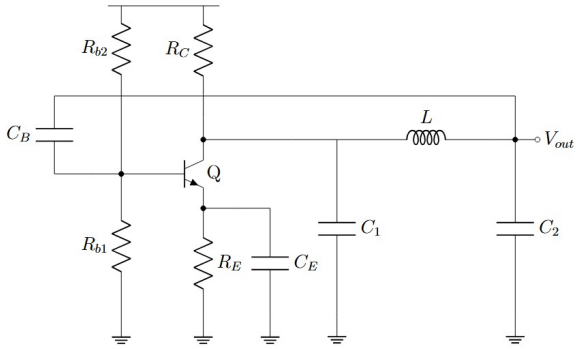


Fig. 6.1 From [296]: standard architecture of a Colpitts Oscillator.

Component	Value	Role	Type
C_E	1 µF	Emitter bypass capacitor	Fixed
R_E	1 kΩ	Emitter resistor	Fixed
R_C	2.2 kΩ	Collector resistor	Fixed
R_{b1}, R_{b2}	50, 100 kΩ	Base voltage divider	Fixed
BJT	BC547	NPN transistor	Fixed
L	See Table 6.2	Tank inductor	Variable
$C_1 = C_2$	68 pF – 6.6 nF	Tank capacitors	Variable

Table 6.1 Component values of the Colpitts oscillator circuit. Fixed components define the biasing and operating point; variable components set the oscillation frequency.

microcontroller uses its hardware quad timers to count rising edges of the oscillator output over a 1 s gate time (100 accumulation intervals of 10 ms each). The accumulated count equals the frequency in hertz, yielding one reading per second with a resolution of 1 Hz. The design of the PCB is not optimal. Since the invention of the Colpitts Oscillator, many variations have been proposed [297, 298], but in this work the basic circuit was used. The principal sources of this drift are: (i) the temperature sensitivity of the BJT operating point, (ii) the temperature coefficients of the discrete passive components (C_1, C_2, R_C, R_E), and (iii) the absence of oscillation amplitude regulation, which allows the oscillation amplitude to vary with environmental conditions and thereby pull the resonant frequency.

6.2.2 Coils

In this work, two main inductive sensors with respective interfaces are used: the

1. A custom-made Colpitts Oscillator interface, offering flexibility in choice of both capacitances and hand-wound inductances (cf infra). This offers frequency tunability, enabling the nanoparticle susceptibility to be probed between 500 kHz and 10 MHz within a single hardware platform. Basic electronic interface with little to no optimisation, thus a significant noise.
2. The off-the-shelf LDC1614EVM (Texas Instruments, Dallas, USA) with a planar coil integrated on the PCB, operating at approximately 2 MHz by default. Optimised electronics, lower noise-floor, better stability. This coil is of interest for two reasons: it serves both as benchmark for sensitivity and allows to compare another sensor geometry.

The planar vs tubular geometry offers the advantage that nanoparticles can be excited parallel and transversal to the NC sheet: this is further leveraged in Section 6.4.

6.2.2.1 Wound Coils for Colpitts Oscillator

The supports on which the inductor coils are wound are shown in Fig. 6.2. These are 3D-printed with Clear V4 resin from FormLabs. Two morphologies of coils

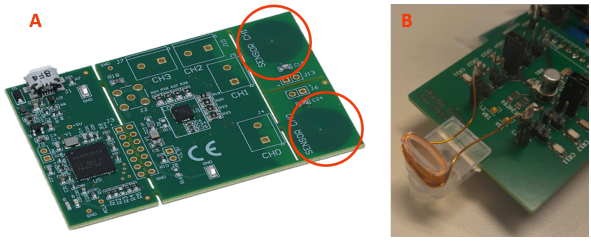


Fig. 6.2 Planar Coil (A) connected to LDC and Wound coil L1 around printed Support (B) connected to Colpitts Oscillator

were used with properties listed in Table 6.2:

1. **L1 and L2:** elliptical cross-section (minor and major axis: 2 mm and 10 mm) to ease the introduction of the paper sample on which the nanoparticles are deposited, while minimizing the void at the center of the coil. This enables us to maximize the influence of the nanoparticles on the value of the inductance, and thus increase the signal amplitude per unit mass. L1 is illustrated on Fig. 6.2 B.
2. **LE1 and LE2:** were designed to contain 2 mL eppendorfs. They have been wound around the eppendorf over 1 cm height and have a perfectly circular

	N	d [mm]	L [µH]	C [pF]	SRF [MHz]	cross-section
L1	9	0.48	0.49	0.12	670	ellips (2 × 10 mm)
L2	18	0.48	1.91	5.4	49.4	ellips (2 × 10 mm)
LE1	27	0.48	5.72	21	14	circle ⌀10.3 mm
LE2	80	0.48	21.8	28.9	6.46	circle ⌀10.3 mm

Table 6.2 Main properties of coils used in this chapter: number of turns, wire diameter, inductance, capacitance, SRF

cross-section. Their windings have been fixed with glue and the inductances are positioned in a wooden holder, allowing for the eppendorfs to be inserted and removed easily without moving the inductance.

Depending on the exact configuration of the oscillator, the magnetic field at the center of the coil is estimated at 80 – 120 A/m (0.10 – 0.15 mT), based on the oscillation current amplitude obtained from LTspice transient simulations of the Colpitts circuit. Table 6.2 contains the main properties of the coils used in this chapter. Stray capacitance is deduced from the SRF measured with E4991 impedance analyzer.

6.2.2.2 Off-the-shelf Benchmark: TI LDC 1614 EVM

An LDC 1614 'inductance to digital converter' EVM board was purchased from Texas Instruments (Dallas, USA). Two identical 19.4 μH planar coils with 64 turns each (32 turns per layer, 2-layer PCB, 14 mm diameter) are implemented on this board, each connected in parallel with a 330 pF capacitor to form the LC tank. From Eq. 6.1, the resulting resonant frequency is approximately 2 MHz. The LDC1614 derives the external LC tank with a programmable current source and measures the resonant frequency by counting sensor oscillation cycles against a 43 MHz reference clock. Two features[1] of the LDC1614 further reduce the noise floor compared to the Colpitts Oscillator:

- **Auto-calibrated sensor drive.** The device dynamically adjusts its drive current (programmable from 16 μA to 1.56 mA) to maintain a constant oscillation amplitude. This closed-loop amplitude control prevents the frequency-pulling effects that arise in the Colpitts oscillator when the transistor operating point shifts.
- **Integrated analog front-end.** The LDC1614 combines the oscillator drive, amplitude regulation and frequency digitisation on a single die. On-chip

[1] A third feature is the second identical planar coil on the PCB connected to a matched channel, which allows differential detection: common-mode drift from temperature, supply voltage variations and component aging is rejected by computing the channel difference. For the sake of consistence with the Colpitts Oscillator, we will only consider the inductance change caused by analysed samples in one coil.

components are thermally matched and factory-trimmed, reducing the sensitivity to temperature and component tolerances that affect the discrete Colpitts circuit.

While the planar coil geometry determines the signal amplitude ($\Delta L/L$ per μg), the readout electronics determine the noise floor, the minimum detectable $\Delta L/L$, and therefore the LoD.

6.2.3 Measurement Protocol: MNP in Nitrocellulose

6.2.3.1 NP samples in NC

The samples used in this section are on a 160 µm thick NC sheet (CN95, Sartorius, Germany), backed with polyester ($\approx$ 100 µm thick). This nitrocellulose is a common substrate for commercial LFA [6]. On NC squares 7x7 mm (unless different dimensions are specifically mentioned), nanoparticles from a mother suspension with known concentration (by ICP measurements made in suspension) were pipeted. Care was taken to avoid overflow. When several pipeted volumes were required to obtain the desired mass, an intermediate drying time of at least 20 minutes was implemented between successive depositions to reduce the coffee ring effect. After the final deposition, samples were dried at ambient conditions for at least 90 minutes before measurement. All used nanoparticles are made with CP, unless stated otherwise, for two reasons: (1) available amount was higher due to higher synthesis yield and (2) suspension is already in water, required to leave NC unaffected.

As a reminder, Table 6.3 displays the nanoparticle median diameters $\tilde{D}_{\mathrm{TEM}}$ (from Table 3.5) as well as the bulk magnetocrystalline anisotropy constants K_{m} and the specific saturation magnetisation $\sigma_{M,s}$ at room temperature (from Table 4.3).

Composition	**Sample**	$\tilde{D}_{\mathrm{TEM}}$ **(nm)**	$\sigma_{M,s}\left(\frac{\mathrm{Am^2}}{\mathrm{kg}}\right)$	$K_{\mathrm{m}}\left(\frac{\times 10^4 \mathrm{J}}{\mathrm{m^3}}\right)$
$MnFe_2O_4$	Mn–CP2	*9.7*	80	0.3
	Mn–CP3	*8.0*		
$CoFe_2O_4$	Co–CP1	5.1 / 13.4*	80	20
Fe_3O_4	Fe–CP1	*9.6*	92	1.1

Table 6.3 Bulk magnetic properties (300 K) and median TEM diameters of nanoparticle samples used in the inductive sensing experiments. Italic data are derived from mean and γ assuming a lognormal distribution. * Note that Co–CP1 has a bimodal size distribution: cf Table 3.5.

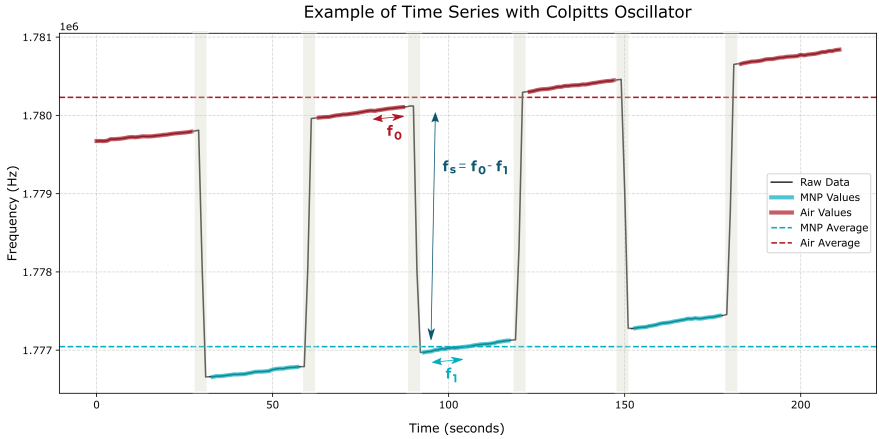


Fig. 6.3 Example of timeseries for measurement of nanoparticles in nitrocellulose

6.2.3.2 Measurement process

Fig. 6.3 represents a typical measurement for one sample, which takes 210 s in total. To detect changes in inductance caused by nanoparticles within a coil connected to the Colpitts Oscillator, the following procedure is applied:

- Measure of the empty ("air-filled") inductance for 30 s. Introduction of the NC sample and keep it for 30 s. Repeated 3 times. End by 30 s of empty inductance.
- Consider a "dead time" of 2 seconds before the transition and 2 seconds after the transition, represented by the gray zones in Fig. 6.3. This window was determined empirically to account for the manual insertion and retraction of the sample, which does not occur instantaneously, as well as for the subsequent mechanical and electrical stabilisation of the oscillator.
- Consider the average frequency f_0 over the 5 seconds immediately before each dead time, and the average frequency f_1 over the 5 seconds immediately after each dead time. The 5-second window represents a trade-off between averaging over enough oscillation cycles to suppress short-term noise and keeping the window short enough to limit the influence of oscillator drift. We consider that the frequency change induced by the insertion or removal of the sample is $f_s = |\Delta(f_0, f_1)|$.
- Over one sequence, we get 6 different values for f_s. The mean $f_{s,m}$ and standard deviation $\sigma(f_s)$ of their absolute values are considered to obtain the frequency change (and its distribution) caused by the sample.

- A measurement is considered significant when $\Delta f_{s,m} > 3 \cdot \sigma(f_s)$, i.e. when the mean frequency shift exceeds three times its own standard deviation across repetitions. This ensures that the observed signal is repeatable rather than dominated by measurement scatter.

To obtain the relative frequency change $\Delta f / f_0$ induced by the sample, we consider the average frequency for the empty coil (excluding dead times) over the 210 seconds $f_{air,avg}$, corresponding to the red dotted line in Fig. 6.3.

$$\Delta f / f_0 = \frac{\Delta f_{s,m}}{f_{air,avg}} \tag{6.7}$$

$$\sigma(\Delta f / f_0) = \frac{\sigma(f_s)}{f_{air,avg}} \tag{6.8}$$

Considering relative frequency change allows to compare the impact of a sample throughout different measurements: varying $C_1 = C_2$ in the Colpitts analyser changes the initial oscillation frequency f_0, and the LDC1614 oscillates at approximately 2 MHz. This metric is only valid when the frequency changes are "small enough" (cf Eq. 6.2): all samples induce $\Delta f / f_0$ smaller than 1%, which justifies the use of this linear approximation throughout this work.

Justification for considering individual frequency changes: Considering each insertion or removal frequency change individually, rather than against a single fixed baseline, isolates the differential measurement from long-term oscillator drift. To verify this, the air-filled segments of 48 measurement files acquired on the same day with coil L2 (six nanoparticle samples across eight $C_1 = C_2$ configurations spanning 1.0 to 6.2 MHz) were analysed. Transitions between air-filled and sample-loaded states were identified from abrupt frequency jumps (> 50 Hz between consecutive 1 s readings), with 2 s masked on each side of every transition. Within individual air segments (≈ 26 s), the standard deviation of the 1 s frequency readings, σ_w, stays below 45 Hz across all configurations. Over the full 210 s measurement however, the mean frequency of successive air segments drifts by tens to hundreds of Hz, as visible in Fig. 6.3. This drift exceeds σ_w by an order of magnitude or more in every configuration tested. The differential protocol therefore operates within the regime of short-term stability rather than against a drifting baseline.

6.3 Results: linearity within working range

6.3.1 Sensitivity: Frequency change induced by known MNP mass

6.3.1.1 Colpitts Oscillator Sensitivity

Fig. 6.4 displays the relative frequency change defined in Eqn. 6.7, induced by 4 samples made by coprecipitation: Fe - CP1, Mn - CP2, Mn - CP3, Co - CP1. Note

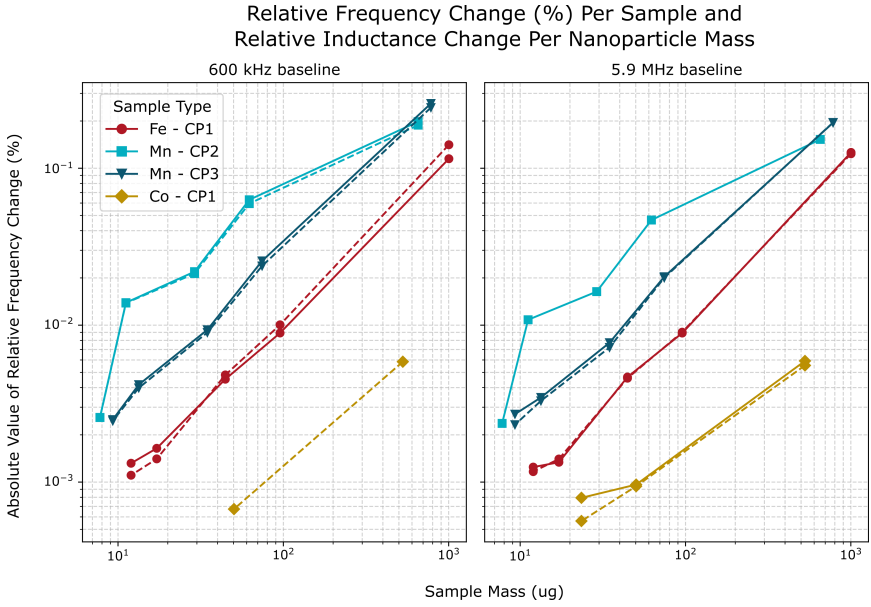


Fig. 6.4 Variation of sensing signal over mass, with L1 on the Colpitts oscillator, at 600 kHz (left) and 5.9 MHz (right). Dashed lines represent duplicate measurements. Missing datapoints for cobalt are due to insufficient SNR.

that an increase in inductance leads to a decrease in frequency, which is why the ordinate displays absolute values.

Table 6.4 summarizes sensitivity and relative sensitivity per working frequency. Assuming linearisation for sensitivity induces a fitting error which is quantified by R^2. The fitted slope was forced to pass through the origin. The corresponding relative inductance change has been derived with Eq. 6.3, assuming constant capacitance, which is not totally correct: it can be interpreted as an upper bound of inductance variation. While no finer distributed range of masses was tested to determine the exact limit of detection, one should observe that 8.6 μg is detected with $S_r > 3 \cdot \sigma(S_r)$ and in a repeatable manner for Mn–CP3. On the other hand, 11.5 μg was the limit for cobalt ferrite at 6MHz. The stability of the oscillator being lower at lower frequency, only 14 μg was the minimum detection signal for f_0 = 603 kHz.

$\mathbf{f_0}$	**Sample**	Sensitivity (Hz/μg)	Rel. sens. (%/μg)	R^2	$\Delta L/L$ (%/μg)
603 kHz	Mn – CP2	1.819	3.03×10^{-4}	0.9151	6.06×10^{-4}
	Mn – CP3	1.929	3.21×10^{-4}	0.9999	6.42×10^{-4}
	Fe – CP1	0.764	1.27×10^{-4}	0.9993	2.54×10^{-4}
	Co – CP1	0.067	1.11×10^{-5}	0.9990	2.22×10^{-5}
5.9 MHz	Mn – CP2	14.354	2.39×10^{-4}	0.9230	4.78×10^{-4}
	Mn – CP3	15.020	2.50×10^{-4}	0.9999	5.00×10^{-4}
	Fe – CP1	7.453	1.24×10^{-4}	0.9991	2.48×10^{-4}
	Co – CP1	0.657	1.10×10^{-5}	0.9787	2.20×10^{-5}

Table 6.4 Sensitivity analysis for Colpitts oscillator coil measurements with L1. All linear fits are forced through the origin. Each entry averages over both available measurement dates per frequency. The relative inductance change $\Delta L/L$ is derived from the relative sensitivity by inverting Eq. 6.3.

Linearity of the frequency change as a function of mass is validated at both 600 kHz and 6 MHz. In Chapter 4 it was suggested, based on initial magnetisation curves, that nanoparticle density within a membrane might affect initial susceptibility due to interactions. The effects of these interactions seem below the measurability of this set-up: linear fitting is reliable for Fe–CP1 and Mn–CP3. However, a higher granularity in measured masses is required to confirm this. Note that Mn, CP2 exhibits a markedly lower R^2 ($\sim$ 0.92) compared to the other samples ($R^2 > 0.99$), we assume some error occurred during pipetting, affecting the normalisation per iron mass. Comparing with the susceptibilities summarized in

Table 4.14, one can observe:

1. Mn–CP2 & Mn–CP3 cause the largest inductance variations, consistent with the fact that they have the highest susceptibilities. At 603 kHz the Mn–CP3/Fe–CP1 sensitivity ratio is 2.5; at 5.9 MHz it is 2.0 (Table 6.4). These ratios are consistent with the initial susceptibility ratio $\chi_i(\text{Mn–CP3})/\chi_i(\text{Fe–CP1}) = 14.8/6.36 \approx 2.3$ obtained by SQUID magnetometry (Subsection 4.3.2.3, Table 4.14) and with the Debye-fitted static susceptibility ratio $33.9/11.3 \approx 3.0$ from E4991 measurements (Table 4.13).
2. The relative sensitivity is lower at 603 kHz than at 5.9 MHz for both Mn–CP and Fe–CP samples. Given the decade change in frequency, it might be related to the order-of-magnitude decrease in initial susceptibility observed in the powder forms, Fig. 4.16. Indeed, susceptibility of Mn–CP3 shows a stronger decay-rate than Fe–CP1, and the sensitivity decrease is strongest for these samples. No one-on-one comparison on the slopes can be made given that the set-up is not the same: interactions affect the susceptibility differently in powder and in membrane, but the qualitative consisency between Fe–CP1 and Mn–CP3 is encouraging.
3. Co–CP1 had higher initial susceptibility (Table 4.14) than Fe–CP1 due to total demagnetization in initial magnetisation measurements. Here no demagnetization was done: Co–CP1 samples generate little inductance change given their high magnetocrystalline anisotropy (confirmed by coercivity observed in Section 4.3).

It was argued in Subsection 6.2 that the capacitance contribution $\Delta C/C$ is negligible for these nanoparticle loadings on nitrocellulose: this hypothesis is not rejected by the observations made here: sensitivity seems mainly correlated with magnetic susceptibility. Note that the operation frequencies are at least two decades below the SRF of the coil (cf Table 6.2): operating near SRF-range might make changes in stray capacitance more dominant. The obtained sensitivity values can be compared with the benchmark in Table 5.1.

- Richardson et al. [265] reported a detection limit of 1.2 μg Fe with a PLL oscillator at 529 kHz using 2.8 μm beads, achieving an absolute sensitivity of $\sim$3 Hz/μg Fe, i.e. a relative sensitivity of $\sim 5.7 \times 10^{-4}$ %/μg Fe.

- Marques-Fernandez et al. [244] later achieved 5821 Hz/μg Fe_3O_4 with a 150 μm planar coil operating at a baseline SRF of $\sim$50 MHz on LFA strips. While this represents a $\times$1940 improvement in absolute sensitivity, it combines two effects: the higher operating frequency and the near-field coupling of the planar geometry. The relative sensitivity is $\sim 1.16 \times 10^{-2}$ %/μg Fe_3O_4, i.e. $\sim 1.6 \times 10^{-2}$ %/μg Fe (accounting for the 72.4 wt% iron content of magnetite).

The Colpitts oscillator with wound coil L1 at 603 kHz yields a relative sensitivity of 3.21×10^{-4} %/μg Fe for Mn–CP3 (Table 6.4), comparable to Richardson's value despite using sub-10 nm nanoparticle cores rather than 2.8 μm polymer beads. It remains roughly a factor of 50 below Marques-Fernandez's result, a gap attributable to the planar coil geometry and higher operating frequency of the latter.

6.3.1.2 TI LDC1614 Planar Coil Sensitivity

Fig. 6.5 shows similar measurements made with the planar coils on the LDC, as benchmark.

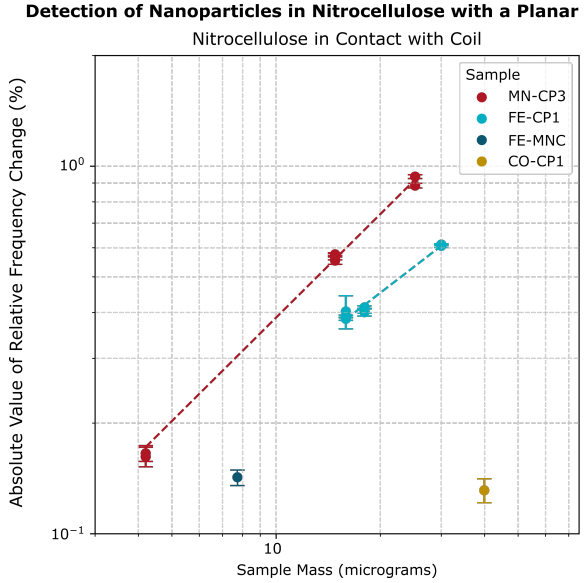


Fig. 6.5 Inductance changes induced by different ferrite samples in nitrocellulose membranes, deposited on the planar LDC coil.

Sample	Sensitivity (Hz/μg)	Rel. sensitivity (%/μg)	R^2	Avg. $\Delta L/L$ (%/μg)
Mn – CP3	1117.0	3.72×10^{-2}	0.9967	7.78×10^{-2}
Fe – CP1	587.3	1.96×10^{-2}	0.9846	3.82×10^{-2}

Table 6.5 Sensitivity analysis for the planar coil at 2 MHz baseline. Linear fits forced through the origin.

Again, the frequency change induced by iron oxide is half as high as for manganese ferrite. Note that Fe–CP1 has only two data points (and the origin), so the R^2 value has limited statistical meaning. Co–CP1 and MNC give little signal: in Section 4.3 we demonstrated that the former have coercivity corresponding to 20 mT for the former and 5 mT for the latter: this is much larger than the ≈ 0.15 mT (corresponding to 120 A/m) amplitude applied during the measurement.

For Mn–CP3, the planar coil connected to the TI LDC1614 yields an absolute sensitivity of 1117 Hz/μg at 2 MHz, compared to 15.0 Hz/μg for the wound coil L1 on the Colpitts oscillator at 5.9 MHz. The relative sensitivity, which factors out the baseline frequency, differs by a factor of ≈ 116 for Mn–CP3. This is mainly attributed to the coil shape. Indeed, the inductance change induced scales with the fraction of the coil's magnetic energy that overlaps with the sample volume. Richardson et al. showed that minimising the dead space of the coil, so that a larger fraction of the electromagnetic field passes through the sample, is essential for sensitivity [265]. In the wound coil L1 (Table 6.2), the 160 μm thick membrane occupies only a small fraction of the coil's internal volume, leaving most of the magnetic energy in air that contains no nanoparticles. By contrast, a planar spiral concentrates its magnetic field near the coil surface rather than inside a bore [271, 299]. The nitrocellulose membrane (7×10 mm) is placed directly on the 14 mm diameter planar coil, covering ≈ 45 % of its surface area, and the SPNF layer sits in direct proximity to the conductor traces where the field intensity is highest (membrane thickness is ≈ 160 μm). Barnett et al. confirmed that this proximity is critical, reporting that the field from surface-mount coils extends only a few mm and using a spring mechanism to press the sample against the coil surface [276]. Salvador et al. further confirmed that adapting the coil footprint to match the sample geometry maximises the filling factor [97]. This probably explains the substantially higher relative sensitivity of the planar configuration.

6.3.2 Results: Constant signal ratio with varying Oscillation Frequency

$C_1 = C_2$	L1	L2
270 pF	17.7 MHz	11.7 MHz
470 pF	14.0 MHz	8.20 MHz
1 nF	10.0 MHz	–
4 nF	5.33 MHz	2.85 MHz

Table 6.6 Oscillation frequencies for L1 and L2 coils at different capacitances for C_1 and C_2 (cf Fig. 6.1).

Table 6.7 summarizes the dilutions and corresponding masses for the samples

used in this section. Coils L1 and L2 (0.49 and 1.91 uH respectively) were used and combined with the capacitances listed in Table 6.6, allowing for a sweep over f_0 between 2.8 MHz and 19 MHz. The measurement was executed according to the protocol described in 6.2.3.2. For Mn3 samples the signal of every mass dilution is plotted in Fig. 6.6. The response over frequency is not identical for L1 and L2. This is because varying capacitances while keeping L constant varies the total L/C ratio of the oscillator, and as a consequence a same sample does not induce the same relative changes frequency: thus the sensor has a varying "operating point sensitivity" varying over frequency, independently of sample variations over frequency (e.g. decay in χ' as expected by Debye model for SPM samples). When L1 is connected to the Colpitts oscillator, its operating-point sensitivity is more stable in the swept frequency range (i.e. when varying capacitances connected in the Colpi tts LC tank), likely because its SRF is higher.

Mn – CP2		**Mn – CP3**		**Fe – CP1**	
Mass (μg)	**Name**	**Mass** (μg)	**Name**	**Mass** (μg)	**Name**
653.2	Mn20	780.9	Mn30	1002	Fe10
62.21	Mn21	74.37	Mn31	95.51	Fe11
		34.71	Mn32		
		13.35	Mn33		

Table 6.7 Samples used for studying behaviour of nitrocellulose samples over frequency.

To isolate the frequency dependence of the sensor's response, a normalized differential signal ratio was calculated for Mn–CP2, Mn–CP3 and Fe–CP1. Using Mn21, Mn31 and Fe11 as references, the relative signal $D(f)$ added by samples Mn20, Mn30 and Fe10 was determined using the relationship:

$$D(f) = \frac{\Delta f_{\text{sample}} - \Delta f_{\text{ref}}}{\Delta f_{\text{ref}}} \tag{6.9}$$

where Δf_{sample} and Δf_{ref} represent the relative frequency shifts induced by the mother solution and its corresponding first dilution, respectively. This metric captures the proportional excess signal provided by the higher concentration relative to the reference baseline. To isolate the influence of the operating frequency from the absolute signal magnitude, the values were normalized by the mean response at the lowest measured frequency, f_0. The resulting normalized ratio, $D_{\text{norm}}(f)$, is defined as:

$$D_{\text{norm}}(f) = \frac{\bar{D}(f)}{\bar{D}(f_0)} \tag{6.10}$$

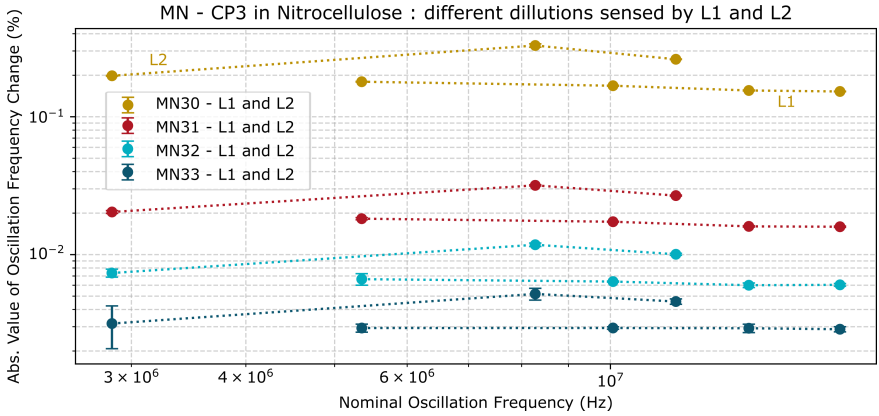


Fig. 6.6 Mn3 samples measured (masses indicated in Table 6.7) by inductances L1 (between approx 5 and 11 MHz) and L2 (between approx 3 and 10 MHz). One trendline per inductance. Errorbars represent standard deviation as defined in Eq. 6.8.

where $\bar{D}(f)$ is the mean differential ratio across 5 measurements per operating frequency. Fig. 6.7 shows that $D_{\text{norm}}(f)$ remains within 10% of unity for Mn–CP2, Fe–CP1 and Co–CP1 across the 3–19 MHz range despite the different operating point sensitivities and the different $\chi'(f)$ profiles of each nanoparticle type. Between 5 and 10.2 MHz, measurements alternate between L1 and L2 (as shown in Fig. 6.6). This indicates that the frequency-dependent factors, both the oscillator's transduction gain ("operating point sensitivity") and the nanoparticle susceptibility, affect sample and reference signals proportionally, so that they cancel in the differential ratio - even when using different inductors. In practice, this indicates that the concentration-response relationship would be independent of operating frequency: a calibration curve obtained at one frequency could be applied at another without systematic bias.

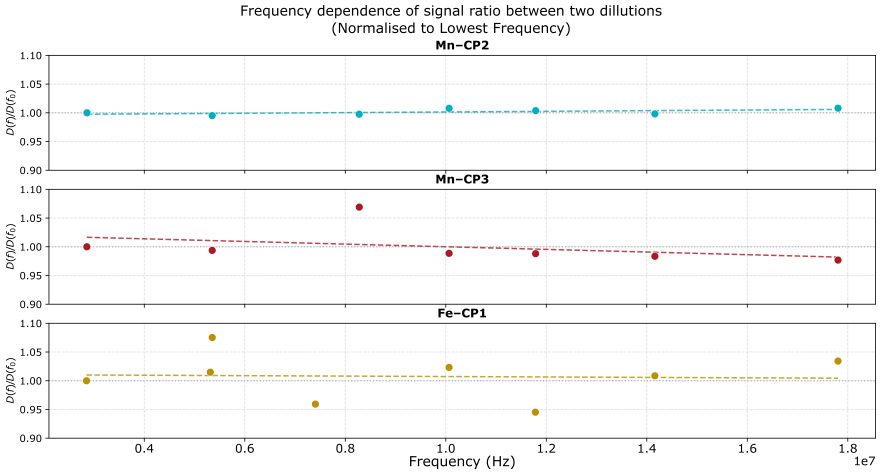


Fig. 6.7 $D_{\text{norm}}(f)$ calculated according to Eq. 6.10 for CP samples in NC membranes measured with the Colpitts oscillator (overlap of L1 and L2). Concentration-response relationship seems independent of operating frequency and used coil.

Section summary

Nanoparticle samples (Mn–CP2, Mn–CP3, Fe–CP1, Co–CP1) deposited on nitrocellulose membranes were measured with wound coils (600 kHz to 19 MHz) and a planar coil (2 MHz) interfaced with a PCB. The section establishes the linearity, sensitivity and frequency behaviour of the inductive detection signal.

Consolidated conclusions:

- The frequency change induced by nanoparticles is linear with mass at both 600 kHz and 5.9 MHz ($R^2 > 0.99$ for Fe–CP1 and Mn–CP3, Fig. 6.4). All measured samples induce $\Delta f / f_0 < 1\%$, validating the linear approximation of Eq. 6.2 correlating frequency change with inductance change throughout this work.
- The sensitivity ranking Mn–CP2 $\approx$ Mn–CP3 $>$ Fe–CP1 $\gg$ Co–CP1 is consistent with the initial susceptibility hierarchy from SQUID magnetometry (Table 4.14). The Mn–CP3 / Fe–CP1 sensitivity ratio (2.0–2.5, Table 6.4) matches the initial susceptibility ratio ($\chi_i = 14.8/6.36 \approx 2.3$) and the Debye-fitted static susceptibility ratio from E4991 measurements ($33.9/11.3 \approx 3.0$, Table 4.13). This indicates that the inductive signal is a reliable proxy for real magnetic susceptibility.
- Co–CP1 generates the weakest signal despite exhibiting the highest initial susceptibility when fully demagnetised (Table 4.14). In the absence of prior demagnetisation and with the low excitation field of the oscillator (≈ 0.15 mT), the

high coercivity of cobalt ferrite prevents significant magnetisation change. This makes cobalt ferrite unsuitable for inductive LFA sensing under low-field excitation conditions.

- The planar coil yields a relative sensitivity approximately 116 times higher than the wound coil for Mn–CP3 (Table 6.5). This is attributed to the near-field concentration of the planar geometry and the higher fraction of the magnetic energy volume overlapping with the nanoparticle layer.

Observed trends requiring further investigation:

- The normalised differential signal $D_{\mathrm{norm}}(f)$ remains within 10% of unity over the studied frequency decade (3–19 MHz) for all tested nanoparticle types (Fig. 6.7), including measurements alternating between two wound coils. Operating-point sensitivity and nanoparticle susceptibility affect sample and reference signals proportionally: a calibration obtained at one frequency could probably be applied at another without systematic bias.

- Concentration-dependent changes in susceptibility, attributed to dipolar interactions in Section 4.3, are below the detection threshold of the used sensors. This does not exclude interactions-effects but indicates that they are unresolvable with the current sensitivity and the few masses that were analysed.

- The assumption $\Delta C/C \approx 0$ for membrane samples, required to correlate measured frequency changes with susceptibility changes (Eq. 6.2), is supported by the correlation between signal strength and magnetic susceptibility. However, this assumption may break down when operating near the SRF of the coil, where stray capacitance contributions become more significant. This is especially true for the planar coil, where nanoparticles on the coil surface would have higher impact on stray capacitance.

Perspectives:

- The demonstrated linearity and the frequency independence of the calibration ratio are prerequisites for quantitative LFA sensing. Together, they support the design of a single-frequency calibration protocol applicable across the operating range of the Colpitts oscillator.

- The sensitivity advantage of the planar geometry (factor ≈ 116) motivates adapting the coil footprint to match the LFA test-line dimensions, as proposed by Salvador et al. [97], in order to maximise the filling factor.

- While deriving relative values of susceptibilities was possible, deriving absolute susceptibility values remains out of reach: the non-uniform distribution of nanoparticles within the coil cavity (due to the flat nature of nitrocellulose) or over the coil surface (due to random distribution of MNP on the nitrocellulose fibers, and coffee ring effect) invalidates effective medium approximations. Furthermore the frequency dependence of permittivity has not been characterised for these samples. These limitations are revisited in Section 6.5, where homogeneous filling conditions of a coil are met by winding it around filled eppendorf.

6.4 EA orientation within Nitrocellulose

In practical applications, MNP can be subjected to DC magnetic fields of several thousands of Oersteds for motion, concentration or transduction purposes. When they are free to rotate, this results in an alignment of their EA by Brownian rotation [300]. Theoretical models are insufficient to fully predict their magnetic response in complex biological systems due to surface effects and clustering [50]. The effects of MNP orientation have mainly been studied for hyperthermia applications. It was found that the exposure of a group of magnetite SPION within a cell-like environment creates chain-like structures, affecting the shape anisotropy and the relaxation time [301]. The imaginary susceptibility is increased, resulting in more efficient heat dissipation [302]. However, the effects of nanoparticle pre-orientation on the real part of complex susceptibility are less investigated but equally important in inductive sensing applications. Martin et al. [18] found through simulation that when the EA were oriented parallel to the sensing field, Zeeman energy and anisotropy contributions cooperate, resulting in a directional susceptibility increased with roughly 10 %. When EA were transverse to sensing field, susceptibility was decreased by roughly 10 %. In the experiments reported in this section, a similar symmetry has been observed.

6.4.1 Pre-Orientating EA: Materials and Methods

In this experiment, we study how EA alignment affects the directional susceptibility and can be used to improve sensor sensitivity for inductive nanoparticle detection in porous substrates. MNP are dispensed on nitrocellulose membranes, mimicking magnetic LFA, in the absence or presence of an external static magnetic field during the drying process (i.e. at least 90 min after sample is applied).

- In the absence of such a drying field, the MNP are shown to have randomly distributed EA.
- Conversely, when the drying occurs under a static magnetic field $\overline{H_z^D}$, the nanoparticles experience a torque that reorients their EA along the direction of the external field (Brownian motion). Upon completion of the drying process, the MNP become immobilized within the nitrocellulose matrix, preserving the alignment of their EA.

As summarized in Fig. 6.8, we assess the consequences for inductive sensing with planar and tubular coils, which generate an excitation field respectively parallel ($\overline{H_z^E}$) and orthogonal ($\overline{H_y^E}$) to the external field imposed during drying.

Sample preparation

Three types of MNP with varying magnetocrystalline anisotropies are studied: 10.1 nm magnetite Fe_3O_4 (Fe–CP1), 8.9 nm $MnFe_2O_4$ (Mn–CP3) and 11.1 nm

$CoFe_2O_4$ (Co–CP1).

Square sample of 7x7 mm were cut and volumes of 5.3 μl of different nanoparticle suspensions were pipetted onto them resulting in the different SPN masses in Fig. 6.10. This volume was chosen to avoid the coffee ring effect (excessive nanoparticle accumulation on the borders). Within 10 seconds after the liquid was applied, the square was either kept in a Petri dish ('no field drying'), or put in a 500 mT C-core magnet ('field drying'), as represented by the table columns in Fig. 6.8. Drying (with or without field) was done for at least 90 minutes.

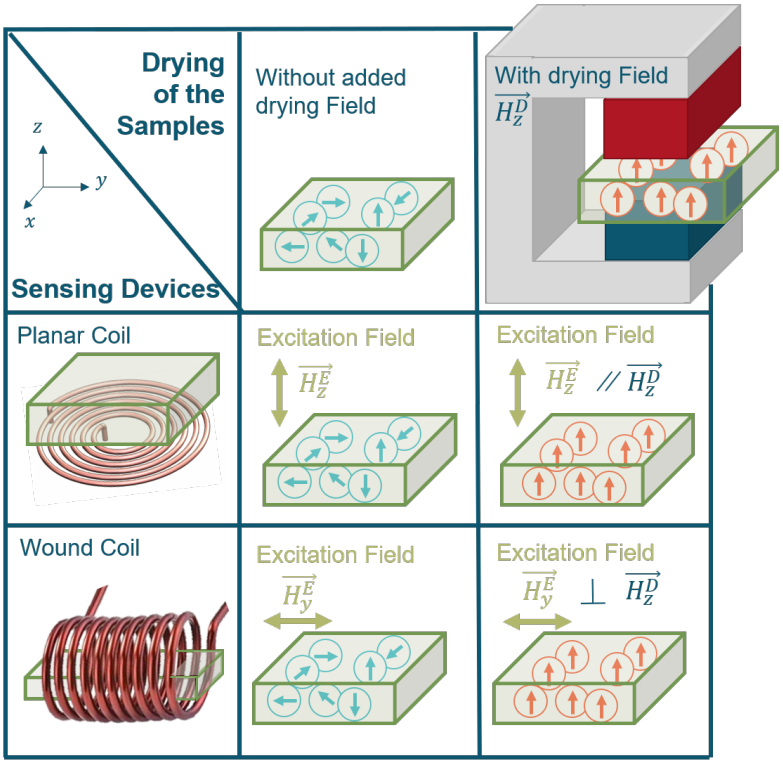


Fig. 6.8 Nanoparticles within nitrocellulose squares are either dried without or with external magnetic field, generated by a C-magnet of 0.5 T resulting in a non-arbitrary orientation of the easy axis. They are then measured in both a planar and wound coil. For the samples dried under field, this results in an excitation that is respectively parallel or transverse to the easy axis orientation. (Drawing not at scale)

Measurement

The sensors were sensed with two different coils: the L2 "tubular" coil connected to the Colpitts oscillator and the planar coil connected to the TI LDC (cf supra). In the former, sensing field is parallel to the paper and thus transversal to the drying field. In the latter, the sensing field is transversal to the paper plane and thus parallel with the drying field. Samples were inserted in the wound coil or positioned on the planar coil in a repeatable way. Each sample is added and removed at least eight times with a 30-seconds interval. As illustrated by the rows of Fig. 6.8, the samples were measured by two types of inductors with different conditioning chains. The measurement process corresponds to the description in Subsection 6.2.3.2.

6.4.2 Results: Pre-orienting EA improves inductive sensing

Agglomeration: Since a detailed study of clustering dynamics of MNP within membranes is not found at the start of this work, Fe_3O_4 MNP (Fe–Comm) were suspended within a glass fiber membrane, both without and with external field. Although diameter ($\tilde{D}_{\mathrm{TEM}}$ = 130 nm) is larger than the critical SPM diameter for magnetite (Fig. 2.3), their coercivity is low enough and the external drying field high enough, to serve as an informative approximation. SEM analysis on Fig. 6.9 reveals morphological differences between drying without and with static magnetic field. In the former, clusters are smaller and tend to be elongated along the fiber. In the latter, clusters are larger and can be orthogonal to the fiber direction. This cluster formation is similar to what was previously observed in agarose [301], suggesting that the clustering dynamics and the rotational dynamics induced by the external field, occur simultaneously.

SPNF types: Fig. 6.10 shows the relative change in frequency expressed in % per nanoparticle mg for samples respectively measured with the planar and the wound coil. The wound coil combined with the Colpitts oscillator has too low SNR for the 4.2 μg $MnFe_2O_4$ samples. First, a clear distinction exists between the signal amplitude caused by the three ferrite compositions, no matter the magnetisation or coil, which can be explained by the magnetocrystalline anisotropy constant K_{m} in Table 6.3. For similar saturation magnetisation, K_{m} greatly affects the initial susceptibility χ_i: the lower K_{m}, the higher χ_i [171]. This explains why $MnFe_2O_4$ samples have the highest signal and $CoFe_2O_4$ the lowest, exactly as in Fig. 6.4.

Pre-orienting EA: Fig. 6.10 shows that on the planar coil drying the sample in a field parallel to the excitation field improves the signal amplitude by 6 to 16 % compared to sample dried without field. With the tubular coil, detection signal is reduced by 6 to 16 % when drying field was transverse to sensing field. The effect is visible on all three types of SPNF.

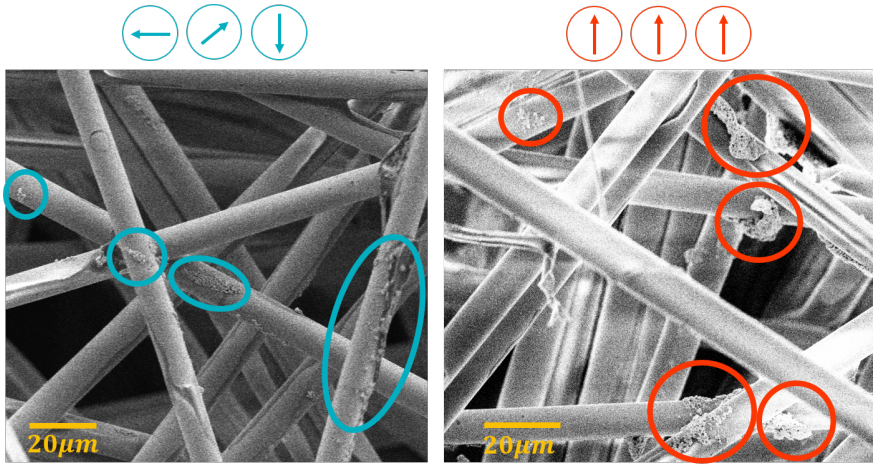


Fig. 6.9 SEM images of 50 nm magnetite nanoparticles dried in glass fiber membrane. When dried under field (resulting in aligned easy axis) the particles have a higher tendency to cluster.

6.4.3 Discussion on EA Pre-Orientation

Clustering witin NC membranes: In Chapter 4, magnetic characterisation of SPNF dispersed in cellulose membranes revealed that nanoparticles form clusters of distributed sizes during the drying process. This was inferred from three independent observations: (i) a large gap $\Delta T = T_{\text{irr}} - T_B > 100$ K in FC-ZFC curves that cannot be attributed to the narrow intrinsic size distribution measured by TEM (Section 4.4), (ii) a systematically broadened Chantrell-fitted shape factor γ for membrane samples compared to powder (Table 4.6), and (iii) Mydosh parameters $\Phi < 0.3$ indicating interacting regimes for all membrane samples (Table 4.10). However, these conclusions were drawn from magnetic data alone, without direct morphological evidence. In this experiment, SEM imaging of nanoparticles dried within membranes provides direct visual confirmation of clustering and reveals that the cluster morphology depends on the drying conditions.

Regardless of EA orientation, a clear distinction can be made in signal strength for the three materials, correlated with the magnetocrystalline anisotropy (Table 6.3): the lower the crystalline anisotropy (and thus magnetic energy barrier), the higher the directional susceptibility. This is coherent with the trends obtained in Subsection 6.3.1. While K_{m} differs by nearly two orders of magnitude across the three compositions (Table 4.3), the improvement or deterioration factor of the sensing signal induced by drying under field is of the same order of magnitude for all three materials.

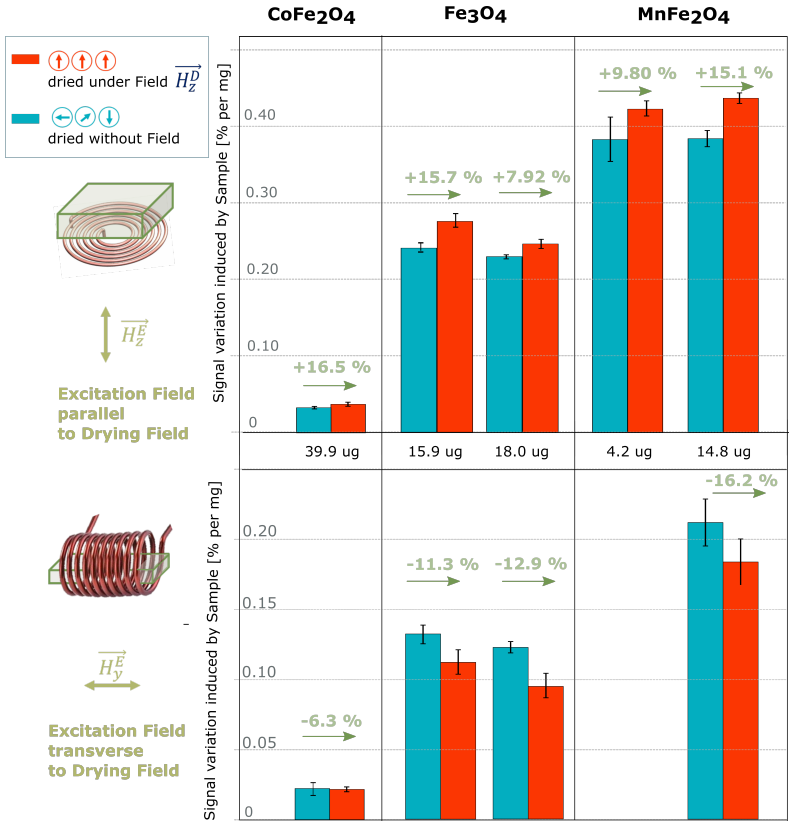


Fig. 6.10 Signal amplitude ($\Delta(f)/f_0$ per mass, cf Eq. 6.8) for Co–CP1, Fe–CP1 and Mn–CP3 in both planar and wound coil. When EA are aligned parallel [transverse] to the excitation field through an external field during the drying process, signal amplitude is increased [decreased] with 6 to 16 %.

The effective anisotropy K_{eff} was found to be 7–24 times above bulk K_{m} in membranes (Tables 4.8 and 4.15), with dipolar interactions contributing substantially. These composition-scaled interaction effects are directly relevant to the interpretation of the EA pre-orientation experiments in this section. It is consistent with the hypothesis formulated in Section 4.4 that dipolar interactions scale the effective anisotropy in a composition-dependent manner, as proposed by Serantes et al. [220].

While the directional nature of the set-up clearly differentiates the contribution of pre-detection EA orientation, it was also demonstrated that an external drying field affects the clustering dynamics. The effects of altered dipolar interactions on the effective anisotropy should be studied further. Performing magnetisation curves on membrane samples dried with and without external field would allow to quantify the effect of chain formation on the static magnetisation, independently from the inductive measurement. In Section 4.3, the initial susceptibility χ_i was shown to decrease with increasing nanoparticle mass in the membrane (Fig. 4.4), attributed to larger clusters and stronger dipolar interactions at higher concentration. A similar comparison between pre-oriented and randomly oriented samples could isolate the contribution of cluster morphology to the effective susceptibility, and determine whether the 6–16% signal difference observed here is primarily due to EA alignment or also partly due to modified inter-particle coupling.

Improving LFA with EA pre-orientation: The difference between the 'best configuration' where EA orientation is parallel to the sensing field, and the worst in which both orientations are orthogonal, is over 31% for the 14.8 μg $MnFe_2O_4$ sample, which is significant for sensing applications. Notably, none of the MNP detection studies benchmarked in Tables 5.1 and 5.2 report on the effect of easy axis pre-orientation. Yet this 31% signal difference is of the same order of magnitude as many of the hardware-based sensitivity improvements reported in the literature (e.g. differential measurement, bridge balancing), suggesting that controlling the magnetic microstructure of the label layer is an underexplored lever for improving inductive biosensor performance.

External field for drying was only applied after the SPNF suspension had already wicked through the membrane. Given this induces a repeatable difference, we validated that while nanoparticles tend to attach to the nitrocellulose pore walls when dried, this attachment does not occur immediately after application. Nitrocellulose, already widely used in immunosensing applications, therefore seems a medium fit for exploiting the advantages of MNP orientation without requiring an extra manipulation step in which the MNP are under field before entering the nitrocellulose.

Section summary

Nanoparticles of three ferrite compositions (Fe–CP1, Mn–CP3, Co–CP1) were deposited on nitrocellulose membranes and dried either without or under a 500 mT static magnetic field. The resulting EA orientation was probed with a planar coil (excitation parallel to drying field) and a wound coil (excitation transverse to drying field). SEM imaging provided direct morphological evidence of clustering within the membrane.

Consolidated conclusions:

- Drying SPNF-loaded nitrocellulose under a 500 mT field produces a clear change in the inductive signal: a 6 to 16% increase when the EA are aligned parallel to the sensing field, and a 6 to 16% decrease when they are transverse (Fig. 6.10). The effect is observed on all three ferrite compositions and with both coil geometries.
- The total signal difference between the best configuration (EA parallel to sensing field) and the worst (EA transverse) reaches 31% for the 14.8 μg $MnFe_2O_4$ sample. This is comparable in magnitude to hardware-based sensitivity improvements reported in the benchmark of Chapter 5 (Tables 5.1 and 5.2), yet none of those studies report on EA pre-orientation.
- SEM imaging (Fig. 6.9) confirms that nanoparticles form clusters within membranes and that the cluster morphology depends on drying conditions: field-dried samples exhibit larger, chain-like clusters, while field-free samples show smaller clusters elongated along the membrane fibres. This provides visual support for the clustering previously inferred from magnetic data alone in Chapter 4 (broadened Chantrell shape factor in Table 4.6, Mydosh parameters below 0.3 in Table 4.10, FC-ZFC gap in Section 4.4).
- The external field was applied after the SPNF suspension has wicked through the membrane, confirming that nanoparticle attachment to nitrocellulose pore walls is not instantaneous. This is relevant for practical LFA fabrication, as it means no additional sample manipulation support is required to exploit pre-orientation of EA.

Observed trends requiring further investigation:

- No correlation was observed between the relative signal change due to pre-orientation and the bulk magnetocrystalline anisotropy K_m of the ferrite. This is consistent with the observation from FC-ZFC and ACS analysis (Table 4.15) pointing towards approximate preservation of the bulk K_m ratios. Possible interpretation is offered the scaling framework from Serantes et al [220], in which the dipolar interaction effect is material-scaled rather than a composition-independent additive constant. Better differentiation of the impact of changes in clustering morphology and changes in EA orientation would allow to study this more in-depth.

Perspectives:

- The external drying field simultaneously alters EA orientation and cluster morphology. The individual contributions of these two effects to the observed signal change could not be separated. Measuring magnetisation curves on field-dried versus non-field-dried membrane samples would help to quantify changes in directional susceptibility and coercivity more precisely. Measuring initial magnetisation curves at 2 – 5 K as proposed by Thamm et al. [213] would allow if changes in directional susceptibility can be attributed to changes in interactions (hence, clustering morphology).
- The minimum field strength required to induce the orientation effect was not determined. The 500 mT field used in these experiments exceeds what a compact permanent magnet could provide in a portable device. Repeating the experiment with decreasing drying field strengths (e.g. 10, 50, 100, 200 mT) should identify the practical threshold for integration of a DC drying field into an LFA portable reader, and determine whether the effect saturates.

6.5 Inductive Detection as complementary characterisation tool: the Influence of Particle Mobility

In this section, we use inductors LE1 and LE2 (cf Table 6.2) wound around 2 mL eppendorfs. These are filled with nanoparticle suspensions in either DI (free to rotate) or agar-agar (immobilized). This allows us to measure how real susceptibility is affected by particle mobility. Both types of suspensions are considered homogeneous, allowing to apply the linear mixing rule described in Subsection 4.6.2.3.

6.5.1 Literature: Mobility affects susceptibility

In [105] ACS measurements were obtained for FeraSpin XL [2] particles in different media (aqueous suspension, water-glycerol solution, and freeze-dried). The viscosity of the suspension medium affects particle mobility, therefore the interplay between Néel and Brownian relaxation (cf SubSubsection 2.3.3)... and thus the signature of $\chi(f)$. This is illustrated in Fig. 6.11 showing the susceptibility spectra for nanoparticles in water and glycerol (higher viscosity), compared to the freeze-dried counterparts (immobilized).

- When nanoparticles are immobilized, Brownian rotation is suppressed: the particle's magnetic response is dominated by the Néel mechanism (internal spin relaxation). Only a small frequency dependence of the magnetisation response is observed between 0.1 Hz and 25 kHz.
- When nanoparticles are suspended liquid samples, the magnetisation response is strongly frequency-dependent due to the Brownian contribution. Higher viscosity makes the Brownian contribution less distinguishable.

The effect nanoparticle mobility on susceptibility is proposed by some authors to be leveraged directly for biodetection. For example, Tian et al. [303] perform biodetection of Zikavirus by measuring immunologically stimulated agglomeration. This affects the hydrodynamic diameter of the particle agglomerates, thus the brownian relaxation time constant τ_B. While a clear decrease of imaginary susceptibility maximum frequency (from 1 kHz to 10 Hz) is observed with an increase of biomarker concentration (from 32aM to 1fM), this is neither linked to actual agglomerate sizes nor correlated with data of the real susceptibility.

In the benchmark Table 5.1 summarising inductive measurements, the nanoparticle matrix varies from aqueous solutions to dried surfaces and LFA strips, yet the effect of particle mobility on the measured signal is never explicitly addressed. However, as suggested by Viereck et al. [105] and as proven in the

[2] FeraSpin XL are said to be multicore nanoparticles, hydrodynamic size 65nm, core diameter 25nm, crystalite size 6-7nm, elemental composition not specified

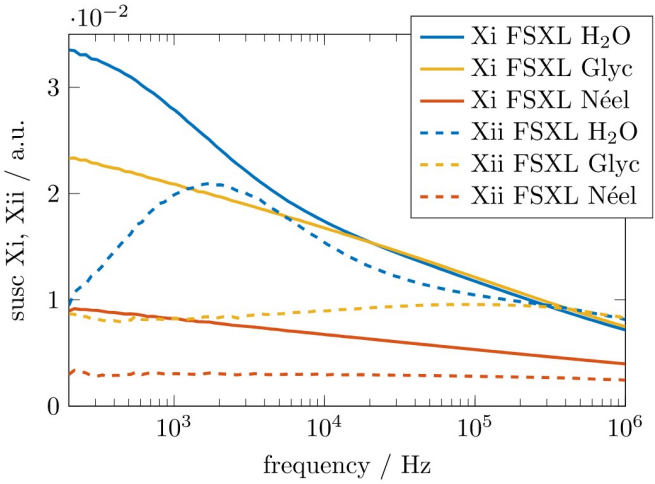


Fig. 6.11 From [105]: Real and imaginary part of susceptibility for FeraSpin XL nanoparticles in resp. water, glycerol and freeze-dried (called "Néel" in the legend).

following sections, nanoparticle mobility should be considered when designing and calibrating a sensor.

6.5.2 Observing MNP mobility with Impedance Analyser LCR4284

6.5.2.1 LCR4284: Materials and Methods

The used nanoparticles for these measurements are listed in Table 6.8. Alongside the Mn–CP3, Fe–CP1 and Co–CP1 samples used throughout this work, the Nanomag-D nanoparticles (micromod Partikeltechnologie GmbH, Rostock, Germany) [304], are beads with radii >200 nm containing superparamagnetic cores. Given their large size, they are a control sample since their brownian relaxation time is much larger than the other samples with 8-10 nm diameter. These store-bought samples were not analysed with TGA or ICP so their exact mass density and the corresponding filling factor are unknown. Nevertheless, given their large hydrodynamic diameter, their frequency-dependent signature is a relevant point for comparison.

0.50 mL of suspensions with known concentrations were pipeted in 2mL eppendorfs (outer diameter 10.3mm) which were already containing either 1.50 mL DI water or liquid agar-agar. Upon addition of the MNP, the eppendorfs were closed and shaken heavily resulting in a homogeneous dispersion. The eppendorfs containing agar-agar were then kept still for 20 min while the agar-agar was

hardening. It is worth emphasising the colloidal stability of the samples made by CP as explained in Subsection 3.3.2: no deposition/agglomeration was observed in the eppendorfs even after several days. Nevertheless, they were sonicated for 5 minutes before every measurement.

Sample	NP Mass [mg]	MNP Mass Density [mg/mm^3]	Filling Factor v_f in 2 mL eppendorf
Mn–CP3	3.90	4.96	2.02 e-4
Fe–CP1	5.01	5.18	1.93 e-4
Nanomag-D	4.17	?	?
Co–CP1	2.604	5.30	1.89 e-4

Table 6.8 Measured samples with the LCR impedance analyser in eppendorfs (suspended in DI or agar-agar). For the commercial 250 nm Nanomag-D samples the mass fraction of Fe was not known.

The eppendorfs were placed in the LE1 coil (cf Table 6.2) and measured with the LCR4284 impedance analyser, between 1 kHz and 1 MHz. Blank measurements involved eppendorfs containing only agar-agar or DI. As in Subsection 4.6.1, permeability change "induced by the sample" was derived based on the difference ΔL between the sample and the blank (filled with only DI or agar-agar), relative to the air filled ("empty") inductance L_a (Eq. 4.15). All measurements were performed with a 5 mA sensing current in the LE1 coil and an AC voltage ranging from 0.37 mV (at 1 kHz) to 150-180 mV around 1 MHz. Data between 1 and 8 kHz was very noisy (due to low impedance) and therefore mostly omitted.

A methodologically similar study is worth mentioning: Cui et al. [305] propose a four-tap solenoid coil sensor coupled to a commercial LCR meter for measuring the complex permeability of particle mixtures (Al_2O_3/Fe) between 1 kHz and 100 kHz. As in our approach, effective permeability is derived from the inductance change between an empty and a sample-filled coil. Their set-up additionally uses an oscilloscope for reading the secondary coils and a signal generator with voltage amplifier for excitation. While the frequency range and measurement principle are comparable to the LCR measurements presented here, Cui et al. characterise static mixtures at varying volume fractions and do not address the influence of particle mobility on the measured susceptibility, which is the central question of this section.

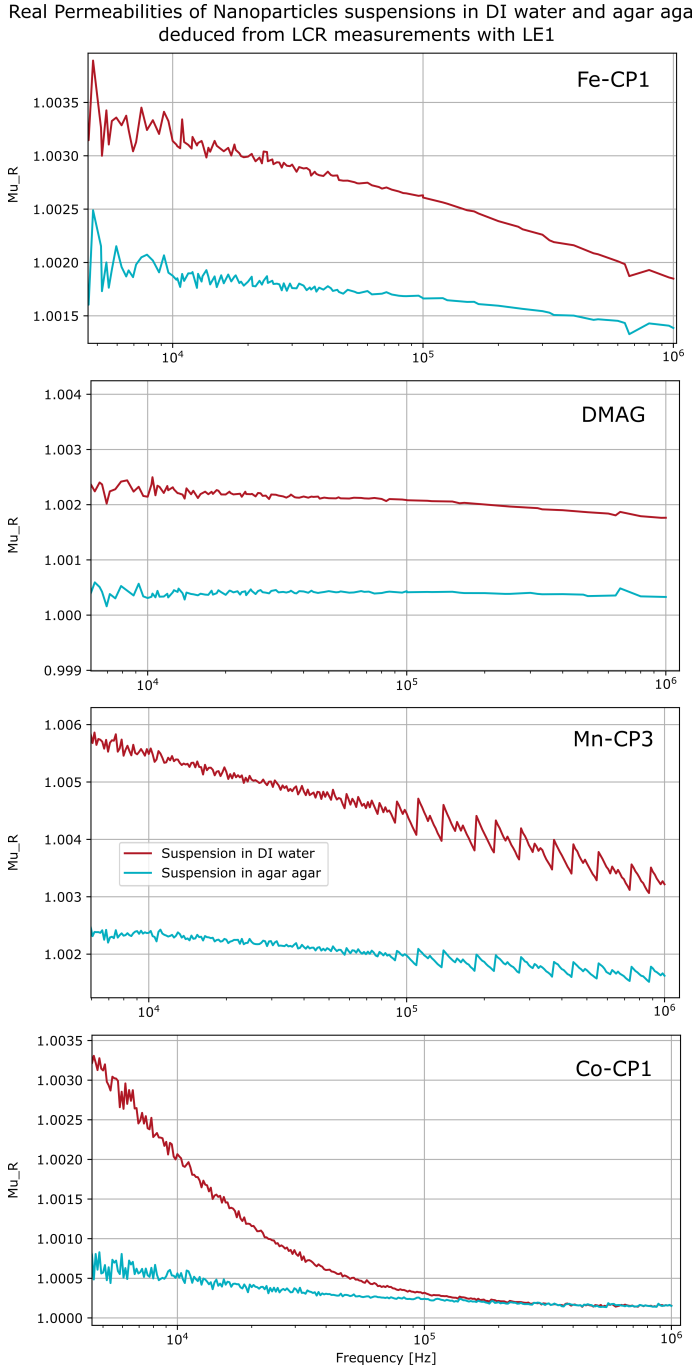


Fig. 6.12 Variation in real relative permeability obtained with the LCR4284 for SPNF (Mn–CP3, Fe–CP1, Co–CP1) and Nanomag-D samples in eppendorfs (cf. Table 6.8): suspended in agar-agar and in DI water.

6.5.2.2 LCR4284 Results: MNP mobility increases μ_r (10kHz - 1MHz)

Volume susceptibility χ was derived from the measured relative permeability μ_r (Eq. 2.6) and corrected for the filling factor v_f (Eq. 4.16). The same precautions as applied when analysing powder with the E4991 impedance analyser (cf sub-Subsection 4.6.2.3) should be taken regarding the filling factor. The used samples and corresponding v_f are summarised in Table 6.8. Fig. 6.12 summarises the effective relative permeabilities μ_r deduced from the coils during measurement. Fe–CP1 and Mn–CP3 exhibit a higher susceptibility in suspension than in immobilized form (cf. Fig. 4.16). This enhancement can be understood through the interplay of the two relaxation mechanisms described in Section 2.3.3. For these particle sizes, the Néel relaxation time is shorter than the Brownian relaxation time (Fig. 2.5), which renders internal moment reversal the dominant relaxation pathway. Through this mechanism, the magnetic moment preferentially aligns along the nearest energy minimum of the easy axis (cf. Fig. 2.4), but remains at an angular offset from the applied field direction. When the excitation frequency lies below the Brownian relaxation threshold, the Zeeman torque exerted by the external field additionally drives a physical rotation of the particle, further aligning the easy axis with the field. This supplementary Brownian contribution effectively reduces the angular mismatch between the moment and the field, yielding a net increase in the measured susceptibility. For the Co–CP1 sample, a sharp decrease is observed, corresponding to brownian relaxation. This decrease is sharper than for Fe–CP1 and Mn–CP3 since there is less interplay with the Néel relaxation due to their high anisotropy (cf. Table 4.3, Table 6.4). The Nanomag-D samples vary little with frequency since the measurement time is shorter than their brownian relaxation time, given their large hydrodynamic size (bead diameter > 200 nm). The very small observed decay can be attributed to Néel relaxation of their superparamagnetic cores.

In Fig. 6.13 volume susceptibility χ' of the CP samples is deduced based on these relative permeabilies (and assumed v_f). Debye fitting is performed on these data.

6.5.2.3 Fitting the Debye equation

Method: fitting Debye considering Néel and Brown relaxation simultaneously:

Because the Brownian and Néel processes take place in parallel, the effective relaxation time τ_{eff} (Eq. 2.36) is dominated by the shorter of the two time constants [31]. Based on the obtained real susceptibilities for "immobilised" (agar-agar) and "rotating" (DI) suspensions, a combined fitting is done on the real part of the lognormal Debye function (Eq. 2.47). For samples in agar-agar, the size-dependent relaxation time $\tau(D_{\text{mag}})$ reduces to the Néel relaxation time τ_N alone, since physical rotation of the particle is suppressed. For the samples in DI water, the effective relaxation time additionally includes the Brownian contribution τ_B (Eq. 2.35), so

that τ_{eff} is computed from Eq. 2.36 for each particle size in the distribution.

Both datasets are fitted simultaneously by minimising a single cost function $\mathcal{J}$ defined as the sum of squared residuals over both conditions:

$$\mathcal{J} = \sum_i \left(\chi'_{\text{AA},i} - \chi'_{\text{N}}(\omega_i)\right)^2 + \sum_i \left(\chi'_{\text{DI},i} - \chi'_{\text{eff}}(\omega_i)\right)^2 \tag{6.11}$$

where $\chi'_{\text{AA},i}$ and $\chi'_{\text{DI},i}$ are the measured real susceptibilities at angular frequency ω_i for the immobilised (agar-agar) and suspended (DI) samples respectively, $\chi'_{\text{N}}(\omega_i)$ is the modelled real susceptibility computed from Eq. 2.47 using only τ_N, and $\chi'_{\text{eff}}(\omega_i)$ is the modelled real susceptibility using the combined τ_{eff} from Eq. 2.36. Because the concentration and size distribution remain unchanged in both suspensions, the fitting parameters χ_{hf}, C, τ_0, K_{eff}, $\tilde{D}_{\text{mag}}$, and γ are shared between both terms of Eq. 6.11. Only the hydrodynamic factor h, defined such that $V_H = h \cdot V_{\text{mag}}$, enters exclusively in the second term through τ_B. This is a simplification since it assumes that h is constant across the size distribution; it would be more correct to assume h has a probability density function as well. However, this simplified model yields interpretable results.

The integral in Eq. 2.47 is evaluated numerically (trapezoidal rule) over a grid of 250 radii between 1 and 40 nm. Minimisation is performed using a sequential least-squares algorithm (SLSQP) with bound constraints listed in Table 6.9.

Parameter	Description	Min	Max	Unit
χ_{hf}	High-frequency susceptibility offset	0	0.5	–
C	Prefactor $\propto \mu_0 M_S^2 N / k_B T$ (Eq. 2.45)	1e-10	1e-3	nm^{-6}
τ_0	Néel–Arrhenius attempt time	1e-11	1e-9	s
K_{eff}	Effective anisotropy constant	1e4	1e7	J/m^3
$\tilde{D}_{\text{mag}}$	Median magnetic diameter (Chantrell/Debye fitting)	7	10	nm
γ	Lognormal shape factor	0	1.1	–
h	Hydrodynamic-to-magnetic volume ratio	2	1e6	–

Table 6.9 Bounds on fitting parameters for the lognormal Debye model (Eq. 2.47) applied to susceptibilities measured for MNP samples suspended in agar-agar (Néel relaxation only) and DI water (Néel + Brownian relaxation).

Table 6.9 summarises the bounds used for fitting. Mathematically, the results are not exactly comparable since there are fewer datapoints above 100 kHz for

Fe–CP1 (which affect the weighting of the fitting) and more noisy datapoints for Mn–CP3. However, the visual agreement is sufficient to accept the tendencies and principal conclusions.

Results of Debye fitting: Fig. 6.13 shows $\chi'(f)$ resulting from the Debye fitting in blue. The red datapoints correspond to impedance measurements points.

- The derived static susceptibilities χ_0 (based on Eq. 2.48) are 14.05 for Mn–CP3, 11.87 for Fe–CP1 and 16.84 for Co–CP1. The classification (i.e Co–CP the highest and Fe–CP the lowest) is consistent with the initial susceptibility χ_i measured on their powder forms (cf Table 4.14).

- The obtained anisotropy constant K_{eff} for Co–CP1 is unsurprisingly higher than for the counterparts. It should be noted that for Mn–CP3 the fitted anisotropy is ten times higher than the corresponding bulk magnetocristalline anisotropy (cf Table 4.3). The order of magnitude is coherent with the results obtained by applying Vogel-Fulcher to ACS measurements on Mn–CP2 (cf Table 4.15).

- For the Fe–CP1 the fitted anisotropy constant is smaller than the bulk magnetite counterpart. This might be explained by the size distribution and/or an over-estimation of the magnetic diameter (since K_{eff} is multiplied by magnetic volume to determine anisotropy energy). Indeed the model fits the median magnetic diameter $\tilde{D}_{\text{mag}}$ at 9.9 nm, which is higher than Chantrell fitting in Chapter 4 (cf Table 4.6). Also, since the nanoparticle is a mix of magnetite and maghemite, the fraction of maghemite (with lower bulk magnetocrystalline anistotropy) may decrease the effective anisotropy.

- Looking at the parameter h, the hydrodynamic volume of cobalt ferrite would be 38 times its magnetic volume, which is higher than the fitted equivalent h parameters for the Fe–CP1 and Mn–CP3. The three samples were at similar concentration and have a citric acid corona. Since the data is situated at the "high end tail" of brownian relaxation frequencies, and since the contrast is sharpest for Co–CP (given its high magnetocristaline anisotropy), it is most probable that the h factor is underestimated in the other two fittings. Another option would be that since they have higher anisotropy, the nanoparticles are more clustered despite sonication because of remanent magnetisation. While we did not observe a difference between colloidal stability or agglomeration tendency with Mn–CP3 and Fe–CP1, we cannot exclude this hypothesis. Extending the measurement frequency range below 100 Hz would allow to observe the -supposed- Brownian relaxation peak more precisely. Comparative DLS measurements on the three DI suspensions would directly quantify hydrodynamic diameters and reveal whether Co–CP1 forms larger agglomerates than Fe–CP1 or Mn–CP3:

however, they would require dilluting the measured solutions, potentially affecting the clustering dynamics.

Material	τ_0 (s)	C (nm^{-6})	χ_0	χ_{hf}	K_{eff} (kJ/m^3)	$\tilde{D}_{\text{mag}}$ (nm)	γ	h
Co-CP1	1.00e-11	1.00e-03	16.8	5.00e-01	140	9.83	0.10	38.31
MN-CP3	7.01e-11	1.00e-03	14.05	5.00e-01	47.8	9.04	0.17	15.18
FE-CP1	1.00e-09	2.37e-04	11.8	1.59e-04	10.5	9.92	0.26	2.48

Table 6.10 Extracted parameters from the Debye Model fitting on χ' for Co-CP1, MN-CP3, and FE-CP1 in Liquid and Agar-Agar.

Comparison with E4991 Debye fitting on powders: The same Debye model was applied in Chapter 4 to CP powders measured with the E4991 impedance analyser over the 1 MHz–1 GHz range (Table 4.13).

- The fitted median magnetic diameters $\tilde{D}_{\text{mag}}$ are substantially larger in the present LCR fitting than in the E4991 powder fitting: 9.92 nm versus 5.32 nm for Fe–CP1 and 9.04 nm versus 6.30 nm for Mn–CP3. The E4991 diameters were already noted to be 33–43% smaller than Chantrell-fitted values from magnetisation curves (Table 4.5). The LCR-fitted diameters are closer to these Chantrell references (7.95 nm for Fe–CP1, 11.0 nm for Mn–CP3). Correspondingly, the fitted shape factors γ are narrower in the LCR fitting (0.26 and 0.17 versus 0.45 and 0.44), potentially indicating that the broad distributions obtained in the E4991 fitting were partly compensating for the underestimated diameters.

- This difference in fitted diameters (smaller $\tilde{D}_{\text{mag}}$ for E4991 Debye fitting) may be associated with the fact that the Debye fitting on LCR data is performed on the real susceptibilities χ' obtained for both mobile and immobile nanoparticles, both dominated by volume-weighted dynamic as explained in Section 4.5.1. The E4991 fitting was done on χ' and χ'' of immobilized powders: since the latter is attributed to mainly number weighted phenomena, the impact of the largest nanoparticles on the total fitting results was more mitigated.

- In the E4991 powder fitting, the effective anisotropy K_{eff} converged to the imposed lower bound of 10 kJ/m^3 for both Fe–CP1 and Mn–CP3, reflecting a degeneracy between K_{eff} and the fitted volume (Table 4.13). In the present LCR fitting, Mn–CP3 converges to $K_{\text{eff}} = 47.8$ kJ/m^3, consistent with Vogel-Fulcher analysis of ACS data on Mn–CP2 (Table 4.15). This improvement arises because the effective relaxation time τ_{eff} now depends on both Néel and Brownian contributions, and the additional fitting parameter

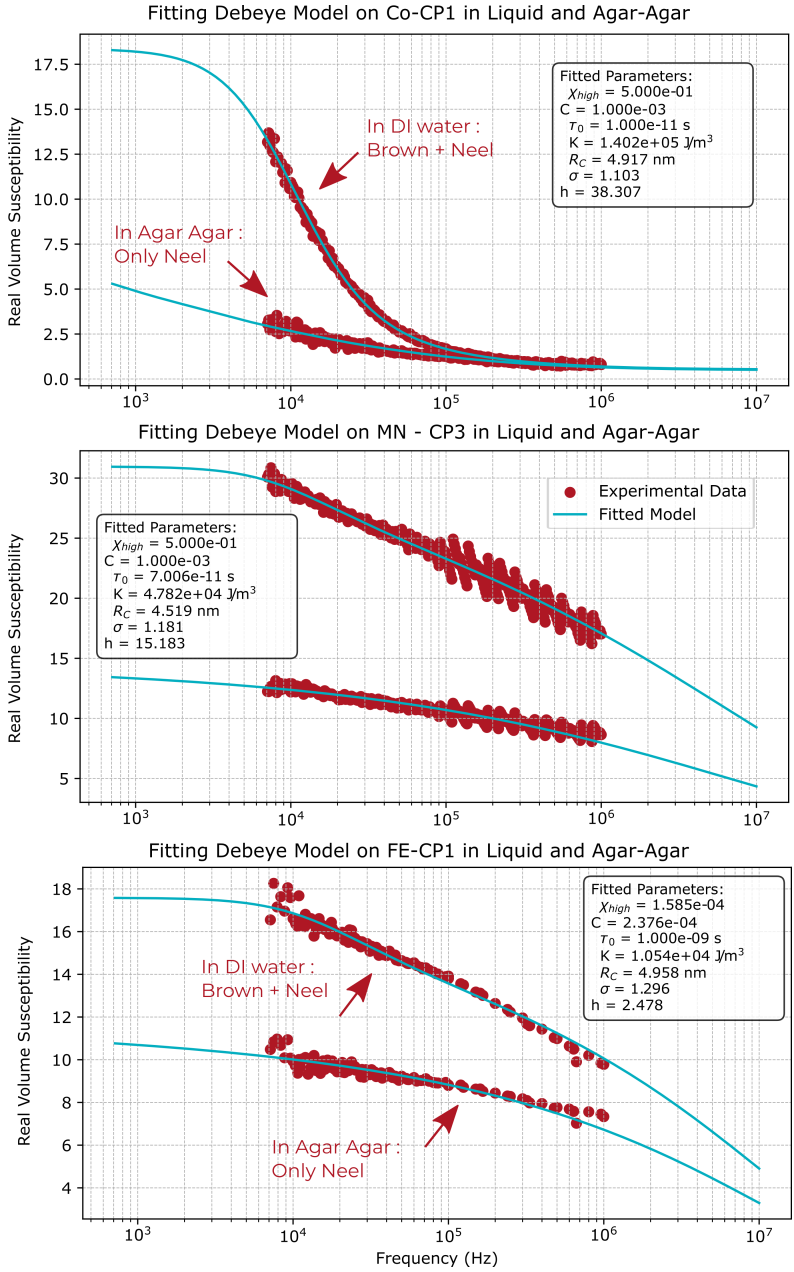


Fig. 6.13 Debye fitting on derived volume susceptibility from LCR measurements, considering a linear filling factor. The red points represent datapoints while the blue line corresponds to the fitted Debye models for real susceptibility with effective relaxation time constant depending on either Brown and Néel relaxation, or just Néel. The resulting fitting parameters are applicable to both curves (except for h, determining the hydrodynamic volume).

h (hydrodynamic-to-magnetic volume ratio) absorbs the direct correlation between τ_0 and K_{eff}, probably allowing K_{eff} to settle at a more physically meaningful value.

- The substrate state may also contribute to the observed differences. In the E4991 toroidal holders, the powder is compressed, leading to stronger dipolar interactions that can shift the apparent relaxation behaviour and suppress the fitted diameter. In the LCR liquid suspensions, the particles are dilute (v_f 10^{-4}–10^{-3}), reducing the influence of dipolar interactions.

The impact of the introduction of the h factor needs further study: physically it makes more sense to consider that the distribution of hydrodynamic diameters does not exactly scale the distribution of magnetic diameters. This would require to consider h as a PDF rather than a constant, and to measure a wide variety of nanoparticles suspension concentrations where clustering is known with e.g. DLS. However, the Debye fitting on LCR data methods yield consistent rankings of χ_0 (cf. Table 4.14) and the obtained $\tilde{D}_{\text{mag}}$ are consistent with Chantrell fitted diameters on magnetisation curves. Connecting handwound coils to an impedance analyzer is not only cheaper than a SQUID (and the E4991 impedance analyser with appropriate sample-holder, to lesser extend), it also offers greater flexibility in sample geometry, enabling characterisation of nanoparticles in conditions close to the final biomedical application in which they will be used. Finally, it is worth underlining that by differentiating the combined effect of Brownian + Néel relaxation with Néel relaxation only, coherent K_{eff} and χ_0 from Co–CP1 could be extracted without needing to demagnetize the sample. While the results above yield interesting orders of magnitude, it should be kept in mind that the Debye model is an important simplification since it does not consider interactions. A system of strongly magnetic, non-touching particles, such as a ferrofluid, is dominated by interactions. On the other hand, if the particles are touching, exchange coupling between spins at contact points can occur, giving raise to exchange interactions [50]. In [306], it was demonstrated how dipolar interactions between magnetic nanoparticles significantly alter their magnetisation dynamics, leading to a coupling between the internal (Néel) and rotational (Brownian) relaxation processes, which invalidates the common theoretical framework used for non-interacting systems.

6.5.3 Observing Particle Mobility with the Colpitts Oscillator

6.5.3.1 Materials and Methods: Observing MNP mobility with Colpitts Oscillator

The samples in DI and agar-agar eppendorfs were also measured with the Colpitts oscillator with both LE1 and LE2 inductances. The used capacitance values ($C_1 = C_2$) resulted in oscillation frequencies in Table 6.11.

$C_1 = C_2$	LE1	LE2
470 pF	4 MHz	2 MHz
2 nF	2 MHz	1 MHz
22 nF	600 kHz	330 kHz
100 nF	330 kHz	150 kHz

Table 6.11 Resonance frequencies for LE1 and LE2 coils at different capacitances for C_1 and C_2 (cf Fig. 6.1).

In Fig. 6.14 the process of a measurement is indicated: every 20 seconds, alternations are made: measuring an empty ("air filled") coil, the blank (pure DI or agar-agar) eppendorf in the coil, then the eppendorf containing nanoparticles. Unlike for measurements with membranes, the NP suspension medium does have significant relative permittivity ($\epsilon_{r,water} \approx 80$) and fills up the whole coil volume. A non-negligible stray capacitance change affects the oscillation frequency. Therefore, the oscillation frequency change induced by the nanoparticles f_s is defined wrt. to blank eppendorfs (DI or agar-agar filled), as illustrated in Fig. 6.14. Besides that, the relative frequency and standard deviation are determined in the same manner as Subsection 6.2.3.2.

Between the blank measurements and the nanoparticle measurements, the change in capacitance is considered identical: since AA is DI-water based, its permittivity is very similar. According to [307] the relative permittivity of Fe3O4 nanoparticles is 80, which is close to that of DI water at room temperature. Thus, we assume that the difference in frequency change induced by MNP, compared to their blank, is affected to changes in permeability.

6.5.3.2 Results

Fig. 6.15 plots the frequency changes per nanoparticle mass for both LE1 and LE2. Nanomag-D and Mn–CP3 measurements were confirmed by dilluting the sample ten times (blue curves). The dotted lines represent DI samples, the full lines represent agar-agar samples. Since we operate near the SRF of LE2 (SRF = 6.46 MHz, cf Table 6.2), the operating point sensitivity is more unstable than for LE1 (SRF = 14 MHz), resulting in higher standard deviation of the measurements and higher frequency-dependency of the signal for a given sample. This is consistent with the observations in Fig. 6.6 where NC membrane samples are measured with L1 rather than L2, the former showing a more stable operating point sensitivity probably due to the higher SRF. Both on LE1 and LE2, a clear tendency is observed for the CP samples: samples in DI-water systematically cause a higher signal per nanoparticle mass (as defined in Eq. 6.8) and show a stronger downwards

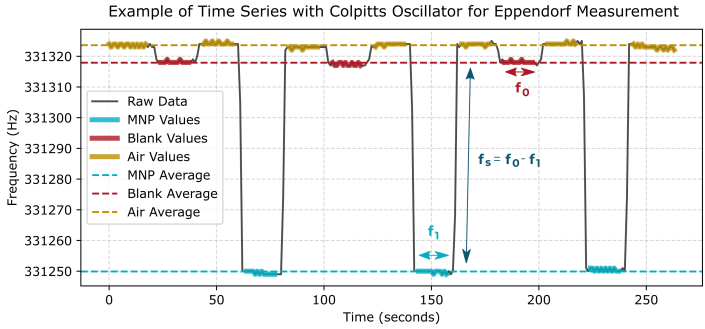


Fig. 6.14 Example of timeseries for the eppendorf measurement protocol: every 20 s, the coil alternates between empty (air), a blank eppendorf (pure DI or agar-agar), and a nanoparticle suspension eppendorf. The frequency change induced by nanoparticles is defined relative to the corresponding blank.

trend with frequency, consistent with the permeability increase observed for DI suspensions with the LCR analyser (Fig. 6.12). On the other hand, Nanomag-D samples show no significant difference in slope due to change in suspension medium, again in agreement with the LCR analyser results (Fig. 6.12).

These results demonstrate that a simple Colpitts oscillator, built from standard discrete components at negligible cost, is sufficient to distinguish the effect of nanoparticle mobility on the inductive signal, reproducing the tendencies observed with the LCR4284 impedance analyser. This is encouraging for the development of portable sensing platforms where autonomous read-out electronics should replace (some functionalities of) laboratory-grade instrumentation. A natural next step would be to quantify the sensitivity of this oscillator-based read-out more precisely with samples that vary in nanoparticle concentration and hydrodynamic diameter. Using the planar coil and a more stable interface, it would be relevant to try measuring LFA strips when they are still drying, since it was observed that mobility increases the effective μ_r change of the coil. A trade-off exists here: larger beads (such as Nanomag-D) are preferred in LFA design (cf. Section 5.4) yet due to their high hydrodynamic radius, their Brownian relaxation occurs below 1kHz: operating inductive sensing with small coils at these frequencies might be counterproductive. As a result, the gain in "increased magnetic mass per nanoparticle" and offered by multicore beads is probably not compatible with the gain of "increasing signal by particle mobility".

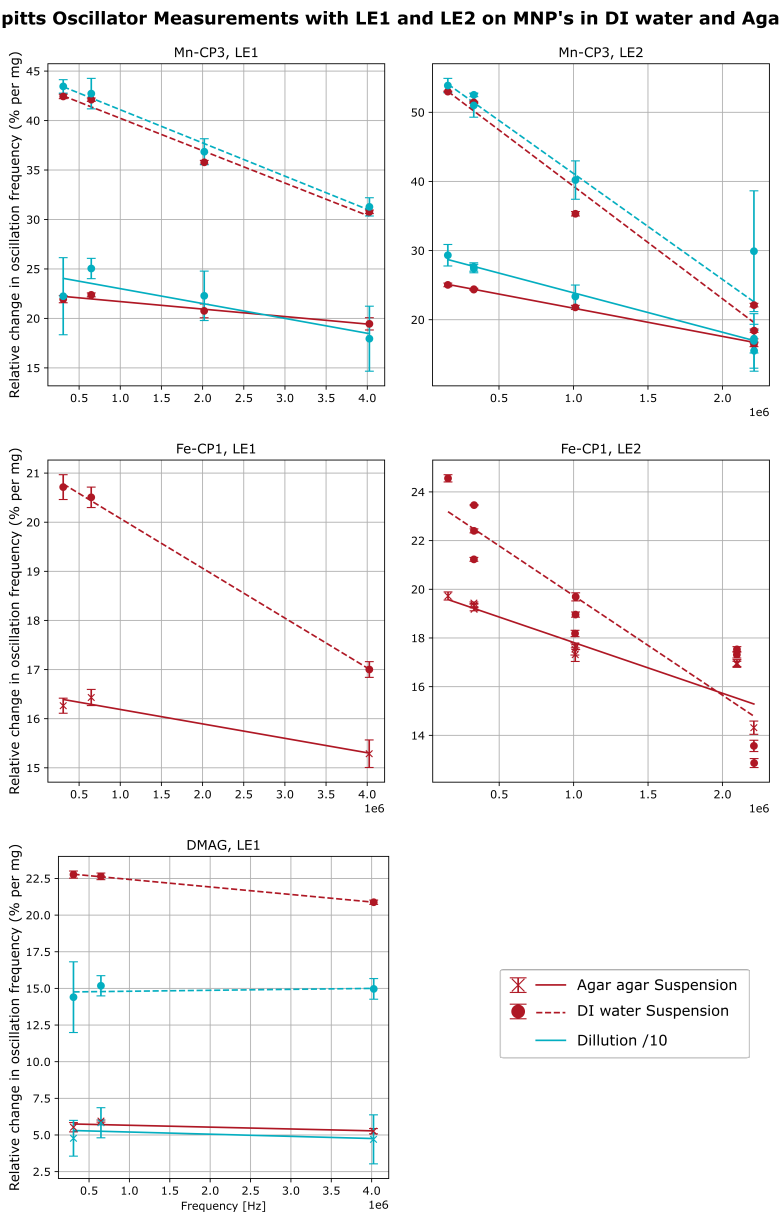


Fig. 6.15 Relative change in oscillation frequency per unit mass for the Colpitts oscillator with coils LE1 and LE2. Solid lines: samples in agar-agar; dotted lines: samples in DI water. Rows correspond to Mn–CP3, Fe–CP1 and Nanomag-D. Capacitances are varied according to Table 6.11 to sweep the operating frequency.

Section summary

SPNF suspensions (Fe–CP1, Mn–CP3, Co–CP1) and Nanomag-D control beads were measured in both DI water (mobile) and agar-agar (immobilised): coils were wound around the eppendorf and inductance changes were measured using an LCR4284 impedance analyser (10 kHz–1 MHz) and the Colpitts oscillator (150 kHz–4 MHz). A combined Debye fitting was performed on the LCR data to extract magnetic and hydrodynamic parameters from the two conditions simultaneously.

Consolidated conclusions:

- LCR measurements unambiguously distinguish mobile from immobilised SPNF: for all three ferrite types, the real susceptibility in DI water exceeds that in agar-agar at every measured frequency (Fig. 6.12). This is because the Brownian contribution provides an additional relaxation channel that supplements Néel relaxation by allowing physical rotation of the particle toward the field direction. The Nanomag-D beads (hydrodynamic diameter > 200 nm) confirm this: they show negligible frequency dependence across the full measurement range, consistent with a Brownian relaxation time much longer than the measurement period.
- The sharp susceptibility decrease for Co–CP1 in DI water is steeper than for Fe–CP1 and Mn–CP3 (Fig. 6.12), consistent with cobalt ferrite's high magnetocrystalline anisotropy: the Néel contribution is weaker, making the Brownian contribution more distinct and its frequency dependence more visible.
- The Colpitts oscillator confirms the tendencies observed with the LCR analyser: CP samples yield systematically higher signal per mass in DI than in agar-agar, and Nanomag-D shows no significant difference between the two media (Fig. 6.15). While the resolution is much lower, this is a proof of concept that a simple PCB and wound coil can detect the influence of particle mobility on the macroscopic magnetic response.

Observed trends requiring further investigation:

- The combined Debye fitting on DI and agar-agar data yields static susceptibilities χ_0 of 14.05 (Mn–CP3), 11.87 (Fe–CP1) and 16.84 (Co–CP1). Their relative ranking is consistent with SQUID measurements (Table 4.14). The fitted median magnetic diameters (9.04 and 9.92 nm for Mn–CP3 and Fe–CP1) are closer to Chantrell-fitted values from magnetisation curves (Section 4.3) than the E4991 powder fits (Table 4.13), probably because the LCR fitting uses real susceptibility data from two complementary conditions rather than real and imaginary data from a single immobilised condition.
- The scaling between hydrodynamic and magnetic volume, h varies from 2.5 (Fe–CP1) to 38 (Co–CP1). Whether this reflects genuine differences in clustering or a fitting artefact from probing only the tail of the Brownian relaxation spectrum could not be resolved. Comparative DLS measurements would directly quantify hydrodynamic diameters.

- The inclusion of the Brownian channel and the additional parameter h appears to resolve the K_{eff}/diameter degeneracy that limited the E4991 powder fitting (Table 4.13): Mn–CP3 converges to $K_{\text{eff}} = 47.8\ \text{kJ/m}^3$, consistent with Vogel-Fulcher analysis of ACS data (Table 4.15). The Fe–CP1 value ($10.5\ \text{kJ/m}^3$) remains below bulk magnetite anisotropy, possibly due to the maghemite fraction.

Perspectives:

- Combining Néel and Brown relaxation in a single Debye fit by adding a scaling factor h was not done before to the best of our knowledge and yields more relevant magnetic results since the model is constraint by two different (complementary) dynamics. Treating the hydrodynamic factor h as a probability distribution rather than a constant would better represent the diversity of cluster sizes in suspension. This requires measuring a range of nanoparticle concentrations with validated hydrodynamic diameters from DLS.

- Extending the LCR measurement frequency below 100 Hz with a stronger inductor would allow direct observation of the Brownian relaxation peak. Combined with ACS data from Section 4.5 (0.1 Hz–1 kHz) and E4991 data from Section 4.6 (1 MHz–1 GHz), this would provide a nearly continuous susceptibility spectrum from sub-Hz to GHz frequencies, as compiled in Table 6.12.

- The increased susceptibility of mobile nanoparticles compared to immobilized ones could be exploited by in LFA measurements, traditionally performed after drying is completed. This would require better characterisation of the fluidics and clustering dynamics within the nitrocellulose. A trade-off exists for bead selection: larger multicore beads (such as Nanomag-D) are preferred in LFA for their higher magnetic mass per particle (Section 5.4), but their Brownian relaxation occurs below 1 kHz, making the mobility-induced signal enhancement inaccessible at typical inductive sensing frequencies.

6.6 Conclusion and Perspectives

This section lists the key contributions of Chapter 6. The chapter pursued three objectives: (i) demonstrating inductive nanoparticle detection on an LFA-like substrate with simple, low-cost hardware compatible with the ASSURED criteria, (ii) evaluating wound coils as complementary characterisation tools for SPNF in biosensor-relevant substrates (nitrocellulose membranes and aqueous suspensions), and (iii) correlating the obtained results with the magnetic properties established in Chapter 4. Each contribution is followed by an outlook on remaining open questions.

Table 6.12 compiles the susceptibility values obtained across all instruments and configurations used in this work, illustrating that the "same" quantity takes different values depending on instrument, frequency, substrate and fitting model.

Sample	Magnetometer	ACS		LCR			E4991			
	Measured initial χ_i	@ 1 Hz	@ 1 kHz	Deduced χ_0	@ 10 kHz	@ 1 MHz	Deduced χ_0	@ 1 MHz	@ 50 MHz	@ 1 GHz
Fe–Comm p.	3.01	—	—	—	—	—	[a]	4.1	4.3	7.7
Fe–CP1 p.	6.36	—	—	—	—	—	11.3	8	5.3	—
Fe–CP1 m.	27.1	10.8	10.1	—	—	—	—	—	—	—
Fe–CP1 susp.	—	—	—	11.87	17 (DI) 10 (AA)	10 (DI) 8.2 (AA)	—	—	—	—
Fe–TDH4 p.	4.76	—	—	—	—	—	[b]	[b]	3.6	—
Fe–TDH4 m.	13.2	—	—	—	—	—	—	—	—	—
Mn–CP1 p.	5.35	—	—	—	—	—	—	—	—	—
Mn–CP2 m.	53.4	14.5	12.5	—	—	—	—	—	—	—
Mn–CP3 p.	14.8	—	—	—	—	—	33.9	15.3	9.62	4
Mn–CP3 susp.	—	—	—	14.05	28 (DI) 12.5 (AA)	16 (DI) 8.1 (AA)	—	—	—	—
Co–CP1 p.	21	—	—	—	—	—	—	—	—	—
Co–CP1 susp.	—	—	—	16.8	11.5 (DI) 2.5 (AA)	0.7 (DI) 0.7 (AA)	—	—	—	—

[a] Debye model not applicable: no SPM behaviour.
[b] Signal too noisy for reliable fitting.

Table 6.12 Summary of the obtained susceptibilities through different measurements in this work. In the "Conf." column, "p." stands for powder, "m." for cellulose membrane and "susp." for inductor suspension. "Deduced χ_0" refers to the zero-frequency extrapolation obtained by fitting the Debye model to AC data. In the LCR columns, values are given for deionised water (DI) and agar-agar (AA) suspensions where both were measured.

6.6.1 Summary of the workflow

The experimental work of this chapter is divided into three blocks. First, CP nanoparticles of four types (Mn–CP2, Mn–CP3, Fe–CP1, Co–CP1) deposited on 160 µm thick nitrocellulose membranes were measured with two coil geometries: wound coils connected to a custom Colpitts oscillator PCB, and a planar coil connected to the TI LDC1614 evaluation board (Section 6.2). These measurements established the linearity of the inductive signal with nanoparticle mass, the sensitivity ranking across ferrite compositions, and the frequency dependence of the detection signal between 600 kHz and 19 MHz (Section 6.3.1).

Second, nitrocellulose membranes loaded with Fe–CP1, Mn–CP3 and Co–CP1 were dried under a 500 mT static field to pre-orient the EA of the nanoparticles (Section 6.4). The resulting directional susceptibility was probed with both planar and wound coils, whose excitation fields are respectively parallel and transverse to the drying field direction. SEM imaging provided morphological evidence of field-induced clustering within the membrane.

Third, the same nanoparticle types were suspended in DI water (mobile) and agar-agar (immobilised) inside 2 mL eppendorfs, around which coils were wound (Section 6.5). Impedance measurements with the LCR4284 (10 kHz–1 MHz) and frequency measurements with the Colpitts oscillator (150 kHz–4 MHz) quantified the influence of particle mobility on the effective permeability. A combined Debye fitting on the DI and agar-agar datasets extracted magnetic and hydrodynamic parameters from the two conditions simultaneously.

6.6.2 Conclusions regarding the nanoparticle samples

The sensitivity ranking observed with the inductive sensors, Mn–CP2 $\approx$ Mn–CP3 $>$ Fe–CP1 $\gg$ Co–CP1, is consistent across all measurement configurations: Colpitts oscillator with wound coils, LDC planar coil, and LCR impedance analyser. This ranking reproduces the initial susceptibility hierarchy established by SQUID magnetometry in Chapter 4 (Table 4.14). The Mn–CP3/Fe–CP1 sensitivity ratio measured with the Colpitts oscillator (2.0–2.5, Table 6.4) is coherent with the initial susceptibility ratio from SQUID ($\chi_i = 14.8/6.36 \approx 2.3$) and the Debye-fitted static susceptibility ratio from E4991 measurements ($33.9/11.3 \approx 3.0$, Table 4.13). We conclude that the initial susceptibility measured with laboratory instruments is a reliable proxy for predicting the relative signal strength of these portable inductive sensors (operating below SRF of the inductors).

Co–CP1 generates the weakest signal despite exhibiting the highest initial susceptibility among the three ferrites when fully demagnetised (Table 4.14). Under

the low excitation field of the oscillator ($\approx$ 0.15 mT), the high magnetocrystalline anisotropy of cobalt ferrite (Table 4.3) results in a coercive field that prevents significant magnetisation change. However, when Co–CP1 is suspended in DI water and measured with the LCR analyser, the Brownian relaxation channel provides sufficient additional susceptibility to make it detectable (Fig. 6.12). This observation is consistent with the high anisotropy: Néel relaxation contributes less, so the Brownian dynamics accounts for a larger fraction of the total response.

Nanomag-D control beads (hydrodynamic diameter $>$ 200 nm) show no difference between the two media (Fig. 6.15). The invariance of Nanomag-D confirms that the frequency-dependent differences observed for the smaller nanoparticles are of Brownian origin and not a measurement artefact.

6.6.3 Conclusions regarding the measurement set-up

Proof of concept: Linearity and frequency stability on the portable set-up: The frequency change induced by nanoparticles in the LC-tank oscillator is linear with nanoparticle mass, validated at both 600 kHz and 5.9 MHz with $R^2 > 0.99$ for Fe–CP1 and Mn–CP3 (Fig. 6.4). The normalised differential signal $D_{\mathrm{norm}}(f)$ remains within 10 % of unity across the 3–19 MHz range (Fig. 6.7), including measurements alternating between two different wound coils. These two properties, linearity with mass and stability of the calibration ratio over frequency, are prerequisites for quantitative LFA sensing.

Flexibility offered by the set-up: A practical advantage of inductive sensing is that the coil geometry can be adapted to match the sample container: a coil wound around a 2 mL eppendorf probes a suspension volume, while a planar coil placed underneath a nitrocellulose strip probes a thin membrane. This geometrical flexibility allows characterisation to be performed in conditions close to the final biosensor configuration, so that the obtained data are directly representative of the intended application. With this approach, LCR measurements between 10 kHz and 1 MHz unambiguously distinguish mobile nanoparticles (DI water) from immobilised ones (agar-agar) using a hand-wound coil connected to a laboratory impedance meter. The Colpitts oscillator, a low-cost portable reader, confirms this tendency: CP samples in DI water yield systematically higher signal per mass than in agar-agar.

For identical nitrocellulose samples, the planar coil yields a relative sensitivity approximately 116 times higher than the wound coil for Mn–CP3 (Table 6.5 versus Table 6.4). This is attributed to the near-field concentration of the planar geometry: the nanoparticle layer sits directly on the coil surface where the field intensity is highest, whereas the 160 µm thick membrane occupies only a small fraction of the wound coil bore. Conversely, wound coils are better suited for volumetric sam-

ples such as eppendorf tubes or liquid suspensions, where the sample fills a larger fraction of the coil bore. The two geometries are therefore complementary.

The leverage of easy-axis orientation: The combination of planar and wound coils is particularly relevant for probing EA orientation effects. The planar coil generates a sensing field parallel to the membrane plane, whereas the wound coil generates a field transverse to it. Measuring the same field-dried sample with both geometries therefore provides two orthogonal projections of the directional susceptibility.

Drying nanoparticle-loaded membranes under a 500 mT static field produces a repeatable change in the inductive signal: 8 to 16 % increase when the EA are aligned parallel to the sensing field, and 6 to 16 % decrease when they are transverse (Fig. 6.10). The total signal difference between the best and worst configurations reaches 31 % for the 14.8 µg $MnFe_2O_4$ sample. This is comparable in magnitude to hardware-based sensitivity improvements reported in the benchmark tables of Chapter 5 (Tables 5.1 and 5.2). SEM imaging (Fig. 6.9) revealed that the drying field simultaneously alters EA orientation and cluster morphology. The individual contributions of these two effects to the observed signal change could not be separated. The minimum drying field strength required to induce the orientation effect was not determined. Repeating the experiment with decreasing field strengths would identify the practical threshold for integration into a portable LFA reader.

6.6.4 Conclusions regarding the applied models

Debye fitting on LCR data: comparison with E4991 results from Chapter 4: The polydisperse Debye model (Eq. 2.47) was applied in two distinct configurations across this thesis: to immobilised CP powders measured with the E4991 impedance analyser over 1 MHz–1 GHz (Table 4.13), and to CP suspensions measured with the LCR4284 over 10 kHz–1 MHz (Fig. 6.13). Both applications fit the same mathematical expression to frequency-dependent susceptibility data. The key difference is that the LCR fitting exploits two complementary conditions: agar-agar data, where only Néel relaxation contributes, and DI water data, where both Néel and Brownian relaxation are active. Combining these two distinct dynamics within the same Debye framework constrains the fit based on two different physical mechanisms rather than on a single relaxation channel.

The LCR fitting yields static susceptibilities χ_0 of 14.05 (Mn–CP3), 11.87 (Fe–CP1) and 16.84 (Co–CP1). While these are underestimations compared to SQUID-derived values, the relative ranking between samples is correct and consistent with Table 4.14. The expanded susceptibility compilation in Table 6.12 illustrates clearly the challenge of heterogeneous reporting identified in the literature survey (Section 5.3): the “same” quantity, initial susceptibility, takes different

values depending on the instrument, frequency range, sample preparation and fitting model.

The fitted median magnetic diameters from LCR data (9.92 nm for Fe–CP1, 9.04 nm for Mn–CP3) are closer to Chantrell-fitted values from magnetisation curves (7.95 and 11.0 nm respectively, Table 4.15) than the E4991 powder fits (5.32 and 6.30 nm, Table 4.13). The E4991 diameters were already noted to be 33–43 % smaller than the Chantrell references (Section 4.6). We make the hypothesis that this increase arises (among other things) because the LCR fitting uses real susceptibility data from two complementary conditions (mobile and immobilised), both dominated by volume-weighted dynamics, whereas the E4991 fitting included both χ' and χ'' on a single immobilised condition, where the imaginary component is more sensitive to number-weighted phenomena (Section 4.6).

6.6.4.1 Validity of the Debye model for cross-comparison of immobilised and mobile MNP samples

As expected, the fitted K_{eff} of Co-CP1 is an order of magnitude above Mn–CP3 and Fe–CP1. However, the fitting does not respect the ordering between Fe–CP1 and Mn–CP3. Since K_{eff} scales with the magnetic volume, this inconsistency is likely introduced by the fact that the fitted V_{mag} distribution is constrained to be proportional to the V_H distribution. The hydrodynamic-to-magnetic volume ratio h is treated as a single constant for the entire size distribution, which is a simplification: in reality, the cluster size distribution in suspension introduces a distribution of h values. Since this would add extra freedom to the fitting, it should be contraint by repeated measures at different concentrations. Comparative DLS measurements would help quantify hydrodynamic diameters independently.

The Debye model provides a consistent framework for describing this decay across both frequency ranges, despite the different physical mechanisms at play (Néel only in powder, Néel + Brownian in suspension). The fact that the model yields a correct relative ranking of χ_0 and plausible orders of magnitude for K_{eff} across both configurations supports its use as a semi-quantitative tool, provided its limitations are kept in mind. From a practical standpoint, preparing agar-agar and DI water suspensions is straightforward, provided the nanoparticles have adequate colloidal stability. Since each condition isolates a different relaxation channel, comparing the two responses with an impedance analyser or oscillator circuit offers a simple manipulation to cross-check magnetic parameters obtained by other techniques, or to gain additional insight into quantities such as K_{eff} and hydrodynamic diameter that are not directly accessible from a single immobilised measurement.

6.6.5 Key contributions of this chapter

1. **Characterisation of SPNF within biosensor-relevant substrates in the kHz–MHz range.** Nanoparticles were measured in nitrocellulose membranes

(Section 6.3.1) and in aqueous suspensions (Section 6.5), configurations that are directly representative of bio-applications. The susceptibility data obtained in this chapter complement the SQUID, ACS and E4991 measurements of Chapter 4, extending the multi-instrument susceptibility compilation (Table 6.12) to cover the 10 kHz–6 MHz range. **Perspective:** Deriving absolute susceptibility from the Colpitts oscillator data was not achieved, owing to the non-uniform distribution of nanoparticles within the coil volume and the incomplete characterisation of their permittivity over frequency. Covering the full surface of a planar coil with a homogeneous membrane and independently measuring the frequency-dependent permittivity of each sample type would allow the effective medium approach to be applied (Lichtenecker's equation) and convert inductance changes into absolute susceptibility values.

2. **Joint Debye fitting of mobile and immobilised suspensions with the hydrodynamic parameter h.** By fitting the Debye model simultaneously to DI and agar-agar data with a shared parameter set and a single additional parameter h (Eq. 6.11), the Néel and Brownian contributions could be separated within the same measurement framework. To the best of our knowledge, this joint-fitting approach has not been reported previously. **Perspective:** Treating the hydrodynamic factor h as a probability distribution rather than a constant would better represent the diversity of cluster sizes in suspension. This requires measuring nanoparticle suspensions at multiple concentrations with validated hydrodynamic diameters from DLS, and extending the LCR measurement frequency below 100 Hz (with larger coils) to observe the Brownian relaxation peak directly.
3. **Demonstration that relevant magnetic parameters can be extracted with equipment from an electrical engineering laboratory.** The wound coils used in this work are hand-wound copper wire on 3D-printed supports, connected to either an LCR meter or a Colpitts oscillator built from standard discrete components (total component cost below thirty euros). Despite this simplicity, the set-up reproduces the qualitative susceptibility trends observed with laboratory-grade instruments: the correct sample ranking, frequency-dependent Néel relaxation (Fig. 6.15), and the distinction between mobile and immobilised nanoparticles. The Colpitts oscillator measurements confirm the frequency trends observed by the LCR meter for both mobile and immobilised samples. The planar coil on the LDC evaluation board further confirms these observations with higher sensitivity. This validates inductive sensing as a practical bridge between advanced characterisation and portable biosensing. Coils offer flexibility in geometry and can measure samples with a configuration close to the final application. The relevance of characterising nanoparticles in aqueous suspension is supported by several bio-application contexts described in this work. In

LFA, nanoparticles are suspended in the liquid front during wicking before being captured at the test line (Section 5.4); the susceptibility during this mobile phase differs from that of the immobilised state, as demonstrated in Section 6.5. Furthermore, Tian et al. [303] showed that monitoring the Brownian relaxation frequency of suspended nanoparticles enables biodetection of Zikavirus through immunologically stimulated agglomeration, and Viereck et al. [105] demonstrated that discriminating bound from free nanoparticles via ACS is a viable detection modality. These examples confirm that suspension-based inductive measurements address configurations that are directly encountered in biosensing workflows.

4. **Proof of concept inductive SPNF sensor on nitrocellulose** The frequency change is linear with nanoparticle mass ($R^2 > 0.99$) and the calibration ratio is stable over a frequency decade (Fig. 6.7). These are prerequisites for quantitative LFA sensing. The minimum detectable mass is 7 µg for Mn–CP3 at 6 MHz with the Colpitts oscillator (Section 6.3.1). **Perspective:** The planar coil geometry was identified as the most sensitive configuration for thin-membrane samples (Table 6.5), owing to the concentration of the sensing field at the coil surface. Further development of the proof-of-concept reader for LFA applications should therefore focus on optimising the planar coil design: track width, number of turns, and substrate permittivity can be tailored to maximise the filling factor for nitrocellulose membranes of standard thickness. Additionally, the higher susceptibility observed for mobile nanoparticles (Section 6.5) raises the question of whether performing the readout during the wicking phase, while nanoparticles are still suspended in the liquid front, could yield a stronger signal than measuring the dried strip. Investigating this would require characterising the time window during which nanoparticles remain mobile in the membrane and the reproducibility of the signal during capillary flow.

5. **Identification of easy axis pre-orientation as an underexplored lever for signal improvement.** Drying nanoparticle-loaded membranes under a static field improves the inductive signal by up to 16 % (Fig. 6.10), without any modification to the nanoparticles or the interfacing electronics. The total signal difference between the best and worst EA configurations reaches 31 %. None of the detection studies benchmarked in Tables 5.1 and 5.2 report on practical implementation of this effect, yet the improvement in signal strength is significant. **Perspective:** The drying field simultaneously alters EA orientation and cluster morphology (Fig. 6.9). Measuring magnetisation curves on field-dried versus non-field-dried membrane samples, at room temperature and 3–5 K, would help to distinguish the contributions of each phenomenon more precisely.

Chapter Summary

This chapter integrates the SPNFs (made by CP) of Part I into simple inductive sensing platforms, to provide both a proof of concept for LFA-compatible detection and a complementary characterisation of the same batches in the kHz–MHz range. Three configurations were investigated: nitrocellulose membranes loaded with CP nanoparticles, field-dried membranes with pre-oriented EAs, and aqueous suspensions (DI water and agar-agar) in 2 mL eppendorfs. Two coil geometries were used, hand-wound copper coils and a planar coil on the TI LDC1614 evaluation board, connected to either a custom Colpitts oscillator or to laboratory impedance meters.

Inductive signal on nitrocellulose membranes: The frequency shift of the Colpitts oscillator is linear with deposited nanoparticle mass ($R^2 > 0.99$) and the normalised differential signal remains within 10 % of unity across the 3–19 MHz range. The sensitivity ranking Mn–CP2 $\approx$ Mn–CP3 $>$ Fe–CP1 $\gg$ Co–CP1 reproduces the initial susceptibility hierarchy established by SQUID magnetometry in Chapter 4. The Mn–CP3/Fe–CP1 sensitivity ratio (2.0–2.5) is coherent with the SQUID χ_i ratio (2.3) and the Debye-fitted χ_0 ratio from E4991. The minimum detectable mass is 7 µg for Mn–CP3 at 6 MHz. For identical nitrocellulose samples, the planar coil yields a relative sensitivity approximately 116 times higher than the wound coil, which we attribute to the near-field concentration of the planar geometry and the high filling factor of a thin membrane at the coil surface. In contrast, the simplicity of hand-winding a copper wire is a qualitative advantage compared to integrating planar coils on a PCB design.

Easy-axis pre-orientation: Drying nanoparticle-loaded membranes under a 500 mT static field produces a repeatable change in the inductive signal: an 8 to 16 % increase when the EAs are aligned parallel to the sensing field, and a 6 to 16 % decrease when they are transverse. The total signal difference between the best and worst configurations reaches 31 % for a 14.8 µg $MnFe_2O_4$ sample. SEM imaging reveals that the drying field simultaneously alters EA orientation and cluster morphology, and the individual contributions of these two effects could not be separated from the inductive data alone. To the best of our knowledge, no detection study benchmarked in Tables 5.1 and 5.2 exploits this lever for signal improvement.

Aqueous suspensions and joint Debye fitting: LCR measurements between 10 kHz and 1 MHz distinguish mobile (DI water) from immobilised (agar-agar) nanoparticles using a hand-wound coil connected to a laboratory impedance meter. The Colpitts oscillator, a low-cost portable reader, confirms this tendency: CP samples in DI water yield systematically higher signal per mass than in agar-agar, while Nanomag-D control beads (hydrodynamic diameter $>$ 200 nm)

show no such difference, confirming a Brownian origin. The polydisperse Debye model was fitted jointly to the DI and agar-agar datasets with a shared parameter set and a single additional hydrodynamic factor h, separating Néel and Brownian contributions within the same framework. The fitted χ_0 values (14.05 for Mn–CP3, 11.87 for Fe–CP1, 16.84 for Co–CP1) underestimate the SQUID-derived χ_i but preserve the correct ranking. The fitted median magnetic diameters (9.92 nm for Fe–CP1, 9.04 nm for Mn–CP3) are closer to the Chantrell references than the E4991 powder fits. The approach is presented as a cross-check rather than an absolute measurement: treating h as a constant rather than a distribution is a limitation, to be addressed by varying the concentration and combining with independent DLS data.

Multi-instrument susceptibility compilation: Table 6.12 assembles the susceptibility values obtained across all instruments and configurations used in this work, from SQUID magnetometry in powder and membrane, through ACS at 1 Hz–1 kHz, LCR at 10 kHz–1 MHz, and E4991 at 1 MHz–1 GHz. The "same" quantity, initial susceptibility, takes different numerical values depending on instrument, frequency, substrate and fitting model, which illustrates the heterogeneous-reporting issue identified in the literature survey of Chapter 5. Within a single instrument and substrate, however, the relative ranking between compositions is preserved, which supports the use of a subset of measurements for evaluating the relative impact of e.g. changes in concentration, substrate,...

7

Conclusion and Perspectives : Integrating MNP in Biosensors

This final chapter proposes (parts of) answers to the scientific and engineering questions (SQ and EQ) raised in the introduction. It then summarizes the main contributions of the thesis, and closes with a set of perspectives organised by effort and expected impact. A degree of redundancy between the two parts is accepted, so that the answers to the SQs and EQs remain self-contained.

7.1 Scientific Questions on SPNF Properties

SQ 1: What intrinsic parameters set the magnetic response of SPNF?

Superparamagnetic behaviour arises when the magnetic anisotropy energy $K_{\text{eff}}V$ of a monodomain nanoparticle becomes comparable to the thermal energy k_BT, so that the magnetic moment spontaneously reverses on a timescale shorter than the measurement window. The characteristic reversal time is described by the Néel–Arrhenius law (Eq. 2.30). Assuming good crystallinity, two intrinsic properties set this balance: composition and size.

Composition: The elemental composition of a ferrite nanoparticle principally governs two intrinsic bulk quantities: the saturation magnetisation M_s and the magnetocrystalline anisotropy constant K_{m} (Table 4.3). While the three ferrite compositions studied in this work (Fe_xO_y, $MnFe_2O_4$ and $CoFe_2O_4$) have comparable bulk saturation magnetisations (80–92 Am^2/kg), their magnetocrystalline anisotropies differ by nearly two orders of magnitude: K_{m} ranges from 3 kJ/m^3 for $MnFe_2O_4$ to 200 kJ/m^3 for $CoFe_2O_4$. This difference directly determines which compositions display superparamagnetic behaviour at a given particle size. The 13.4 nm cobalt ferrite nanoparticles (Co–CP1) exhibited significant coercivity (approximately 20 mT) in magnetisation curves (Section 4.3), while 8–12 nm magnetite and iron oxide SPNF showed (near-)superparamagnetic behaviour at room temperature depending on interactions. Manganese ferrite nanoparticles of similar sizes showed the lowest effective anisotropy across all characterisation techniques (Table 4.15), resulting in higher initial susceptibility and a more pronounced superparamagnetic response.

Size: Two diameters govern the magnetic behaviour of ferrite nanoparticles as a function of their physical size (Fig. 2.3, Table 2.3): the polydomain limit D_p and the critical diameter for superparamagnetism D_c. Above D_p, magnetisation reversal is dominated by domain wall motion rather than coherent rotation. Below D_c, the anisotropy energy barrier $K_{\text{eff}}V$ becomes comparable to k_BT and superparamagnetic behaviour appears. This was confirmed experimentally in this work: the 33 nm Mn–CP1 and 130 nm Fe–Comm samples show coercivity in magnetisation curves, while the 8–10 nm counterparts (Fe–CP1, Mn–CP2, Mn–CP3) showed

(nearly, depending on interactions) superparamagnetic behaviour in magnetisation measurements, FC-ZFC and ACS characterisation.

SQ 2: How do configurations modify these intrinsic properties?

A central finding of this work is that the macroscopic magnetic properties of SPNF depend not only on intrinsic particle parameters (composition, size, crystallinity; SQ 1) but also on the physical configuration in which they are measured.

Mobility: For nanoparticles suspended in a liquid medium, two parallel relaxation pathways are simultaneously available: Néel relaxation (internal moment reversal) and Brownian relaxation (physical particle rotation). Brownian rotation provides an additional alignment pathway: the particle physically rotates to reduce the Zeeman energy, thereby shortening τ_{eff} (Eq. 2.36) and increasing χ' at frequencies below the Brownian relaxation frequency. This was observed directly in LCR impedance measurements (Section 6.5): for all three ferrite compositions, the real part of susceptibility was systematically higher in deionised water (mobile) than in agar-agar (immobilised) at the same concentration. The control beads (Nanomag-D, hydrodynamic diameter > 200 nm) showed little difference in frequency dependency between the two media between 1 kHz and 1 MHz, confirming that the effect is of Brownian origin (Fig. 6.12).

Dipolar interactions and K_{eff}: In any concentrated ensemble, dipolar interactions modify the effective energy barrier. Morüp et al. [69] classify both dense colloidal suspensions and compacted powders as "high-interaction" regimes. In this work, the effective anisotropy K_{eff} extracted from FC-ZFC and ACS measurements was systematically one order of magnitude above the bulk K_{m} for all compositions and configurations (Table 4.15). This is consistent with the observation by Demortiere et al. [38] of a significant increase in T_B for 9 nm nanoparticles in concentrated assemblies. Within the Dormann–Bessais–Fiorani (DBF) framework, these interaction contributions are folded into K_{eff}, which is therefore a configuration-dependent effective parameter rather than a material constant (modelling aspect developed in SQ 4).

Nitrocellulose as specific substrate for LFA: The nitrocellulose membrane in which nanoparticles are embedded for LFA applications exerts a significant effect on the macroscopic magnetic properties. Dipolar interactions are reduced compared to powder form: superparamagnetic samples that appear blocked at room temperature in the former configuration appear unblocked in the latter. The initial susceptibility of membrane-dispersed samples was three to four times higher than for the same batches in compacted powder (Table 4.14), for both SPION and Mn-SPNF. Simultaneously, the Chantrell-fitted shape factor γ was systematically broader in membranes, which we interpret as reflecting a distribution of agglomerate sizes formed during capillary flow and drying rather than a change in the

intrinsic single-particle size distribution. The FC-ZFC measurements strengthen this interpretation: the gap between irreversibility temperature T_{irr} and T_B exceeds 100 K for all membrane samples, consistent with a broad distribution of energy barriers arising from heterogeneous clustering.

Cobalt ferrite as explicit illustration: The case of cobalt ferrite provides a clear illustration of how the measurement configuration determines which magnetic properties are accessible to a given sensor. Cobalt ferrite nanoparticles (Co–CP1):

1. exhibit the highest *demagnetised* initial susceptibility among the three ferrites when measured by SQUID at quasi-static conditions (Table 4.14),
2. produce the *weakest* inductive signal across all sensor configurations when immobilised in membranes (Figs. 6.4 and 6.5),
3. yet show the *largest* susceptibility contrast between mobile and immobilised states in LCR measurements. At 10 kHz, the real part of the volume susceptibility of Co–CP1 is approximately 11.5 in deionised water versus 2.4 in agar-agar (Fig. 6.12); the Debye-fitted DC value χ_0 over the full 10 kHz–1 MHz range is 16.84 (Section 6.5).

All three observations are mutually consistent: the high K_{m} of cobalt ferrite (Table 4.3) results in a Néel relaxation time too long for the sensing field to induce reversible magnetisation changes in immobilised particles, but Brownian rotation can still provide alignment when the particles are free to rotate in suspension.

SQ 3: How are appropriate SPNF with required properties for Lateral Flow Assays made?

Synthesis route: The choice of nanoparticle synthesis is a trade-off between monodispersity and practical yield. Given the limited reliability of the properties of commercially available nanoparticles [5], it is beneficial to be closely involved with the synthesis process in order to understand and control the resulting magnetic properties.

In this work, TD was performed to obtain monodisperse SPION batches ($\gamma^2 < 0.05$ for the majority of batches, Table 3.4). However, repeatability between batches was limited: median diameters varied between 7.5 and 11 nm across eleven syntheses (Section 3.2.3.1). The yield is approximately 150 mg of powder per batch. We demonstrated that doubling the initial reagent quantities does not significantly affect the size distribution, which is relevant for research purposes but not substantial enough for industrial purposes. The TD SPION did not reach saturation at 7 T and showed specific magnetisations at 55–65 % of the bulk value. This is attributed to a dominant dead layer contribution, which is expected to be more pronounced for nanoparticles below 12 nm [83]. Better control of the heating

ramp and performing the synthesis under inert atmosphere (argon flow) might improve both repeatability and oxidation control.

CP offers practical advantages regarding mass yield, hydrophilicity and colloidal stability. However the shape factors of the CP samples (γ= 0.25–0.46, Table 3.5) indicate broader size distributions than those obtained by TD. The CP nanoparticles showed higher initial susceptibility per unit mass but also higher T_B: the increased γ contributes to both phenomena, since the largest fraction of the distribution pulls χ_i up through its dominant magnetic volume and pulls T_B up through its higher energy barrier.

Material composition: Iron oxide (Fe_xO_y) introduces complexity due to the coexistence of magnetite and maghemite phases and the associated dead layer. However, for *in vivo* applications where toxicity is a primary concern, iron oxide remains the established standard [8]. Manganese ferrite ($MnFe_2O_4$) demonstrated a more favourable magnetic response throughout this work, owing to its lower crystalline anisotropy (Table 4.3): higher initial susceptibility was observed across all characterisation techniques and configurations (Table 4.14). Manganese ferrite is also less prone to oxidation than iron oxide under ambient conditions. Nevertheless, the stoichiometry of its surface may be affected when the pH is lowered, as the preferential dissolution of Mn^{2+} documented by Ma et al. [172] and confirmed by the ICP data in this work (Section 3.3.2.2) demonstrates that manganese ferrite nanoparticles are not chemically inert in acidic environments. This can be a local effect e.g. due to citric acid corona.

Corona and coating: At the ensemble level, the corona governs colloidal stability and hence the degree of clustering, which modifies dipolar interactions and the effective anisotropy (see SQ 2). Towards quantification purposes in biosensors, controlling colloidal stability is essential since it determines the number of nanoparticles linked to one immunological binding. A practical consequence of poor colloidal stability is reduced precision in pipetting and mass determination: the iron concentration per volume, once measured, must remain reliable across dilutions and extractions, and colloidally unstable samples can deposit on pipette walls, introducing systematic losses.

To improve the colloidal stability and biocompatibility of hydrophobic TD nanoparticles, two SiO_2-coating methods were compared. The reverse microemulsion method of Hou et al. [195] yielded the most homogeneous silica shell and the best control of shell thickness, although it requires several days of incubation with fractionated TEOS additions, which is a practical constraint. Silica-coated TD iron oxide nanoparticles (Fe–TDH4@Si) showed an increase in susceptibility per iron mass of approximately 20 % relative to the uncoated counterpart, observed in both magnetisation curves (Fig. 4.5) and E4991 impedance

measurements (Fig. 4.18). We attribute this to improved surface state, either due to ligand exchange or the coating itself, which reduces the broken-symmetry surface anisotropy K_S and dead layer effects. This observation is based on a single coated batch and requires confirmation on additional samples before a definitive conclusion can be drawn.

SQ 4: What models are appropriate to describe macro-properties of MNP at room temperature, from DC to 1 GHz?

Four theoretical models, summarised in Table 2.5, are applied throughout the 1 Hz to 1 GHz characterisation range of this work. An additional framework is applied regarding the defintion of effective anisotropy.

Langevin–Chantrell model: The Langevin function (Eq. 2.39) describes the equilibrium magnetisation of a superparamagnetic nanoparticle ensemble as a function of the Zeeman-to-thermal energy ratio. Chantrell extended this to polydisperse samples, enabling extraction of the median magnetic diameter and geometric standard deviation from measured $M(H)$ curves. Although the underlying hypotheses (non-interacting particles,...) are not strictly fulfilled in any experimental configuration of this work, Chantrell fitting (and its SSE) offers a good indicator of how "perfectly" the SPNF system behaves from a macroscopic point of view. In this work it helps identify that CP samples have more ideal superparamagnetic behavior than TD samples, probably due to stronger dead layer in the latter (Table 4.6). Since the Chantrell model does not account for anisotropy, interactions that effectively increase the energy barrier tend to manifest as a smaller fitted magnetic diameter.

Néel–Arrhenius and Vogel–Fulcher laws: The Néel–Arrhenius law (Eq. 2.30) relates the relaxation time to the energy barrier $K_{\text{eff}}V$ and temperature for non-interacting particles. For systems with significant inter-particle dipolar interactions, the empirical Vogel–Fulcher law introduces the interaction temperature T_0, which shifts the effective energy barrier. In this work, a sensitivity study (Section 4.5) revealed that the Vogel–Fulcher parameters (τ_0, K_{eff}, T_0) are strongly correlated: relaxing the τ_0 bound shifted the fitted K_{eff} by approximately 50 % with no change in fit quality. The Vogel–Fulcher law should therefore be used primarily as a relative measure of interaction strength across samples measured under identical conditions. The model-free Mydosh parameter Φ (Section 4.5) complements the Vogel–Fulcher fit by classifying the interaction regime without any assumption on τ_0 or particle diameter.

Debye model for complex AC susceptibility: The single-relaxation-time Debye model, extended to a lognormal distribution of relaxation times (Eq. 2.45), with the initial susceptibility given by Eq. 2.40, is the central tool for interpreting frequency-domain measurements. It is applied across the 1 kHz to 1 GHz

range: LCR impedance analysis (1 kHz–1 MHz) and coaxial impedance analysis with the E4991 (1 MHz–1 GHz). Despite the simplifying assumptions of a linear response regime and a single effective relaxation process, the model yields physically plausible initial susceptibilities and a correct relative ranking between samples (Tables 4.14 and 6.12). The addition of Brownian relaxation as a parallel pathway (Eq. 2.36) further extends the validity of the Debye framework to mobile suspensions (Fig. 6.13). The joint fitting of deionised water and agar-agar datasets within the same Debye framework (Section 6.5) constrains the fit using two distinct physical mechanisms rather than a single relaxation channel, which improves the reliability of the extracted parameters. The approach is not without limits: with a single hydrodynamic-to-magnetic volume ratio treated as a constant, the fit reproduces the K_{eff} of Co–CP1 but does not preserve the K_{eff} ordering between Fe–CP1 and Mn–CP3, which points to distributions of cluster sizes as the natural next refinement.

Stoner–Wohlfarth model: Strictly valid for coherently rotating single-domain particles with uniaxial anisotropy (Table 2.5), the Stoner–Wohlfarth model is applied in this work primarily as a qualitative framework: it provides the energy-landscape picture (Fig. 2.4) that underpins the understanding of easy-axis orientation effects (Section 6.4).

The K_{eff} umbrella: DBF framework and Serantes scaling: The Dormann–Bessais–Fiorani (DBF) approach folds inter-particle interactions, surface anisotropy and dead-layer effects into a single effective anisotropy constant K_{eff} (Section 2.3.6). This is a deliberate simplification: the physical origins of the energy barrier are not separated, and K_{eff} is therefore not a material constant but a configuration-dependent parameter (observed consequences in SQ 2). The framework is retained throughout this work because it delivers a single scalar that is comparable across techniques (SQUID magnetometry, FC-ZFC, ACS, E4991) and across configurations (powder, membrane). Serantes et al. [220] propose that the dipolar contribution to K_{eff} scales with the intrinsic material anisotropy K_{m} rather than adding a fixed offset. This scaling is consistent with the cross-composition ratios observed in this work: the FC-ZFC-derived ratio $K_{\text{eff}}(\text{Fe})/K_{\text{eff}}(\text{Mn})$ is 1.8–2.5 in membranes (Table 4.15), which falls within the bulk reference bracket $K_m(\gamma\text{-}Fe_2O_3)/K_m(MnFe_2O_4) = 1.5$ to $K_m(Fe_3O_4)/K_m(MnFe_2O_4) = 3.6$ (Table 4.3). This observation should be treated as indicative rather than conclusive: it is based on two compositions only, the magnetite/maghemite fraction of the iron oxide cores is not known, and the Mn-depleted surface of the manganese ferrite samples (Section 3.3.2.2) introduces uncertainty on the effective K_{m}. Verification on additional compositions would be required to confirm the generality of this scaling.

Practical applicability despite violated hypotheses: The key assumptions systematically violated in practice are: (i) the non-interaction hypothesis, since dipo-

lar interactions are present in any concentrated ensemble; and (ii) strict lognormality of the sample size distributions. Despite this, the Debye and Langevin–Chantrell frameworks remain the most practically useful models because they yield reliable relative comparisons and realistic orders of magnitude, provided that fitting boundaries are constrained by independent physical measurements from the analysis workflow of Fig. 4.20. The Vogel–Fulcher law requires low-temperature measurements and cannot be as easily deployed as impedance measurements at room temperature, but joint interpretation with the Mydosh parameter Φ provides a means to classify the set-up specific interaction regimes.

SQ 5: Which MNP properties govern the signal of an inductive LFA reader?

Superparamagnetism is not a prerequisite for colloidal stability: The framing adopted in this work treated superparamagnetism as the defining regime for MNP used as biomedical labels. The sensing results of Part II invite a narrower reading of this requirement for inductive LFA readout. The single-particle magnetic moment scales with the magnetic volume (Eq. 2.38) and the initial susceptibility scales with its square (Eq. 2.40), so a label in the $[D_c, D_p]$ window (Fig. 2.3) delivers more signal per particle than a strictly superparamagnetic counterpart below D_c. The operational constraint on inductive readout is not zero remanence but that the AC excitation field exceed the coercivity of the particles, which opens this monodomain-but-not-superparamagnetic window. It is often argued in the literature that nanoparticles must be superparamagnetic because zero remanence avoids magnetic dipole-induced clustering [58, 158]. The validity of this argument may be questioned, since colloidal stability is determined by a competition between multiple forces in which magnetic attraction is only one factor among van der Waals interactions, steric or electrostatic repulsion from the corona, ionic strength and pH. In this work, the thermally decomposed SPION (Fe–TDH4), while fully superparamagnetic, exhibited poor colloidal stability and agglomerated rapidly under a magnetic field[1]. By contrast, the 33 nm Mn–CP1, although not superparamagnetic, showed excellent colloidal stability owing to their well-controlled citric acid corona; applying a magnet to their container did not produce visible precipitation. Given that χ_i increases with particle volume, it is worth exploring the diameter range $[D_c, D_p]$ where nanoparticles are still monodomain but not strictly superparamagnetic, such as 20–30 nm particles. The main constraint is that the excitation field should exceed the coercivity of these particles: as an illustration, Mn–CP1 has a coercivity of approximately 3 mT in powder form, although this may be lower in a dispersed configuration where dipolar interactions are reduced. From a fluidic perspective, the size of agglomerates is more relevant than the size of individual

[1] Interestingly, agglomeration was slowed down when silica coating was applied, illustrating the competition between magnetic forces and drag forces.

nanoparticles. For nitrocellulose membranes with pore sizes between 1 and 10 µm, clusters of a few 30 nm particles would migrate without difficulty.

Easy axis pre-orientation: Drying nanoparticle-loaded membranes under a 500 mT static field improves the inductive signal by 8–16 % along the drying direction, by pre-aligning the easy axes of the nanoparticles with the sensing field (Fig. 6.10). The constraint that $K_{\text{eff}}V$ should remain small enough for the Néel relaxation time to be much shorter than the measurement time constant remains valid regardless of pre-orientation. Full figures of merit (directional spread, SEM evidence of cluster morphology changes, conditions for integration into a portable reader) are discussed under EQ 2.

Exploiting Brownian relaxation: Nanoparticles with rotational mobility exhibit higher susceptibility when the measurement time is close to the Brownian relaxation time (Section 6.5, Fig. 6.12; physical mechanism under SQ 2). This is not compatible with pre-aligning the easy axis (which requires drying), but it deserves further exploration, for instance by performing the readout during the wicking phase before the membrane has fully dried. Exploiting mobility has the advantage that nanoparticles with high anisotropy (which may be required in other bio-applications such as hyperthermia), or nanoparticles with $D > D_p$, can produce a relevant signal at excitation fields lower than their coercivity.

Maximising the inductive signal: frequency vs diameter The initial susceptibility χ_i is directly proportional to the signal strength for a sensor based on inductive impedance. Since $\chi_i \propto V_{\text{mag}}^2$ (Eq. 2.40), the MNP diameter should be as close as possible to D_c - or even beyond if strict SPM behavior is not required- to maximise the signal per particle while minimising the relative contribution of the dead layer (Subfigure 7.1 A). For inductive sensing with immobilized nanoparticles, the measurement should remain in the "following" range of the Debye response where χ' is maximal, which requires that $K_{\text{eff}}V$ be small enough for the Néel relaxation frequency to lie well above the measurement frequency. The measurement frequency is bounded from below by the requirements of inductive transduction and from above by the SRF of the coil and interfacing electronics. This work proposed two tracks worth exploring for further LFA design: pre-orientation of EA and exploiting mobility during drying. For the former it is not required to operate at sensing frequencies below brownian relaxation threshold: increasing operation frequency at the cost of decreasing nanoparticle volume is probably a relevant trade-off for inductive purposes. For the latter it is required to operate at a frequency which is low enough for significant Brownian relaxation to occur: V_H is the limiting parameter. If other factors remain identical, the V_H "budget" is best allocated clusters with few large particles than many small particles.

Maximising the inductive signal: field amplitude vs diameter To maintain a linear relationship between nanoparticle mass and sensor signal, which simplifies

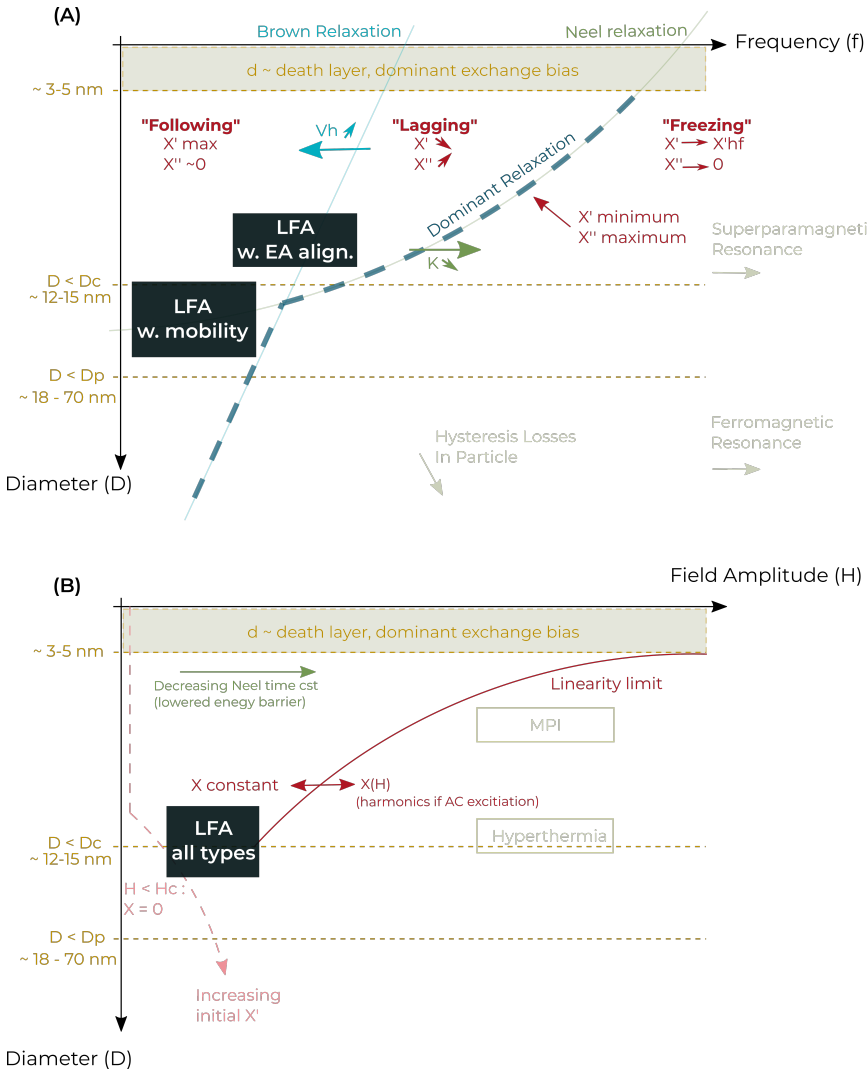


Fig. 7.1 Main phenomena affecting susceptibility: diameter vs frequency and diameter vs field amplitude. The indicated diameter values are representative for magnetite. The linearity limit is determined by the Langevin equation (Eq. 2.39); Néel and Brownian relaxation fronts are determined by Eq. 2.30 and 2.35. Red labels identify the different behaviours of susceptibility χ with "following, lagging and freezing" elaborated in Section 2.3.5.1. In (A) the green (resp. blue) arrow indicates how the Néel (Brownian) relaxation front moves with values of anisotropy K (hydrodynamic volume V_H).

quantification, Subfigure 7.1 B illustrates that the nanoparticles should be excited within the linear range of the Langevin function as defined in 2.3.4.1. For sensor design, the excitation field amplitude is limited by power consumption and shielding considerations: operating below or at the linearity limit with large monodomain nanoparticles almost naturally fulfills these conditions. For comparison: magnetic particle imaging (MPI) exploits the non-linear magnetisation response and therefore favours low-anisotropy nanoparticles that respond quickly and symmetrically around zero field [16]. Magnetic hyperthermia operates in the hundreds of kHz range at mT-range AC fields and relies on hysteretic losses, which favour higher-anisotropy nanoparticles where each cycle dissipates heat [9].

7.2 Engineering Questions on Inductive LFA Design

EQ 1: What magnetic characterisation steps are necessary for inductive SPNF sensor design on specific substrates?

The characterisation techniques applied in this work span three levels of instrumentation complexity. Their complementarity is summarised in the workflow of Fig. 4.20: each technique accesses the magnetic properties through a different physical variable (field, temperature, frequency) and yields partially overlapping but not identical parameter sets.

Structural preliminaries: Before any magnetic measurement, two inputs are required per batch: TEM (number-weighted diameter and polydispersity), ICP (iron mass fraction, Fe/Mn ratio for mixed ferrites). Dynamic light scattering (DLS; hydrodynamic diameter) offers an important benchmark if nanoparticle mobility contributes to the desired sensor signal. These measurements define the "what is in the sample" baseline that the magnetic workflow then interprets.

Level 1: Low-cost oscillator-based characterisation: The Colpitts oscillator and the LDC planar coil (Chapter 6) operate between 100 kHz and 19 MHz with a total component cost below 30 euros. Despite this simplicity, they correctly reproduce the relative susceptibility ranking established by laboratory instruments: manganese ferrite consistently generates approximately twice the signal of iron oxide across all frequencies and configurations (Table 6.4). The distinction between mobile and immobilised nanoparticles is also detectable (Fig. 6.15). Winding copper wire fifteen times around an eppendorf is sufficient to observe the impact of Brownian relaxation at the nanoscale.

Level 2: Benchtop impedance analysis: The LCR4284 (10 kHz–1 MHz) and E4991 (1 MHz–1 GHz) impedance analysers provide quantitative complex susceptibility spectra from which the Debye model extracts initial susceptibility, effective anisotropy, and magnetic diameter (Tables 4.13 and 6.12). Measuring inductive

impedance is less affected by permittivity changes than an oscillator-based system (if operating sufficiently below the coil SRF). Both impedance analysers are complementary: to achieve an overview of frequency-dependent properties although more nanoparticle mass is required at frequencies (coils need to be larger to operate in inductive range at lower frequencies). Both measurements are non-destructive when applied to powder or liquid samples, which is relevant given the small yields of thermal decomposition synthesis (approximately 150 mg per batch, SQ 3). Dispersing nanoparticles in agar-agar de facto sacrifices them. LCR4284 measurements are done on hand-wound coils that can adapt to any container morphology (contraint is inductance value) while E4991 equipment imposes two toroid holder sizes. Exploring other inductance layouts for characterisation is feasible on the latter. Applying the Debye model simultaneously to mobile and immobilised suspensions (Section 6.5) resolves the K_{eff}–diameter degeneracy that limits single-configuration fitting. These instruments remain benchtop equipment, but the measurements themselves (impedance spectroscopy and Debye fitting) require no specialised magnetic infrastructure and can be performed entirely in an electronics laboratory.

Level 3: SQUID magnetometry: The SQUID magnetometer (Chapter 4) provides the deepest physical insight. Magnetisation curves at room temperature yield the saturation magnetisation and initial susceptibility; Chantrell fitting extracts the magnetic diameter and size distribution. FC-ZFC measurements access the blocking temperature and, combined with an assumed diameter, the effective anisotropy (Table 4.15). ACS measurements classify the interaction regime through the Mydosh parameter (Table 4.10). SQUID measurements offer more fundamental insights in the batches, such as the coexistence of two relaxation populations (well below room temperature) in SPION samples. The dead-layer contribution and the role of dipolar interactions, both of which affect the effective susceptibility in the final application, require this technique to be better understood. However, SQUID measurements are time-consuming, require cryogenic infrastructure, and characterise nanoparticles under conditions (compacted powder, high fields, cryogenic temperatures) that differ substantially from the sensing configuration.

One-time versus per-batch characterisation: Characterisation steps recommended during iterations of inductive sensor design:

- **Once per substrate:** when changing membranes and pore size, SQUID measurements (magnetisation curves and FC-ZFC) on the same batch in different media can help identify the clustering dynamics, oxydation effects,... This mapping in magnetic behavior is a relevant complement to TEM or SEM images (more complex on 3D samples and non-conductive materials). When the influence of the substrate is understood it can be transposed to similar nanoparticles (but remains subject to investigation if inconsistencies occur).

- **Once per synthesis route:** Magnetisation curves and initial magnetisation are needed to extract saturation magnetisation and initial susceptibility data. FC-ZFC and ACS measurements to establish the blocking temperature, effective anisotropy, and interaction regime. The full LCR4284 and E4991 Debye spectrum provides the frequency-dependent susceptibility profile. These measurements are resource-intensive but need not be repeated for every batch of the same composition and synthesis protocol.

- **Per batch:** TEM offers insights in diameter and polydispersity, and helps assess validity of comparison with previous structural benchmarks. ICP correlates sample mass with magnetic content and should ideally be done systematically unless reproducibility of the batches synthes (and coating) is validated. One magnetic measurement should validate coherence with the exhaustive magnetic characterisation done for the synthesis route, to exclude outliers: magnetisation curves require little sample mass but SQUID operation is resource consuming, while impedance analysis needs more magnetic content but is quick, non-destructive and available in most sensor design lab. Decent Debye fitting requires to be done in at least three frequency decades and on two (complementary) datasets: either mobile and immobile nanoparticles (requires two measurements but poses better constraints on diameter fitting) or real-imaginary parts of susceptibility (requires only one).

EQ 2: What sensor properties are achieved with the proof of concept sensor? How does this compare to literature? What recommendations for improved figures of merit?

Proof-of-concept sensor: The inductive sensing set-up developed in this work consists of a hand-wound solenoidal copper-wire inductor (coil properties listed in Table 6.2), off-the-shelf discrete capacitors, a Colpitts oscillator topology (Fig. 6.1), and a Teensy microcontroller for frequency counting, with a total component cost below approximately 30 euros. Two coil configurations were tested: wound coils (operating between 600 kHz and 19 MHz) and a commercial planar coil on the TI LDC1614 evaluation module (operating at $\sim$2 MHz).

Achieved figures of merit: With the wound coil L1, the absolute sensitivity for Mn–CP3 is 1.93 Hz/µg Fe at 603 kHz and 15.0 Hz/µg Fe at 5.9 MHz (Table 6.4). The corresponding relative sensitivities are 3.21×10^{-4} %/µg and 2.50×10^{-4} %/µg respectively, the same order of magnitude obtained by Richardson et al. [265] with a wound coil. The frequency change is linear with nanoparticle mass ($R^2 > 0.99$ for Fe–CP1 and Mn–CP3, Fig. 6.4), validating the linear approximation of Eq. 6.2. The smallest mass demonstrating linear response is approximately 7 µg for Mn–CP3 at 5.9 MHz. The exact limit of detection was not formally determined, since the granularity of the mass samples was not fine enough to resolve the noise floor at

the 3σ level (Section 6.3.1). A denser mass series in the sub-10 µg range would be required. Nevertheless, the demonstrated linearity ($R^2 > 0.99$) and the frequency independence of the calibration ratio are prerequisites for quantitative LFA sensing. The planar coil on the LDC1614 achieves an absolute sensitivity of 1117 Hz/µg Fe for similar Mn–CP3 masses at 2 MHz, corresponding to a relative sensitivity of 3.72×10^{-2} %/µg (Table 6.5), the same order of magnitude as obtained by Marques-Fernandez et al. [244] with a planar coil. . The improvement is attributed to the near-field concentration of the planar geometry, where the membrane sits directly on the conductor traces, and to the higher fraction of the coil's magnetic energy volume that overlaps with the nanoparticle layer. This is comparable to other single-frequency, inductive impedance-based nanoparticle detections.

Easy-axis pre-orientation: Drying nanoparticle-loaded membranes under a 500 mT static field produces a repeatable directional change in the inductive signal: 8 to 16 % increase when the EA are aligned parallel to the sensing field, and 6 to 16 % decrease when they are transverse, for a total directional spread of 31 % on a 14.8 µg $MnFe_2O_4$ sample (Fig. 6.10). The enhancement requires no modification to the sensor electronics. The minimum drying field required to induce the orientation effect was not determined (see Perspectives).

Gap relative to LFA requirements: The smallest nanoparticle mass demonstrating linear response in this work is approximately 7 µg for $MnFe_2O_4$ with the Colpitts wound coil at 5.9 MHz (Table 6.4). The nanoparticle masses tested in this work are consistent with single-frequency inductive readers [244], but remain above the sub-microgram regime relevant for low-abundance biomarker detection on LFA [97]. Planar coil design close to the testline, frequency mixing [3] and magnetic pre-enrichment, which concentrates the analyte before application to the strip, can further compensate for the sensitivity gap by increasing the local nanoparticle mass at the test line [1].

EQ 3: Are inductive LFA good candidates to respond to the ASSURED standards?

The ASSURED criteria (Affordable, Sensitive, Specific, User-friendly, Rapid and robust, Equipment-free, Deliverable to end-users) were defined by Kosack et al. [2] for point-of-care screening in low-resource settings, primarily with binary outcomes. Applied strictly to the quantitative biomarker detection that motivates magnetic LFA, several criteria either become mutually exclusive with quantitation or are governed by the assay rather than by the transducer.

Leverages towards ASSURED:

- The Colpitts reader of this work (Chapter 6) uses below 30 euros of components (EQ 2), fits in a handheld envelope with no static bias magnet, no

cryogenic stage and no lock-in amplifier, and sits below the price point of most commercial optical strip readers. Towards sensors with which disposable LFAs are read, this proof of concept is both affordable and portable.

- Inductive transduction is volumetric: it probes the full thickness of the nitrocellulose membrane, whereas optical readout senses only the top ∼10 µm [3]. Combined with the intrinsic matrix tolerance of permeability-based sensing (the SPNF-to-matrix contrast is orders of magnitude larger than any optical or dielectric contrast), this opens readout on opaque whole blood and turbid environmental samples, closed to AuNP.

- Magnetic pre-enrichment of the analyte upstream of the strip [1] is a direct lever on the captured mass at the test line, which acts on the binding-limited regime (see bottlenecks below) without complicating the reader electronics.

- A reader-based output removes the operator-dependent subjectivity of naked-eye AuNP readout identified by Li et al. [278], returns a quantitative value.

- The same inductor that enables the low-cost reader also extracts physically meaningful magnetic parameters (initial susceptibility, effective anisotropy, magnetic diameter, Brownian-to-Néel balance) via impedance spectroscopy and Debye fitting, using instruments standard in an electronics laboratory (EQ 1). This cross-disciplinary reduction lowers the interdisciplinarity barrier that the commercialisation survey (Section 5.5) identified as a recurring failure mode of the magnetic LFA community.

Bottlenecks towards ASSURED:

- The dynamic range of the reader does not equal assay dynamic range. The antibody–antigen kinetics compress the useful analyte concentration range to three or four orders of magnitude regardless of the transducer (Section 5.4), so pushing reader noise below the mass captured at the test line yields negligible returns on the overall LoD. This is why even sub-nanogram reader performance [3] has not translated into clinical dominance (Section 5.5).

- The sensitivity–simplicity trade-off established in the Chapter 5 benchmark (Section 5.3) bounds what a portable inductive reader can achieve: the best commercial platforms are not inductive (Atellica VTLi optomagnetic [284], MagArray spin-valve GMR [281]) and rely on static bias fields and proprietary cartridges incompatible with standard nitrocellulose strips. True portability and sub-nanogram LoD have not been reconciled in a single device, relating the difficulty of achieving sufficient sensitivity.

- ASSURED "Specific" is set by the antibody–antigen recognition, not by the transducer. Marquina et al. [5] obtained a fourfold difference in assay sensitivity between two functionalisation strategies on identical nanoparticles, so coupling chemistry of the corona dominates the overall response. Optimising antibody orientation requires bio-conjugation expertise outside the skillset of an electronics laboratory, and is the bottleneck least addressed by the magnetic LFA community. The inductive reader inherits this constraint without being able to influence it.

- The label itself is constrained: the single-domain moment scales as d^3 while nitrocellulose pores (1 to 10 µm) cap the hydrodynamic diameter, with ∼200 nm reported as the practical optimum [3]. Multicore beads reconcile moment and migration but rely on a coating step whose industrial supply chain is not yet standardised, and most commercial MNPs suffer from broad size distributions, significant non-magnetic mass fractions and poor batch-to-batch reproducibility [5], which propagates into any reader calibration.

- Deployed cost is not the reader cost. Regulatory approval, clinical validation and reimbursement dominate the total cost of any diagnostic platform [13, 14], and the manufacturing scale at which colloidal AuNP strips are produced sets a high bar. These barriers are largely independent of the sensing principle, but they are the reason the six surveyed magnetic ventures mostly underwent acquisition, pivot or cessation (Section 5.5), and they directly affect how "deliverable to end-users" magnetic LFA's are.

- Robustness to storage, humidity and temperature has not been characterised in this work and remains a gap towards Rapid-and-robust. Readout itself is sub-second, but the dominating timescale (5 to 15 minutes of wicking) is set by the assay and is identical across AuNP and MNP labels.

A window of relevance rather than a scorecard: Applied strictly, ASSURED suggests that inductive MNP-LFA partially meets four criteria (Affordable, Specific, User-friendly, Sensitive with pre-enrichment), is structurally unable to meet Equipment-free once quantitation is required, and remains insufficiently evaluated on Rapid-and-robust and Deliverable. More usefully, the tensions above delimit a window of relevance: inductive MNP-LFA is not the right tool for high-abundance binary screening, where AuNP with naked-eye readout outperforms on every ASSURED criterion. It becomes competitive when the target requires (i) quantitation over three to four orders of magnitude, (ii) sufficient analyte to leverage magnetic pre-enrichment, or (iii) readout of matrices where optical methods fail. Within that window, the relevant competitors are not AuNP strips but GMR [5] and frequency-mixing [3] readers. Inductive readout occupies the simplicity corner of that design

space: the least sensitive of the magnetic family, but also the cheapest and compatible with standard nitrocellulose strips. The contribution of this thesis to narrowing this gap is the methodological bridge between nanoparticle metrology and sensor design established in EQ 1, which directly addresses the cross-disciplinary barrier the commercialisation survey (Section 5.5) identified as a recurring failure mode of the magnetic LFA community.

7.3 Contributions and key findings

Multi-instrument susceptibility dataset: This work provides, to the best of our knowledge, the first systematic comparison of frequency-dependent complex susceptibility $\chi'(\omega)$ and $\chi''(\omega)$ for well-characterised ferrite nanoparticles across eight decades of frequency (sub-Hz to 1 GHz), measured in three distinct configurations: compacted powder, nitrocellulose membrane, and liquid suspension. The same batches of iron oxide, manganese ferrite, and cobalt ferrite were characterised by four complementary techniques (SQUID magnetometry, FC-ZFC, ACS, and E4991 impedance analysis), enabling a direct cross-comparison of the extracted parameters (Tables 4.14, 4.15, and 6.12).

K_{eff} is configuration-dependent, not a material constant: The effective anisotropy constant K_{eff}, extracted from FC-ZFC and ACS measurements, is one order of magnitude above the bulk magnetocrystalline anisotropy K_{m} for all compositions and configurations (Table 4.15). This is consistent with the Dormann–Bessais–Fiorani (DBF) framework, in which dipolar interactions, surface anisotropy, and dead-layer effects are folded into a single effective parameter. Critically, dipolar interactions are always present in the configurations relevant to biosensing; their magnitude depends on the local concentration and cluster geometry, and they affect both the susceptibility amplitude and its frequency dependence. The cross-composition ratio $K_{\text{eff}}(\text{Fe})/K_{\text{eff}}(\text{Mn})$ is consistent with the Serantes scaling hypothesis, in which the interaction contribution scales with K_{m} rather than adding a fixed offset, although this observation is based on two compositions only and should be considered indicative (SQ 5 and SQ 6). Current analytical models (Debye, Langevin–Chantrell) do not explicitly account for interactions; frameworks such as the Ilg–Kröger model [306] or Monte Carlo approaches [18] represent the most promising paths forward but have not yet been validated against the experimental data of this thesis.

Substrate-dependent susceptibility: membrane vs powder: Nanoparticles embedded in nitrocellulose membranes exhibit initial susceptibilities three to four times higher than the same batch in compacted powder (Table 4.14). This discrepancy is attributed to reduced dipolar interactions in the membrane, where nanoparticles are distributed in agglomerates within the porous structure rather

than in dense contact. The Chantrell-fitted shape factor γ is systematically broader in membranes, probably reflecting the agglomerate size distribution (SQ 5).

Manganese ferrite as preferred composition for inductive sensing: Manganese ferrite ($MnFe_2O_4$) consistently outperforms iron oxide in initial susceptibility across all measurement techniques and configurations. The underlying reason is its lower bulk magnetocrystalline anisotropy ($K_m = 3$ kJ/m^3 vs 4.6–11 kJ/m^3 for iron oxide, Table 4.3), which places the Néel relaxation frequency well above the sensor operating range. In the inductive sensor, the Mn–CP3/Fe–CP1 sensitivity ratio is 2.0–2.5 (Table 6.4), consistent with the SQUID-derived susceptibility ratio of 2.3 (Table 4.14). Note that for cytotoxicity concerns, this advantage is mainly relevant for in-vitro applications.

Silica coating improves susceptibility of thermally decomposed SPION: Silica-coated TD iron oxide nanoparticles (Fe–TDH4@Si) showed an increase in susceptibility per iron mass of approximately 20 % relative to the uncoated counterpart, observed in both magnetisation curves (Fig. 4.5) and E4991 impedance measurements (Fig. 4.18). We attribute this improvement to improved surface state, either through ligand exchange or the coating itself, which reduces the broken-symmetry surface anisotropy K_S (SQ 4). This observation is consistent throughout measurement techniques but based on a single coated batch and requires confirmation.

Joint Debye fitting of mobile and immobilised suspensions: A Debye model fitted simultaneously to nanoparticle suspensions in deionised water (Néel + Brownian relaxation) and in agar-agar (Néel only) resolves the K_{eff}–diameter degeneracy that limits single-configuration fitting (where effective relaxation time depends on the product of K_{eff} and V_{mag} which are both fitting parameters). The extracted K_{eff} values are physically consistent with those obtained independently from FC-ZFC and ACS measurements (Section 6.5). This approach also yields the hydrodynamic-to-magnetic volume ratio h. The method requires only an LCR impedance analyser and two sample preparations based with the same batch, making it accessible without specialised magnetic instrumentation.

Easy-axis pre-orientation as signal enhancement leverage: Drying nanoparticle-loaded membranes under a 500 mT static field improves the inductive signal by 8–16 % (Fig. 6.10). The effect is attributed to Brownian rotation aligning the easy axes of the nanoparticles along the sensing field direction before immobilisation upon drying. This enhancement requires no modification to the sensor electronics. SEM imaging (Fig. 6.9) revealed that the drying field simultaneously alters EA orientation and cluster morphology; the individual contributions could not be separated.

Low-cost oscillator reproducing laboratory susceptibility rankings: The Colpitts oscillator (total component cost below 30 euros) correctly reproduces the relative susceptibility hierarchy established by SQUID magnetometry and

E4991 impedance analysis. The distinction between mobile and immobilised nanoparticles is detectable with this set-up (Fig. 6.15). The planar coil on the LDC1614 achieves a relative sensitivity approximately 116 times higher than the wound coil (Table 6.5), demonstrating that coil geometry is the dominant lever for sensitivity improvement.

7.4 Perspectives

Low effort, high impact

Inductive readout during the wicking phase: The observed cooperation between Néel and Brownian relaxation results in increased susceptibility at certain frequencies (Section 6.5). Performing the inductive readout during the wicking phase, before the membrane has fully dried, is a relevant track to explore. It is not compatible with easy-axis pre-orientation (which requires drying), and the transient nature of the wicking phase introduces timing constraints that must be characterised.

Medium effort, high impact

Determination of the minimum drying field for easy axis alignment: Drying nanoparticle-loaded membranes under a 500 mT static field improves the inductive signal by 8–16 % (Section 6.4, Fig. 6.10), but the minimum field strength required to produce this effect was not determined. Repeating the experiment at field strengths of 10, 50, 100, and 200 mT using permanent magnets of known surface field would yield a saturation curve of signal improvement vs. applied field. The result would determine whether a compact permanent magnet can be integrated into a portable cassette (no power consumption) or whether an electromagnet is needed (power budget constraint), which is directly relevant to the ASSURED criteria discussed in Section 5.3.

Dedicated planar coil matched to the LFA test line: The 116× relative sensitivity gain obtained by switching from a wound coil to the LDC1614 planar coil (Table 6.5) confirms that coil geometry is the dominant hardware lever. For LFA applications, the test line is typically 1–4 mm wide and extends across the full strip width [97]. Designing a planar coil whose footprint matches this geometry would maximise the filling factor and therefore the sensitivity. Existing implementations include the 150 µm planar coil of Marqués-Fernández et al. [244] and the surface-mount spiral coils of Barnett et al. [276].

Origin of the secondary blocking temperature in iron oxide: All iron oxide samples in this work exhibit a secondary FC-ZFC peak at 15–20 K, which is absent in every manganese ferrite sample and attenuated in silica-coated iron oxide (Section 4.7). The current hypothesis attributes this peak to a subpopulation of strongly

oxidised particles with reduced magnetic cores, supported by its non-interacting Mydosh parameter ($\Phi = 0.21$ for Fe–CP1). A single Mössbauer spectroscopy measurement on one Fe–CP batch would help clarify the question by quantifying the magnetite-to-maghemite ratio and identifying whether a distinct population with a smaller effective core exists. While this question has limited direct consequences for sensor design at room temperature, it would clarify the interpretation of K_{eff} values extracted from FC-ZFC data and offer more fundamental insights in the nanomagnetic behavior of SPION.

High effort, high impact

Low-temperature magnetisation programme on membrane samples: Two complementary experiments on nanoparticles dispersed in nitrocellulose membranes would clarify the role of dipolar interactions and drying-field-induced structural changes by EA orientation. First, magnetisation curves at 5 K (suppression of thermal fluctuations) on membrane and powder samples, analysed within the Thamm and Hesse framework, would classify the sign and relative strength of inter-particle interactions in each configuration. Second, comparing magnetisation curves of membranes dried with and without an applied field, in different orientations relative to the probing field would reveal whether signal improvement after field-drying within nitrocellulose (Fig. 6.10) originates from easy-axis alignment alone or also from field-induced chain formation affecting the interaction landscape.

7.4.1 High effort, medium impact

Validated dipolar interaction model for LFA configurations: Implementing Monte Carlo simulations of interacting superparamagnetic nanoparticles following the framework of Martin et al. [18], would allow to improve the DBF convention applied in this work. It should be adapted to the particle sizes and concentrations typical of LFA membranes and validated against the powder/membrane susceptibility ratio (Table 4.14) and the Vogel-Fulcher T_0 values (Table 4.10).

Closing remarks

Effective magnetic susceptibility of superparamagnetic nanoferrites, key figure for inductive LFA detection, is not a fixed material property. It depends on composition, size distribution, surface state, inter-particle interactions, substrate, and measurement frequency. The mantra introduced at the outset, *"Weet wat je meet"*, is not merely a reminder to calibrate carefully; it is a statement about the physics: the same nanoparticle batch yields different macroscopic properties depending on how it is measured.

For sensor designers, this work provides both a warning and a toolkit. The warning is that no single characterisation technique captures all the relevant parameters. The toolkit is a set of complementary methods, from a 30-euro Colpitts oscillator to SQUID magnetometry, whose cross-validation narrows the uncertainty on the quantities that ultimately determine the sensor signal. If this thesis contributes to shortening the path between nanoparticle synthesis and functional inductive biosensors, it will have served its purpose.


ALL MODELS ARE WRONG,
BUT SOME ARE USEFUL
— GEORGE BOX
sketchplanations

Appendices

A.1 Suppl. Chap. 2 : Electromagnetism : Maxwell Equations

A.1.1 Steady Current generates a Magnetic Field (1820's)

In 1820, Hans Christian Oersted (°1777 in Denmark[2]) demonstrated that electric current produces magnetic field by rotating a compass needle transversally to a current-carrying wire.[3] Oersted's publication created a frenzy at the French Academy of Sciences and greatly inspired two contemporaries : Jean-Baptiste Biot and André-Marie Ampère. [4]

Jean-Baptiste Biot (°1774 in France[5]) and his apprentice Félix Savart (°1791 in France) studied the forces exerted by a current-carrying wire on a magnetic dipole, leading to the **Biot-Savart Law**. They empirically correlated a stationary current I in a long straight wire and the magnetic field H around the wire. The law gives the magnetic field component $\delta\mathbf{B}(\mathbf{x})$ in a given point $\mathbf{x}$ generated by an infinitesimal element of a current-carrying wire $Id\mathbf{l}$ at point $\mathbf{l}$:

$$\delta\mathbf{B}(\mathbf{x}) = -\frac{\mu_0}{4\pi} I \frac{\mathbf{r}(\mathbf{x}) \times \delta\mathbf{l}}{\mathbf{r}(\mathbf{x})^3} \tag{1}$$

with **r = x-l** the displacement vector from the wire element to the point at which the magnetic field is computed.

André-Marie Ampère (°1775 in France[6]) further investigated Oersted's observations at the French Academy of Science. He demonstrated that two current-carrying parallel wires attract each other when currents flow in the same direction, and repel each other when currents flow in the opposite direction. He established the more general **Ampère's Law**, correlating the circulation of a magnetic field **B** around a closed loop C to the electric current enclosed by the loop I_{enc}.

[2]H.C. Oersted was born in the middle of the Danish Golden Age. His close friendship with H.C. Anderssen feeds the imagination on the fruitful intersection between art and science at the time. 'Interdisciplinarity' was already hot.

[3]While Oersted is mainly remembered for his work in electromagnetics, it is interesting to note that he also discovered aluminium in 1825. Only 30 years later it started to be industrially produced and has been an essential part of industry ever since.

[4]Founded in 1666 under Louis XIV and predominant for european scientific developments in the 17th, 18th and 19th century.

[5]Before his contributions to electromagnetism, Biot had already joined J.L. Gay-Lussac in a hot-air balloon ride to measure how Earth's magnetic field varies with elevation, in 1804.

[6]Ampère's youth has been marked by the French revolution. His father was guillotined in 1793, plunging the young mathematician even more in his craft. He started his career as a teacher in mathematics until new research positions were opened by the Napoleonic regime.

$$\oint_C \mathbf{B} \cdot d\mathbf{l} = \mu_0 I \tag{2}$$

Consider $\mathbf{J}\left[\frac{\mathrm{A}}{\mathrm{m}^2}\right]$ the electric current density in a point. The differential form of Ampère's Law is then

$$\nabla \times \mathbf{B} = \mu_0 \mathbf{J} \tag{3}$$

Ampère's Integral law can be derived from the Biot-Savart Law using Stokes' Theorem[7]. They are however not equivalent. While Ampères Law is -in its differential form- a local expression (i.e. describing the magnetic field in a given point with the current density at that exact same point), Biot-Savart fundamentally describes the causality between the current in a point and the field in another point. It is important to note that both Ampère's Law and Biot-Savart Law are **magnetostatic** : they consider stationary current and no variations in time.

A.1.2 Changing Magnetic Field generates a Current (1830's)

In the 1830's, it was well established that a steady current creates magnetic fields. Michael Faraday (°1791 in the Kingdom of Great Britain) and Emil Lenz (°1804 in Estonia, then part of the Russian Empire) laid the foundations for our current understanding of electromagnetism by questioning how magnetic field could create current. While they worked independently from one another, their observations lead to the same, fundamental conclusion : a time-varying magnetic field creates a current in a closed loop[8]. Faraday discovered that a changing magnetic flux Ψ induces a voltage $\mathcal{E}[\mathrm{V}]$ through the wire. This voltage is called the Electromotive Force (EMF)[9]. Lenz's contribution concerns the direction of the induced voltage : the induced current will flow in a direction so that the corresponding created magnetic field opposes the change in flux that created it. This makes perfect sense from an energy-conservation point-of-view : if a change in magnetic flux created a current that were to enforce this change, a small change in flux would create infinite current. Hence the $-$ sign in the Lenz-Faraday Law :

$$\mathcal{E} = -\frac{d\Phi_B}{dt} \tag{4}$$

It is important to note that the **Lenz-Faraday Law** is electrodynamic : time variation of the Magnetic flux density is a necessary condition to induce EMF.

[7] The Stokes' Theorem only appeared in the 1850's and was proven ten years later by Hermann Hankel.

[8] While these truly fundamental discoveries were made, Belgium had just been created, and was still squabbling with the House of Orange-Nassau over the distribution of territories around Antwerp, Limburg and Luxembourg.

[9] But careful, this is not a proper 'force' in Newtons, it's actually a voltage.

A.1.3 Maxwell : One Ring to Rule all Fields (1870's)

In 1864, James Clerk Maxwell dedicated an important part of his life to unifying previous electrical and magnetic observations. That same year he presented a set of equations to the Royal Society, laying the groundwork for what is now known as the "Maxwell's Equations". These equations fundamentally describe electrical fields, magnetic field and their interactions. Some interesting (a)symmetries exist in this set of equations and are discussed below.

Law Name	Integral Form	Local (Differential) Form
Gauss's Law	$\oint_S \mathbf{E} \cdot \mathrm{d}\mathbf{A} = \frac{Q_{\text{enc}}}{\epsilon_0}$	$\nabla \cdot \mathbf{E} = \frac{\rho}{\epsilon_0}$
Gauss's Law for Magnetism	$\oint_S \mathbf{B} \cdot \mathrm{d}\mathbf{A} = 0$	$\nabla \cdot \mathbf{B} = 0$
Faraday's Law of Induction	$\oint_C \mathbf{E} \cdot \mathrm{d}\mathbf{l} = -\frac{\mathrm{d}\Phi_B}{\mathrm{d}t}$	$\nabla \times \mathbf{E} = -\frac{\partial \mathbf{B}}{\partial t}$
Ampere-Maxwell Law	$\oint_C \mathbf{B} \cdot \mathrm{d}\mathbf{l} = \mu_0 I_{\text{enc}} + \mu_0 \epsilon_0 \frac{\mathrm{d}\Phi_E}{\mathrm{d}t}$	$\nabla \times \mathbf{B} = \mu_0 \mathbf{J} + \mu_0 \epsilon_0 \frac{\partial \mathbf{E}}{\partial t}$

Table A.1.1 Maxwell's Equations in Integral and Differential Form

First two Maxwell Equations : Gauss' Laws

Gauss's Law states that the surface integral of electrical field $\mathbf{E}$ $\left[\frac{\mathrm{V}}{\mathrm{m}}\right]$ entering any closed loop is proportional to the enclosed electrical charge Q_{enc} [C]. In local form, the divergence of $\mathbf{E}$ is proportional to ρ $\left[\frac{\mathrm{C}}{\mathrm{m}^3}\right]$, the charge density. The magnetic counterpart of this law states that the integral of $\mathbf{B}$ [T], as well as $\mathbf{B}$'s divergence, are always zero. This has two fundamental implications :

1. Any closed surface in an $\mathbf{E}$ field can contain a net charge, an electric monopole. This is equivalent to saying that sinks and sources can exist in a electrical field (i.e. its divergence is non-zero)
2. Any $\mathbf{B}$-fieldline entering a closed surface must leave it, since the net balance on a closed surface is always zero. No magnetic sources or sinks can exist (i.e. $\mathbf{B}$'s divergence is always zero.) This implies that **no magnetic monopoles can exist, the fundamental magnetic unit are dipoles.**

Third and Fourth Maxwell Equations : Faraday's and Ampère-Maxwell Law

The integral form of the third Maxwell Law is exactly the Lenz-Faraday Law described in section A.1.2. The Electromotive Force (EMF) [V] generated by a time-varying magnetic flux within a contour is exactly the non-zero line-integral of the $\mathbf{E}$ $\left[\frac{\mathrm{V}}{\mathrm{m}}\right]$ parallel to every segment of the contour. A vector field is called conservative

when its curl is zero. In conservative fields, the line integral of the field between two points is independent of the path taken between these two points, meaning that the work done by the field on an object moving from one point to another is the same regardless of the chosen route. The third Maxwell equation teaches us that an electrical field is conservative in any magnetostatic situation (i.e. when magnetic flux does not vary over time). This has important consequences :

1. When in any magneto- or electrostatic context, the electrical field is always conservative. Since $\nabla \mathbf{E} = 0$ we can express $\mathbf{E}$ as the gradient of a scalar field V which is the electric potential : $\mathbf{E} = -\nabla V$. Thus the electric potential of an electric charge is always the same in a given point, regardless of the paths it has traveled.
2. In a magnetodynamic context, the electrical field is never conservative, thus $\mathbf{E} \neq -\nabla V$. A particle cannot have a well-defined potential energy that depends only on its position. When a particle returns to its initial position, the electrical field has done some path-dependent work W_{loop} on it : $W_{loop} = \oint \mathbf{F} d\mathbf{l} = \oint q\mathbf{E} d\mathbf{l} = q\mathcal{E}$ with q [C] the charge and $\mathcal{E}$ [V] the electromotive force. The work done by the **E**-Field changes the kinetic energy of the particle[10].

The fourth Maxwell Equation is called the "Ampère-Maxwell Law" : Maxwell observed that Ampères Law was incomplete in electrodynamic situations. Consider a simple circuit where a current I is flowing to charge up a parallel-plate capacitor. We draw a circular loop (the "Amperian Loop") around the wire. The **B**-field on that loop depends on the current enclosed by *any* surface bounded by the loop. First consider the surface to be a flat disk : the current passes through that surface, thus $\oint \mathbf{B} d\mathbf{l} = \mu_0 I$. Now consider the surface to be a "bag" that extends to the middle of both plates. Since the capacitor is charging, no current is flowing, thus $\oint \mathbf{B} d\mathbf{l} = 0$. This contradiction is due to the fact that Ampère's law is valid in electrostatic situations. Maxwell added an electrodynamic term : the displacement current $I_D = \epsilon_0 \frac{\partial \mathbf{E}}{\partial t}$. Not only a conduction current is source of magnetic field, also a time-varying electric field[11]. This thought exercise has a mathematical counterpart. Consider the differential form of the initial Ampère's Law :

$$\nabla \times \mathbf{B} = \mu_0 \mathbf{J}. \tag{5}$$

A key identity in vector calculus is that the divergence of a curl is always zero:

$$\nabla \cdot (\nabla \times \mathbf{B}) = 0. \tag{6}$$

[10] In a perfect vacuum, the work done by the EMF increases the kinetic energy of the charge.

[11] A capacitor is often said to store electrical energy as electrostatic potential energy (a 'conservative' electric field). This is actually incomplete, a charging capacitor creates a small magnetic field who will in turn generate an electrical field that opposes the charging capacitor. This induced electrical field is non-conservative but almost always negligible.

If we take the divergence of Ampere's Law, we get

$$\nabla \cdot (\mu_0 \mathbf{J}) = 0, \tag{7}$$

which implies that the divergence of the current density **J** is zero. This condition, $\nabla \cdot \mathbf{J} = 0$, is only true for steady currents (magnetostatics) and is derived from the continuity equation, which relates current density to charge density ρ: $\nabla \cdot \mathbf{J} = -\frac{\partial \rho}{\partial t}$. Thus, the original law holds only when charge density is not changing anywhere. This is what breaks down, for example, when charging a capacitor.

Considering a region with no conduction current, the symmetry of the third and fourth Maxwell Law is striking. A time-varying **B**-field creates an **E**-field, and vice-versa.[12]

$$\nabla \times \mathbf{E} = -\frac{\partial \mathbf{B}}{\partial t} \tag{8}$$

$$\nabla \times \mathbf{B} = \mu_0 \epsilon_0 \frac{\partial \mathbf{E}}{\partial t} \tag{9}$$

In Short The Maxwell Equations relate the electrical and magnetic fields **E** and **B** in free space to the distribution of electric charge and current densities in the surrounding space, highlighting the coupling between oscillatory electric and magnetic fields. These equations are however asymmetric in the fields **E** and **B** : no magnetic counterpart of electric charge, 'magnetic monopoles', has been ever identified in nature. The building block of magnetism, magnetic dipoles, are equivalent to current loops. [17]

Biot-Savart in the Maxwell-Equations?
Why is it that Biot-Savart's equation (Eq. 1) is not in the Maxwell Equations while Ampère's Law (Eq. 2) is? Section A.1.1 points out that Ampère's Law can be derived from Biot-Savart's law when applying certain geometrical symmetries, so wouldn't Biot-Savart be more fundamental? Biot-Savart describes an "action at a distance" while the differential form of the Ampère equation is local, as are the other Maxwell equations. It states that the curl (a measure of circulation or "vorticity") of the magnetic field at a single point in space is determined by the current density at that exact same point. Note that while Maxwell created an electrodynamic counterpart of Ampères' law, Jefimenko's equations [308] are a particular solution of Maxwell's equations and can be used as an "electrodynamic" equivalent of Biot-Savart's Law. They are out of scope for this introduction.

[12] While Faraday had experimentally proven the interaction between light and magnetic field, Maxwell was the first to mathematically prove that light actually is an electromagnetic wave. He correctly suggested that the propagation speed of electromagnetic waves within a material depends on the physical constants μ and ϵ

A.1.4 Lorentz : Forces on Electrical Charges

Hendrik Lorentz (°1853, The Netherlands[13]) established a simple yet accurate description of the force on a charge moving in a magnetic and electric field. This equation is general, i.e. valid in both static and time-varying fields.

$$\mathbf{F_L} = q \cdot \mathbf{E} + q\mathbf{v} \times \mathbf{B} \tag{10}$$

A very important insight given by this simple equation is that **a magnetic field never can do work on a moving charge, while an electric field can.** Consider the rate at which work is done, i.e. the power P_L:

$$\begin{aligned} P_L &= \mathbf{F_L} \cdot \mathbf{v} && (11)\\ &= q(\mathbf{E} + \mathbf{v} \times \mathbf{B}) \cdot \mathbf{v} && (12)\\ &= q\mathbf{E} \cdot \mathbf{v} + q(\mathbf{v} \times \mathbf{B}) \cdot \mathbf{v} && (13)\\ &= q\mathbf{E} \cdot \mathbf{v} + 0 && (14) \end{aligned}$$

Indeed, $(\mathbf{v} \times \mathbf{B})$ is always perpendicular to $\mathbf{v}$, thus $(\mathbf{v} \times \mathbf{B}) \cdot \mathbf{v}$ is zero. This means that a magnetic field can deflect a moving charge but never accelerate or decelerate it.

Lorentz' Force equation fundamentally interacts the Maxwell's equations. The latter describe the "source" fields of the Lorentz Force. When they vary, the $\mathbf{F_L}$ varies, altering $\mathbf{J}$ and ρ, thus altering the fields again.

We cannot associate a potential energy function with the magnetic force. It is necessary to consider the work done by the transient electric fields when establishing a particular magnetic configuration, or in setting up a particular current distribution, in order to calculate the associated energy [28].

A.1.5 Recurring Spatial Configurations

A.1.5.1 Torque on a Magnetic Loop or Dipole

Consider a small rigid dipole $\mathbf{m}$ in a steady $\mathbf{B}$ field. The moment experiences a torque $\mathbf{\Gamma}$ [Nm]:

$$\mathbf{\Gamma} = \mathbf{m} \times \mathbf{B} \tag{15}$$

[13] Lorentz worked in close collaboration with Pieter Zeeman who gave its name to "Zeeman Energy" which will be introduced later. They won the Physics Nobel Prize in 1902.

A.1.5.2 Magnetic Field and Distance

Field around a Straight infinite wire Applying Maxwell's equation, the azimuthal flux density component B_θ at a distance h from the wire is given by

$$B_\theta = \frac{\mu_0 I}{2\pi h} \tag{16}$$

A current loop 'from nearby' Consider a conducting loop with current I and radius R; and its axis in the z direction. On its middle axis, only B_z components do not cancel out. At a distance z from the center of the loop, the magnetic flux density is :

$$B_z = \frac{\mu_0}{2} \frac{IR^2}{(R^2 + z^2)^{3/2}} \tag{17}$$

At the center of loop, when $z = 0$, the magnetic field is given by

$$B_z = \frac{\mu_0 I}{2R} \tag{18}$$

Aligning N coils over a length l gives the magnetic field within a solenoid :

$$B_{solenoid} = \frac{\mu_0 IN}{l} \tag{19}$$

A current loop 'from far away'

Considering a dipole field from "far away" (i.e. distance of observation is much bigger than equivalent circuit loop), the dipole field in spherical coordinates becomes :

$$B_r = 2\left(\frac{\mu_0 m}{4\pi r^3}\right) cos(\theta) \tag{20}$$

$$B_\theta = \left(\frac{\mu_0 m}{4\pi r^3}\right) sin(\theta) \tag{21}$$

$$B_\phi = 0 \tag{22}$$

with m the magnetic moment of the dipole, $cos(\theta)$ parallel to the vector r and $sin(\theta)$ orthogonal. Note that this field has axial symmetry around $\mathbf{m}$.

For an infinite wire, the field circulates around the wire and spreads only radially in a cylindrical shell. Since its circumference grows as $2\pi r$, the field weakens as $1/r$. Since we consider the wire is indefinitely long, there is no significant can-

cellation of field contributions from different parts of the wire. Around a dipole, magnetic flux density decreases in $1/r^3$ with the radial component having twice the amplitude of the polar component. This has its importance in understanding dipolar interactions between nanoparticles : the strength of the interactions decay with the cube of the distance. The induced magnetization field of a particle, $\mathbf{B_{NP}}$ is approximated by

$$\mathbf{B_{NP}} = \frac{\mu_0}{4\pi} \frac{3(\mathbf{r} \cdot \mathbf{m_{NP}})\mathbf{r} - (\mathbf{r} \cdot \mathbf{r})\mathbf{m_{NP}}}{r^5} \tag{23}$$

with $\mathbf{r}$ the vector from the centre of the nanoparticle to the point of observation, $r = \|\mathbf{r}\|$ its norm, and $\mathbf{m_{NP}}$ the magnetic moment of the particle. The nanoparticle's induced magnetisation decays with the cube of the distance r [249]. A detailed modeling of the field around a nanoparticle is given in [255].

A.2 Suppl. Chap. 2 : Interpreting the Bohr Magneton with Classical Physics

In Lecture 22 of Walter Lewin's online course (MIT OpenCourseWare), an interesting derivation of the amplitude of the Bohr magneton μ_B is given. Note that while classical physics can reproduce the correct order of magnitude, quantum physics are required to explain that all electrons have a magnetic moment which is a multiple of μ_B (quantization) and that the spin magnetic dipole moment is always exactly μ_B.

A classical model of the magnetic dipole moment of an atom, such as hydrogen, considers an electron (e^-) orbiting a nucleus. The model uses the electron mass $m_e \approx 9.11 \times 10^{-31}$ kg, the elementary charge $e \approx 1.6 \times 10^{-19}$ C, and the Bohr radius $R \approx 5.10 \times 10^{-11}$ m.

The magnetic moment μ is defined as the product of the equivalent current I and the area of the orbital loop A.

$$\mu = I \cdot A$$

The area A is given by $A = \pi R^2$, which is approximately 8.1×10^{-21} m^2.

The current I must be determined. It is derived from the motion of the electron. The electrostatic Coulomb force between the electron and the proton provides the centripetal force that maintains the orbit.

$$F_{\text{coulomb}} = F_{\text{centripetal}}$$

$$\frac{e^2}{4\pi\varepsilon_0 R^2} = \frac{m_e v^2}{R}$$

Solving this force balance for the orbital velocity v yields a value of approximately

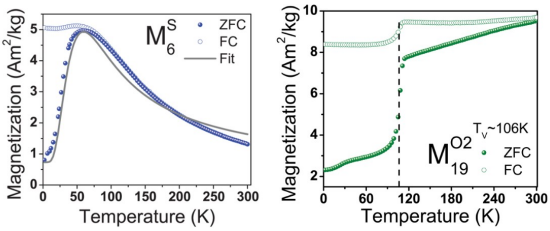


Fig. A.3.1 From [143] : Verwey transition observed in 19 nm powders but absent in 6 nm particles (measurement made in powders form)

$2.3 \times 10^6\,\mathrm{m\,s^{-1}}$.

The time T required for one orbit (the period) is the circumference of the orbit divided by the velocity.

$$T = \frac{2\pi R}{v}$$

$$T = \frac{2\pi(5.10 \times 10^{-11}\,\mathrm{m})}{2.3 \times 10^6\,\mathrm{m\,s^{-1}}} \approx 1.4 \times 10^{-16}\,\mathrm{s}$$

The orbiting electron constitutes an equivalent electrical current I, defined as the charge e passing a point per unit time T.

$$I = \frac{e}{T}$$

$$I = \frac{1.6 \times 10^{-19}\,\mathrm{C}}{1.4 \times 10^{-16}\,\mathrm{s}} \approx 1.1 \times 10^{-3}\,\mathrm{A}$$

Finally, the magnetic moment can be calculated from the product of the current and the area.

$$\mu = I \cdot A \approx 9.3 \times 10^{-24}\,\mathrm{A\,m^2}$$

This calculated value corresponds to the accepted value of the Bohr magneton, μ_B.

A.3 Suppl. Chap. 2, 4 : Verwey Transition in Iron Oxide Nanoparticles

The Verwey transition in magnetite (Fe3O4), traditionally occuring near 120-125 K in perfect bulk crystals, exhibits varied and complex behaviour in nanoparticles depending on their size, shape, stoichiometry, and how they are assembled. With the reduction in particle size, the Verwey temperature tends to shift towards lower values [141]. In the studies cited below, information concerning Verwey Transition was gained from FC-ZFC curves measured on compacted powder samples, unless stated otherwise.

A.3.0.1 Absence or Suppression in SPIONS $<$ 20 nm

:

- For nanoparticles smaller than 20 nm with purely superparamagnetic behaviour, Klomp et al. report a complete vanishing of the Verwey Transition in FC-ZFC curves. [309]. At 32 nm size, VT is observed. They make the hypothesis that this is linked to faceting of the nanoparticles at that size.
- Prozorov et al. similarly noted that no Verwey transition was observed in 7-10 nm nanoparticles [91].
- Mitra et al. reported a Verwey transition in very small (6-14 nm) amine-coated octahedral magnetite nanoparticles, while it was absent in similarly sized spherical particles [92]. This is attributed to (1) better stoichiometry and surface coordination in octahedral particles and a larger blocking temperature for octahedral nanoparticles due to higher shape anisotropy (thus these nanoparticles do not have superparamagnetic behaviour at the VT).
- Martins et al. observed that 9.3 nm nanoparticles without hydrothermal treatment did not display the Verwey transition, attributing it to their smaller size and non-stoichiometry from surface effects [141]. Hydrothermally treated nanoparticles (17-20 nm) did show VT at 102 K : due to the hydrothermal treatment, stoichiometry was improved and surface effects were reduced. Measurements were made by suspending nanoparticles in gelatin capsules.
- Hevroni et al. observed a sharp Verwey transition in individual 10 nm magnetite nanocrystals, but at a lowered temperature of 101 +/- 2 K compared to bulk. This lowering was suggested to be an intrinsic finite size effect, possibly due to the surface, rather than solely stoichiometry changes [88]. The study emphasizes VT-STS as a direct probe of electronic structure, effectively circumventing the difficulties that superparamagnetism might pose for magnetometry at these small sizes.

Relevant literature for the occurrence of Verwey Transition in nanoparticles larger than 20 nm can be found in Appendix A.3.

A.3.1 Verwey Transition in Larger Nanoparticles ($>$ 20 nm)

- Frandsen et al. concluded that the Verwey transition persists in Fe3O4 nanoparticles in the size range of 20 nm, as evidenced by a "kink at about 120 K" in FC/ZFC curves made on tightly compacted powder samples [95] while it was not observed for measurements on 5 nm.

- Prozorov et al. observed a Verwey temperature (TV) in 50nm particles, although much lower than the bulk : around 20 K [91]. For these measurements, nanoparticles were suspended in agarose.

- In Goya et al., bulk-like properties such as saturation magnetization, hyperfine parameters, coercive field, and Verwey transition are observed in 150 nm particles. For decreasing particle size, the Verwey temperature shifts down to 20 K for 50 nm and is no longer observable for smaller particles [49].

- Wang et al. reported that 45 nm Fe3O4 nanoparticles exhibit a Verwey transition at approximately 120 K, similar to bulk samples [310]. However, it vanished in the Fe3O4 nanoparticles that were formed under a 0.25 T magnetic field, supposedly due to magnetic field-induced oxidation of some Fe2+ ions on octahedral sites to Fe3+ during the nanoparticle formation. This would've led to a deficiency of Fe2+ in certain layers, which disrupted the long-range charge ordering. The Verwey transition was detected as an abrupt decrease in the signal of Electron Paramagnetic Resonance (EPR).

- López Maldonado et al. observed the Verwey transition at 90 K for 40 nm nanoparticles. This reduction compared to the bulk value (125 K) was attributed to the small average crystallite size and increased surface energy [87]. The Verwey transition was identified by observing a "slope change" in the in-phase magnetic susceptibility curves.

- Kim et al. studied 44 ± 3 nm nanoparticles and observed an evolution of the Verwey transition due to slow oxidation. For measurements, the powdered sample was pelletized and mounted onto the sample stage. The nanoparticles were then subjected to slow oxidation by exposure to controlled oxygen partial pressures at an ambient temperature of 30 °C, with measurements taken over periods up to 1071 days. The VT initially dropped to a minimum of 70 K (after 75 days) and then recovered to a persistent value of 95 K (after 160 days) [89].

These studies suggest that the Verwey transition persists in Fe_3O_4 nanoparticles down to approximately 20 nm, albeit at temperatures below the bulk value of 125 K. Below 20 nm, it appears to be no longer detectable. The transition temperature is also sensitive to oxidation state and sample preparation.

A.4 Suppl. Chap. 3 : Literature Review for TD synthesis and Silica coating

A.4.1 Literature Review for TD synthesis

The two tables below complement the literature overview on thermal decomposition given in Subsection 3.2.1. Table A.4.1 compares the reagents, synthesis conditions, and post-treatment steps across protocols reported in literature. Table A.4.2 summarises the size control strategies employed and the resulting size distributions.

Author	Precursor	Solvent	Surfactant	Extra reagent	Atm.	Time at max T (h)	Heating Rate (°/min)	Max T (°C)	Washing method	Washing mixture	Storage	D (nm)
Baaziz 2014 [83]	Iron Stearate	octyl ether, hexadecene, octadecene, eicosene, hexadecanol, docosene	Oleic Acid		Air	2	5	287 - 365	centri. (14000 rmp)	hexane / acetone	Storage under Arto preserve surface state. In Chloroform	4 - 28
Balakrishnan 2019 [132]	Iron(III) Oleate	1 - octadecene & docosane	Oleic Acid		Ar	20 min	6.6	320 - 370	centri. (6000rpm)	hexane / acetone	stored in chloroform (10ml/mg)	6 to 13 (octa-docene) & 18 to 25 (do-cosane)
Belaid 2018 [139]	Iron (III) acetylaceto-nate	dibenzylether	Oleic Acid & Oleyamine (1:1 mix)	reducing agent : 1,2 - hexadecanediol	Inert	<2		200 - 300	Magnetic separation & centri.	ethanol	n - heptane	4 to 8
Cavelius 2012 [129]	Iron(II) - , iron(II)oxalates	Tri - n - octylamine	Oleyic Acid, Oleyamine	oxidizing agent : Trimethylamine - N - oxide for size control & post - synthesis oxidation	N_2	1 - 2	5	280 - 385	centri.	ethanol		6 - 25
Chen 2008 [311]	Iron(III) Oleate	1 - octadecanol	Oleic Acid		N_2	30 min	3.3		centri. & magnetic separation	etanol	ligand exchange before storage in water	10
Cotin 2022 [145]	Iron Stearate	dioctylether	Oleic Acid		Air	2	5	280 - 290	centri.	chloroform / acetone	suspension in THF	10
Demortiere 2011 [38]	Iron(III) Oleate	di - n - hexyl ether, hexadecene, dibenzyl ether, octadecene & eicosene	Oleic Acid		Ar	1	5	290				2.5 - 14

Continued on next page

Table A.4.1 - continued from previous page

Author	Precursor	Solvent	Surfactant	Extra reagent	Atm.	Time at max T (h)	Heating Rate (°/min)	Max T (°C)	Washing method	Washing mixture	Storage	D (nm)
Fokina 2022 [156]	Iron(III) Oleate	1 - octadecene, trioctylamine, & n - docosane	Oleic Acid, oleylamine, & trioctylphosphine		Ar	30 min	1 - 10	320 - 370	decantation	THF, ethanol		6 - 24
Guardia 2010 [137]	Iron (III) acetylacetonate	Dibenzylether, phenyl ether, octyl ether	Oleic Acid, Decanoic acid	reducing agent : 1,2 - hexadecanediol	Ar	1 - 2			centri.	isopropanol, acetone, ethanol	suspended in hexane & Oleic Acid	4 - 20 (Oleic Acid) & 45 (decanoic acid)
Hufschmid 2015 [151]	Iron(III) oleate, iron pentacarbonyl, iron oxyhydroxide	1 - octadecene, octyl ether	Oleic Acid (5:1–20:1 to precursor)	oxidizing agent : Trimethylamine - N - oxide (post synthesis oxidation)	Ar	1 - 24	3 - 10	280 - 320	Magnetic separation	3:2 chloroform methanol	in chloroform & hexane	2 - 30
Hyeon 2001 [157]	iron pentacarbonyl	octyl ether	Oleic Acid, Lauric Acid	trimethylamine oxide for oxidative decomposition	Ar	1		300	centri.	ethanol	hexane, toluene	4 - 16
Jiang 2014 [154]	Iron(III) Oleate	1 - octadecene	Oleic Acid		Inert	2	5	315 - 320	centri.	ethanol	n - hexane	15
Lak 2013 [155]	Iron(III) Oleate	1 - octadecene & tetracosane	Oleic Acid		Ar	30 - 60 min	1 - 3	317 - 337	centri.	acetone / hexane	chloroform	12 - 25
Lin 2006 [138]	iron oxyhydroxide	1 - octadecene or docosane	Oleic Acid		N_2	1 - 5		320 - 340			same solvent as synthesis	11 - 18
Manuelli 2014 [108]	Iron (III) acetylacetonate	octadecene	Oleyic Acid, Oleyamine	reducing agent : 1,2 - Hexadecanediol	N_2	3h	5	320				7 - 12
Meftah 2024 [153]	Iron(III) Oleate, iron dodecanoate, & iron octanoate	1 - hexadecene & 1 - octadecene	Oleic Acid, Dodecanoic Acid, Octanoic Acid		Air	30 min, 1 h, 1.5 h	10	320 - 370	centri.	acetone	chloroform	3.3 - 12

Continued on next page

Table A.4.1 - continued from previous page

Author	Precursor	Solvent	Surfactant	Extra reagent	Atm.	Time at max T (h)	Heating Rate (°/min)	Max T (°C)	Washing method	Washing mixture	Storage	D (nm)
Orozco - Henao 2016 [143]	Iron (III) acetylaceto-nate	benzyl ether	Oleic Acid & Oleyamine	Reducing agend : 1,2 - Hexadecane-diol (2.6 g)	N_2	2.5	2 - 4	290	centri.	toluene	toluene	5 - 19
Park 2004 [136]	Iron(III) Oleate	1 - octadecene, 1 - hexadecene, octyl ether, 1 - eicosene & trioctylamine	Oleic Acid		Air	30 min 1, 1.5	3,3	320	centriguation	ethanol	hexane, toluene	5 - 22
Patsula 2016 [126]	Iron(lll) glucuronate	ocatadecene, squalene, icosane, mPEG / Brij O10 mixture	Oleic Acid		Air	30 min		285 - 343	magnetic separation	hot ethanol	toluene	11 - 32
Pazik 2020 [130]	Iron (III) acetylaceto-nate	Acetophenone	none		Ar	4		202	centri.	ethanol	ethanol	10
Perez 2013 [312]	Iron (III) acetylaceto-nate	diphenyl ether, Benzyl ether	Oleic Acid (12 mmol), oleylamine (12 mmol)		Air	45 min		260 - 298	centifugation	ethanol	n - hexane	3 - 17
Roca 2006 [128]	Iron(III) acetylaceto-nate & Iron(III) Oleate	Phenyl ether & octyl ether	Oleic Acid	reducing agent : 1,2 - Hexade-canediol (for some samples)	N_2	30 min - 4		254 - 287	centifugation	ethanol	powder	5 - 11
Salvador 2020 [97]	Iron(III) Oleate	octadecene	Oleic Acid	DMSA for ligand exchange	Air	1	3.4	320				8 - 23
Sharifi 2017 [140]	Iron(III) acetylaceto-nate	benzyl ether	Oleic Acid, Oleylamine	reducing agent : 1,2 Hexade-canediol	N_2	2	3.3 - 6.5	300	centri.	toluene/ ethanol/ acetone	toluene & hexane	6 - 24
Sharifi 2018 [133]	Iron(III) acetylaceto-nate	benzyl ether	Oleic Acid & Oleyamine	reducing agent : 1,2 Hexade-canediol	N_2		6 - 7	300				9 - 12

Continued on next page

Table A.4.1 - continued from previous page

Author	Precursor	Solvent	Surfactant	Extra reagent	Atm.	Time at max T (h)	Heating Rate (°/ min)	Max T (°C)	Washing method	Washing mixture	Storage	D (nm)
Sun 2002 [150]	Iron(III) acetylaceto-nate	phenyl ether & stearyl alcohol	Oleic Acid & Oleyamine	reducing agent : 1,2 Hexade-canediol	N_2	30 min		265	precipitation	ethanol	n - hexane	3 - 20
Unni 2017 [81]	Iron(III) acetylaceto-nate	trioctylamine, docosane & 1 - octadecene	Oleic Acid		Ar & N_2	1 - 5	3.3 - 8	330 - 350	centri.	hexane/ acetone	Oleic Acid coated particles stored in hexane, PEG - coated particles stored in water	
Xu 2009 [135]	Iron(III) acetylaceto-nate	benzyl ether	Oleyamine		N_2	1	20 (fast!)	300	centri.	ethanol		7 - 10

Table A.4.1 Thermal Decomposition protocols : Author, Reagents, Synthesis Conditions, Post - Treatement, Obtained Diameter. *"centri." refers to centrifugation, "Atm." refers to the ambient atmosphere in which the synthesis occurs.*

Author	D (nm)	Size control method	Distribution width	Size measurement	Notes
Baaziz 2014 [83]	4–28	Parameters investigated include reflux time, nature of solvents, nature of ligands, oleic acid/iron stearate ratio, and the introduction and influence of a hold at 250 °C (nucleation temperature). The stability of the iron complex, which dictates its decomposition kinetics, was found to be a key factor.	Selected batches had standard deviation between 7 and 9 %. Mean sample: 11.2 ± 0.9 nm	TEM (at least 300 particles), XRD, Mosbauer, IR	
Balakrishnan 2019 [132]	6 to 13 (octadocene) and 18 to 25 (docosane)	The drying time of the iron oleate complex was used as a single and reliable control parameter. This parameter influenced the number ratio of Fe species available for nucleation and particle growth. A longer drying time led to larger particles	"polidispersity of less than 5%". 11.9 ± 0.4 nm	TEM, XRD	
Belaid 2018 [139]	4 to 8	Varying heating temperature, heating time, and surfactant amount.	4.3 ± 1.7, 8.0 ± 2.0 nm, polidispersity INDEX (PDI) ranging from 1.1 to 1.5	TEM (between 600 and 1000 particles), XRD, PCS	This study used a "hot injection" method where a solution of iron(III) acetylacetonate in dibenzylether was rapidly injected into a hot mixture of solvent, surfactants, and a reducing agent. The reaction was then held at the target temperature for 0 to 120 minutes
Cavelius 2012 [129]	6–25	Adjusting decomposition temperature, addition of oxidants, reaction time	10 to 40% polydispersity	HR-TEM and XRD	
Chen 2008 [311]	10	This study did not focus on size control but on a reproducible method for synthesizing 10 nm particles and making them water-soluble	Not specified	TEM and PCS	
Cotin 2022 [145]	10	Specific heating and aging conditions in the protocol appear to be the primary control factors	10.3 ± 0.8 nm, 10.2 ± 0.9 nm	DSL, S(W)AXS, TEM, AFM	high temperature and Liquid-Cell TEM (LCTEM): Used for directly imaging particle size, morphology, and observing the nucleation and growth of nanocrystals
Demortiere 2011 [38]	2.5–14	The key parameters for controlling the growth process and thus the final size were the type of solvent used (specifically its boiling point) and the ligand/precursor molar ratio. Increasing the solvent boiling point or the ligand concentration generally led to larger particles	polidispersity from 6 to 20%	TEM, XRD	nanoparticles from 3 to 14 nm were obtained by adapting the solvent and the ligand/precursor ratio. 'polidispersity' is mentioned as distribution spread measure but is expressed as σ (%)

Continued on next page

Table A.4.2 – continued from previous page

Author	D (nm)	Size control method	Distribution	Size measurement	Notes
Fokina 2022 [156]	6–24	Higher reaction temperatures, higher precursor concentrations, and lower heating rates generally lead to larger nanoparticles. Crucially, a thermal pretreatment (drying time) of the iron oleate precursor was found to be essential for reproducible size control.	The study focused on synthesizing monodisperse iron oxide nanoparticles (SPIONs) in a diameter range of 6–24 nm with reproducible size control of $\pm$ 0.5 nm	TEM, VSM size estimation assuming log-normal distribution	
Guardia 2010 [137]	4–20 (oleic acid) and 45 (decanoic acid)	The type of surfactant (oleic acid vs. decanoic acid) was shown to significantly control both particle size and shape. Oleic acid yielded smaller (4–20 nm) pseudospherical/faceted particles, while decanoic acid led to much larger (45) pseudocubic particles with a wider size distribution	DTEM = 7.4 (0.8) , DXRD = 7.2 (0.7) DTEM = 8.1 (0.7), DXRD = 8.2 (0.5). DTEM = 45 (9), DXRD = 46 (5) DTEM = 4.2 (0.5), DXRD = 3.9 (0.5). DTEM = 17 (1), DXRD = 16.8 (0.8).	TEM for at least 100 particles and XRD	
Hufschmid 2015 [151]	2–30	Increasing the amount of excess surfactant (oleic acid) slows the reaction kinetics, allowing for the growth of larger particles, though often at the cost of a broader size distribution.		TEM and VSM (Chantrell Method)	
Hyeon 2001 [157]	4–16	Particle size is controlled by the precursor-to-surfactant ratio; smaller ratios (e.g., 1:1, 1:2) produce smaller nanoparticles (4 nm, 7 nm). Comparison of post-synthesis oxidation (seed-mediated resulting in larger NPs) with oxidative decomposition.	highly monodisperse'	TEM, XRD	
Jiang 2014 [154]	15	Increasing the oleic acid concentration led to larger particles but with a broader size distribution and irregular shapes, likely due to Ostwald ripening.	cubic nanoparticles, uniformity not quantified	TEM, HR-TEM, XRD, SAED	

Continued on next page

Table A.4.2 – continued from previous page

Author	D (nm)	Size control method	Distribution	Size measurement	Notes
Lak 2013 [155]	12–25	A high heating rate (3 °C/min) favors burst nucleation, leading to smaller (∼12–14 nm) and more monodisperse particles. A slow heating rate (1 °C/min) leads to gradual nucleation and growth, resulting in larger (∼22–24 nm) particles with broader size distributions. Hydrodynamic size increases with increasing reaction time, temperature, and precursor concentration	standard deviation between 1.2 and 3.3 nm	TEM (150 nanoparticles)	
Lin 2006 [138]	11–18	Particle size increases with an increasing molar ratio of oleic acid. Using a higher boiling point solvent (docosane vs. 1-octadecene) allows for higher reaction temperatures and thus the synthesis of larger nanoparticles.	standard deviation of sizes less than 5%	TEM (500 nanoparticles)	
Manuelli 2014 [108]	7–12	A two-step, seed-mediated process was used. First, 7.6 ± 0.7 nm "seed" particles were synthesized. These seeds were then used in a second reaction to grow larger particles with a final average size of 11.3 ± 1.2 nm.	7.6 ± 0.7 and 11.3 ± 1.2 nm	TEM (600np)	Seed-mediated growth procedure. Obtained nanoparticles are spheric.
Meftah 2024 [153]	3.3–12	The study shows that no single rule applies for size control due to the different decomposition behaviors of the precursors. A combination of solvent choice, reactant concentrations, and reaction time must be optimized for each specific precursor-ligand system to achieve a target size.	4–14% polidispersity	TEM (700np)	
Orozco - Henao 2016 [143]	5–19	Particle size is highly sensitive to the final refluxing temperature and surfactant concentration. Critically, exposure to oxygen during the final synthesis stage substantially promotes particle growth, likely by redissolving smaller nanoparticles and favoring the growth of larger ones.	standard deviation (σ) from a log-normal fit, ranging from 0.1 to 0.17.	TEM (100np)	

Continued on next page

Table A.4.2 – continued from previous page

Author	D (nm)	Size control method	Distribution	Size measurement	Notes
Park 2004 [136]	5–22	Size can be systematically controlled by selecting a solvent with an appropriate boiling point, based on the principle that higher reaction temperatures promote greater particle growth. The size could be fine-tuned by varying the concentration of oleic acid.	<4.1% polydispersity	TEM	
Patsula 2016 [126]	11–32	Monodisperse nanoparticles are formed only at sufficiently high temperatures (>300 °C) where nucleation and growth stages are well separated. Higher stabilizer (oleic acid) concentration leads to the formation of more nuclei, resulting in smaller final nanoparticles.	PDI between 1.02 and 1.3	TEM (900 np), DLS	
Pazik 2020 [130]	10	Compared nanoparticles made by two different methods (co-precipitation and thermal decomposition)	< 0.21 PDI	XRD, SAED, TEM	Compares thermal decomposition and coprecipitation
Perez 2013 [312]	3–17	Tuning np size using iron salt:surfactant:solvent molar ratio and the nature of the solvent	For sample M1, the arithmetic mean was 8.9 nm with a geometric standard deviation (σ_g) of 1.2	TEM (636 and 1165 particle count) and DLS	
Roca 2006 [128]	5–11	The choice of precursor and solvent has a primary effect on particle size, with higher boiling point solvents and the iron oleate precursor leading to larger, more crystalline, and anisometric particles. Seeded growth offers a route to intermediate sizes.	Specific sizes reported (mean particle size ± standard deviation): MAG 1: 11.0 ± 1.4 nm, MAG 2: 6.9 ± 1.2 nm, MAG 3: 5.7 ± 1.1 nm. Polidispersity <20%. Logarithmic standard deviation of around 0.15 was obtained in all cases, supporting a narrow size distribution	TEM (measuring 100particles) and data fitting to log-normal distribution function to obtain logarithmic standard deviation. XRD for crystal size. VSM (with Chantrell equation) for magnetic particle size at room temperature (also providing a lognormal std!)	
Salvador 2020 [97]	8–23	particle size was increased by reducing the amount of oleic acid in the reaction media	NP8 (mean TEM diameter D_0 = 7.6 nm, σ = 0.15 nm), NP12 (D_0 = 11.6 nm, σ = 0.08 nm), and NP23 (D_0 = 22.6 nm, σ = 0.11 nm). Their hydrodynamic diameters (DBB DLS) before biofunctionalization were 94 nm (PDI 0.36) for NP8, 22 nm (PDI 0.20) for NP12, and 44 nm (PDI 0.35) for NP23		8 and 23nm also obtained by adapting oleic acid. Dissolution of reactants at 60 °C.

Continued on next page

Table A.4.2 – continued from previous page

Author	D (nm)	Size control method	Distribution	Size measurement	Notes
Sharifi 2017 [140]	6–24	Nanoparticle size does not change monotonically with precursor concentration. The trend depends on a competition between monomer concentration (which promotes growth) and the surfactant-to-precursor ratio (which affects nucleation). A higher surfactant ratio stabilizes monomers, reducing nucleation and leading to larger particles.	The "standard sample" had a mean size of 13.00 nm with a standard deviation of 1.1 nm, resulting in a polydispersity of ∼8.5%. It mentions 24.1 ± 5.7 nm, 9.1 ± 0.71 nm, 6 ± 0.9 nm, 5.8 ± 0.8 nm and 13 ± 1.1 nm.	TEM for size distribution (over 2000!!), HR TEM for crystalline structure.	
Sharifi 2018 [133]	9–12	oleic acid/ oleyamine ratio should be 3 for monodisperse synthesis. reflux time and heating rate should be tuned for nanoparticle size	7–14% PDI	TEM for size distribution (over 2000!), XRD for crystallinity (Scherrer's formula)	
Sun 2002 [150]	3–20	Size control is achieved through a seed-mediated growth method. By adjusting the quantity of the initial nanoparticle "seeds," the final size of the nanoparticles can be controlled.	"narrow size distribution" but no actual quantification	TEM, XRD	Seed-mediated growth procedure.
Unni 2017 [81]		In the presence of oxygen, increasing the reaction time from 2 hours to 5 hours resulted in a controlled growth of both physical and magnetic diameters, for instance, from ∼13 nm to ∼18 nm. "continuous addition of molecular oxygen at a molar flow rate slightly above stoichiometry was key to matching physical and magnetic diameters during growth"	Physical diameter (Dp) of 15.4 ± 1.9 nm (CV = 12.3%), magnetic diameter (Dm) of 14.1 ± 1.7 nm (CV = 12%).	TEM, XRD, HAADF-STEM	
Xu 2009 [135]	7–10	A higher ratio of oleylamine to benzyl ether results in smaller nanoparticles. If the ratio of oleylamine to benzyl ether was less than 1:1, the size distribution became broad.	7 ± 0.5 nm, 8 ± 0.4 nm, 9 ± 0.6 nm, and 10 ± 0.8 nm.		Start formation of magnetic nanocristals at 170 °C

Table A.4.2 Synthesis Summary: Size Control Methods and Results. Note that distribution width is described with the terminology used in the article, i.e. this might be inconsistent with the vocabulary developed in subsection 3.1.3.2.

A.4.2 Alternatives to LaMer Nucleation

Two alternative routes to LaMer nucleation exist for the decomposition of metal precursors:

- **Seed-mediated growth** consists in making small nanoparticles (4–6 nm) and subsequently mixing them with more precursor materials and heating the mixture as in the synthesis. By controlling the quantity of nanoparticle seeds, various MNP sizes can be formed. For example, mixing and heating 62 mg of 8 nm Fe_3O_4 nanoparticles with 2 mmol of $Fe(acac)_3$, 10 mmol stearyl alcohol, 2 mmol of oleic acid, and 2 mmol oleylamine led to 12 nm Fe_3O_4 nanoparticles, while changing the mass of seeds to 15 mg led to 16 nm Fe_3O_4 nanoparticles in the research of Sun et al. [150].

- **Finke's method** relies on slow, continuous nucleation and fast, autocatalytic surface growth. It consists in transforming a precursor through chemical reduction of the metal centre by H_2 within the precursor complex. The applied external heat is limited (up to 50 °C) [147].

A.4.3 Competing Mechanisms of Surfactant Influence on Particle Size

The precursor-to-surfactant ratio influences final particle size through several competing mechanisms. The net effect depends on which mechanism dominates under the specific reaction conditions, and an optimum ratio is generally identified [83].

Mechanisms leading to **larger** particles with increased surfactant:

- Stabilisation and Slower Nucleation: An increase in the amount of ligand or surfactant generally leads to the formation of more stable intermediate metal complexes or monomers. This stabilisation slows down the nucleation step, meaning fewer nuclei are formed. With fewer nuclei competing for the available monomer (iron species), each nucleus can grow into a larger nanoparticle [83, 133, 153].

- Enhanced Monomer Availability: In certain conditions, an increased concentration of growth species (monomers) in the reaction medium promotes faster growth rates, leading to larger particles [140].

- Desorption and Anisotropic Growth: At very high surfactant concentrations or ratios beyond an optimum, desorption of the bonded oleate from the nanoparticle surface can occur. This leaves the surface unprotected, leading to uncontrolled, anisotropic, or colossal growth and often resulting in larger, irregularly shaped, and polydisperse nanoparticles [133].

- Delayed Nucleation and Extended Growth: Excess surfactant can also delay the onset of nucleation and slow down the subsequent growth process [151].

Mechanisms leading to **smaller** particles with increased surfactant:

- Blocking Growth Sites: An excess of ligands can inhibit nanoparticle growth by covering the growth sites on the nascent particles, thereby resulting in smaller nanoparticles [153].
- Stabilising More Nuclei: Higher amounts of oleic acid can stabilise more nuclei, which could lead to a reduction in the final nanoparticle size by effectively distributing the available monomer among a larger number of growing particles [126].

A.4.4 Coating Hydrophilic (and vitrophilic) Magnetic Nanoparticles with Silica

In the context of coating, the magnetic nanoparticles introduced into the reaction mixture act as "seeds" or substrates. It is often energetically more favourable for silica monomers to condense onto these existing surfaces rather than expending the energy required to form entirely new nuclei in the bulk solution [313]. This is called 'heterogeneous nucleation' as opposed to 'homogeneous nucleation' when pure silica spheres are formed [187, 314]. If homogeneous nucleation is not suppressed, the reaction will produce a mixture of the desired core-shell particles and undesirable, core-free silica particles, which are formed independently in the bulk solution [191]. Silica monomers/oligomers will prefer to attach to existing nanoparticles rather than creating new ones when the kinetic conditions are such that the rate of silica deposition onto the core particles is significantly faster than the rate of self-nucleation in the bulk solution. This happens for example when the surface of the nanoparticles are rich in hydroxyl ($-OH$) groups [177, 314], or when the concentration of hydrolyzed silica monomers is 'below a critical threshold' [315] (which would be similar to the supersaturation threshold in Lamer's nucleation theory). Green et al. revealed that the formation of the first silica nanostructures is thermodynamically controlled by reaching a critical supersaturation concentration of hydrolyzed monomers [316]. Table A.4.3 summarises 13 'modified Stober' protocols for silica coating around magnetite nanoparticles, found in literature with 'convincing TEM images'. Based on this overview, the main control parameters are identified :

- TEOS concentration : Barnakov et al. demonstrate that the concentration or volume of tetraethyl orthosilicate (TEOS) directly influences the thickness of the silica shell [317]. To avoid the creation of core-free particles however, Urena-Horno et al. demonstrated that the supply of TEOS should not be larger than to the total available surface area of the seed particles [191] 'at

all times'. This points the need to tailor the amount of TEOS not just to the desired shell thickness, but also to the concentration and size of the core particles being coated. This is coherent with Sharifi et al. who demonstrated that -all other parameters alike- increasing the initial TEOS concentration from 0.1% to 0.2% (v/v) eliminated the coating process and instead produced large, core-free silica spheres [133].

- Catalyst concentration : Reducing the initial concentration of the base catalyst for a short period and then gradually increasing it to an optimal level can minimise nucleation and effectively prevent the agglomeration of magnetite nanoparticles during coating [318]. This is coherent with the findings of Liu et al. : as the hydrolysis and condensation of TEOS proceed, the ionic strength of the medium increases due to the formation of byproducts and charged species. This increased ionic strength compresses the electrical double layer surrounding the core particles, reducing their electrostatic repulsion and making them highly susceptible to irreversible agglomeration. If this aggregation occurs before a continuous and mechanically stable silica shell (even thin) has been formed, the result is not individually coated nanoparticles but large clusters of magnetic cores entrapped within a single, oversized silica matrix [313].

- Catalyst type : NaOH is noted for providing more precise control over the process compared to NH_4OH [318, 319].

- Pre-treatment of nanoparticles to stabilise the cores. This can involve coating the particles with a layer of citrate anions (either during the synthesis as done by Qiu et al. [320] or post-synthesis [177, 182]) or amines as done by Kobayashi et al. on silver nanoparticles [183]. This pre-coating serves a dual purpose: it provides electrostatic or steric stabilisation to prevent core agglomeration in the reaction medium, and it functionalizes the surface with groups (e.g., hydroxyls, carboxyls) that can act as effective anchoring points for the initial deposition of silica [58].

Hydrophobic nanoparticles (typically obtained by thermal decomposition) can be rendered hydrophillic through a silinization process using aminosilanes such as (3-aminopropyl)triethoxysilane (APTES) and are then coated with the Stober method discussed above [58]. This was done by Barnakov et al. and Digigow et al. [317, 321]. This sililation process can also be applied to nanoparticles already coated with silica, to provide extra binding sites for covalent binding of bioconjugation molecules [195].

Author	Initial MNP Pre-treatment?	MNP Medium	MNP (mg)	TEOS (ml)	EtOH (ml)	DI water (ml)	Base : Ammonia (ml)	Base : NaOH (ml)	Extra reactant	Reaction time	RESULT	LESSONS
Barnakov 2005 [317]	8-10 nm Fe3O4, oleic acid in toluene Removing OA with methanol and coating with APTMS	3 ml EtOH		0.5	10	2.5	3			48 h	Core-shell	
Dang 2010 [319] (hydrol-ysis under ultra-sonic irradia-tion)	30 nm Fe3O4, sonochemical synthesis	200 ml EtOH/H2O (80/20)		6	20			2 M, mass not specified		2h	Core-shell	Ultrasonic irradiation during reaction reduces agglomeration. Lower coating temperatures and lower pH values (when pH > 10) generally resulted in smaller agglomerate particle sizes. Higher pH values resulted in a higher weight ratio of silica.
Digigow 2014 [321] (co-condensation TEOS and APTES)	10 nm Fe3O4 from co-precipitation pH adjustement	sodium citrate	1.45	varied	80	20	1 (25%)		APTES, varied mass	3 h	Multiple cores - shell	The co-condensation of APTES and TEOS led to the formation of a multiple SPIONs core – silica shell architecture. The particles were amine-functionalized on the surface.
Furlan 2019 ('green' Stober : water as a solvent)	5 - 40 nm Fe3O4 from coprecipita-tion	powder	100	2	2	100	5 ('resulting pH is 11')			24 h	ultrafine' shell	Water's higher polarity enabled better dispersion of MNPs and slower TEOS condensation, favoring effective and uniform coating

Continued on next page

Table A.4.3 - continued from previous page

Author	Initial MNP Pre-treatment?	MNP Medium	MNP (mg)	TEOS (ml)	EtOH (ml)	DI water (ml)	Base : Ammonia (ml)	Base : NaOH (ml)	Extra reactant	Reaction time	RESULT	LESSONS
Gabelica 2021 [322]	20 nm Fe3O4 from microwave-assisted synthesis	powder	0.5	TEOS:EtOH:DI:NH3 molar ratio 1:100:32:0.003								The particle size, dispersion, and magnetic properties of the Fe3O4@SiO2 composite nanoparticles can be adjusted by changing the volume ratio of TEOS and magnetite colloid
Gao 2011 [194]	Fe3O4 from coprecipita-tion Sonication of initial suspension	water	380	varied	80	19	2 (25% wt.)			12 h	Core-shell	Silica coated magnetite are resistent to oxidation even during 800° heat treatment
Kuzminska 2015 [323]	11 - 13 nm Fe3O4 from coprecipita-tion	powder	281	0.043 (thin) and 0.215 (thick)		165	3 (25%)		Isopropanol : 80 mL	3 h	Core-shell APTES grafted	Tunable silica layer thicknesses by varying the amount of TEOS used in the Stober process
Lu 2002 [324]	5 - 15 nm Fe3O4 commercial ferrofluid	water, 0.3 mL		varied		4 + 0.3	0.5 (30%)		Isopropanol : 20 mL	3h	Core-shell (2-100nm thickness shell)	Silica in shell is amorphous. The thickness of the silica shell could be conveniently and reproducibly controlled by changing the concentration of the TEOS precursor. Fluorescent organic dyes could be incorporated into the silica shells, creating multifunctional nanoparticles with both magnetic and optical properties

Continued on next page

Table A.4.3 - continued from previous page

Author	Initial MNP Pre-treatment?	MNP Medium	MNP (mg)	TEOS (ml)	EtOH (ml)	DI water (ml)	Base : Ammonia (ml)	Base : NaOH (ml)	Extra reactant	Reaction time	RESULT	LESSONS
Ma 2013 [325] (CTAB assisted)	13 nm Fe_3O_4 from thermal decomposition, oleic acid in chloroform Transfer to aqeous solution by CTAB enrobement	water and CTAB (2mM), 0.5 mL		0.05		10		0.020 (2M)	TEOS suspended in methanol	24h	Amine-functionalized core-shell (8nm thick shell)	Obtained biocompatible silica coated SPIONS
Qui 2015 [320]	Fe_3O_4 from solvothermal synthesis (citrate)	ethanol (3mL)	150	2 (dropwise)	280	70	4 (28%)		Sonication of reagents (15 min) before adding TEOS		Core-shell for further modification	
Sharafi 2018 [318]	8 nm Fe_3O_4 from coprecipitation (citrate)	ethanol (80 mL) and water (20mL)	100 mg	0.1	80	20		1 (2M)	NaOH added in 0.1mL portions over 2h	6h	Core-shell (2-5nm shell tickness)	Agglomeration was prevented without additives by decreasing the initial concentration of the catalyst (NaOH) for a short period to minimize nucleation (reducing TEOS hydrolysis rate) and then gradually increasing its concentration
Sun 2005 [173] (Silicate pre-treatment)	7.6 nm Fe_3O_4 from coprecipitation (citrate) Sodium-silicate pre-treatment	ethanol (2 ml)	4 mg	varied (5 -250)	2	4	1.4 (27%)			12 h	Core-shell (shell thickness 1.5 – 60 nm)	The thickness of the silica shell can be easily tuned by different volumes of TEOS precursor. With an increased TEOS volume (from 5 ml to 20 ml), the mean hydrodynamic diameters and polydispersity decreased, indicating improved sheltering of magnetic interactions by the silica coating.

Continued on next page

Table A.4.3 - continued from previous page

Author	Initial MNP Pre-treatment?	MNP Medium	MNP (mg)	TEOS (ml)	EtOH (ml)	DI water (ml)	Base : Ammonia (ml)	Base : NaOH (ml)	Extra reactant	Reaction time	RESULT	LESSONS
Zelepukin 2017 [326]	Fe3O4 from coprecipitation (citrate and dextran)	water and CTAB (2mM), 0.5 mL	50 mg	0.010 - 0.200	1	50 ml	('resulting in pH 10)		Alcohol (1ml) varies between (ethanol, methanol or isopropyl alcohol)	24h	Multiple cores - shell	The type of alcohol solvent significantly affected the mean silica particle size: 10 nm in methanol, 100 nm in ethanol, and 500 nm in isopropanol

Table A.4.3 Modified Stober Protocols. All processes are done at room temperature except for Dang et al. in which temperature was varied from 10 to 50 °for different samples. All processes occur under stirring (260 - 800rpm) except for Dang et al. in which reaction was done under ultrasonic irradiation and Furlan et al. that alternated manual shaking, sonication and stirring.

A.5 Suppl. Chap. 4 : Magnetisation Curves at Room Temperature

A.5.1 Validation of SQUID measurements with AGFM measurements

Powder samples measured by the SQUID magnetometer are generally 1-2 mg of powder within a small polymer tube. To validate the obtained results and the measurement set-up, we compared magnetisation curves of Fe–Comm (magnetite 50 nm nanoparticles, commercial origin) samples and Fe–TD samples (magnetite 10 nm nanoparticles, obtained with thermal decomposition) in both SQUID and AGFM. In the AGFM, 0.05-0.1 mg of powder was encapsulated in a small piece of kapton tape.

Figure A.5.1 displays curves for both samples in both measurement set-ups. While the sensing principles, sample masses and sample holders are different, the conclusions per set-up are the same, i.e. that the superparamagnetic nanoparticles have a higher initial susceptibility but saturate slower, compared to the 50 nm nanoparticles. The AGFM saturation slope of both Fe-COMM and Fe–TD samples are consistently extended by the SQUID measurements which allow for higher DC field measurements. However, in absolute terms, one can not compare data from several set-ups : the SQUID measurements obtain slightly higher magnetisation for both TD and COMM. For superparamagnetic nanoparticles, a small opening of the hysteresis curve is observed with the AGFM measurement : this is considered an artefact due to less precise DC field calibration.

A.5.2 Validation of superparamagnetism in manganese ferrite SPNF and SPION

Spinel ferrites ($M^{2+}Fe_2^{3+}O_4$) containing 3d metals allow for excellent fine-tuning of magnetic properties [171]. $MnFe_2O_4$, $CoFe_2O_4$ and Fe_3O_4 nanoparticles are available for study in this case. Figure A.5.2 displays magnetisation curves obtained on powder samples of each available sample type made by coprecipitation. Note that ICP and TEM data on these samples are summarized in Tables 3.5.

The nickel ferrite nanoparticles do not have a superparamagnetic behavior : while nickel ferrite can display superparamagnetic behavior around 10 nm [327], the obtained particles are too small, making surface effects (e.g. spin canting as explained in Subsection 2.3.7.1) dominant.

Cobalt ferrite nanoparticle powder shows a high saturation magnetisation (61.2 emu/g at 7 T) but significant coercivity (23 mT), due to its high magnetocrystalline anisotropy K_m as specified in Table 4.3. As a result, initial susceptibility is small.

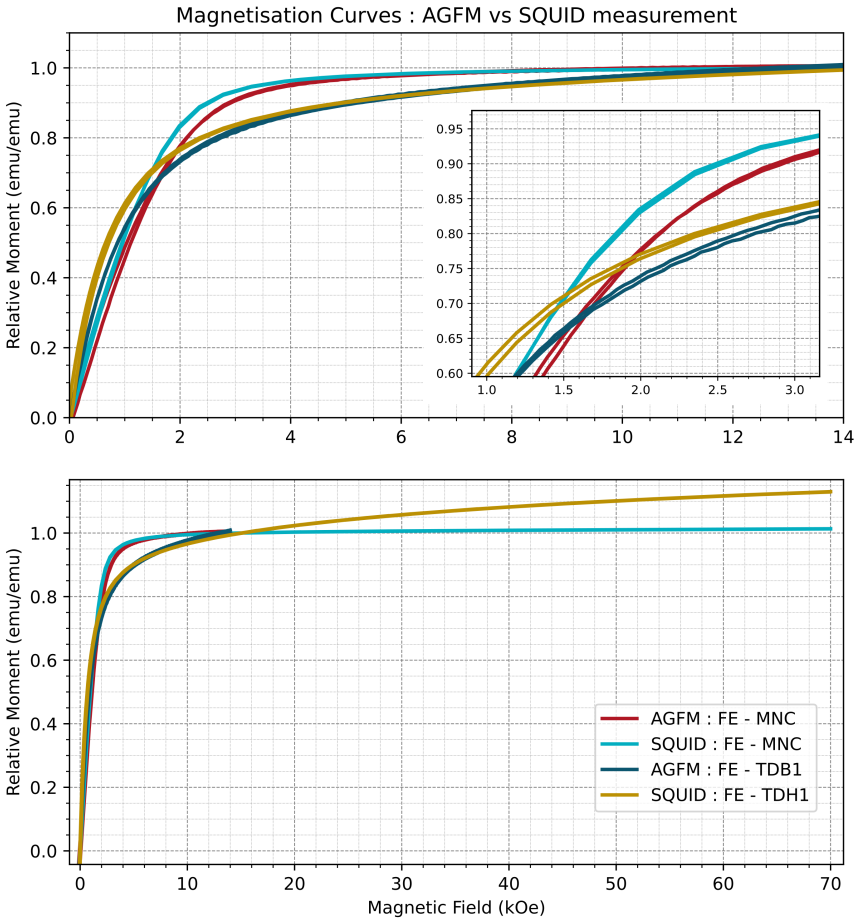


Fig. A.5.1 Comparison of magnetisation of magnetite powders (commercial 50 nm MNC and thermally decomposed 10 nm TD) extracted by both SQUID and AGFM magnetometers. Note : 70 kOe magnetic field corresponds to 7 T flux density.

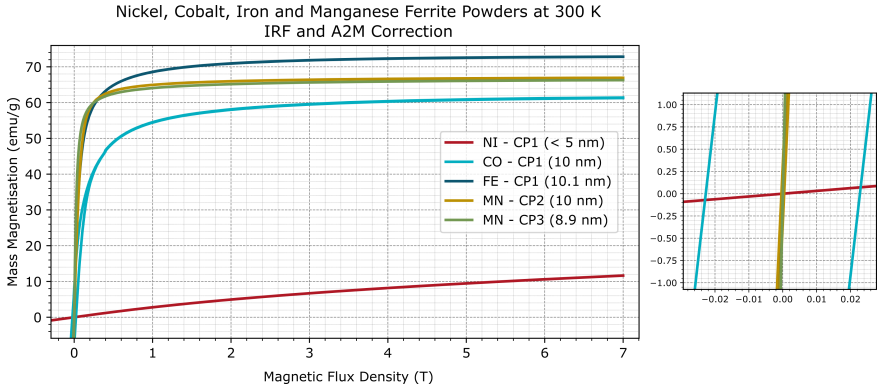


Fig. A.5.2 Magnetisation of Manganese, Iron, Cobalt and Nickel Ferrites. Mass Magnetisation relative to total powder mass, in emu/g corresponds to Am^2/kg

Both the manganese ferrite powders converge to similar mass magnetisation : the slightly lower value of the 8.9 nm Mn–CP3 (66.3 emu/g at 7 T) compared to the 10 nm Mn–CP3 (66.9 emu/g at 7 T) is probably due to a higher surface/volume ratio. The magnetite nanoparticles (which might have maghemite at the surface) converge to the highest saturation value : (72.9 emu/g at 7 T).

Referring to bulk counterparts of superparamagnetic samples in Table 4.3, it is consistent that SPION have the highest M_s while cobalt ferrites have the lowest. The manganese ferrite powders saturate at 82% of the bulk value, while the magnetite saturates at 79%. This might be explained by the presence of maghemite at the surface of the iron oxide nanoparticles due to oxidation, or by a thicker dead layer.

A.5.3 Correcting Magnetisation Curves for Measurement

A.5.3.1 High Field slope Correction

As illustrated in Figure 2.2 in Chapter 2, diamagnetic effects (which are always present in a material, albeit overshadowed by its ferromagnetism) correspond to a constant negative slope of the magnetisation curve. Paramagnetic effects are a positive slope : while paramagnets can saturate in certain conditions, we consider they do not saturate below 7 [T] (maximum flux density applied during measurement) at room temperature [17] [14]. SPNF on the other hand do saturate at room temperature, since they are ferromagnetic materials and thus have larger magnetic

[14] As a reminder : atomic magnetic moments in paramagnetic materials are really small (low positivie susceptibility) which makes it virtually impossible to overcome the randomizing thermal energy (and thus to saturate by aligning all moments).

moments. Therefore, to correct for the diamagnetism of the sample and the sample holder, and the non-saturating paramagnetism, the average slope between 5 and 7 [T] (assumed to be a linear range)) is calculated and subtracted from the measured magnetisation curve $M_{meas}(H)$.

$$\chi_{hf} = \frac{M(7\ [\mathrm{T}]) - M(5\ [\mathrm{T}])}{7\ [\mathrm{T}] - 5\ [\mathrm{T}]} \tag{24}$$

$$M_{corr}(H) = M_{meas}(H) - \chi_{hf} H \tag{25}$$

This slope in the assumed linear range is the high field susceptibility χ_{hf}. Note that in the more advanced correction explained below, it is considered that a small massic fraction of the magnetic particles still hasn't reached saturation at these fields, due to e.g. dead layer effect. As a result, the "high field part" of the curve is not considered strictly linear.

A.5.3.2 Remanent Flux and High Field asymptotic Correction (IRF and A2S)

In [328, 329] a more advanced correction method is detailed for magnetisation data obtained with a SQUID magnetometer, addressing two potential sources of measurement errors :

1. Superconducting magnets without active field feedback control can trap magnetic "frozen flux", creating a remanent field (H_{ff}). This causes the actual field (H_{actual}) at the sample to differ from the nominal field ($H_{nominal}$) set by the instrument. This discrepancy is most pronounced near $H = 0$ and is a major source of artifacts for paramagnetic and superparamagnetic samples, often manifesting as apparently open hysteresis loops, significantly shifted branches, or even non-physical negative coercivity (H_c) [329].
2. While true paramagnetic materials do not saturate ferromagnetically, accurately determining their linear susceptibility requires correct field values. For superparamagnetic nanoparticles, achieving complete magnetic saturation of the particle moments can require high fields (due to e.g. dead layer), and distinguishing the particle contribution from the linear background susceptibility relies on accurate high-field data.

Step 1: Correction for Instrumental Remanent Field (IRF)

This IRF is particularly relevant for low-coercivity materials (such as superparamagnetic samples). Following the method of Spassov and Egli [329], the applied field axis (H) is corrected to account for the discrepancy between the "nominal field" and the actual field experienced by the sample, mainly attributed to trapped magnetic flux within the superconducting magnet of the SQUID.

1. **Measurement of a Paramagnetic Standard:** A hysteresis loop is recorded for a known paramagnetic standard (in this case Palladium, exhibit-

ing temperature-independent Pauli Magnetism as described in Subsection 2.2.2.5, chapter 2). This measurement utilises the *exact measurement sequence* (field range $\pm H_{max}$, sweep rate, temperature, etc.) intended for the samples. The standard's measured moment is denoted as $M^{\pm}_{std}(H_{nominal})$.

2. **Determination of the Field Error Curve:** The difference in nominal field, $\Delta H(H_{nominal})$, required to produce the same moment M between the descending (+) and ascending (-) branches of the standard's loop is calculated. This is typically achieved by interpolating the inverse functions $H_{nominal}(M_{std})$. This ΔH curve represents approximately $2 \times H_{ff}$ as a function of the nominal field.
3. **Modelling of the Error Curve:** The $\Delta H(H_{nominal})$ curve is modelled using appropriate functions, with the positive ($H_{nominal} > 0$) and negative ($H_{nominal} < 0$) field ranges treated separately to account for potential asymmetry. Example functions in [329] include:

$$f_P(H) = a \tanh\left(\frac{1}{bH}\right) + \sum_{i=0}^{n} c_i H^i \quad \text{for } H > 0 \tag{26}$$

$$f_N(H) = -a' \tanh\left(\frac{1}{b'H}\right) + \sum_{i=0}^{n} c'_i H^i \quad \text{for } H < 0 \tag{27}$$

   The coefficients are determined via weighted fitting to the ΔH data, where H is $H_{nominal}$.
4. **Correction of the Sample Data Field Axis:** The nominal field values for the actual sample measurement ($M^{\pm}_{sample}(H_{nominal})$) are adjusted to obtain the corrected field H_{corr}:

$$\text{Descending Branch (+): } H_{corr} = H_{nominal} - \frac{1}{2} f_{P/N}(H_{nominal}) \tag{28}$$

$$\text{Ascending Branch (-): } H_{corr} = H_{nominal} + \frac{1}{2} f_{N/P}(H_{nominal}) \tag{29}$$

   The appropriate fit function (f_P or f_N) is selected based on the sign of $H_{nominal}$ in each measurement quadrant. This yields the field-corrected loop, $M^{\pm}_{sample}(H_{corr})$.

This correction enables the accurate determination of the true (near-zero) H_c and M_{rs} for superparamagnetic samples, as well as the correct field dependence required for the extraction of paramagnetic susceptibility in the subsequent correction step.

Step 2: Analysis and Correction of High-Field Slope (A2S)

The A2S method proposed in [328] models the convergence of the magnetisation $M(H)$ toward its saturation value M_s as the applied field H tends towards infinity

($H \to \infty$). It allows to distinguisch the sample magnetisation from its background more precisely than the linear High Field Slope Correction in Subsection A.5.3.1. The model used is:

$$M(H) = M_s + \chi_{hf} H + \alpha H^{\beta} \tag{30}$$

- The term αH^{β} (where $\beta < 0$ for a valid approach) represents the deviation of the ferromagnetic component from full saturation. As $H \to \infty$, this term asymptotically approaches zero ($\alpha H^{\beta} \to 0$).
- The purely ferromagnetic component of the magnetisation, $M_{ferro}(H) = M(H) - \chi_{hf} H$, asymptotically approaches the constant value M_s.
- The total measured magnetisation $M(H)$ asymptotically approaches the line $M = M_s + \chi_{hf} H$.

Exactly like the high field slope correction, linear regression is performed on the data points within the identified high-field linear region of $M_{sample}(H_{corr})$ versus H_{corr}. The slope of this fit yields χ_{hf}, incorporating both purely diamagnetic and paramagnetic behaviours. The linear contribution is subtracted from the entire dataset:

$$M_{intrinsic}(H_{corr}) = M_{sample}(H_{corr}) - \chi_{hf} H_{corr} \tag{31}$$

For superparamagnetic samples, $M_{intrinsic}(H_{corr})$ represents the magnetisation curve of the nanoparticle assembly approaching its saturation value M_s. The slope of β is calculated by considering the second derivative $\ln |M''_{intrinsic}(H_{corr})|$ vs $\ln(H_{corr})$. The correlation derived from the second derivative of the general approach model $M(H) = M_s + \chi_{hf} H + \alpha H^{\beta}$, is given by:

$$\ln |M''(H)| = \ln |\alpha\beta(\beta - 1)| + (\beta - 2) \ln(H) \tag{32}$$

The slope in the high-field region is fitted, allowing for the calculation of $\beta = \text{Slope} + 2$.

A strongly negative β indicates a well-behaved high-field regime, supporting the validity of the linear fit for χ_{hf}. Conversely, a β value near or above zero suggests potential issues, such as incomplete saturation of particle moments, significant sample drift, or other measurement artifacts affecting the high-field curvature.

In this work, the A2S correction was applied only in cases exhibiting a strongly negative β. These corrections were performed by Dr. Simo Spassov.

A.6 Suppl. Chap. 4 : reported Mydosh parameters for SPIONs

Table A.6.1 compiles experimentally reported Φ values for ferrite and iron oxide nanoparticle systems from the literature. The values are organised by material family (magnetite, maghemite, manganese ferrite, mixed ferrites) to highlight the influence of composition on the interaction regime.

Material	Size (nm)	Φ	Classification	Cond.	Comp.	f range [Hz]	Ref.
Magnetite (Fe_3O_4)							
Fe_3O_4	—	0.050	SSG	p.	—	—	[233][a]
Fe_3O_4	5	0.07	Weakly int. SPM	p.	χ''[b]	0.02–1000	[49]
Fe_3O_4	6.5	0.13	Weakly int. SPM	p.	χ'	9–941 Hz	[330]
Ag@Fe_3O_4	6.5 (+ 2 Ag)	0.029	SG (interface)	p.	χ'	9–941	[330]
Fe_3O_4 (oleic acid)	6.9	0.33 / 0.076	SPM / SSG	p.	χ''	107–9693	[223]
Maghemite (γ-Fe_2O_3)							
γ-Fe_2O_3/SiO_2	11 (shell 0.5)	—	SSG	c.s.	χ'	1.2–1190	[234]
γ-Fe_2O_3/SiO_2	11 (shell 18)	—	SPM (Arrhenius)	c.s.	χ''	1.2–1190	[234]
Manganese ferrite ($MnFe_2O_4$)							
$MnFe_2O_4$	4–8	0.02–0.03	SSG	p.	χ'	33–1000	[232]
Mixed / substituted ferrites							
$Zn_{0.5}Ca_{0.5}Fe_2O_4$	∼11	0.026	SSG	p.	χ'	11–9984	[233]
$Zn_xFe_{3-x}O_4$	fine	0.028	SSG	p.	—	—	[233][a]
$MgFe_2O_4$	—	0.030	SSG	p.	—	—	[233][a]
$Zn_{0.5}Ni_{0.5}Fe_2O_4$	—	0.032	SSG	p.	—	—	[233][a]
$LiFe_5O_8$	—	0.03–0.05	SG	p.	—	—	[233][a]
Co/Ag multilayer	—	0.050	SSG transition	film	—	—	[233][a]
Canonical spin glasses (for reference)							
CuMn (1–6 at%)	bulk	0.005	Canonical SG	alloy	—	—	[228]
$Mn_{64}Fe_{36}Si_{16}$	bulk	0.007	Canonical SG	alloy	—	—	[233][a]

[a] Value compiled from Table 4 in [233], citing original sources therein; frequency ranges not reported.
[b] Arrhenius analysis explicitly from χ''; the paper does not state which component was used for Φ.

Table A.6.1 Reported Mydosh parameter values for ferrite and iron oxide nanoparticle systems. "Conditions" indicates whether the sample was measured as powder (p.), ferrofluid (f.f.), membrane (m.), or core-shell assembly (c.s.). The "Component" column indicates whether Φ was computed from the real (χ') or imaginary (χ'') susceptibility peak temperatures. The "f range" column gives the frequency window over which $T_B(f)$ was tracked to compute Φ.

- Goya et al. [49] measured 5 nm spherical Fe_3O_4 powder over 0.02–1000 Hz and obtained $\Phi = 0.07$ from χ'', placing the system in a weakly interacting

SPM regime. A Néel-Arrhenius fit yields $\tau_0 = 9 \times 10^{-13}$ s and a K_{eff} an order of magnitude above bulk magnetite, a discrepancy attributed to dipolar interactions that inflate the apparent barrier under the low-field ACS conditions but are suppressed in high-field static measurements.

- The uncoated 6.5 nm Fe_3O_4 particles of Singh et al. [330] ($\Phi = 0.13$) are nearly non-interacting[15], whereas the same particles coated with silver ($\Phi = 0.029$) exhibit spin-glass behaviour due to the magnetically disordered interface layer.

- Modestino et al. [223] observed two χ'' peaks for 6.9 nm oleic-acid-coated Fe_3O_4: a low-T peak (37 K, $\Phi \approx 0.33$, SPM) and a high-T peak (225 K, $\Phi \approx 0.076$, SSG). The nature of each is confirmed by the DC-field dependence: the SPM peak follows an H^2 law, while the SSG peak follows the de Almeida–Thouless $H^{2/3}$ line. Both regimes coexist within a single monomodal size distribution, the SSG fraction arising from closely aggregated particles.

- In the study of Hiroi et al. [234], maghemite (γ-Fe_2O_3) nanoparticles in the controlled interparticle-distance demonstrated a clear transition from SSG to SPM behaviour as the silica shell thickness (and thus interparticle distance) was increased. The critical interparticle distance for the SSG transition was found to be 15–18 nm for 11 nm cores, corresponding to a dipolar interaction energy of 6–12% of the anisotropy energy.

- Aslibeiki et al. [232] found $\Phi = 0.02$–0.03 for closely packed $MnFe_2O_4$ powders (4–8 nm). Néel-Arrhenius fits give unphysical τ_0 (10^{-29}–10^{-47} s), while a critical slowing-down model recovers $\tau_0 \sim 10^{-8}$–10^{-10} s and $z\nu \approx 5$, confirming SSG freezing driven by dipolar interactions whose strength grows with particle size.

- Tiwari et al. [233] reported $\Phi = 0.026$ for $\sim$11 nm $Zn_{0.5}Ca_{0.5}Fe_2O_4$ nanoferrites, with coexistence of SPM and SSG confirmed by an unphysical Arrhenius $\tau_0 \sim 10^{-57}$ s, physically reasonable Vogel-Fulcher and power-law fits ($\tau_0 \sim 10^{-9}$ s, $T_g \approx 115$ K), and a ZFC stop-and-wait memory dip, a hallmark of glassy freezing absent in canonical SPM systems. Table 4 of this reference compiles Φ values for numerous ferrite systems and serves as the source for several entries in Table A.6.1.

[15] The 6.5 nm particles are measured in powder form. Nearly non-interacting SPM behaviour can be explained by the small size, thus small magnetic moment of the particles (accounting for e.g. dead layer) that reduce interaction effects.

A.7 Suppl. Chap. 4 : RF analysis of magnetic samples

A.7.1 Notifying an Error in the Internal Correction of the E4991 Permeability Mode

After calibration (open, short, 50 Ω load, and low-loss capacitance) the E4991 Analyzer can be set to two relevant modes for magnetic materials characterisation : permeability mode and impedance mode.

- In permeability mode, properties of the test-fixture are pre-encoded (electrical length,...). A short compensation for the fixture is required. The user has the possibility of entering the dimensions of the toroid (which should not take the whole cavity) after which real and imaginary permeability is automatically calculated, based on the developments above.
- In impedance mode, the properties of the test-fixture need to be entered manually. Short and open compensation for the fixture can be entered. The obtained data are impedance modulus and phase, with corresponding resistance and reactance, for the whole test fixture volume as a whole. Correction for the sample dimensions should be done in post-treatment.

We draw the reader's attention to the following issue regarding correction for the blank, i.e. for the small contribution of the capsule to the measured impedance. In theory, both scenarios should result in very similar data :

1. Performing a short compensation of the fixture containing no capsule. Measuring an empty capsule and a filled capsule, and subtracting the former's impedance from the latter.
2. Performing the short compensation of the fixture containing an empty capsule. Then measuring a filled capsule.

In the lower part of Figure A.7.1 we observe that in impedance mode, both scenarios correspond: "blank correction" corresponding to scenario 1, and "blank calibration" corresponding to scenario 2, coincide. In the upper figure, the permeability data ("MU data") that have been automatically calculated by the E4991 based on material dimensions, coincide. For permeability based on corresponding impedance data, a difference is observed in real permeability; i.e. the outlying blue 'blank calibration' curve. This is due to the fact that the short compensation, while correctly integrated in the permeability calculation, is not correctly integrated in corresponding reactance data. When measuring the blank and filled capsule separately, this inconsistency is transposed to both measurements but canceled out after subtraction, resulting in the red "blank correction" curve being consistent with the other data. This observation was confirmed with Dr. Ron Goldfarb who equally has access to an E4991 in the NIST laboratories [240].

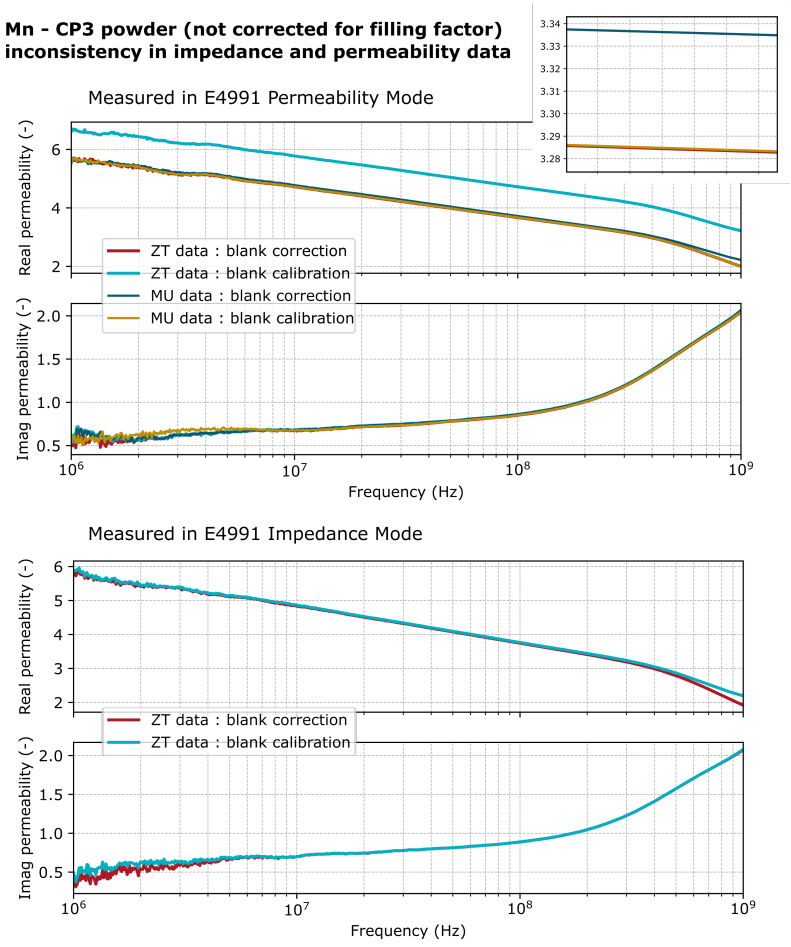


Fig. A.7.1 The light blue curve illustrates an error in the fixture compensation from E4991.

A.7.1.1 Other geometries and set-ups for RF properties of magnetic materials

For extraction of material properties at radio frequency, various geometries exist (solenoid, coaxial line, waveguide, toroid), each with trade-offs in frequency range, sample preparation, and calibration complexity. In order to effectively utilise the permeability in GHz range, high magnetic resonance frequency (i), high permeability (ii), magnetic isotropy (iii), and a low loss (iv) are requested for the magnetic material [60]. Noteworthy studies analysing material permeability between MHz to sub-GHz range include :

- Wu et al. [331] measured the permeability of composite materials toroids of rod-shaped CrO_2 nanoparticles in epoxy resin, up to 16 GHz. An interparticular interaction factor is introduced to fit the theoretical model (based on Bruggeman's effective medium theory for composites) and the experimental result. However, no physical interpretation is associated to this factor.

- Yamaguchi et al. [332, 333] propose a permeameter for both metallic and insulating thin-films in the 10MHz-20GHz range based on coplanar wave guides. Dependence on geometry of the thin-film and of the wave-guide was demonstrated and discussed in [334]. Waveguides demonstrate a high SNR below 100MHz frequencies. Tamaru et al. proposed the coupling of two shorted wave-guides to improve the SNR and characterised 200um ferromagnetic flakes [335].

- Sakharov et al. [336] characterized the frequency dependencies of dense cobalt nanoparticle composites between 10 MHz and 10 GHz, based on a custom coaxial transmission line. The study concludes that this oxidation causes both the real and imaginary parts of the permeability to decrease. The reduction in the real part is attributed to the formation of an antiferromagnetic shell, reducing the effective ferromagnetic volume. The decrease in the imaginary part is attributed to this insulating shell, which reduced conductive pathways between nanoparticles, thereby suppressing eddy current losses.

- At lower frequencies (1 kHz – 100 kHz), Cui et al. [305] proposed a four-tap solenoid coil sensor coupled to a commercial LCR meter for measuring the effective permeability of particle mixtures (Al_2O_3/Fe) at varying volume fractions. A correction factor accounts for the non-uniform field distribution in the finite solenoid, and results are validated against the Maxwell mixing model with a relative error below 5.35%.

A.8 Suppl. Chap. 5 : Sensors - Key Concepts

Noise Floor

The **noise floor** of a sensor is the minimum signal level that can be detected above the intrinsic noise of the measurement system. It is quantified by the standard deviation σ_{blank} of the sensor output in the absence of any analyte or stimulus [337]. Any signal smaller than the noise floor is indistinguishable from random fluctuations. In the context of frequency-shift measurements (e.g. a Colpitts oscillator monitoring an LC resonance), the noise floor corresponds to the standard deviation $\sigma(f_s)$ of the frequency differences obtained from repeated insertion/removal cycles of a blank or of a given sample.

Sensitivity

The **sensitivity** of a sensor is the slope of its calibration curve, i.e. the ratio of the change in sensor output to the change in the quantity being measured [337]:

$$S = \frac{\partial y}{\partial x} \tag{33}$$

where y is the sensor output and x the measurand. A sensor with higher sensitivity produces a larger output change for the same input change. For inductive nanoparticle sensing, the sensitivity is the slope of the linear fit relating the frequency change Δf (or relative frequency change $\Delta f/f$) to the analyte mass, expressed e.g. in Hz/μg.

Limit of Detection

The **LoD** is the smallest quantity of analyte that can be reliably distinguished from the absence of analyte. The IUPAC framework [337] formalises detection in terms of a *critical value* L_C (the decision threshold above which a signal is declared "detected") and a *detection limit* L_D (the true analyte level that will be detected with probability $1-\beta$). For Gaussian noise with known variance and default error rates $\alpha = \beta = 0.05$, these evaluate to $L_C = 1.645\,\sigma_o$ and $L_D = 3.29\,\sigma_o$. In practice, a widely adopted simplification sets both thresholds equal to $3\,\sigma_{blank}$, as applied e.g. in [338]. The LoD then becomes:

$$\mathrm{LoD} = 3 \cdot \frac{\sigma_{blank}}{S} \tag{34}$$

where σ_{blank} is the standard deviation of the blank measurement (the noise floor) and S is the sensitivity. Under the assumption of Gaussian-distributed noise, this corresponds to a one-sided false positive probability of $1-\Phi(3) \approx 1.35 \times 10^{-3}$, i.e. $\approx 0.13\,\%$ [337]. In terms of signal-to-noise ratio, this threshold corresponds to

$SNR_{dB} \approx 9.54\,\text{dB}$. In practice, a measurement is therefore considered **significant** when the observed signal exceeds three times the standard deviation of the noise:

$$\Delta y > 3\,\sigma_{blank} \tag{35}$$

For the frequency-shift measurements in Chapter 5, the noise floor is $\sigma(f_s)$ (standard deviation of repeated frequency-shift values for a given sample), the sensitivity S is the slope of the mass-versus-frequency calibration curve, and the detection criterion becomes $\Delta f_{s,m} > 3 \cdot \sigma(f_s)$.

A.9 Suppl. Chap. 5 : Commercial MNP Sensors applications, patents and evolution

The following subsections detail the technology, intellectual property, target applications, and corporate evolution of six ventures that have attempted to commercialise MNP detection for point-of-care diagnostics. A comparative summary is given in Table 5.3 (Chapter 5).

MagnaBioSciences, LLC (San Diego, CA, USA)

- **Founded:** 2000, as an affiliate of Quantum Design International[16]. A related entity, MagnaBioAnalytics, also operates under the Quantum Design umbrella[17].

- **Sensing principle:** Inductive readout of the AC magnetic response. A C-shaped electromagnet applies a strong AC field (∼100 kHz) across a small air gap; an array of thin-film induction coils in a gradiometer configuration measures the magnetic signal from the labels.

- **Platform / hardware:** MICT (Magnetic Immuno-Chromatographic Test). Both a benchtop and a handheld reader were developed, using disposable cassettes encoded with 2D barcodes for assay identification and calibration[18]. The company reported improved sensitivity over conventional gold or latex LFA, attributed to the ability of magnetic detection to probe the full membrane depth (∼200 µm) rather than only the top ∼10 µm accessible to optical methods.

- **Assay substrate:** Lateral flow strip.

[16] https://www.qdusa.com/

[17] https://magnabioanalytics.com/

[18] US Army WMD Detector Selector, https://www.wmddetectorselector.army.mil/detectorPages/188.aspx

- **Nanoparticle labels:** Superparamagnetic iron oxide polymer beads, 60–380 nm range; a Taenia solium validation study used 200 nm carboxyl particles from Ademtech (France).

- **Key patents:** US 6,046,585 ("Method and apparatus for making quantitative measurements of localised accumulations of target particles having magnetic particles bound thereto", Quantum Design, 2000)[19]; US 6,597,176 B2 ("…patterns of magnetic particles in lateral flow membranes and microfluidic systems", 2003)[20]; US 6,607,922 B2 ("Immunochromatographic assay method and apparatus", 2003)[21].

- **Target applications:** Biodefense, the MICT platform was featured on the US Army WMD Detector Selector.

- **Company evolution:** As of 2025, the original website (`https://magnabiosciences.com/`) appears inactive.

LifeAssays AB (Lund, Sweden)

- **Founded:** 2000, based on technology developed at Lund University [283].

- **Sensing principle:** Magnetic permeability detection. An inductance coil measures the permeability change caused by bound superparamagnetic nanoparticle labels [283]. A later patent (US 10,705,162 B2) adds temperature control for measurement stability.

- **Platform / hardware:** Proprietary magnetic permeability reader; after the 2015 acquisition of Magnasense Technologies Oy, also the CE-marked Magnia Reader for magnetic LFA.

- **Assay substrate:** Lateral flow strip (Magnia Reader platform).

- **Nanoparticle labels:** 70 nm dextran-coated iron oxide (Fe_3O_4) nanoparticles [283].

- **Key patents:** US 10,705,162 B2 ("Temperature controlled magnetic permeability detector", 2020) and US 8,790,917 B2[22].

- **Target applications:** Point-of-care diagnostics (CRP demonstrated in [283]).

[19] `https://patents.google.com/patent/US6046585`
[20] `https://patents.google.com/patent/US6597176B2/en`
[21] `https://patents.google.com/patent/US6607922B2/en`
[22] `https://patents.google.com/patent/US10705162B2/en`

- **Company evolution:** In November 2015, LifeAssays acquired Magnasense Technologies Oy (Tampere, Finland)[23]. In 2021, LifeAssays was itself acquired by AegirBio AB, which subsequently renamed itself Magnasense AB in July 2024[24].

Senova Immunoassay Systems (Weimar, Germany)

- **Founded:** 1997. Primarily a LFA and immunofiltration manufacturer rather than a magnetic reader company.

- **Sensing principle:** Frequency mixing magnetic detection (FMMD), developed jointly by Forschungszentrum Jülich and Senova [271, 288]. Senova contributed the ABICAP immunoassay substrate; the frequency mixing detection principle originated at Forschungszentrum Jülich.

- **Platform / hardware:** FMMD reader (Forschungszentrum Jülich); Senova's own portfolio centres on lateral flow rapid test manufacturing.

- **Assay substrate:** ABICAP (Antibody Binding Immunocolumn for Analytical Purpose) 3D immunofiltration column, a sintered polyethylene filter (5 mm diameter $\times$ 5 mm height) inside an 8 mm outer-diameter column (used with FMMD); lateral flow strips (for Senova's broader product line).

- **Nanoparticle labels:** PVA-SAV1 beads from Chemagen AG (Baesweiler, Germany), 0.5–1 µm diameter; magnetite crystallites embedded in a polyvinylalcohol matrix, streptavidin-coated [271].

- **Key patents:** WO 2004/077044 A1[25] ("Method and device for selectively detecting ferromagnetic or superparamagnetic particles", Forschungszentrum Jülich GmbH, inventors: P. Miethe, H.-J. Krause et al.), held by Forschungszentrum Jülich, not Senova.

- **Target applications:** Extensive lateral flow portfolio: Troponin I, D-Dimer, CRP, hCG; first Ebola LFA worldwide (2015)[26].

- **Company evolution:** ISO 13485 certified as IVD manufacturer since 2011. Remains active with over 30 employees: `https://www.senova.de/`.

[23] `https://www.bionity.com/en/companies/14646/lifeassays-ab.html`

[24] `https://www.nasdaq.com/press-release/change-company-name-aegirbio-ab-changes-name-magnasense-ab-2024-07-08`

[25] `https://patents.google.com/patent/WO2004077044A1/en`

[26] `https://www.senova.de/en/history/`

Magnotech (Philips, Eindhoven, Netherlands)

- **Founded:** Developed internally at Philips Research, led by Menno Prins.
- **Sensing principle:** Optomagnetic biosensing. The early proof of concept used a GMR sensor chip with magnetic actuation [291]; the platform then evolved to optical detection based on frustrated total internal reflection (FTIR): bound magnetic nanoparticles at the sensor surface absorb and scatter the evanescent wave, causing a measurable reduction in reflected light intensity [284]. Electromagnets actuate the nanoparticles through the sample to accelerate binding kinetics and perform bound/free separation, all magnetically controlled.
- **Platform / hardware:** Minicare product line (Philips, 2016), then Atellica VTLi Patient-Side Immunoassay Analyser[27] (Siemens Healthineers).
- **Assay substrate:** Disposable cartridge (sandwich immunoassay format).
- **Nanoparticle labels:** 500 nm superparamagnetic particles.
- **Key patents:** US 8,449,833 B2[28] ("Frustrated total internal reflection biosensor cartridge", Philips, 2013) and US 9,658,219 B2[29] ("Microelectronic sensor device for detecting label particles", Philips, 2017). Both now reassigned to Siemens Healthineers Nederland B.V.
- **Target applications:** Cardiac markers from fingerstick blood samples.
- **Company evolution:** Philips launched Minicare (2016); spun out as Minicare BV (2018); acquired by Siemens Healthineers (July 2019). Now deployed in hospitals as the Atellica VTLi.

Magnisense (Paris, France)

- **Founded:** 2003, by Ingmar Adlerberg; core technology invented by Dr Petr Nikitin (Chief Scientific Officer), based on a Russian patent from 2000.
- **Sensing principle:** Nonlinear magnetisation detection, the MIAtek (Magnetic ImmunoAssay technology) platform exploits the nonlinear magnetisation of superparamagnetic labels [272, 293]. Conceptually similar to the FMMD technique from Forschungszentrum Jülich but independently invented, based on a Russian priority patent from 2000.

[27] https://www.siemens-healthineers.com/cardiac/cardiac-systems/atellica-vtli

[28] https://patents.google.com/patent/US8449833B2

[29] https://patents.google.com/patent/US9658219B2

- **Platform / hardware:** Portable reader for emergency diagnostics. Commercialised as MIAstrip (lateral flow format) and MIAflo (disposable cartridge for food/water safety)[30].

- **Assay substrate:** Multi-format: lateral flow strips and porous immunofiltration filters [272]; commercially available as disposable cartridges (MIAstrip, MIAflo).

- **Nanoparticle labels:** Superparamagnetic iron oxide beads, ∼200 nm. Nikitin et al. used Dynabeads MyOne (∼1 µm) and M-280 (∼2.8 µm) commercial superparamagnetic beads for calibration and detection [272]; Orlov et al. used 200 nm carboxyl-modified Fe_3O_4 particles from Merck Chimie SAS (France) [3].

- **Key patents:** US 7,785,902 ("Method for analysing a mixture of biological and/or chemical components using magnetic particles", priority 2000) and its divisional US 8,865,068 B2[31]. A separate patent family covers the immunochromatographic test device: EP 1996945 A1 (priority 2006, inventors R. Legastelois, P. I. Nikitin, A. Billiotte).

- **Target applications:** Emergency cardiovascular diagnostics (acute myocardial infarction markers); more recently, obstetric and gynecological point-of-care diagnostics (under OVVI Diagnostics).

- **Company evolution:** R&D facilities near Lyon; planned expansion into the Belgian diagnostics ecosystem[32]. Acquired by OVVI Diagnostics (Liège, Belgium) in July 2020[33], which continues development.

MagArray, Inc. (Milpitas, CA, USA)

- **Founded:** 2005[34], by Stanford University researchers [282, 285]. Technology adapted from the hard drive industry.

- **Sensing principle:** Giant Magnetoresistive (GMR) spin-valve nanosensor arrays. Arrays of GMR sensors detect the stray magnetic field from bound magnetic nanotags, providing real-time, multiplexed, quantitative detection.

[30] BioSpace, "Magnisense's Cornerstone Patent Is Issued In The United States", July 2010, https://www.biospace.com/article/releases/magnisense-s-cornerstone-patent-is-issued-in-the-united-states-/

[31] https://patents.google.com/patent/US8865068

[32] Cited by L'Echo in 2018: https://www.lecho.be/entreprises/pharma-biotechnologie/la-biotech-francaise-magnisense-integre-l-ecosysteme-wallon/10062934.html

[33] https://www.ovvidx.com/our-history.php

[34] https://magarray.com/

- **Platform / hardware:** Silicon chip with GMR sensor array. Demonstrated matrix-insensitive protein assays with sensitivities surpassing conventional ELISA [281].
- **Assay substrate:** Silicon chip.
- **Nanoparticle labels:** ∼50 nm MACS MicroBeads (Miltenyi Biotec); clusters of 13 nm Fe_2O_3 cores in a dextran shell, streptavidin-coated [282, 285].
- **Key patents:** US 9,863,939 B2 ("Analyte detection with magnetic sensors", Stanford/MagArray, 2018)[35], US 9,164,100 B2, and US 9,151,763 B2.
- **Target applications:** Lung cancer blood diagnostics, the REVEAL Lung Nodule Characterization test (launched 2018, covered by Medicare[36]) and the Knodule ID multianalyte risk stratification test, clinically validated in a 918-patient study across four US and one Canadian medical center[37].
- **Company evolution:** Remains active: `https://magarray.com/`.

A.10 Suppl. Chap. 6 : Coil Geometries

A.10.1 Solenoid Coils

The inductance of a solenoid coil, its stray capacitance and its intrinsic resistance (ignoring skin effect) are [339]:

$$L_{solenoid} = N^2 \mu_0 \frac{A}{l} \tag{36}$$

$$C_s = \frac{\epsilon_0 \pi^2 D}{(N-1)\ln(\frac{p}{d} + \sqrt{(p/d)^2 - 1})} \tag{37}$$

$$R_{DC} = 4\rho \frac{ND}{d^2} \tag{38}$$

with N the number of turns, D the coil diameter, A the intersection surface, l the coil length, ϵ_0 the dielectric constant, p the winding pitch, d the wire diameter and ρ the wire resistivity

[35] `https://patents.google.com/patent/US9863939B2/en`

[36] MagArray states REVEAL "is already covered by Medicare" in their Nov. 2022 press release; however, several private insurers still classify the test as investigational.

[37] Cleveland Clinic, University of Pennsylvania, San Francisco VA Medical Center, Vanderbilt University, and British Columbia Cancer Research Institute. See: `https://www.globenewswire.com/news-release/2022/11/21/2559774/0/en/MagArray-Inc-Announces-the-Publication-of-Knodule-ID-Clinical-Validation-Results-in-CHEST.html`

A.10.2 Planar Coils

The geometry of planar coils is determined by 4 independent parameters among d_{out}, d_{in}, n, s and w; the fifth is always dependent on the others : outer diameter, inner diameter, number of turns, space between traces, and width of the traces.

Like wire-wound coils, planar coils also produce a magnetic field when excited. However, while the magnetic field of a coil that is long relative to its core diameter is strongly focused within the core of the coil, a planar structure (comparable to a short coil with many layers) creates a relatively strong magnetic field on the surface of the coil. [299] Three common approximations for planar coil inductance values are elaborated in [340] : the Modified Wheeler Formula, the Current Sheet Approximation and the Data Fitted Monomial.

The empirical Wheeler formula for planar inductance based on Wheelers' work in 1928 [341] and improved by [340] states :

$$L_{Wheeler} = \mu_0 N^2 d_{avg} \frac{K_1}{1/K_2\zeta} \tag{39}$$

with $\zeta = \frac{d_{out}-d_{in}}{d_{out}+d_{in}}$ the filling ratio, $d_{avg} = 0.5(d_{out} + d_{in})$ the average diameter and layout-dependent coefficients K_1 and K_2 that are summarized in table A.10.1. Two inductors with the same average diameter but different fill ratios will, of course, have different inductance values. The full one has a smaller inductance because its inner turns are closer to the center of the spiral and contribute less positive mutual inductance and more negative mutual inductance [340]. This expression is correlated to $L \propto A$ in the inductance expression of a solenoid (equation 36).

A second approach consists in approximating the sides of the spirals by symmetrical **current sheets** of equivalent current densities [263, 342].

$$L_{CS} = \mu_0 N^2 d_{avg} \frac{c_1}{2} \left[\ln\left(\frac{c_2}{\zeta}\right) + c_3\zeta + c_4\zeta^2 \right] \tag{40}$$

where ζ is the same fill ratio as in the Wheeler formula (not to be confused with the wire resistivity ρ used in the wire-wound coil expressions above). Note that this approximation requires that $s < 3w$.

A third approach is based on **monomial datafitting** done in [340], yielding the following expression :

$$L_{monomial} = \beta d_{out}^{a_1} w^{a_2} d_{avg}^{a_3} n^{a_4} s^{a_5} \tag{41}$$

Note that while the exact geometry of planar coils is constrained by 4 parameters, only 3 of those (dout, din, n) are used in the Wheeler and Current Sheet

	Wheeler Expression		Current Sheet Expression				Data-Fitted Monomial Expression					
	K_1	K_2	c_1	c_2	c_3	c_4	β (e-3)	a_1	a_2	a_3	a_4	a_5
Square	2.34	2.75	1.27	2.07	0.18	0.13	1.62	-1.21	-0.147	2.40	1.78	-0.030
Hexagonal	2.33	3.82	1.09	2.23	0.00	0.17	1.28	-1.24	-0.174	2.47	1.77	-0.049
Octogonal	2.25	3.55	1.07	2.29	0.00	0.19	1.33	-1.21	-0.163	2.43	1.75	-0.049
Circle			1.00	2.46	0.00	0.20						

Table A.10.1 Coefficients for different analytical expressions for planar coil inductance values as gathered in [340]

models : the pitch $s + w$ is decisive for the inductance, similar to the solenoid coil in which the inductance is determined by the number of turns per solenoid length. However, while the inductance can be identical for various s and w values as long as their sum stays the same, varying the ratio s/w affects the quality factor of the coil. The inner turns, which do not have a significant area, do not contribute significantly to the overall inductance while they still increase R_s which deteriorates the quality factor. Therefore, a general rule of thumb is that $d_{in}/d_{out} > 0.3$ However, for applications where the target is very close to the sensor, such as touch-on-metal, a ratio as low as 0.05 is often acceptable, as the inner turns provide increased sensitivity [343].

Circular spiral windings[38] present lower series resistance and interwinding capacitance due to their lower area to perimeter ratio, with respect to other geometries [259].

Resistance of a planar coil

The resistance is expressed by

$$R_S = \frac{\rho l}{A} = \frac{\rho l}{wt}$$

where ρ is the resistivity of the material, l is the length of the current sheet, w, t are the width and thickness of the wire. For a planar coil, the length of the current sheet can be approximated using

$$l = N \cdot d_{avg} N_{sides} \tan\left(\frac{\pi}{N_{sides}}\right)$$

with N the number of turns, N_{sides} the number of sides (e.g. 4 for a square) and d_{avg} defined in formula A.10.2.

For high frequency applications, skin depth must be taken into account, which

[38] Texas Instruments provides a user-friendly online coil design calculator which you can easily play around with : *https://webench.ti.com/wb5/LDC/#/spirals*

is why t should be the effective thickness t_{eff} approximated by [263] :

$$t_{eff} = \int_0^t e^{\frac{-z}{\delta}} dz = A \cdot (1 - e^{\frac{-t}{A}}) \tag{42}$$

$$A = \sqrt{\frac{\rho}{\pi f \mu}} \tag{43}$$

Capacitance of planar coils

A lumped model for planar capacitors can be found in [344].

Bibliography

[1] M. Salvador, J. L. Marqués-Fernández, A. Bunge, J. C. Martínez-García, R. Turcu, D. Peddis, *et al.*, "Magnetic nanoclusters increase the sensitivity of lateral flow immunoassays for protein detection: Application to pneumolysin as a biomarker for streptococcus pneumoniae," *Nanomaterials*, vol. 12, no. 12, p. 2044, Jan. 2022. DOI: 10.3390/nano12122044.

[2] C. S. Kosack, A.-L. Page, and P. R. Klatser, "A guide to aid the selection of diagnostic tests," *Bulletin of the World Health Organization*, vol. 95, no. 9, pp. 639–645, Sep. 2017. DOI: 10.2471/BLT.16.187468.

[3] A. V. Orlov, V. A. Bragina, M. P. Nikitin, and P. I. Nikitin, "Rapid dry-reagent immunomagnetic biosensing platform based on volumetric detection of nanoparticles on 3d structures," *Biosensors & Bioelectronics*, vol. 79, pp. 423–429, May 2016. DOI: 10.1016/j.bios.2015.12.049.

[4] A. Moyano, E. Serrano-Pertierra, M. Salvador, J. Martínez-García, Y. Piñeiro, S. Yañez-Vilar, *et al.*, "Carbon-coated superparamagnetic nanoflowers for biosensors based on lateral flow immunoassays," *Biosensors*, vol. 10, no. 8, p. 80, Jul. 2020. DOI: 10.3390/bios10080080.

[5] C. Marquina, J. M. de Teresa, D. Serrate, J. Marzo, F. A. Cardoso, D. Saurel, *et al.*, "Gmr sensors and magnetic nanoparticles for immuno-chromatographic assays," *Journal of Magnetism and Magnetic Materials*, Fifth Moscow international symposium on magnetism, vol. 324, no. 21, pp. 3495–3498, Oct. 2012. DOI: 10.1016/j.jmmm.2012.02.074.

[6] G. Le Brun, M. Hauwaert, A. Leprince, K. Glinel, J. Mahillon, and J.-P. Raskin, "Electrical characterization of cellulose-based membranes towards pathogen detection in water," *Biosensors*, vol. 11, p. 57, Feb. 2021. DOI: 10.3390/bios11020057.

[7] A. Sena-Torralba, R. Alvarez-Diduk, C. Parolo, A. Piper, and A. Merkoçi, "Toward next generation lateral flow assays: Integration of nanomaterials," *Chemical Reviews*, vol. 122, no. 18, pp. 14 881–14 910, 2022. DOI: 10.1021/acs.chemrev.1c01012.

[8] Y. Huang, J. C. Hsu, H. Koo, and D. P. Cormode, "Repurposing ferumoxytol: Diagnostic and therapeutic applications of an FDA-approved nanoparticle," *Theranostics*, vol. 12, no. 2, pp. 796–816, 2022. DOI: 10.7150/thno.67375.

[9] L. S. Ganapathe, M. A. Mohamed, R. M. Yunus, and D. D. Berhanuddin, "Magnetite (Fe_3O_4) nanoparticles in biomedical application: From synthesis to surface functionalisation," *Magnetochemistry*, vol. 6, no. 4, p. 68, 2020. DOI: 10.3390/magnetochemistry6040068.

[10] J. B. Haun, T.-J. Yoon, H. Lee, and R. Weissleder, "Magnetic nanoparticle biosensors," *WIREs Nanomedicine and Nanobiotechnology*, vol. 2, no. 3, pp. 291–304, 2010. DOI: 10.1002/wnan.84.

[11] M. Wang, L. Jin, P. H.-M. Leung, F. W.-N. Chow, X. Zhao, H. Chen, *et al.*, "Advancements in magnetic nanoparticle-based biosensors for point-of-care testing," *Frontiers in Bioengineering and Biotechnology*, vol. 12, p. 1 393 789, 2024. DOI: 10.3389/fbioe.2024.1393789.

[12] Wahajuddin and Arora, "Superparamagnetic iron oxide nanoparticles: Magnetic nanoplatforms as drug carriers," *International Journal of Nanomedicine*, p. 3445, Jul. 2012. DOI: 10.2147/IJN.S30320.

[13] H.-Y. Chen and C. Chen, "The development, characteristics, and challenges of biosensors: The example of blood glucose meters," *Chemosensors*, vol. 13, no. 8, p. 300, Aug. 2025. DOI: 10.3390/chemosensors13080300.

[14] A. A. Seyhan, "Lost in translation: The valley of death across preclinical and clinical divide – identification of problems and overcoming obstacles," *Translational Medicine Communications*, vol. 4, no. 1, p. 18, Dec. 2019. DOI: 10.1186/s41231-019-0050-7.

[15] S. Dash, T. Das, P. Patel, P. K. Panda, M. Suar, and S. K. Verma, "Emerging trends in the nanomedicine applications of functionalized magnetic nanoparticles as novel therapies for acute and chronic diseases," *Journal of Nanobiotechnology*, vol. 20, p. 393, 2022. DOI: 10.1186/s12951-022-01595-3.

[16] R. M. Ferguson, K. R. Minard, A. P. Khandhar, and K. M. Krishnan, "Optimizing magnetite nanoparticles for mass sensitivity in magnetic particle imaging," *Medical Physics*, vol. 38, no. 3, pp. 1619–1626, 2011. DOI: 10.1118/1.3554646.

[17] "Chap 1 : Introduction," in *Magnetism and Magnetic Materials*, J. M. D. Coey, Ed., Cambridge: Cambridge University Press, 2010, pp. 1–23, ISBN: 978-0-521-81614-4. DOI: 10.1017/CBO9780511845000.002.

[18] É. Martin, Y. Gossuin, S. Bals, S. Kavak, and Q. L. Vuong, "Monte carlo simulations of the magnetic behaviour of iron oxide nanoparticle ensembles: Taking size dispersion, particle anisotropy, and dipolar interactions into account," *The European Physical Journal B*, vol. 95, no. 12, p. 201, Dec. 2022. DOI: 10.1140/epjb/s10051-022-00468-w.

[19] W. F. Brown, "Thermal fluctuations of a single-domain particle," *Physical Review*, vol. 130, no. 5, pp. 1677–1686, Jun. 1963. DOI: 10.1103/PhysRev.130.1677.

[20] R. B. Goldfarb, "The permeability of vacuum and the revised international system of units," *IEEE Magnetics Letters*, vol. 8, pp. 1–3, 2017. DOI: 10.1109/LMAG.2017.2777782.

[21] R. B. Goldfarb, "Electromagnetic units, the giorgi system, and the revised international system of units," *IEEE magnetics letters*, vol. 9, 10.1109/LMAG.2018.2868654, 2018. DOI: 10.1109/LMAG.2018.2868654.

[22] J. C. R. De Araújo, C. A. De Moraes Iglesias, R. B. Da Silva, S. Araujo Barbosa, J. Xavier, E. D. D. Silva Filho, *et al.*, "Experimental evidence of exchange forces between nanoparticles in a superparamagnetic system," *Journal of Physics D: Applied Physics*, vol. 55, no. 36, p. 365 002, Sep. 2022. DOI: 10.1088/1361-6463/ac7268.

[23] "Chap 7 : Micromagnetism, domains and hysteresis," in *Magnetism and Magnetic Materials*, J. M. D. Coey, Ed., Cambridge: Cambridge University Press, 2010, pp. 231–263, ISBN: 978-0-521-81614-4. DOI: 10.1017/CBO9780511845000.008.

[24] F. Mederos Henry, "Decoration of nanocarbon supports with magnetic nanoparticles for the control of electromagnetic propagation," Ph.D. dissertation, UCLouvain, Louvain La Neuve, 2019.

[25] F. Fiorillo, "Measurements of magnetic materials," *Metrologia*, vol. 47, no. 2, S114–S142, Apr. 2010. DOI: 10.1088/0026-1394/47/2/S11.

[26] B. D. Cullity and C. D. Graham, "Chap 9 : Domains and the magnetization process," in *Introduction to Magnetic Materials*, John Wiley & Sons, Ltd, 2008, ch. 9, pp. 275–333, ISBN: 978-0-470-38632-3. DOI: 10.1002/9780470386323.ch9.

[27] "Chap 5 : Ferromagnetism and exchange," in *Magnetism and Magnetic Materials*, J. M. D. Coey, Ed., Cambridge: Cambridge University Press, 2010, pp. 128–194, ISBN: 978-0-521-81614-4. DOI: 10.1017/CBO9780511845000.006.

[28] "Chap 2 : Magnetostatics," in *Magnetism and Magnetic Materials*, J. M. D. Coey, Ed., Cambridge: Cambridge University Press, 2010, pp. 24–61, ISBN: 978-0-521-81614-4. DOI: 10.1017/CBO9780511845000.003.

[29] M. Salvador Fernández, "Biofunctional nanoparticles for magnetic immunoassays: Application to the detection of pneumolysin for the rapid diagnosis of pneumococcal pneumonia.," doctoral thesis, Feb. 2022. [Online]. Available: https://digibuo.uniovi.es/dspace/handle/10651/64388.

[30] J. Adams Stratton, *Electromagnetic Theory*. Boston: McGraw-Hill Book Company, 1941.

[31] R. E. Rosensweig, "Heating magnetic fluid with alternating magnetic field," *Journal of Magnetism and Magnetic Materials*, Proceedings of the 9th International Conference on Magnetic Fluids, vol. 252, pp. 370–374, Nov. 2002. DOI: 10.1016/S0304-8853(02)00706-0.

[32] B. D. Cullity and C. D. Graham, *Introduction to Magnetic Materials*, 1st ed. Wiley, Nov. 2008, ISBN: 978-0-471-47741-9 978-0-470-38632-3. DOI: 10.1002/9780470386323.

[33] "Chap 3 : Magnetism of electrons," in *Magnetism and Magnetic Materials*, J. M. D. Coey, Ed., Cambridge: Cambridge University Press, 2010, pp. 62–96, ISBN: 978-0-521-81614-4. DOI: 10.1017/CBO9780511845000.004.

[34] B. D. Cullity and C. D. Graham, "Chap 3 : Diamagnetism and paramagnetism," in *Introduction to Magnetic Materials*, John Wiley & Sons, Ltd, 2008, ch. 3, pp. 87–114, ISBN: 978-0-470-38632-3. DOI: 10.1002/9780470386323.ch3.

[35] R. K. Kotnala and J. Shah, "Chapter 4 - ferrite materials: Nano to spintronics regime," in *Handbook of Magnetic Materials*, K. H. J. Buschow, Ed., vol. 23, Elsevier, Jan. 2015, pp. 291–379. DOI: 10.1016/B978-0-444-63528-0.00004-8.

[36] T. Pasinszki and M. Krebsz, "Synthesis and application of zero-valent iron nanoparticles in water treatment, environmental remediation, catalysis, and their biological effects," *Nanomaterials*, vol. 10, no. 5, p. 917, May 2020. DOI: 10.3390/nano10050917.

[37] C. P. Bean and J. D. Livingston, "Superparamagnetism," *Journal of Applied Physics*, vol. 30, no. 4, S120–S129, Apr. 1959. DOI: 10.1063/1.2185850.

[38] A. Demortière, P. Panissod, B. P. Pichon, G. Pourroy, D. Guillon, B. Donnio, *et al.*, "Size-dependent properties of magnetic iron oxidenanocrystals," *Nanoscale*, vol. 3, no. 1, pp. 225–232, 2011. DOI: 10.1039/C0NR00521E.

[39] B. D. Cullity and D. L. Graham, "Chap 11 : Fine particles and thin films," in *Introduction to Magnetic Materials*, John Wiley & Sons, Ltd, 2008, ch. 11, pp. 359–408, ISBN: 978-0-470-38632-3. DOI: 10.1002/9780470386323.ch11.

[40] R. F. Butler and S. K. Banerjee, "Theoretical single-domain grain size range in magnetite and titanomagnetite," *Journal of Geophysical Research*, vol. 80, no. 29, pp. 4049–4058, 1975. DOI: 10.1029/JB080i029p04049.

[41] Q. Li, C. W. Kartikowati, S. Horie, T. Ogi, T. Iwaki, and K. Okuyama, "Correlation between particle size/domain structure and magnetic properties of highly crystalline Fe_3O_4 nanoparticles," *Scientific Reports*, vol. 7, p. 9894, 2017. DOI: 10.1038/s41598-017-09897-5.

[42] D. J. Dunlop, "Superparamagnetic and single-domain threshold sizes in magnetite," *Journal of Geophysical Research*, vol. 78, no. 11, pp. 1780–1793, 1973. DOI: 10.1029/JB078i011p01780.

[43] A. R. Muxworthy and W. Williams, "Critical superparamagnetic/single-domain grain sizes in interacting magnetite particles: Implications for magnetosome crystals," *Journal of the Royal Society Interface*, vol. 6, no. 41, pp. 1207–1212, 2009. DOI: 10.1098/rsif.2008.0462.

[44] S. Bedanta and W. Kleemann, "Supermagnetism," *Journal of Physics D: Applied Physics*, vol. 42, no. 1, p. 013 001, Jan. 2009. DOI: 10.1088/0022-3727/42/1/013001.

[45] K. M. Krishnan, "Biomedical nanomagnetics: A spin through possibilities in imaging, diagnostics, and therapy," *IEEE Transactions on Magnetics*, vol. 46, no. 7, pp. 2523–2558, 2010. DOI: 10.1109/TMAG.2010.2046907.

[46] T. Viereck, "Magnetic particle imaging applications of magnetic nanoparticles for analytics and imaging," Ph.D. dissertation, TU Braunschweig, Braunschweig, 2015.

[47] E. F. Huda and S. I. Putri, "Tailored functional oxide nanomaterials: From design to multi-purpose applications," *Contemporary Physics*, vol. 63, no. 3, pp. 243–244, Jul. 2022. DOI: 10.1080/00107514.2022.2154393.

[48] K. L. Livesey, S. Ruta, N. R. Anderson, D. Baldomir, R. W. Chantrell, and D. Serantes, "Beyond the blocking model to fit nanoparticle zfc/fc magnetisation curves," *Scientific Reports*, vol. 8, no. 1, p. 11 166, Jul. 2018. DOI: 10.1038/s41598-018-29501-8.

[49] G. F. Goya, T. S. Berquó, F. C. Fonseca, and M. P. Morales, "Static and dynamic magnetic properties of spherical magnetite nanoparticles," *Journal of Applied Physics*, vol. 94, no. 5, pp. 3520–3528, Sep. 2003. DOI: 10.1063/1.1599959.

[50] R. Egli, "Magnetic susceptibility measurements as a function of temeperature and freqeuncy i: Inversion theory," *Geophysical Journal International*, vol. 177, no. 2, pp. 395–420, May 2009. DOI: 10.1111/j.1365-246X.2009.04081.x.

[51] A. G. Roca, D. Niznansky, J. Poltierova-Vejpravova, B. Bittova, M. A. González-Fernández, C. J. Serna, *et al.*, "Magnetite nanoparticles with no surface spin canting," *Journal of Applied Physics*, vol. 105, no. 11, p. 114 309, Jun. 2009. DOI: 10.1063/1.3133228.

[52] F. Bødker, S. Mørup, and S. Linderoth, "Surface effects in metallic iron nanoparticles," *Physical Review Letters*, vol. 72, no. 2, pp. 282–285, Jan. 1994. DOI: 10.1103/PhysRevLett.72.282.

[53] I. J. Bruvera, P. Mendoza Zélis, M. Pilar Calatayud, G. F. Goya, and F. H. Sánchez, "Determination of the blocking temperature of magnetic nanoparticles: The good, the bad, and the ugly," *Journal of Applied Physics*, vol. 118, no. 18, p. 184 304, Nov. 2015. DOI: 10.1063/1.4935484.

[54] L. Vajtai, N. M. Nemes, M. D. P. Morales, K. Molnár, B. G. Pinke, and F. Simon, "Incidence of the brownian relaxation process on the magnetic properties of ferrofluids," *Nanomaterials*, vol. 14, no. 7, p. 634, Apr. 2024. DOI: 10.3390/nano14070634.

[55] S. B. Trisnanto and Y. Kitamoto, "Field-dependent brownian relaxation dynamics of a superparamagnetic clustered-particle suspension," *Physical Review E*, vol. 90, no. 3, p. 032 306, Sep. 2014. DOI: 10.1103/PhysRevE.90.032306.

[56] D. B. Reeves and J. B. Weaver, "Simulations of magnetic nanoparticle brownian motion," *Journal of Applied Physics*, vol. 112, no. 12, p. 124 311, Dec. 2012. DOI: 10.1063/1.4770322.

[57] B. U. Felderhof and R. B. Jones, "Orientational relaxation and brownian motion," in *Dynamics: Models and Kinetic Methods for Non-equilibrium Many Body Systems*, J. Karkheck, Ed., Dordrecht: Springer Netherlands, 2000, pp. 31–38, ISBN: 978-0-7923-6554-9 978-94-011-4365-3. DOI: 10.1007/978-94-011-4365-3_3.

[58] S. Laurent, D. Forge, M. Port, A. Roch, C. Robic, L. Vander Elst, *et al.*, "Magnetic iron oxide nanoparticles: Synthesis, stabilization, vectorization, physicochemical characterizations, and biological applications," *Chemical Reviews*, vol. 108, no. 6, pp. 2064–2110, Jun. 2008. DOI: 10.1021/cr068445e.

[59] E. A. Elfimova, A. O. Ivanov, and P. J. Camp, "Static magnetization of immobilized, weakly interacting, superparamagnetic nanoparticles," *Nanoscale*, vol. 11, no. 45, pp. 21 834–21 846, 2019. DOI: 10.1039/C9NR07425B.

[60] D. Hasegawa, H. Yang, T. Ogawa, and M. Takahashi, "Challenge of ultra high frequency limit of permeability for magnetic nanoparticle assembly with organic polymer—application of superparamagnetism," *Journal of Magnetism and Magnetic Materials*, vol. 321, no. 7, pp. 746–749, Apr. 2009. DOI: 10.1016/j.jmmm.2008.11.041.

[61] S. E. Sandler, B. Fellows, and O. T. Mefford, "Best practices for characterization of magnetic nanoparticles for biomedical applications," *Analytical Chemistry*, vol. 91, no. 22, pp. 14 159–14 169, Nov. 2019. DOI: 10.1021/acs.analchem.9b03518.

[62] R. Chantrell, J. Popplewell, and S. Charles, "Measurements of particle size distribution parameters in ferrofluids," *IEEE Transactions on Magnetics*, vol. 14, no. 5, pp. 975–977, Sep. 1978. DOI: 10.1109/TMAG.1978.1059918.

[63] D. Schmidt, D. Eberbeck, U. Steinhoff, and F. Wiekhorst, "Finding the magnetic size distribution of magnetic nanoparticles from magnetization measurements via the iterative kaczmarz algorithm," *Journal of Magnetism and Magnetic Materials*, vol. 431, pp. 33–37, Jun. 2017. DOI: 10.1016/j.jmmm.2016.09.108.

[64] B. Amorim, M. Morales, F. Bohn, A. Carriço, S. De Medeiros, and A. Dantas, "Synthesis of stoichiometric ca2fe2o5 nanoparticles by high-energy ball milling and thermal annealing," *Physica B: Condensed Matter*, vol. 488, pp. 43–48, May 2016. DOI: 10.1016/j.physb.2016.01.029.

[65] A. T. Ngo, P. Bonville, and M. P. Pileni, "Spin canting and size effects in nanoparticles of nonstoichiometric cobalt ferrite," *Journal of Applied Physics*, vol. 89, no. 6, pp. 3370–3376, Mar. 2001. DOI: 10.1063/1.1347001.

[66] P. V. Hendriksen, S. Linderoth, and P. .-. Lindgard, "Magnetic properties of heisenberg clusters," *Journal of Physics: Condensed Matter*, vol. 5, no. 31, pp. 5675–5684, Aug. 1993. DOI: 10.1088/0953-8984/5/31/029.

[67] P. Fannin, C. Mac Oireachtaigh, L. Cohen-Tannoudji, E. Bertrand, and J. Bibette, "Complex susceptibility measurements of a suspension of magnetic beads," *Journal of Magnetism and Magnetic Materials*, vol. 300, no. 1, e210–e212, May 2006. DOI: 10.1016/j.jmmm.2005.10.082.

[68] R. M. Ferguson, A. P. Khandhar, C. Jonasson, J. Blomgren, C. Johansson, and Krishnan, "Size-dependent relaxation properties of monodisperse magnetite nanoparticles measured over seven decades of frequency by ac susceptometry," *IEEE Transactions on Magnetics*, vol. 49, no. 7, pp. 3441–3444, Jul. 2013. DOI: 10.1109/TMAG.2013.2239621.

[69] S. Mørup, M. F. Hansen, and C. Frandsen, "Magnetic interactions between nanoparticles," *Beilstein Journal of Nanotechnology*, vol. 1, pp. 182–190, 2010. DOI: 10.3762/bjnano.1.22.

[70] R. Cabreira-Gomes, F. G. Silva, R. Aquino, P. Bonville, F. Tourinho, R. Perzynski, *et al.*, "Exchange bias of mnfe 2 o 4 @ γ fe 2 o 3 and cofe 2 o 4 @ γ fe 2 o 3 core/shell nanoparticles," *Journal of Magnetism and Magnetic Materials*, vol. 368, pp. 409–414, Nov. 2014. DOI: 10.1016/j.jmmm.2014.03.003.

[71] K. Nadeem, H. Krenn, T. Traussnig, R. Würschum, D. Szabó, and I. Letofsky-Papst, "Effect of dipolar and exchange interactions on magnetic blocking of maghemite nanoparticles," *Journal of Magnetism and Magnetic Materials*, vol. 323, no. 15, pp. 1998–2004, Aug. 2011. DOI: 10.1016/j.jmmm.2011.02.041.

[72] G. S. Abo, Y.-K. Hong, J. Park, J. Lee, W. Lee, and B.-C. Choi, "Definition of magnetic exchange length," *IEEE Transactions on Magnetics*, vol. 49, no. 8, pp. 4937–4939, Aug. 2013. DOI: 10.1109/TMAG.2013.2258028.

[73] D. Kechrakos and K. Trohidou, "Competition between dipolar and exchange interparticle interactions in magnetic nanoparticle films," *Journal of Magnetism and Magnetic Materials*, vol. 262, no. 1, pp. 107–110, May 2003. DOI: 10.1016/S0304-8853(03)00029-5.

[74] F. H. Sánchez, P. M. Zélis, M. L. Arciniegas, G. A. Pasquevich, and M. B. F. van Raap, "Dipolar interaction and demagnetizing effects in magnetic nanoparticle dispersions: Introducing the mean field interacting superparamagnet model (mfisp model)," 2015. DOI: 10.48550/ARXIV.1507.05192.

[75] J. L. Dormann, D. Fiorani, and E. Tronc, "On the models for interparticle interactions in nanoparticle assemblies: Comparison with experimental results," *Journal of Magnetism and Magnetic Materials*, vol. 202, no. 1, pp. 251–267, 1999. DOI: 10.1016/S0304-8853(98)00627-1.

[76] O. Iglesias and A. Labarta, "Magnetic relaxation in terms of microscopic energy barriers in a model of dipolar interacting nanoparticles," *Physical Review B*, vol. 70, no. 14, p. 144 401, 2004. DOI: 10.1103/PhysRevB.70.144401.

[77] A. Kuncser, N. Iacob, and V. E. Kuncser, "On the relaxation time of interacting superparamagnetic nanoparticles and implications for magnetic fluid hyperthermia," *Beilstein Journal of Nanotechnology*, vol. 10, pp. 1280–1289, 2019. DOI: 10.3762/bjnano.10.127.

[78] J. L. Dormann, L. Bessais, and D. Fiorani, "A dynamic study of small interacting particles: Superparamagnetic model and spin-glass laws," *Journal of Physics C: Solid State Physics*, vol. 21, no. 10, pp. 2015–2034, 1988. DOI: 10.1088/0022-3719/21/10/019.

[79] J. L. Dormann, D. Fiorani, and E. Tronc, "Magnetic relaxation in fine-particle systems," *Advances in Chemical Physics*, vol. 98, pp. 283–494, 1997. DOI: 10.1002/9780470141571.ch4.

[80] P. García-Acevedo, M. A. González-Gómez, Á. Arnosa-Prieto, L. de Castro-Alves, Y. Piñeiro, and J. Rivas, "Role of dipolar interactions on the determination of the effective magnetic anisotropy in iron oxide nanoparticles," *Advanced Science*, vol. 10, no. 5, p. 2 203 397, 2023. DOI: 10.1002/advs.202203397.

[81] M. Unni, A. M. Uhl, S. Savliwala, B. H. Savitzky, R. Dhavalikar, N. Garraud, *et al.*, "Thermal decomposition synthesis of iron oxide nanoparticles with diminished magnetic dead layer by controlled addition of oxygen," *ACS Nano*, vol. 11, no. 2, pp. 2284–2303, Feb. 2017. DOI: 10.1021/acsnano.7b00609.

[82] A.-H. Lu, E. L. Salabas, and F. Schüth, "Magnetic nanoparticles: Synthesis, protection, functionalization, and application," *Angewandte Chemie International Edition*, vol. 46, no. 8, pp. 1222–1244, Feb. 2007. DOI: 10.1002/anie.200602866.

[83] W. Baaziz, B. P. Pichon, S. Fleutot, Y. Liu, C. Lefevre, J.-M. Greneche, *et al.*, "Magnetic iron oxide nanoparticles: Reproducible tuning of the size and nanosized-dependent composition, defects, and spin canting," *The Journal of Physical Chemistry C*, vol. 118, no. 7, pp. 3795–3810, Feb. 2014. DOI: 10.1021/jp411481p.

[84] T. Kahmann and F. Ludwig, "Magnetic field dependence of the effective magnetic moment of multi-core nanoparticles," *Journal of Applied Physics*, vol. 127, no. 23, p. 233 901, Jun. 2020. DOI: 10.1063/5.0011629.

[85] G. K. Rozenberg, M. P. Pasternak, W. M. Xu, Y. Amiel, M. Hanfland, M. Amboage, *et al.*, "Origin of the verwey transition in magnetite," *Physical Review Letters*, vol. 96, no. 4, p. 045 705, Feb. 2006. DOI: 10.1103/PhysRevLett.96.045705.

[86] I. Leonov, A. N. Yaresko, V. N. Antonov, M. A. Korotin, and V. I. Anisimov, "Charge and orbital order in f e 3 o 4," *Physical Review Letters*, vol. 93, no. 14, p. 146 404, Sep. 2004. DOI: 10.1103/PhysRevLett.93.146404.

[87] K. L. López Maldonado, P. De La Presa, E. Flores Tavizón, J. R. Farias Mancilla, J. A. Matutes Aquino, A. Hernando Grande, *et al.*, "Magnetic susceptibility studies of the spin-glass and verwey transitions in magnetite nanoparticles," *Journal of Applied Physics*, vol. 113, no. 17, 17E132, May 2013. DOI: 10.1063/1.4797628.

[88] A. Hevroni, M. Bapna, S. Piotrowski, S. A. Majetich, and G. Markovich, "Tracking the verwey transition in single magnetite nanocrystals by variable-temperature scanning tunneling microscopy," *The Journal of Physical Chemistry Letters*, vol. 7, no. 9, pp. 1661–1666, May 2016. DOI: 10.1021/acs.jpclett.6b00644.

[89] T. Kim, S. Sim, S. Lim, M. A. Patino, J. Hong, J. Lee, *et al.*, "Slow oxidation of magnetite nanoparticles elucidates the limits of the verwey transition," *Nature Communications*, vol. 12, p. 6356, Nov. 2021. DOI: 10.1038/s41467-021-26566-4.

[90] F. Walz, "The verwey transition - a topical review," *Journal of Physics: Condensed Matter*, vol. 14, no. 12, R285–R340, Apr. 2002. DOI: 10.1088/0953-8984/14/12/203.

[91] R. Prozorov, T. Prozorov, S. K. Mallapragada, B. Narasimhan, T. J. Williams, and D. A. Bazylinski, "Magnetic irreversibility and the verwey transition in nanocrystalline bacterial magnetite," *Physical Review B*, vol. 76, no. 5, p. 054 406, Aug. 2007. DOI: 10.1103/PhysRevB.76.054406.

[92] A. Mitra, J. Mohapatra, S. S. Meena, C. V. Tomy, and M. Aslam, "Verwey transition in ultrasmall-sized octahedral fe_3 o_4 nanoparticles," *The Journal of Physical Chemistry C*, vol. 118, no. 33, pp. 19 356–19 362, Aug. 2014. DOI: 10.1021/jp501652e.

[93] L. Maldonado-Camargo, M. Unni, and C. Rinaldi, "Magnetic characterization of iron oxide nanoparticles for biomedical applications," *Methods in molecular biology (Clifton, N.J.)*, vol. 1570, pp. 47–71, 2017. DOI: 10.1007/978-1-4939-6840-4_4.

[94] S. Husain and A. Kumar, "Verwey transition in fe3o4," in *Ferrite Nanostructured Magnetic Materials*, ser. Woodhead Publishing Series in Electronic and Optical Materials, J. Pal Singh, K. H. Chae, R. C. Srivastava, and O. F. Caltun, Eds., Woodhead Publishing, Jan. 2023, pp. 693–719, ISBN: 978-0-12-823717-5. DOI: 10.1016/B978-0-12-823717-5.00012-7.

[95] B. A. Frandsen, C. Read, J. Stevens, C. Walker, M. Christiansen, R. G. Harrison, *et al.*, "Superparamagnetic dynamics and blocking transition in ${\mathrm{fe}}_{3}{\mathrm{o}}_{4}$ nanoparticles probed by vibrating sample magnetometry and muon spin relaxation," *Physical Review Materials*, vol. 5, no. 5, p. 054 411, May 2021. DOI: 10.1103/PhysRevMaterials.5.054411.

[96] S. Mishra and M. D. Yadav, "Magnetic nanoparticles: A comprehensive review from synthesis to biomedical frontiers," *Langmuir*, vol. 40, no. 33, pp. 17 239–17 269, 2024. DOI: 10.1021/acs.langmuir.4c01532.

[97] M. Salvador, Á. Gallo-Cordova, A. Moyano, J. C. Martínez-García, M. C. Blanco-López, M. Puerto Morales, *et al.*, "Improved magnetic lateral flow assays with optimized nanotags for point-of-use inductive biosensing," *The Analyst*, vol. 145, no. 17, pp. 5905–5914, 2020. DOI: 10.1039/D0AN00849D.

[98] M. Frenea-Robin and J. Marchalot, "Basic principles and recent advances in magnetic cell separation," *Magnetochemistry*, vol. 8, no. 1, p. 11, 2022. DOI: 10.3390/magnetochemistry8010011.

[99] P.-O. Champagne, N. T. Sanon, L. Carmant, D. K. Nguyen, S. Deschênes, P. Pouliot, *et al.*, "Superparamagnetic iron oxide nanoparticles-based detection of neuronal activity," *Nanomedicine: Nanotechnology, Biology, and Medicine*, vol. 40, p. 102 478, Feb. 2022. DOI: 10.1016/j.nano.2021.102478.

[100] P.-O. Champagne, N. T. Sanon, L. Carmant, P. Pouliot, A. Bouthillier, and M. Sawan, "Feasibility of implantable iron oxide nanoparticles in detecting brain activity-proof of concept in a rat model," *Epilepsy Research*, vol. 172, p. 106 585, May 2021. DOI: 10.1016/j.eplepsyres.2021.106585.

[101] A. Pant, G. Singh, R. P. Barnwal, T. Sharma, and B. Singh, "Qbd-driven development and characterization of superparamagnetic iron oxide nanoparticles (spions) of a bone-targeting peptide for early detection of osteoporosis," *International Journal of Pharmaceutics*, vol. 654, p. 123 936, Apr. 2024. DOI: 10.1016/j.ijpharm.2024.123936.

[102] L. Wu, Y. Zhang, G. Steinberg, H. Qu, S. Huang, M. Cheng, *et al.*, "A review of magnetic particle imaging and perspectives on neuroimaging," *American Journal of Neuroradiology*, vol. 40, no. 2, pp. 206–212, Feb. 2019. DOI: 10.3174/ajnr.A5896.

[103] T. M. Buzug, G. Bringout, M. Erbe, K. Gräfe, M. Graeser, M. Grüttner, *et al.*, "Magnetic particle imaging: Introduction to imaging and hardware realization," *Zeitschrift für Medizinische Physik*, vol. 22, no. 4, pp. 323–334, Dec. 2012. DOI: 10.1016/j.zemedi.2012.07.004.

[104] T. Knopp and T. M. Buzug, "How magnetic particle imaging works," in *Magnetic Particle Imaging*. Berlin, Heidelberg: Springer Berlin Heidelberg, 2012, pp. 11–70, ISBN: 978-3-642-04198-3 978-3-642-04199-0. DOI: 10.1007/978-3-642-04199-0_2.

[105] T. Viereck, C. Kuhlmann, S. Draack, M. Schilling, and F. Ludwig, "Dual-frequency magnetic particle imaging of the brownian particle contribution," *Journal of Magnetism and Magnetic Materials*, vol. 427, pp. 156–161, Apr. 2017. DOI: 10.1016/j.jmmm.2016.11.003.

[106] S. Laurent, A. A. Saei, S. Behzadi, A. Panahifar, and M. Mahmoudi, "Superparamagnetic iron oxide nanoparticles for delivery of therapeutic agents: Opportunities and challenges," *Expert Opinion on Drug Delivery*, vol. 11, no. 9, pp. 1449–1470, Sep. 2014. DOI: 10.1517/17425247.2014.924501.

[107] F. Garello, Y. Svenskaya, B. Parakhonskiy, and M. Filippi, "Micro/nanosystems for magnetic targeted delivery of bioagents," *Pharmaceutics*, vol. 14, no. 6, p. 1132, May 2022. DOI: 10.3390/pharmaceutics14061132.

[108] M. Manuelli, S. Fallarini, G. Lombardi, C. Sangregorio, C. Nativi, and B. Richichi, "Iron oxide superparamagnetic nanoparticles conjugated with a conformationally blocked α-tn antigen mimetic for macrophage activation," *Nanoscale*, vol. 6, no. 13, pp. 7643–7655, 2014. DOI: 10.1039/C4NR00070F.

[109] R. J. Tackett, J. Thakur, N. Mosher, E. Perkins-Harbin, R. E. Kumon, L. Wang, *et al.*, "A method for measuring the néel relaxation time in a frozen ferrofluid," *Journal of Applied Physics*, vol. 118, no. 6, p. 064 701, Aug. 2015. DOI: 10.1063/1.4928202.

[110] B. Mehdaoui, A. Meffre, J. Carrey, S. Lachaize, L.-M. Lacroix, M. Gougeon, *et al.*, "Optimal size of nanoparticles for magnetic hyperthermia: A combined theoretical and experimental study," *Advanced Functional Materials*, vol. 21, no. 23, pp. 4573–4581, Dec. 2011. DOI: 10.1002/adfm.201101243.

[111] C. Caizer, "Nanoparticle size effect on some magnetic properties," in *Handbook of Nanoparticles*, M. Aliofkhazraei, Ed., Cham: Springer International Publishing, 2016, pp. 475–519, ISBN: 978-3-319-15337-7 978-3-319-15338-4. DOI: 10.1007/978-3-319-15338-4_24.

[112] J. Winsett, A. Moilanen, K. Paudel, S. Kamali, K. Ding, W. Cribb, *et al.*, "Quantitative determination of magnetite and maghemite in iron oxide nanoparticles using mössbauer spectroscopy," *SN Applied Sciences*, vol. 1, no. 12, p. 1636, Nov. 2019. DOI: 10.1007/s42452-019-1699-2.

[113] J. Ranville and M. D. Montano, "Chapter 3 - size distributions," in *Frontiers of Nanoscience*, ser. Characterization of Nanomaterials in Complex Environmental and Biological Media, M. Baalousha and J. R. Lead, Eds., vol. 8, Elsevier, Jan. 2015, pp. 91–121. DOI: 10.1016/B978-0-08-099948-7.00003-8.

[114] B. Zang, K. Suzuki, and A. C. Y. Liu, "Estimation of volume-weighted average grain size in fe-based nanocrystalline soft magnetic materials by autocorrelation function," *Materials Characterization*, vol. 142, pp. 577–583, Aug. 2018. DOI: 10.1016/j.matchar.2018.06.023.

[115] F. V. Gutierrez, I. S. Lima, A. De Falco, B. M. Ereias, O. Baffa, C. Diego De Abreu Lima, *et al.*, "The effect of temperature on the synthesis of magnetite nanoparticles by the coprecipitation method," *Heliyon*, vol. 10, no. 4, e25781, Feb. 2024. DOI: 10.1016/j.heliyon.2024.e25781.

[116] U. Kätzel, M. Vorbau, M. Stintz, T. Gottschalk-Gaudig, and H. Barthel, "Dynamic light scattering for the characterization of polydisperse fractal systems: Ii. relation between structure and dls results," *Particle & Particle Systems Characterization*, vol. 25, no. 1, pp. 19–30, Apr. 2008. DOI: 10.1002/ppsc.200700005.

[117] T. Mudalige, H. Qu, D. Van Haute, S. M. Ansar, A. Paredes, and T. Ingle, "Chapter 11 - characterization of nanomaterials: Tools and challenges," in *Nanomaterials for Food Applications*, ser. Micro and Nano Technologies, A. López Rubio, M. J. Fabra Rovira, M. martínez Sanz, and L. G. Gómez-Mascaraque, Eds., Elsevier, Jan. 2019, pp. 313–353, ISBN: 978-0-12-814130-4. DOI: 10.1016/B978-0-12-814130-4.00011-7.

[118] C. M. Hoo, N. Starostin, P. West, and M. L. Mecartney, "A comparison of atomic force microscopy (afm) and dynamic light scattering (dls) methods to characterize nanoparticle size distributions," *Journal of Nanoparticle Research*, vol. 10, no. 1, pp. 89–96, Dec. 2008. DOI: 10.1007/s11051-008-9435-7.

[119] R. C. Woodward, J. Heeris, T. G. St. Pierre, M. Saunders, E. P. Gilbert, M. Rutnakornpituk, *et al.*, "A comparison of methods for the measurement of the particle-size distribution of magnetic nanoparticles," *Journal of Applied Crystallography*, vol. 40, no. s1, s495–s500, Feb. 2007. DOI: 10.1107/S002188980700091X.

[120] P. Eneren, A. Sergievskaya, Y. T. Aksoy, P. Umek, S. Konstantinidis, and M. R. Vetrano, "Time-resolved in situ nanoparticle size evolution during magnetron sputtering onto liquids," *Nanoscale Advances*, vol. 5, no. 18, pp. 4809–4818, 2023. DOI: 10.1039/D3NA00312D.

[121] "Chapter 2 - estimation of probability densities," in *Stochastic Processes*, K. Najim, E. Ikonen, and A.-K. Daoud, Eds., Oxford: Kogan Page Science, Jan. 2004, pp. 93–166, ISBN: 978-1-903996-55-3. DOI: 10.1016/B978-190399655-3/50011-6.

[122] S.-P. Yu, Y.-H. Liu, A.-C. Sun, and J.-H. Hsu, "Determining the size distribution of magnetic nanoparticles based on analysis of magnetization curves," *Journal of Applied Physics*, vol. 106, no. 10, p. 103 905, Nov. 2009. DOI: 10.1063/1.3259424.

[123] D. Henrard, Q. L. Vuong, S. Delangre, X. Valentini, D. Nonclercq, M. F. Gonon, *et al.*, "Monitoring of superparamagnetic particle sizes in the langevin law regime," *Journal of Nanomaterials*, vol. 2019, pp. 1–9, Nov. 2019. DOI: 10.1155/2019/6409210.

[124] D. Eberbeck, F. Wiekhorst, S. Wagner, and L. Trahms, "How the size distribution of magnetic nanoparticles determines their magnetic particle imaging performance," *Applied Physics Letters*, vol. 98, no. 18, p. 182 502, May 2011. DOI: 10.1063/1.3586776.

[125] S. M. Dadfar, D. Camozzi, M. Darguzyte, K. Roemhild, P. Varvarà, J. Metselaar, *et al.*, "Size-isolation of superparamagnetic iron oxide nanoparticles improves mri, mpi and hyperthermia performance," *Journal of Nanobiotechnology*, vol. 18, no. 1, p. 22, Dec. 2020. DOI: 10.1186/s12951-020-0580-1.

[126] V. Patsula, L. Kosinová, M. Lovrić, L. Ferhatovic Hamzić, M. Rabyk, R. Konefal, *et al.*, "Superparamagnetic fe_3 o_4 nanoparticles: Synthesis by thermal decomposition of iron(iii) glucuronate and application in magnetic resonance imaging," *ACS Applied Materials & Interfaces*, vol. 8, no. 11, pp. 7238–7247, Mar. 2016. DOI: 10.1021/acsami.5b12720.

[127] C. E. Ribeiro, M. Vinícius-Araújo, and A. F. Bakuzis, "Multicore manganese ferrite nanoparticles for theranostics," *ACS Applied Nano Materials*, vol. 8, no. 14, pp. 7061–7072, Apr. 2025. DOI: 10.1021/acsanm.5c00309.

[128] A. G. Roca, M. P. Morales, K. O'Grady, and C. J. Serna, "Structural and magnetic properties of uniform magnetite nanoparticles prepared by high temperature decomposition of organic precursors," *Nanotechnology*, vol. 17, no. 11, pp. 2783–2788, May 2006. DOI: 10.1088/0957-4484/17/11/010.

[129] C. Cavelius, K. Moh, and S. Mathur, "Chemically designed growth of monodisperse iron oxide nanocrystals," *Crystal Growth & Design*, vol. 12, no. 12, pp. 5948–5955, Nov. 2012. DOI: 10.1021/cg300936t.

[130] R. Pazik, A. Lewińska, J. Adamczyk-Grochala, M. Kulpa-Greszta, P. Kłoda, A. Tomaszewska, *et al.*, "Energy conversion and biocompatibility of surface functionalized magnetite nanoparticles with phosphonic moieties," *The Journal of Physical Chemistry B*, vol. 124, no. 24, pp. 4931–4948, Jun. 2020. DOI: 10.1021/acs.jpcb.0c02808.

[131] A. D. Wulandari, S. Sutriyo, and R. Rahmasari, "Synthesis conditions and characterization of superparamagnetic iron oxide nanoparticles with oleic acid stabilizer," *Journal of Advanced Pharmaceutical Technology & Research*, vol. 13, no. 2, pp. 89–94, 2022. DOI: 10.4103/japtr.japtr_246_21.

[132] T. Balakrishnan, M.-J. Lee, J. Dey, and S.-M. Choi, "Sub-nanometer scale size-control of iron oxide nanoparticles with drying time of iron oleate," *CrystEngComm*, vol. 21, no. 27, pp. 4063–4071, 2019. DOI: 10.1039/C9CE00112C.

[133] H. Sharifi Dehsari, R. A. Harris, A. H. Ribeiro, W. Tremel, and K. Asadi, "Optimizing the binding energy of the surfactant to iron oxide yields truly monodisperse nanoparticles," *Langmuir : the ACS journal of surfaces and colloids*, vol. 34, no. 22, pp. 6582–6590, May 2018. DOI: 10.1021/acs.langmuir.8b01337.

[134] H. Sharifi Dehsari, V. Ksenofontov, A. Möller, G. Jakob, and K. Asadi, "Determining magnetite/maghemite composition and core–shell nanostructure from magnetization curve for iron oxide nanoparticles," *The Journal of Physical Chemistry C*, vol. 122, no. 49, pp. 28 292–28 301, Dec. 2018. DOI: 10.1021/acs.jpcc.8b06927.

[135] Z. Xu, C. Shen, Y. Hou, H. Gao, and S. Sun, "Oleylamine as both reducing agent and stabilizer in a facile synthesis of magnetite nanoparticles," *Chemistry of Materials*, vol. 21, no. 9, pp. 1778–1780, May 2009. DOI: 10.1021/cm802978z.

[136] J. Park, K. An, Y. Hwang, J.-G. Park, H.-J. Noh, J.-Y. Kim, *et al.*, "Ultra-large-scale syntheses of monodisperse nanocrystals," *Nature Materials*, vol. 3, no. 12, pp. 891–895, Dec. 2004. DOI: 10.1038/nmat1251.

[137] P. Guardia, A. Labarta, and X. Batlle, "Tuning the size, the shape, and the magnetic properties of iron oxide nanoparticles," *The Journal of Physical Chemistry C*, vol. 115, no. 2, pp. 390–396, Dec. 2010. DOI: 10.1021/jp1084982.

[138] C.-R. Lin, R.-K. Chiang, J.-S. Wang, and T.-W. Sung, "Magnetic properties of monodisperse iron oxide nanoparticles," *Journal of Applied Physics*, vol. 99, no. 8, 08N710, Apr. 2006. DOI: 10.1063/1.2172891.

[139] S. Belaïd, D. Stanicki, L. Vander Elst, R. N. Muller, and S. Laurent, "Influence of experimental parameters on iron oxide nanoparticle properties synthesized by thermal decomposition: Size and nuclear magnetic resonance studies," *Nanotechnology*, vol. 29, no. 16, p. 165 603, Apr. 2018. DOI: 10.1088/1361-6528/aaae59.

[140] H. Sharifi Dehsari, A. Halda Ribeiro, B. Ersöz, W. Tremel, G. Jakob, and K. Asadi, "Effect of precursor concentration on size evolution of iron oxide nanoparticles," *CrystEngComm*, vol. 19, no. 44, pp. 6694–6702, 2017. DOI: 10.1039/c7ce01406f.

[141] C. Martins, C. Rolo, V. R. G. Cacho, L. C. J. Pereira, J. Paulo Borges, J. Carvalho Silva, *et al.*, "Enhancing the magnetic properties of superparamagnetic iron oxide nanoparticles using hydrothermal treatment for magnetic hyperthermia application," *Materials Advances*, vol. 6, no. 5, pp. 1726–1743, 2025. DOI: 10.1039/D4MA01120A.

[142] M. M. Lin, D. K. Kim, A. J. El Haj, and J. Dobson, "Development of superparamagnetic iron oxide nanoparticles (spions) for translation to clinical applications," *IEEE Transactions on NanoBioscience*, vol. 7, no. 4, pp. 298–305, Dec. 2008. DOI: 10.1109/TNB.2008.2011864.

[143] J. M. Orozco-Henao, D. F. Coral, D. Muraca, O. Moscoso-Londoño, P. Mendoza Zélis, M. B. Fernandez van Raap, *et al.*, "Effects of nanostructure and dipolar interactions on magnetohyperthermia in iron oxide nanoparticles," *The Journal of Physical Chemistry C*, vol. 120, no. 23, pp. 12 796–12 809, Jun. 2016. DOI: 10.1021/acs.jpcc.6b00900.

[144] C. B. Whitehead, S. Özkar, and R. G. Finke, "Lamer's 1950 model of particle formation: A review and critical analysis of its classical nucleation and fluctuation theory basis, of competing models and mechanisms for phase-changes and particle formation, and then of its application to silver halide, semiconductor, metal, and metal-oxide nanoparticles," *Materials Advances*, vol. 2, no. 1, pp. 186–235, 2021. DOI: 10.1039/D0MA00439A.

[145] G. Cotin, B. Heinrich, F. Perton, C. Kiefer, G. Francius, D. Mertz, *et al.*, "A confinement-driven nucleation mechanism of metal oxide nanoparticles obtained via thermal decomposition in organic media," *Small*, vol. 18, no. 20, p. 2 200 414, May 2022. DOI: 10.1002/smll.202200414.

[146] A. Lassenberger, T. A. Grünewald, P. D. J. van Oostrum, H. Rennhofer, H. Amenitsch, R. Zirbs, *et al.*, "Monodisperse iron oxide nanoparticles by thermal decomposition: Elucidating particle formation by second-resolved in situ small-angle x-ray scattering," *Chemistry of Materials*, vol. 29, no. 10, pp. 4511–4522, May 2017. DOI: 10.1021/acs.chemmater.7b01207.

[147] M. A. Watzky and R. G. Finke, "Transition metal nanocluster formation kinetic and mechanistic studies. a new mechanism when hydrogen is the reductant: Slow, continuous nucleation and fast autocatalytic surface growth," *Journal of the American Chemical Society*, vol. 119, no. 43, pp. 10 382–10 400, Oct. 1997. DOI: 10.1021/ja9705102.

[148] C. B. Whitehead, S. Özkar, and R. G. Finke, "Lamer's 1950 model for particle formation of instantaneous nucleation and diffusion-controlled growth: A historical look at the model's origins, assumptions, equations, and underlying sulfur sol formation kinetics data," *Chemistry of Materials*, vol. 31, no. 18, pp. 7116–7132, Sep. 2019. DOI: 10.1021/acs.chemmater.9b01273.

[149] S. Arshadi, J. Moghaddam, and M. Eskandarian, "Lamer diagram approach to study the nucleation and growth of cu2o nanoparticles using supersaturation theory," *Korean Journal of Chemical Engineering*, vol. 31, no. 11, pp. 2020–2026, Nov. 2014. DOI: 10.1007/s11814-014-0130-3.

[150] S. Sun and H. Zeng, "Size-controlled synthesis of magnetite nanoparticles," *Journal of the American Chemical Society*, vol. 124, no. 28, pp. 8204–8205, Jul. 2002. DOI: 10.1021/ja026501x.

[151] R. Hufschmid, H. Arami, R. M. Ferguson, M. Gonzales, E. Teeman, L. N. Brush, *et al.*, "Synthesis of phase-pure and monodisperse iron oxide nanoparticles by thermal decomposition," *Nanoscale*, vol. 7, no. 25, pp. 11 142–11 154, 2015. DOI: 10.1039/c5nr01651g.

[152] M. Görke, S. Okeil, D. Menzel, B. Semenenko, and G. Garnweitner, "Tuning the properties of iron oxide nanoparticles in thermal decomposition synthesis: A comparative study of the influence of temperature, ligand length and ligand concentration," *Particle & Particle Systems Characterization*, vol. 41, no. 10, p. 2 400 059, Oct. 2024. DOI: 10.1002/ppsc.202400059.

[153] S. Meftah, A.-T. Ngo, L. Bouteiller, V. Russier, D. Hrabovsky, A. Konaté, *et al.*, "Synthesis and magnetic properties of spherical maghemite nanoparticles with tunable size and surface chemistry," *Langmuir : the ACS journal of surfaces and colloids*, vol. 40, no. 43, pp. 22 673–22 683, Oct. 2024. DOI: 10.1021/acs.langmuir.4c02495.

[154] F. Jiang, X. Li, Y. Zhu, and Z. Tang, "Synthesis and magnetic characterizations of uniform iron oxide nanoparticles," *Physica B: Condensed Matter*, vol. 443, pp. 1–5, Jun. 2014. DOI: 10.1016/j.physb.2014.03.009.

[155] A. Lak, F. Ludwig, J. M. Scholtyssek, J. Dieckhoff, K. Fiege, and M. Schilling, "Size distribution and magnetization optimization of single-core iron oxide nanoparticles by exploiting design of experiment methodology," *IEEE Transactions on Magnetics*, vol. 49, no. 1, pp. 201–207, Jan. 2013. DOI: 10.1109/TMAG.2012.2224325.

[156] V. Fokina, M. Wilke, M. Dulle, S. Ehlert, and S. Förster, "Size control of iron oxide nanoparticles synthesized by thermal decomposition methods," *The Journal of Physical Chemistry C*, vol. 126, no. 50, pp. 21 356–21 367, Dec. 2022. DOI: 10.1021/acs.jpcc.2c05380.

[157] T. Hyeon, S. S. Lee, J. Park, Y. Chung, and H. B. Na, "Synthesis of highly crystalline and monodisperse maghemite nanocrystallites without a size-selection process," *Journal of the American Chemical Society*, vol. 123, no. 51, pp. 12 798–12 801, Dec. 2001. DOI: 10.1021/ja016812s.

[158] M. Salvador, A. Moyano, J. C. Martínez-García, M. C. Blanco-López, and M. Rivas, "Synthesis of superparamagnetic iron oxide nanoparticles: Swot analysis towards their conjugation to biomolecules for molecular recognition applications," *Journal of Nanoscience and Nanotechnology*, vol. 19, no. 8, pp. 4839–4856, Aug. 2019. DOI: 10.1166/jnn.2019.16931.

[159] R. Massart, "Preparation of aqueous magnetic liquids in alkaline and acidic media," *IEEE Transactions on Magnetics*, vol. 17, no. 2, pp. 1247–1248, Mar. 1981. DOI: 10.1109/TMAG.1981.1061188.

[160] J. Schemberg, A. E. Abbassi, A. Lindenbauer, L.-Y. Chen, A. Grodrian, X. Nakos, *et al.*, "Synthesis of biocompatible superparamagnetic iron oxide nanoparticles (spion) under different microfluidic regimes," *ACS Applied Materials & Interfaces*, vol. 14, no. 42, pp. 48 011–48 028, Oct. 2022. DOI: 10.1021/acsami.2c13156.

[161] N. Ajinkya, X. Yu, P. Kaithal, H. Luo, P. Somani, and S. Ramakrishna, "Magnetic iron oxide nanoparticle (ionp) synthesis to applications: Present and future," *Materials*, vol. 13, no. 20, p. 4644, Oct. 2020. DOI: 10.3390/ma13204644.

[162] F. Mirdavardoost and K. Ludtke-Buzug, "Optimization of the coprecipitation in the synthesis of spions with rigorize control of process conditions," *International Journal on Magnetic Particle Imaging IJMPI*, vol. 9, no. 1 Suppl 1, Mar. 2023. DOI: 10.18416/IJMPI.2023.2303019.

[163] M. S. Yusuf, Sutriyo, and R. Rahmasari, "Synthesis processing condition optimization of citrate stabilized superparamagnetic iron oxide nanoparticles using direct co-precipitation method," *Biomedical and Pharmacology Journal*, vol. 14, no. 3, pp. 1533–1542, Sep. 2021. [Online]. Available: https://biomedpharmajournal.org/vol14no3/synthesis-processing-condition-optimization-of-citrate-stabilized-

superparamagnetic-iron-oxide-nanoparticles-using-direct-co-precipitation-method/.

[164] A. Atrei, F. F. Mahdizadeh, M. C. Baratto, and A. Scala, "Effect of citrate on the size and the magnetic properties of primary fe3o4 nanoparticles and their aggregates," *Applied Sciences*, vol. 11, no. 15, p. 6974, Jan. 2021. DOI: 10.3390/app11156974.

[165] F. A. Tourinho, R. Franck, and R. Massart, "Aqueous ferrofluids based on manganese and cobalt ferrites," *Journal of Materials Science*, vol. 25, no. 7, pp. 3249–3254, Jul. 1990. DOI: 10.1007/BF00587682.

[166] J. Y. Park, P. Daksha, G. H. Lee, S. Woo, and Y. Chang, "Highly water-dispersible peg surface modified ultra small superparamagnetic iron oxide nanoparticles useful for target-specific biomedical applications," *Nanotechnology*, vol. 19, no. 36, p. 365 603, Sep. 2008. DOI: 10.1088/0957-4484/19/36/365603.

[167] E. Tombácz, I. Tóth, D. Nesztor, E. Illés, A. Hajdú, M. Szekeres, *et al.*, "Adsorption of organic acids on magnetite nanoparticles, ph-dependent colloidal stability and salt tolerance," *Colloids and Surfaces A: Physicochemical and Engineering Aspects*, vol. 435, pp. 91–96, Oct. 2013. DOI: 10.1016/j.colsurfa.2013.01.023.

[168] S. C. McBain, H. H. P. Yiu, A. El Haj, and J. Dobson, "Polyethyleneimine functionalized iron oxide nanoparticles as agents for dna delivery and transfection," *Journal of Materials Chemistry*, vol. 17, no. 24, p. 2561, 2007. DOI: 10.1039/b617402g.

[169] R. Aquino, F. Tourinho, R. Itri, M. E Lara, and J. Depeyrot, "Size control of mnfe2o4 nanoparticles in electric double layered magnetic fluid synthesis," *Journal of Magnetism and Magnetic Materials*, vol. 252, pp. 23–25, Nov. 2002. DOI: 10.1016/S0304-8853(02)00607-8.

[170] V. Pilati, R. Cabreira Gomes, G. Gomide, P. Coppola, F. G. Silva, F. L. O. Paula, *et al.*, "Core/shell nanoparticles of non-stoichiometric zn–mn and zn–co ferrites as thermosensitive heat sources for magnetic fluid hyperthermia," *The Journal of Physical Chemistry C*, vol. 122, no. 5, pp. 3028–3038, Feb. 2018. DOI: 10.1021/acs.jpcc.7b11014.

[171] V. Pilati, M. Salvador, L. B. Fraile, J. L. Marqués-Fernández, F. G. da Silva, M. Fadel, *et al.*, "Mn-ferrite nanoparticles as promising magnetic tags for radiofrequency inductive detection and quantification in lateral flow assays," *Nanoscale Advances*, vol. 6, pp. 4247–4258, Jul. 2024. DOI: 10.1039/D4NA00445K.

[172] H. Ma, L. Guo, H. Zhang, Y. Wang, Y. Miao, X. Liu, *et al.*, "The metal ion release of manganese ferrite nanoparticles: Kinetics, effects on magnetic resonance relaxivities, and toxicity," *ACS Applied Bio Materials*, vol. 5, no. 6, pp. 3067–3074, Jun. 2022. DOI: 10.1021/acsabm.2c00338.

[173] Y. Sun, L. Duan, Z. Guo, Y. DuanMu, M. Ma, L. Xu, *et al.*, "An improved way to prepare superparamagnetic magnetite-silica core-shell nanoparticles for possible biological application," *Journal of Magnetism and Magnetic Materials*, vol. 285, no. 1, pp. 65–70, Jan. 2005. DOI: 10.1016/j.jmmm.2004.07.016.

[174] M. H. Sousa, J. C. Rubim, P. G. Sobrinho, and F. A. Tourinho, "Biocompatible magnetic fluid precursors based on aspartic and glutamic acid modified maghemite nanostructures," *Journal of Magnetism and Magnetic Materials*, Proceedings of the Third International Conference on Scientific and Clinical Applications of Magnetic Carriers, vol. 225, no. 1, pp. 67–72, Jan. 2001. DOI: 10.1016/S0304-8853(00)01229-4.

[175] H. L. Ding, Y. X. Zhang, S. Wang, J. M. Xu, S. C. Xu, and G. H. Li, "Fe_3 o_4 @sio_2 core/shell nanoparticles: The silica coating regulations with a single core for different core sizes and shell thicknesses," *Chemistry of Materials*, vol. 24, no. 23, pp. 4572–4580, Dec. 2012. DOI: 10.1021/cm302828d.

[176] R. M. Fratila, S. G. Mitchell, P. Del Pino, V. Grazu, and J. M. De La Fuente, "Strategies for the biofunctionalization of gold and iron oxide nanoparticles," *Langmuir*, vol. 30, no. 50, pp. 15 057–15 071, Dec. 2014. DOI: 10.1021/la5015658.

[177] S. E. Favela-Camacho, E. J. Samaniego-Benitez, A. Godinez-Garcia, L. M. Aviles-Arellano, and J. F. Perez-Robles, "How to decrease the agglomeration of magnetite nanoparticles and increase their stability using surface properties," *Colloids and Surfaces A: Physicochemical and Engineering Aspects*, vol. 574, pp. 29–35, Aug. 2019. DOI: 10.1016/j.colsurfa.2019.04.016.

[178] N. Petersen, M. Girard, A. Riedinger, and O. Valsson, "The crucial role of solvation forces in the steric stabilization of nanoplatelets," *Nano Letters*, vol. 22, no. 24, pp. 9847–9853, Dec. 2022. DOI: 10.1021/acs.nanolett.2c02848.

[179] O. Hiroyuki, "Dlvo theory of colloid stability," in *Interface Science and Technology*, vol. 37, Elsevier, 2024, pp. 217–244, ISBN: 978-0-443-16116-2. DOI: 10.1016/B978-0-443-16116-2.00009-6.

[180] A. F. C. Campos, E. P. Marinho, M. D. A. Ferreira, F. A. Tourinho, F. L. D. O. Paula, and J. Depeyrot, "X-dlvo interactions between nanocolloidal magnetic particles: The quantitative interpretation of the ph-dependent phase diagram of edl-mf," *Brazilian Journal of Physics*, vol. 39, no. 1a, Apr. 2009. DOI: 10.1590/S0103-97332009000200018.

[181] P. Y. Furlan, A. Y. Furlan, K. Kisslinger, M. E. Melcer, D. W. Shinn, and J. B. Warren, "Water as the solvent in the stober process for forming ultrafine silica shells on magnetite nanoparticles," *ACS Sustainable Chemistry & Engineering*, vol. 7, no. 18, pp. 15 578–15 584, Sep. 2019. DOI: 10.1021/acssuschemeng.9b03554.

[182] R. C. Popescu, E. Andronescu, and B. S. Vasile, "Recent advances in magnetite nanoparticle functionalization for nanomedicine," *Nanomaterials*, vol. 9, no. 12, p. 1791, Dec. 2019. DOI: 10.3390/nano9121791.

[183] Y. Kobayashi, H. Katakami, E. Mine, D. Nagao, M. Konno, and L. M. Liz-Marzán, "Silica coating of silver nanoparticles using a modified stöber method," *Journal of Colloid and Interface Science*, vol. 283, no. 2, pp. 392–396, Mar. 2005. DOI: 10.1016/j.jcis.2004.08.184.

[184] W. Stöber, A. Fink, and E. Bohn, "Controlled growth of monodisperse silica spheres in the micron size range," *Journal of Colloid and Interface Science*, vol. 26, no. 1, pp. 62–69, Jan. 1968. DOI: 10.1016/0021-9797(68)90272-5.

[185] D. Navas, S. Fuentes, A. Castro-Alvarez, and E. Chavez-Angel, "Review on sol-gel synthesis of perovskite and oxide nanomaterials," *Gels*, vol. 7, no. 4, p. 275, Dec. 2021. DOI: 10.3390/gels7040275.

[186] S. Esposito, ""traditional" sol-gel chemistry as a powerful tool for the preparation of supported metal and metal oxide catalysts," *Materials*, vol. 12, no. 4, p. 668, Feb. 2019. DOI: 10.3390/ma12040668.

[187] Y. Han, Z. Lu, Z. Teng, J. Liang, Z. Guo, D. Wang, *et al.*, "Unraveling the growth mechanism of silica particles in the stöber method: In situ seeded growth model," *Langmuir*, vol. 33, no. 23, pp. 5879–5890, Jun. 2017. DOI: 10.1021/acs.langmuir.7b01140.

[188] D. Zeng, H. Zhang, B. Wang, K. Sang, and J. Yang, "Effect of ammonia concentration on silica spheres morphology and solution hydroxyl concentration in stober process," *Journal of Nanoscience and Nanotechnology*, vol. 15, no. 9, pp. 7407–7411, Sep. 2015. DOI: 10.1166/jnn.2015.10595.

[189] B. Vörös-Horváth, A. Salem, B. Kovács, A. Széchenyi, and S. Pál, "Systematic study of reaction conditions for size-controlled synthesis of silica nanoparticles," *Nanomaterials*, vol. 14, no. 19, p. 1561, Jan. 2024. DOI: 10.3390/nano14191561.

[190] C.-L. Chang and H. S. Fogler, "Kinetics of silica particle formation in nonionic w/o microemulsions from teos," *AIChE Journal*, vol. 42, no. 11, pp. 3153–3163, Nov. 1996. DOI: 10.1002/aic.690421115.

[191] E. Ureña-Horno, M.-E. Kyriazi, and A. G. Kanaras, "A method for the growth of uniform silica shells on different size and morphology upconversion nanoparticles," *Nanoscale Advances*, vol. 3, no. 12, pp. 3522–3529, 2021. DOI: 10.1039/D0NA00858C.

[192] R. P. Bagwe, C. Yang, L. R. Hilliard, and W. Tan, "Optimization of dye-doped silica nanoparticles prepared using a reverse microemulsion method," *Langmuir*, vol. 20, no. 19, pp. 8336–8342, Sep. 2004. DOI: 10.1021/la049137j.

[193] X.-H. Pham, E. Hahm, H.-M. Kim, B. S. Son, A. Jo, J. An, *et al.*, "Silica-coated magnetic iron oxide nanoparticles grafted onto graphene oxide for protein isolation," *Nanomaterials*, vol. 10, no. 1, p. 117, Jan. 2020. DOI: 10.3390/nano10010117.

[194] M. Gao, W. Li, J. Dong, Z. Zhang, and B. Yang, "Synthesis and characterization of superparamagnetic fe3o4@sio2 core-shell composite nanoparticles," *World Journal of Condensed Matter Physics*, vol. 1, no. 2, pp. 49–54, May 2011. DOI: 10.4236/wjcmp.2011.12008.

[195] X. Hou, C. Zhao, Y. Tian, S. Dou, X. Zhang, and J. Zhao, "Preparation of functionalized fe3o4@sio2 magnetic nanoparticles for monoclonal antibody purification," *Chemical Research in Chinese Universities*, vol. 32, no. 6, pp. 889–894, Dec. 2016. DOI: 10.1007/s40242-016-6251-y.

[196] M. A. Garcia, E. Fernandez Pinel, J. de la Venta, A. Quesada, V. Bouzas, J. F. Fernández, *et al.*, "Sources of experimental errors in the observation of nanoscale magnetism," *Journal of Applied Physics*, vol. 105, no. 1, p. 013 925, Jan. 2009. DOI: 10.1063/1.3060808.

[197] F. Farshidfar, M. Lapolla, A. Fattahi, and K. Ghandi, "On the structural and electrical properties of mgfe2o4, mgmn0.2fe1.8o4, and mn3o4," *Heliyon*, vol. 9, no. 11, e21677, Oct. 2023. DOI: 10.1016/j.heliyon.2023.e21677.

[198] A. C. Velazquez-Albino, A. Nozka, A. Melnyk, H. J. Good, and C. M. Rinaldi-Ramos, "Post-synthesis oxidation of superparamagnetic iron oxide nanoparticles to enhance magnetic particle imaging performance," *ACS applied nano materials*, vol. 7, no. 1, pp. 279–291, Jan. 2024. DOI: 10.1021/acsanm.3c04442.

[199] P. Kucheryavy, J. He, V. T. John, P. Maharjan, L. Spinu, G. Z. Goloverda, *et al.*, "Superparamagnetic iron oxide nanoparticles with variable size and an iron oxidation state as prospective imaging agents," *Langmuir*, vol. 29, no. 2, pp. 710–716, Jan. 2013. DOI: 10.1021/la3037007.

[200] T. Kohler, A. Feoktystov, O. Petracic, E. Kentzinger, T. Bhatnagar-Schoffmann, M. Feygenson, *et al.*, "Mechanism of magnetization reduction in iron oxide nanoparticles," *Nanoscale*, vol. 13, no. 14, pp. 6965–6976, 2021. DOI: 10.1039/D0NR08615K.

[201] C. Iacovita, A. Florea, L. Scorus, E. Pall, R. Dudric, A. I. Moldovan, *et al.*, "Hyperthermia, cytotoxicity, and cellular uptake properties of manganese and zinc ferrite magnetic nanoparticles synthesized by a polyol-mediated process," *Nanomaterials*, vol. 9, no. 10, p. 1489, Oct. 2019. DOI: 10.3390/nano9101489.

[202] R. B. Goldfarb and J. V. Minervini, "Calibration of ac susceptometer for cylindrical specimens," *Review of Scientific Instruments*, vol. 55, no. 5, pp. 761–764, May 1984. DOI: 10.1063/1.1137813.

[203] J. D. A. Gomes, M. H. Sousa, F. A. Tourinho, R. Aquino, G. J. Da Silva, J. Depeyrot, *et al.*, "Synthesis of core-shell ferrite nanoparticles for ferrofluids: Chemical and magnetic analysis," *The Journal of Physical Chemistry C*, vol. 112, no. 16, pp. 6220–6227, Apr. 2008. DOI: 10.1021/jp7097608.

[204] J. Peng, L. Giordano, T. C. Davenport, and Y. Shao-Horn, "Stability design principles of manganese-based oxides in acid," *Chemistry of Materials*, vol. 34, no. 17, pp. 7774–7787, Sep. 2022. DOI: 10.1021/acs.chemmater.2c01233.

[205] M. Pannetier-Lecoeur and C. Fermon, "Magnetic sensors," in *Handbook of Magnetism and Magnetic Materials*, M. Coey and S. Parkin, Eds., Cham: Springer International Publishing, 2020, pp. 1–25, ISBN: 978-3-030-63101-7. DOI: 10.1007/978-3-030-63101-7_30-1.

[206] J. M. Martinis and K. Osborne, *Superconducting qubits and the physics of josephson junctions*, 2004. DOI: 10.48550/ARXIV.COND-MAT/0402415.

[207] J. W. Harrell, "Effect of ac gradient field on magnetic measurements with an alternating gradient magnetometer," *Journal of Magnetism and Magnetic Materials*, vol. 205, no. 1, pp. 121–129, Oct. 1999. DOI: 10.1016/S0304-8853(99)00487-4.

[208] K. O'Grady, V. G. Lewis, and D. P. E. Dickson, "Alternating gradient force magnetometry: Applications and extension to low temperatures (invited)," *Journal of Applied Physics*, vol. 73, no. 10, pp. 5608–5613, May 1993. DOI: 10.1063/1.353613.

[209] M. Pérez, I. de Mendizábal Vázquez, C. Aroca, R. Ranchal, and P. Cobos, "Combined alternating gradient force magnetometer and susceptometer system," *Review of Scientific Instruments*, vol. 86, no. 1, Jan. 2015. DOI: 10.1063/1.4905686.

[210] B. R. Sankhi and E. Turgut, "A low-cost vibrating sample magnetometry based on audio components," *Journal of Magnetism and Magnetic Materials*, vol. 502, p. 166 560, May 2020. DOI: 10.1016/j.jmmm.2020.166560.

[211] Quantum Design, *MPMS3 SQUID magnetometer: Product description*, Document No. 1500-102, Rev. C2. Quantum Design, San Diego, CA, 2016.

[212] A. Ugulava, S. Chkhaidze, and Z. Rostomashvili, "Magnetization of superparamagnets in the state of mechanical anisotropy," *Physics of Metals and Metallography*, vol. 118, no. 4, pp. 334–340, Apr. 2017. DOI: 10.1134/S0031918X1704010X.

[213] S. Thamm and J. Hesse, "A simple plot indicating interactions between single-domain particles," *Journal of Magnetism and Magnetic Materials*, vol. 154, no. 2, pp. 254–262, Apr. 1996. DOI: 10.1016/0304-8853(95)00585-4.

[214] O. Petracic, "Superparamagnetic nanoparticle ensembles," *Superlattices and Microstructures*, vol. 47, no. 5, pp. 569–578, May 2010. DOI: 10.1016/j.spmi.2010.01.009.

[215] D. Peddis, F. Orrù, A. Ardu, C. Cannas, A. Musinu, and G. Piccaluga, "Interparticle interactions and magnetic anisotropy in cobalt ferrite nanoparticles: Influence of molecular coating," *Chemistry of Materials*, vol. 24, no. 6, pp. 1062–1071, 2012. DOI: 10.1021/cm203280y.

[216] Z. Nedelkoski, D. Kepaptsoglou, L. Lari, T. Wen, R. A. Booth, S. D. Oberdick, *et al.*, "Origin of reduced magnetization and domain formation in small magnetite nanoparticles," *Scientific Reports*, vol. 7, p. 45 997, Apr. 2017. DOI: 10.1038/srep45997.

[217] B. Martinez, X. Obradors, L. Balcells, A. Rouanet, and C. Monty, "Low temperature surface spin-glass transition in γ-Fe_2O_3 nanoparticles," *Physical Review Letters*, vol. 80, no. 1, pp. 181–184, 1998. DOI: 10.1103/PhysRevLett.80.181.

[218] M. Kubisztal, J. Kubisztal, M. Karolus, K. Prusik, and G. Haneczok, "Evolution of frozen magnetic state in co-precipitated $Zn_\delta Co_{1-\delta}Fe_2O_4$ ($0 \leq \delta \leq 1$) ferrite nanopowders," *Journal of Magnetism and Magnetic Materials*, 2018. DOI: 10.1016/j.jmmm.2018.02.001.

[219] F. T. Dias, V. N. Vieira, D. L. Silva, F. Wolff-Fabris, E. Kampert, M. L. Almeida, *et al.*, "Paramagnetic moments and time effects in melt-textured ndbacuo system with nd422 inclusions," *Journal of Physics: Conference Series*, vol. 592, p. 012 064, Mar. 2015. DOI: 10.1088/1742-6596/592/1/012064.

[220] D. Serantes, M. Pereiro, R. Chantrell, and D. Baldomir, "Scaling the effect of the dipolar interactions on the ZFC/FC curves of random nanoparticle assemblies," *Journal of Magnetism and Magnetic Materials*, vol. 460, pp. 28–33, 2018. DOI: 10.1016/j.jmmm.2018.03.026.

[221] E. H. Sánchez, M. Vasilakaki, S. S. Lee, P. S. Normile, M. S. Andersson, R. Mathieu, *et al.*, "Crossover from individual to collective magnetism in dense nanoparticle systems: Local anisotropy versus dipolar interactions," *Small*, vol. 18, no. 28, p. 2 106 762, 2022. DOI: 10.1002/smll.202106762.

[222] C. V. Topping and S. J. Blundell, "A.C. susceptibility as a probe of low-frequency magnetic dynamics," *Journal of Physics: Condensed Matter*, vol. 31, no. 1, p. 013 001, 2019. DOI: 10.1088/1361-648X/aaed96.

[223] M. Modestino, A. Galluzzi, M. Sarno, and M. Polichetti, "The effect of a dc magnetic field on the ac magnetic properties of oleic acid-coated fe3o4 nanoparticles," *Materials*, vol. 16, no. 12, p. 4246, Jan. 2023. DOI: 10.3390/ma16124246.

[224] A. O. Ivanov, V. S. Zverev, and S. S. Kantorovich, "Revealing the signature of dipolar interactions in dynamic spectra of polydisperse magnetic nanoparticles," *Soft Matter*, vol. 12, no. 15, pp. 3507–3513, 2016. DOI: 10.1039/C5SM02679B.

[225] F. Ludwig, E. Heim, S. Mäuselein, D. Raber, and M. Schilling, "Analysis of AC susceptibility spectra for the characterization of magnetic nanoparticles," *IEEE Transactions on Magnetics*, vol. 53, no. 11, pp. 1–4, 2017. DOI: 10.1109/TMAG.2017.2693420.

[226] S. Shtrikman and E. P. Wohlfarth, "The theory of the Vogel-Fulcher law of spin glasses," *Physics Letters A*, vol. 85, no. 8–9, pp. 467–470, 1981. DOI: 10.1016/0375-9601(81)90441-2.

[227] O. E. Ayala-Valenzuela, J. A. Matutes-Aquino, J. T. E. Galindo, and C. E. Botez, "Ac susceptibility study of a magnetite magnetic fluid," *Journal of Applied Physics*, vol. 105, no. 7, 07B524, Apr. 2009. DOI: 10.1063/1.3072783.

[228] J. A. Mydosh, *Spin Glasses: An Experimental Introduction*. London: Taylor & Francis, 1993, ISBN: 978-0-7484-0038-6.

[229] S. H. Masunaga, R. F. Jardim, P. F. P. Fichtner, and J. Rivas, "Role of dipolar interactions in a system of Ni nanoparticles studied by magnetic susceptibility measurements," *Physical Review B*, vol. 80, no. 18, p. 184 428, 2009. DOI: 10.1103/PhysRevB.80.184428.

[230] J. A. Ramos-Guivar, F. J. Litterst, and E. C. Passamani, "AC susceptibility studies under DC fields in superspinglass nanomaghemite-multiwall carbon nanotube hybrid," *Magnetochemistry*, vol. 7, no. 4, p. 52, 2021. DOI: 10.3390/magnetochemistry7040052.

[231] M. Roy-Chowdhury, M. S. Seehra, and S. Thota, "Optimized analysis of the AC magnetic susceptibility data in several spin-glass systems using the Vogel–Fulcher and power laws," *AIP Advances*, vol. 13, no. 11, p. 115 020, 2023. DOI: 10.1063/5.0169800.

[232] B. Aslibeiki, P. Kameli, H. Salamati, M. Eshraghi, and T. Tahmasebi, "Superspin glass state in $MnFe_2O_4$ nanoparticles," *Journal of Magnetism and Magnetic Materials*, vol. 322, no. 19, pp. 2929–2934, 2010. DOI: 10.1016/j.jmmm.2010.05.007.

[233] S. Tiwari, G. Lal, H. Bhoi, K. Punia, S. S. Meena, and S. Kumar, "Coexistence of superparamagnetism and superspin glass in non-stoichiometric $Zn_{0.5}Ca_{0.5}Fe_2O_4$ nanoferrite," *Journal of Magnetism and Magnetic Materials*, vol. 570, p. 170 466, 2023. DOI: 10.1016/j.jmmm.2023.170466.

[234] K. Hiroi, K. Komatsu, and T. Sato, "Superspin glass originating from dipolar interaction with controlled interparticle distance among γ-Fe_2O_3 nanoparticles with silica shells," *Physical Review B*, vol. 83, no. 22, p. 224 423, 2011. DOI: 10.1103/PhysRevB.83.224423.

[235] K. Bai, J. Casara, A. Nair-Kanneganti, A. Wahl, F. Carle, and E. Brown, "Effective magnetic susceptibility of suspensions of ferromagnetic particles," *Journal of Applied Physics*, vol. 124, no. 12, p. 123 901, Sep. 2018. DOI: 10.1063/1.5041750.

[236] S. Ota and Y. Takemura, "Characterization of néel and brownian relaxations isolated from complex dynamics influenced by dipole interactions in magnetic nanoparticles," *The Journal of Physical Chemistry C*, vol. 123, no. 47, pp. 28 859–28 866, Nov. 2019. DOI: 10.1021/acs.jpcc.9b06790.

[237] L. Tu, T. Klein, W. Wang, Y. Feng, Y. Wang, and J.-P. Wang, "Measurement of brownian and néel relaxation of magnetic nanoparticles by a mixing-frequency method," *IEEE Transactions on Magnetics*, vol. 49, no. 1, pp. 227–230, Jan. 2013. DOI: 10.1109/TMAG.2012.2224853.

[238] W. T. Coffey and Y. P. Kalmykov, "Thermal fluctuations of magnetic nanoparticles: Fifty years after Brown," *Journal of Applied Physics*, vol. 112, no. 12, p. 121 301, 2012. DOI: 10.1063/1.4754272.

[239] R. Moreno, S. Jenkins, W. Williams, and R. F. L. Evans, "Atomistic calculation of the τ_0 inverse attempt frequency in Fe_3O_4 magnetite nanoparticles," *Physical Review B*, vol. 112, p. 024 429, 2025. DOI: 10.1103/vmwp-q427.

[240] R. B. Goldfarb, "Radio-frequency toroid susceptometry of magnetic nanoparticles: What goes around comes around," *IEEE Access*, vol. 14, pp. 22 335–22 355, Jan. 2026. DOI: 10.1109/ACCESS.2026.3637951.

[241] A. Rasmussen, A. Enfield, and A. Hesse, "Advances in the design and application of the radiofrequency permeameter," *Journal of Research of the National Bureau of Standards*, vol. 56, no. 5, pp. 261–268, May 1956.

[242] R. B. Goldfarb and H. E. Bussey, "Method for measuring complex permeability at radio frequencies," *Review of Scientific Instruments*, vol. 58, no. 4, pp. 624–627, Apr. 1987. DOI: 10.1063/1.1139227.

[243] A. Sihvola, *Electromagnetic Mixing Formulas and Applications*. Institution of Engineering and Technology, Jan. 1999, ISBN: 978-0-85296-772-0 978-1-84919-400-6. DOI: 10.1049/PBEW047E.

[244] J. L. Marqués-Fernández, M. Salvador, J. C. Martínez-García, P. Fernández-Miaja, A. García-Arribas, and M. Rivas, "New perspective on planar inductive sensors: Radio-frequency refractometry for highly sensitive quantification of magnetic nanoparticles," *Sensors*, vol. 23, no. 5, p. 2372, Feb. 2023. DOI: 10.3390/s23052372.

[245] N. Marconato, "Design of integrated micro-fluxgate magnetic sensors: Advantages and challenges of numerical analyses," *Sensors*, vol. 22, no. 3, p. 961, Jan. 2022. DOI: 10.3390/s22030961.

[246] J. Lenz, "A review of magnetic sensors," *Proceedings of the IEEE*, vol. 78, no. 6, pp. 973–989, Jun. 1990. DOI: 10.1109/5.56910.

[247] E. A. H. Ladino, N. Zufelato, A. F. Bakuzis, A. A. O. Carneiro, D. T. Covas, and O. Baffa, "Detection of magnetic nanoparticles with a large scale ac superconducting susceptometer," *Superconductor Science and Technology*, vol. 30, no. 8, p. 084 007, Aug. 2017. DOI: 10.1088/1361-6668/aa7666.

[248] R. Popović, "Hall-effect devices," *Sensors and Actuators*, vol. 17, no. 1-2, pp. 39–53, May 1989. DOI: 10.1016/0250-6874(89)80063-0.

[249] O. Florescu, M. Mattmann, and B. Boser, "Fully integrated detection of single magnetic beads in complementary metal-oxide-semiconductor," *Journal of Applied Physics*, vol. 103, no. 4, p. 046 101, Feb. 2008. DOI: 10.1063/1.2840062.

[250] L. K. Quynh, B. D. Tu, C. V. Anh, N. H. Duc, A. T. Phung, T. T. Dung, *et al.*, "Design optimization of an anisotropic magnetoresistance sensor for detection of magnetic nanoparticles," *Journal of Electronic Materials*, vol. 48, no. 2, pp. 997–1004, Feb. 2019. DOI: 10.1007/s11664-018-6822-4.

[251] L. Li, K. Y. Mak, C. W. Leung, S. M. Ng, Z. Q. Lei, and P. W. T. Pong, "Detection of 10-nm superparamagnetic iron oxide nanoparticles using exchange-biased gmr sensors in wheatstone bridge," *IEEE Transactions on Magnetics*, vol. 49, no. 7, pp. 4056–4059, Jul. 2013. DOI: 10.1109/TMAG.2013.2237889.

[252] M. Volmer, C. Musuroi, M. Oproiu, A. Avram, M. Avram, and E. Helerea, "On detection of magnetic nanoparticles using a commercial gmr sensor," in *2021 International Aegean Conference on Electrical Machines and Power Electronics (ACEMP) & 2021 International Conference on Optimization of Electrical and Electronic Equipment (OPTIM)*, Brasov, Romania: IEEE, Sep. 2021, pp. 1–6, ISBN: 978-1-6654-0298-9. DOI: 10.1109/OPTIM-ACEMP50812.2021.9590055.

[253] Z. Jin, T. M. Koo, M. S. Kim, M. Al-Mahdawi, M. Oogane, Y. Ando, *et al.*, "Highly-sensitive magnetic sensor for detecting magnetic nanoparticles based on magnetic tunnel junctions at a low static field," *AIP Advances*, vol. 11, no. 1, p. 015 046, Jan. 2021. DOI: 10.1063/9.0000189.

[254] F. A. Cardoso, J. Germano, R. Ferreira, S. Cardoso, V. C. Martins, P. P. Freitas, *et al.*, "Detection of 130nm magnetic particles by a portable electronic platform using spin valve and magnetic tunnel junction sensors," *Journal of Applied Physics*, vol. 103, no. 7, 07A310, Apr. 2008. DOI: 10.1063/1.2836713.

[255] K. Fodil, M. Denoual, C. Dolabdjian, A. Treizebre, and V. Senez, "Model calculation of the magnetic induction generated by magnetic nanoparticles flowing into a microfluidic system: Performance analysis of the detection," *IEEE Transactions on Magnetics*, vol. 50, no. 4, pp. 1–8, Apr. 2014. DOI: 10.1109/TMAG.2013.2291546.

[256] D. T. Huong Giang, D. X. Dang, N. X. Toan, N. V. Tuan, A. T. Phung, and N. H. Duc, "Distance magnetic nanoparticle detection using a magnetoelectric sensor for clinical interventions," *Review of Scientific Instruments*, vol. 88, no. 1, p. 015 004, Jan. 2017. DOI: 10.1063/1.4973729.

[257] C. Bai, H. Zhang, L. Zeng, X. Zhao, and L. Ma, "Inductive magnetic nanoparticle sensor based on microfluidic chip oil detection technology," *Micromachines*, vol. 11, no. 2, p. 183, Feb. 2020. DOI: 10.3390/mi11020183.

[258] Y.-X. Guo, C. Lai, Z.-B. Shao, K.-L. Xu, and T. Li, "Differential structure of inductive proximity sensor," *Sensors*, vol. 19, no. 9, p. 2210, May 2019. DOI: 10.3390/s19092210.

[259] S. Baglio, S. Castorina, and N. Savalli, "Integrated inductive sensors for the detection of magnetic microparticles," *IEEE Sensors Journal*, vol. 5, no. 3, pp. 372–384, Jun. 2005. DOI: 10.1109/JSEN.2004.839892.

[260] S. Krishnapriya, R. S. Komaragiri, and K. J. Suja, "Via-free single metal level planar microcoil sensors for detection of magnetic microbeads," *Journal of Magnetism and Magnetic Materials*, vol. 541, p. 168 469, Jan. 2022. DOI: 10.1016/j.jmmm.2021.168469.

[261] Y. Zhao, Y. Fang, J. Yang, W. Zhang, X. Ge, S. Cao, *et al.*, "An implementation method for an inductive proximity sensor with an attenuation coefficient of 1," *Energies*, vol. 13, no. 24, p. 6482, Dec. 2020. DOI: 10.3390/en13246482.

[262] M. Bartunik, H. Unterweger, C. Alexiou, R. Schober, M. Lübke, G. Fischer, *et al.*, "Comparative evaluation of a new sensor for superparamagnetic iron oxide nanoparticles in a molecular communication setting," preprint, Jan. 2021. DOI: 10.36227/techrxiv.13554401.v1.

[263] J. Makiranta, J. Verho, J. Lekkala, and N. Matintupa, "Novel measurement method for magnetic particles," in *2006 International Conference of the IEEE Engineering in Medicine and Biology Society*, New York, NY: IEEE, Aug. 2006, pp. 4598–4601, ISBN: 978-1-4244-0032-4. DOI: 10.1109/IEMBS.2006.259441.

[264] Y. Zheng, N. Shang, P. S. Haddad, and M. Sawan, "A microsystem for magnetic immunoassay based on planar microcoil array," *IEEE Transactions on Biomedical Circuits and Systems*, vol. 10, no. 2, pp. 477–486, Apr. 2016. DOI: 10.1109/TBCAS.2015.2434618.

[265] J. Richardson, A. Hill, R. Luxton, and P. Hawkins, "A novel measuring system for the determination of paramagnetic particle labels for use in magneto-immunoassays," *Biosensors and Bioelectronics*, vol. 16, no. 9, pp. 1127–1132, Dec. 2001. DOI: 10.1016/S0956-5663(01)00241-X.

[266] T. Yoshida, K. Ogawa, T. Tsubaki, N. B. Othman, and K. Enpuku, "Detection of magnetic nanoparticles using the second-harmonic signal," *IEEE Transactions on Magnetics*, vol. 47, no. 10, pp. 2863–2866, Oct. 2011. DOI: 10.1109/TMAG.2011.2157805.

[267] A. Moyano, E. Serrano-Pertierra, M. Salvador, J. C. Martínez-García, M. Rivas, and M. C. Blanco-López, "Magnetic lateral flow immunoassays," *Diagnostics*, vol. 10, no. 5, p. 288, May 2020. DOI: 10.3390/diagnostics10050288.

[268] S. Rzeszowski, G. A. Ferrier, T. Cabel, M. Nikolic-Jaric, D. Weber, S. F. Romanuik, *et al.*, "Inductive detection of 4.5 um superparamagnetic beads in a microfluidic device," in *2010 14th International Symposium on Antenna Technology and Applied Electromagnetics & the American Electromagnetics Conference*, Ottawa, ON, Canada: IEEE, Jul. 2010, pp. 1–4, ISBN: 978-1-4244-5049-7. DOI: 10.1109/ANTEM.2010.5552520.

[269] R. Dowling, R. Narkowicz, K. Lenz, A. Oelschlägel, J. Lindner, and M. Kostylev, "Resonance-based sensing of magnetic nanoparticles using microfluidic devices with ferromagnetic antidot nanostructures," *Nanomaterials (Basel, Switzerland)*, vol. 14, no. 1, p. 19, Dec. 2023. DOI: 10.3390/nano14010019.

[270] U. M. Engelmann, B. Simsek, A. Shalaby, and H.-J. Krause, "Key contributors to signal generation in frequency mixing magnetic detection (fmmd): An in silico study," *Sensors*, vol. 24, no. 6, p. 1945, Mar. 2024. DOI: 10.3390/s24061945.

[271] H.-J. Krause, N. Wolters, Y. Zhang, A. Offenhäusser, P. Miethe, M. H. Meyer, *et al.*, "Magnetic particle detection by frequency mixing for immunoassay applications," *Journal of Magnetism and Magnetic Materials*, vol. 311, no. 1, pp. 436–444, Apr. 2007. DOI: 10.1016/j.jmmm.2006.10.1164.

[272] P. I. Nikitin, P. M. Vetoshko, and T. I. Ksenevich, "New type of biosensor based on magnetic nanoparticle detection," *Journal of Magnetism and Magnetic Materials*, Proceedings of the Sixth International Conference on the Scientific and Clinical Applications of Magnetic Carriers, vol. 311, no. 1, pp. 445–449, Apr. 2007. DOI: 10.1016/j.jmmm.2006.10.1180.

[273] A. Rabehi, B. Garlan, S. Achtsnicht, H.-J. Krause, A. Offenhäusser, K. Ngo, *et al.*, "Magnetic detection structure for lab-on-chip applications based on the frequency mixing technique," *Sensors*, vol. 18, no. 6, p. 1747, Jun. 2018. DOI: 10.3390/s18061747.

[274] K. R. Minard, M. H. Littke, W. Wang, Y. Xiong, J. G. Teeguarden, and B. D. Thrall, "Magnetic particle detection (mpd) for in-vitro dosimetry," *Biosensors and Bioelectronics*, vol. 43, pp. 88–93, May 2013. DOI: 10.1016/j.bios.2012.12.011.

[275] A. Kuwahata, M. Kaneko, S. Chikaki, M. Kusakabe, and M. Sekino, "Development of device for quantifying magnetic nanoparticle tracers accumulating in sentinel lymph nodes," *AIP Advances*, vol. 8, no. 5, p. 056 713, May 2018. DOI: 10.1063/1.5006668.

[276] J. M. Barnett, P. Wraith, J. Kiely, R. Persad, K. Hurley, P. Hawkins, *et al.*, "An inexpensive, fast and sensitive quantitative lateral flow magneto-immunoassay for total prostate specific antigen," *Biosensors*, vol. 4, no. 3, pp. 204–220, Sep. 2014. DOI: 10.3390/bios4030204.

[277] B. N. Khlebtsov, R. S. Tumskiy, A. M. Burov, T. E. Pylaev, and N. G. Khlebtsov, "Quantifying the numbers of gold nanoparticles in the test zone of lateral flow immunoassay strips," *ACS Applied Nano Materials*, vol. 2, no. 8, pp. 5020–5028, 2019. DOI: 10.1021/acsanm.9b00956.

[278] S.-L. Li, H.-L. Lin, H.-F. Mi, Q.-Q. Meng, Y. Yan, X.-L. Zhang, *et al.*, "Evaluation of the diagnostic performance of an immunochromatographic test for *Chlamydia trachomatis*," *Practical Laboratory Medicine*, vol. 40, e00412, 2024. DOI: 10.1016/j.plabm.2024.e00412.

[279] R. H. Christenson, L. D. S. Frenk, H. J. de Graaf, T. S. Y. van Domburg, F. P. G. Wijnands, H. W. J. Foolen, *et al.*, "Point-of-care: Roadmap for analytical characterization and validation of a high-sensitivity cardiac troponin I assay in plasma and whole blood matrices," *The Journal of Applied Laboratory Medicine*, vol. 7, no. 4, pp. 971–988, 2022. DOI: 10.1093/jalm/jfac028.

[280] C. M. Florkowski, V. Buchan, B. V. Li, F. Taylor, M. Phan, M. Than, *et al.*, "Analytical verification of the Atellica VTLi point of care high sensitivity troponin I assay," *Clinical Chemistry and Laboratory Medicine*, vol. 63, no. 2, pp. 433–439, 2024. DOI: 10.1515/cclm-2024-0312.

[281] R. S. Gaster, D. A. Hall, C. H. Nielsen, S. J. Osterfeld, H. Yu, K. E. Mach, *et al.*, "Matrix-insensitive protein assays push the limits of biosensors in medicine," *Nature Medicine*, vol. 15, no. 11, pp. 1327–1332, 2009. DOI: 10.1038/nm.2032.

[282] D. Hall, R. Gaster, T. Lin, S. Osterfeld, S. Han, B. Murmann, *et al.*, "Gmr biosensor arrays: A system perspective," *Biosensors and Bioelectronics*, vol. 25, no. 9, pp. 2051–2057, May 2010. DOI: 10.1016/j.bios.2010.01.038.

[283] F. Ibraimi, D. Kriz, M. Lu, L.-O. Hansson, and K. Kriz, "Rapid one-step whole blood c–reactive protein magnetic permeability immunoassay with monoclonal antibody conjugated nanoparticles as superparamagnetic labels and enhanced sedimentation," *Analytical and Bioanalytical Chemistry*, vol. 384, no. 3, pp. 651–657, Feb. 2006. DOI: 10.1007/s00216-005-0094-6.

[284] D. M. Bruls, T. H. Evers, J. a. H. Kahlman, P. J. W. van Lankvelt, M. Ovsyanko, E. G. M. Pelssers, *et al.*, "Rapid integrated biosensor for multiplexed immunoassays based on actuated magnetic nanoparticles," *Lab on a Chip*, vol. 9, no. 24, pp. 3504–3510, Nov. 2009. DOI: 10.1039/B913960E.

[285] S. J. Osterfeld, H. Yu, R. S. Gaster, S. Caramuta, L. Xu, S.-J. Han, *et al.*, "Multiplex protein assays based on real-time magnetic nanotag sensing," *Proceedings of the National Academy of Sciences*, vol. 105, no. 52, pp. 20 637–20 640, 2008. DOI: 10.1073/pnas.0810822105.

[286] S. Workman, S. K. Wells, C.-P. Pau, S. M. Owen, X. F. Dong, R. LaBorde, *et al.*, "Rapid detection of HIV-1 p24 antigen using magnetic immunochromatography (MICT)," *Journal of Virological Methods*, vol. 160, no. 1–2, pp. 14–21, 2009. DOI: 10.1016/j.jviromet.2009.04.003.

[287] S. Handali, M. Klarman, A. N. Gaspard, X. F. Dong, R. LaBorde, J. Noh, *et al.*, "Development and evaluation of a magnetic immunochromatographic test to detect *Taenia solium*, which causes taeniasis and neurocysticercosis in humans," *Clinical and Vaccine Immunology*, vol. 17, no. 4, pp. 631–637, 2010. DOI: 10.1128/CVI.00511-09.

[288] M. H. Meyer, M. Hartmann, H.-J. Krause, G. Blankenstein, B. Mueller-Chorus, J. Oster, *et al.*, "Crp determination based on a novel magnetic biosensor," *Biosensors and Bioelectronics*, vol. 22, no. 6, pp. 973–979, Jan. 2007. DOI: 10.1016/j.bios.2006.04.001.

[289] S. Achtsnicht, C. Neuendorf, T. Faßbender, G. Nölke, A. Offenhäusser, H.-J. Krause, *et al.*, "Sensitive and rapid detection of cholera toxin subunit B using magnetic frequency mixing detection," *PLoS ONE*, vol. 14, no. 7, e0219356, 2019. DOI: 10.1371/journal.pone.0219356.

[290] J. Pietschmann, N. Voepel, L. Voß, S. Rasche, M. Schubert, M. Kleines, *et al.*, "Development of fast and portable frequency magnetic mixing-based serological SARS-CoV-2-specific antibody detection assay," *Frontiers in Microbiology*, vol. 12, p. 643 275, 2021. DOI: 10.3389/fmicb.2021.643275.

[291] W. Dittmer, P. De Kievit, M. Prins, J. Vissers, M. Mersch, and M. Martens, "Sensitive and rapid immunoassay for parathyroid hormone using magnetic particle labels and magnetic actuation," *Journal of Immunological Methods*, vol. 338, no. 1-2, pp. 40–46, Sep. 2008. DOI: 10.1016/j.jim.2008.07.001.

[292] V. Jarrige, J.-M. Broglio, A. Josselin, N. Bischoff, J. Schläpfer, and R. Beeler, "A new point-of-care iSTAT platform for the determination of intact parathyroid hormone," *Clinical Chemistry and Laboratory Medicine*, vol. 49, no. S1, S397, 2011, PTH measurement using Magnotech / Philips Minicare platform; concordance with reference assay.

[293] L. Motte, F. Benyettou, C. De Beaucorps, M. Lecouvey, I. Milesovic, and Y. Lalatonne, "Multimodal superparamagnetic nanoplatform for clinical applications: Immunoassays, imaging & therapy," *Faraday Discuss.*, vol. 149, pp. 211–225, 2011. DOI: 10.1039/C005286H.

[294] A. M. Skirda, A. V. Orlov, J. A. Malkerov, S. L. Znoyko, A. S. Rakitina, and P. I. Nikitin, "Enhanced analytical performance in CYFRA 21-1 detection using lateral flow assay with magnetic bioconjugates: Integration and comparison of magnetic and optical registration," *Biosensors*, vol. 14, no. 12, p. 607, 2024. DOI: 10.3390/bios14120607.

[295] A. V. Goncharenko, V. Z. Lozovski, and E. F. Venger, "Lichtenecker's equation: Applicability and limitations," *Optics Communications*, vol. 174, no. 1, pp. 19–32, Jan. 2000. DOI: 10.1016/S0030-4018(99)00695-1.

[296] N. Trifiro, "Development of an inductive sensor for superparamagnetic nanoparticles detection and quantification," M.S. thesis, UCLouvain, Jun. 2023.

[297] M. Azadmehr, I. Paprotny, and L. Marchetti, "100 years of colpitts oscillators: Ontology review of common oscillator circuit topologies," *IEEE Circuits and Systems Magazine*, vol. 20, no. 4, pp. 8–27, 2020. DOI: 10.1109/MCAS.2020.3027334.

[298] X. Lu, G. Tian, Z. Wang, W. Li, D. Yang, H. Li, *et al.*, "Research on the time drift stability of differential inductive displacement sensors with frequency output," *Sensors*, vol. 22, no. 16, p. 6234, Aug. 2022. DOI: 10.3390/s22166234.

[299] M. Bartunik, S. Faghih-Naini, T. Maiwald, and J. Kirchner, "Planar coils for detection of magnetic nanoparticles in a testbed for molecular communication," in *Proceedings of the 9th ACM International Conference on Nanoscale Computing and Communication*, ser. NANOCOM '22, New York, NY, USA: Association for Computing Machinery, Oct. 2022, pp. 1–6, ISBN: 978-1-4503-9867-1. DOI: 10.1145/3558583.3558844.

[300] C. Scherer and H.-G. Matuttis, "Rotational dynamics of magnetic particles in suspensions," *Physical Review E*, vol. 63, no. 1, p. 011 504, Dec. 2000. DOI: 10.1103/PhysRevE.63.011504.

[301] H. Gavilán, K. Simeonidis, E. Myrovali, E. Mazarío, O. Chubykalo-Fesenko, R. Chantrell, *et al.*, "How size, shape and assembly of magnetic nanoparticles give rise to different hyperthermia scenarios," *Nanoscale*, vol. 13, no. 37, pp. 15 631–15 646, Oct. 2021. DOI: 10.1039/D1NR03484G.

[302] E. Myrovali, N. Maniotis, A. Makridis, A. Terzopoulou, V. Ntomprougkidis, K. Simeonidis, *et al.*, "Arrangement at the nanoscale: Effect on magnetic particle hyperthermia," *Scientific Reports*, vol. 6, no. 1, p. 37 934, Nov. 2016. DOI: 10.1038/srep37934.

[303] B. Tian, Z. Qiu, J. Ma, T. Zardán Gómez de la Torre, C. Johansson, P. Svedlindh, *et al.*, "Attomolar zika virus oligonucleotide detection based on loop-mediated isothermal amplification and ac susceptometry," *Biosensors and Bioelectronics*, vol. 86, pp. 420–425, Dec. 2016. DOI: 10.1016/j.bios.2016.06.085.

[304] micromod Partikeltechnologie GmbH, *Nanomag-d*, https://micromod.de/en/shop/nanomag-d-09-00-252/.

[305] Z. Cui, W. Zhang, and H. Wang, "Magnetic permeability measurement method for particle materials," in *2018 IEEE International Instrumentation and Measurement Technology Conference (I2MTC)*, Houston, TX: IEEE, May 2018, pp. 1–6, ISBN: 978-1-5386-2222-3. DOI: 10.1109/I2MTC.2018.8409702.

[306] P. Ilg and M. Kröger, "Dynamics of interacting magnetic nanoparticles: Effective behavior from competition between brownian and néel relaxation," *Physical Chemistry Chemical Physics*, vol. 22, no. 39, pp. 22 244–22 259, 2020. DOI: 10.1039/D0CP04377J.

[307] B. Du, Q. Liu, Y. Shi, and Y. Zhao, "The effect of fe3o4 nanoparticle size on electrical properties of nanofluid impregnated paper and trapping analysis," *Molecules*, vol. 25, no. 16, p. 3566, Aug. 2020. DOI: 10.3390/molecules25163566.

[308] O. Dushek and S. V. Kuzmin, "The fields of a moving point charge: A new derivation from jefimenko's equations," *European Journal of Physics*, vol. 25, no. 3, p. 343, Mar. 2004. DOI: 10.1088/0143-0807/25/3/001.

[309] S. Klomp, C. Walker, M. Christiansen, B. Newbold, D. Griner, Y. Cai, *et al.*, "Size-dependent crystalline and magnetic properties of 5–100 nm fe $_3$ o $_4$ nanoparticles: Superparamagnetism, verwey transition, and feo–fe $_3$ o $_4$ core–shell formation," *IEEE Transactions on Magnetics*, vol. 56, no. 11, pp. 1–9, Nov. 2020. DOI: 10.1109/TMAG.2020.3018154.

[310] J. Wang, Q. Chen, X. Li, L. Shi, Z. Peng, and C. Zeng, "Disappearing of the verwey transition in magnetite nanoparticles synthesized under a magnetic field: Implications for the origin of charge ordering," *Chemical Physics Letters*, vol. 390, no. 1-3, pp. 55–58, May 2004. DOI: 10.1016/j.cplett.2004.04.005.

[311] Z. P. Chen, Y. Zhang, S. Zhang, J. G. Xia, J. W. Liu, K. Xu, *et al.*, "Preparation and characterization of water-soluble monodisperse magnetic iron oxide nanoparticles via surface double-exchange with dmsa," *Colloids and Surfaces A: Physicochemical and Engineering Aspects*, vol. 316, no. 1, pp. 210–216, Mar. 2008. DOI: 10.1016/j.colsurfa.2007.09.017.

[312] I. O. Perez De Berti, M. V. Cagnoli, G. Pecchi, J. L. Alessandrini, S. J. Stewart, J. F. Bengoa, *et al.*, "Alternative low-cost approach to the synthesis of magnetic iron oxide nanoparticles by thermal decomposition of organic precursors," *Nanotechnology*, vol. 24, no. 17, p. 175 601, Apr. 2013. DOI: 10.1088/0957-4484/24/17/175601.

[313] S. Liu, R. Eijkelenkamp, J. Duvigneau, and G. J. Vancso, "Silica-assisted nucleation of polymer foam cells with nanoscopic dimensions: Impact of particle size, line tension, and surface functionality," *ACS Applied Materials & Interfaces*, vol. 9, no. 43, pp. 37 929–37 940, Nov. 2017. DOI: 10.1021/acsami.7b11248.

[314] H.-X. Wu, T.-J. Wang, and Y. Jin, "Effects of -oh groups on fe3o4 particles on the heterogeneous coating in a hydrous alumina coating process," *Industrial & Engineering Chemistry Research*, vol. 46, no. 3, pp. 761–766, Jan. 2007. DOI: 10.1021/ie060987z.

[315] N. T. K. Thanh, N. Maclean, and S. Mahiddine, "Mechanisms of nucleation and growth of nanoparticles in solution," *Chemical Reviews*, vol. 114, no. 15, pp. 7610–7630, Aug. 2014. DOI: 10.1021/cr400544s.

[316] D. Green, S. Jayasundara, Y.-F. Lam, and M. Harris, "Chemical reaction kinetics leading to the first stober silica nanoparticles – nmr and saxs investigation," *Journal of Non-Crystalline Solids*, vol. 315, no. 1-2, pp. 166–179, Jan. 2003. DOI: 10.1016/S0022-3093(02)01577-6.

[317] Y. A. Barnakov, M. H. Yu, and Z. Rosenzweig, "Manipulation of the magnetic properties of magnetite-silica nanocomposite materials by controlled stober synthesis," *Langmuir*, vol. 21, no. 16, pp. 7524–7527, Aug. 2005. DOI: 10.1021/la0508893.

[318] Z. Sharafi, B. Bakhshi, J. Javidi, and S. Adrangi, "Synthesis of silica-coated iron oxide nanoparticles: Preventing aggregation without using additives or seed pretreatment," *Iranian Journal of Pharmaceutical Research : IJPR*, vol. 17, no. 1, pp. 386–395, 2018. [Online]. Available: https://www.ncbi.nlm.nih.gov/pmc/articles/PMC5937108/.

[319] F. Dang, N. Enomoto, J. Hojo, and K. Enpuku, "Sonochemical coating of magnetite nanoparticles with silica," *Ultrasonics Sonochemistry*, vol. 17, no. 1, pp. 193–199, Jan. 2010. DOI: 10.1016/j.ultsonch.2009.05.013.

[320] P. Qiu, K. Kang, K. Kim, W. Li, M. Cui, and J. Khim, "Facile synthesis of uniform yolk–shell structured magnetic mesoporous silica as an advanced photo-fenton-like catalyst for degrading rhodamine b," *RSC Advances*, vol. 5, no. 116, pp. 96 201–96 204, Nov. 2015. DOI: 10.1039/C5RA15693A.

[321] R. G. Digigow, J.-F. Dechézelles, H. Dietsch, I. Geissbühler, D. Vanhecke, C. Geers, *et al.*, "Preparation and characterization of functional silica hybrid magnetic nanoparticles," *Journal of Magnetism and Magnetic Materials*, vol. 362, pp. 72–79, Aug. 2014. DOI: 10.1016/j.jmmm.2014.03.026.

[322] I. Gabelica, L. Ćurković, V. Mandić, I. Panžić, D. Ljubas, and K. Zadro, "Rapid microwave-assisted synthesis of fe3o4/sio2/tio2 core-2-layer-shell nanocomposite for photocatalytic degradation of ciprofloxacin," *Catalysts*, vol. 11, no. 10, p. 1136, Sep. 2021. DOI: 10.3390/catal11101136.

[323] M. Kuzminska, N. Carlier, R. Backov, and E. M. Gaigneaux, "Magnetic nanoparticles: Improving chemical stability via silica coating and organic grafting with silanes for acidic media catalytic reactions," *Applied Catalysis A: General*, vol. 505, pp. 200–212, Sep. 2015. DOI: 10.1016/j.apcata.2015.08.005.

[324] Y. Lu, Y. Yin, B. T. Mayers, and Y. Xia, "Modifying the surface properties of superparamagnetic iron oxide nanoparticles through a sol-gel approach," *Nano Letters*, vol. 2, no. 3, pp. 183–186, Mar. 2002. DOI: 10.1021/nl015681q.

[325] M. Ma, Y. Zhang, H. Gong, F. Li, and N. Gu, "Silica-coated magnetite nanoparticles labeled by nimotuzumab, a humanised monoclonal antibody to epidermal growth factor receptor: Preparations, specific targeting and bioimaging," *Journal of Nanoscience and Nanotechnology*, vol. 13, no. 10, pp. 6541–6545, Oct. 2013. DOI: 10.1166/jnn.2013.6640.

[326] I. V. Zelepukin, V. O. Shipunova, A. B. Mirkasymov, P. I. Nikitin, M. P. Nikitin, and S. M. Deyev, "Synthesis and characterization of hybrid core-shell fe3o4/sio2 nanoparticles for biomedical applications," *Acta Naturae*, vol. 9, no. 4, pp. 58–65, 2017. [Online]. Available: https://www.ncbi.nlm.nih.gov/pmc/articles/PMC5762829/.

[327] K. Nejati and R. Zabihi, "Preparation and magnetic properties of nano size nickel ferrite particles using hydrothermal method," *Chemistry Central Journal*, vol. 6, no. 1, p. 23, Dec. 2012. DOI: 10.1186/1752-153X-6-23.

[328] K. Fabian, "Approach to saturation analysis of hysteresis measurements in rock magnetism and evidence for stress dominated magnetic anisotropy in young mid-ocean ridge basalt," *Physics of the Earth and Planetary Interiors*, vol. 154, no. 3-4, pp. 299–307, Mar. 2006. DOI: 10.1016/j.pepi.2005.06.016.

[329] S. Spassov and R. Egli, "Method for correcting remanent fields in magnetic property measurement systems without field compensation," in *COST Action TD1402 RADIOMAG Technical Note – WG2*, 2016.

[330] P. Singh, M. Shukla, and C. Upadhyay, "Signatures of consolidated superparamagnetic and spin-glass behavior in magnetite–silver core–shell nanoparticles," *Nanoscale*, vol. 10, no. 47, pp. 22 583–22 592, 2018. DOI: 10.1039/C8NR08401G.

[331] L. Z. Wu, J. Ding, C. P. Neo, L. F. Chen, and C. K. Ong, "Studies of high-frequency magnetic permeability of rod-shaped cro_2 nanoparticles," *physica status solidi (a)*, vol. 204, no. 3, pp. 755–762, Mar. 2007. DOI: 10.1002/pssa.200622015.

[332] M. Yamaguchi, Y. Miyazawa, K. Kaminishi, and K.-I. Arai, "A new 1 mhz-9 ghz thin-film permeameter using a side-open tem cell and a planar shielded-loop coil," *Transactions of the Magnetics Society of Japan*, vol. 3, no. 4, pp. 137–140, 2003. DOI: 10.3379/tmjpn2001.3.137.

[333] M. Yamaguchi, S. Yabukami, and K. Arai, "Development of multilayer planar flux sensing coil and its application to 1 mhz–3.5 ghz thin film permeance meter," *Sensors and Actuators A: Physical*, vol. 81, no. 1-3, pp. 212–215, Apr. 2000. DOI: 10.1016/S0924-4247(99)00124-7.

[334] S. G. Cho, J. Kim, I. Kim, K. H. Kim, and M. Yamaguchi, "Effect of measurement geometry on permeability extracted by a broadband method," *physica status solidi (a)*, vol. 204, no. 12, pp. 4133–4136, Dec. 2007. DOI: 10.1002/pssa.200777230.

[335] S. Tamaru, N. Kikuchi, T. Igarashi, S. Okamoto, H. Kubota, and S. Yoshida, "Broadband and high-sensitivity permeability measurements on a single magnetic particle by transformer coupled permeameter," *Journal of Magnetism and Magnetic Materials*, vol. 501, p. 166 434, May 2020. DOI: 10.1016/j.jmmm.2020.166434.

[336] V. K. Sakharov, R. A. Booth, and S. A. Majetich, "High-frequency permeability of ni and co particle assemblies," *Journal of Applied Physics*, vol. 115, no. 17, 17A517, May 2014. DOI: 10.1063/1.4866234.

[337] L. A. Currie, "Nomenclature in evaluation of analytical methods including detection and quantification capabilities (IUPAC recommendations 1995)," *Pure and Applied Chemistry*, vol. 67, no. 10, pp. 1699–1723, 1995. DOI: 10.1351/pac199567101699.

[338] N. Bidoul, "Potential of vanadium dioxide for artificial sensory neurons," Ph.D. dissertation, UCLouvain, Aug. 2024. [Online]. Available: http://hdl.handle.net/2078.1/293131.

[339] G. Grandi, M. Kazimierczuk, A. Massarini, and U. Reggiani, "Stray capacitances of single-layer solenoid air-core inductors," *IEEE Transactions on Industry Applications*, vol. 35, no. 5, pp. 1162–1168, Sept.-Oct./1999. DOI: 10.1109/28.793378.

[340] S. Mohan, M. del Mar Hershenson, S. Boyd, and T. Lee, "Simple accurate expressions for planar spiral inductances," *IEEE Journal of Solid-State Circuits*, vol. 34, no. 10, pp. 1419–1424, Oct. 1999. DOI: 10.1109/4.792620.

[341] H. Wheeler, "Simple inductance formulas for radio coils," *Proceedings of the IRE*, vol. 16, no. 10, pp. 1398–1400, Oct. 1928. DOI: 10.1109/JRPROC.1928.221309.

[342] *Calculation of the self-inductance of single-layer coils*. National Bureau of Standards, Aug. 1906. [Online]. Available: http://archive.org/details/calcul216118719063131unse.

[343] Y. Su, X. Liu, C. K. Lee, and S. Hui, "On the relationship of quality factor and hollow winding structure of coreless printed spiral winding (cpsw) inductor," *IEEE Transactions on Power Electronics*, vol. 27, no. 6, pp. 3050–3056, Jun. 2012. DOI: 10.1109/TPEL.2011.2174654.

[344] F. Tounsi, M. H. Said, M. Hauwaert, S. Kaziz, L. A. Francis, J.-P. Raskin, *et al.*, "Variation range of different inductor topologies with shields for rf and inductive sensing applications," *Sensors*, vol. 22, no. 9, p. 3514, Jan. 2022. DOI: 10.3390/s22093514.